



ALPEN-ADRIA
UNIVERSITÄT
KLAGENFURT



FIRST
INTERNATIONAL WORKSHOP
ON
NONLINEAR DYNAMICS AND
SYNCHRONIZATION

INDS '08

July 18-19, 2008
(Klagenfurt, Austria)

<http://indso8.uni-klu.ac.at>



We thank our sponsors



Bundesministerium für Wissenschaft und Forschung
<http://www.bmwf.gv.at/>



Kärntner Wirtschaftsförderungs Fonds
<http://www.kwf.at/>



Logicx Consulting & Workflow Integration GmbH
<http://www.logicx.at/>



Raiffeisen Landesbank Kärnten
<http://www.raiffeisen.at/>



Alpen-Adria-Universität Klagenfurt
<http://www.uni-klu.ac.at>



IEEE Austria Section
<http://ieee.ict.tuwien.ac.at/>



ASFiNAG
<http://www.asfinag.at/>



Kapsch TrafficCom
<http://www.kapsch.at/>



Österreichisches Rotes Kreuz Landesverband Kärnten
<http://www.k.rotekreuz.at/>



Applied Informatics Software Engineering GmbH
<http://www.appinf.com/>

Message from the Chair

In the name of the organization committee I welcome you to the First International Workshop on Nonlinear Dynamics and Synchronization (INDS'08) located at the Alpen-Adria University Klagenfurt in the beautiful small town Klagenfurt. INDS'08 brings together researchers, developers and practitioners from different horizons, with the main aim to establish a platform for discussing the latest advances and applications of nonlinear dynamics and synchronization. INDS'08 is an interdisciplinary workshop and will serve as a forum to present current and future works as well as to exchange research ideas pertaining to various aspects in this exciting and challenging field. With great pleasure I can inform you that we have received a substantial number of high-quality contributions and we thank all authors for their overwhelming response. The best papers were selected through a thorough review process and we have an acceptance rate of approximately 40%. In addition to the contributed papers, INDS'08 also features invited papers as well as poster and demo sessions.

We could win eleven international renowned experts to present exceptionally interesting insights and ideas in nonlinear dynamics and synchronization in keynotes and invited talks. We thank them for their availability and precious time: L.O. Chua, G.R. Chen, J. Kacprzyk, D. Helbing, J. Kurths, W. Mathis, D. Ruan, F. Rulkov, M.C. Mackey, M. Rosenblum and H.B. Hwarng.

We also thank all our reviewers for their efforts to ensure the high standard of this workshop's contributions. Additionally, our thanks are directed to both the local organization committee at the Alpen-Adria University Klagenfurt (especially the staff of the Institute for Smart System Technologies) and to the program and organization chairs for their distinguished work and their efforts to make this first edition of INDS'08 a great success. We do hope that all participants will enjoy two interesting and stimulating workshop days and the stay in our beautiful city Klagenfurt, which is the capital of the federal state of Carinthia in Austria. Carinthia - the southernmost state of Austria, sharing borders with Italy and Slovenia - is situated in a basin of the Alps and has the longest hours of sunshine in the region as well a large number of crystal clear alpine lakes.

We plan to organize this interdisciplinary workshop every year. Thus, this is also an invitation to join and actively participate in INDS'09. We further advertise the possibility to submit either an extended paper version or a fully new paper to one or more of the four INDS'08 post conference publications. The deadlines and guidelines will be posted on our website <http://inds08.uni-klu.ac.at> in the next days. After undergoing a thorough further review process, selected papers will be published either in one of two books (one with Springer and one with World Scientific Publisher) or in one of two special journal issues (one with "The Open Cybernetics and Systemics Journal" published by Bentham publishing and the second with the "International Journal of Computational Intelligence Systems" published by Atlantis Press).

Kyandoghene Kyamakya
General Chair, INDS'08

Organization Committee

General Chair

Kyandoghere Kyamakya, *University of Klagenfurt, Austria*

Program Co-Chairs

Guanrong Ron Chen, *City University of Hong Kong, Hong Kong*
Wolfgang A. Halang, *University of Hagen, Germany*
Da Ruan, *Belgian Nuclear Research Centre, Belgium*
Nikolai Rulkov, *University of California, San Diego, USA*

Organization Chairs

Abdelhamid Bouchachia, *University of Klagenfurt, Austria*
Jean Chamberlain Chedjou, *University of Klagenfurt, Austria*
Zhong Li, *University of Hagen, Germany*

Local Organization Committee

Koteswara Rao Anne, *University of Klagenfurt, Austria*
Claus Dabringer, *University of Klagenfurt, Austria*
Simone Fuchs, *University of Klagenfurt, Austria*
Annemarie Korenjak, *University of Klagenfurt, Austria*
Martin Salcher, *University of Klagenfurt, Austria*

Technical Program Committee

Dirk Aeyels, *University of Gent, Belgium*
Paolo Arena, *University of Catania, Italy*
Peter Ashwin, *University of Exeter, UK*
Gunther Auer, *DoCoMo Communications Laboratories Europe GmbH, Germany*
Antoine B. Bagula, *University of Cape Town, South Africa*
Abdellah Benzaouia, *University Cadi Ayyad, Morocco*
Christian Bettstetter, *University of Klagenfurt, Austria*
Christophe Bobda, *University of Potsdam, Germany*
József Bokor, *Budapest University of Technology and Economics, Hungary*
Abdelhamid Bouchachia, *University of Klagenfurt, Austria*
Leonid Bunimovich, *Georgia Institute of Technology, USA*
Giulio Casati, *University of Insubria, Italy*
Massimo Cencini, *Università degli Studi di Roma "La Sapienza", Italy*
Jean Chamberlain Chedjou, *University of Klagenfurt, Austria*
Guanrong Ron Chen, *City University of Hong Kong, Hong Kong*
D. Cheng, *University of Yaounde I, Cameroon*
Leon O. Chua, *University of California, Berkeley, USA*
Alberto Delgado, *National University of Colombia, Colombia*
Mingzhou Ding, *University of Florida, Florida, USA*
Mariagrazia Dotoli, *Politecnico di Bari, Italy*
Saber Elaydi, *Trinity University, Texas, USA*
Maria Pia Fanti, *Politecnico di Bari, Italy*
Luigi Fortuna, *University of Catania, Italy*

- Mattia Frasca, *University of Catania, Italy*
 Jason Gallas, *University of Stuttgart, Germany*
 José Esteban García, *Telefonica I+D, Intelligent Environment Services, Spain*
 Carlos Gershenson, *New England Complex Systems Institute, USA*
 Wolfgang A. Halang, *University of Hagen, Germany*
 Martin Hasler, *EPFL, Switzerland*
 Michael Hofbauer, *University of Graz, Austria*
 Yiguang Hong, *Chinese Academy of Sciences, China*
 Mario Huemer, *University of Klagenfurt, Austria*
 H. Brian Hwang, *National University of Singapore, Singapore*
 Felix Izrailev, *Universidad de Puebla, Mexico*
 Janusz Kacprzyk, *Polish Academy of Sciences, Poland*
 Tomasz Kapitaniak, *Technical University of Lodz, Poland*
 Ljupco Kocarev, *University of California, San Diego, USA*
 Timoleon C. Kofane, *University of Yaounde I, Cameroon*
 Krzysztof Kozłowski, *Poznan University of Technology, Poland*
 Jürgen Kurths, *University of Potsdam, Germany*
 Kyandoghere Kyamakya, *University of Klagenfurt, Austria*
 Henry Leung, *University of Calgary, Alberta, Canada*
 Frank Lewis, *University of Texas at Arlington, USA*
 Michael C. Mackey, *McGill University, Canada*
 Marko Marhl, *University of Maribor, Slovenia*
 Wolfgang Mathis, *University of Hannover, Germany*
 Peter V. E. McClintock, *Lancaster University, Lancaster, UK*
 José Fernando Mendes, *University of Aveiro, Portugal*
 Jose Tito Mendonca, *Instituto Superior Técnico, Portugal*
 Carlos H. Muravchik, *Universidad Nacional de La Plata, Argentina*
 V. Nguyen, *Hanoi University of Technology, Vietnam*
 G.V. Osipov, *Nizhny Novgorod University, Russia*
 Luca Patané, *University of Catania, Italy*
 Lou Pecora, *Naval Research Laboratory, USA*
 Jürgen Pilz, *University of Klagenfurt, Austria*
 Kęstutis Pyragas, *Semiconductor Physics Institute, Italy*
 Marko Robnik, *University of Maribor, Slovenia*
 Valery Romanovski, *University of Maribor, Slovenia*
 Da Ruan, *Belgian Nuclear Research Centre, Belgium*
 Nikolai Rulkov, *University of California, San Diego, USA*
 V.D. Shalfeev, *Nizhny Novgorod University, Russia*
 Patrick Siarry, *University of Paris, Paris*
 Ruedi Stoop, *Swiss Federal Institute of Technology Zurich, Switzerland*
 Johan Suykens, *Katholieke Universiteit Leuven, Belgium*
 Kazuo Takatsuka, *University of Tokyo, Japan*
 Mbusa Claude Takenga, *University of Hannover, Germany*
 Wallace Kit-Sang Tang, *City University of Hong Kong, Hong Kong*
 Ken Umeno, *National Taiwan University of Science and Technology, Taiwan*
 Guido Vagliasindi, *University of Catania, Italy*
 Mihail Voicu, *Technical University of Iasi, Romania*
 P. Wofo, *University of Yaounde I, Cameroon*
 Chai Wah Wu, *BM T.J. Watson Research Center, USA*

Keynotes

We could win international experts from various fields of non-linear dynamics and synchronization to fascinate us with their exciting keynote speeches and invited talks. The speaker's biographies and a short abstract of their planned talks are presented on the next pages.



Prof. Leon O. Chua, University of California, Berkeley, USA

Leon O. Chua received the MSEE from Massachusetts Institute of Technology in 1961, and the Ph.D. from University of Illinois, Urban-Champaign in 1964. After that he was Assistant and Associate Professor at Purdue University until 1970. He became a Professor of Electrical Engineering and Computer Sciences at University of California at Berkeley since 1971.

Dr. Chua is known internationally as a pioneer in 3 major research areas, namely, neural networks, chaos and nonlinear circuits. His work in these areas has been recognized internationally through numerous major awards, including 11 honorary doctorates from major universities in Europe and Japan, and 7 USA patents. He was elected Fellow of IEEE in 1974, a foreign member of the European Academy of Sciences (Academia Europea) in 1997, and a foreign member of the Hungarian Academy of Sciences in 2007. He was honored with many major IEEE prizes, including the IEEE Browder J. Thompson Memorial Prize

Award in 1972, the IEEE W. R. G. Baker Prize Award in 1978, the Frederick Emmons Award in 1974, twice winner of the IEEE M.E. Van Valkenburg Award (1995 and 1998). He is also a Recipient of the top 15 most cited authors Award in 2002 from all fields of engineering published during the 10-year period from the Current Contents (ISI) database, the IEEE Neural Networks Pioneer Award in 2000, the IEEE Gustav Kirchhoff Award in 2005, and the IEEE Vitold Belevitch Award in 2007. Throughout his career, Dr. Chua has authored around 500 papers and 8 books. He is widely recognized as the father of nonlinear circuit theory and cellular neural networks (CNN). Dr. Chua also invented a five-element electronic circuit for generating chaotic signals. Known internationally as the Chua Circuit, it is used by many researchers to design secure communication systems based on chaos and has become a standard paradigm for teaching chaos in textbooks on nonlinear dynamics.

Keynote: A nonlinear dynamics perspective of Wolfram's new kind of science

Wolfram's monumental best seller entitled "A new kind of science" was based almost entirely on brute-force computer simulations. In sharp contrast, this 2-hour lecture presents a rigorous *analytical* theory based on *attractors* from a nonlinear dynamics perspective.

New results and concepts to be presented include the partitioning (via Felix Klein's Vierergruppe) of all 256 local Boolean rules studied empirically by Wolfram into 88 global equivalence classes, one of which contains 4 topologically-conjugate rules capable of universal computation, and endowed with a $1/f$ spectrum. Another major result is the rigorous characterization of the time-asymptotic dynamics (attractors) of 112 local rules via an explicit generalized *Bernoulli shift formula*.

Even more surprising, we have discovered the attractors of 170 local rules are blessed with the remarkable property of *time-reversality*. For such rules, the *past* evolution in time can be recovered from the *future* evolutions of a corresponding "twin" rule. Only 86 local rules exhibit an "arrow of time".

One of our most fascinating discoveries is a new phenomenon, dubbed an "*isle of Eden*," having no counter part in hyperbolic differential equations, which has neither a past, nor a future!

In addition to providing a mathematical foundation for brainlike dynamics, the discoveries cited above provide a simple dynamical mechanism for mimicking many exotic phenomena from brain science, relativity, quantum physics, cosmology, etc.



Prof. Guanrong Ron Chen, City University of Hong Kong, Hong Kong

Guanrong Chen received the M.Sc. Degree in Computer Science from the Sun Yat-sen, China and the Ph.D. Degree in Applied Mathematics from Texas A&M University, USA. He is an IEEE Fellow (1996) and currently is a Chair Professor and the Founding Director of the *Centre for Chaos and Complex Networks* at the City University of Hong Kong.

Prof. Chen served and is serving as Chief Editor, Deputy Chief Editor, Advisory Editor and Associate Editor for several international journals including the IEEE Circuits and Systems Magazine, IEEE Transactions on Circuits and Systems (I and II), IEEE Transactions on Automatic Control and the International Journal of Bifurcation and Chaos. He received the 1998 Harden-Simons Prize for the Outstanding Journal Paper Award from the American Society of Engineering Education, the 2001 M. Barry Carlton Best Annual Transactions Paper Award from the IEEE Aerospace and Electronic Systems

Society, the 2002 Best Paper Award from the Institute of Information Theory and Automation, Academy of Science of the Czech Republic and the 2005 IEEE Guillemin-Cauer Best Transaction Annual Paper Award from the Circuits and Systems Society. He is an honorary professor at different ranks in more than twenty universities in Argentina, Australia, China and USA.

Keynote: On the Synchronizability of Complex Dynamical Networks

Some concerned issues on synchronization and synchronizability of complex networks are addressed, regarding synchronized regions, synchronization conditions and the relationships between the topology and the synchronizability. The presentation will first be motivated by showing two simple examples of regular symmetrical graphs, which have identical structural parameters (average distance, degree distribution and node betweenness centrality) but have very different synchronizabilities. These simple examples demonstrate the intrinsic complexity of the network synchronizability problem. I will then show that for a complex network with identical node dynamics in any topology, two key factors influencing the network synchronizability are the structure of the network inner-linking matrix and the eigenvalues of the network outer-linking matrix. Some more examples will then be provided to show that an addition of new edges to a network can either increase or decrease the network synchronizability, depending on the underlying network topology and where the edges are added. Therefore, to search for some conditions under which the network synchronizability may be increased through adding edges, research found that graph theory is very helpful. It will be demonstrated that for networks with disconnected complementary graphs, adding edges never decreases their synchronizabilities. This implies that better understanding and careful manipulation of the complementary graphs are important and useful for enhancing the network synchronizability. Moreover, it will be shown that an unbounded synchronized region is always easier to analyze than a bounded synchronized region for any complex network. Consequently, to effectively enhance the network synchronizability for the case where the synchronous state is an equilibrium point of the network, a new design method will be presented for determining a rank-1 inner-linking matrix, which means only one state variable is used for coupling therefore very cost-effective, such that the resulting network has an unbounded synchronized region. Throughout this presentation, both theoretical analysis and computer simulations will be presented with comparisons, revealing the essence of graph theory for studying complex network synchronization.

Prof. Chen has been nominated lately for the "2008 National Natural Science Award of China". As the date of final interview coincides with the workshop, he will not be able to attend and give his interesting talk. We wish Professor Chen all the best for the competition and strongly hope that he is going to win the award.

**Prof. Dirk Helbing, Swiss Federal Institute of Technology Zürich (ETH Zürich)**

Since June 1st 2007, Dirk Helbing (born on January 19, 1965) is Professor of Sociology, in particular of Modeling and Simulation at ETH Zurich. Before, he worked as Managing Director of the Institute for Transport & Economics at Dresden University of Technology, where he was appointed full professor in 2000. Having studied Physics and Mathematics in Göttingen, his master thesis dealt with the nonlinear modeling and multi-agent simulation of observed self-organization phenomena in pedestrian crowds. Two years later, he finished his Ph.D. at Stuttgart University on modeling social interaction processes by means of game-theoretical approaches, stochastic methods and complex systems theory, which was awarded two research prizes.

After having completed his habilitation on traffic dynamics and optimization in 1996, he received a Heisenberg scholarship. Both theses were printed by international publishers. Apart from this, Helbing has (co-)organized several international conferences and (co-)edited proceedings or special issues on material flows in networks and cooperative dynamics in socio-economic and traffic systems. He has given 250 talks and published more than 200 papers, including several contributions to journals like Nature, Science or PNAS, which were discussed by the public media (newspapers, radio and TV) more than 200 times. He collaborates closely with international scientists. For example, he worked at the Weizmann Institute in Israel, at Xerox PARC in Silicon Valley, at INRETS in Paris and the Collegium Budapest - Institute for Advanced Study in Hungary, where he is now a member of the external faculty.

Keynote: From emergent crowd behavior to self-organized traffic light control

Crowds and traffic flows have been successfully modeled as driven many-particle systems. Due to the non-linear interactions and delayed adaptations in these systems, one finds a rich spectrum of self-organization phenomena. This includes, for example, various forms of traffic jams, noise-induced breakdowns, freezing-by-heating and slower-is-faster effects, self-organized oscillations, and spontaneous synchronization phenomena. We also discuss instabilities in the motion of dense crowds and the occurrence of turbulence-like phenomena that have been discovered by high-performance video analysis techniques.

Non-linear interactions do not automatically lead to a system optimum. The system may be rather trapped in a local optimum or behave in an unstable way. Therefore, one interesting question is how to modify many-particle interactions in order to avoid this. Future traffic assistance systems will, for example, be able to increase the stability and capacity of traffic flows. Moreover, self-organized traffic light and production scheduling based on decentralized control approaches will allow for better adaptation to variations in capacities and demands. This will lead to a higher quality and performance of traffic and production systems in the future.



Prof. Jürgen Kurths, Potsdam University, Germany

Keynote: Synchronization in Oscillatory Networks

The formation of collective behaviour in large ensembles or networks of coupled oscillatory elements is one of the most fundamental aspects of dynamical systems theory. Applications range from physics and chemistry via neuroscience to engineering and social sciences. Here some basic properties, potentials but also open problems will be discussed.

Recent research has revealed a rich and complicated network topology in the cortical connectivity of mammalian brains. A challenging task is to understand the implications of such network structures on the functional organization of the brain activities. This is studied here basing on dynamical complex networks. We investigate synchronization dynamics on the cortico-cortical network of the cat by modelling each node (cortical area) of the network with a sub-network of interacting excitable neurons. We find that the network displays clustered synchronization behaviour and the dynamical clusters coincide with the topological community structures observed in the anatomical network. Our results provide insights into the relationship between the global organization and the functional specialization of the brain cortex.

This approach of a network of networks seems to be of general importance, especially for spreading of diseases or opinion formation in human societies or socio-economic dynamics.

References:

- Osipov, G.V., J. Kurths, and C. Zhou, Synchronization in Oscillatory Networks, Springer Complexity, Berlin 2007.
- Motter, A., C. Zhou, and J. Kurths, Europhys. Lett. 2005, 69, 334.
- Motter, A., C. Zhou, and J. Kurths, Phys. Rev. E 2005, 71, 016116.
- Zhou, C., A. Motter, and J. Kurths, Phys. Rev. Lett. 2006, 96, 034101.
- Zhou, C., L. Zemanova, G. Zamora, C. Hilgetag, and J. Kurths, Phys. Rev. Lett. 2006, 97, 238103.

**Prof. Da Ruan, Belgian Nuclear Research Centre, Belgium**

Da Ruan (PhD in Math, Ghent U, Belgium 1990) is a scientific staff member at the Belgian Nuclear Research Centre (SCK•CEN). He was a Post-Doctoral Researcher from 1991-93 and since 1994 has been a senior researcher and FLINS Project Leader at SCK•CEN. He is the principal investigator for the research project on intelligent control for nuclear reactors, cost-estimation for large nuclear projects under uncertainty, and computerized decision making systems for society and policy support at SCK•CEN. He was a guest research scientist at the OECD Halden Reactor Project (HRP), Norway from April 2001 to September 2002 as a principal investigator for the research project on computational intelligent systems for feedwater flow measurements at HRP. His major research interests lie in the areas of mathematical modelling, computational intelligence methods, uncertainty analysis and information/sensor fusion, decision support systems to information management, cost/benefit analysis, and safety and security

related fields.

Dr. Ruan currently serves as Scientific advisor at the National Institute for Nuclear Research of Mexico for the project "Adaptive fuzzy control and its applications in nuclear systems" (Mexico), Regional editor for Europe of *Int. J. of Intelligent Automation and Soft Computing* (TSI Press, Albuquerque, NM), co-editor-in-chief of *Int. J. of Nuclear Knowledge Management* (Interscience Publishers, Geneva), editor-in-chief of *Int. J. of Computational Intelligence Systems* (Atlantis Press, Paris), Editor of the book series of *Intelligent Information Systems* and the proceedings series of *Computer Engineering and Information Science*, Part time Professor at the Dept. of Applied Math. and CS in Ghent University and Adjunct Professor in the Faculty of Information Technology at University of Technology, Sydney, Australia.

Keynote: The role of computational intelligence in complex decision systems

In recent years there has been a growing interest in the need for designing intelligent systems to address complex engineering problems. One of the most challenging issues for the intelligent system is to effectively handle real-world uncertainties that cannot be eliminated. These uncertainties include sensor imprecision, instrumentation and process noise and disturbances, unpredictable environmental factors, to name a few. These uncertainties result in a lack of the full and precise knowledge of the system including its state, dynamics, and interaction with the environment. Computational intelligent techniques including fuzzy logic, neural networks, and genetic algorithms etc., as complimentary to the existing traditional techniques, have shown great potential to solve these demanding, real-world problems that exist in uncertain and unpredictable environments. These technologies have formed the foundation for intelligent systems. An overview on computational intelligence in control and decision making for complex systems will be given over the last four decades. Some real-world cases on power plant operation, information-driven safeguards, cost estimation under uncertainty for a large engineering project, and decision support for long-term options of energy policy will be illustrated for the potential use of computational intelligence related techniques in complex systems. Essential steps on implementing computational intelligence related techniques in industry will be presented via R&D, demonstration, and commercialization. Challenges and future research directions will be concluded in this talk.



Prof. Janusz Kacprzyk, Polish Academy of Sciences, Poland Janusz Kacprzyk is Professor of Computer Science at the Systems Research Institute, Polish Academy of Sciences, and Honorary Professor at the Department of Mathematics, Yli Normal University, Shanxi, China. He has been a visiting professor at many universities in the USA, England, Italy, UK and Mexico. He is an Academician (Member) of the Polish Academy of Sciences and Foreign Member of the Spanish Royal Academy of Economic and Financial Sciences.

His research interests include intelligent systems, soft computing, fuzzy logic, decision making, decision analysis and decision support, database querying, information retrieval, data analysis, data mining, etc.

He is president of the IFSA (International Fuzzy Systems Association) and president of the Polish Society for Operational and Systems Research. He is fellow of IEEE and IFSA. He received the 2005 IEEE CIS Fuzzy Pioneer Award for pioneering works on multistage fuzzy control, notable fuzzy dynamic

programming and the Sixth Kaufmann Prize and Gold Medal for pioneering works on the use of fuzzy logic in economy and management.

His publication record is: 5 books, 30 volumes, 300 papers. He is Editor in chief of 3 Springer's book series and a co-editor of one Springer book series, is on the editorial boards of approx. 30 journals and a member of the IPC at more than 200 conferences.

Keynote: Towards a more efficient complex problem solving using human centric type computing paradigms

We start with a brief account of complex decision making problems, and advocate the use of modern approaches to real world decision making emphasizing the concept of a decision making process that involves more factors and aspects like: the use of explicit and tacit knowledge, intuition, emotions, individual habitual domains, non-trivial rationality, different paradigms, etc. We stress the need for computer based decision support systems that should exhibit some "intelligence" which is meant in an individual and collective perspective, and give an overview of main types of decision support systems. We present some new so-called computing paradigms that try to attain a synergy, and bridge the gap between the human user and computer systems that is mainly caused by the fact that natural language is the only fully natural means of communication and articulation for a human being but it "strange" to the computer. We advocate the so-called: human centric computing, human centered computing, human computing, etc. that can help bridge this gap.

We also point some relations of the proposed approach to the analysis and explanation of decision making and decision processes, both of a decision analytic and game type, with elements of approaches to decision making based on neuroeconomics.

Then, we present Zadeh's paradigm of computing with words (and perceptions) as a tool that may help bring computing closer to the human being by an explicit use of (quasi)natural language in many phases of computing, problem solving, etc. We indicate relations between the computing with words and human centric computing paradigms, and indicate - first - that the former can be viewed as an attempt at providing proper tools to implement the latter, and that both can play a crucial role in intelligent decision support systems.

We show some implementations of using linguistic data summaries in a business context and show that they can be viewed as extremely human consistent data mining tools, notably for novice users.



Prof. Dr.-Ing. Wolfgang Mathis, *Leibniz University of Hannover, Germany*

Wolfgang Mathis was born in Celle (Germany) on May 13, 1950. He received the Dipl.-Phys. degree in 1980 and the Dr.-Ing. degree, (Ph.D.) in electrical engineering in 1984 (TU Braunschweig) and was granted with the Habilitation Degree. He became a full professor at the Universities of Wuppertal (1990) and Magdeburg (1996). In 2000 he became a full professor at the Leibniz University Hannover and holds the chair of Theoretical Electrical Engineering (TET). His research interests include theory of nonlinear circuits and dynamical systems (incl. noise), RF CMOS circuit analysis and design, parallel computation, nanoelectronics, quantum computing, analysis and numerics of electromagnetic fields. He is chair of the IEEE Circuits and Systems Society German chapter since 2001 and became an IEEE senior member since 1998, received the IEEE Fellow award in 1999 and became He is a member of IEEE, VDE/ITG, DPG (German Physical Society). Furthermore he is member of the Nordrhein-Westfälische Academy of

Science since 2001 and received the VDE/ITG Award.

Keynote: Oscillatory Circuits and Synchronization in RF Circuit Design



Prof. Michael C. Mackey, *McGill University, Montreal, Quebec, Canada*

Prof. Mackey has an undergraduate degree in Mathematics and made his doctorate in Physiology and Biophysics in Washington. Currently he is a Joseph Morley Drake professor of Physiology and the director of the Centre for Nonlinear Dynamics in Physiology and Medicine at McGill University in Montreal, Canada. Before going to McGill University in 1971, Prof. Mackey did research at the National Institutes of Health (NIH). His current research involves dynamical systems theory applied to physiological systems including the regulation of cell proliferation and differentiation as well as gene regulatory networks. Additionally, Prof. Mackey works on problems related to the origins of microscopic irreversibility and foundational issues in non-equilibrium statistical mechanics.

Keynote: Using mathematical modeling to understand and treat periodic hematological disease

There are a range of fascinating periodic hematological diseases in humans. These are characterized by oscillations in the numbers of one or more blood cell types (white blood cells, red blood cells, or platelets) with periods ranging from days to months. Extensive mathematical modeling efforts over the past 30 years have yielded progressively more detailed models for the regulation of blood cell production that now allow us, in some instances, to pinpoint the location of the dynamic defects that lead to these periodic hematological diseases. All of the defects that have been identified have been associated, in one way or another, with derangements of cellular death mechanisms (apoptosis) and have given rise to supercritical Hopf bifurcations. In this talk I will discuss three of these: cyclical neutropenia, periodic leukemia, and cyclical thrombocytopenia. In the case of cyclical neutropenia the mathematical modeling has actually offered insight into how the clinical symptoms can be brought under control (though not eliminated).



Dr. Nikolai Rulkov, *University of California, San Diego, USA*

Nikolai F. Rulkov received the M.S. and Ph.D. degrees, both in physics and mathematics, from the University of Nizhny Novgorod, Nizhny Novgorod, Russia, in 1983 and 1991, respectively. In 1983, he joined the Radio Physics Department of the University of Nizhny Novgorod, where he worked as a Researcher until 1993. He has been with the Institute for Nonlinear Science, University of California, San Diego, from 1993 through the present. His research interests are in the areas of bifurcation theory, nonlinear phenomena, theory of synchronization, chaos and applications of nonlinear dynamics in science and engineering. Starting form 2004 he is with the Information Systems Labs, San Diego, where he works on a wide spectrum of nonlinear problems in the areas of signal processing, biologically inspired control systems, biomimetic robotics and modeling of neurobiological networks.

Keynote: Modeling of oscillations and synchronization phenomena in large-scale neuronal networks

Intrinsic neuronal and synaptic properties control the responses of networks of thousands of neurons by creating spatio-temporal patterns of activities, which are used for muscle control, sensory processing, memory formation and other cognitive tasks. The modeling of such systems requires single neuron models capable of displaying both realistic response properties and computational efficiency.

We use difference equations (map-based models) to simulate the individual dynamics of neurons and synapses. Such phenomenological models can be designed to capture the main intrinsic dynamical properties of specific type of neurons. This approach allows fast simulation and efficient parametric analysis of networks containing hundreds of thousands of neurons of different cell types using a conventional workstation.

This paper presents results of the modeling of spatio-temporal behavior of large-scale models of a cortical network, formation and synchronization of fast oscillations and restructuring of synchronization patterns as a function of parameters of synaptic interconnections and the intrinsic states of the neurons. The paper also discusses the application of map-based models in the design of a real-time CPG network model that controls undulatory locomotion of a biomimetic lamprey-based robot.



Dr. Michael Rosenblum, *Potsdam University, Germany*

Michael Rosenblum has been a research associate in the Department of Physics, University of Potsdam, since 1997. His main research interests are synchronization theory, time series analysis, and application of nonlinear dynamics to biological systems. He was a Humboldt fellow in the Max-Planck research group on nonlinear dynamics at Potsdam University, and a visiting scientist at Boston University. Michael Rosenblum studied physics at Moscow Pedagogical University, and went on to work in the Mechanical Engineering Research Institute of the USSR Academy of Sciences, where he was awarded a PhD in physics and mathematics. He received his habilitation degree in theoretical physics from Potsdam University.

Keynote: Self-organized quasiperiodic dynamics in ensembles of nonlinearly coupled oscillators

We briefly discuss synchronization and appearance of collective motion in large ensembles of all-to-all coupled oscillators. We illustrate the effect by several real world examples and present a theoretical description in the framework of the Kuramoto model. Next, we present recent results on collective dynamics of populations of nonlinearly coupled oscillators and discuss a corresponding generalization of the Kuramoto model. In particular, we demonstrate a transition from fully synchronous periodic oscillations to partially synchronous quasiperiodic dynamics in ensembles of identical oscillators with coupling that nonlinearly depends on the generalized order parameters. We present an analytically solvable model that predicts a regime where the mean field does not entrain individual oscillators, but has a frequency incommensurate to theirs. The self-organized onset of quasiperiodicity is illustrated with Landau-Stuart oscillators, Josephson junction array with a nonlinear coupling, and ensembles of chaotic Roessler oscillators.

Invited Talk



H. Brian Hwang, PhD, *National University of Singapore, Singapore*

H. Brian Hwang is an Associate Professor at the Department of Decision Sciences and a former Academic Director of Asia-Pacific Executive (APEX) MBA Program, School of Business, National University of Singapore. He received his Ph.D. in Industrial and Management Systems Engineering from Arizona State University, USA. Prior to joining National University of Singapore, he worked as an Industrial Engineer for Delta Electronics in Taiwan and as a Material System Analyst for Allied-Signal Aerospace in Phoenix, Arizona, USA. His current research interests focus on applying computational algorithms and techniques such as chaos analysis, neural networks and simulation modeling to investigate system dynamics and quality issues in the context of process control and supply chain management. His pioneer works in pattern recognition on statistical process control charts have been widely cited. He was a recipient of the 2000 Commonwealth Fellowship Award in the UK and has been involved in a global supply chain modeling effort for Glaxo Wellcome and a large-scale innovative technology research project for the specialty chemical industry. Brian is a member of the Decision Science Institute (USA), a senior member of the American Society for Quality (ASQ), of the ASQ Six Sigma Forum and a life-time member of Alpha Pi Mu (American Industrial Engineering Honor Society).

Decisions and chaos in a complex supply chain

A supply chain involves multiple entities encompassing activities of moving goods and adding value from the raw material state to the final delivery stage. Along the chain, there exist various types of uncertainties, e.g. demand uncertainty, production uncertainty and delivery uncertainty. Making decisions as to how much and when to replenish, often involves a feedback process triggering interaction between system entities, which may result in system nonlinearity. A time delay is observed when there is a lag between when a decision is made and when its effect is felt, which often further complicates the interaction between entities. Feedback, time delay and interaction are inherent to many processes in a supply chain. Feedback, time delay and interaction induce variability, instability and complex behaviors that make supply chain management awfully challenging.

In this talk, I would like to discuss, under various supply chain factors, how decisions concerning inventory replenishment contribute to the complex dynamics and chaotic behaviors. We are interested in a general class of multi-level supply chains that can be represented by the well-known beer distribution model. Various supply chain factors are considered, such as demand pattern, ordering policy, demand-information sharing and lead time, with different options or levels. Simulation models are developed to observe system dynamics, particularly the inventory across all levels of the supply chain. Using the Lyapunov exponent, we quantify the degree of system chaos in terms of inventory across all supply chain levels.

The primary purpose of this talk is to share our findings, from a chaos perspective, on (1) how inventory replenishment decisions may impact a complex supply-chain system; (2) how various supply-chain factors act or interact to affect the system dynamics which in many cases lead to chaos; and (3) some managerial insights into more effective management of supply chains.

Content

Day One

Poster Session 1 - Application of Nonlinear Dynamics and Synchronization (NDS)

Performing Compression and Encryption Simultaneously using Chaotic Map	19
<i>Kwok-Wo Wong, Ching-Hung Yuen</i>	
Neural Networks for Approximating the Cost and Production Functions	24
<i>Efthymios G. Tsionas, Panayotis G. Michaelides, Angelos T. Vouldis</i>	
Implementation of One Dimensional CNN array on FPGA, Based-on Verilog HDL	31
<i>Alireza Fasih, Jean Chedjou, Kyandoghere Kyamakya</i>	
Clustering In VANETs	35
<i>Sadaf Momeni, Mahmood Fathy</i>	
Performance Comparison of Band-limited Baseband Synchronous CDMA Using between Walsh-Hadamard Sequence and ICA Sequence	40
<i>Ryo Takahashi, Ken Umeno</i>	
Evaluation of nonlinear system behaviors in Military Supply chain	45
<i>S.K. Bhagavatula, J.C. Chedjou, K.R. Anne, K. Kyamakya</i>	
A Periodical Time-Variable Effect in OFDM Systems with Aliasing and a Sampling Frequency Offset	52
<i>Ilias Trachanas, Norbert J. Fliege</i>	
Anticipation and Delocalization in Cellular Models of Pedestrian Traffic	61
<i>Alexander Makarenko, Dmitry Krushinsky, Boris Goldengorin</i>	
Modeling of a Three-echelon Supply Chain: Stability analysis and synchronization issues	65
<i>K.R. Anne, J.C. Chedjou, S.K. Bhagavatula, K. Kyamakya</i>	
A Stable Path Selection Algorithm for Protecting Optical Networks using OBGp Backup Routing	72
<i>Wen-Fong Wang, Lih-Chyau Wu</i>	
Component-based Face Detection in Colour Images	79
<i>Jamal Ahmad Dargham, Ali Chekima</i>	

Parallel Session P1 - Nonlinear Dynamics in Supply Chains and Economy

Non-Linear Dynamics in a Small-Open-Economy Model in the Euro Area	83
<i>Panayotis G. Michaelides, Angelos T. Vouldis</i>	
Self-organized optimization and synchronization of material flow networks with decentralized control	87
<i>Reik Donner, Stefan Lämmer, Dirk Helbing</i>	
Multiple-Model Seismic Structural Control	97
<i>Alexandar Ichtev, Svetla Radeva</i>	

Parallel Session P2 - Applications of NDS in Technical Systems - 1

Self-Organising Sync in a Robotic Swarm	104
<i>Vito Trianni, Stefano Nolfi</i>	
Adaptive frequency oscillators and applications	112
<i>Ludovic Righetti, Jonas Buchli, Auke Jan Ijspeert</i>	
Controlling EMI with A Chaotic Peak Current-mode Boost Converter	118
<i>H. Li, Z. Li, W.A. Halang, Juan Gonzalo Barajas Ramirez</i>	
Application of Asynchronous Channels Method to the W-CDMA Systems	125
<i>Etsushi Nameda, Hideaki Terai, Minghui Kao, Ken Umeno</i>	

Day Two

Poster Session 2 - Theory of NDS

Recursive Backstepping for Synchronization of Chaotic Systems	131
<i>Ashraf A. Zaher</i>	
Cumulant Analysis of Rössler Attractor	137
<i>Luis A. Beltrán, V. Kontorovich, Z. Lovtchikova</i>	
Detecting dynamical interdependence and generalised synchronisation using the Lorenz method of analogues	146
<i>Erik Casagrande, David Lowe, Avgis Hadjipapas</i>	
Instabilities driven by dipole resonances in cold atoms	154
<i>Hugo Terças, José Tito Mendonça</i>	
Ultrasonic Sensor Data Processing using Support Vector Machines	158
<i>D. Isa, R. Rajkumar</i>	
System Identification using Symbolic Chaotic Sequence	164
<i>Ajeesh P. Kurian, Henry Leung</i>	
Models of Oscillatory Nonlinear Mappings	170
<i>Wieslaw Citko, Wieslaw Sienko</i>	
Generation and Circuitry Implementation of N-double Scroll Delayed Chaotic Attractors	177
<i>Lidan Wang, Shukai Duan, Xiaofan Yang</i>	
Ultra Fast Object Counting Based On Cellular Neural Network	181
<i>Alireza Fasih, Jean Chedjou, Kyandoghere Kyamakya</i>	

Parallel Session P3 - Theory of Synchronization

A linear path towards self-synchronization: Analysis of the fully locked transition of the Kuramoto model	184
<i>David C. Roberts, Razvan Teodorescu</i>	
Ragged Synchronizability and Clustering in a Network of Coupled Oscillators	188
<i>Przemyslaw Perlikowski, Andrzej Stefanski, Tomasz Kapitaniak</i>	
Designing Couplings for Synchronization	194
<i>Ioan Grosu, Servilia Oancea</i>	
Adaptive Synchronization of Lorenz System and Its Uses in Cryptanalysis	197
<i>Ying Liu, Wallace K.S. Tang</i>	

Parallel Session P4 - Application of NDS - 2 (Computational Intelligence Issues)

Ensemble Learning for Time Series Prediction	205
<i>Abdelhamid Bouchachia, Saliha Bouchachia</i>	
Feature extraction for the prognosis of electromechanical faults in electrical machines through the DWT	213
<i>J.A. Antonino-Daviu, M. Riera-Guasp, M. Pineda-Sánchez, J. Pons-Llinares, R. Puche-Panadero</i>	
Networks of Mixed Canonic-Dissipative Systems and Dynamic Hebbian Learning	220
<i>Julio Rodriguez, Max-Olivier Hongler</i>	
About a New Kind of Autonomous, Self-Adapting Agents and the Library Game Environment	225
<i>Herwig Unger, Daniel Berg</i>	
Global Structure Constraint Model for Object Representation	232
<i>Miao Liu, Dongwei Guo, Jie Ma, Yanbin Liu, Chunguang Zhou</i>	

Performing Compression and Encryption Simultaneously using Chaotic Map

Kwok-Wo Wong

Department of Electronic Engineering
City University of Hong Kong
Hong Kong, P.R. China
itkwong@cityu.edu.hk

Ching-Hung Yuen

Department of Electronic Engineering
City University of Hong Kong
Hong Kong, P.R. China
chyuen@cityu.edu.hk

Abstract—An algorithm for performing compression and encryption simultaneously using a chaotic map is proposed. The look-up table used for encryption is determined adaptively by the probability of occurrence of plaintext symbols. As a result, more probable symbols will have a higher chance to be visited by the chaotic search trajectory. The required number of iterations is small and can be represented by a short code. The compression capability is thus achieved. Simulation results show that the compression performance on standard test data and image files is satisfactory while the security is not compromised. Therefore, our scheme can be applied for lossless data and lossy image compression.

Keywords— chaos, cryptography, compression, encoding

I. INTRODUCTION

In recent years, the size of multimedia files as well as the need for the secure transmission of confidential data over public networks keeps rising. This leads to a growing interest in the investigation of joint operation of compression and encryption on the same set of data, i.e., perform these two operations simultaneously, instead of separately. There are in general two different research directions in this area, to embed encryption into compression algorithms or to incorporate compression in cryptographic schemes.

It is natural to embed encryption in entropy coding such as arithmetic coding and Huffman coding since both cryptographic ciphers and entropy coders bear certain resemblance in the sense of secrecy. An entropy coder is easy to be turned to a cipher by using a secret key to govern the statistical model used in coding. The decoder can track the changes in the statistical model and produces the correct output only if the secret key is available.

The work of embedding encryption into arithmetic coding mainly focused on the control of interval allocation using a secret key. In [1], an arithmetic coding scheme with the functions of encryption, data compression and error detection was proposed. Another scheme utilizes a randomized arithmetic coding paradigm based on key-controlled interval swapping [2]. There was also a suggestion to combine binary arithmetic coding with encryption [3]. By incorporating permutation at the input and output of the encoder, the same research group has recently proposed a modified arithmetic coding scheme with a higher security but negligible coding efficiency penalty [4]. Besides arithmetic coding, other entropy coding schemes such as Huffman coding can also be used for embedding encryption. In [5], a scheme based on multiple

Huffman tables was proposed. However, it was lately found that this approach suffers from the chosen-plaintext attack if the Huffman tables are not selected properly [6].

There are some reports on the use of chaos in the joint operation of compression and encryption. In [7], a chaos-based adaptive arithmetic coding technique was proposed. The arithmetic coder's statistical model is made varying in nature according to a pseudo-random bitstream generated by coupled chaotic systems. A similar idea was reported in [8] that the mapping intervals of the arithmetic coder are changed irregularly using a keystream generated from both the chaotic logistic map and the plaintext. A chaotic stream cipher for the selective encryption of video streams was proposed recently [9]. Among all the data in the video stream, only the encoded discrete cosine transform (DCT) coefficients and the sign of the motion vector are encrypted by masking them with a pseudo-random bit sequence generated by two piecewise linear chaotic maps. While all these papers [7-9] utilize chaos in their schemes, they are actually not based on the architecture of chaotic systems, but rather built on the framework of compression such as entropy coding or transform coding. Chaotic systems only play the role of pseudo-random bitstream generators there.

In this paper, an approach for embedding compression in the Baptista-type chaotic cryptosystem [10] is proposed. It roots on the architecture of chaotic cryptosystems rather than the compression framework. The look-up table used for encryption is determined adaptively by the probability of occurrence of plaintext symbols. As a result, more probable symbols will have a higher chance to be visited by the chaotic search trajectory. The required number of iterations is thus small and so can be represented by a short code. Simulation results verify that the proposed scheme can compress standard test files to a satisfactory degree while performing the encryption. Moreover, our scheme ensures that the ciphertext is not longer than the plaintext.

The rest of this paper is organized as follows. In next section, the Baptista-type chaotic cryptosystem is reviewed. Our approach for embedding compression in this class of chaotic cryptosystem is described in Section III. Simulation results and analyses can be found in Section IV. In the last section, conclusions will be drawn.

II. BAPTISTA-TYPE CHAOTIC CRYPTOSYSTEM

Simple one-dimensional chaotic maps such as the logistic map and the tent map are usually employed for data and document encryption. A typical chaos-based cryptographic scheme was proposed by Baptista [10]. The phase space of

the logistic map is divided into a number of equal-width partitions, each maps to a possible plaintext symbol uniquely. A secret chaotic trajectory generated from the key-dependent chaotic map parameters and initial condition is utilized to search for the partition mapped to the plaintext symbol being encrypted. The length of the searching trajectory is equal to the number of iterations of the logistic map, which is then taken as the ciphertext. In other words, the partitioned phase space together with the corresponding plaintext mapping can be considered as a look-up table or a codebook for encryption. In the decryption process, the same secret chaotic search trajectory is re-generated and the correct plaintext symbols are recovered only if the same secret key and the look-up table are available.

There are some variants of the Baptista-type chaotic cryptosystem. Wong *et al* modified it to obtain a flatter ciphertext distribution [11]. A dynamic look-up table version was proposed so that the mapping between the phase space partitions and the plaintext symbols keeps changing for different plaintext blocks [12]. As the look-up table is updated dynamically according to the order of appearance of plaintext symbols, it is plaintext dependent and can be considered as a hash or message authentication code (MAC) of the plaintext sequence [13]. In [14], the Baptista-type chaotic cryptographic scheme was further analyzed in detail.

Like other cryptographic schemes, attempts to crack the original Baptista-type chaotic cryptosystem and its variants were made [15, 16]. The causes of vulnerability were investigated and remedial operations were suggested [17-19].

The Baptista-type chaotic cryptosystem suffers from the problem of long ciphertext which is usually about 1.5 to twice the plaintext length [10, 17]. A short-ciphertext variant was suggested in [20] so that the ciphertext is only slightly longer than the plaintext by a short header. Nevertheless, it is believed that the ciphertext cannot be shorter than the plaintext for this type of cryptosystems. In the next section, an algorithm for incorporating compression in Baptista-type chaotic cryptosystems is proposed for lossless and lossy compression.

III. THE PROPOSED APPROACH

The proposed approach of performing compression and encryption simultaneously can be applied in three different areas, namely, lossless data compression using zero-order and first-order plaintext entropy, and also lossy image compression.

A. Lossless Data Compression using Zero-order Entropy

In this approach, the dynamic look-up table is built adaptively using the plaintext zero-order entropy. By doing so, certain compression capability is achieved along with encryption while the security is not compromised.

First, the whole plaintext sequence is scanned once to find out the probability of occurrence of each plaintext symbol. The phase space of the chaotic map is divided into a number of fixed-width partitions and the number of partitions mapped to a particular symbol is proportional to its probability of occurrence. As an example, suppose that there are only 4 possible plaintext symbols (A, B, C, D) with

probability of occurrence 0.5, 0.25, 0.125, and 0.125, respectively. If the phase space (0,1) is divided into 256 partitions, then 128 of them should map to symbol A, 64 to symbol B, 32 to symbol C, and finally 32 to symbol D, as shown in Fig. 1. It should be noticed that the partitions mapped to the same symbol are not necessarily at adjacent positions.

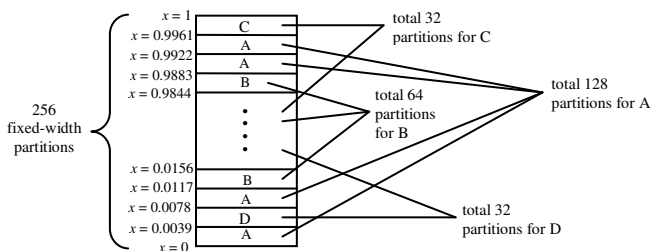


Fig. 1 Mapping of plaintext symbols to partitions in the phase space of the chaotic map.

The advantage of having more partitions for more probable symbols is that the chance for the chaotic trajectory to land on those partitions is also higher. As a result, the required number of iterations is smaller and fewer bits are used to encode it. For example, if each plaintext symbol is represented by a byte and the chaotic search trajectory usually lands on the target partition corresponding to that symbol within 16 iterations. Then a maximum of 4 bits are required for encoding and the ciphertext for that symbol is equal to or shorter than half of the plaintext symbol length. This leads to the compression capability.

While the number of iterations for more probable symbols is small, it can be very large for less probable symbols since there are only one or a few partitions mapped to them. Therefore we cannot include all the plaintext symbols in the mapping table, but can only choose a limited number of more probable ones. Less probable symbols not found in the mapping table are encrypted by masking them with a pseudo-random bitstream also generated by the chaotic map. As a result, the proposed compression and encryption scheme can be considered as a hybrid one: more probable symbols are encrypted by searching in the dynamic look-up table like block ciphers while less probable ones are masked by a pseudo-random bitstream as performed in stream ciphers. A special symbol is required to distinguish between these two modes and it causes certain overhead to the ciphertext. If this overhead exceeds the gain from encrypting more probable symbols, the ciphertext will become longer than the plaintext. In this case, the whole plaintext sequence will be encrypted solely by masking so as to ensure that the ciphertext is not longer than the plaintext.

B. Lossless Data Compression using First-order Entropy

Besides using the zero-order entropy of the plaintext, the first-order one can also be utilized. This means that the a priori information of the relationship between consecutive plaintext symbols is used to build the look-up table adaptively. By doing so, the chance for the chaotic trajectory to fall into the target partitions increases. The number of iterations required is then small and can be encoded by a short code.

Suppose that there are a total of S possible symbols in the plaintext sequence. For each symbol, scan the whole plaintext sequence to find out all the symbols immediately after it. Then sort them in descending order according to their number of occurrence and select the top K symbols only. As a result, each symbol s_i has its own set $N_i = \{n_{i1}, n_{i2}, n_{i3}, \dots, n_{iK}\}$ of more probable next symbols, where $i=1, 2, \dots, S$. The storage requirement could be very large if the number of occurrence of these K more probable next symbols is stored for each symbol. Therefore the average is taken instead so that all the symbols share the same model of probability of occurrence of next symbols, $P = \{p_1, p_2, \dots, p_K\}$ where p_j is a byte value given by Eq. (1).

$$p_j = \left\lfloor \frac{\sum_{i=1}^S u(n_{ij})}{\sum_{i=1}^S \sum_{j=1}^K u(n_{ij})} \times 256 \right\rfloor + 1 \quad (1)$$

where $u(n_{ij})$ is the number of occurrence of next symbol n_{ij} .

Encrypt the plaintext sequentially by finding the previous symbol and then use the corresponding set N_i . For the first plaintext symbol, there is no previous symbol and so we arbitrarily choose it as 0. Divide the phase space of the chaotic map into M equal-width partitions, with $M > K$. Starting from n_{i1} , map the K more probable next symbols to the M partitions randomly according to criterion given by Eq. (2), until all the partitions are mapped.

$$v(n_{ij}) = \left\lfloor \frac{p_j}{\sum_{j=1}^K p_j} \times M \right\rfloor + 1 \quad (2)$$

where $v(n_{ij})$ is the number of partitions mapped to n_{ij} .

C. Lossy Image Compression

For lossless joint compression and encryption, the reconstructed plaintext must be identical to the original one. No error or tolerance is allowed. However, for the lossy counterpart, certain amount of error or tolerance is allowed. This means that we don't need to find out the exactly matched symbol in the codebook. A nearby one is still acceptable. Under the framework of lossless joint compression and encryption mentioned above, this tolerance relaxes the restriction for the chaotic search trajectory to land on the partition exactly mapped to the symbol to be encoded. In fact, a single partition can be mapped to a group of symbols close to each other. If there is overlapping in the grouping of symbols, a particular symbol may belong to more than one group and the chance of getting the chaotic search orbit to land on the target partitions is higher. The corresponding number of iterations is fewer and the compression ratio is improved. In the decoding process, each partition maps to the mean value of the group of symbols, which is then used to represent all the symbols belonging to this group, similar to the principle of vector quantization.

There is another implementation of this relaxation. Instead of having multiple symbols mapped to a single partition, each partition is mapped to one symbol only. However, there is tolerance on the requirement of matching. For example, if the plaintext symbol is 97 and the chosen tolerance limit is 5, the chaotic trajectory landed on any one of the partitions mapped to symbols within the range of 92 to 102 is said to have hit the target. Again, the corresponding number of iterations is fewer and the compression ratio is raised.

IV. SIMULATION RESULTS

To implement the proposed algorithm for joint operation of compression and encryption, the logistic map given by Eq. (3) is chosen as the chaotic map.

$$x_{n+1} = bx_n(1-x_n) \quad (3)$$

The gain b is selected as 3.999999991 while the initial condition x_0 is 0.3388. The plaintext symbols are read in bytes and the chaotic map phase space is divided into 256 equal-width partitions. The maximum number of iterations for the search mode is chosen as 15. The proposed algorithm is implemented in C++ programming language running on a personal computer with an Intel Core2 2.13GHz processor and 1GB memory. The following data are collected.

To test the compression capability of the proposed scheme, the standard files from the Calgary Corpus are used [21]. There are 18 distinct files of different types, including text, executable, geophysical data and picture. Two simulation configurations are chosen for zero-order entropy. The first one is that only 16 more probable plaintext symbols are selected and they are all mapped to one table. In the second case, 128 more probable plaintext symbols are chosen and they are distributed to 16 tables, each has 8 symbols. The ciphertext-to-plaintext ratio (R) calculated by Eq. (4) is listed in Table 1.

$$R = \frac{\text{CiphertextLength}}{\text{PlaintextLength}} \times 100\% \quad (4)$$

TABLE 1: CIPHERTEXT-TO-PLAINTEXT RATIO OF THE CALGARY CORPUS FILES USING ZERO-ORDER ENTROPY.

File	1 map, 16 symbols	16 maps, 8 symbols each
pic	32.88%	31.43%
book1	83.36%	71.09%
paper2	83.95%	72.19%
paper3	84.30%	73.54%
paper4	84.27%	73.97%
progl	86.00%	74.82%
book2	85.05%	75.43%
paper5	86.30%	77.50%
progp	85.63%	77.73%
paper1	86.88%	78.38%
paper6	87.12%	78.81%
news	87.97%	81.73%
progc	88.74%	82.15%
bib	89.07%	82.34%
geo	83.98%	85.22%
trans	93.25%	86.98%
obj1	88.60%	89.62%
obj2	92.85%	94.03%

Table 1 shows that all files can be compressed using the two configurations. However, the compression performance of the second configuration (16 maps, 8 symbols each) is better for most of the files. The image file (pic) is the easiest to compress due to the redundancy of image pixels. The corresponding ciphertext length is about one-third the plaintext length. The executable files (obj1 and obj2) are the most difficult to compress as the distribution of plaintext symbols is comparatively uniform. The corresponding ciphertext sequences are only about 10% shorter than the plaintext ones.

The compression performance using first-order entropy can be found in Table 2. Eight next symbols, *i.e.*, $K=8$, are selected. The data in the bracket of the rightmost column are the ratio when the necessary secret parameters are included as a header of the ciphertext. All the values are below 100% which imply that all the files can be compressed. The performance is the best for the pic file that the ciphertext length is only about one-third of the plaintext, due to the high redundancy in the picture.

TABLE 2: CIPHERTEXT-TO-PLAINTEXT RATIO OF THE CALGARY CORPUS FILES USING FIRST-ORDER ENTROPY.

File	Size (byte)	Ciphertext-to-plaintext ratio (With Header)
pic	513,216	31.67% (32.11%)
progp	49,379	68.31% (72.87%)
progl	71,646	69.49% (72.63%)
paper4	13,286	71.90% (88.76%)
paper5	11,954	72.08% (90.84%)
paper2	82,199	72.20% (74.94%)
trans	93,695	72.23% (74.64%)
obj1	21,504	72.71% (83.16%)
bib	111,261	72.81% (74.84%)
paper3	46,526	72.85% (77.68%)
progc	39,611	73.39% (79.08%)
paper6	38,105	73.49% (79.39%)
book1	768,771	73.50% (73.79%)
paper1	53,161	74.07% (78.30%)
book2	610,856	74.68% (75.05%)
obj2	246,814	74.74% (75.65%)
news	377,109	78.63% (79.23%)
geo	102,400	79.27% (81.47%)

The performance of our algorithm for lossy image compression is tested using eight standard 512 x 512 gray-scale images in bitmap format. The tolerance limit of the pixel value is set to 20. The ciphertext-to-plaintext ratio can be found in Table 3. It ranges from around 25% to 43% which shows that the compression performance is satisfactory. The corresponding peak signal-to-noise ratio (PSNR) of the reconstructed image is around 30dB.

TABLE 3: CIPHERTEXT-TO-PLAINTEXT RATIO OF LOSSY IMAGE COMPRESSION.

Image	Original Size (byte)	Ciphertext-to-plaintext ratio (With Header)
goldhill	262,144	24.80% (25.66%)
lena	262,144	25.65% (26.51%)
sailboat	262,144	27.18% (28.04%)
peppers	262,144	28.63% (29.49%)
frog512	262,144	31.48% (32.34%)
aerial	262,144	35.57% (36.43%)
barb	262,144	40.17% (41.03%)
baboon	262,144	41.91% (42.77%)

To evaluate the key sensitivity, encryptions using the all-mask mode for first-order entropy were performed by introducing a very small change in one of the secret parameters. Then the resultant ciphertext sequence is

compared with the original one bit-by-bit and the percentage of bit change is calculated. For parameters b and x_0 , the 15th digit after decimal point is changed from 0 to 1. For c_{-1} , the least significant bit (bit 0) is toggled from 0 to 1. The measured bit change percentages are 49.97%, 50.03% and 49.99% for b , x_0 and c_{-1} , respectively. All the data are close to 50% which indicate that the ciphertext is very sensitive to the key.

To measure the plaintext sensitivity, a bit is changed at different positions of the plaintext sequence while the key remains unchanged. The two resultant ciphertext sequences are compared bit-by-bit and the percentage of bit change is calculated. The results are 50.00% (bit change at the beginning of plaintext), 50.03% (middle) and 49.98% (end), respectively. They are all close to 50%, which imply that the ciphertext is very sensitive to the plaintext.

The randomness of the binary mask sequence is confirmed by the statistical test suite recommended by the U.S. National Institute of Standards and Technology (NIST) [22]. Ten sequences, each of 1,000,000 bits, are extracted for testing and they all pass the statistical tests including frequency, block-frequency, cumulative-sums, runs, longest-run, rank, and FFT.

V. CONCLUSION

An algorithm for the simultaneous compression and encryption using chaotic maps has been proposed. It can be applied to lossless data compression as well as lossy image compression. The effectiveness of the proposed scheme is confirmed by the satisfactory ciphertext-to-plaintext ratio using standard data and image files. Simulation results verify that the ciphertext is very sensitive to a tiny change in the key or the plaintext and so the security is maintained.

ACKNOWLEDGEMENT

The work described in this paper was fully supported by a grant from CityU [Project No. 7002070].

REFERENCES

- [1] X. Liu, P. Farrell, and C. Boyd, "A unified code" *IMA - Crypto & Coding'99, LNCS 1746*, pp. 84-93, 1999.
- [2] M. Grangetto, E. Magli, and G. Olmo, "Multimedia selective encryption by means of randomized arithmetic coding," *IEEE Trans. Multimedia*, vol. 8, no. 5, pp. 905-917, 2006.
- [3] J. Wen, H. Kim, and J. Villasenor, "Binary arithmetic coding with key-based interval splitting," *IEEE Signal Processing Letters*, vol. 13, no. 2, pp. 69-72, 2006.
- [4] H. Kim, J. Wen, and J. Villasenor, "Secure arithmetic coding," *IEEE Trans. Signal Process.*, vol. 55, no. 5, pp. 2263-2272, 2007.
- [5] C. Wu and C. Kuo, "Design of integrated multimedia compression and encryption systems," *IEEE Trans. Multimedia*, vol. 7, no. 5, pp. 828-839, 2005.
- [6] J. Zhou, Z. Liang, Y. Chen, and O.C. Au, "Security analysis of multimedia encryption schemes based on multiple Huffman table," *IEEE Signal Processing Letters*, vol. 14, no. 3, pp. 201-204, 2007.
- [7] R. Bose and S. Pathak, "A novel compression and encryption scheme using variable model arithmetic coding and coupled chaotic system," *IEEE Trans. Circuits and Sys. I*, vol. 53, no. 4, pp. 848-857, 2006.
- [8] Bo Mi, X. Liao, and Y. Chen, "A novel chaotic encryption scheme based on arithmetic coding," to appear in *Chaos Solitons and Fractals*.

- [9] S. Lian, J. Sun, J. Wang, and Z. Wang, "A chaotic stream cipher and the usage in video protection," to appear in *Chaos, Solitons and Fractals*.
- [10] M.S. Baptista, "Cryptography with chaos," *Physics Letters A*, vol. 240, no. 1-2, pp. 50-54, 1998.
- [11] W.K. Wong, L.P. Lee and K.W. Wong, "A modified chaotic cryptographic scheme," *Computer Physics Communications*, vol. 138, no. 3, pp. 234-236, 2001.
- [12] K.W. Wong, "A fast chaotic cryptography scheme with dynamic look-up table," *Physics Letters A*, vol. 298, pp. 238-242, 2002.
- [13] K.W. Wong, "A combined chaotic cryptographic and hashing scheme," *Physics Letters A*, vol. 307, no. 5-6, pp. 292-298, 2003.
- [14] S. Li, G. Chen, K.W. Wong, X. Mou, and Y. Cai, "Baptista-type chaotic cryptosystems: problems and countermeasures," *Physics Letters A*, vol. 332, pp. 368 - 375, 2004.
- [15] G. Alvarez, F. Montoya, M. Romera, G. Pastor, "Cryptanalysis of an ergodic chaotic cipher," *Physics Letters A*, vol. 311, pp. 172-179, 2003.
- [16] G. Alvarez, F. Montoya, M. Romera, G. Pastor, "Cryptanalysis of dynamic look-up table based chaotic cryptosystems," *Physics Letters A*, vol. 326, no. 3-4, pp. 211-218, 2004.
- [17] K.W. Wong, K.P. Man, S. Li, X. Liao, "A more secure chaotic cryptographic scheme based on dynamic look-up table," *Circuits, Systems and Signal Processing*, vol. 24, no. 5, pp. 571-584, 2005.
- [18] J. Wei, X. Liao, K.W. Wong, T. Zhou, and Y. Deng, "Analysis and improvement for the performance of Baptista's cryptographic scheme," *Physics Letters A*, vol. 354, no. 1-2, pp. 101-109, 2006.
- [19] D. Xiao, X. Liao, and K.W. Wong, "Improving the security of a dynamic look-up table based chaotic cryptosystem," *IEEE Trans. Circuits and Sys. II*, vol. 53, no. 6, pp. 502-506, 2006.
- [20] K.W. Wong, S.W. Ho, C.K. Yung, "A chaotic cryptographic scheme for generating short ciphertext," *Physics Letters A*, vol. 310, no. 1, pp.67-73, 2003.
- [21] <ftp://ftp.cpsc.ucalgary.ca/pub/projects/text.compression.corpus>
- [22] A. Rukhin, J. Soto, *et al*, "A Statistical Test Suite for the Validation of Random Number Generators and Pseudo Random Number Generators for Cryptographic Applications," NIST Special Publication 800-22, http://csrc.nist.gov/groups/ST/toolkit/rng/documentation_software.html



Kwok-Wo Wong graduated with a BSc(EE) degree from The Chinese University of Hong Kong and a PhD degree from City University of Hong Kong. Currently, he is an Associate Professor in Department of Electronic Engineering, City University of Hong Kong. His research interests include chaos and cryptography.



Ching-Hung Yuen graduated with a Bachelor of Engineering in Computer Engineering from City University of Hong Kong in 2006. He is working as a research assistant in the Department of Electronic Engineering, City University of Hong Kong. His research interests include chaos and cryptography.

Neural Networks for Approximating the Cost and Production Functions

Efthymios G. Tsionas
 Department of Economics
 Athens University of Economics and Business
 Athens, Greece
tsionas@aueb.gr

Panayotis G. Michaelides and Angelos T. Vouldis
 Department of Applied Mathematics and Physical Sciences
 National Technical University of Athens
 Athens, Greece
pmichael@central.ntua.gr and avouldis@biosim.ntua.gr

Abstract— Most business decisions depend on accurate approximations to the cost and production functions. Traditionally, the estimation of cost and production functions in economics relies on standard specifications which are less than satisfactory in numerous situations. However, instead of fitting the data with a pre-specified model, Artificial Neural Networks let the data itself serve as evidence to support the model's estimation of the underlying process. In this context, the proposed approach combines the strengths of economics, statistics and machine learning research and the paper proposes a global approximation to arbitrary cost and production functions, respectively, given by ANNs. Suggestions on implementation are proposed and empirical application relies on standard techniques. All relevant measures such as scale economies and total factor productivity may be computed routinely.

Keywords— Neural networks, Econometrics, Production and Cost Functions, RTS, TFP.

I. INTRODUCTION

Business decisions often depend on accurate approximations and analyses of the cost and production functions [1]. Commonly used specifications such as the Cobb-Douglas or the Translog are intuitively appealing and computationally straightforward. However, they are often less than satisfactory because they attempt to explain the complex variation in cost or production with a quite simple mathematical function despite the fact the real – world data are much more complicated. As a result their explanatory power is quite low. On the contrary, the nonparametric feature of Artificial Neural Networks (ANNs) makes them quite flexible and attractive in modelling economic phenomena where the theoretical relationship is not known a priori [2].

Consequently, instead of fitting the data with a pre-specified model, ANNs let the data itself serve as evidence to support (or reject) the model's estimation of the underlying process [2]. ANNs have found numerous applications in financial modelling [3]-[9]. However, with the exception of

very few papers ([1], [10]) no systematic research on pure economic modelling using ANNs has been done.

This paper focuses on scholars and researchers in applied mathematics and attempts to combine tools from the statistical community with neural network technology. It proposes new flexible cost and production functions, respectively, which are based on ANNs allowing for multiple outputs. Contrary to widely used local approximations like the Translog [11], the generalized Leontief [12] or the symmetric McFadden form [13] the proposed flexible functions are global approximations to the unknown functions. The Fourier flexible form [14], [15] is also a global approximation but it requires an excessive number of parameters. The neural functions provide a better approximation using considerably less parameters [16].

II. ELEMENTS OF NEURAL NETWORKS

Neural networks are “data-driven, self-adaptive nonlinear methods that do not require specific assumptions about the underlying model” [2]. By combining simple units with multiple intermediate nodes, ANNs can approximate any smooth nonlinearity [17]. As demonstrated in Hornik et al. [18], [19], they have the ability to approximate arbitrarily well a large class of functions while keeping the number of free parameters to a minimum.

In mathematical terms, ANNs are collections of transfer functions that relate an output variable Y to certain input variables $X' = [X_1, \dots, X_n]$. The input variables are combined linearly to form m intermediate variables Z_1, \dots, Z_m where

$$Z_i = X \phi_i, \quad i = 1, \dots, m \quad (1)$$

where $b_i \hat{=} R^n$ are parameter vectors. The intermediate variables are combined nonlinearly to produce Y :

$$Y = \mathring{\mathbf{a}} \sum_{i=1}^m a_i f(Z_i) \quad (2)$$

where f is an activation function, the a_i 's are parameters and m is the number of intermediate nodes [20]. For various activation functions see, for instance, [21].

III. THE COST FUNCTION

In economics, the cost function is a function of input prices and output quantity and its value expresses the cost of producing that output given the input prices. Let $p \hat{=} R^n$ denote a price vector corresponding to n factors of production, and $y \hat{=} R_+^J$ the output vector. The neural cost function has the form:

$$\ln C(p, y) = a_0 + \mathring{\mathbf{a}} \sum_{k=1}^m a_k f(\ln p \times b_k + \ln y \times g_k) + \ln p \times q \quad (3)$$

where $C(p, y)$ is the cost function, $a_k \hat{=} R$, $b_k \hat{=} R^n$, $g_k \hat{=} R^J$ and $q \hat{=} R^n$ are parameters, and m is the number of intermediate nodes. For vectors a and b , $a \times b$ denotes the inner product.

Factor share equations are derived by (3) via formal differentiation with respect to prices using Shephard's lemma [22]:

$$w_i(p, y) = \frac{\mathring{\nabla} \ln C(p, y)}{\mathring{\nabla} \ln p_i} = \mathring{\mathbf{a}} \sum_{k=1}^m a_k b_{ki} f'(\ln p \times b_k + \ln y \times g_k) + q_i, \quad (4)$$

$$i = 1, \dots, n$$

In order for (3) to represent a proper cost function, $C(p, y)$ must be concave in p , which is expressed by the condition that the Hessian matrix $D^2 C(p)$ is negative semidefinite for every $p \hat{=} R_+^n$. Concavity is, traditionally, not imposed *a priori* but checked *a posteriori*.

A. Returns to Scale

In econometric studies, returns to scale describe what happens as the scale of production increases. Returns to scale refers to a technical property of production that examines changes in output subsequent to a proportional change in all inputs. If output increases by the same proportional change then there are constant returns to scale (CRTS). If output increases by less than that proportional change, there are decreasing returns to scale (DRS). If output increases by more than that proportion, there are increasing returns to scale (IRS) [23].

The neural cost function does not place *a priori* restrictions on the behavior of returns to scale like other functional forms.

It is known that if $\frac{\mathring{\nabla} \ln C(p, y)}{\mathring{\nabla} \ln y} < 1$ (≥ 1) the production

technology is characterized by increasing (non-increasing) returns to scale. For the neural cost function:

$$RTS = \mathring{\mathbf{a}} \sum_{i=1}^J \frac{\mathring{\nabla} \ln C(p, y)}{\mathring{\nabla} \ln y_i} = \mathring{\mathbf{a}} \sum_{i=1}^J \mathring{\mathbf{a}} \sum_{k=1}^m a_k g_{ki} f'(\ln p \times b_k + \ln y \times g_k) \quad (5)$$

B. Total Factor Productivity

In economics, growth in total-factor productivity (TFP) represents output growth not accounted for by the growth in inputs [23] and presumably changes over time. It is traditionally used as a proxy for technical change.

If we modify (3) to include time (t) as an index of technical change, we have:

$$\ln C(p, y) = a_0 + \mathring{\mathbf{a}} \sum_{k=1}^m a_k f(\ln p \times b_k + \ln y \times g_k + d_k t) + \ln p \times q \quad (6)$$

Therefore:

$$\frac{\mathring{\nabla} \ln C(p, y)}{\mathring{\nabla} t} = \mathring{\mathbf{a}} \sum_{k=1}^m a_k d_k f'(\ln p \times b_k + \ln y \times g_k + d_k t) \quad (7)$$

By definition, total factor productivity measure is given by $TFP = \frac{\mathring{\nabla} \ln y}{\mathring{\nabla} t}$. Since: $TFP = \frac{\mathring{\nabla} \ln C(p, y) / \mathring{\nabla} t}{\mathring{\nabla} \ln C(p, y) / \mathring{\nabla} \ln y}$ it follows that:

$$TFP = \frac{\mathring{\mathbf{a}} \sum_{k=1}^m a_k d_k f'(\ln p \times b_k + g_k \ln y + d_k t)}{\mathring{\mathbf{a}} \sum_{k=1}^m a_k g_k f'(\ln p \times b_k + g_k \ln y + d_k t)} \quad (8)$$

Apparently, TFP as derived from the neural cost function is a weighted average of coefficients $\frac{d_k}{g_k}$. The weights are normalized first-order derivatives of the activation functions at the different nodes of the neural network.

C. Model Building

Empirical estimation is based on the cost function and the system of share equations. The system is highly nonlinear in the parameters. Although the system is nonlinear in terms of the parameters b_k and g_k the neural cost function's global approximation properties do not depend on this nonlinearity. As has been shown in [16], one may select the nonlinear parameters by a random search procedure, fix their values at the outcome of the random search, and estimate the linear parameters by the usual econometric methods. This will not

affect the global approximation properties of the network. The weights are estimated and refit from scratch instead of being updated from previous data with a learning algorithm [18]. A modification of the Stinchcombe and White [16], procedure has to be followed here, because we have a system of equations instead of a single equation. The procedure is as follows:

Step 1: Let $b_k^{(i)}$ and $g_k^{(i)}$ ($k = 1, \dots, m$) be drawn from a uniform distribution.

Step 2: Given these parameters, estimate a_k ($k = 1, \dots, m$) and q by least squares applied to the cost function:

$$\ln C(p_t, y_t) = a_o + \sum_{k=1}^m a_k f(\ln p_t \times b_k + g_k \ln y_t) + \ln p_t \times q + v_t, \quad t = 1, \dots, T \quad (9)$$

where T denotes the number of observations, p_t the vector of factor prices of date t , and y_t the output level of date t .

Step 3: Compute the residual sum of squares $SSR^{(i)}$ or $SSR(b^{(i)}, g^{(i)})$. Repeat for $i = 1, \dots, I$ and select the values \bar{b} and \bar{g} that yield the minimum value of $SSR^{(i)}$.

Step 4: Estimate the following system of equations:

$$\ln C(p_t, y_t) = a_o + \sum_{k=1}^m a_k f(\ln p_t \times \bar{b}_k + \bar{g}_k \ln y_t) + \ln p_t \times q + e_{o,t} \quad (10a)$$

$$w_{it} = \sum_{k=1}^m a_k \bar{b}_k f(\ln p_t \times \bar{b}_k + \bar{g}_k \ln y_t) + q_t + e_{i,t}, \quad i = 1, \dots, n - 1 \quad (10b)$$

where $e_t \in [e_{0t}, e_{1t}, \dots, e_{n-1,t}]$ is a vector random variable, distributed as i.i.d. $N(0, S)$ where Σ is a covariance matrix. System (10a) and (10b) is linear in the parameters $[a, q] \in R^{n+m}$ and can be estimated using standard, iterative seemingly unrelated regressions equations technique (SURE) [25]. This is feasible even for extremely large systems.

IV. THE PRODUCTION FUNCTION

Let $x \in R^n$ denote an input vector corresponding to n factors of production, and $Y \in R^J$ the output vector. The neural production function, for each output, has the form:

$$\ln Y_i(x) = a_{0i} + \sum_{k=1}^{m_i} a_{ki} f_i(\ln x \times b_{ki}) + \ln x \times q_i \quad (11)$$

where $Y_i(x)$ is the production function of output i , $a_{ki} \in R$, $b_{ki} \in R^n$, $q_i \in R^n$ are parameters and m_i is the number of intermediate nodes. For the last output J the equation governing its production process has the following form:

$$\ln Y_J(x) = a_{0J} + \sum_{k=1}^{m_J} a_{kJ} f_J(\ln x \times b_{kJ}) + \ln Y \times g + \ln x \times x \quad (12)$$

where $g \in R^J$, $x \in R^n$ are parameters, and m_J is the number of intermediate nodes for output J .

In addition, for (11) to represent a proper production function $Y_i(x)$ must be increasing in x and $Y_i(x)$ decreasing in Y . Also, quasi-concavity of $Y_i(x)$ and $Y_j(x)$ is implied by economic theory. These assumptions are not imposed *a priori* but rather checked *a posteriori*. Finally, $Y_j(x)$ must be homogeneous of degree one, a fact which places parametric restrictions on the production function. More precisely, homogeneity of degree one implies:

$$\sum_{j=1}^J g_j = 0 \quad (13)$$

A. Returns to Scale

As we have seen, returns to scale (RTS) describe what happens as the scale of production increases. The neural production function does not place a priori restrictions on the behavior of returns to scale. It is known that typically the RTS are equal to the sum of the output elasticities of the various inputs. Let e^j denote the elasticity of output with respect to factor x^j :

$$e^j = \frac{\partial \ln Y(x)}{\partial \ln x_j} = \frac{\partial \ln Y(x)}{\partial x_j} \times \frac{x_j}{Y(x)}, \quad j = 1, \dots, n \quad (14)$$

where $x \in R^n$ denotes the input vector corresponding to n factors of production.

Therefore, for the neural production function RTS for each output are equal to:

$$RTS^i = \sum_{j=1}^n \frac{\partial \ln Y_i(x)}{\partial \ln x_j}, \quad i = 1, \dots, J - 1 \quad (15)$$

Consequently:

$$RTS^i = \mathring{\mathbf{a}} \mathring{\mathbf{a}} \mathring{\mathbf{b}}_{kj} a_{ki} f_i(\ln x \times b_{ki}) + \mathring{\mathbf{a}} \mathring{\mathbf{a}}_{q=1}^n q_{iq}, \quad i = 1, \dots, J-1, \quad j = 1, \dots, n \quad (16)$$

For the last output J, we have:

$$RTS^J = \mathring{\mathbf{a}} \mathring{\mathbf{a}} \mathring{\mathbf{b}}_{jkl} a_{klJ} f_j(\ln x \times b_{kl}) + \mathring{\mathbf{a}} \mathring{\mathbf{a}}_{i=1}^{J-1} g_i \left(\mathring{\mathbf{a}} \mathring{\mathbf{a}} \mathring{\mathbf{b}}_{kj} a_{ki} f_i(\ln x \times b_{ki}) \right) + \mathring{\mathbf{a}} \mathring{\mathbf{a}}_{q=1}^n x_q \quad (17)$$

B. Total Factor Productivity

If we modify (11) to include time (t) as an index of technical change, we have:

$$\ln Y_{it}(x) = a_{0i} + \mathring{\mathbf{a}} \mathring{\mathbf{a}}_{k=1}^{m_i} a_{ki} f_i(\ln x \times b_{ki} + d_{ki}t) + \ln x \times q_i \quad (18)$$

$i = 1, \dots, J-1$

By definition Total Factor Productivity (TFP) measure, for each output, is given by:

$$TFP_{it} = \frac{\mathring{\mathbf{a}} \ln Y_{it}(x)}{\mathring{\mathbf{a}} t} \quad (19)$$

Therefore, it follows that:

$$TFP_{it} = \mathring{\mathbf{a}} \mathring{\mathbf{a}}_{k=1}^{m_i} d_{ki} a_{ki} f_i(\ln x \times b_{ki} + d_{ki}t), \quad i = 1, \dots, J-1 \quad (20)$$

For the last output J, we have:

$$TFP_{Jt} = \mathring{\mathbf{a}} \mathring{\mathbf{a}}_{k=1}^{m_J} d_{kJ} a_{kJ} f_j(\ln x \times b_{kJ} + d_{kJ}t) + \mathring{\mathbf{a}} \mathring{\mathbf{a}}_{i=1}^{J-1} g_i \left(\mathring{\mathbf{a}} \mathring{\mathbf{a}}_{k=1}^{m_i} d_{ki} a_{ki} f_i(\ln x \times b_{ki} + d_{ki}t) \right) \quad (21)$$

We can see that TFP depends on time and inputs.

C. Model Building

Similarly to the cost function, estimation is based on the system of production functions (11) – (12). The system is highly nonlinear in the parameters. The procedure is, practically, the same as earlier:

Step 1: Let $b_k^{(i)}$ be drawn from a uniform distribution.

Step 2: Given these parameters, estimate $a_k^{(i)}$, $g_k^{(i)}$, $\theta^{(i)}$ and $\xi^{(i)}$ by means of the system:

$$\ln Y_{it}(x_t) = a_{0i} + \mathring{\mathbf{a}} \mathring{\mathbf{a}}_{k=1}^{m_i} a_{ki} f_i(\ln x_t \times b_{ki}) + \ln x_t \times q_i + e_{i,t} \quad (22a)$$

$$\ln Y_{Jt}(x_t) = a_{0J} + \mathring{\mathbf{a}} \mathring{\mathbf{a}}_{k=1}^{m_J} a_{kJ} f_j(\ln x_t \times b_{kJ}) + \ln y_t \times g + \ln x_t \times x + e_{J,t} \quad i = 1, \dots, J-1 \quad (22b)$$

where x_t denotes the vector of inputs of date t , y_t the output levels of date t , $e_t \circ [e_{0t}, e_{1t}, \dots, e_{J,t}]$ is a vector random variable, distributed as i.i.d. $N(0, S)$, S is a covariance matrix. The system of equations (22a) and (22b) is linear in the parameters $a_k^{(i)}$, $g_k^{(i)}$, $\theta^{(i)}$ and $\xi^{(i)}$ and can be estimated using standard, iterative SURE. This is feasible even for extremely large systems.

Step 3: Compute the determinant of the covariance matrix $\det S^{(i)} \circ \det S(b)$. Repeat for $i = 1, \dots, I$ and select the values \bar{b} that yield the minimum value of $\det S^{(i)}$.

Step 4 : For \bar{b} that yield the minimum value of $\det S^{(i)}$ re-estimate the system and keep the estimated values for parameters $a_k^{(i)}$, $g_k^{(i)}$, $\theta^{(i)}$ and $\xi^{(i)}$.

V. MODEL SELECTION

Although it has been demonstrated that ANNs can approximate any nonlinear function with arbitrary accuracy, no accepted guideline exists in choosing the appropriate model for empirical applications [2]. Consequently, the number of nodes m could be selected using one of the following methods: (a) the R_{adj}^2 criterion, (b) Schwartz's criterion [25] or (c) Akaike's criterion [26].

R^2 is a statistical measure of how well the estimated line approximates the real data point and a value equal to 1

indicates perfect fit to the data. In this framework, R_{adj}^2 is a modification of R^2 that adjusts for the number of explanatory terms in a model, i.e. the number of independent variables and the number of data points. According to this very popular criterion in model selection one should select the number of nodes that maximizes the R_{adj}^2 . When R_{adj}^2 finds a global maximum one should stop adding explanatory terms [18].

According to the Bayesian Information Criterion or the so-called Schwartz's criterion [25], one should select the number of nodes that minimizes the BIC which is defined as:

$$BIC = -2 \ln(L) + k \ln(n) \quad (23)$$

where n is the number of observations, k is the number of free parameters to be estimated and L is the maximized value of the likelihood function for the estimated model. The BIC minimizing model keeps a balance between bias and variance, in that additional complexity must be justified by a correspondingly large improvement in fit. BIC has been shown to be statistically consistent [18].

According to Akaike [26], one should determine the number of nodes that minimizes the AIC criterion defined as:

$$AIC = 2k - 2 \ln(L) \quad (24)$$

where k is the number of free parameters to be estimated and L is the maximized value of the likelihood function for the estimated model. The AIC rewards the goodness of fit but also includes a penalty that is an increasing function of the number of parameters.

Finally, it should be noted that the algorithm for randomly drawing parameters from a hyper-rectangle to estimate the cost and production functions shall be refined by means of more sophisticated optimization techniques in case of very large dimensional problems.

VI. EMPIRICAL RESULTS

A. Data and Variables

The data are taken from the commercial bank and bank holding company database managed by the Federal Reserve Bank of Chicago over the 1989-2000 time span. The dataset is based on the Report of Condition and Income (Call Report) for all U.S. commercial banks that report to the Federal Reserve banks and the FDIC. The output variables are: (1) instalment loans (to individuals for personal/household expenses), (2) real estate loans, (3) business loans, (4) federal funds sold and securities purchased under agreements to resell, and (5) other assets (assets that cannot be properly included in any other asset items in the balance sheet). The input variables are: (1) labor, (2) capital, (3) purchased funds, (4) interest-bearing deposits in total transaction accounts and (5) interest-bearing deposits in total non-transaction accounts.

B. Results for the Cost Function

We followed the procedure described earlier and estimated the parameters $[\alpha, \theta] \in R^{n+m}$. However, the desirable number of nodes m also has to be selected using one of the methods described earlier. R_{adj}^2 criterion is depicted in Fig. 1 whereas Schwartz's (1978) and Akaike's (1973) criteria are depicted in Fig. 2.

It is clear that the BIC finds a global minimum for $m=7$ while the Akaike criterion, which punishes less strictly the increase in the number of nodes, finds also other local minimums for greater numbers of nodes. However, even for the Akaike criterion $m=7$ is the global minimum. Also, the R^2 and R_{adj}^2 find a global maximum for $m=7$ nodes. So, for an ANN with $m=7$ nodes and activation function $f(x) = (1 + e^{-x})^{-1}$ the estimated coefficients α, θ are statistically significant for almost all of the estimated coefficients.

Next, the Returns to Scale are computed through equation (5) and are found to follow a Gaussian-like distribution around unity (1). This result implies, roughly speaking, constant returns to scale and can be characterized as expected (see Figs. 3-4) because, as is well known, as a result of the optimization principle the production function for the firm will generally exhibit constant returns to scale.

The factor shares of the five (5) inputs were calculated and were found to range between 0 and 1, as expected.

Subsequently, the issue of concavity is investigated. As it has already been mentioned, the concavity condition can be checked by calculating the eigenvalues of the Hessian matrix for each observation and examining if they are all negative. It was confirmed that the vast majority of eigenvalues are negative implying that the cost function is, practically, globally concave with respect to prices, a result which is consistent with economic theory [21]. For each observation there were five eigenvalues equal to the dimension of the Hessian matrix.

More precisely, for each observation, the four greater (in absolute value) eigenvalues were negative. Also, the lower eigenvalues for each observation have generally a much greater absolute value than its most positive eigenvalue. In total, approximately 90% of all eigenvalues were found to be negative. Any deviation from this rule can be attributed to omitted variables, measurement errors, and inefficiency. A failure of the proposed functional form to comply with this assumption would imply empirical findings non-consistent with neo-classical economic theory. However, not all cost functions proposed, so far, in the empirical literature satisfy this assumption, despite it being dictated by economic theory.

Finally, in Fig. 5, the histogram of all TFP values (%) is depicted. We see that TFP is negative on the average with a longer tail to the left indicating the prevalence of negative technical progress for the organizations of the US Banking sector in the 1989-2000 time span.

B. Results for the Production Function

The estimation procedure described earlier was used to estimate the parameters $[a, \theta, \gamma, \xi] \in R^{J(n+1) + \sum_{i=1}^J m_i - 1}$. However, a choice has to be made regarding the number of nodes of the neural network. The system R^2_{wide} had a maximum for $m_i = 3$ nodes (Fig. 6). Consequently, for the rest of our analysis of production functions we set $m_i = 3$ ($i = 1, \dots, J$).

As it can be inferred from the value of the R^2_{wide} , the neural network production function provides a very good approximation to the actual production function. Also, almost all of the estimated coefficients of the production functions were statistically significant.

Next, the RTS are also calculated and the results are shown in Fig. 7.

The histogram of the TFP values is depicted in Fig. 8.

Finally, the hypothesis that $Y_i(x)$ is increasing in x , decreasing in $Y_j(x)$, for $i = 1, \dots, J-1$, $i \neq j$ and the quasi-concavity of $Y_i(x)$ and $Y_j(x)$ were checked *ex post* and were found to be, in general terms, consistent with economic theory.

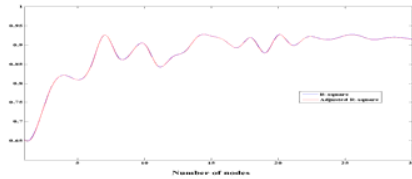


Figure 1. R^2 and R^2_{adj} and the number of number of nodes

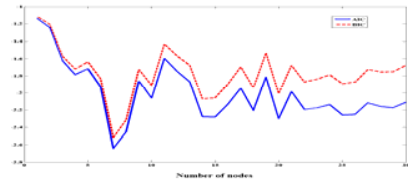


Figure 2. Akaike's Information Criterion, Bayesian Information Criterion and the number of nodes

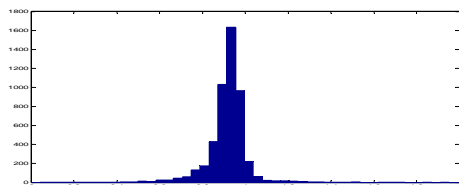


Figure 3. Histogram of RTS (Unconstrained regression)

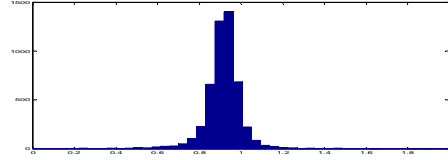


Figure 4. Histogram of RTS (Constrained regression)

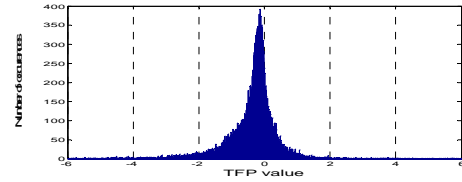


Figure 5. Histogram of TFP values

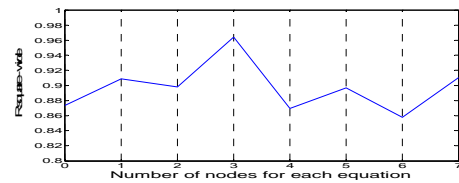


Figure 6. \tilde{R}^2 and the number of nodes

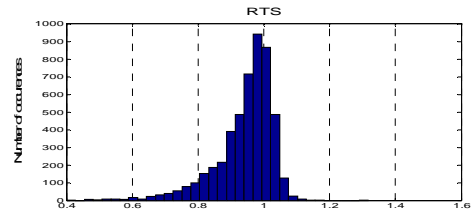


Figure 7. Histogram of RTS for the J th output

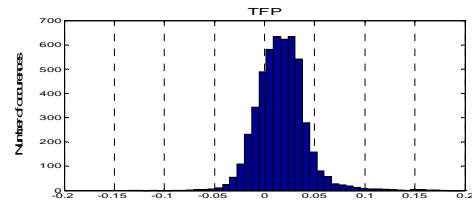


Figure 8. Histogram of TFP for the J th output

VII. CONCLUSIONS

Commonly used production and cost functions usually estimated by means of linearized multifactor models are known to be less than satisfactory in numerous situations. However, ANNs let the data itself serve as evidence to support the model's estimation of the underlying process. In this context, the proposed procedure attempted to combine the strengths of economics, statistics and machine learning research. The

paper proposed a global approximation to arbitrary cost and production functions, respectively, given by ANN specifications. All relevant measures such as scale economies and total factor productivity were computed routinely. The empirical application referred to a large panel data set consisting of all U.S. commercial banks that report to the Federal Reserve banks over the time period 1989-2000. The results of the empirical implementation were consistent with conventional economic theory.

REFERENCES

- [1] U. Anders, O. Korn, and C. Schmitt, "Improving the pricing of options: A neural network approach," *J. Forecasting*, vol. 17, pp. 369-388, 1998.
- [2] M. Hanke, "Neural networks versus Black-Scholes: An empirical comparison of the pricing accuracy of two fundamentally different option pricing methods," *J. Comput. Intell. Finance*, vol. 5, pp. 26-34, 1999.
- [3] J. M. Hutchinson, A.W. Lo, and T. Poggio, "A nonparametric approach to pricing and hedging derivative securities via learning networks," *J. Finance*, vol. 49, pp. 851-889, 1994.
- [4] J. Y. Campbell, A. W. Lo, and A. C. MacKinley, *The Econometrics of Financial Markets*. Princeton, NJ: Princeton Univ. Press, 1997.
- [5] J.N. Tsitsiklis, and B.V.Roy, "Regression Methods for Pricing Complex American-Style Options", *IEEE Trans. Neural Networks*, Vol. 12, No. 4, pp. 694-703, 2001.
- [6] M. Magdon-Ismael, "The Equivalent Martingale Measure: An Introduction to Pricing Using Expectations", *IEEE Trans. Neural Networks*, Vol. 12, No. 4, pp. 684-693, 2001.
- [7] B. LeBaron and A.S. Weigend, "A Bootstrap Evaluation of the Effect of Data Splitting on Financial Time Series", *Letters IEEE Trans. Neural Networks*, Vol. 9, No. 1, pp. 213-220, 1998.
- [8] H. White, and J. Racine, "Statistical Inference, The Bootstrap, and Neural-Network Modeling with Application to Foreign Exchange Rates", Vol. 12, No. 4, pp. 657-673, 2001.
- [9] Christensen, L.R., D.W. Jorgenson and L.J. Lau, "Conjugate duality and the transcendental production function", *Econometrica*, 39, pp. 206-218, 1971.
- [10] Diewert, E., "An application of the Shephard duality theorem: A generalized Leontief production function", *J. Political Economy*, 79, pp. 481-507, 1971.
- [11] Diewert, E., and J.T. Wales, "Flexible functional forms and global curvature conditions", *Econometrica*, 55, pp. 43-68, 1987.
- [12] Gallant, A.R., "On the bias in flexible functional forms and an essentially unbiased form: The Fourier flexible form", *J. Econometrics*, 15, pp. 211-246, 1981.
- [13] Gallant, A.R., "Unbiased determination of production technologies", *J. Econometrics*, 20, pp. 285-323, 1982.
- [14] Stinchcombe, M., and H. White, "Using feedforward neural networks to distinguish multivariate populations", Proceedings of the International Joint Conference on Neural Networks, 1994.
- [15] Kuan, C.M., and H. White, "Artificial neural networks: An econometric perspective", *Econometric Reviews*, 13, pp. 1-91, 1994.
- [16] Chan, N. H and Genovese, R. C., "A Comparison of Linear and Nonlinear Statistical Techniques in Performance Attribution", *IEEE Trans. Neural Networks*, Vol. 12, No. 4, July, pp. 922-928, 2001.
- [17] Hornik, K., M. Stinchcombe, and H. White, "Multilayer feedforward networks are universal approximators", *Neural Networks*, 2, pp. 359-366, 1989.
- [18] Hornik, K., M. Stinchcombe, and H. White, "Universal approximation of an unknown mapping and its derivatives using multilayer feedforward networks", *Neural Networks*, 3, pp. 551-560, 1990.

- [19] Haykin, S., *Neural Networks*, New Jersey: Prentice-Hall, 1999.
- [20] Shephard, R., *Cost and Production Functions*, Princeton, NJ: Princeton University Press, 1953.
- [21] Varian, H., *Microeconomic Analysis*, New York: W.W. Norton, 1992.
- [22] Hornstein, A. and P. Krusell, "Can Technology Improvements Cause Productivity Slowdowns?",
- [23] *NBER Macroeconomics Annual 11*, MIT Press: Cambridge MA, pp. 209-259, 1996.
- [24] Greene, W., *Econometric Analysis*, New Jersey: Prentice Hall.
- [25] Schwartz, G., "Estimating the dimension of a model", *Annals of Statistics* 6 (2), pp. 461-464, 1978.
- [26] Akaike, H., "A new look at the statistical model identification", *IEEE Trans. Automatic Control*, Vol. 19, No. 6, pp. 716-723, 1974.

Efthymios Tsionas is Associate Professor of Econometrics at Athens University of Economics and Business (AUEB), Greece. In total, he has conducted studies and research in three (3) institutions including AUEB, Greece, University of Minnesota, USA and University of Toronto, Canada. He has given lectures in Greek and foreign universities at international conferences. Dr. Tsionas has authored or coauthored more than sixty (60) papers appearing in refereed Journals including *Review of Economic Studies*, *Journal of the American Statistical Association*, *Journal of Econometrics*, *Journal of Applied Econometrics*, *Journal of Economic Dynamics and Control*, *Empirical Economics*, etc. He has authored one textbook and serves as reviewer for numerous scholarly journals. His research relates to many fields of econometrics and has supervised numerous MSc and PhD Theses.

Panayotis Michaelides is Lecturer in Economics (407/80) at National Technical University of Athens (NTUA), Greece. He received the Diploma Degree in Mechanical Engineering from NTUA. Then, he earned an MSc in Economics, followed by an MBA in Business Administration and an MSc in Mathematics. Dr. Michaelides completed his PhD on a full scholarship. In total, he has conducted studies or research in three (3) institutions including Athens University of Economics and Business and University of Groningen, The Netherlands. He has given lectures in Greek and foreign universities at international conferences and speaks English, French and German fluently. Dr. Michaelides has authored one textbook, two scholarly books, a lot of teaching material and serves as reviewer for scholarly journals. Also, he has authored or co-authored more than sixty (60) papers published or forthcoming in refereed journals or appearing in refereed international conferences and collective volumes, including *Cambridge Journal of Economics*, *History of Political Economy*, *History of Economics Review*, *Review of Political Economy*, *European Journal of the History of Economic Thought*, *Applied Economics*, *Energy Economics*, *Journal of Economics and Business*, *Economics Letters*, *The Journal of Technology Transfer*, *East-West Journal of Economics and Business*, *Journal of Transport and Shipping*, *IEEE Trans. Neural Networks*, *SPOUDAI*, etc. Dr. Michaelides was recipient of three (3) scholarships for academic excellence and has received the NTUA award for the promotion of Sciences. Also, he has supervised numerous Diploma Theses and has participated in numerous research projects with an active role. His research relates to many fields of economics, econometrics and applied mathematics. He is member of a variety of scientific organizations.

Angelos Vouldis is a Researcher at National Technical University of Athens (NTUA), Greece, since 2001. He received the Diploma degree in Electrical and Computer Engineering in 2000 and the PhD degree in 2007 both from NTUA. He has authored or co-authored papers published or forthcoming in international refereed journals such as *Review of Political Economy*, *Journal of Economics and Business*, *Economics Letters*, *IEEE Trans. Neural Networks*, *IEEE Trans. Instrumentation and Measurement*, *Journal of the Optical Society of America A* or appearing in refereed international conferences. Also, he has participated in several research projects. His research interests include economics, econometrics, applied mathematics and the development of computational algorithms.

Implementation of One Dimensional CNN Array on FPGA - A Design Based on Verilog HDL

Alireza Fasih

Transportation Informatics Group
fasih@qazviniau.ac.ir

Jean C. Chedjou

Transportation Informatics Group
University of Klagenfurt
Klagenfurt-Austria
jean.chedjou@uni-klu.ac.at

Kyandoghene Kyamakya

Transportation Informatics Group
University of Klagenfurt
Klagenfurt-Austria
kyandoghene.kyamakya@uni-klu.ac.at

Abstract— In this paper an FPGA based Implementation of a 1D-CNN with a 3×1 template and 8×1 length will be described. The Cellular Neural Networks (CNN) is a parallel processing technology that has been generally used for image processing. This system is a reduced version of a Hopfield Neural Network. The local connections between a cell and the neighbors in this implementation of this technology is easier than in the case of Hopfield Neural Networks. There are various implementation options of CNN on chips, the best solution being using ASIC technology. The next best is an emulation on top of a digital reconfigurable chip such as FPGA. Designing and developing universal CNN based machines using these technologies is possible. Since FPGAs are COTS components and their growth is high, a simple and economical architecture is obtained by designing an CNN emulation on FPGA chips. This digital designing on FPGA does however have a tradeoff between speed and area. One key target is therefore to reach to a best performance for this emulation architecture under the mentioned constraints.

Keywords— Cellular Neural Network; CNN Emulation on FPGA; Simulation; HDL.

I. INTRODUCTION

This paper briefly introduces a the design of digital emulation of CNN based on hardware description languages. Cellular Neural Network has been introduced by Chua and Yang from the University of California at Berkeley in 1988 [4]. This type of neural networks is a reduced version of Hopfield Neural Networks. One of the most important features of CNN is the local connectivity; in this technology each cell is connected only to its neighbor cells. Due to local connection between a cell and the neighbors a hardware implementation of this type of neural networks is easily realizable [5]. By digitizing the analog behavior of this system (i.e. emulation on a digital platform) one is able realize this system based on FPGA. Due to the local connectivity and processing around each cell the global system works like a parallel processor system [6].

The behavior of a CNN system is based on the settings of the template values. By changing these template values the CNN behavior is affected. This is a very feature for realizing a

universal machine by using CNN [7]. A test-bed for CNN emulation on an FPGA evaluation board is a relatively cheap option and the required development time should be significantly low.

II. CNN DIGITAL EMULATION/MODELLING

CNN mathematical models for each cell are first-order equations like Eq-1 shown below.

Eq-1:

State Equation

$$C \frac{dv_{xij}(t)}{dt} = -\frac{1}{R_x} v_{xij}(t) + \sum_{C(k,l) \in N_r(i,j)} A(i,j;k,l) v_{ykl}(t) + \sum_{C(k,l) \in N_c(i,j)} B(i,j;k,l) v_{ykl} + I$$

$$1 \leq i \leq M; 1 \leq j \leq N$$

For modeling this equation in HDL, we must simplify nonlinear terms. The simplified equation takes the form of equation (Eq-2) as following.

Eq-2:

$$\dot{x} = -x + A * v_y + B * v_u + I$$

In this equation 'A' is a template for feedback operator and 'B' is a template for control.

Eq-3:

Output Equation :

$$v_{yij}(t) = \frac{1}{2} (|v_{xij}(t) + 1| - |v_{xij}(t) - 1|)$$

$$1 \leq i \leq M; 1 \leq j \leq N$$

The output Equation is a linear sigmoid function for limiting the output state value. In some references the sigmoid function is noted by $f(\cdot)$.

Converting equation-2 to a discrete time model is possible. A Discrete Time CNN can easily be mapped to an FPGA by defining digital integrators, multipliers, adders and other digital operators. After defining fundamental operators in FPGA and wiring of/between these operators, a dynamic modeling of CNN is possible [7]. A single CNN cell model is like a first-order differential equation; therefore, solving this equation by this architecture is possible.

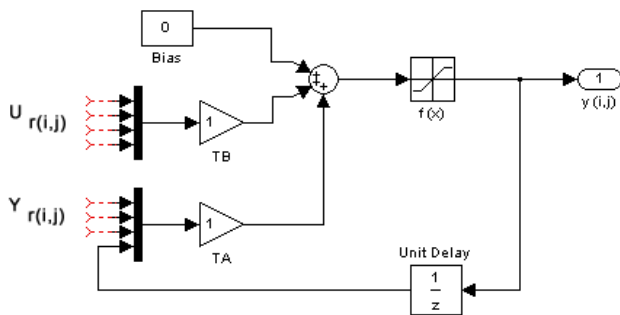


Figure 1. Simplify CNN Cell Dynamic Model

The architecture of this module consists of two main parts, hardware and behavioral sequential units. In the hardware part we must define the relationships of the CNN cells with their neighbors by the template values. These connections are based on convolution operators. With array cloning of convolution modules in HDL we are able to develop/extent the size of the CNN module. Using this approach we can realize a growth of the CNN structure up to a simple 8×1 width. In the CNN structure, there are 2 type templates: control templates and feedback templates. Due to the architecture of the feedback path we have to define a memory block for a appropriate handling of this path. Another main memory unit is defined for integrators components. In this system, all convolution unit should work together concurrently. Therefore the results of $TA*Y$ and $TB*U$ are immediately accessible (see Fig.1).

In the top-level CNN module Verilog code defines 16-Bit 2's complement variables for loading data and templates to this module. One bit for sign and 3 bit for round value and 12 bit float value. Therefore, we are able to load values to this module in the range of $[-7, +7]$. For the 12 bit fixed float register, the accuracy is $1/(2^{12})$. Input data range is limited to the range of $[-1, +1]$; -1 means black and +1 is white value. This procedure means that for image processing purposes we must rescale the image values to this range. On the other hand, value of each gray pixel must be in range of $[-1, +1]$.

According to the Equation-4, we are able to normalize the input data.

Eq-4:

$$U = \text{Pixel_value} * 2 - 1$$

The convolution module loads template values and inputs data and then return the product of these values. The following block diagram shows the convolution operator I/O (see Fig.2). We set zero for out of bound values in the CNN array. The module cloning based on this diagram is simple in HDL code.

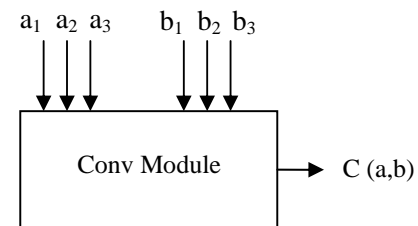


Figure 2. Convolution I/O Block Diagram

This module of Fig.2 operates according to Equation-5.

Eq-5:

$$C(i, j) = \sum_{i=1}^3 (a_i \times b_i)$$

This module is common for $TA*Y$ and $TB*U$.

The code below shows the calling conv2 function for solving the convolution between Control Template and Input Data on cell 7:

```
conv2 ccn7 (M0[7], VB1, VB2, VB3, 16'd0, u7, u6)
```

Further, the convolution on feedback template and output state is similar to the code below:

```
conv2 fcn7 (M1[7], VA1, VA2, VA3, 16'd0, Y[7], Y[6])
```

More details on the convolution module are presented in the paper appendix. Other main important units for developing this module are the integrator and linear sigmoid function. To implement an integrator in HDL we need a register. In previous steps we determined the convolution for feedback and control templates. In the integrator unit we must sum the result in each new cycle with previous values of the register. The convolution module's length defines on 18bits. According to the length of M0 and M1, the length of the integrator register should be 32 bit. The following code below is

obtained after synthesis and is like an 8 integrator that work concurrently.

```

always @(posedge clk)
begin
for (j=0;j<=7;j=j+1)
begin
res[j] = S2[j];
end
end
    
```

In this code the term of S2 is the sum of C(TA,Y) and C(TB,U) from the previous cycle.

The best method to design a sigmoid function is to use an if-then rule. The following code below shows the way this unit operates. "Greater than values" will be limited by this procedure between +1 and -1.

```

for (j=0;j<=7;j=j+1)
begin
if (res[j]>32'sh00000_000) // > 0
begin
Y[j]=16'h1_000; // +1
res[j]=32'h00001_000;
end
if (res[j]==32'sh00000_000) // = 0
begin
Y[j]=16'h0_000; // 0
res[j]=32'h00000_000;
end
if (res[j]<32'sh00000_000) // < 0
begin
Y[j]=16'hf_000; // -1
res[j]=32'hfffff_000;
end
end
    
```

End

In these units the "res" vector is a temporary register for simulating the integrator and "Y" variable is a memory for storing CNN output state. We used 2 level memories for designing totally a simple 8x1 CNN..

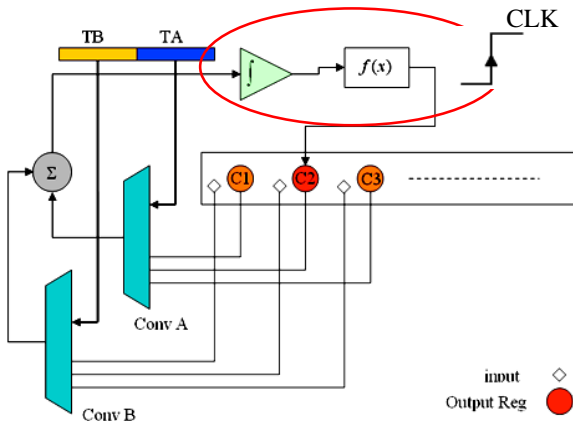


Figure 3. Digital Architecture of CNN

Figure 3 shows the digital architecture of a CNN cell introduced in this paper. According to this architecture the system is synchronous. Parts of integrator, sigmoid function and loading state variable are triggered by a rising clock.

III. SIMULATION RESULTS

To simulate this system we use ModelSim 6 software. The result is very closed to the one obtained from a simulation in Matlab.

For example, by setting TA= [0.5, +1, -1] and TB=Bias=0, the following wave form appears. The converge time for this case in this architecture is 200ns (8 clock).

u= [+1,-1,-1, +1, +1,-1,-1, +1]

TA= [0.5, +1, -1]

TB=Bias=0

The output for this defined template is

xt=[+1,-1,+1,-1,+1,-1,+1,-1]

The converge time for the case below in this architecture is 150ns (6 clock).

u= [+1,-1,-1, +1, +1,-1,-1, +1]

TA= [-1, +2, +1]

TB=Bias=0

The output for this defined template is

xt=[+1,+1,+1,+1,-1,+1,-1,+1]

In an advanced mode, there is another way for simulating the HDL code. In Matlab 2006a we have been able to establish a connection between Modelsim simulator and Simulink.

By a TCP/IP connection between Simulink in Matlab and the Modelsim simulator we were able to test this CNN code on Images. We must operate this CNN module on each Image line separately.

TA= [-1, +2, +1]

TB=Bias=0

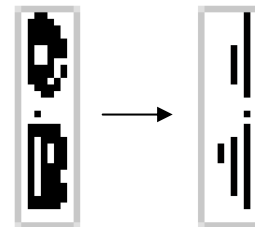


Figure 4. Hole Counting Sample, (Left) Input Image, (Right) output result.

TA= [+1, -1, +1]
 TB= [0, 1, 0]
 Bias = 0

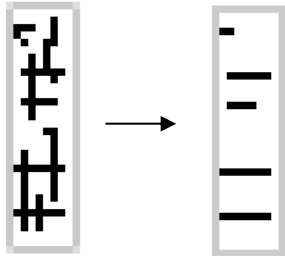


Figure 5. Filter Sample: (Left) Input Image, (Right) output result.

IV. CONCLUSION

In this paper we introduced a new model for simulation and digital implementation/emulation of digital CNN. Finally, the model could be simulated and validate by several templates. Future works are going to improve this module to realize a large-scale CNN based universal machine system.

REFERENCES

- [1] Martinez, J. J., F. J. Toledo, et al. "New emulated discrete model of CNN architecture for FPGA and DSP applications." Lecture notes in computer science: 33-40.
- [2] T. Roska, A. Rodriguez-Vazquez, "Review of CMOS implementations of the CNN universal machine-type visual microprocessors", IEEE Int. Symp. on Circuits and Systems, ISCAS 2000, Geneva-Italia, vol. 2, pp. 120-123, 2000.
- [3] Chua, L. O. and L. Yang (1988). "Cellular neural networks: applications." Circuits and Systems, IEEE Transactions on **35**(10): 1273-1290.
- [4] Chua, L. O. and L. Yang (1988). "Cellular neural networks: theory." Circuits and Systems, IEEE Transactions on **35**(10): 1257-1272.
- [5] J.Zhao, Q. Ren, J. Wang, and H. Meng, "A New Approach for Image Restoration Based on CNN Processor", ISNN 2007, Part III, LNCS 4493, pp. 821-827, 2007.
- [6] Toledo, F. J., J. J. Martínez, et al. (2005). "Image processing with CNN in a FPGA-based augmented reality system for visually impaired people." 8° Int. Work-Conference on Artificial and Natural Neural Networks, IWANN: 906-912.
- [7] Martinez-Alvarez, J. J., F. J. Garrigos-Guerrero, et al. "High Performance Implementation of an FPGA-Based Sequential DT-CNN."
- [8] Eric Y. Chou, Bing J. Sheu, Topzy H. Wu, Robert C. Chang, "VLSI Design of Densely-Connected Array Processors", Proceedings of the International Conference on Computer Design: VLSI in computers & Processor (ICCD '95)
- [9] Lai, K. and P. Leong "Implementation of Time-Multiplexed CNN Building Block Cell." Proc. MicroNeuro 96: 80-85.
- [10] Sadeghi-Emamchaie, S., G. A. Jullien, et al. (1998). "Digital arithmetic using analog arrays." VLSI, 1998. Proceedings of the 8th Great Lakes Symposium on: 202-205.
- [11] Espejo, S., A. Rodriguez-Vazquez, et al. (1994). "Smart-pixel cellular neural networks in analog current-mode CMOS technology." Solid-State Circuits, IEEE Journal of **29**(8): 895-905.

APPENDIX

// 1x3 Convolution Module

```

module conv2 (conv,VA1,VA2,VA3,Y1,Y2,Y3);
    output [17:0] conv; //17
    input [15:0]VA1;
    input [15:0]VA2;
    input [15:0]VA3;
    input [15:0]Y1;
    input [15:0]Y2;
    input [15:0]Y3;
    wire signed [17:0] conv;
    wire signed [15:0] out1;
    wire signed [15:0] out2;
    wire signed [15:0] out3;
    signe_mul MUL1(out1,VA1,Y1);
    signe_mul MUL2(out2,VA2,Y2);
    signe_mul MUL3(out3,VA3,Y3);
    assign conv = out1+out2+out3;
endmodule

// resule range [-7,+7] accuracy 12bit Fixed Float
module signe_mul (out,a,b);
    output [15:0] out;
    input [15:0] a;
    input [15:0] b;
    wire signed [15:0] out;
    wire signed [31:0] mul_out;
    assign mul_out = a*b;
    assign out = {mul_out[31],mul_out[26:12]};
endmodule

```

Clustering In VANETs

Sadaf Momeni

Department of Computer
Iran University of Science and Technology
Tehran, Iran
sadaf_momeni@comp.iust.ac.ir

Mahmood Fathy

Department of Computer
Iran University of Science and Technology
Tehran, Iran
mahfathy@iust.ac.ir

Abstract—We present our proposed algorithm in this paper, a reactive Location Routing Algorithm with Directional Cluster-Based Flooding (LORA-DCBF) for inter-vehicle communication in the context of optimizing traffic flow and increasing vehicular safety. We consider the performance and motorway environment with associated high mobility in highway and compare LORA-DCBF with Location Routing Algorithm with Cluster-Based Flooding(LORA-CBF).In our proposed algorithm, it is possible to have more than one cluster heads in the limited area, but with two opposite direction, this strategy have more stability in the clusters form and more effective. We use a microscopic traffic model, developed in OPNET, to simulate our proposed algorithm to validate our research and shows that LORA-DCBF is more effective in Vehicular communications.

Keywords—Location routing algorithm with directional cluster based flooding, Ad-Hoc networks, VANET networks, inter-vehicular communication, rotating.

I. INTRODUCTION

Generic routing protocols have the design goals of optimality, simplicity and low overhead, robustness and stability, rapid convergence, and flexibility [1]. However, since mobile nodes have less available power, processing speed and memory, low overhead becomes more important than in fixed networks. The high mobility present in vehicle-to-vehicle communication also places great importance on rapid convergence [2]. Therefore, it is imperative that ad-hoc protocols deal with any inherent delays in the underlying technology, be able to deal with varying degrees of mobility, and be sufficiently robust in the face of potential transmission loss due to drop out. In addition, such protocols should also require minimal bandwidth and efficiently route packets [3].

The past few years have witnessed the growth of wireless technologies that have gained increased relevance and acceptance in the form of laptops, PDA's, and personal area networks, all of which require ad-hoc connectivity [4]. The areas of personal computing and communications are converging and evolving to create new patterns of technological deployment and human behavior because of communication-enabled technology [5]. Our hypothesis is that a vehicular point-to-multipoint deployment is likely to become

the first properly mature ad-hoc implementation of these emerging technologies [6].

Economic costs due to transportation delays are reflected in the billions of dollars spent on construction projects and the resulting loss of productivity caused by billions of man hours of lost time on the congested streets and freeways, not to mention health costs related to increased air pollution levels and fuel consumption of stationary automobiles [7]. Presently, according to model simulations, the most common cause of transportation delay in the United States is vehicular accidents, representing nearly 40 percent of nonrecurring delays of freeways and principal arteries.

Although passive safety systems such as seat belts and air bags have been used to significantly reduce the total number of major injuries and deaths due to motor vehicle accidents, they do not improve traffic flow or lower the actual number of automobile collisions [8]. In order to actually lower the number of vehicular accidents, computer and network experts propose active safety systems, including Intelligent Transportation Systems (ITS) that are based on Inter-vehicle Communication (IVC) and Vehicle-to-Roadside Communication (VRC). Presently, technologies related to these architectures and their related technologies may, in the future, significantly optimize traffic flow, which, in turn, can have important economic and safety ramifications [9].

Active vehicular systems employ wireless ad-hoc networks and Geographic Positioning System (GPS) to determine and maintain the inter-vehicular separation necessary to insure the one hop and multi hop communications needed to maintain spacing between vehicles [10]. Location based routing algorithms form the basis of any Vehicular Ad-hoc Network (VANET) because of the flexibility and efficiency they provide with regards inter-vehicular communication. Although several location-based algorithms already exist, including Grid Location Service (GLS), Location Aided Routing (LAR), Greedy Perimeter Stateless Routing (GPSR), and Distance Routing Effect Algorithm for Mobility (DREAM) to name a few.

This paper proposes a Location-Based Routing Algorithm with Cluster-Based Flooding (LORA-CBF) as an option for present and future automotive applications due to the following three advantages:

1. It employs local information to improve the traditional routing used in non-positional algorithms
2. It minimizes flooding of its control traffic by using only the selected nodes, called gateways nodes, to disseminate its messages.
3. We can have two cluster head in limited area with two opposite directions so will have more stability in clusters form.

II. LORA-DCBF SUGGESTED PROTOCOL

LORA-CBF is formed with one cluster head, zero or more members in every cluster and one or more gateways to communicate with other cluster heads. Each cluster head maintains a "Cluster Table," which is a table that contains the addresses, directions and geographic locations of the member and gateway nodes [11].

We propose a reactive algorithm for mobile wireless ad-hoc networks, which we have called Location Routing Algorithm with Directional Cluster-Based Flooding (LORA_DCBF). The algorithm inherits the properties of reactive routing algorithms and has the advantage of acquiring routing information only when a route is needed [12]. LORA_DCBF has the following features: Firstly, this protocol improves the traditional routing algorithms, based on non-positional algorithms, by making use of location information provided by GPS. Secondly, it minimizes flooding of its Location Request (LREQ) packets. Flooding, therefore, is directive for control traffic as it uses only the selected nodes, called gateways, to diffuse LREQ messages. The function of gateway nodes is to minimize the flooding of broadcast messages in the network by reducing duplicate retransmissions in the same region. Member nodes are converted into gateways when they receive messages from more than one cluster head. All the members in the cluster read and process the packet, but do not retransmit the broadcast message. This technique significantly reduces the number of retransmissions in a flooding or broadcast procedure in dense networks. Therefore, only gateway nodes retransmit packets between clusters (hierarchical organization) [13]. Moreover, gateways only retransmit a packet from one gateway to another in order to minimize unnecessary retransmissions, and only if the gateway belongs to a different cluster head and the direction of packet receiving is same with itself.

Apart from normal Hello messages, the protocol does not generate extra control traffic in response to link failures and additions. Thus, it is suitable for networks with high rates of geographical changes. As the protocol keeps only the location information of the [source, destination] pairs in the network, the protocol is particularly suitable for large and dense networks with very high mobility.

The protocol is also designed to work in a completely distributed manner and does not depend upon any central entity. The protocol does not require reliable transmission for its control messages, because each node sends its control messages periodically and can, therefore, sustain some packet loss. This is, of course, important in radio networks like the one being considered here, where deep fades are possible.

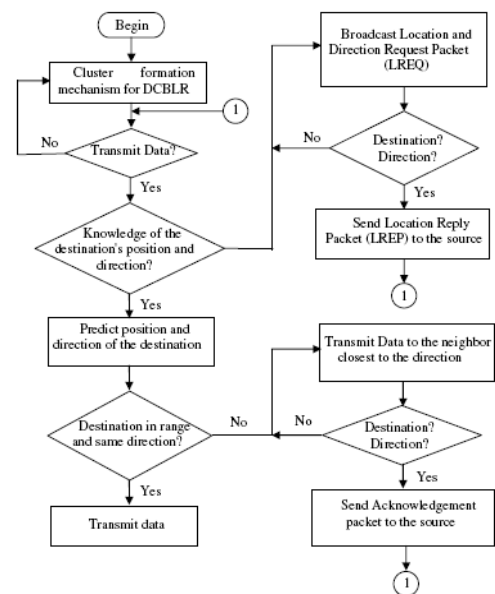
The algorithm we propose in this work does not operate in a source routing manner. Instead, it performs hop-by-hop routing as each node uses its most recent location information of its neighbor nodes to route a packet. Hence, when a node is moving, its position and direction is registered in a routing table so that the movements can be predicted, which is necessary to correctly route the packets to the next hop to the destination.

Upon receiving a location request, each cluster head checks to see if the destination is a member of its cluster. Success triggers a Location Reply (LREP) packet that returns to the sender using geographic routing, because each node knows the position and direction of the source and the closest neighbor based on the information from the LREQ received and the Simple Location Service (SLS). Failure triggers retransmissions by the cluster head to adjacent cluster-heads (Reactive Location Service, RLS). The destination address is recorded in the packet. Cluster-heads and gateways, therefore, discard a request packet that they have already seen. Once the source receives the location of the destination, it retrieves the data packet from its buffer and sends it to the closest neighbor to the destination.

Basically, the algorithm consists of four stages:

1. Cluster formation
2. Location and Direction discovery (LREQ and LREP)
3. Routing of data packets
4. Maintenance of location information.

Figure 1 shows the flow diagram of LORA-DCBF Algorithm.



A. Cluster Formation

The LORA_DCBF algorithm initializes by first forming clusters. When the communications start, every node begins as undecided, starts a timer, and broadcasts a Hello message [14]. If the undecided node receives a Hello message from a cluster head before the timer expires, it becomes a member. Otherwise, it becomes a cluster head.

Cluster heads are responsible for their clusters and have to send a Hello Message periodically. When a member receives a Hello message, it registers the cluster head and responds with a reply Hello message. The cluster head then updates the Cluster Table with the address, position (longitude and latitude) and direction of every member in the cluster. When a member receives a Hello packet from a different cluster head, it first registers the cluster head and changes its status to a gateway and broadcasts the new information to the cluster heads. After receiving the Hello packet, the cluster head updates the Cluster Table with the new information.

In the case where the source wants to send a message to the destination, it first checks its routing table to determine if it has a "fresh" route to the destination. If it does, it first searches its Cluster Table to determine the closest neighbor to the destination. Otherwise, it starts the location discovery process.

B. Location and Direction discovery (LREQ and LREP)

When the source of the data packet wants to transmit to a destination that is not included in its routing table, or if its route has expired, it first puts the data packet in its buffer and broadcasts a Location Request (LREQ) packet.

When a cluster head receives a LREQ packet, it checks the identification field of the packet to determine if it has previously seen the LREQ packet. If it has, it discards the packet. Otherwise, if the destination node is a member of the cluster head, it unicasts the Location Reply (LREP) packet to the source node.

If the destination node is not a member of the cluster head, it first records the address and direction of the LREQ packet in its list and if the source is the same direction with the source, it will be rebroadcasts the LREQ packet to its neighboring cluster heads, otherwise it discards the packet.

Each cluster head node forwards the packet only once. The packets are broadcast only to the neighboring cluster head by means of a directional antenna that routes them via the gateway nodes. Gateways only retransmit a packet from one gateway to another in order to minimize unnecessary retransmissions, and only if the gateway belongs to a different cluster head. When the cluster head destination receives the LREQ packet, it records the source address, direction and location. From this, the destination's cluster head can determine the location of the source node. The destination then sends a LREP message back to the source via its closest neighbor.

Finally, the packet reaches the source node that originated the request packet. If the source node does not receive any LREP after sending out a LREQ for a set period of time, it goes into an exponential back off before re-transmitting the LREQ. Hence, only one packet is transmitted back to the source node. The reply packet does not have to maintain a routing path from the source to the destination, and the path is determined from the location information given by the source node. It is important to note that the path traversed by the LREQ may be different from that traveled by the LREP.

C. Routing of data packets

The actual routing of data packets is then based on the location of source, destination and neighbors and directions of source and destination. Since the protocol is not based on source routing, packets travel the path from source to a destination based on locations. The packets find paths to the destinations individually each time they transmit between the source and the destination. Packets are transmitted based on the knowledge of their relative position. Because the transmission is in the direction of the destination node, the path found will be shorter and stronger than in other routing mechanisms. In non-positional-based Routing strategies, the shortest path is measured in hops. Therefore, the path found may not be the shortest, but the path found using location information will be significantly shorter. If the source of the data packet does not receive the acknowledgement packet before its timer expires, it will retransmit the data packet again. This situation might occur during packet loss due to drop out or network disconnection.

D. Maintenance of location information

The LORA_DCBF algorithm is suitable for networks with very fast mobile nodes because it maintains and updates the direction and location information of the source and the destination every time the pairs send or receive data and acknowledgment packets. The source updates its direction and location information before sending each data packet. When the destination receives the data packet, its direction and location information is updated and an acknowledgment packet is sent to the source.

LORA_DCBF uses MFR (most forward within radius) as its forwarding strategy. In MFR the packet is sent to the neighbor with the greatest progress to the destination. The advantage of this method is that it decreases the probability of collision and end-to-end delay between the source and the destination.

III. NEIGHBOR SENSING

Each node must detect the neighbor nodes with which it has a direct link. To accomplish this, each node periodically broadcasts a Hello message, containing its location information, address, direction and status. These control

messages are transmitted in broadcast mode in one direction and received by all one-hop neighbors that they located in same direction with the source, but they are not relayed to any further nodes. A Hello message contains the following information:

- Node Address.
- Type of node (Undecided, Member, Gateway or Cluster head)
- Location (Latitude and Longitude)
- Node moving direction.

A. Forwarding strategy

LORA_DCBF uses MFR (most forward within radius) as its forwarding strategy. In MFR the packet is sent to the neighbor with the greatest progress to the destination. The advantage of this method is that it decreases the probability of collision and end-to-end delay between the source and the destination.

IV. LORA-DCBF IN COMPARE WITH LORA-CBF

To validate LORA-DCBF, we compared LORA-DCBF against the results of LORA-CBF algorithm. The simulator for evaluating two routing protocols is implemented in OPNET. The simulation models a network of 250 mobiles nodes, moving around a 6283 m length circular road.

The LORA-DCBF and LORA-CBF algorithms employed periodic beaconing to inform neighboring nodes about their presence and both used source-initiated on-demand ad hoc routing protocols to discover routes and they make use of their predictive algorithm to select the best route based on the geographic locations of their neighbor nodes. The main difference here is that LORA-CBF makes the cluster that each cluster has the cluster members with different mobility direction. On the other hand LORA-DCBF makes use of member direction to form the cluster that cluster head and all the cluster members move in same direction. So we could have two cluster head near each other in a geographical limited area, but they must be in different mobility direction.

Figure 2 and 3 show routing overhead result for LORA-CBF and LORA-DCBF. Results show similar behavior for two algorithms, but LORA-CBF has slightly greater routing overhead compared with Routing Overhead.

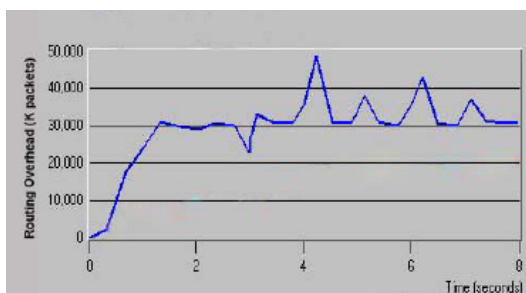


Figure 2. LORA-CBF Routing Overhead

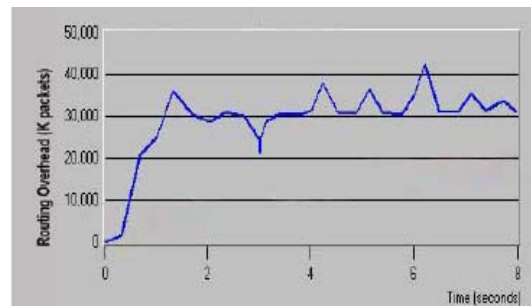
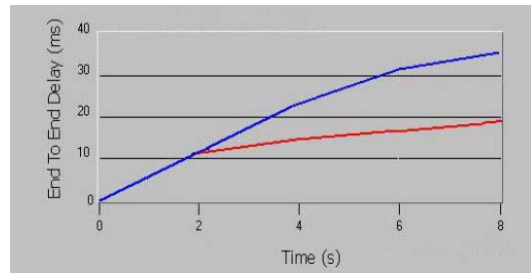
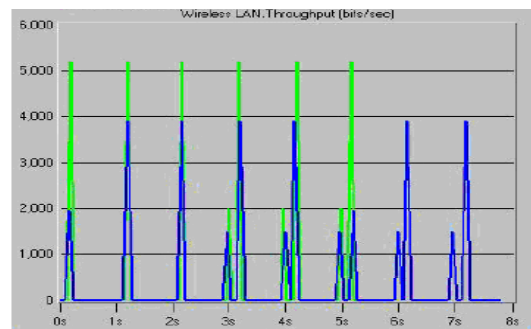


Figure 3. LORA-DCBF Routing Overhead



■ LORA-CBF
■ LORA-DCBF

Figure 4. End to End Delay



■ LORA-DCBF
■ LORA-CBF

Figure 5. Throughput

End-to-End delay (EED), which is presented in Figure 4, LORA-DCBF performs better because it has the more stable cluster formation.

Figure 5 compares the throughput of the algorithms considered. LORA_DCBF shows good results, because one of the factor for LORA_DCBF is to select the cluster based on node direction so it make a robustness rout between cluster head and cluster member.

V. CONCLUSIONS AND FUTURE WORK

In the near future, automobiles may have factory installed wireless ad-hoc network capabilities to improve traffic flow and safety, in part, because it is more cost effective than continually undertaking massive construction projects, which are proving to have limited success. Consequently, future developments in automobile manufacturing will include new communication technologies to help provide more effective

spacing and collision avoidance systems. In order to avoid communication costs and guarantee the low delays required for the exchange of safety-related data between cars, inter-vehicle communication (IVC) systems based on wireless ad-hoc networks represent a promising solution for future road communication scenarios, as it permits vehicles to organize themselves locally in ad-hoc networks without any pre-installed infrastructure.

LORA-DCBF is an algorithm that can possibly be used in future wireless ad-hoc networks because of its reactive geographic routing algorithm, which employs GPS in conjunction with its predictive algorithm, both of which are necessary in mobile networks. Furthermore, LORA-DCBF uses a gateway selection mechanism and direction to determine the cluster to reduce contention in dense networks, which is a predictable scenario in highly congested traffic conditions. Finally, the hierarchical structure of LORA-DCBF facilitates its deployment as part of vehicular ad hoc networks because it requires minimal deployed infrastructure. Future work related to the development of LORA-DCBF will include the integration of GPS, predictive algorithms and geographical maps into a sole architecture and deploy it on a test bed.

REFERENCES

- [1] Carl-Herbert Rokitansky and Christian Wietfeld. Comparison of Adaptive Medium Access Control Schemes for Beacon-Vehicle Communications. IEEE-IEE Vehicle Navigation & Information Systems Conference, 1993.
- [2] Jaime Barceló et al. Smartest Simulation Report, <http://www.its.leeds.ac.uk/smartest>.
- [3] P. Basu, N. Khan, and T. D.C. Little. "A Mobility Based Metric for Clustering in Mobile Ad Hoc Networks." in Proc. IEEE ICDCSW' 01, Apr. 2001, pp. 413-18.
- [4] Xukai Zou, Byrav Ramamurthy and Spyros Magliveras. Routing Techniques in Wireless Ad Hoc Networks Classification and Comparison. Proceedings of the Sixth World Multiconference on Systemics, Cybernetics and Informatics, SCI, July 2002.
- [5] Demetrio Carmine Festa, Giovanni Longo, Gabriella Mazzulla and Giuseppe Musolino. Experimental analysis of different simulation models for motorway traffic flow. Proceedings of the IEEE Intelligent Transportation Systems Conference, 2001.
- [6] Santos, R. A., Edwards, A., Edwards, R. M. and Seed, N. L. (2005) 'performance evaluation of routing protocols in vehicular ad-hoc networks', International Journal Ad Hoc and Ubiquitous Computing, vol. 1, nos. 1/2, pp. 80-91.
- [7] Jatinder Pal Singh, Nicholas Bambos, Bhaskar Srinivasan and Detlef Clawinn. Proposal and Demonstration of Link Connectivity Assessment based Enhancements to Routing in Mobile Ad-hoc Networks. IEEE 58th Vehicular Technology Conference (VTC2003- Fall), vol. 5, pp. 2834-2838.
- [8] Plamondon, R., Lorette, G., "Automatic Signature Verification and Writer Identification - The State of the Art", Pattern Recognition, Vol. 22, pp. 107-131, 1989.
- [9] Object Management Group. Unified Modeling Language: Superstructure, Version 2.0, ptc/03-07-06, July 2003, <http://www.omg.org/cgi-bin/doc?ptc/2003-08-02>.
- [10] Robert Morris, John Jannotti, Frans Kaashock, Jinyang Li and Douglass De couto. CarNet: A Scalable Ad-hoc Wireless Network System. In Proceedings of the 9th ACM SIGOPS European workshop: Beyond the PC: New Challenges for the Operating System, Kolding, Denmark, September 2000.
- [11] Holger Füßler, Martin Mauve, Hannes Hartenstein, Michael Käsemann and Dieter Vollmer. MobiCom Poster: Location-Based Routing for Vehicular Ad- Hoc Networks. ACM SIGMOBILE Mobile Computing and Communication Review, volume 7 issue 1, 2003.
- [12] Christian Lochert, Holger Füßler, Hannes Hartenstein, Dagmar Hermann, Jiang Tian and Martin Mauve. A Routing Strategy for Vehicular Ad-hoc Networks in City Environments. IEEE Intelligent Vehicles Symposium, 2003.
- [13] Michael Möske, Holger Füßler, Hannes Hartenstein and Walter Franz. Performance Measurements of a Vehicular Ad-hoc Network. IEEE 59th Vehicular Technology Conference (VTC2004-spring), vol. 4, pp. 2116-2120, 2004.
- [14] Raúl Aquino S. and Arthur Edwards B." A Reactive Location Routing Algorithm with Cluster-Based Flooding for Inter- Vehicle Communication". Computación y Sistemas Vol. 9 Núm. 4, pp. 297-313, 2006.



Sadaf Momeni received a Master degree of Computer Engineering from Iran University of Science and Technology (IUST) in 2007, She is now involved in researching of Clustering in Vehicular Ad-Hoc Network's. She is a member of R&D department of Parsian e-commerce. assistance to Prof M.Fathy. Her current research interests include Clustering in Vehicular Ad-Hoc Network's.



Mahmood Fathy has received his M.Sc in Microprocessor Engineering from Bradford university (UK) in 1986, and his Ph.D from university of Manchester (UMIST,UK) in 1991. At present, he is an associate professor in Computer Engineering Department, Iran University of Science and Technology. His primary fields of interest include QOS in wireless Ad-Hoc Networks and Computer system Architecture.

Performance Comparison of Band-limited Baseband Synchronous CDMA Using between Walsh-Hadamard Sequence and ICA Sequence

Ryo Takahashi

Next Generation Mobile Communications Laboratory,
Center for Intellectual Property Strategies, RIKEN
2-1, Hirosawa, Wako-shi, Saitama 351-0198, Japan
Email: ryo-takahashi@riken.jp

Ken Umeno

Next Generation Mobile Communications Laboratory,
Center for Intellectual Property Strategies, RIKEN
2-1, Hirosawa, Wako-shi, Saitama 351-0198, Japan
Email: chaosken_umenno@riken.jp

Abstract—Performance of band-limited baseband synchronous CDMA using the orthogonal Independent Component Analysis (ICA) spreading sequences is compared with that using the Walsh-Hadamard sequences. The system we focus on here is where the transmitted signal powers after passing band-limiting filter are not controlled. The orthogonal ICA sequences are generated by ICA. We use ICA not as separator for received signal but as generator of spreading sequences. These performances are also compared with that in the band-unlimited system using orthogonal sequences. We calculate Bit Error Rates (BERs) of these systems by numerical simulation. The quantities BERs in the band-limited baseband systems are lower than that in the band-unlimited baseband system. However, BER in the band-limited system using the orthogonal ICA sequences is much lower than that using the Walsh-Hadamard sequences.

I. INTRODUCTION

In Code Division Multiple Access (CDMA), each of the signals existing in the same frequency band at the same time is assigned as the spreading sequences which are to be orthogonalized as much as possible. In the synchronous CDMA, such as the down-link, the Walsh-Hadamard sequences which realize zero interference are used.

On the other hand, Independent Component Analysis (ICA) for blind source separation attracts much attention in various fields [1], [2]. This technique makes it possible to recover the original signals from only the mixed observed signal data, without knowing how to mix original signals. The observed data $\mathbf{X}(t)$ at time t is expressed as $\mathbf{X}(t) = \mathbf{A}\mathbf{S}(t)$, where each row of the matrix $\mathbf{S}(t)$ means the original signal and \mathbf{A} is an unknown mixing matrix. Under the assumption that each original signal is independent variable and their probability distributions

are nongaussian, the separating matrix \mathbf{W} , such that $\mathbf{S}^{\text{ICA}}(t) = \mathbf{W}\mathbf{X}(t)$, is found by maximizing the nongaussianity of the data. Here, $\mathbf{S}^{\text{ICA}}(t)$ is the recovered signal data by ICA which are scaled and permuted version of the original source signals.

Recently, we have originally proposed the new orthogonal spreading sequences as the Walsh-Hadamard sequences for CDMA, which are generated by ICA [3–6]. In this proposal, ICA is used in information and communication fields not as the separator for received signal, such as Zero Forcing and Minimum Mean Square Error (MMSE) methods, but as the generator of spreading sequences. These orthogonal ICA spreading sequences can be obtained by the following simple procedure. That is to say, we apply the centering process to the original sequences, mix the sequences' data linearly and recover the sequences by ICA. The ICA sequences have almost the same waveform as the original sequences. Thus, The orthogonal ICA sequences can realize the ideal correlation property which the Walsh-Hadamard sequences do not have, although the orthogonal ICA sequences have the orthogonality like the Walsh-Hadamard sequences have.

In this paper, the performance of the band-limited baseband synchronous CDMA using the orthogonal ICA sequences is investigated and compared with that using the Walsh-Hadamard sequence. In [4], [5], the performances of these systems are investigated in the case that the frequency band is not limited. In that case, it is found that Bit Error Rate (BER) in these system using the orthogonal ICA sequence is almost the same as that using the Walsh-Hadamard sequence. In the practical CDMA system, however, the frequency bandwidth is limited. For this, the orthogonality between the simul-

taneous signals in the synchronous CDMA, which is realized by using the orthogonal spreading sequences, are broken. In addition, a certain amount of bit energy is cut by a filter introduced for limiting transmitted signals' bandwidth. In this study, we investigate the system where the transmitted signal powers after passing the filter are not controlled. Thus, we investigate the performance in the band-limited CDMA using the orthogonal ICA sequence and the Walsh-Hadamard sequences by numerical method. For limiting the frequency f bandwidth, we use a Raised Cosine filter whose impulse response $H(f)$ is given as

$$H(f) = \begin{cases} 1, & 0 \leq |f| < \frac{1-\alpha}{2T} \\ \cos^2 \left[\frac{\pi T}{2\alpha} \left(|f| - \frac{1-\alpha}{2T} \right) \right], & \frac{1-\alpha}{2T} \leq |f| < \frac{1+\alpha}{2T} \\ 0, & \text{otherwise} \end{cases}$$

where α is a roll-off factor. In this study, we set $\alpha = 0.22$. By using this filter, the bandwidth is limited as $(1 + \alpha)/T$.

II. ORTHOGONAL ICA SEQUENCE

In this paper, we consider the data recovered by ICA as the spreading sequences, namely ICA sequence. Here, we use FastICA [7] which is one of the ICA algorithms. In brief, the FastICA takes the following steps for recovering the original sequences from the observed data. First, each of the mean values of data is removed from the observed data, namely centering $E\{\mathbf{X}\} = 0$, and be whitened $E\{\mathbf{X}\mathbf{X}^T\} = \mathbf{I}$, as preprocessing. Here, \mathbf{I} means the identity matrix. Next, the mixing matrix \mathbf{W} is guessed by maximizing the property of the nongaussian of these data. Finally, we can obtain K spreading sequences which length are N , but there are restriction such as $K < N$. Here, we use the program of the FastICA in IT++ [8] which is a C++ library in the numerical simulation.

The ICA sequence have several unique properties compared with the original sequences although the waveforms of the recovered ones are almost the same as those of original ones [3], [4]. Because of using this ICA algorithm, the sequences recovered by ICA, namely $\{S_{k,j}^{\text{ICA}}\}$, satisfy the following relations:

$$S_{k,j}^{\text{ICA}} \simeq S_{k,j}/D_{S_k}, \quad (1)$$

$$S_{k,j}^{\text{ICA}} = S'_{k,j} + \overline{S}_k/D_{S_k}, \quad (2)$$

where \overline{S}_k and D_{S_k} mean the length of the sequence N average and the standard deviation of $\{S_{k,j}\}$, respectively. Because of using the centering and the whitening

in the ICA algorithm, $S'_{k,j}$ which is the part of data recovered by ICA satisfies the following relations:

$$\overline{S'_k} = \sum_{j=0}^{N-1} S'_{k,j}/N = 0, \quad (3)$$

$$\sum_{j=0}^{N-1} S'_{p,j} S'_{q,j}/N = \delta_{p,q}. \quad (4)$$

Here, by applying the centering process to the original sequences, namely $\overline{S}_k = 0$, the sequences recovered by ICA have orthogonality as

$$\sum_{j=0}^{N-1} S_{p,j}^{\text{ICA}} S_{q,j}^{\text{ICA}}/N = \delta_{p,q}. \quad (5)$$

We call these sequences the orthogonal ICA sequences. By using sequences which have the good correlation property as the original ones, we can obtain the sequences which realize orthogonality in the synchronous case and can be used in the asynchronous system. In the case where the synchronization is broken, the performance of the sequences recovered by ICA is almost the same as the original sequences because of almost the same waveform each other.

The sequences which have these properties can be realized by the other ICA algorithms, such as the Equivariant Adaptive Separation via Independence (EASI) [6], [9], [10]. This algorithm have simple parallel structure and can be implemented simply into the hardware [10].

Here, we use the Chebyshev chaotic spreading sequences as the original for the orthogonal ICA sequences. It is known that these Chebyshev sequences have good correlation property and arbitrary number of the sequences, whose code lengths are also arbitrary, can be obtained easily [11], [12]. The k -th sequence is defined as follows:

$$S_{k,j+1} = T_q(S_{k,j}), \quad q \geq 2. \quad (6)$$

Here, $T_q(x)$ is the q -th order Chebyshev polynomial defined by $T_q(\cos \theta) = \cos(q\theta)$ and j is time or position in this code sequence. It is known that this Chebyshev map is ergodic and it has the ergodic invariant measure

$$\rho(x)dx = \frac{dx}{\pi\sqrt{1-x^2}} \quad (7)$$

and it satisfies the orthogonal relation

$$\int_{-1}^1 T_i(x)T_j(x)\rho(x)dx = \delta_{i,j} \frac{1 + \delta_{i,0}}{2}, \quad (8)$$

where $\delta_{i,j}$ is the Kronecker delta function. From the above facts these chaotic sequences generated from

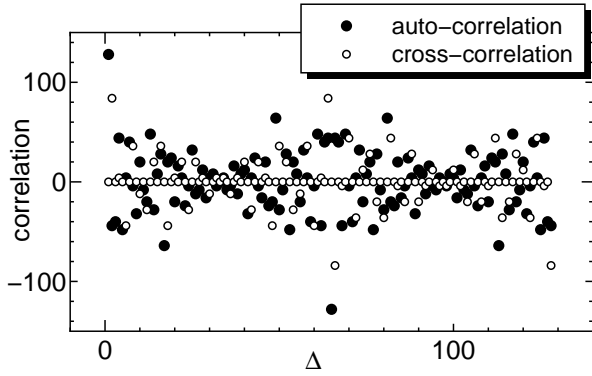


Fig. 1. Correlation property of the Walsh-Hadamard sequences.

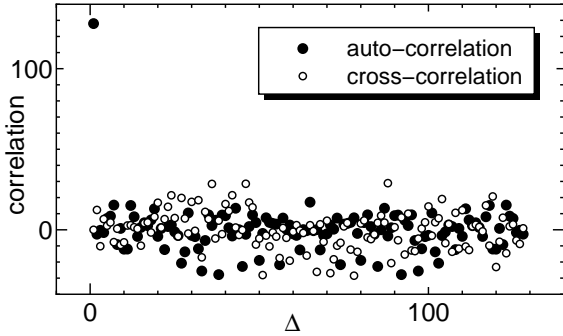


Fig. 2. Correlation property of the orthogonal ICA sequences whose originals are Chebyshev chaotic sequences.

$T_q(x)$ of different orders can be used as the naturally orthogonal spreading sequence in CDMA from the ergodic principle [11–14].

III. CORRELATION PROPERTY

We compare the correlation property of the orthogonal ICA sequences whose original sequences are the above Chebyshev chaotic sequences with that of the Walsh-Hadamard sequences. We calculate the auto-correlations and the cross-correlations given by $\sum_{j=0}^{N-1} S_{k,j} S_{k,j+\Delta}$ and $\sum_{j=0}^{N-1} S_{k,j} S_{i,j+\Delta}$ ($i \neq k$), respectively. Here, the sequence code satisfies the relation $S_{k,0} = S_{k,N}$ and Δ means the phase difference. Figures 1 and 2 show examples of correlation properties of the Walsh-Hadamard sequences and the orthogonal ICA sequences as functions of the phase difference Δ for these code length $N = 128$, respectively. From these figures, it is found that the orthogonal ICA sequences have better correlation properties to be synchronized with the received signal at the correlation receiver than the Walsh-Hadamard sequences.

IV. BIT ERROR RATE

We compare the performance of the band-limited baseband synchronous CDMA using the orthogonal ICA sequence with that using the Walsh-Hadamard sequence. For this, we calculate the BERs by numerical simulations.

In this study, we set the number of users for $K = 10$ and the spreading factor for $N = 128$. The average power of each chip of spreading sequence is set for unity 1. Thus, the initial spread bit energy E is equal to N . Here, we investigate the system where the transmitted signal powers after passing the filter are not controlled. Thus, the transmitted signal energy in the air, whose bandwidth is limited, is usually lower than E . This is because a filter for limiting the bandwidth cut a certain amount of bit energy. For limiting the bandwidth, we use the Raised Cosine filter and the bandwidth $(1 + \alpha)/T$ is set for $(1 + \alpha)T_c$, where $1/T_c$ is a chip rate. We consider the channel where the additive white Gaussian channel noise whose power is σ^2 exists. We obtain the distribution of the correlation output of the receiver by 10000 sample bits numerical simulation and calculate the mean value and the variance of this distribution. We use the randomly selected sequences from the set obtained in $N = 128$. By using these two values and the complementary error function, BERs are estimated. Finally, we can obtain the average BERs in the systems using the orthogonal ICA sequences or the Walsh-Hadamard sequences.

We also compare these BERs with those in band-unlimited synchronous CDMA. The quantity BER in the band-unlimited CDMA using the orthogonal spreading sequence is already known in [4]. The quantity in baseband system can be estimated by using the standard Gaussian approximation and Signal to Interference plus Noise Ratio (SINR) obtained analytically in [4]. Based on Pursley [15], we have derived the SINR of the orthogonal sequences in the band-unlimited baseband synchronous CDMA as

$$\text{SINR} = \sqrt{\frac{E}{\sigma^2}}. \quad (9)$$

Figure 3 shows the BERs as functions of initial bit energy per noise power. Initial bit energy means the one before passing the RC filter. The line is drawn by using the above analytical SINR and the standard Gaussian approximation. Each point is the data obtained by numerical simulation. Table I shows the a part of the BER data in Fig. 3. These values are for 18 dB.

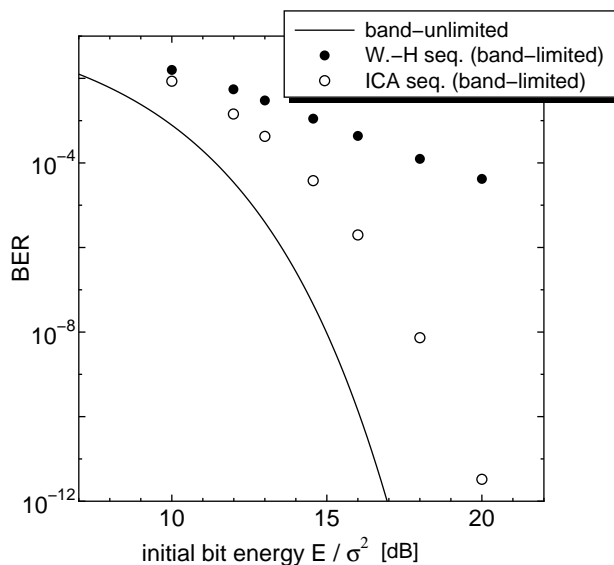


Fig. 3. BERs in synchronous CDMA using the several orthogonal sequences as functions of initial bit energy per noise power. The line is drawn by using the analytical formula and each point is obtained by numerical simulation for $K = 10$, $E = 128$.

Theoretical figure of BER in band-unlimited baseband system using the orthogonal sequences for the same parameters as the above simulation are 9.84449×10^{-16} .

TABLE I
BERs IN BAND-LIMITED BASEBAND SYNCHRONOUS CDMA FOR ABOUT 18 dB.

Walsh-Hadamard seq.	1.25026×10^{-4}
Orthogonal ICA seq.	7.36994×10^{-9}

From these values and figure, it is found that the BERs in the band-limited baseband system are larger than that in band-unlimited baseband system. However, the BER in the band-limited system using the orthogonal ICA sequences is much closer to that in the band-unlimited system than that using the Walsh-Hadamard sequences.

V. DISCUSSION AND CONCLUSION

In the present paper, the performance of the band-limited baseband synchronous CDMA using the orthogonal ICA sequences is investigated and be compared with that using the Walsh-Hadamard sequences. Here, these are the systems where the transmitted signal powers after passing the filter are not controlled. We calculate the BER of these systems by numerical simulation. We focus on the relation between the BER and initial bit energy per noise power which is the one before passing the RC filter. In addition, these BERs in the band-limited synchronous

CDMA are compared with those in the band-unlimited synchronous CDMA using orthogonal sequences. It is found that the BERs in the band-limited systems are larger than that in the band-unlimited baseband system. However, the BER in the band-limited baseband system using the orthogonal ICA sequences is much closer to the band-unlimited system than that using the Walsh-Hadamard sequences. The orthogonal ICA sequences can realize much lower BER than the Walsh-Hadamard sequences in the band-limited synchronous CDMA. This is because it is highly possible that the part of signal energy which are cut off by the Raised Cosine filter in the system using the orthogonal ICA sequences is much lower than that using the Walsh-Hadamard sequences. That is to say, it is highly possible that the spectrum density of the orthogonal ICA sequences inside the limited bandwidth is larger than that of the Walsh-Hadamard sequences. In addition, the orthogonality realized in the band-unlimited system is broken in the band-limited system.

For the band-unlimited synchronous CDMA, the Walsh-Hadamard sequence is one of the most effective spreading sequences. Thus, this sequence is used now in the actual system, namely the band-limited synchronous CDMA such as down-link, as the most effective spreading sequence based on the performance in the band-unlimited system. However, from these results, it is found that the orthogonal ICA sequences are more effective significantly for the band-limited synchronous CDMA than the Walsh-Hadamard sequences.

ACKNOWLEDGMENT

The authors would like to thank Dr. Etsushi Nameda who is the visiting scientist at Next Generation Mobile Communications Laboratory, RIKEN, for fruitful discussions.

REFERENCES

- [1] A. Hyvärinen, J. Karhunen and E. Oja, ed, Independent Component Analysis, Wiley, 2001.
- [2] K. Umeno, "Chaos and codes in communication systems", *Proc. IPSJ Symposium*, vol.19, pp.312–316, 2005.
- [3] R. Takahashi, S.J. Kim and K. Umeno, "Super amplification of SNR with an independent component analysis in chaos CDMA", *Technical Report of IEICE*, vol. 106, no. 413, NLP2006–102, pp. 1–6, Dec. 2006.
- [4] R. Takahashi, S.J. Kim and K. Umeno, "Analysis of bit error rate using the chaos spreading sequence with an independent component analysis filter", *Technical Report of IEICE*, vol. 106, no. 573, NLP2006-142, pp. 1–6, March 2007.

- [5] R. Takahashi, S.J. Kim and K. Umeno, "Performance of the recovered pseudo-noise binary sequences by independent component analysis for CDMA", *Proc. 2007 Int. Symposium on Nonlinear Theory and Its Applications (NOLTA2007)*, pp.148–151, Sept. 2007.
- [6] R. Takahashi, S.J. Kim and K. Umeno, "Generating complete orthogonal spreading sequences by equivariant adaptive separation via independence for CDMA", *Proc. 15th IEEE Int. Workshop on Nonlinear Dynamics of Electronic Systems (NDES2007)*, pp.126–128, July, 2007.
- [7] A. Hyvärinen, "Fast and robust fixed-point algorithms for independent component analysis", *IEEE Trans. Neural Netw.*, vol.10, pp.626–634, May 1999.
- [8] Available: <http://itpp.sourceforge.net/>
- [9] J.F. Cardoso and B.H. Laheld, "Equivariant adaptive source separation", *IEEE Trans. Signal Processing*, vol.44, pp.3017–3030, Dec. 1996.
- [10] S.J. Kim, K. Umeno and R. Takahashi, "FPGA implementation of EASI algorithm", *IEICE Electron. Express*, vol.4, no.22, pp.707–711, 2007.
- [11] K. Umeno and K. Kitayama, "Spreading sequences using periodic orbits of chaos for CDMA", *Electron. Lett.*, vol. 35, no. 7, pp. 545–546, 1999.
- [12] K. Umeno and K. Kitayama, "Improvement of SNR with chaotic spreading sequences for CDMA", *Proc. 1999 IEEE Information Theory Workshop*, p. 106, 1999.
- [13] K. Umeno and A. Yamaguchi, "Construction of optimal chaotic spreading sequence using Lebesgue spectrum filter", *IEICE Trans. Fundamentals*, vol.E85–A, no.4, pp.849–852, April 2002.
- [14] C.C. Chen, K. Yao, K. Umeno and E. Biglieri, "Design of spread-spectrum sequences using chaotic dynamical systems and ergodic theory," *IEEE Trans. Circuits Syst. I*, vol. 48, pp. 1110–1114, Sep. 2001.
- [15] M.B. Pursley, "Performance evaluation for phase-coded spread-spectrum multiple-access communication - Part I: System analysis", *IEEE Trans. Commun.*, vol. 25, pp. 795–799, 1977.



Ken Umeno received his BSc degree in electronic communication from Waseda University, Japan, in 1990. He received his MSc and PhD degrees in physics from University of Tokyo, Japan, in 1992 and 1995, respectively. From 1995 to 1998, he was a special postdoctoral fellow of RIKEN, Japan. He joined the National Institute of Information and Communications Technology (NICT), Japan, in 1998. He led the Chaos-CDMA project team of Japan Science and Technology Corporation during the term 2000–2003. Currently, he is a CEO and president of ChaosWare Inc. and a senior researcher of NICT. His research interests include chaos-based computation and chaos-based communication networks as well as the fundamental theory of dynamical systems and computer science. He received LSI IP Award in 2003.



Ryo Takahashi received his BSc, MSc and PhD degrees in physics from Tokyo University of Science, Japan, in 2001, 2003 and 2006, respectively. He was an expert researcher at National Institute of Information and Communications Technology (NICT), Japan, and be currently a research scientist at RIKEN, Japan. His research interests include statistical physics, nonlinear dynamical systems, and information and communications theory. He is a member of the IEEE, the Physical Society of Japan and the Japan Society for Industrial and Applied Mathematics.

Evaluation of nonlinear system behaviors in Military Supply chain

S.K. Bhagavatula, J.C. Chedjou, K.R. Anne, K.Kyamakya
Institute for Smart Systems-Technologies
University of Klagenfurt
Klagenfurt, Austria

Abstract—This paper discusses the concepts of military supply chains and make comparisons with commercial supply chains. After an introduction, the major observations concerning military supply chain deficiencies like unmanageable demand forecasting are addressed. Furthermore, the uncertainties and invalid priorities in military inventory operations are described. Further considerations do examine the required optimization models and analyze both the product and information flows during warfare in military supply chains. Finally, a new model which withdraws the nonlinear system behaviors in military supply chain is suggested.

Keywords—Military Logistics, Military Supply Chain, Inventory visibility, Nonlinear System Behavior.

I. INTRODUCTION

Supply chain management is a combination of management and science. The concern of supply chain management is how firms utilize their suppliers' processes, technology and capability to increase competitive advantages. We see these supply chain networks in many sectors such as computers, toys, pharmaceuticals, automotive, consumer goods, military, etc. The formal definition of military supply chain is "All entities belonging to military or nation logistics separately, which are involved in military logistics, and network system formed by activities and interactions of the entities"[6]. Where as military has very large, complex distribution and supply systems. The basic need of military forces is to deter war and build the security to the nation. While considering the supply chain perspective/objective, in military, services are provided to prepare for warfare, not for profit. Military supply chains serve far away, always moving and have other high-risk operations in harsh conditions. In military supply chains commodities vary from every day supplies to specialized military equipments such as weapons, tanks etc. To build the same advantages, logistics management and distribution are also viewed as the key components in supply chain management (figure.1) [3].



Figure.1. The relationship among distribution, logistics management, and supply chain management

At around 700 BC, a provision has made in advance to stock supplies. During this period military were employing more number of animals as means of transportation to feed and equip a force. To improve logistics and supply chain networks one initiated the soldiers to carry much of their equipment and supplies. However, in the fifth century AD armies expanded their supply chains by constructing roads, interior lines of communication and getting stock details earlier to an attack. As the centuries passed, rapid changes fall out in military operations. However, the evolved solutions are not of long duration in military supply chains.

During the Crimean war, one identified the primary courses of the warfare as logistics, supply chain, training and team coordination were recognized. At this instant one introduced the hierarchy system in military sector for provision of supply chain support. The view of administration and logistic support to the troops in the field afforded greater extent. Until this period, supplies were determined for one or two battles. When established foundations for a long war then required to uphold the supply chain between large populations with mass mobilization was necessary. To meet the majority of supplies, military tied with the railway system and kept the operations functioning.

During the first world war, military found it difficulty to predict the demand or re-supply, when military kept on the move. One could identify cases where military people had stopped or expected to stay for long term; and such event makes consumption more than the pre-war estimates. Such unanticipated changes in the global military operations aimed to unify the supply chain networks with all military groups/hierarchical levels. At once military planners have achieved readiness on large inventories to reduce inventory on hand.[1]

During the second world war, again railways showed to meet armies' requirements. However, air and sea mode also made important contributions during this warfare. From eighteenth century onwards, the total process of the supply chain, which is making support to commercial business, is now being adapted by and adapted within the military environment. The larger and faster moving of military, the longer the supply chain became, the more difficult it became to re-supply. To defeat such aspects, initially 'Lean' and 'Focussed' Logistics were developed by the US military and acknowledged by the UK Military to support the military operations. As well one could initiate to verify the total

integral stockholding and transportation systems. In addition, one extended the third party support to military operations with civilian contractors. At the end of the 20th century, military maintains main supply bases to meet the demand and move the demand through the supply chain as required [1-2].

II. COMMERCIAL VS MILITARY

The military environment is of high complexity as it uses isolated, independent and incompatible systems, processes and data. Therefore, the modeling of military scenarios is of necessary importance as models can provide in-depth explanation of the scenarios and control their occurrence and evolution in both time and space domains as well. In military, as well the supply chain management strives for qualitative changes. In commercial supply chain, a consumer's demand for a product can be changed within a period of months to acquire gain. The supply chain management conceptual models for both commercial and military are remarkably same. However, some significant differences are imparted to an evident difference in between commercial and military supply chains (figure.2). In commercial supply chains, the first issue is about absence of maintenance and another is that the flow of products/materials between suppliers and retailer, which is in unidirectional. In military supply chain the transportation, distribution/warehousing are bidirectional, that means from producer to military user and vice versa. Since military move the materials for maintenance and for medical care. The other differences are external factors including deployment of forces i.e. soldier, military regulations, joint interoperability, mission requirements [3-4].

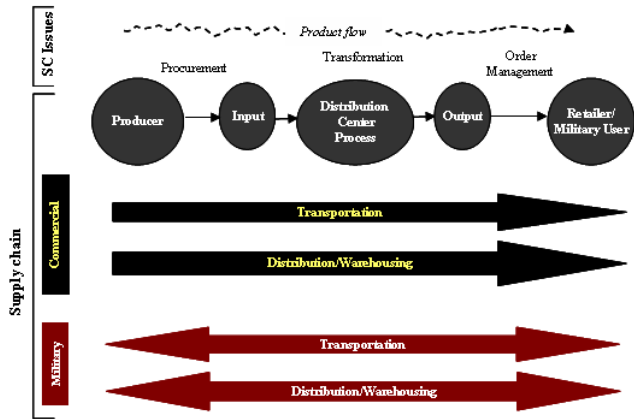


Figure.2. Commercial and Military Supply Chain Management

In commercial supply chains, people can see what is going on and they can change the business processes they have. They can take what they see and embed that into an improved method of doing business i.e. reengineering. Whereas in military supply chain, data transparency and embed into the new or improved system is an unmanageable issue because of security crisis [4]. Another major issue is concern in military supply chain is material families.

In military, materials are places in different categories as classes. It is difficult to analyze the demand issues in terms of

range of supplies, movement of supplies, and reserving supplies for warfare. The resources consist of a complicated web of supplies, ranging from food and clothing to nuclear weapons. In military, inventory management must keeps records and stores the material to take the possibility of war at any moment. The necessity to store resources is to use on a daily basis as well as store resources for times of war. The military organizes all supplies into ten different classes as below (figure. 3) [7].

CLASS TYPE OF SUPPLY					
Class	Symbol		Class	Symbol	
CLASS I	(☾)	Subsistence and commercially bottled water	CLASS VI	(⊙)	Personal demand items
CLASS II	(☒)	Clothing, individual equipment, tools, administrative supplies	CLASS VII	(☉)	Major end items, such as launchers, tanks
CLASS III	(☉)	POL includes bulk fuels and packaged products such as antifreeze	CLASS VIII	(⊕)	Medical supplies, including repair parts for medical equipment
CLASS IV	(☒)	Construction items, including fortification and barrier material	CLASS IX	(⊗)	Repair parts and components,
CLASS V	(☒)	Ammunition of all types	CLASS X	(CA)	Materiel to support nonmilitary programs

Figure.3: Class Type of military supply

Each class consists of subclasses, which gives thorough information about supplies. The subclasses data presents as follows (fig. 4) [7].

CLASS & SUB CLASSES			
Class	Sub Classes		
CLASS I	A - Nonperishable C - Combat Rations R - Refrigerated	S - Non refrigerated W - Water	
CLASS II	A - Air B - Ground Support Materiel E - General Supplies	F - Clothing G - Electronics M - Weapons	T - Industrial Supplies
CLASS III	A - POL for Aircraft W - POL for Surface Vehicles P - Packaged POL		
CLASS IV	A - Construction B - Barrier		
CLASS V	A - Air Delivery W - Ground		
CLASS VI	A - Personal Demand Items M - Personal and Official Mail P - Ration Supplemental Sundry Pack		
CLASS VII	A - Air B - Ground Support Materiel D - Admin. Vehicles	J - Tanks, Racks, Adapters & Pylons L - Missiles M - Weapons	N - Special Weapons T - Industrial Materiel X - Aircraft Engines
CLASS VIII	A - Medical Materiel B - Blood/Fluids		
CLASS IX	A - Air B - Ground Support Materiel D - Admin. Vehicles G - Electronics	K - Tactical Vehicles L - Missiles M - Weapons N - Special Weapons T - Industrial Materiel	

Figure.4: Class and sub classes of military supply chain

In supply chain management, the flow carries in two ways i.e. downstream and upstream from factory to the end user. The end user may commercial customer or military user or any other depends on sector. In military, at initial point, the product will examine to determine accuracy, quality and condition. Hence, the products examination induces less status for reverse logistics. The baseline of military Supply Chain throughput was unavailable to secondary markets for military unique products like weapons, ammunition etc. In military,

funding, purchasing actions, and technology changes are not reliable, since the risk is too high for industry to pre-position the components for the military.

In almost all supply chain networks, the raw material suppliers are at one end of the supply chain. In commercial, suppliers are connecting to manufacturers and distributors, which are in turn connecting to a retailer and the end customer. In general, the number of organizations begins with suppliers, who provide raw materials to manufacturers, which manufacture products and keep those manufactured goods in the warehouses. Then they send them to whole sales or distribution centers that ship the goods to retailers. The customers then buy products from retailers [10].

The sectors have slight differences concerning the structures of the supply chain networks. The figure.5 illustrates the scenario between commercial and military supply chains. In both supply chains consists of material and information flow.

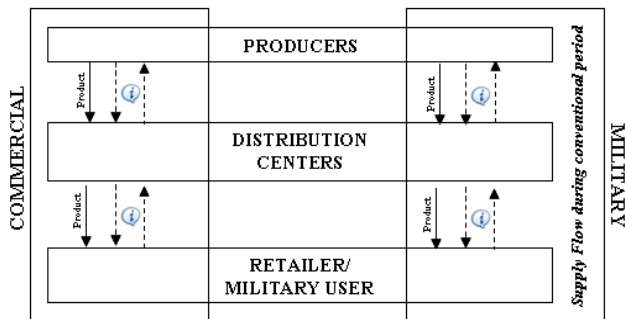


Figure.5: Three-Level supply chain networks

In commercial supply chain, retailer identifies the demand; communicate the demand information to distributor. When distributor receives the order information from retailer, checks the inventory level. If finds low, send the order information to producer otherwise accomplish the retailer request by supplying the product with prior information. If distributor finds low inventory then producer receives demand information from distributor to produces the products. As per distributor demand producer produces the product and sends the product to distributor with prior supply information. The above process exercised between three troops such as producer, distributor and retailer in commercial supply chain [10].

In military, as well, supply chain network can considered as three levels between producer, distributor and military user. The significant changes between military and commercial supply chain is product flow. In military, material flow can be view in two scenarios. One is conventional flow, which processed between producer, distribution centers and military user. The other one is nuclear flow, which comes at warfare. Where as the customer in military, may vary as Army, Marines, Air Force and Navy. In addition, figure.5 also presents military supply flow, which states the same scenario of commercial supply network. The military user identifies the demand and communicates the demand information to distribution centers. When receives the order information from military user, checks the inventory level at depots. From

figure 4, it supposes that the material flows in military are in many forms. Existences of different material are stored at different depots thru distribution centers. If the depot find low inventory, send the order information to distribution centers otherwise accomplish the distribution centers request by supplying the product with prior information to distribution centers. In other case, a distribution center finds information about low inventory then sends demand information to producer, to produces the required products. With prior information producer produces and send product to distribution centers with supply information. Now distribution center directs the supplied product with supply information to distribution centre. The above process exercised between three troops such as producer, distribution centers and military user during conventional period [9]. Whenever the military posited in warfare, supply chain needs to transfers the information and material flow. Since the warfare is an emergency state of affairs which needed to support the operations with an essential materials such as arms and ammunitions. If the supply lines are, too long i.e. three level supply chain flows, it is extremely difficult to meet the military operations.

In Section III will briefly describe present scenario of military supply chain and their deficiencies. Moreover, describes the uncertainties in military supply chain. We consider the Lorenz system model to describe new model during warfare in Section IV. Finally presents the brief conclusions.

III. MILITARY SUPPLY CHAIN NETWORKS

A. Present scenario of military supply chain

During the First World War, military supply chains were managed as groups. Individual groups run their own processes for placing orders, maintaining and moving inventory to war fighters. With rapid changes in the global military operations, supply chain networks are coupled with all military groups/hierarchical levels. In Military, war operations are rare events. During peacetime, as well, the military consumes resources that are similar to a commercial supply chain. However, military supply chain decisions heavily depend on strategy, tactics and intelligence than cost efficiency. During wartime, the supply chain decisions are depend on operational and tactical. The ancient warfare conducted by using conventional military weapons and battlefield tactics between two or more states with an open challenge. The idea behind the conventional warfare is to weaken or destroy the opponent's military force. With this conventional warfare, the supply chain and logistics issues can handle according to scenario. However, many changes influence the present military systems. The present situations were unable to predict the wartime and conduct the warfare without conforming to legality, moral law, or social convention. As each individual nation perceiving their welfare and getting more influence by political bodies. To support this enhanced speed, creating new challenges for military supply chain. However, the present military supply chain is becoming dynamic and getting more influence by political individuals.

The idea behind the present military supply chain upholders is to support their transformed combat force with fast, accurate and flexible supply line. To meet these challenges introduced many practical application of science and models. Also employs technologies, information systems and procedures to predict and prioritize military requirements and allowing for appropriate sustainment. Military supply chain models allowed the nation to new challenges for conducting surge operations. Combining the military and commercial strengths for better turnout and attaining optimal procurement, supply, maintenance and distribution times for efficient supply chain system. Real-time stock age information, just-in-time deliveries are also promoting by military sections [5]. In fact, military achieved possibility of future success, still receiving state of problems that needs to be resolve. From these problems military supply line is getting trouble. The problems makes ineffective to inventory management, waste, inefficiency, and delay across the supply chain. Military planners are attempting a set of scenarios and various probabilities to resolve problems.

B. Uncertainties in Military Supply Chain Networks

Even though in military, supply chain brings different uncertain demands to supply line. Because demand may occur with in short time and unpredictable. In military, the need may arise from basic supplies needs to with major items such as tanks, weapons. According to priority, indicated the supply line condition and made decision by hierarchic officials. The idea behind the military inventory is to ensure the stock on hand when required at warfare.

The above statements suppose that to anticipate or forecast the wartime. In urgency, military place an order and wait for the stock. Some time stock may get delay. In that situation military needs to accept the unnecessary prices even if stock gets too late or earlier. The situation may sort out as inventory holding costs for storage of stock or the cost for out dated items such as perishable. So here in military supply chain, the major identified problem as inventory visibility. Without stock visibility retailers as well as customers (i.e. military) struggles to commit an orders. The lack of visibility on inventory, results in miscalculated order quantities. In addition, peak time orders based on pinch demand causes shipping delays. Due to this poor visibility, military planners were unable to order in urgency. Therefore, inventory gets into trouble with this invalid prioritize. To accurate, the inventory level throughout the military supply chain needs to improve visibility and reduce transit delays [5].

The attention of a military supply chain is entirely different from that of a commercial supply chain. The military operates on an operational base, where the required commodities have to be transport to a soldier at the war front. The unique characteristic of military supply chain is its back-pipeline, which moves the 'goods' like injured troops and damaged equipment, in the reverse direction i.e. from the front line to its operational base . The military has tried to adopt many models practices from the commercial supply chains. However, the present military supply line head-on with demand. The head-on problem is that uncertainty demand occurrence with in short time. This uncertainty was unable to

be identified in advance. From section II, the last statements state the military inventory maintenance. In inventory maintenance, activities are getting trouble in about events that keeps the stock on hand before the warfare. Inaccurate inventory forecasts can affect at a variety of process areas includes supply management, transportation, distribution depots, and depot maintenance. This in turn will have an impact on the cost of commodities, also a conflict occurs, increasing demand for supplies, and existing stock of material are insufficient. Accurate inventories are critical to maintaining readiness in the presence of variable demand.

IV. SYSTEM MODEL

The modeling process in this section exploits the results in Ref. [8]. Indeed this reference discusses some scenarios related to the flow of materials along a three-echelon commercial supply chain and models them by three coupled equations.

In this paper, we consider the case of a three-echelon military supply chain and explain some specific scenarios related to the flow of materials (i.e. arms and ammunitions). This interesting consideration can lead to various possible cases when dealing with the flow of materials from supplier to military user. Two striking cases can be envisaged. The first case (which is an ideal case) supposes the traffic of materials (with no inconvenience) along the three echelons of the supply chain and a good communication or exchanges between them as well. This case does not however describe a realistic scenario since an emergency (see second case below) can occur due to the malfunctioning of a significant number of arms or lack of ammunitions during warfare [11,12]. This situation is discussed later.

The modeling process of the first case is based on a comparative analysis between commercial and military supply chains in order to show that this specific scenario can be modeled by the set of the equations in Ref. [8].

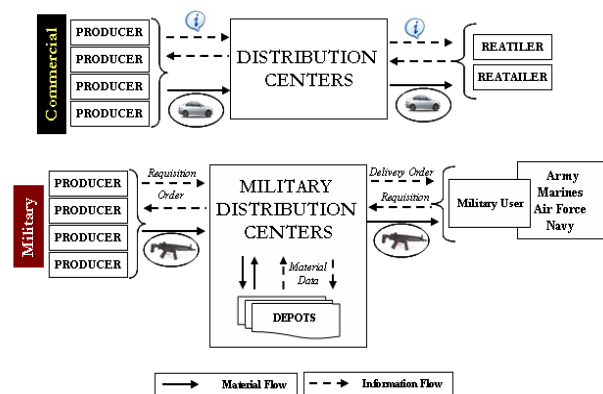


Figure.6: In First case the Material and Product flows in Military and Commercial supply chains

In figure.6, the demand information is transmitting with in the layers of the military supply chain with a delay of one unit time. This indicates the information flow from military user to producer and vice versa. In addition, the materials flow from the producer to military user via distribution center. As

illustrated in figure.6, three-layer military supply chain model can show in mathematical expression as equations. The equations are derived from the Ref. [8].

The quantity demanded by military user for material in current period is decides that how much of demand is satisfied in previous period. The demand can obtain from previous inventory level at distributor, delivery efficiency of distributor and the user (i.e. military) demand satisfaction. This can be represented as shown in equation (1)

$$x_i = my_{i-1} - nx_{i-1} \dots\dots\dots (1)$$

At distributor level, needs to take the combined effect of military user and producer into consideration before making an order. In distributor center, makes their decision on inventory levels Apart from this distributor, also need to take into consideration the expected loss rate that can take place on the producer's supplies. This can be represented as shown in equation (2)

$$y_i = rx_{i-1} - x_{i-1}z_{i-1} \dots\dots\dots (2)$$

The producer's production typically depends on the distributor's orders and the safety stock. However, distributor's orders are again depended on military user order, i.e., the producer needs to take the combined effect of military user and distribution into account before making production at producer position. This can be represented as shown in equation (3)

$$z_i = x_{i-1}y_{i-1} + kz_{i-1} \dots\dots\dots (3)$$

- Notations:
- i* Time period
 - m* Distributors efficiency while delivering the product
 - n* Ratio of customer demand satisfaction
 - r* Distortion coefficient
 - k* Safety stock coefficient
 - x_i* The quantity demanded for products
 - y_i* Inventory level of distributor
 - z_i* The quantity produced by producer

Where

- ◆ $x_i < 0$ denotes that the supply is less than military demand in the previous period.
- ◆ $y_i < 0$ denotes that critical information without adjustment is necessary to inventory level.
- ◆ $z_i < 0$ denotes the cases of overstock or return and no new productions [8].

The three differences equations are quantity demanded by military user, inventory level or quantity demanded by distributors and quantity produced by producers. The above equations and statements are considered as first case. The three-echelon military supply chain model is accepted from a well-known model i.e. Lorenz model and described in Ref. [8].

However, in military the major concern and purpose of optimizing the supply chain is warfare. During these situations, the military user communicates demand and expects the material supply with an immediate affect. In these

situations, if supply lines are too long then it is extremely difficult to support the warfare operations. To reduce the time delay and to improve the supply flow from producer to the military user need to introduce a novel scenario. The new proposed model needs immediate deliver or transmission of material to the military user at war locations. However, the first case does not supply the material with an immediate affect during warfare.

The second case seems to be more interesting as it could describe a realistic scenario (an emergency case) which can occur due to the malfunctioning of a significant number of arms or lack of ammunitions during warfare [11,12]. This is a specific case where a stretch forward action is needed to provide arms and ammunitions to military user. To satisfy the demand, a direct flow of material from supplier to military user is justified since the material flow thru distributor will be not only time consuming but also not appropriate as a situation can occur at the level of distributors (accident, some problems during transportation etc.). Therefore, this second case is an emergency scenario, which will be combines to the first case in order to describe a more realistic scenario.

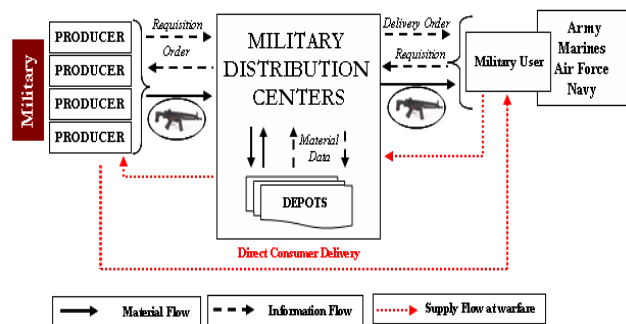


Figure.7: In second case (during emergency), the material flows in military supply chains

In military, war is an essential consequence, must be ready to move to the conflict location and need to carry the sufficient material. If the military users waiting time increases or delays then the flow of supply products are delayed, this gives unmanageable impression to entire military operations. The consideration of second case intends to deliver or transmission of material to the military user at war locations. While considering the second case, initially necessary to conceive the key points such as quantity produced, safety stock coefficient during emergency.

Considering such a scenario, the supplier unit suppliers in both directions (z_i : in the former direction in the directions through distributor) and (w_i in a straightforward (direct) way (i.e. directly to military user)).

Therefore:

- Additional Notations:
- w_i quantity produced by producer (due to emergency)
 - l loose in safety stock coefficient (due to emergency)
 - $(k-l)$ current safety stock coefficient

Under these considerations, equation (3) is modified as follows:

$$z_i = x_{i-1}y_{i-1} + (k - l)z_{i-1} \dots\dots (3')$$

Where by this new form of equation (3) takes into account the current safety stock.

Further, the flow in the direction due to emergency is expressed as follows:

$$w_i = kz_{i-1} - lw_{i-1} \dots\dots\dots (4)$$

Where kz_{i-1} is the previous stock and lw_{i-1} is the quantity subtracted on the previous stock due to emergency case.

There the following complete equations describe the scenarios envisaged in the second case:

$$x_i = my_{i-1} - nx_{i-1} \dots\dots\dots (1)$$

$$y_i = rx_{i-1} - x_{i-1}z_{i-1} \dots\dots\dots (2)$$

$$z_i = x_{i-1}z_{i-1} - (k - l)z_{i-1} \dots\dots\dots (3')$$

$$w_i = kz_{i-1} - lw_{i-1} \dots\dots\dots (4)$$

CONCLUSION

This paper was concerned with the modeling of material flow (arms and ammunitions) along a military supply chain. The structure of the proposed military supply chain is made up of a three-echelon. The first part of this work has dealt which a general overview which aimed to position the work and to explain current scenario encountered in military supply chain. The model process was inspired on that carried out in reference [8]. The first case showed a scenario along military supply chain which is comparable to that exhibited in a three-echelon commercial supply chain. A comparative analysis aimed to show that this case could be modeled by the equations in reference [8]. However, the scenario in the first case has been shown not to be more realistic. Indeed many references (see references [11,12]) have shown an interesting scenario which currently occur in a military supply chain in addition to the scenario discussed in the first case. This interesting scenario in addition to the scenario case one could described a realistic scenario (an emergency case) which can occur due to the malfunctioning of a significant number of arms or lack of ammunitions during warfare [11][12] This paper has discussed such a scenario and appropriate model (i.e. set of equations) was proposed to model this scenario.

The work in this paper is the first step towards complete modeling of the realistic scenario encountered in military supply chain. Therefore, it will of high interest the use of the proposed model to analyze various scenario that can be exhibited along military supply chain. This is an interesting issue as the results from the modeling process may be compared to the real scenario encountered in military supply chain in order to validate the proposed model.

REFERENCES

[1] Antill, P. *Military Logistics: A Brief History*, by Military History Encyclopedia on the Web, 22 August 2001.
 [2] Steve John Simon, *The art of military logistics*, by Association for computing machinery, Volume 44, No.6, June 2001.

[3] Eric Peltz, "Logistics: supply based or Distribution based ?", by RAND Arroyo center, Volume 39, Issue 2 PB 700-08-02, 2007.
 [4] Major Joshua M.Lenzini, " Anticipatory Logistics: The army's Answer to supply chain management", by Army Logisitian, issue 2002, PB 700-02-5.
 [5] F.Barahone, P.Chowdhary, M.Ettl, P.Huang, T.Kimbrel, L.Landanyi, Y.M.Lee,B.Schieber, K.Souriranjan, M.I.Sviridenko, G.M.Swirszcz, "Inventory allocation and transportation scheduling for logistics of network-centric military operations" by IBM J.RES. & DEV., volume.51 No. 3/4, 2007.
 [6] Wang Jinfa, Li Li, *Military Supply Chain Management - the Science and Art Supporting Military Operation*, Beuing: National Defense University Press, 2004.
 [7] DoD Logistics, Chapter 4, Joint Publication 4-09 "Joint Doctrine For Global Distribution" issu-e JP 4-09, 14 December 2001.
 [8] Z.Lei, L.Yi-jun, and X.Yaoqun, "Chaos Synchronization of bullwhip Effect in a Supply Chain," presented at Management Science and Engineering, 2006. ICMSE'06. 2006 International conference on, Lille, Date: 5 - 7 Oct. 2006.
 [9] Mark Y.D.Wang, "Factory to Foxhole:Improving the Army's supply chain", presented by RAND Corporation, September'2006.
 [10] David F. Pyke and M. Eric Johnson (editors), "Supply Chain Management: Innovations for Education", by Production and Operations Management Society, POMS Series in Technology and Operations Management Volume 2, , 2000
 [11] Daniel W.Engels, Robin Koh, Elaine Lai, Edmund W.Schuster, "An introductory analysis of Auto-ID applications in the department of defense supply chains", by Auto ID Center, 2002
 [12] Michael Brzoska, Frederic S, "Arms and Warfare: Escalation, De-escalation, and Negotiation", Book, Published 2006 DIANE Publishing Company, ISBN:142235296X



Sreeram Kumar Bhagavatula received his BSc in Computer Science and MSc in Computer Science from Andhra University, India, in 2001 and 2003, respectively. He worked as project operations in Indian railways from 2004 – 2007. He is now a Ph.D. student at the University of Klagenfurt in Austria. His research interests include military supply chains, city logistics, multi-agent systems, chaos and its applications.



Jean Chamberlain Chedjou received in 2004 his doctorate in Electrical Engineering at the Leibniz University of Hanover, Germany. He has been a DAAD (Germany) scholar and an AUF research Fellow (Postdoc.). From 2000 to date, he has been a Junior Associate researcher in the Condensed Matter section of the ICTP (Abdus Salam International Centre for Theoretical Physics) Trieste, Italy. Currently, he is a senior researcher at the Institute for Smart Systems Technologies of the Alpen-Adria University of Klagenfurt in Austria. His research interests include Electronics Circuits Engineering, Chaos Theory, Analog Systems Simulation, Cellular Neural Networks, Nonlinear Dynamics, Synchronization and related Applications in Engineering. He has authored and co-authored 2 books and more than 22 journals and conference papers.



Koteswara Rao Anne received his BE in Electronics and Communication and MSc in Electrical engineering and Information Technology from Bharathiyar University, Coimbatore, India and Leibniz University of Hanover, Germany, in 2001 and 2006, respectively. He is now a Ph.D. student at the University of Klagenfurt in Austria. His research interests include advanced planning and scheduling in production systems, Intelligent supply chains, systems dynamics, multi-agent systems, chaos and its applications.



Kyandoghene Kyamakya obtained the M.S. in Electrical Engineering in 1990 at the University of Kinshasa. In 1999, he received his Doctorate in Electrical Engineering at the University of Hagen in Germany. He then worked three years as post-doctorate researcher at the Leibniz University of Hannover in the field of Mobility Management in Wireless Networks. From 2002 to 2005, he was junior professor for Positioning Location Based Services at Leibniz University of Hannover. Since 2005, he is full Professor for Transportation Informatics and Director of the Institute for Smart Systems Technologies at the University of Klagenfurt in Austria.

A Periodical Time-Variable Effect in OFDM Systems with Aliasing and a Sampling Frequency Offset

Ilias Trachanas and Norbert J. Fliege
 Chair of Electrical Engineering
 Faculty of Mathematics & Computer Science
 University of Mannheim, Mannheim, Germany
 Email: ilias.trachanas@ti.uni-mannheim.de

Abstract—Aliasing constitutes a well-known drawback of digital communication systems and causes time-invariable effects, which affect the signal to noise ratio (SNR) at the digital receiver. Orthogonal Frequency Division Multiplexing (OFDM) systems suffer besides from intercarrier interference (ICI) caused by the non-perfectly synchronized clock of the receiver. This work focuses on the study of the effects caused by the interference of these both system impediments. The infinite aliased copies of the insufficiently filtered OFDM base-band spectrum generated at the transmitter are additionally phase-distorted due to the sampling frequency offset between the receiver and the transmitter. A thorough analysis of the frequency components at every OFDM subcarrier position at the receiver shows that the received power is a periodical function of time. We explain how this effect depends on the transfer function of the utilised reconstruction and anti-aliasing low-pass filters as well as the value of the sampling frequency offset and the transmission channel. Two realistic as well as one unrealistic scenarios are investigated in order to demonstrate the theoretically studied relationships.

Index Terms—Aliasing, Frequency Offset, OFDM, Synchronization, Periodical Time-Variable Effect.

I. INTRODUCTION

Numerous advantages of the OFDM modulation technique have led to the fact that it is nowadays widely used in standards about data transfer over various mediums including telephone cables, the air, powerlines etc. However, OFDM is very sensitive to system's imperfections caused by the disability to perfectly fulfil important theoretical assumptions in practically implemented systems. Such a theoretical consideration of vital importance for every digital communication system, the discussion of which is widely found in the literature (e.g. in [1]), is the perfect low-pass filtering at the transmitter (reconstruction filtering) and at the receiver (anti-aliasing filtering).

Especially in OFDM systems a number of implementation issues concerning the computing power of modern digital signal processors or the dispose of limited bandwidth have contributed to the standardization of the policy to use the lowest possible sampling rate. By exploiting the properties of the discrete Fourier transform (DFT) in order to generate and transmit a real signal it is a common practice to add the complex-conjugated parts of the signal in the frequency domain. As a consequence of the imperfections of the re-

construction filter frequencies near to the system's Nyquist frequency are occupied, which could obstruct the parallel use of other systems that utilize these frequencies. Moreover, because of the fact that the anti-aliasing filter is also imperfect such frequency parts of the transmitted signal cause aliasing at the receiver.

The limited accuracy of the sampling frequency oscillators, which are utilized in every implemented OFDM system, counts as an additional origin for difficulties and system quality degradations. Intercarrier interference (ICI) and intersymbol interference (ISI) are the best examples of problems caused by a sampling frequency offset between transmitter and receiver [2], [3], [4]. The impact at the bit error rate is actually visible for small sampling frequency offsets. Some systems deal with the problem by measuring the offset and correcting it by means of a voltage controlled oscillator or signal interpolation techniques (e.g. interpolation of the twiddle factors [5]). Other systems use ICI correction methods [6], [7], [8], [9]. However, for reasons of cost and computing resource conservations or even simplicity and robustness other systems tolerate the sampling frequency offset by using sophisticated techniques e.g. differential phase modulation or timing offset correction methods. Moreover, the accuracy of the methods is limited and depends on the fulfilling of certain conditions, which is particularly difficult if other effects (e.g. aliasing) occur at the same time or if the channel's transfer function is still unknown.

Main objective of this work is the investigation of the effects caused by the parallel existence of aliasing and a sampling frequency offset, which is in different degrees the fact in every implemented OFDM system. In many systems yet the effect is particularly noticeable at the beginning of the link establishment during the channel measurement. While considering a number of different effects caused by the previously mentioned system's imperfections in section II we analyse the OFDM signal in different interesting positions of the communication path. Section III begins with a thorough discussion of the effects caused by aliasing and a sampling frequency offset alone. At the end of the part of the section that analyses aliasing an exact formula for the power of the signal per

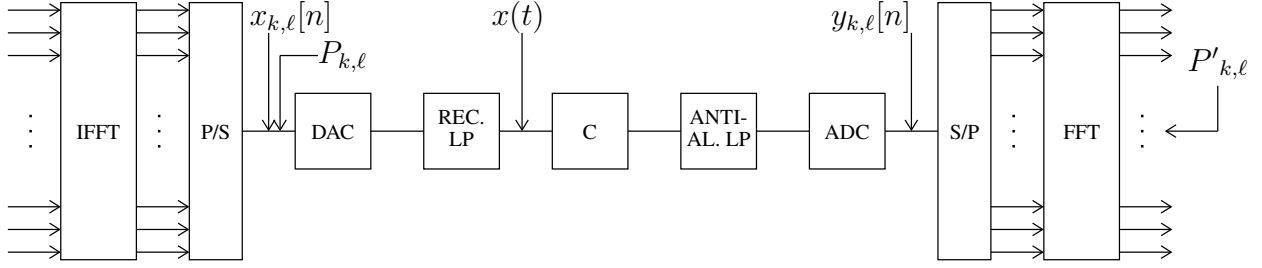


Fig. 1. A typical OFDM system

subcarrier and symbol at the output of the receiver's fast Fourier transform (FFT) is provided. As next a discussion of the effects that dominate in case of the interaction of aliasing and a sampling frequency offset as well as the analysis of the periodical time-variable received power effect caused by this interaction follows. The results of the previous paragraphs are used in section IV to demonstrate the effect in three different scenarios and show how it can be approximately eliminated and the work is closed by the conclusions.

II. THE OFDM SYSTEM

A typical OFDM system is shown in Fig. 1. At the transmitter the information bits are separated into packets and appropriately used as input of a modulator that calculates $\frac{M}{2} - 1$ complex values, the Fourier coefficients. These values determine the amplitude $\alpha_{k,\ell}$ and the initial phase $\phi_{k,\ell}$ in the k -th OFDM symbol of $\frac{M}{2} - 1$ modulated subcarriers (hereafter also called "useful" subcarriers), where ℓ denotes the subcarrier index ($1 \ll \ell \ll \frac{M}{2} - 1$). Note that the subcarrier with zero index is not used because it produces zero frequency signal parts, which cannot be practically used. In order to produce a real signal at the output of the transmitter a well-known property of the FFT is utilised according to which the output of the inverse FFT (IFFT) is real only when the description of the basis-band output signal in the frequency domain (the input of the IFFT) is complex-conjugated symmetrical. For that reason the rest of the $\frac{M}{2} - 1$ subcarriers (hereafter also called "useless" subcarriers as they can carry no extra information) are modulated with the same amplitude and the opposite phase of their correspondent "useful" subcarrier (subcarrier index symmetrical to $\frac{M}{2}$). Due to the fact that the signal is discrete described the hypothetical spectrum of the digital transmitted signal is composed of infinite copies of the "useful" and the "useless" subcarriers, that are moved by multiples of 2π to other frequency areas, which is graphically illustrated in Fig. 2. After the IFFT with length M the discrete time domain signal of subcarrier ℓ reads:

$$x_{k,\ell}[n] = \alpha_{k,\ell} \cdot \left(\frac{1}{2} e^{j(\Omega_\ell n + \phi_{k,\ell})} + \frac{1}{2} e^{-j(\Omega_\ell n + \phi_{k,\ell})} \right) \cdot \text{rect}_M[n - (M-1)/2],$$

where $\Omega_\ell = 2\pi \frac{\ell}{M}$ denotes the angular frequency normalised to the sampling frequency f_s and

$$\text{rect}_M[n] = \begin{cases} 1, & |n| \leq \frac{M-1}{2} \\ 0, & \text{otherwise} \end{cases}$$

denotes a discrete rectangular sequence. The transmitted power per symbol is then given by:

$$P_{k,\ell} = \frac{\alpha_{k,\ell}^2}{M} \sum_{n=0}^{M-1} \cos^2(\Omega_\ell n + \phi_{k,\ell}) = \frac{\alpha_{k,\ell}^2}{2} \quad (1)$$

In order to depict the fact that before the reconstruction filter the OFDM signal contains infinite, periodically copied "useful" and "useless" subcarriers we assume that the transmitter always sends the same information bits at all subcarriers and every subcarrier is loaded with the same power. Considering the fact that the discrete Fourier transform of a discrete rectangular sequence is a Dirichlet function the frequency domain signal reads:

$$X(\Omega) = \alpha_{k,\ell} \pi \sum_{i=-\infty}^{+\infty} e^{j\phi_{k,\ell}} \cdot \text{di}(\Omega - \Omega_\ell - 2\pi i) + \alpha_{k,\ell} \pi \sum_{i=-\infty}^{+\infty} e^{-j\phi_{k,\ell}} \cdot \text{di}(\Omega + \Omega_\ell - 2\pi i)$$

After the FFT and a parallel to serial converter the data are given to the DAC. As already mentioned the DAC and ADC are normally of type "sample and hold" and will be hereafter handled as filters with the following transfer function (ideally exactly the same f_s is utilized at the transmitter and the receiver):

$$H_{da}(\Omega) = H_{ad}(\Omega) = \text{si}(\Omega T_s/2) \cdot e^{-j\Omega T_s/2} \quad (2)$$

The si- shape of H_{da} is caused by the fact that every sample is held until the next comes, which means that the sample values are multiplied with a rectangular function ($\text{rect}(\frac{t-T_s/2}{T_s/2})$), the Fourier transform of which is a si function.

The output of the DAC is connected to the reconstruction filter. This is an analog low-pass filter, which attenuates the "useless" subcarriers and the continuously periodical copies of them and those of the "useful" subcarriers. Depending on the form and grade of the realised reconstruction filter the amplitudes at the infinite frequency positions of the transmitted signal are decreasing with frequency to almost but not exactly

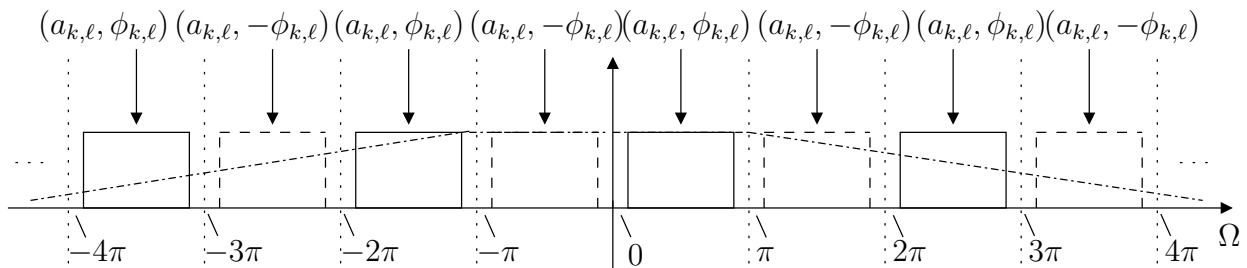


Fig. 2. Graphical illustration of the "useful" and "useless" subcarriers

zero. As a consequence of this fact the continuous output signal $x(t)$ of the OFDM transmitter consists of infinite cosine-shaped signals most of which are heavily attenuated.

As next the output of the OFDM transmitter is further attenuated and phase-rotated by the transmission channel. Because of the fact that the scope of this work is to analyse and demonstrate time-variable effects caused by the OFDM system itself we assume that the transfer function of the channel does not change within one OFDM symbol, a sufficient guard interval is used and that the noise samples all over the transmission path are equal to zero.

At the receiver the continuous time signal is first filtered from the anti-aliasing low-pass analog filter. Afterwards it is passing through the ADC, where it is sampled with the sampling frequency f'_s of the local oscillator, which is generally unequal (very close though) to f_s and once again si-shaped filtered. At this position of the communication path aliasing as well as a frequency shift of the aliased components of the signal and other effects, which will be thoroughly discussed in the next session, occur.

III. INTERACTION OF ALIASING AND A SAMPLING FREQUENCY OFFSET

As already mentioned main goal of this paragraph is to investigate the effects, which are caused due to the parallel existence of aliasing and a sampling frequency offset. For that reason and in order to provide a distinct analysis we divide it in three main parts. At first the effects caused by aliasing alone are explained and the received power per subcarrier is analytically computed in case of a zero sampling frequency offset by hypothetically applying a IFFT after the FFT at the receiver in order to get the time domain signal (in that way calculations are simplified). In that case the power per subcarrier remains the same before and after the FFT because there are no leakage effects [10]. As second, we assume perfect reconstruction and anti-aliasing filters and discuss the effects originating from the sampling frequency offset. Finally, the effects are combined and formulas, which show that the received power is a periodical function of time, are given.

A. Aliasing

Considering Fig. 1 aliasing is a phenomenon that occurs due to the sampling after the ADC. Actually, aliasing occurs always in real OFDM systems because the amplitude of the

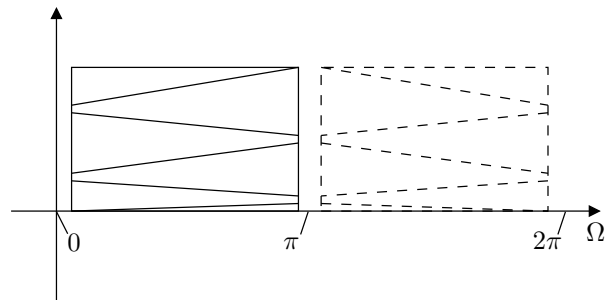


Fig. 3. The effects of aliasing in the interesting (for the FFT) spectrum

infinite - already generated at the transmitter - "useful" and "useless" subcarriers is never ideally attenuated (by the low-pass filters) to zero. Due to the sampling at the receiver the remaining frequency blocks shown in Fig. 2, which are already non-ideally filtered by the reconstruction and the anti-aliasing filter, are again infinitely copied to the corresponding frequencies, which are the original frequencies of the transmitted subcarriers (the "useful" lie between zero and π and the "useless" between π and 2π) shifted by multiples of $\pm 2\pi$. As a consequence of this fact and in respect to the sampling theorem the receiver by using the FFT "looks" to the frequencies between zero and π and reads more power as it was originally transmitted at the subcarrier positions ℓ . This extra power is coming from the aliased subcarriers, which were originally lying in frequency areas, which are the exact subcarrier positions ℓ plus all the infinite multiples of $\pm f_s$. The same happens for the complex conjugated of them (shown in Fig. 3) from π to 2π .

If we now assume a zero sampling frequency offset then no additional effects (e.g. leakage) are caused during the FFT. Because of the fact that it is more convenient to make the calculations shown below in the time domain we assume that we have applied the IFFT to the signal at the output of the FFT again. Because the FFT causes no leakage the output of the hypothetically applied IFFT is the same as the input of the FFT before. If we theoretically separate the time samples of the different subcarriers then we can use $y_{k,\ell}[n]$ shown in Fig. 1 in order to calculate the received power of the signal after the FFT per subcarrier and OFDM symbol, which is in case of aliasing alone the same as the power per subcarrier before the FFT and eventually the deciding value for the system.

Regarding that zero noise samples are assumed we can express the signal after the ADC as follows:

$$y_{k,\ell}[n] = \sum_{i=0}^{+\infty} \alpha_{k,\ell} |H(iM + \ell)| \cos(\Omega_\ell n + \phi_{al}(iM + \ell)) + \sum_{i=1}^{+\infty} \alpha_{k,\ell} |H(-iM + \ell)| \cos(\Omega_\ell n + \phi_{al}(-iM + \ell)), \quad (3)$$

where $|H(iM + \ell)|$ is the total absolute signal attenuation of the "useful" subcarriers (and all its infinite copies) and given by:

$$|H(iM + \ell)| = |H_{rf}(iM + \ell)| \cdot |H_{af}(iM + \ell)| \cdot |H_c(iM + \ell)| \cdot |H_{da}(iM + \ell)| \cdot |H_{ad}(iM + \ell)| \quad (4)$$

As we already explained in section II the attenuation is caused by the reconstruction and anti-aliasing filters, the channel and the non-ideal ADC and DAC. The total phase rotation ϕ_{al} for the "useful" subcarriers reads:

$$\begin{aligned} \phi_{al}(iM + \ell) &= \phi_{rf}(iM + \ell) + \phi_{af}(iM + \ell) + \phi_c(iM + \ell) \\ &\quad + \phi_{da}(iM + \ell) + \phi_{ad}(iM + \ell) + \phi_{k,\ell} \\ &= \phi_e(iM + \ell) + \phi_{k,\ell}, \end{aligned} \quad (5)$$

where ϕ_e is caused by the filters, the channel, the ADC/DAC and $\phi_{k,\ell}$ by the modulated data.

In respect to Fig. 3 we notice that a part of the aliased subcarriers (the ones which were originally lying in the frequency positions $iM + \ell$) keep their phases and another part (the ones which were originally lying in the frequency positions $iM - \ell$) have to negate their phases. In order to explain this one should consider that the part of the aliased subcarriers that get their phases negated are the complex conjugated from the "useless" subcarriers and were actually positioned in negative frequencies ($-iM + \ell$). Another way to understand this would be to hypothetically position imaginary half-permeable mirrors at zero, π , 2π etc. and imagine that the mirrors transfer the information from the right to the left from $+\infty$ until zero. That means that these aliased subcarriers inherit the amplitude of the "useless" subcarriers ($|H(-iM + \ell)| = |H(iM - \ell)|$), but get the negative phase:

$$\begin{aligned} \phi_{al}(-iM + \ell) &= \phi_{rf}(-iM + \ell) + \phi_{af}(-iM + \ell) + \phi_c(-iM + \ell) \\ &\quad + \phi_{da}(-iM + \ell) + \phi_{ad}(-iM + \ell) + \phi_{k,\ell} \\ &= -\phi_{rf}(iM - \ell) - \phi_{af}(iM - \ell) - \phi_c(iM - \ell) \\ &\quad - \phi_{da}(iM - \ell) - \phi_{ad}(iM - \ell) + \phi_{k,\ell} \\ &= -\phi_e(iM - \ell) + \phi_{k,\ell} = -\phi_{al}(iM - \ell) \end{aligned} \quad (6)$$

If we now calculate the received power per symbol and

subcarrier we get:

$$\begin{aligned} P'_{k,\ell} &= \frac{1}{M} \sum_{n=0}^{M-1} y_{k,\ell}^2[n] = \frac{1}{M} \sum_{n=0}^{M-1} \left(\sum_{i=0}^{+\infty} A + \sum_{i=1}^{+\infty} B \right)^2 \\ &= \frac{1}{M} \sum_{n=0}^{M-1} \left(\sum_{i=0}^{+\infty} A \right)^2 + \frac{1}{M} \sum_{n=0}^{M-1} \left(\sum_{i=1}^{+\infty} B \right)^2 \\ &\quad + \frac{2}{M} \sum_{n=0}^{M-1} \left(\sum_{i=0}^{+\infty} A \cdot \sum_{i=1}^{+\infty} B \right), \end{aligned} \quad (7)$$

where:

$$A = \alpha_{k,\ell} \cdot |H(iM + \ell)| \cos(\Omega_\ell n + \phi_{al}(iM + \ell))$$

and

$$B = \alpha_{k,\ell} \cdot |H(iM - \ell)| \cos(\Omega_\ell n - \phi_{al}(iM - \ell))$$

It can be shown that for every $\theta, \phi, \rho \in [0, 2\pi]$:

$$\begin{aligned} 2 \cos(\theta + \phi) \cdot \cos(\theta + \rho) &= \cos(\phi - \rho) \\ + \cos(2\theta) \cdot \cos(\phi + \rho) - \sin(2\theta) \cdot \sin(\phi + \rho) \end{aligned} \quad (8)$$

That means that for every $\phi_1, \phi_2 \in [0, 2\pi]$:

$$\sum_{n=0}^{M-1} (2 \cos(\Omega_\ell n + \phi_1) \cos(\Omega_\ell n + \phi_2)) = M \cdot \cos(\phi_1 - \phi_2)$$

because:

$$\sum_{n=0}^{M-1} \cos(2\Omega_\ell n) = \sum_{n=0}^{M-1} \sin(2\Omega_\ell n) = 0$$

By using (1) we can calculate the double sums in (7) as shown below:

$$\begin{aligned} \frac{1}{M} \sum_{n=0}^{M-1} \left(\sum_{i=0}^{+\infty} A \right)^2 &= P_{k,\ell} \left(\sum_{i=0}^{+\infty} |H(iM + \ell)|^2 \right. \\ &\quad + \sum_{j=0}^{+\infty} \sum_{i=0}^{+\infty} |H(jM + \ell)| \cdot |H((i+1)M + \ell)| \\ &\quad \cdot \cos(\phi_{al}(jM + \ell) - \phi_{al}((i+1)M + \ell)) \Big) = C \cdot P_{k,\ell} \end{aligned} \quad (9)$$

$$\begin{aligned} \frac{1}{M} \sum_{n=0}^{M-1} \left(\sum_{i=1}^{+\infty} B \right)^2 &= P_{k,\ell} \left(\sum_{i=1}^{+\infty} |H(iM - \ell)|^2 \right. \\ &\quad + \sum_{j=1}^{+\infty} \sum_{i=1}^{+\infty} |H(jM - \ell)| \cdot |H((i+1)M - \ell)| \\ &\quad \cdot \cos(-\phi_{al}(jM - \ell) + \phi_{al}((i+1)M - \ell)) \Big) = D \cdot P_{k,\ell} \end{aligned} \quad (10)$$

$$\begin{aligned} \frac{2}{M} \sum_{n=0}^{M-1} \left(\sum_{i=0}^{+\infty} A \cdot \sum_{i=1}^{+\infty} B \right) &= P_{k,\ell} \sum_{j=0}^{+\infty} \sum_{i=1}^{+\infty} |H(jM + \ell)| \cdot \\ |H(iM - \ell)| \cdot \cos(\phi_{al}(jM + \ell) + \phi_{al}(iM - \ell)) &= E \cdot P_{k,\ell} \end{aligned} \quad (11)$$

That means that the power for every subcarrier at the receiver (after the FFT) is directly dependent of the transmitted power at the same frequency as shown below:

$$P'_{k,\ell} = (C + D + E) P_{k,\ell} \quad (12)$$

Because the filters' and the channel's attenuation factors and phases are constant with time (that means that C,D and E are also independent of time) the value $\frac{P'_{k,\ell}}{P_{k,\ell}}$ remains also constant with time. Furthermore, it can be shown that the series which are added in C, D and E are converging when using Butterworth or Chebychev low-pass filters. This happens because $|H(iM - \ell)| < 1$ and $|H((i+1)M - \ell)| < |H(iM - \ell)|$. Finally, the larger the filter's order the less the error that is done when a small finite number of "useful" and "useless" subcarriers is used for the calculation of the power at the receiver.

B. Sampling Frequency Offset

In the second step of the analysis we discuss the effects originating from the sampling frequency offset Δf_s alone. For that reason we assume perfect channel conditions as well as perfect initial timing synchronization and low-pass filtering. In this case the sampling frequency at the receiver is slightly different as at the transmitter, which means that the M equidistant subcarrier positions of the FFT at the receiver do not meet the maximum locations of the Dirichlet functions. Indeed, the positioning error grows for larger subcarrier positions and the orthogonality of all the subcarriers is destroyed (ICI occurs). This fact is responsible for the generation of three effects: a) every subcarrier is slightly attenuated (H_{di}) and phase rotated (ϕ_{di}), b) ICI noise is added to every subcarrier and caused by all the other used subcarriers and c) a constantly growing timing offset occurs. The ICI attenuation, which is plotted in Fig. 4 for $M = 128$, depends on the subcarrier index, the FFT-length and the value of the sampling frequency offset and reads:

$$H_{di}(\ell) = \text{di}_M\left(\frac{\ell}{M} \cdot \frac{\Delta f_s}{f_s}\right), \quad (13)$$

where di_M denotes the Dirichlet kernel [11].

As it can be clearly seen in Fig. 4 the Dirichlet attenuation is very small for realistic values of the normalized sampling frequency offset $\frac{\Delta f_s}{f_s}$ e.g. 10 – 100 ppm. The same applies for the phase rotation. The second effect of ICI is the noise added to every subcarrier caused by every other subcarrier because the orthogonality is lost. The amplitude of the ICI noise can be written as a sum of noise amplitudes:

$$N_{ici}(f'_\ell) = \alpha_{k,\ell} \sum_{\ell=1, \ell \neq \ell'}^{\frac{M}{2}-1} \text{di}_M(f'_\ell - f_\ell), \quad (14)$$

where $f'_\ell = \ell \frac{f'_s}{M}$ are the new subcarrier frequency positions at the receiver.

The ICI noise power reads:

$$P_{ici}(f'_\ell) = \alpha_{k,\ell}^2 \left(\sum_{\ell=1, \ell \neq \ell'}^{\frac{M}{2}-1} \text{di}_M(f'_\ell - f_\ell) \right)^2 \quad (15)$$

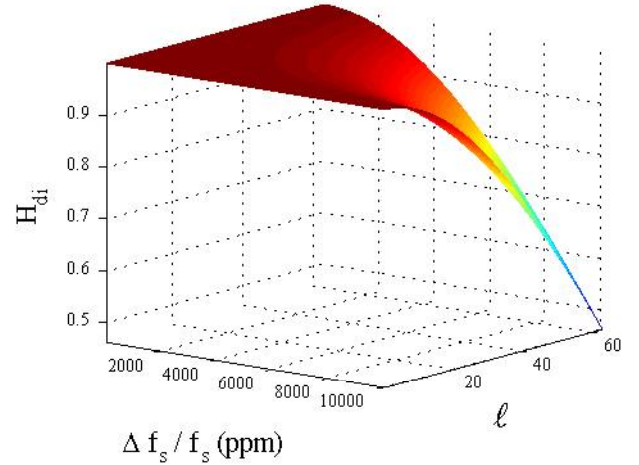


Fig. 4. ICI attenuation due to the sampling frequency offset for $M=128$

The ICI noise power is a size that is practically neglectable because it is very low for small offsets, so that for 100 ppm the SNR is always larger than 60 dB if no other noise source than ICI exists.

The last effect that is caused by a tolerated sampling frequency offset is a timing offset, which is constantly growing with time if not corrected. Of course, in order to achieve stable OFDM links the timing offset should be always corrected by a correction algorithm. However, there are systems that do not correct the timing offset during the channel and SNR measurement. If so, the phase of every subcarrier is growing with time as shown below:

$$\phi_{\Delta T}(\ell) = 2\pi \ell k(1 + \gamma), \quad (16)$$

where $\gamma = \frac{\Delta T_s}{T_s}$ is the normalized sampling period offset and is related to the sampling frequency offset according to:

$$\gamma = \frac{\Delta T_s}{T_s} = \left(\frac{1}{f'_s} - \frac{1}{f_s}\right) f_s = -\frac{\Delta f_s}{f'_s}, \quad (17)$$

which means that for small values of the normalized sampling frequency offset (e.g. 10-100ppm) γ is approximately its negative.

From (16) it is clear that the phase rotation due to a continuously growing timing offset (caused by the uncorrected sampling frequency offset) is linearly growing with time (here the symbol index k). Also, the larger the frequency position of the subcarrier the larger the increase of the phase rotation. This fact applies, of course, for all the infinite "useful" and "useless" subcarriers and is essential for the explanation of the periodicity of the received power, which is discussed in the following paragraph.

C. Aliasing and a Sampling Frequency Offset

A more realistic approach, where real low-pass filters and non-ideal sampling frequency oscillators are utilized, is analysed in the present subsection. In this case all the effects described in the previous paragraphs are combined in a rather

complicated way. All the "useless" as well as all the "useful" subcarriers at the receiver do not meet the exact frequencies of the transmitter so that the infinite alias subcarriers' frequencies slightly differ from each other. As a consequence after the FFT ICI occurs, where the noise is even larger than in the case described in the previous paragraph because all the aliased subcarriers contribute to the generation of the ICI noise. Furthermore, because of the leakage in the FFT the power of every subcarrier after the FFT is less than its power before it. However, as we already showed the ICI attenuation and phase rotation as well as the ICI noise are so low for realistic values of the frequency offset that they can be practically neglected. As a consequence, we can assume that these effects are minimal and again $y_{k,\ell}[n]$ can be used for the calculation of the power.

In respect to the discussion given at the previous paragraph the effect, which results from the sampling frequency offset itself and should be taken into consideration in the combined case is the constantly growing phase rotation $\phi_{\Delta T}$. That means that the new phase rotation of the infinite "useful" subcarriers and of the complex conjugated "useless" subcarriers, which are used for the calculation of the received power, read:

$$\phi_{al,fo}(iM + \ell) = \phi_{al}(iM + \ell) + \phi_{\Delta T}(iM + \ell) \quad (18)$$

$$\phi_{al,fo}(-iM + \ell) = -\phi_{al}(iM - \ell) + \phi_{\Delta T}(-iM + \ell) \quad (19)$$

So, if one calculates the new received power then the form of (12) remains, but the arguments of the cosines in C, D and E change. The new arguments read:

$$\begin{aligned} \phi_C &= \phi_{al,fo}(jM + \ell) - \phi_{al,fo}((i+1)M + \ell) = \\ & \phi_e(jM + \ell) + \phi_e((i+1)M - \ell) + 2\pi k(j - i - 1)M(1 + \gamma) \end{aligned} \quad (20)$$

$$\begin{aligned} \phi_D &= \phi_{al,fo}(-jM + \ell) - \phi_{al,fo}(-(i+1)M + \ell) = \\ & -\phi_e(jM - \ell) - \phi_e((i+1)M - \ell) - 2\pi k(j - i - 1)M(1 + \gamma) \end{aligned} \quad (21)$$

$$\begin{aligned} \phi_E &= \phi_{al,fo}(jM + \ell) - \phi_{al,fo}(-iM + \ell) = \\ & \phi_e(jM + \ell) - \phi_e(iM - \ell) + 2\pi k(j + i)M(1 + \gamma), \end{aligned} \quad (22)$$

for the cosines in C, D and E respectively. By combining (12), (9), (10), (11), (20), (21) and (22) we get the final formula that gives the received power for every subcarrier and symbol in case of aliasing and a sampling frequency offset.

Considering the new form of the arguments in the cosines in C, D and E and the forms of C, D and E itself it can be easily derived that the received power is a periodical function of time (here expressed by the OFDM symbol index k). Moreover, the function contains infinite frequencies, the values of which depend on the normalized sampling frequency offset and the FFT-length. Finally, the more the indices i and j in the sums grow the more the amplitudes of these frequencies tend to become zero.

IV. THREE DEMONSTRATING SCENARIOS

In the last section the periodical time-variable effects affecting the received power are demonstrated using the formulas given above. The three following scenarios are examined: a) No reconstruction and no anti-aliasing filter is utilized, b) two 4th order Chebychev filters are used as reconstruction and anti-aliasing filters, c) two 6th order Cauer filters are utilized. Please note that because of the fact that the scope of this work is to analyse phenomena resulting from the OFDM system itself we have normalized the channel's coefficients to 1. Finally, the normalized sampling frequency offset was kept rather small in the value of 10ppm, the chosen FFT-length was 512 and the transmitted power per subcarrier was normalized to 1.

In the first scenario an unrealistic situation, where no low-pass filters are used is shown. This is actually the worst case for the power at the receiver because the amplitudes of the aliased subcarriers are maximized. In section II it was shown that conventional ADC and DAC of type "sample and hold" behave like filters with a characteristic spectrum that has the form of a si function, which is plotted in Fig. 5. It can be easily seen that the ADC/DAC comprise rather bad "filters" because they not only hardly attenuate the frequencies that cause aliasing (from the half of the normalized sampling frequency to $+\infty$) but also insert an attenuation that has a maximum of almost 4dB in the transmission band (from zero to the half of the normalized sampling frequency). Another important observation is that the attenuation is growing slowly so that it is expected that more than the first aliased frequencies (from 0.5 to 1 - the first "useless" subcarriers) are playing an important role in the form of the received power.

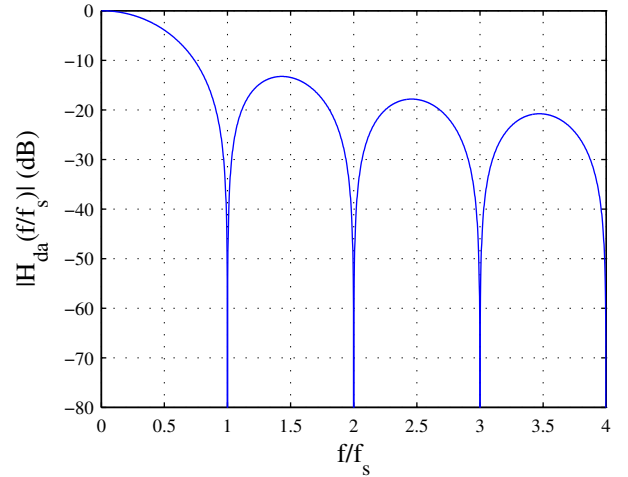


Fig. 5. AD/DA filter's attenuation

Fig. 6 shows the received power at different time points (the OFDM subcarrier index k was changed from 1 to 100) along the frequency in the first scenario. The attenuation of the first "useful" subcarriers as well as the time dependency are clearly observable. The effect is actually so powerful that hardly the first subcarriers could be theoretically utilized for

a data transfer in this case, which would be of course not done because there could be other sources for aliasing than the OFDM system itself so that even the first subcarriers are destroyed. Actually, the worst fact when the received power has the characteristic shown in Fig. 6 is not the attenuation of the utilized subcarriers but the time-variability and the large jumps in the values of the received power that is destroying the SNR. Please note that during the simulations we have sequentially used a growing number of aliased subcarriers starting with the first "useless" (from 0.5 to 1) and the second "useful" (from 1 to 1.5) ones. Thereby we noticed that after the third period (from 2.5 to 3.5) no remarkable impact was seen in the generated figures. It was furthermore observed that changes in the normalised frequency sampling offset didn't affect the form of the 2-D plot but only the period of the power's fluctuation, which is clear due to the form of (20), (21) and (22). This fact can be easily seen by the corresponding 3-D plots (simulations done for different values of γ), where the third dimension is the time and which are not shown for reasons of redundancy.

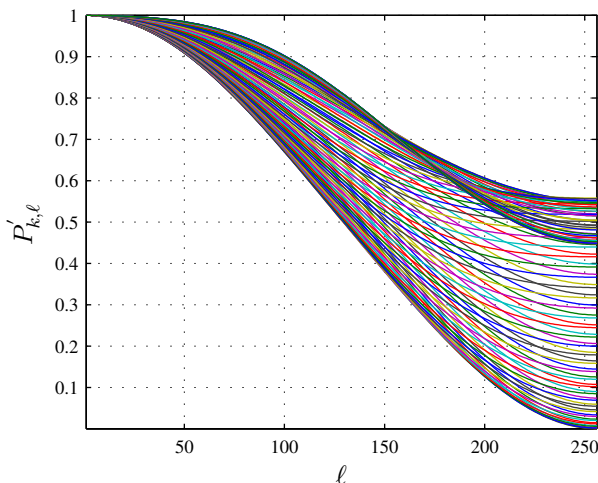


Fig. 6. Received power in the first scenario

In the second scenario we investigate the case, where two 4th order Chebychev filters are utilized (attenuation plotted in Fig. 7 - ripple equal to 0.125dB). This is a realistic scenario, where most of the aliased subcarriers are sufficiently filtered and the filters are relatively easy to implement. Fig. 8 shows the received power per subcarrier in that case. The first "useful" subcarriers are again attenuated by the ADC and the DAC and more than 50 subcarriers are severely affected by the effects. In order to demonstrate how large the power's fluctuation is we assumed that the ADC and DAC are perfect (attenuation caused equals zero), which is even more realistic because the reconstruction and anti-aliasing filters are normally designed in a way that the attenuation caused by the ADC and the DAC is almost eliminated. The results are plotted in Fig. 9. The received power fluctuates in a way that even more power (coming from the aliased subcarriers) than given at the specific frequencies is received according to the OFDM

symbol index. During the simulations we observed that for the specific filters only the first "useless" subcarriers caused noticeable aliasing effects.

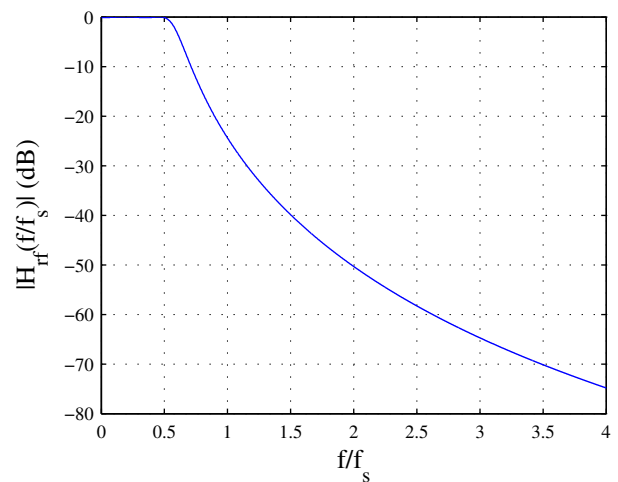


Fig. 7. Anti-aliasing/reconstruction filter's attenuation - Chebychev 4th order

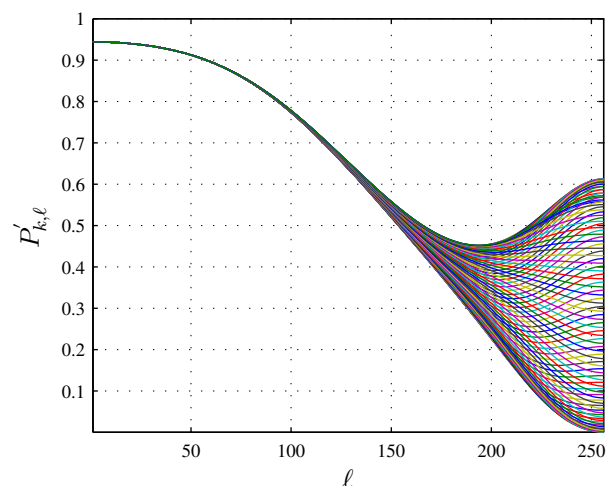


Fig. 8. Received power in the second scenario

In the last scenario two 6th order elliptic (Cauer) filters were used. This is a more optimistic case because the filters are more complicated to implement. From the form of the received power (see Fig. 11, Fig. 12) it is clear that this is the best scenario as the received power remains rather constant in time for the most subcarriers. However, even in this case there are subcarriers near the Nyquist frequency, which are heavily affected and improper for data transfer. This happens because the filters are not steep enough to provide enough attenuation near the Nyquist frequency so that the impact of the first aliased subcarriers is still quite noticeable.

Generally, the fluctuations in the received power grow with the subcarrier index. Actually, the 2-D form of these changes resembles a bouquet of flowers ("Blumenstrauß" in German), which is rotated 90° (see Fig. 8, 9, 11 and 12). This is rather

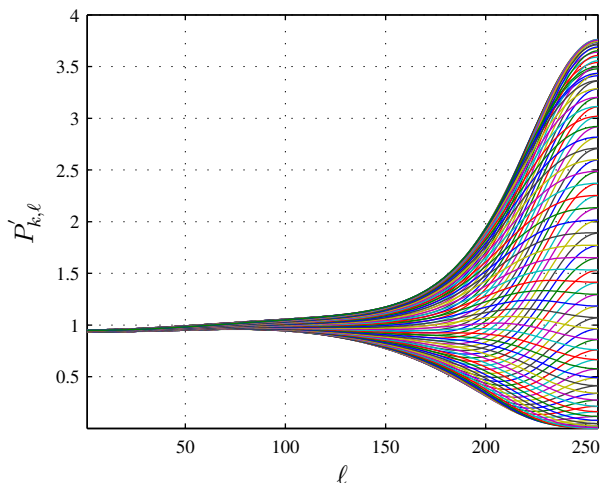


Fig. 9. Received power in the second scenario (perfect AD/DA assumed)

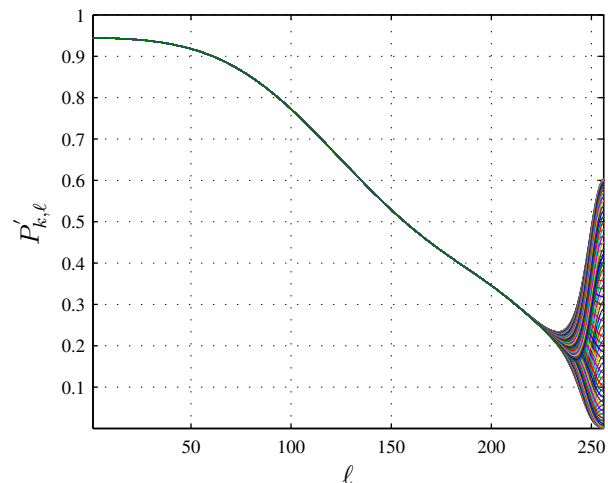


Fig. 11. Received power in the third scenario

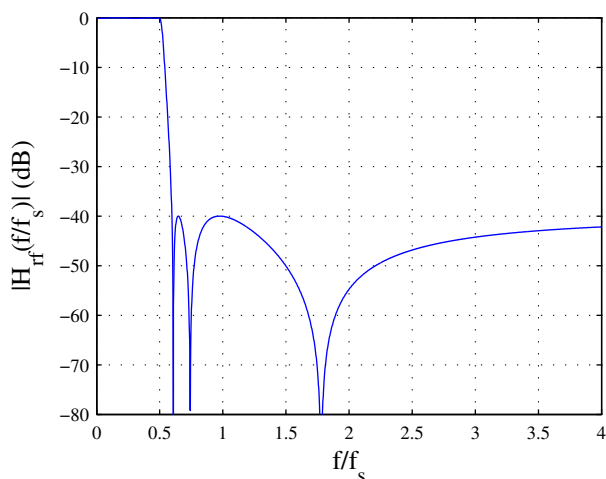


Fig. 10. Anti-aliasing/reconstruction filter's attenuation - Cauer 6th order

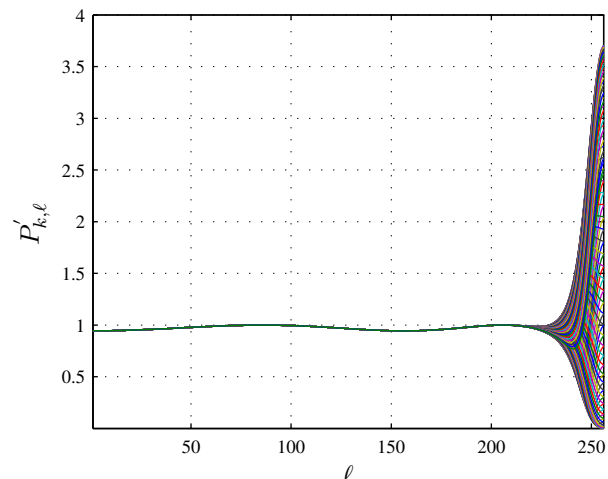


Fig. 12. Received power in the third scenario (perfect AD/DA assumed)

expected because the least filtered frequencies, where the first aliased subcarriers lie, are mirrored in the frequency area between zero and π (see Fig. 3) so that the highest frequencies (close to the Nyquist frequency) are mostly affected. The length of the "stick" of the bouquet as well as the thickness of the "flowers" in the bouquet increases with the abruptness of the low-pass filter (e.g. compare between Fig. 9 and Fig. 12)).

From the results shown in this section it is also clear that most of the theoretically infinite aliased subcarriers play practically no role in the changes of the received power in time. The filtering threshold lies approximately by -25 dB, which means that if normal low-pass filters are utilized, only the subcarriers lying between π and 2π can be used to predict the form of the received power and decide whether the filter is good enough or if some subcarriers should be left out of the transmission scheme. Indeed, the exception of at least one subcarrier (the next one near the Nyquist frequency) seems to be unavoidable if the OFDM system is designed in the way we have described in this work. The number of these subcarriers is

yet dependent on the FFT-length (the larger M is the narrower the available transition bandwidth for the low-pass filters is for a given sampling frequency) and the filter's characteristic. That is why these system parameters should be carefully chosen in respect to the given analysis and the system's specifications.

V. CONCLUSIONS

In this work the effects caused by the combination of two well-known drawbacks of OFDM systems, namely aliasing and a sampling frequency offset, were analysed. It lies in the nature of OFDM that even small sampling frequency offsets cause large phase rotations to the utilized subcarriers, which depend on the subcarrier's frequency and the symbol index. The parallel existence of aliasing yet results in a combined effect, where the aliased subcarriers, which are heavily phase rotated as they lie in large frequencies, are added to their corresponding subcarriers, which lie between zero and the Nyquist frequency and are therefore less phase rotated. The result of these theoretically infinite additions is a large fluctuation of

the received power, which grows with the subcarrier's index, the FFT-length and the inverse of the attenuation factors of the utilized low-pass filters. Due to the power fluctuations, which can be exactly calculated using the given formulas, there are severe degradations in the SNR, which can eventually lead to the exclusion of some subcarriers from the transmission scheme.

REFERENCES

- [1] R. S. A.V. Oppenheim and J. Buck, "Discrete-time signal processing (2nd edition)," Feb 1999.
- [2] M. V. B. T. Pollet and M. Moeneclaey, "Ber sensitivity of ofdm systems to carrier frequency offset and wiener phase noise," *IEEE Transactions on Communications*, vol. 43, no. 234, pp. 191–193, Feb-Mar-Apr 1995.
- [3] Y. Li and L. Cimini, "Bounds on the interchannel interference of ofdm in time-varying impairments," *IEEE Transactions on Communications*, vol. 49, no. 3, pp. 401–404, March 2001.
- [4] S.-G. H. Y. Zhao, "Sensitivity to doppler shift and carrier frequency errors in ofdm systems-the consequences and solutions," *IEEE 46th Vehicular Technology Conference, 1996. 'Mobile Technology for the Human Race'*, vol. 3, pp. 1564–1568, April 1996.
- [5] M. Sliskovic, "Sampling frequency offset estimation and correction in OFDM systems," *The 8th IEEE International Conference on Electronics, Circuits and Systems, 2001. ICECS 2001*, vol. 1, pp. 437 – 440, Sept. 2001.
- [6] J. Armstrong, "Analysis of new and existing methods of reducing intercarrier interference due to carrier frequency offset in ofdm," *IEEE Transactions on Communications*, vol. 47, no. 3, pp. 365–369, March 1999.
- [7] L. Wang and C. Tellambura, "A novel ici cancellation technique for ofdm systems using adaptive mapping signal constellation," *PACRIM. 2003 IEEE Pacific Rim Conference on Communications, Computers and Signal Processing, 2003*, vol. 1, pp. 442–445, Aug 2003.
- [8] S. X. C. Jun, J.W. Mark, "Ici cancellation in ofdm wireless communication systems," *GLOBECOM '02 IEEE Global Telecommunications Conference, 2002*, vol. 1, pp. 656–660, Nov 2002.
- [9] S.-G. H. Y. Zhao, "Inter-carrier interference self-cancellation scheme for ofdm mobile communication systems," *IEEE Transactions on Communications*, vol. 49, no. 7, pp. 1185–1191, July 2001.
- [10] J. Schwarz, "Enhancing the Spectral Selectivity of Discrete Multi-Tone Modulation," Dissertation, Universität Mannheim, 2006.
- [11] K. D. Kammeyer and K. Kroschel, *Digitale Signalverarbeitung*, 5th ed. Stuttgart: B. G. Teubner, 2002.



Ilias Trachanas was born in Athens, Greece, in 1982. He received the Diploma in electrical engineering from the National Technical University of Athens, Athens, Greece, in 2004. Since 2004 he is with the University of Mannheim, Mannheim, Germany, as a research and teaching assistant.

He is currently working on a project about IP communications over the medium voltage network funded by a major European electrical power company. He serves as reviewer for the *IEEE Transactions on Wireless Communications* and is a member of VDE (Germany). His research interests include digital signal processing, OFDM, synchronization, channel characterization and modeling, detection and estimation, interference rejection and their application to powerline and wireless telecommunications.



Norbert J. Fliege (M'89, SM'90) received the diplom degree (Dipl.-Ing.) and the doctor degree (Dr.-Ing.) in 1971, both from the University of Karlsruhe, Germany.

Since 1978, he was an associate professor at the same university. In 1980, he was a visiting professor at ESIEE in Paris. From 1982 to 1996, he was a Full Professor and Head of the Telecommunication Institute at Hamburg University of Technology in Hamburg, Germany. Since 1996, he has been a Full Professor of Electrical Engineering and Computer Technology at University of Mannheim, Germany. Since 1968, Dr. Fliege has been engaged in research work on fields like active filters, digital filters, communication circuits and software, digital audio, and multirate digital signal processing. In addition, he served as a Department Chairman and as Head of a research center. He has also founded a company providing telecommunication equipment.

Dr. Fliege has published more than hundred papers, most of them in international magazines and conference proceedings, and four books, one of them with the title "Multirate Digital Signal Processing", published by John Wiley and Sons in 1994. Dr. Fliege is a Senior Member IEEE, a member of EURASIP, and a member of VDE (Germany). He has received several national and international awards. In 1997, he has got the honorary doctorate from University of Rostock, Germany. In 2000, he was awarded an IEEE Fellow for contributions to analog and digital signal processing, and to engineering education.

Anticipation and Delocalization in Cellular Models of Pedestrian Traffic

Alexander Makarenko, Dmitry Krushinsky
 Institute for Applied System Analysis
 National Technical University of Ukraine "KPI"
 Kyiv, Ukraine
 makalex@i.com.ua

Boris Goldengorin
 Faculty of Economics and Business
 University of Groningen
 Groningen, the Netherlands
 b.goldengorin@rug.nl

Abstract—In this paper an issue of mentality simulation in cellular automata (CA) models of pedestrian traffic is addressed. Anticipation, as one of the major mental properties, plays an important role in behavior of real pedestrians, allowing them to use additional information in a form of sensual perception, knowledge and experience, etc. for optimization of their trajectories. Here we propose an approach to implementation of anticipation property in CA models and discover a relation between anticipation and spatial de-localization of interactions. A number of simulation experiments demonstrated consistency of the proposed approach and revealed some specific features.

Keywords—cellular automata; models of pedestrian traffic; anticipation

I. INTRODUCTION

One of the numerous applied fields, where cellular automata proved to be an extremely powerful tool, is modeling of pedestrian crowd motion [1], [2]. Having started from quite simple models inherited from physics, researchers are developing more and more sophisticated ones with a trend towards an introduction of mentality accounting into these models [3]. However, such "humanization" of a cellular automaton (CA), that is "mechanistic" by its nature, may demand changes not only in local rules, but also in the structure or in the pattern of interaction of cells. Basic property of a classical CA is locality of all interactions, both spatial (every cell interacts only with several neighbors) and temporal (next state of the CA is determined only by its current state). At the same time, when it comes to simulation of real crowds, this locality assumption is not always consistent, as pedestrians can somehow be informed about the situation beyond their immediate neighborhood (e.g. from visual observation or from notification systems). They can also use this information to predict the situation for several steps ahead and use these forecasts for optimization of their trajectories, a phenomenon, usually referred to as "anticipation" [4], [5]. Thus, the next step in development of the model is its de-localization, i.e. construction of a system lying in-between completely localized system (e.g. CA) and completely decentralized system (e.g. ANN¹).

II. A BRIEF DESCRIPTION OF THE BASIC MODEL

All the models presented here are based on a CA discrete in space and time. Thus, the model is [3]:

- microscopic: every pedestrian is simulated by a separate cell;
- stochastic: local rules contain random values;
- space- and time-discrete.

The basic assumptions behind the model are:

- dynamics of pedestrian motion can be represented by a CA;
- global route is pre-determined;
- irrational behavior is rare;
- persons are not strongly competitive, i.e. they do not hurt each other;
- individual differences can be represented by parameters determining the behaviour.

A CA has two layers (Fig. 1). The first one – data layer – embeds the information about the geometry of the scene, i.e. placement of pedestrians and obstacles. Every cell in this layer has 3 possible states: "empty", "obstacle", "pedestrian".

The second layer embeds a vector field of directions and stores the information about the global route. This field of

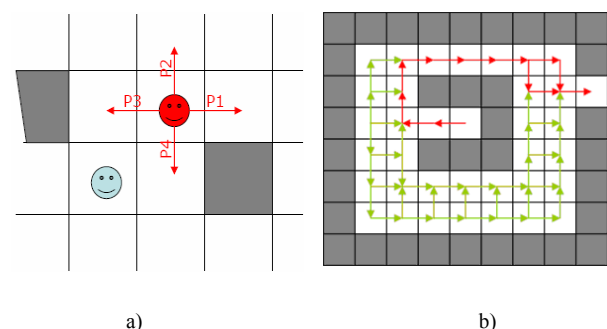


Figure 1. Structure of the model

¹ ANN – artificial neural network

directions is constructed so that to minimize evacuation time of a sole pedestrian. If there are several possibilities at a particular point, they are considered to be equally probable.

At every time step, for every pedestrian probabilities of shift for all the directions are being computed according to the following principles:

- if a target cell is occupied (by obstacle or other pedestrian), the corresponding probability is set to 0;
- pedestrians try to follow the optimal global route.

At every step the order of pedestrians' shifts is randomly chosen. Persons differ in their maximum speed. These differences are implemented via division of every time step into V_{\max} sub-steps $t_0..t_{V_{\max}}$. An i -th person tries to move at a sub-step k only if $v_i < k$, where v_i – his maximum speed.

III. ANTICIPATING PEDESTRIANS

Starting from the described above basic model, a pedestrian, capable of foreseeing the situation within his neighbourhood and accordingly optimizing his movement, may be generated. Further, a pedestrian possessing this property will be referred to as anticipating pedestrian.

As it was mentioned above, at every step a person determines probabilities of shift (P_k , $k=1,2,3,4$). These are these values that may be subjected to influence of anticipation. Let's assume, that pedestrians try to avoid collisions, i.e. a person tries not to move into a particular cell of his neighbourhood if (as he predicts) it will be occupied by another person at the next time step. This may be achieved by changing the probabilities in the following manner:

$$P_k \rightarrow P_k \cdot (1 - \alpha \cdot P_{k,occ}), \quad (1)$$

where α – free parameter expressing influence of anticipation, $P_{k,occ}$ – probability of occupation of k -th cell in the neighborhood by one of the neighbors. It is quite natural, that values P_k have to be normalized, so that their sum =1 (if at least one of them >0). It should be mentioned, that in this case all the pedestrians are assumed to have equal rights. If α is set to 1, a situation, when two pedestrians attempt to let each other move and stand still, may occur. Such deadlocks can be completely excluded only by selecting the value of α less than 1, however, the number of them can also be minimized by granting certain (e.g. fast-moving) pedestrians privileges. In this case the shift probabilities will be transformed into:

$$P_k \rightarrow P_k \cdot (1 - \alpha \cdot (1 - \frac{v}{v_{\max}}) \cdot P_{k,occ}). \quad (2)$$

It means that the fastest pedestrians do not take care of others, while slowly moving ones try to make way for those moving faster. By using in (2) a somewhat greater value instead of v_{\max} , the fastest pedestrians may be forced to be more "polite".

As it was shown above, anticipation is closely related to ability of foreseeing the system state, so the issue of how do the pedestrians predict (in other words, how do they compute

$P_{k,occ}$) remains open. Two variants were considered: observation- and model-based prediction. The first variant is based upon the assumption that pedestrians preserve direction of their movement. So, $P_{k,occ}$ may be considered to be a linear function of the number of pedestrians "looking" at the k -th cell (the direction of their look is defined by the direction of their previous shift):

$$P_{k,occ} = \frac{m}{M}, \quad (3)$$

where m – number of pedestrians "looking" at k -th cell; $M = \langle \text{number of cells in the neighborhood} \rangle - 1$, in our case $M = 3$.

Such an approach, though being the most simple and natural, is, at the same time, the least accurate. Thus, for the sake of comparison, the second approach was considered, according to which a target pedestrian for every cell of his neighborhood computes P_k of its neighbors (excluding himself) and the resulting probability is defined as follows:

$$P_{k,occ} = \sum_{i=1}^3 P_i - \sum_{i \neq j} P_i P_j + \sum_{i \neq j, j \neq k} P_i P_j P_k. \quad (4)$$

It is quite evident that this approach allows more accurate evaluation of $P_{k,occ}$, while being somewhat unnatural, as every pedestrian must know behavioral models of the others.

A number of experiments were held and typical performance of all the mentioned configurations of the model is given below (Fig. 2).

The results of simulation reveal the fact, that granting fast-moving pedestrians a priority results in greater overall evacuation time, thus making little sense. On the other hand, the more accurately $P_{k,occ}$ are computed, the better the performance. This proves the consistency of the proposed method of anticipation accounting (given by (1)).

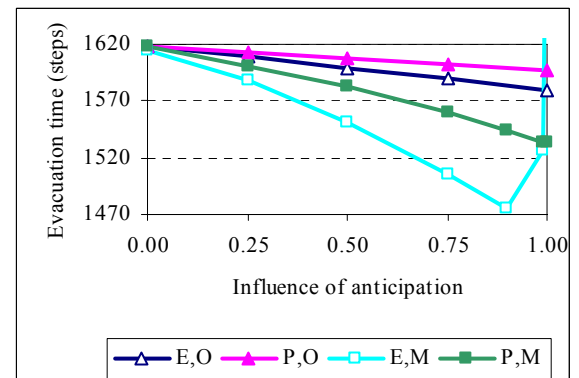


Figure 2. Performance of different configurations of anticipating pedestrians' model. (E/P – equality/priority of fast-moving pedestrians; O/M – observation-/model-based prediction).

IV. SPATIAL “DE-LOCALIZATION”

In the previous section an anticipating pedestrian was generating his prediction based on non-anticipating model of his neighbors. Thus, it is quite straightforward to make his prediction more accurate by involving an anticipating model of neighbors. For that, every pedestrian (within the neighborhood of radius 2) is subjected to the procedure described in section 3 for target pedestrian: calculation of P_k , calculation of $P_{k,occ}$ (4) and correction of P_k (1). It is evident, that in this case cells lying at a distance of 3 from the target pedestrian (center of the neighborhood) are involved in evaluation of $P_{k,occ}$. At the same time, pedestrians standing 2 cells apart from the center used non-anticipating model of their neighbors (standing 3 cells apart from the center). If they have used anticipating model instead, pedestrians standing 4 cells apart from the center of the neighborhood would have become involved. Thus, a neighborhood is growing until it “covers” the entire scene (Fig. 3).

It is clear that this process of neighborhood growth must be interrupted at a certain step, because of two reasons (theoretic and computational):

- every next step destroys spatial localization of the model, thus contradicting the hypothesis of local information (a pedestrian does not know what is happening beyond his neighborhood);
- growth of the neighborhood makes the model more computationally intensive.

Time-cost of calculation of probabilities P_k for one pedestrian is defined by the number of cells in his (extended) neighborhood. In our case (4-cell elementary neighborhood) this number makes up:

$$(r+1)^2 + r^2 - 1 \sim r^2, \quad (5)$$

where r – radius of an extended neighborhood.

So, this radius should be limited by a certain value, through which different extent of information distribution may be simulated. From a point of view of the target pedestrian, this may be given the following interpretation: all the neighbors inside the extended neighborhood are considered to be anticipating, unlike those standing on a border. On the other hand, pedestrians on a border may be also considered to be anticipating under an assumption that there are no

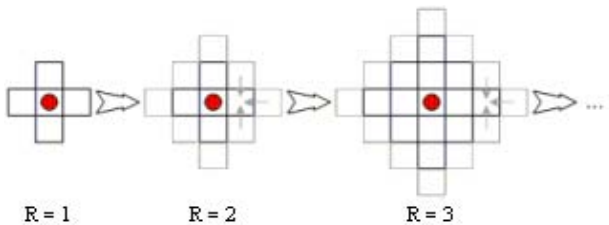


Figure 3. Growth of the neighborhood induced by anticipating model.

pedestrians beyond the neighborhood (in this case for these pedestrians holds $P_{k,occ} = 0$).

The described above scheme may be implemented via the following algorithm:

<neighborhood initialization:

neighborhood of radius r around the target pedestrian is filled with data from the corresponding area of the CA field>

repeat N times

{

for (all empty cells){
calculate $P_{k,occ}$:

$$P_{k,occ} = \sum_{i=1}^4 P_i - \sum_{i \neq j} P_i P_j + \sum_{i \neq j \neq k} P_i P_j P_k - \sum_{i \neq j \neq k \neq l} P_i P_j P_k P_l \quad (6)$$

}

for (all pedestrians){
correction of P_k :

$$P'_{k,occ} = \frac{P_{k,occ} - P_k}{1 - P_k} \quad (7)$$

$$P_k = P_k \cdot (1 - \alpha \cdot P'_{k,occ}) \quad (8)$$

}

}

It is quite straightforward, that if $r=2$ and $N=1$ we have the model described in section 3 (lowest curve in Fig.2), if $r>2$ with growing N distant pedestrians start affecting each other, however this influence decreases exponentially with distance. On the other hand, a problem of finding optimal value of N emerges. It is evident, that values less than $[(r+1)/2]$ make no sense, as information spreads with a “speed” of 2 cells per iteration and cells beyond radius of $2N$ are simply excluded from consideration. Also, growing N increases the time-cost of the model (linearly). So, there are two major questions to be answered:

1) will the further growth of N positively affect pedestrians’ performance;

2) is there an optimal value of N that provides minimum evacuation time.

In order to answer these questions numerous simulations were held. First of all, we have found that growth of N has a positive effect on the model performance, as it decreases the overall evacuation time (see Fig. 4). However, the slope of the curve decreases in exponential fashion, so, on one hand, there is no definite optimal value (or interval) for this parameter. On the other hand, interval 5..7 seems for practical purposes optimal as further growth of N has little effect.

Secondly, a typical relation between optimal values of α and N was discovered (see Fig. 5).

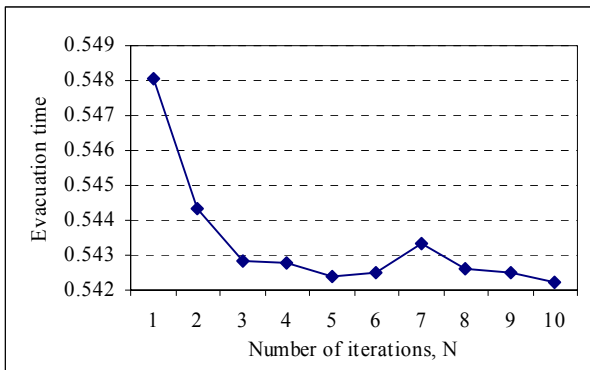


Figure 4. Evacuation time for different values of N . Every data point is obtained for optimal value of α , that depends on N . Evacuation time is given in relative scale with 1.0 corresponding to 150 time steps.

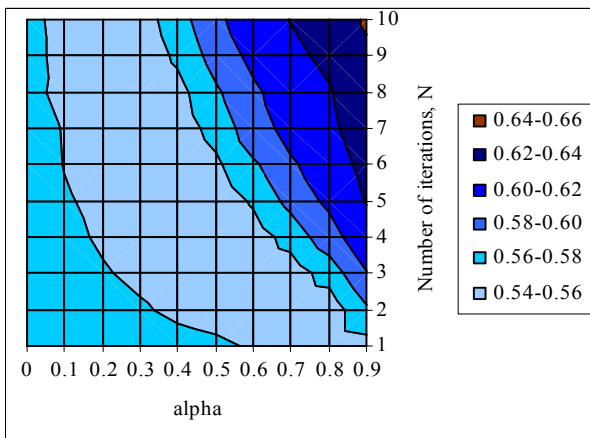


Figure 5. Evacuation time for different values of α and N . Scale is the same as in Fig. 4.

V. CONCLUSIONS

In this paper we have incorporated an anticipation property into a CA-based model of pedestrian traffic. It was demonstrated, how this property may be simulated via quite a simple mechanism and what impact it has on the overall performance of the crowd of pedestrians. The one inherent feature of anticipation is a requirement for additional information, based on which a pedestrian tries to optimize his trajectory. As pedestrians move in space, they need to have an idea about what obstacles they will face further on their way. Thus, a need of additional space-related information and, therefore, certain spatial de-localization occurs. In our case, a pedestrian was provided with relevant information via extension of his neighborhood. We have tried providing a pedestrian with another type of information – knowledge about the model of behavior of others. Though not being critical within the described framework, this additional information improved the performance of the crowd. The approach described allows simulating an arbitrary extent of spatial information distribution by varying the radius of extended neighborhood. At the same time, the model remains

localized in time and pedestrians do not make a full use of the additional information they were given. So, the next step in construction of realistic models is implementation of temporal de-localization by granting pedestrians an ability to construct multi-step predictions. However, it is a matter of further research.

REFERENCES

- [1] N. Gilbert and K. Troitzsch, *Simulation for the social scientist*. Open university press, Surrey, UK, 1999.
- [2] C. Burstedde, K. Klauck, A. Schadschneider, and J. Zittarz, "Simulation of pedestrian dynamics using a 2-dimensional cellular automata," *Physica A*, vol. 295A, 2001, pp. 507-525.
- [3] B. Goldengorin, A. Makarenko, and N. Smilianec, "Some applications and prospects of cellular automata in traffic problems" in *Proceed. Int. Conf. ACRI'06*, vol. 4173. Springer: LNCS, 2006, pp. 532-537.
- [4] R. Rosen, *Anticipatory Systems*. Pergamon Press, 1985.
- [5] D. Dubois, "Introduction to Computing Anticipatory Systems," *International Journal of Computing Anticipatory Systems*, vol. 2, 1998, pp. 3-14.

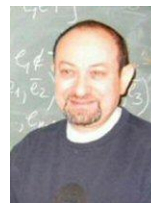
Alexander Makarenko is a head of the Department of Mathematical Methods of System Analysis, National Technical University of Ukraine "Kyiv Polytechnic Institute", Ukraine. He received Doctor of Science degree in mathematical modeling from Institute of Cybernetics, National Academy of Science, Ukraine in 1996. His research interests are in simulation of large socio-economical systems; mathematical modeling and prediction of geopolitical relations; design of geoinformation systems; signal processing and recognition; issues of complexity, symmetry and information.



Dmitry Krushinsky is currently a PhD student at the Institute for Applied System Analysis, National Technical University of Ukraine "Kyiv Polytechnic Institute", Ukraine. He received his M.S. degree in applied mathematics from the same University in 2006. His research interests include: mathematical modeling of complex systems; distributed computations; transportation problems; theory and applications of cellular automata.



Boris Goldengorin is an Associate Professor of Operations Department, University of Groningen, The Netherlands, and Professor of Applied Mathematics Department, Khmelnytsky National University, Ukraine. His research concerns design, complexity analysis (including domination analysis) of exact and heuristic algorithms based on data correcting and tolerances for combinatorial optimization problems (e.g., Traveling Salesman, Quadratic Cost Partition, Simple Plant Location, Maximization of Submodular Functions, Assortment, Max-Cut, Capacitated Vehicle Routing, Tool Switching, Boolean Knapsack, etc.).



Modeling of a Three-Echelon Supply Chain: Stability Analysis and Synchronization Issues

K.R. Anne, J.C. Chedjou, S.K. Bhagavatula, K.Kyamakya
 Institute for Smart Systems-Technologies
 University of Klagenfurt
 Klagenfurt, Austria

Abstract— This paper introduces the supply chain networks integration and discusses the interest of synchronization within them. The evaluation of the causes of uncertainties within the supply chain networks is considered. The structure of a three-echelon supply chain is envisaged and the modeling of this structure is carried out. It is shown that the supply chain network can be exposed to both external and internal perturbations. The origin of these perturbations is discussed and it is shown that the stability of the supply chain network is very sensitive to these perturbations. The effects of the external perturbations on the supply chain network are considered. It is shown that these perturbations can saturate the supply chain network and also create bullwhip effects and chaotic phenomena within the network. A method is developed which is based on an adaptive algorithm for the automatic cancellation of the effects of external perturbations by re-adjusting the internal thresholds of the supply chain network in order to achieve synchronization. Some additional insights into theory and practice in supply chain managements are provided.

Keywords—Synchronization; Supply chain networks; Supply chain network control; Supply chain optimization; Bullwhip effect; Chaos in supply chains

I. INTRODUCTION

Supply chain management (SCM) is the combination of management and science. SCM helps in improving/managing the way a company finds sources for the raw components it needs to make a product and the way it distributes the product to customers. The modern supply chain networks are global in nature and have many interconnections i.e. dependency or coupling between each. The supply chain network comprises of geographically dispersed facilities, like sources of raw materials, manufacturing plants, warehouses and transportation facilities. The facilities may be operated by single entity, many entities within a company, third-party providers or other companies. The primary objective of the supply chain network, or the individual entities in the network, is to deliver the product in the correct quantities at correct time by meeting all the quality measures with competitive price. In addition to this, the threshold of stocked products, quantities must be continuously sustained and uncertainties (that can occur within the supply chain) must be well controlled in order to avoid breaking in stocks and also the well known bullwhip effect at a given level of the supply

chain. This can be achieved through a good coordination or synchronization between the various levels of supply chain.

In order to achieve the stated objective, all the stakeholders in the supply chain network are integrated/coupled. The first part of coupling is concerned with functional integration of purchasing, manufacturing, transportation, and warehousing activities. Besides functional integration intertemporal coupling, also called hierarchical integration, of these activities over strategic, tactical, and operational levels is also important [1, 2]. This intertemporal coupling requires consistency among overlapping supply chain decisions at various levels of planning. However the major role of the intertemporal integration is in product life cycle design. Improved coupling of activities across multiple companies/entities in a supply chain is a concern of increasing importance. Information technology is the key enabler for the coupling in supply chain. The information systems provide the necessary information needed for the integration. Each entity works with their own objective, there by showing a tendency only for loose coupling.

The structure of the paper is as follows, section II is concerned with a brief description of few factors that are contributing for the uncertainties and need to synchronize the uncertainties. Section III deals with supply chain modeling. We present the structure of the supply chain under consideration which is made-up of three levels. The communication between these levels and also the data traffic within them is explained /discussed and it is shown that the scenario/dynamics of the complete supply chain can be modeled by the Lorenz system. In section IV, we will describe what type of synchronization is applied in supply chain networks. Section V describes the effects of the external perturbation on the system and the controlling method. Transitions from regular effects to bullwhip effects or chaotic effects are shown through the stability analysis. Section VI deals with the conclusion and proposals for future works.

II. UNCERTAINTIES IN SUPPLY CHAIN NETWORKS

Even though integration of the stakeholders should provide the ideal solution for the optimization of the supply chain networks, in many cases it is not [1-3]. Business is not usual always; there are many things that happen with time. The major source for uncertainties in supply chain networks originates from the fact that operations are performed over

long period of time and stakeholders are dispersed globally. Supply chain management is a complex set of processes and flows (information flow, product flow, monetary flow) that can either add a great deal of efficiency and profit or can cause serious problems for a company. SCM is technology intensive in some aspects, in some ways it can be compared to a simple game gossip game.

In the game, one passes the secret to his friend, which is then passed around a circle of friends. The secret can be true

either because the capital invested is small or they can arrange financing and storage at advantageous rates, also those whose setup costs are high, will prefer large lot sizes and corresponding large inventory. Retailers with high value of goods but no setup costs will prefer to hold the minimum stock they deem necessary to ensure good customer service. These individual varying factors create demand variability in order to make maximum profits. There are also the problems of misunderstanding the market promotions, social mistrust, forecasting problems. All these leads to more inventory at

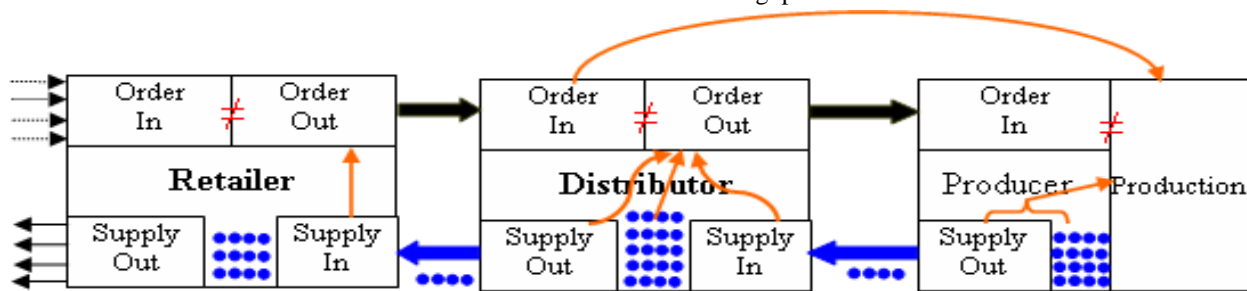


Figure 1: Three level supply chain model

or false, but what is usually the case with the secret is that it becomes exaggerated – if the secret starts out as “there is an insect outside,” it ends as “a monster is in the school”.

The supply chain can often be seen as the same circle. Today’s supply chains pass information relating to item information, forecasting and replenishment upstream and downstream among manufacturers, brokers, distributors, retailers and warehouse, transportation, management and global trade systems. The final result is a flow of information from the creation of a product to the point where that product is sold to the end consumer.

As in the gossip game, the accuracy of information often depends on the quality of the data at the beginning of the cycle, and maintaining same information throughout the supply chain. If the information is wrong in the beginning, it never has a chance of being correct when it finally gets up or down the supply chain. In fact, if inconsistencies remain, there are chances for errors to propagate through the whole supply chain.

The definition of a truly efficient supply chain is when all companies involved are communicating correct or reliable data – a manufacturer is communicating the reliable product information and receiving accurate purchase orders; a retailer is receiving the specific products that were ordered; and the product is available to the end consumer at the right time and at the right price. However communicating the reliable data is always not possible in supply chains as each stake holder has different objectives and constrains. In well-managed supply chains, the inventory flows between members of the chain with little delay. The goal of supply chain management is to optimize the whole system [1-3]. Total chain-wide transportation, holding, and setup costs should be minimized. However, this integration may be difficult to achieve because different members of the chain have conflicting objectives. Supply chain members whose inventory holding cost is small,

different levels and can cause the well known bullwhip effect or forester effect. In this paper, the occurrence of this effect and also the chaotic effect in the supply chain due to external perturbation of the system is shown.

III. SUPPLY CHAIN MODELING

The theoretical framework for the supply chain management underlies the setting, optimization and control of the system model. Here, In this work we use the structure of a three-level supply chain as illustrated in Fig. 1.

i	Time period
m	Ratio of customer demand satisfied
k	Safety stock coefficient
x_i	The quantity demanded for products in current period
y_i	The quantity distributors can supply in current period
z_i	The quantity produced in current period depend on the order

A three echelon model is envisaged in Fig. 1 to describe a simple scenario in a very complex supply chain. Fig. 1 also illustrates the relationship between the three layers. The orders they make may not be equal to orders they receive. The order out quantity depends not only on how much inventory you have already, and how much you want to supply out. Order out quantity at retailer depends on the ratio m at which the demand is satisfied during the previous order. Distributor needs to take into consideration among other things, the distortion rate r that can occur in the inventories. The producer needs to take care about the safety stock k in order to avoid the small production batches. These phenomena are explained below with mathematical modeling.

We consider that the demand information is transmitted within the layers of the supply chain with a delay of one unit time. As illustrated in Fig. 1, the ordering quantity is not same as the requested order quantity at any level. The order quantity at current period of time at retailer is linearly coupled with the distributor and it is influenced by how much of demand is satisfied in previous period of time. This phenomenon can be represented as shown in Eq.1.

$$x_i = m(y_{i-1} - x_{i-1}) \tag{1}$$

m is the ratio at which the demand is satisfied. As it appears from Fig. 1, the dependency or coupling of distributor on producer and retailer is no more linear. Indeed the distributor needs to take the combined effect of retailer and producer into consideration before making his order, i.e., quadratic coupling. Apart from this, the distributor also needs to take into consideration the expected loss rate or distortion that can take place on the producer's supplies. This can be expressed mathematically as shown in Eq. 2.

$$y_i = x_{i-1}(r - z_{i-1}) \tag{2}$$

r is the distortion coefficient. The production quantity from the producer unit typically depends on the distributor's orders and the safety stock. However the distributors' orders again depend on the retailer's orders, i.e., the producer needs to take the combined effect of retailer and distributor into account before making production decisions. This can be represented as

$$z_i = x_{i-1}y_{i-1} + kz_{i-1} \tag{3}$$

Eqs. 1-3 represent the quantity demanded by customers (Eq. 1), the inventory level of distributors (Eq. 2) and the quantity produced by producers (Eq. 3).

- Where $x_i < 0$ denotes that the supply is less than customers demand in the previous period
- $y_i < 0$ denotes that information is severely distorted and no adjustment is necessary to inventory level
- $z_i < 0$ denotes the cases of overstock or return and hence no new productions.

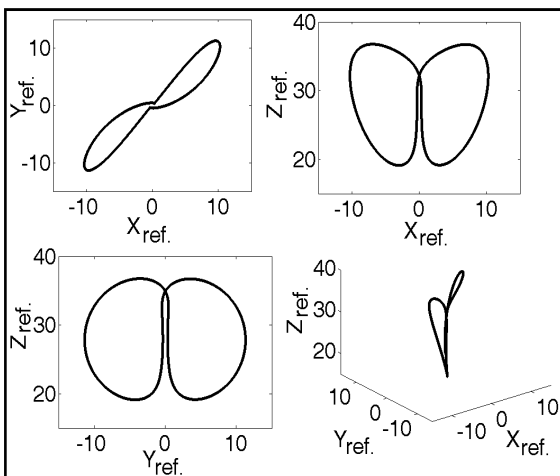


Figure 2: Reference System with given coefficients

Evidently the continuous forms of Eqs 1-3 can be rewritten as Lorenz equations of state:

$$\dot{x} = \sigma(y - x) \tag{4}$$

$$\dot{y} = rx - y - xz \tag{5}$$

$$\dot{z} = xy - bz \tag{6}$$

Depending upon the parameter values, this model produces a wide variety of nonlinear features. In Fig. 2, we showed the reference model with the parameter values $\sigma = 15$, $r = 29$, and $b = 2/3$ to illustrate the regular state of the reference supply chain model.

IV. SYNCHRONIZATION ISSUES IN SUPPLY CHAIN NETWORKS

In this section we briefly introduce the importance of synchronization and present the modern methods to deal with it. When organizations synchronize supply chains and have real-time access to data, they enjoy several competitive advantages:

- Anomalies and exceptions are identified early and the data for intelligent response is immediately available. This greatly minimizes the bullwhip effect and saves downstream partners and customers from needless activity
- Back-end processing of change orders, modified invoices, and updates to inventory systems can happen as decisions are being made
- Visibility into partner systems makes planning easier and enables managers to see opportunities that were not apparent before. This visibility also enables supply chain partners to collaborate more effectively. This cooperation is essential when problem resolution requires the coordination of several supply chain partners
- Easier integration and expansion. Because the synchronization and data passing mechanisms are not based on packages from supply chain software vendors or ERP firms, the software is optimized for all players. Packages can be changed without disrupting the infrastructure and new partners can be added easily

Is supply chain synchronization the ultimate concept? In reality, it is only one of the steps towards the integration of all components of the supply chain. To date, the majority of supply chain efficiencies has come from improvements within the four walls of each individual company. Certainly, there has been collaboration between trading partners in terms of improved communication (EDI and current internet based web information exchanges), better information (point of sale data and the CPFIR initiatives), and a general willingness to work more closely together. But the efficiencies have been gained through improvements that any executive can effect at his or her own workplace by putting in place the appropriate company-wide initiatives aimed at improving the internal business process. Now comes the most difficult part: True coordination between and among all trading partners, which is most difficult. To take the next step, it is critical that companies not only agree to communicate and work together, they must also begin to function as a single entity.

- Apart from all these data discrepancies, there may be other disturbances which occur due to external perturbations. There are different methodologies applied to study these discrepancies and to quantify their effects. In this paper we study the two major synchronization types applied in supply chain networks based on the supply chain model [4]. Complete Synchronization: the cycle time at an upstream stage equal to cycle time of the next downstream stage
- Partial synchronization: the cycle time at an upstream stage is an integer multiple of the cycle time of the next downstream stage

In this paper, we present methodology to control the effects caused by external perturbations through internal measures.

A. Complete synchronization

Complete synchronization enables the supply chain to react quickly to changes in demand and in product design. This type of synchronization is particularly suitable in just-in-time supply chain networks. To achieve the complete synchronization the complete chain should be integrated. Many retailers and manufacturers have looked to the Internet to provide a cost-effective avenue for improving the data deficiencies present in today's supply chains. One of the main ways to decrease the amount of inconsistent item information being passed among companies is to automate many of the item maintenance functions, such as data changes and new item introductions, performed by manufacturers. Synchronization tools automate processes that are traditionally conducted through excessive paperwork, such as informing trading partners of changes to product information. This synchronization method affects the registry and lifecycle management of synchronized products, locations and trading capabilities. Data synchronization involves a strategic combination of technologies, business strategies and implementation of industry standard in messaging that ties together the information management systems of all parties participating in a given supply chain [4, 5].

The modern synchronization tools provide automation of the paper work but not concentrate on what happen if the given data is slightly changed accidentally. Effective data synchronization first involves making information visible within a secured environment, which is again a case that we are discussing throughout this paper.

B. Partial synchronization

Partial synchronization is achieved through the controller item. Apart from the data synchronization as explained in complete synchronization, a controller item is developed to mitigate the effect caused due to time lag. In these synchronization major efforts is placed in modeling the effect and quantifying it. The modeling and quantification of the effect caused by the time lag, information discrepancy, and individual objectives helps in designing the controller/synchronizer element. This controller item can be unique for each entity or supply chain as a whole. Partial synchronization is also achieved indirectly by quantifying the region where uncertainties exists. After identification of

uncertain regions they try to avoid or extra careful in that region [1, 3-7].

In practice, as we discussed in section II and section III, management of commercial supply chains is a challenging issue as diverse pre-defined 'data' thresholds or requirements within them should be currently stabilized with regard to the existence of some uncontrollable effects due to both internal and external perturbations to which the supply chains may be subject. The dynamic character of the information flows within the commercial supply chains is another factor which makes it very difficult to stabilize the overall behavior of the whole supply chain. Therefore, the instability of the supply chain may be directly perceived as the modification of data thresholds or pre-defined requirements based on the uncertainties discussed in section II. In section V, we will describe the effects that can be caused by the external perturbation to the stability of the system and how it can be controlled internally.

V. SYSTEM ANALYSIS AND SYNCHRONIZATION

The causes of supply chain instability can be broadly classified into two categories. The first cause is the dynamical and nonlinear character of the motions (i.e. material/products flow, information exchanges, etc...) between different entities in supply chains. The second cause originates from the effects of both external and internal perturbations to which the supply chain is subjected. An optimal management of the information flows within the supply chains may be of high importance in order to alleviate the effects resulting in negative consequences on the flows within the supply chains. This could be achieved through an adaptive control mechanism which is based on a current comparison of the dynamical data within the supply chains with the pre-defined data fixed by the requirements of the supply chains. Here, an automatic or adaptive control of the flows within the supply chains should be able to detect changes in the flows within the supply chains and act accordingly/consequently (by undertaking a given action within the supply chains) in order to alleviate the undesirable effects and therefore stabilize the system behavior that has been perturbed. The achievement of synchronization is observed when the action undertaken has allowed the recovery of the original behavior (eventually thresholds or reference requirements) of the supply chain.

This paper develops an adaptive method (algorithms and/or tools) for the systematic and automatic control of the flows within the supply chains. The external perturbations can be a consequence of the dynamical behavior of the market demand, forecasting methods, high lead times, etc. In fact, due to the dynamic changes as discussed (in time domain), some pre-defined data or requirements within the supply chains (thresholds like safety stocks) may be varying accordingly as consequence of these perturbations. The internal perturbations within the supply chains are random (or undesirable) effects which can originate from the malfunctioning of a given echelon of the supply chain (e.g. Machine breakdowns, transportation delays etc.). It should be worth mentioning that a combination of the simultaneous effects of both internal and external perturbations may be responsible of the dynamic motion variations (e.g. flow of materials, information

exchange, etc.) within the supply chain. This is a concrete and/or realistic scenario as the supply chains of many companies are currently exposed to the both types of perturbations. This later scenario is however out of scope of this paper, which does concentrate solely on external perturbations and related internal adjustment of parameters to achieve synchronization. Thus, for the sake of simplicity, we consider the case where there is no internal perturbation of the motions within the supply chains. In essence, this work looks at the possibility of re-establishing appropriate data thresholds fixed by the pre-defined behavior requirements. We restrict our analysis to the case where the external perturbations are periodic. It is well-known that periodic waves/signals are characterized by their amplitude and frequency. Considering this restriction, the amplitudes of perturbations can give/show the rate of variation of the products' quantities. The frequency of perturbations determines the rhythm or the sequence of the process related to the variations in the products' quantities.

The development of methods (algorithms) to automatically control and alleviate the effects of external perturbations is of high importance as in practice the overall system behavior may be very sensitive to external perturbations. This may lead to instability.

We develop a method based on an adaptive algorithm for the automatic cancellation of the effects of the external perturbations by re-adjusting the internal thresholds. Indeed, this method is an adaptive numerical code which performs a regulation by currently comparing the perturbed data within a given supply chain with the reference data (which are fixed and pre-defined data) according to the requirements of the three echelon supply chain. Depending upon the key characteristic parameters of the external perturbations, the state of the flows within the reference scheme of the supply chain can even be saturated due to external perturbations as shown in Fig. 3.

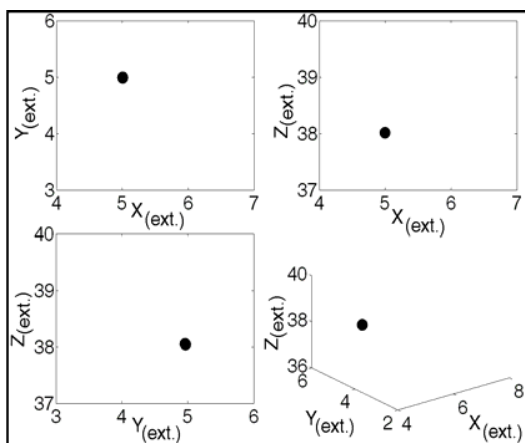
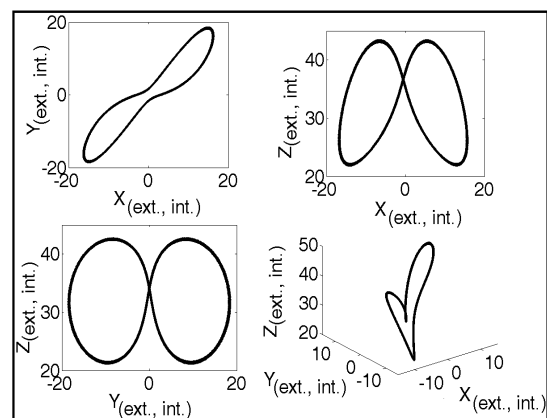


Figure 3: Saturation of the supply chain due to external perturbations

Here, the saturation manifests itself by a sudden exhibition of fixed or constant values/data along each echelon of the globally perturbed three echelon supply chain. Indeed, the states of the reference supply chain are represented by the attractors ($X_{ref.}$, $Y_{ref.}$, $Z_{ref.}$) as shown in Fig. 2. The state of the externally perturbed system is represented by the attractors ($X_{ext.}$, $Y_{ext.}$, $Z_{ext.}$) in Fig. 3. Fig. 3 clearly shows the saturation of the reference system due to external perturbations. To alleviate the effects due to external perturbations, we develop a numerical code based on a regulation feedback. In fact, the numerical code considers the effects of external perturbation and adjust the values of the internal parameters of the three echelon supply chain by incrementing all of them simultaneously whereby the incrementing of each internal parameter is performed in a well defined windows or interval of variation. The numerical code always compares the results from the supply chain submitted to both external perturbation and the internal adjustment of the system parameters with the results of the reference (or original) supply chain behavior. A threshold error was fixed (which is less than approximately 0.1) under which full alleviation of the effects due to external perturbation is supposed to be effective, leading to the achievement of synchronization, which results in the recovery of the reference system behavior. This is clearly illustrated in Fig. 4 where the attractors obtained are almost similar to those of the reference model shown in Fig.2.

Figure 4: Alleviation of the saturation effect caused by



external perturbation with adaptive numerical code

In a further study, we considered the same reference model of the three echelon supply and show that a particular change of the key parameters of the external perturbations can lead to well-known bullwhip and chaotic phenomena. This is clearly illustrated in Fig. 5 which shows chaotic attractors representing the perturbed state of the supply chain.

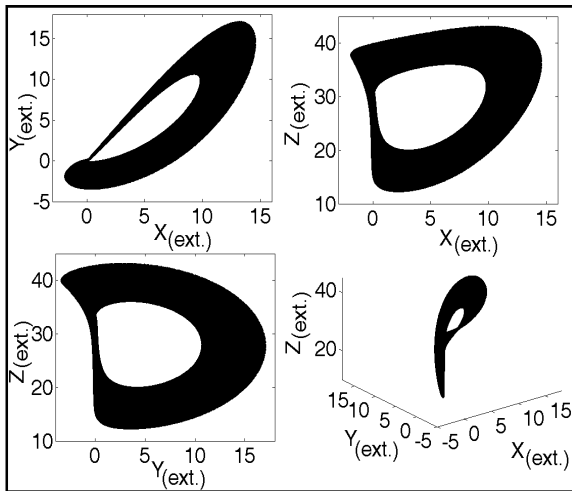


Figure 5: chaotic state of the supply chain due to external perturbations

For these specific states of the perturbed supply chain we obtained that the value of the Largest 1D numerical Lyapunov exponent is equal to $+0.032$. The same feedback/regulation process (see the description above) has been performed and we obtained the achievement of the complete synchronization as shown in Fig.6.

The adjustment of some internal parameters could re-establish the reference supply chain system behavior as shown in Fig. 6. This last case shows the achievement of synchronization with very small values of synchronization errors as illustrated by the attractors in Fig. 6 which are similar to those in Fig. 2.

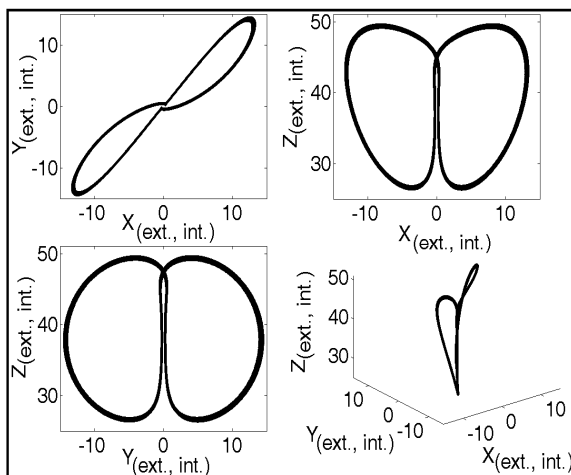


Figure 6: Alleviation of the chaotic effect caused by external perturbation with adaptive numerical code

VI. CONCLUSION

The management of supply chain networks is a complex issue which involves numerous dynamic situations varying with time. In addition to the coupling between the entities, the entire supply chain is customer oriented. In this modern era of globalized supply chains, market demand is short lived,

forecasting methods are prone to dynamics, service contracts are well fixed in advance and many other constrains create uncertainties as discussed throughout this paper. This paper sets up a three-level supply chain, similar to the well known *Lorenz model*, and probes into the causes and presence of the saturation and chaos when the system receives external perturbations. This work illustrates how a supply chain can go into saturation mode under external perturbations. It also details how the same system can go to chaotic mode causing forester effect, if the parameters of the external perturbations are changed. The states illustrated in this work can occur to different parameter values i.e., they are not specific to only a set of values. This paper also proposes an adaptive algorithm for the automatic cancellation of the effects of the external perturbations by re-adjusting the internal thresholds. This method is particularly appealing as it is possible to control or adjust the internal thresholds of the supply chain network. The achievement of synchronization was shown for different sets of the threshold parameters. The simulation results show that the proposed methods are indeed effective. The solutions proposed in this paper offer a new range of possibilities for risk managers and provide a future research direction. The future research is also proposed in arriving at the adaptive synchronization with the help of analog simulation based on CNN (Cellular Neural Network) technology. An interesting and challenging problem of practical interest may be the development of adaptive numerical codes to achieve synchronization within a supply chain network under the cumulative effects of both internal and external perturbations. This is a realistic scenario which currently manifests itself in commercial supply chain networks. It would also be of great interest the analysis the coupling between different structures of supply chains and the achievement of synchronization within them. It is well known that in practice, many commercial supply chains are coupled.

REFERENCES

- [1] L. d. Giacomo and G. Patrizi, "Dynamic nonlinear modelization of operational supply chain," *Journal of Global Optimization*, vol. 34, pp. 503-534, 2006.
- [2] H. B. Hwang and N. Xie, "Understanding supply chain dynamics: A chaos perspective," *European journal of operations research*, pp. 1163-1178, 2006.
- [3] R. Wilding, "The supply chain complexity triangle: Uncertainty generation in the supply chain " *International Journal of Physical Distribution & Logistics Management* vol. 28, pp. 599 - 616 1998.
- [4] M. Khouja, "Synchronization in supply chains: implications for design and management," *journal of the operations research society*, pp. 984-994, 2003.
- [5] Y. Narahari, N. Vishwanadham, and R. Bhattacharya, "Design of synchronized supply chains: A six sigma tolerancing approach," presented at International conference on robotics & automation, Sanfransisco, 2000.

- [6] F. Chen, Z. Drezner, J. K. Ryan, and D. Simchi-Levi, "Quantifying the Bullwhip Effect in a Simple Supply Chain: The Impact of Forecasting, Lead Times, and Information," *Management Science* vol. 46, pp. 436 - 443 2000.
- [7] Z. Lei, L. Yi-jun, and X. Yao-qun, "Chaos Synchronization of Bullwhip Effect in a Supply Chain," presented at Management Science and Engineering, 2006. ICMSE '06. 2006 International Conference on, Lille, Date: 5-7 Oct. 2006.
- [8] J. D. Sterman, "Modeling managerial behavior: misperceptions of feedback in a dynamic decision making experiment," *Management Science* vol. 35 pp. 321 - 339 1989



Kyandoghene Kyamakya obtained the M.S. in Electrical Engineering in 1990 at the University of Kinshasa. In 1999 he received his Doctorate in Electrical Engineering at the University of Hagen in Germany. He then worked three years as post-doctorate researcher at the Leibniz University of Hannover in the field of Mobility Management in Wireless Networks. From 2002 to 2005 he was junior professor for Positioning Location Based Services at Leibniz University of Hannover. Since 2005 he is full Professor for Transportation Informatics and Director of the Institute for Smart Systems Technologies at the University of Klagenfurt in Austria.



Koteswara Rao Anne received his BE in Electronics and Communication and MSc in Electrical engineering and Information Technology from Bharathiyar University, Coimbatore, India and Leibniz University of Hanover, Germany, in 2001 and 2006, respectively. He is now a Ph.D. student at the University of Klagenfurt in Austria. His research interests include advanced planning and scheduling in production systems, Intelligent supply chains, systems dynamics, multi-agent systems, chaos and its applications.



Jean Chamberlain Chedjou received in 2004 his doctorate in Electrical Engineering at the Leibniz University of Hanover, Germany. He has been a DAAD (Germany) scholar and also an AUF research Fellow (Postdoc.). From 2000 to date he has been a Junior Associate researcher in the Condensed Matter section of the ICTP (Abdus Salam International Centre for Theoretical Physics) Trieste, Italy. Currently, he is a senior researcher at the Institute for Smart Systems Technologies of the Alpen-Adria University of Klagenfurt in Austria. His research interests include Electronics Circuits Engineering, Chaos Theory, Analog Systems Simulation, Cellular Neural Networks, Nonlinear Dynamics, Synchronization and related Applications in Engineering. He has authored and co-authored 2 books and more than 22 journals and conference papers.



Sreeram Kumar Bhagavatula received his BSc in Computer Science and MSc in Computer Science from Andhra University, India, in 2002 and 2005, respectively. He worked as programmer operations in Indian railways from 2004 – 2007. He is now a Ph.D. student at the University of Klagenfurt in Austria. His research interests include military supply chains, city logistics, multi-agent systems, chaos and its applications.

A Stable Path Selection Algorithm for Protecting Optical Networks using OBGP Backup Routing

Wen-Fong Wang

Dept. Computer and Communications Engineering
National Yunlin University of Science & Technology
Douliu city, Yunlin, Taiwan
wwf@yuntech.edu.tw

Lih-Chyau Wu

Institute of Information Engineering
National Yunlin University of Science & Technology
Douliu city, Yunlin, Taiwan
wuulc@yuntech.edu.tw

Abstract—BGP is an inter-domain routing protocol that allows an autonomous system (AS) to apply local policies for selecting the best route and decide whether this route is propagated to other ASes or not. When a network failure occurs, BGP withdraws the failed path and selects immediately an alternate path for backup routing. In this investigation, we study the Optical Border Gateway Protocol (OBGP), which can give edge network users in optical networks an automatic control means to establish a lightpath through optical AS domains. Actually, OBGP inherits the features from BGP for optical networks. However, in previous research, it indicates that BGP cannot guarantee the system stability of backup routing under failures; this is due to the inconsistency of local policies between two neighboring ASes. For the stable and safe backup routing of OBGP, we propose a stable path selection scheme for optical AS domains and draw properties for conducting local policies. To verify the scheme, a prototype implementation of our approach and a test environment are fulfilled for functional testing. From the testing, it shows the basic functions of our scheme are correct and effective.

Keywords—OBGP; BGP; Backup Routing; Convergence

I. INTRODUCTION

Optical networks have become more accessible to users on the edge of communications networks after fibre optic cables were laid in and among many communities by carriers. With WDM (Wavelength Division Multiplexing) technology, the users can create high bandwidth connections to their peer groups by employing the leased links and wavelengths of the optical networks. To light up dim fibers, carriers are willing to operate their own “wavelength cloud” to offer such lightpath service to edge network users. In this situation, establishing connectivity of lightpaths requires manual provision and management.

There are few ways for managing and configuring wavelengths between network domains, which allow edge network users to manage their own lightpaths across several wavelength clouds. By shifting the responsibility of administrating lightpaths to users, carriers allow the users to manage their own optical wavelengths better and avoid some expensive services such as lightpath management provided by the carriers. In [1], the authors show that the border gate protocol (BGP) can be extended to allow an edge user to set up a lightpath to peers across AS domains. This approach is

called Optical BGP or OBGP. It is a distributed approach, which gives control to edge users, and allows them to manage their leased objects better. OBGP can provide an inter-domain routing and signaling capability that integrates heterogeneous domains into an end-to-end optical network and can coexist with most of the existing intra-domain solutions.

In the related research, M. Francisco, et al. presented new attributes and tags carried by UPDATE messages to reserve optical wavelengths for a lightpath setup [2]. Another work in [3] proposed a new message type for OBGP, called “OBGP message” to achieve end-to-end signaling and routing for optical networks. The authors created a wavelength table for each OBGP router to store wavelength availability and setup information. In [1], [4], the authors described the applications and functional requirements of OBGP and investigated the lightpath provisioning for inter-domain routing. To extend the BGP protocol for optical networks, a few new optional attributes have been considered and created in the protocol data units of BGP so that wavelength information can be encoded into the routing information base (RIB) of BGP. In [5], the authors discussed a broad range of issues related to the requirements for general inter-domain and inter-area routing in optical networks. They reviewed the applicability of existing routing protocols in the Internet and telecommunications for various optical routing. In our investigation, we follow the results in [1], [4], which seem to be more promising and realizable.

One common weakness in most optical networks is that any link or router failure among ASes would cause the significant loss of transmitted data. In the Internet, there are thousands of ASes connected, whereas an AS is a collection of routers and links operated by a single institution. To increase the reliability of networks under link or router failures, backup routing schemes could be used to withdraw a failed route and select an alternate path to recover the communication service. For this alternate path we can call it a backup path. Nevertheless, the backup path is not easy to select and must be constrained by some commercial relationships between ASes. In some failure scenarios, the backup route would introduce a BGP convergence problem [6], which results in protocol divergence. The work in [7] presents a general model for backup routing while allowing each AS to apply local routing policies that are consistent with the commercial relationships it has with its neighbors. The authors proved their model is inherently safe in the sense that the global system remains safe

This work was supported by the National Science Council, Taiwan, R.O.C., under contracts NSC96-2221-E-224-006.

under any combination of link and router failures. The safe characteristic means that the sets of routing policies would never lead to BGP divergence.

In this study, a stable path selection scheme for OBGp safe backup routing is considered. In our approach, several properties are suggested for an AS to follow in setting its routing policies, and an algorithm is proposed for OBGp to find best safety backup paths. With our approach, OBGp routers can select a best and safe backup path to restore transmission quickly and attain minimum data loss, while a link or router fails. Throughout the paper, the two words, path and route, are used interchangeably.

This paper is organized as follows. Section II describes the OBGp protocol and its incorporated architecture with OXCs. Section III specifies a safety model for backup routing [8], [9], [10], which can avoid the convergent problem of BGP as local policies apply in case a failure occurs in AS domains. In Section IV, our scheme for safe backup routing in optical AS domains is presented. We sketch and formalize the new properties of OBGp to be guidelines, which govern the setting of AS local routing policies. Also, an algorithm is devised to find the best and safe backup route for OBGp entities. In Section V, the implementation of our scheme and a functional testing environment are described. Finally, our work is concluded in Section VI.

II. OBGp SYSTEM ARCHITECTURE

BGP can reach different AS domains by using dedicated AS paths based on path vector routing. The usage of AS paths enables routing decisions to prevent routing loops. Having full path visibility is rather useful to enhance BGP for setting up a lightpath from one AS to others. To allow BGP carrying lightpath information, the BGP's OPEN and UPDATE messages can be used to include lightpath setup information in addition to reachability information [4], [11]. There are two possible ways to perform lightpath reservation using OPEN and UPDATE messages, first carrying a lightpath reservation request between OBGp speaking devices and secondly propagating the status of lightpath reservation information throughout the network.

Optical cross connects (OXCs) are non-blocking, reconfigurable optical switches where an optical signal entering any input port can be directed to any desired output port. In WDM networks, the OXCs may be combined with other optical components, such as optical multiplexers and demultiplexers, optical filters, etc., to fulfill wavelength routing. For OBGp, it is proposed that OXCs can be integrated with BGP routers [1]. As Router B in Fig. 1(a), a new router, called an OBGp router, combines a BGP router with OXCs.

Usually, two pairs of input and output ports are necessary to form a bidirectional link of connecting two routers via an OXC. For the bidirectional link, the two pairs of input and output ports with the connections inside the OXC constitute an optical cross connect as shown in Fig. 1(a). In [1], the basic concept of a virtual BGP router is to bind each optical cross connect with a separate BGP process and administer the bidirectional optical channel; and together for the wavelengths used in an OBGp router, assume mapping can be made

between the wavelengths and IP addresses. The use of a virtual BGP router for each cross connect can allow the use of standard BGP routing with virtually no modifications necessary to support optical lightpaths. As for tunable lasers and filters, which have a limited range of wavelengths, different IP suffixes can be used to indicate the appropriate wavelength range. In addition, the virtual BGP router could be assigned its own private (or public) AS for inter-domain routing. The main purpose of OBGp routers is to be able to announce routes, perform route filtering and classification, and provide enhanced BGP capabilities to other OBGp peers.

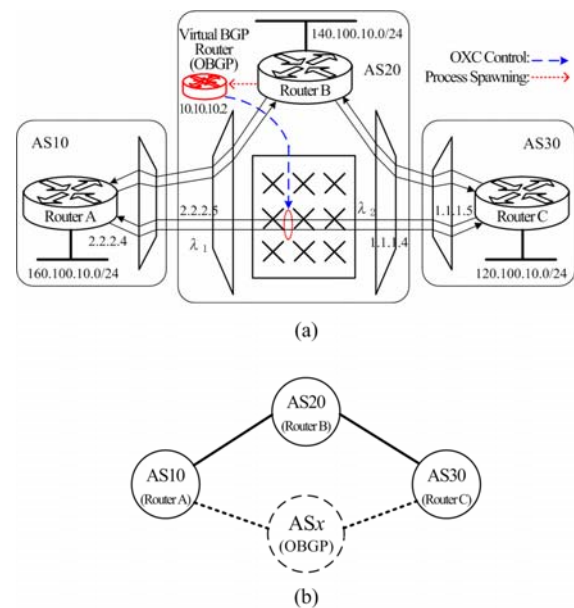


Figure 1. (a) Integration of an OXC and a BGP Router; (b) The abstract AS model

To explain the operation of virtual BGP routers, suppose that Router B receives BGP OPEN messages from Routers A and C (Fig. 1(b)) asynchronously. It can decide to set up an optical cross connect between the two routers if the information about wavelengths (IP addresses), the framing protocol, the preferred destination, etc. is equal in the optional fields of the OPEN messages. Rather than modifying the existing BGP code on Router B, it is envisaged that upon detecting the optional fields in the OPEN messages from Routers A and C, a process, called Lightpath Route Arbiter (LRA), in Router B would spawn a virtual BGP router process that would establish the optical cross connect and BGP peering sessions between Routers A and C through specific input and output ports of the OXC.

Router B's LRA spawns the virtual router process on its own CPU and then creates a configuration file for the virtual router from the information it received in the OPEN messages from Routers A and C. The configuration file for the virtual router might look like as shown in Fig. 2. While Router B is configuring its new virtual router, the LRA processes in routers A and C will update their configuration statements using the information provided in the options field of the OPEN message from Router B. For example, in Fig. 2, it shows the initial configuration of the virtual BGP router. The

loop back address of interface is defined as 10.10.10.2. The wavelength λ_1 is defined to be with suffix $x.x.x.4$ and λ_2 with suffix $x.x.x.5$ as shown in Fig. 1(a). Notably, the symbol $x.x.x$ means the address prefix of the shared network between neighboring ASes. Therefore, the suffix $x.x.x.4$ indicates that λ_1 can pass from AS10 through the OXC to AS30 with the fixed identifier 4 and for λ_2 , vice versa. If the establishment of BGP peering sessions with Routers A and C is successful, the BGP UPDATE messages would be used for exchanging routing information; otherwise, Router B can either decide to leave the virtual BGP router in IDLE mode or close it entirely.

```

Virtual Router Configuration (created by LRA for  $\lambda_1$  and  $\lambda_2$ )
interface loopback()
  ip address 10.10.10.2/32

interface oxc 0/1 ( $\lambda_1$  cross connect)
  ip address xxx.4.80 (by definition  $\lambda_1$  uses suffix xxx.4)
  neighbor xxx.5 update-source loopback0

interface oxc 0/2
  ip address yyy.5.80 (by definition  $\lambda_2$  uses suffix xxx.5)
  neighbor yyy.4 update-source loopback0
    
```

Figure 2. Configuration of a virtual BGP router

Contrary to a normal BGP multi-router configuration, the virtual BGP router would not establish any internal BGP connectivity even though it might be within Router B's AS. It would behave as an independent router carrying its own set of routes, metrics, etc. and advertise itself independently with its own loop back address and its own set of IP addresses for its interfaces.

III. POLICY-BASED CONVERGENT BACKUP ROUTING

In BGP, ASes are allowed to apply local policies for selecting paths and propagating routing information without divulging their policies or internal topology to others. The policies reflect the commercial relationships between neighboring ASes under economic incentive. Typically, the relationship of AS pairs can be customer-provider or peer-peer. To improve the reliability of inter-domain routing, a local backup relationship between ASes can be arranged to prevent link or node failure. There are two kinds of backup arrangements commonly used: multi-homed backup and peer-peer backup [14]. For multi-homed backup, it includes using a secondary customer-provider link as the link to the primary provider fails. For peer-peer backup, an existing peer-peer link is used for backup under a link failure.

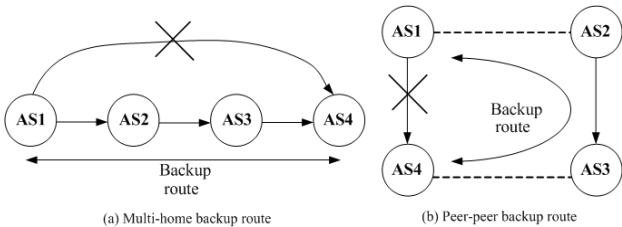


Figure 3. (a) Multi-home backup route; (b) peer-peer backup route

If a path fails, an AS should withdraw the path immediately and select a backup path to recover the interrupted services. Fig. 3 shows two examples, where the provider-customer relationship is represented as a solid line

with an arrow pointing from a provider to its customer and the peer-peer relationship as a dotted line without using an arrow. Given a link failure between AS1 and AS4 in Fig. 3(a), AS4 can choose the backup path via AS3, the secondary provider. For the peer-peer backup in Fig. 3(b), if the link between AS1 and AS4 fails, the backup path can be chosen through the peer-peer links from AS1 to AS2 and AS3 to AS4. In this example, AS3 must advertise backup paths, learned from AS2, to AS4.

Indeed, local backup arrangements bring neighboring ASes more path advertisements to announce backup paths. These additional advertisements would cause global BGP convergence problems [7], [10]; and conflicting local backup policies among a collection of ASes could incur BGP route oscillations [8], [9]. To solve the issues of the BGP routing under the interaction of local backup policies, an abstract model for BGP routing policies in the context of the Stable Paths Problem (SPP) can be considered [10].

A. Stable Paths and Simple Path Vector Routing

Path advertisements in BGP are sent between ASes. These advertisements include attributes **nlri** (network layer reachability information), **next_hop**, **as_path**, **local_pref** (local preference), etc. For the path selection process of BGP, the attributes are used by import and export policies at each router to implement its local routing policies. For example, as a BGP advertisement moves from AS x to AS y , x applies its export policies. If the **as_path** of the advertisement contains y , x filters out the advertisement; if the path advertisement is not filtered out, then x is added to the **as_path**. Finally, the import policies of y are applied to the advertisement. This is where a **local_pref** value is assigned or modified.

Suppose an AS domain is represented by a virtual network node. Consider an AS network as an undirected graph $G = (V, E)$, where $V = \{0, 1, 2, \dots, n\}$ is the set of nodes and E the set of edges. An edge in G is denoted by (i, j) , where $i, j \in V$. For any node u , its neighbors is defined by $neighbors(u) = \{v | (u, v) \in E\}$, which can be further partitioned into three subsets: $providers(u)$, $customers(u)$, and $peers(u)$, the sets of the providers, customers, and peers of u , respectively. A path in G is a sequence of nodes $(v_k v_{k-1} \dots v_0)$, such that $(v_i, v_{i-1}) \in E$, $1 \leq i \leq k$; and it has the direction from v_k to v_0 . An empty path is denoted by ε . Nonempty paths $P = (v_1 v_2 \dots v_k)$ and $Q = (w_1 w_2 \dots w_n)$ can be concatenated if v_k is the same as w_1 . Then PQ denotes the path formed by the *concatenation* of the paths. If $Q = \varepsilon$, we have $P\varepsilon = \varepsilon P = P$. For example, $(123)(345)$ represents the path (12345) , and $\varepsilon(456)$ the path (456) .

In SPP, there is an *origin* node $o \in V$, which is the destination to which all other nodes are trying to establish a path. For each node $v \in V$, it has the corresponding set of permitted paths from v to the origin (node o), denoted by P^v . Let P be the union of all sets P^v . There is a non-negative, integer-valued ranking function λ^v , defined over P^v , which represents the degree of preference to the permitted path. If $P_1, P_2 \in P^v$, and $\lambda^v(P_1) < \lambda^v(P_2)$, then P_2 is said to be preferred over P_1 . Let $\Lambda = \{\lambda^v | v \in V - \{o\}\}$. We say that $S = (G, P, \Lambda)$ is an instance of SPP with a graph, the set of permitted paths

from each node to the origin, and the ranking functions for each node.

A Simple Path Vector Protocol (SPVP) [9], [10] is a distributed algorithm to solve SPP. SPVP can be thought of as an abstract model of BGP. There are two desirable properties for the SPVP with an instance of SPP:

- *Safety* — If the protocol SPVP can never diverge, then we say an instance of SPP is safe.
- *Inherent safety* — If SPP is safe, and remains safe after removing any node, edge, or permitted path, then we say an instance of SPP is inherently safe.

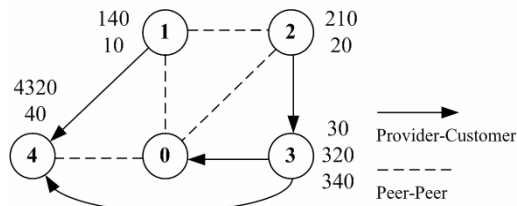


Figure 4. A bad backup arrangement: the routing protocol diverging if link (30) fails

Fig. 4 presents a bad backup arrangement, which is not inherently safe. Assume that in Fig. 4, the vertical list next to each node (except node 0) is the set of permitted paths to the common sink, *i.e.* the node 0 and the paths in each list are ranked from top to bottom for path preference. In this case, the SPVP is safe; it has a set of stable path vectors, $\{(140), (20), (30), (40)\}$, to node 0 from all other nodes. If the link (30) fails, one of the paths (320) and (340) must be chosen as the backup path. Nevertheless, the successive path advertisements for dropping the failed route and selecting a new backup route will cause the SPVP divergence.

B. Safe Backup Routing

Due to conflicting local policies, AS paths may be filtered out by neighboring BGP speakers besides the removal of AS paths due to link or node failures. To study the inherent safety of AS networks to guarantee the safety of backup routing, a specialized SPP under commercial relationships must be considered [7].

In AS domains, transit traffic (non-local traffic) must be constrained by the commercial relationship, which is either customer-provider or peer-peer, of an AS pair. Figs. 3 and 4 show the examples of AS graphs for the specialized SPP with the constraints of commercial relationships. In Fig. 4, the path (1430) is not allowable since node 4, which is a customer AS, cannot transit non-local traffic between node 1 and node 3, its providers. In this situation, we say that the path (1430) has a valley—a provider-customer edge, *e.g.* edge (1, 4), followed by one or more customer-provider edges. For a path with valleys inside, it is not allowed to pass transit traffic. In addition, the paths with one or more edges of customer-provider relationships (or provider-customer relationships) are allowed to pass transit traffic.

In an AS path, a mixture of peer-peer, customer-provider, and provider-customer edges will constrain the ability of relaying transit traffic. To analyze the mixture of commercial relationships in AS paths, consider a path $P_1(uv)P_2$, where (u, v) is a peer-peer edge and P_1 and P_2 might be ε . Edge (u, v) is called a step if either the last edge of P_1 is a peer-peer or provider-customer edge, or the first edge in P_2 is a customer-provider edge. For instance, in Fig. 4, the path (41230) contains no step, but the path (4120) has a step (20), the path (140) a step (40), and the path (304) a step (04). AS paths with steps should not be permitted as far as possible since valleys might exist in them and cause them the violation of commercial relationships. However, peer-peer backup arrangements often involve steps such as the case in Fig. 3(b). Instead, we need to define a slightly weaker notion of reachability, where the set of permitted paths can include paths with steps for backup routing.

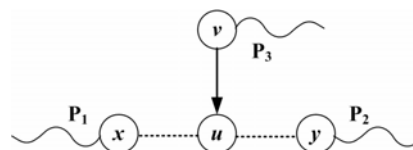


Figure 5. Conditions of permitted backup paths with a step

Fig. 5 shows the conditions of permitted backup paths with a step. Suppose that nodes x and u have peer-peer backup relationship. There are four types of peer-peer backup paths: $(vux)P_1$, $(xuv)P_3$, $(xuy)P_2$, and $(yux)P_1$, as drawn in Fig. 5. For example, in Fig. 3(b), AS4-3-2-1 is a backup path of the second type in Fig. 5, since the link between AS3 and AS4 is a step. It is worthy to recognize three points for backup paths. First, if a path P is a backup path, then $(uv)P$ is also a backup path. Next, a backup path may have one or more steps. Last, a backup path should not be used unless all primary paths are unavailable. More specifically, if path P_1 has no steps and path P_2 has one or more steps, then $\lambda(P_2) < \lambda(P_1)$. Ranking backup paths lower is essential for the safety of SPP.

To select the best backup path for recovering from failures, each node needs to rank among permitted backup paths. In [7], an effective technique is employed to sort permitted backup paths by avoidance levels. The idea of using the avoidance levels is based on counting the number of steps in a path. To utilize the avoidance levels in path selection, a non-negative function $\kappa(P)$, called avoidance classifier that is step aware for a backup path P , is devised. The value of an avoidance level is within the range of κ . In principle, an avoidance classifier κ obeys the rules below.

- As a path traverses additional edges, its avoidance level increases; for instance, if X , Y , and YX are permitted paths, then $\kappa(YX) \geq \kappa(X)$.
- κ is step aware; for any P permitted at v and $(xuv)P$ permitted at x and $(xuv)P$ being one of the above four types of peer-peer backup paths, we have $\kappa((xuv)P) > \kappa((uv)P)$.

By including the notion of avoidance classifiers to the specialized SPP under commercial relationships, the following rules must apply to the path selection process for this new SPP:

- A path with a lower avoidance level is preferred over a path with higher avoidance level; that is, if X and Y are paths permitted at a node and $\kappa(Y) \geq \kappa(X)$, then $\lambda(X) \geq \lambda(Y)$.
- With the same avoidance level, customer paths are preferred over peer and provider paths; for X and Y both permitted at u with $\kappa(X) = \kappa(Y)$, if X is a path through one of $customers(u)$ and Y is not, then $\lambda(X) > \lambda(Y)$.

With the above generalization to the specialized SPP under commercial relationships, permitted paths with steps can be included for save backup routing. In summary, if the specialized SPP S that has the no-valley property, a step aware avoidance classifier κ , and preferring customers with respect to κ , then S is inherently safe.

IV. STABLE PATH SELECTION FOR BACKUP ROUTING

In Section II, the OBGP architecture to provision and manage lightpaths through the optical ASes has been described. However, OBGP inherits the stable convergence issue from BGP in case of link or node failures [1], [4]. In this section, a stable path selection algorithm against the convergence issue for backup routing is considered to guarantee the safety property of OBGP.

In Fig. 1(b), it shows an abstract AS model, which allows AS x containing a virtual BGP router. Suppose that a carrier (represented by AS20) leases ports of the OXC and dark fibers to customers (represented by AS10 and AS30). Then the virtual BGP router is created by Router B to establish an optical cross connect for the backup connection between AS10 and AS30. We can classify this new commercial relationship to the peer-peer relationship. The reason for the classification is that customers rent optical equipment for their private applications such as connections to their peer groups or for backup. As shown in Fig. 1(b), this peer-peer relationship consists of two peer-peer links between AS10 and AS x and between AS x and AS30, respectively. In this situation, the path AS10- x -30 contains one step (AS10- x or AS x -30). More generally, except Router B, if Router A or C itself controls OXCs, the same approach of the new peer-peer relationship can be applied to the connections to more OBGP routers.

According to the specialized SPP under the peer-peer backup relationship stated in Section III.B, the results can be extended to OBGP. Then, we convert formally the properties of the new SPP with the OBGP peer-peer relationship into Properties 4.1 to 4.4. The goal of the first guideline is to include permitted backup paths with OBGP to the set of permitted paths. The other properties can be used to ensure the scheme inherent safety.

Property 4.1 (*obgp peers*) — if a path $(v_k \dots v_l v_0) \in P$ and v_j contains only a virtual BGP router for $j=k-1, \dots, l$, then $v_{j+1}, v_{j-1} \in peers(v_j)$ and the path has at least one step.

Property 4.2 (*no valley*) — if a path $(v_k \dots v_l v_0) \in P$ and $v_{j-1} \in customers(v_j)$ for some $j=k, \dots, l$, then $v_{i-1} \notin providers(v_i)$ for all $i=j-1, \dots, l$.

Property 4.3 (*step aware*) — any avoidance classifier κ must satisfy the following condition; for nodes x, u , and v , if $P \in P^v$,

$(xuv)P \in P^x$, and (xuv) has a step (see Fig. 5), then $\kappa((xuv)P) > \kappa((uv)P)$.

Property 4.4 (*prefer customer*) — if $v \in customers(u)$ and $w \in providers(u) \cup peers(u)$ and $\kappa((uv)P_1) = \kappa((uw)P_2)$, then $\lambda((uv)P_1) > \lambda((uw)P_2)$ for all paths P_1 and P_2 .

The stable path selection algorithm for OBGP convergent backup routing can be divided into three phases. In the first phase, translate the AS graph indicated by the BGP RIB and local policies of a router to an instance of the new SPP using Property 4.1. In the second phase, delete the permitted paths of violating Property 4.2 and update the avoidance level of the remaining permitted paths by following Property 4.3. In the last phase, select the best backup path from the remaining permitted paths according to Property 4.4. The details of notations and the algorithm are described below.

Abbreviations:

- o, V, E , and G : as defined in Section III.A;
- AS $_{local}$: the local AS;
- k : a finite integer;

Stable_Path_Selection()

```
{ // Phase-I
{designate AS $_{local} \rightarrow o$ ;
construct  $G$  from the BGP RIB and local policies;
for each  $u \in V \wedge u \neq o$ 
with Property 4.1,
    enumerate every  $(uv_k \dots v_l o)$ , such that  $v_k, \dots, v_l \in V$ ,
         $v_k \in neighbors(u)$ ,  $v_l \in neighbors(o)$ ,
         $(v_i, v_{i-1}) \in E, i=k, \dots, l$ , and  $v_k \neq \dots \neq v_l \neq v_l$ ;
    include  $(uv_k \dots v_l o)$  to  $P^u$  and  $P$ ; }
// Phase-II
for each  $(v_k \dots v_l v_0) \in P$ 
along  $(v_k \dots v_l v_0)$ , //check Property 4.2
if  $(v_{j-1} \in customers(v_j), \exists j=k, \dots, l) \wedge (v_{i-1} \in providers(v_i), \forall i=j-1, \dots, l)$ 
    delete  $(v_k \dots v_l v_0)$  from  $P^{v_k}$  and  $P$ ;
else //follow Property 4.3
if  $(v_{j+1}, v_{j-1} \in peers(v_j)) \vee ((v_{j+1} \in peers(v_j)) \wedge (v_{j-1} \in providers(v_j))) \vee ((v_{j+1} \in providers(v_j)) \wedge (v_{j-1} \in peers(v_j)))$ ,
     $\forall i=k-1, \dots, l$ 
    //increase the avoidance level of  $(v_k \dots v_l v_0)$ ;
    apply  $\kappa((v_k \dots v_l v_0))$ ; }
// Phase-III
for each  $u \in V \wedge u \neq o$ 
with Property 4.4,
    apply BGP path selection process [11] to  $P$  for the best backup path;
    mark the best backup path in the BGP RIB; }
```

V. EXPERIMENTATION

We implemented an experimental environment (see Fig. 6) and tested the functionality of controlling OXC by using OBGP for wavelength routing. Actually, this experiment is difficult to cover all features of the OBGP scheme due to the

scale and complexity of emulating real networks, which may include many optical links. Consequently, our goal is to build a prototype implementation and verify the basic functions of the scheme.

The experimental network structure of Fig. 6 is very similar to Fig. 1(b). The role of AS20 is a service provider for customers AS10 and AS30; and, AS10 is a peer AS of AS30, and vice versa. In AS20 of Fig. 6, a virtual BGP router will be spawned by Router B2 and controls an OXC (DiCon GP700), which is used to support optical cross connections between different ASes (i.e. AS10 and AS30). Routers A and C are equipped with both ordinary Ethernet and optical gigabit Ethernet, and the remaining routers are linked by ordinary Ethernet with twisted pair cables. The testing optical channel is formed by connecting the optical Ethernet interface of Routers A and C to the I/O ports of the OXC with optical cables. Fig. 6 also shows the network configuration, including IP addresses and prefixes, and those experimental routers are implemented by personal computers with the Quagga routing software [16] installed. Furthermore, in Fig. 6, two personal computers, PCs A and B, are used to establish an FTP (File Transfer Protocol) service connection for testing and observing the change of routing information.

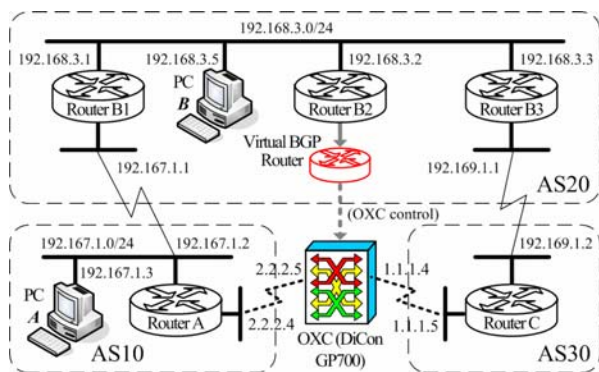


Figure 6. Experimental Environment for OBGP

In the implementation of the OBGP scheme, we develop three software modules, i.e. LRA, the stable path selection algorithm, and the OXC LabVIEW [17] driver, to integrate into the BGP protocol software. As described in Section II, the LRA is responsible to create virtual BGP routers configured according to the example shown in Fig. 2. For the virtual BGP router, its daemon process exchanges the information of lightpath reachability and finally establishes the route of lightpaths through a number of optical cross connects. The establishment of optical cross connects along an optical route is done by giving commands to the OXC driver module, coded by LabVIEW, to control the connection of input and output ports of OXCs in each OBGP node. Subsequently, using BGP UPDATE messages, the daemon process of virtual routers advertises the completed optical routes to its neighbors. For example, in Fig. 6, the optical path AS10-30 will be included in the BGP RIB of AS10 and AS30 eventually. For the stable path selection algorithm, it can be used to find out the inherently safe optical backup path for the local AS by following the properties presented in Section IV.

VI. CONCLUSION

OBGP is a distributed mechanism, which gives managing authority to users for setting up lightpaths to their peers across optical AS domains. As we considered the convergence issue, the leased commercial relationship of wavelengths and dim fibers has been extended to OBGP; and, this extension has been turned into a local policy for BGP routing. Combined with other local policies, we draw the four properties for the inherently safe backup routing of OBGP. In this study, we proposed a stable path selection scheme to cope with the convergent issue of OBGP in case failures occurred in inter-domain optical routing. To verify our approach, an OBGP prototype and an experimental environment have been implemented to conduct a functional testing. From observing the testing activities, we found that the MRAI timer [11] can influence the time for OBGP to converge. This point is very interesting for future investigation.

REFERENCES

- [1] B. St. Arnaud, R. Hatem, W. Hong, M. Blanchet, and F. Parent, "Optical BGP networks," revised draft discussion paper, Mar. 2001, <http://www.canarie.ca/canet4/library/canet4design.html>.
- [2] M. J. Francisco, S. Simpson, L. Pezoulas, C. Hwang, I. Lambadaris, "Interdomain routing in optical networks," *Opticomm 2001, Proceedings of SPIE*, Vol.4599, pp. 120-129, Aug. 2001.
- [3] M. Francisco, L. Pezoulas, C. Huang, and I. Lambadaris, "End-to-end signaling and routing for optical networks," *ICC'2002*, Vol.5, pp. 2870-2875, Apr. 2002.
- [4] M. Blanchet, F. Parent, and B. St. Arnaud, "Optical BGP (OBGP): interAS lightpath provisioning," Internet draft, <draft-parent-obgp-01.txt>, Aug. 2001.
- [5] G. Bernstein, L. Ong, et al., "Optical inter domain routing considerations," Internet draft, <draft-bernstein-obgp-01.txt>, Jul. 2001.
- [6] T.G. Griffin and G. Wilfong, "An analysis of BGP convergence properties," *Proceedings of the ACM SIGCOMM*, Aug. 1999.
- [7] L. Gao, T.G. Griffin, and J. Rexford, "Inherently safe backup routing with BGP," *IEEE INFOCOM*, Vol. 1, pp.547-556, Apr. 2001.
- [8] T. Griffin and G. Wilfong, "A safe path vector protocol," *IEEE INFOCOM*, Mar. 2000.
- [9] T.G. Griffin, F.B. Shepherd, and G. Wilfong, "Policy disputes in pathvector protocols," *Intl. Conf. on Network Protocols*, Nov. 1999.
- [10] T.G. Griffin, F.B. Shepherd, and G. Wilfong, "The stable paths problem and interdomain routing," *IEEE/ACM Trans. Networking*, Vol. 10, Issue 2, Apr. 2002, pp. 232-243.
- [11] Y. Rekhter and T. Li, "A border gateway protocol," RFC 1771 (BGP version 4), Mar. 1995.
- [12] T. Bates, et al., "Multiprotocol extensions for BGP4," RFC 2858, June 2000.
- [13] S.R. Sangli, D. Tappan, et al. "BGP extended communities attribute," Internet draft, <draft-ietf-idr-bgp-ext-community-07.txt>, Mar. 2004.
- [14] E. Chen, and T. Bates, "An application of the BGP community attribute in multi-home routing," RFC 1998, Aug. 1996.
- [15] R. Chandra, P. Traina, and T. Li, "BGP communities attribute," RFC 1997, Aug. 1996.
- [16] K. Ishikuro, et al., "Quagga - A routing software package for TCP/IP networks," Ver. 0.98.6, Jun. 2005.
- [17] A. McDonough, "LabVIEW: Data Acquisition & Analysis for Movement Sciences," Upper Saddle River, NJ, USA: Prentice Hall, 2001.



Wen-Fong Wang received the B.S. degree in Applied Math. from National Chen-Chi University (Taipei, Taiwan) in 1983, and the M.S. degree in Information Engineering and the Ph.D. degree in Electrical Engineering from National Cheng-Kung University (Tainan, Taiwan) in 1989 and 1998, respectively. During 1989-2001, he was

a researcher in Telecommunications Laboratory (TL), Chung-Hua Telecommunications Inc., Taiwan. He is now an Assistant Professor in the Department of Computer and Communications Engineering, National Yunlin University of Science & Technology (Touliu, Taiwan). His current research focuses on switching technology, metropolitan area networks, and optical networking.



Lih-Chyau Wu received her B.S. degree in the Department of Information Engineering from National Taiwan University (Taipei, Taiwan) in 1982, and her Ph.D. degree in the Department of Computer Science from National Tsing Hua University (HsinChu, Taiwan) in 1994. She is currently a Professor in the Department of Electronic Engineering,

National Yunlin Institute of Technology (Touliu, Taiwan). Her research interests include network security, high speed network and distributed self-stabilizing systems.

Component-based Face Detection in Colour Images

Jamal Ahmad Dargham, Ali Chekima

School of Engineering and Information Technology, University Malaysia Sabah,
Locked Bag 2073, Teluk Likas, 88999 Kota Kinabalu, Sabah, Malaysia
{jamalad, Chekima}@webmail.ums.edu.my

Abstract: Face detection is an important process in many applications such as face recognition, person identification and tracking, and access control. The technique used for face detection depends on how a face is modelled. In this paper, a face is defined as a skin region and a lips region that meet certain geometrical criteria. Thus, the face detection system has three main components: a skin detection module, a lips detection module, and a face verification module. The Multi-layer perceptron (MLP) neural networks was used for the skin and lips detection modules. In order to test the face detection system, two databases were created. The images in the first database, called In-house, were taken under controlled environment while those in the second database, called WWW, were collected from the World Wide Web and as such have no restriction on lighting, head pose or background. The system achieved a correct detection rate of 87 and 80 percent on the In-house and WWW databases respectively

Keywords: Face Detection; MLP Neural Network; Component-Based Detection

I. INTRODUCTION

Face detection is defined as the ability to ascertain whether a face is present in the input image and if a face is present to return the location of the face. The technique used for face detection depends on how the face is modelled. In [6] face-processing systems are classified into four categories: template-based, feature-based, appearance-based, and knowledge-based systems. However, these four categories can be grouped into two categories: global and component. In the global category the whole face is modelled either using template-based or appearance-based approaches. While in the second category, the face components and their relationships are used to model the face.

A face detection system proposed by [5] that combines a lips detection neural network (LDNN) and skin distinction neural network (SDNN). The lips are first detected by the LDNN and then the presence of a face is validated by the SDNN if the area around the lips is skin. The LDNN is a multi-layer feed forward neural network trained with the Back propagation algorithm. The network has 300 input neurons, 10 hidden neurons, and one output neuron coded as 1 for lips and 0 otherwise. The size of the lips is restricted to between 5 to 15 pixels vertically and 10 to 30 pixels horizontally. The SDNN is similar to that of the LDNN. However, the

search area for the SDNN is limited to a box centred on the centre of the lips and extend 20 pixels vertically and 40 pixels horizontally. In [4] a face detection system was proposed. The proposed system has two modules: a face localisation module and a facial features detector module. The face localisation module generates potential face candidates in the image based on the chrominance and luminance of the colour image as well as the size of the potential face. The facial feature detector directly locates the eyes, mouth, and face boundary based on measurement derived from the colour-space components of the image. The system was tested on two image databases containing images in different poses from frontal to profile. The performance of the system is found to be dependent of the face pose as well as the occlusion of the facial features. Thus, the detection rate varied from around 75% to 91%.

A trainable, component-based face detection system for frontal and near-frontal images in gray images was presented by [3]. The system consists of a two-level hierarchy of Support Vector Machine classifiers. In the first level fourteen SVM classifiers independently detect the facial components. A single SVM classifier at the second level checks if the geometrical configuration of the detected components in the image matches a geometrical model of a face

II. THE DATABASES

Two databases were developed. The first database is called the In-house database while the second database is called the WWW database. The In-house database comprises 15 subjects both males and females from the various races in Malaysia namely Chinese, Malay, Indian, and Indigenous people. Each subject has 12 images showing the frontal facial image of the subject at three distances from the camera. These distances are called scaling factors. Scale factor 1 represents a distance of 36 cm between the camera and the subject while scale factor 2 and 3 represent a distance of 72 cm and 108 cm respectively. For each scale factor, images for three facial expressions namely neutral, smiling, and laughing were taken as well as with glasses with neutral expression only. These images were all taken indoor with a single digital camera under normal lighting conditions and with uniform background.

The WWW database has 45 images of Asian subjects collected from the World Wide Web. The subjects represent males and females of different ages. Some of the images were taken indoor while others were taken outdoor with varying backgrounds and lighting

conditions. In addition, the pose of the face in the image varied widely from frontal to near portrait. The cameras used for taking these images as well the image processing techniques applied to them are unknown. The only restriction on these images is that they must show a face of an Asian person.

III. THE PROPOSED SYSTEM

The proposed system labels any region in a colour image as a face if that region contains a skin region and a lips region that meet certain geometrical constraints. Fig. 1 shows a block diagram of the proposed face detection system. As can be seen from Fig. 1, skin detection is carried out first on the colour image. Then post-processing operations such as erosion and dilation are carried out on the detected skin pixels followed by connected component labelling to group skin pixels into skin regions. Next, size filtering is performed on these regions to remove objects that are either smaller or larger than a particular size. The skin regions remaining in the image after the size filtering are considered as face candidates. The size of the smallest and largest skin region to be considered as a face candidate is selected as a ratio of the skin region to the size of the image. The values for these ratios were obtained by trials and errors. Then lips detection is carried out only on the face candidates and thus reducing the search space. Then post-processing steps similar to those performed on skin detection are carried out followed by size filtering to determine the lips candidates. The size of the smallest and largest lips region to be considered as a lips candidate is selected as a ratio of the lips region to the size of the image. A face is then assumed to exist when a face candidate and a lips candidate meet certain conditions that relate the ratio of the face size to the lips size as well as the orientation between the face candidate and the lips candidate. Unlike the systems described in this paper, our system does not put any limitation on the image size or on the size of the facial components.

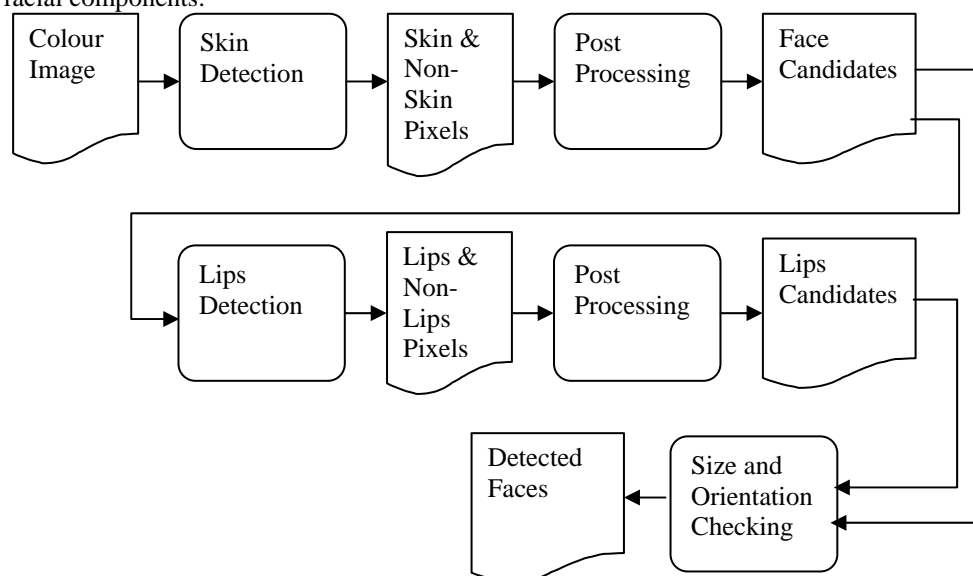


Figure 1 Block Diagram of the Proposed Face Detection System

A. Colour Transformation

For an image having M by N pixels, the r, g, and b component of the normalised rgb colour scheme are obtained from the normal RGB colour scheme as given by Equation 1.

$$\begin{cases} r(x, y) = \frac{R(x, y)}{R(x, y) + G(x, y) + B(x, y)} \\ g(x, y) = \frac{G(x, y)}{R(x, y) + G(x, y) + B(x, y)} \\ b(x, y) = \frac{B(x, y)}{R(x, y) + G(x, y) + B(x, y)} \end{cases} \quad (1)$$

The set of equations given in Equation 1 perform pixel-by-pixel normalization of the RGB components of the RGB colour scheme. Thus, we call this method pixel intensity normalisation. One of the problems of this method is that it breaks down when $R+G+B=0$. Thus, we propose to normalise the RGB components by the maximum value of $(R+G+B)$ over the entire image, we call this method maximum intensity normalisation. Thus, the set of equations in Equation 1 become as expressed in Equation 2.

$$\begin{cases} r(x, y) = \frac{R(x, y)}{\text{Max}(R + G + B)} \\ g(x, y) = \frac{G(x, y)}{\text{Max}(R + G + B)} \\ b(x, y) = \frac{B(x, y)}{\text{Max}(R + G + B)} \end{cases} \quad (2)$$

B. Skin and Lips Detection

The Multi-layer Perceptron neural networks (MLP) were used for the skin and lips detection modules. The network structures for the skin detection and lips detection networks for each database and for each color transformation are given in Tables 1 and 2 respectively. The number of the neurons in the hidden layer was

TABLE I. NETWORK STRUCTURE FOR THE MLP NEURAL NETWORKS USED FOR SKIN DETECTION

Database	Maximum Intensity		Pixel Intensity	
	Chrominance Components	Network Structure	Chrominance Components	Network Structure
In-House	r-b & r-g	18-3-1	r-b & r-g	18-8-1
WWW	r & r-g	18-35-1	r & r-g	18-19-1

determined by using network-growing technique. The networks were trained using the Levenberg-Marquardt training algorithm. For detailed descriptions see [1 and 2] Fig. 2 shows the process of finding the face candidates for an image from the WWW database while Fig. 3 shows the process of finding the lips candidates for the same image.

TABLE II. NETWORK STRUCTURE FOR THE MLP NEURAL NETWORKS USED FOR LIPS DETECTION

Database	Maximum Intensity		Pixel Intensity	
	Chrominance Components	Network Structure	Chrominance Components	Network Structure
In-House	r/g & r+b-2g	2-3-1	r/g & r+b-2g	2-4-1
WWW	r+b-6g & r-g	2-5-1	g & r/g	2-1-1

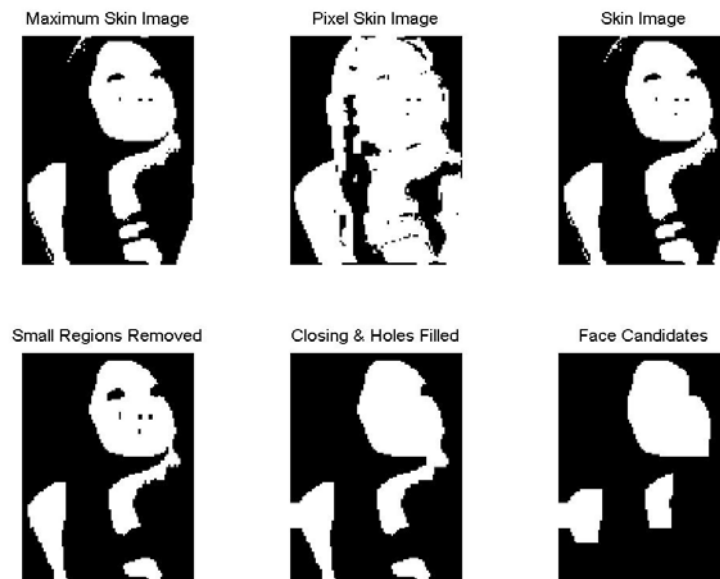


Figure 2. The Process of Finding the Face Candidates

C. Results

As has been mentioned earlier, a face is detected only when a face candidate and a lips candidate meet certain conditions. Thus, as shown in Fig. 4a, when the detected face by the system contains both the correct facial skin and the correct lips then a correct detection is given. However, if either the lips or the facial skin is incorrectly classified, as shown in Fig. 4b, this is termed as false acceptance. Finally, false rejection is defined as when either the facial skin or the lips is not detected when a face exists in an image as shown in Fig. 4c. The

performance of the system on both databases is given in Table 3.

TABLE III PERFORMANCE OF THE FACE DETECTION SYSTEM ON BOTH DATABASES

Database	%Correct	FAR	FRR
In-House	87	6.67	6.67
WWW	80	8.89	11.11

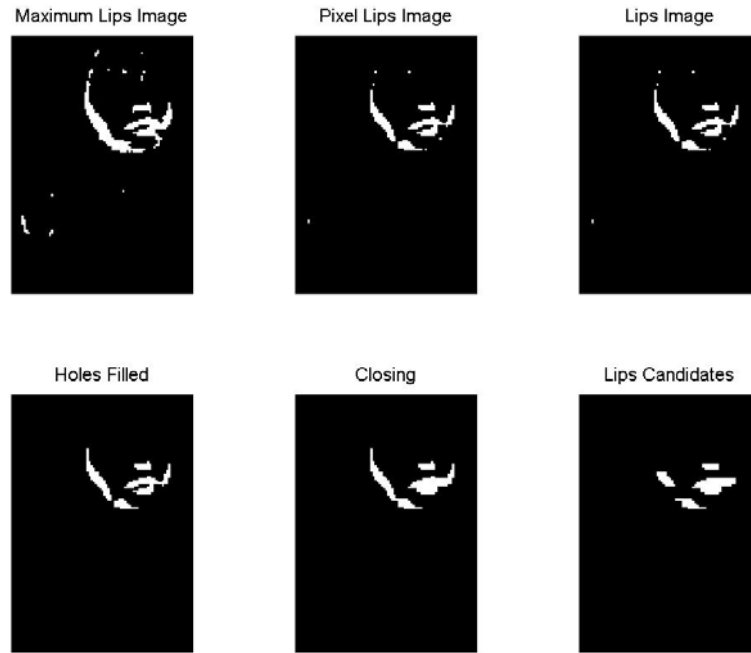


Figure 3. The Process of Finding the Lips Candidates

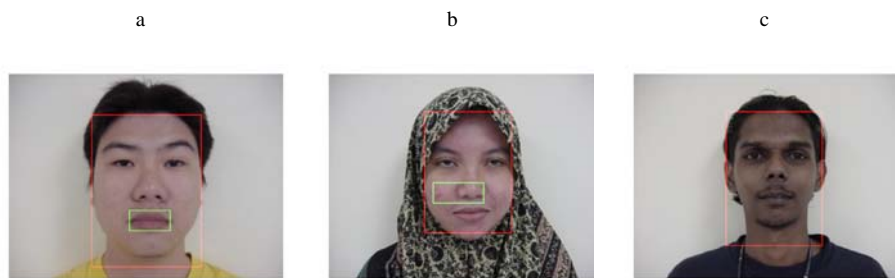


Figure 4 a) Correct Detection, b) False Acceptance, c) False Rejection

IV. CONCLUSIONS

In this paper, a component-based face detection system was presented. The system has two modules: skin detection and a lips detection. The MLP neural networks were used for both skin and lips detections using only the skin and lips colors. Post-processing was carried on the detected skin and lips pixels to detect potential face and lips candidates. If a face candidate and a lips candidate meet certain geometrical conditions then a face is detected. The system was tested on two databases with a correct detection rate of 87 and 80 percent respectively

ACKNOWLEDGMENT

The Authors would like to acknowledge the financial assistance given by the Ministry of Science and Technology, Malaysia under the E-science research grant 03-01-10-SF0045

REFERENCES

- [1] Dargham j., Chekima, A., Omatu, S. Lips detection by use of neural networks. To appears in the Proceedings of the The Thirteenth International Symposium on Artificial Life and Robotics (AROB 13th '08), Beppu, Oita, Japan, 2008
- [2] Dargham j., Chekima, A.. Skin Detection using MLP Neural Networks. Proceedings of the 9th International Conference on Mechatronics Technology, ICMT'05. Kuala Lumpur, Malaysia, December 2005.
- [3] Heisele B., Serre T., Pontil M., and Poggio T.. Component-based face detection. In Proc. IEEE Conference on Computer Vision and Pattern Recognition, volume 1, pages 657–662, Hawaii, 2001.
- [4] Hsu, R.L., Abdel-Mottaleb, M., and Jain, A. K.. Face Detection In Color Images, IEEE Transaction on Pattern Analysis and Machine Intelligence, 24(5): 696-706, 2002
- [5] Mitsukura, Y. Fukumi, E. Akamatsu, N.. A Design of Face Detection System by Using Lip Detection Neural Network and Skin Distinction Neural Network. Proceedings of the International Conference on Systems, Man and Cybernetics, 2789–2793, 2000
- [6] Yang M. H., Roth D., and Ahuja N.. A SNoW-Based Face Detector, Advances in Neural Information Processing Systems. S. A. Solla, T.K. Leen and K.-R. Muller (eds), pp. 855-861, MIT Press. 2000

Non-Linear Dynamics in a Small-Open-Economy Model in the Euro Area

Panayotis G. Michaelides and Angelos T. Vouldis

National Technical University of Athens

Athens, Greece

pmichael@central.ntua.gr and avouldis@biosim.ntua.gr

Abstract— This article focuses on the dynamics of the commodity and money market. The purpose of the article is to study a two-equation linear dynamic model in order to examine its behavior in complex conditions and its dependence on the parameters. Stability conditions are examined by means of the Ruth - Hurwitz criterion. The system and its stability are also examined when non-linear dynamics is introduced. The linear system was stable for any economically admissible values of the parameters. Also, non-linear perturbations were applied in two cases which both led to a stable system. From a theoretical perspective in economics this implies that for any small open economy operating in the Euro area without exchange rate dynamics and operating under the specific conditions, regardless of the possible non-linearity in the investment function, the resulting economic system is asymptotically stable.

Keywords— *small open economy; dynamical system; non-linear; numerical.*

I. INTRODUCTION

The model presented in this paper is primarily of Keynesian inspiration and is based on the Mundell-Fleming theory using IS-LM model [1], [2]. This article models a small open economy without exchange rate dynamics as a two-equation dynamic model in order to examine its behavior. This model could be suitable for modeling the economy of a country such as Greece operating in the Euro area, where exchange rates are absent. In the commodity market, demand for investment and net export is related to savings. Total demand and savings are said to be in equilibrium. The investment demand function depends on the interest rate. The net export demand is considered to be constant. First, we begin with an explanation of the linear model where the economic nature of the parameters results in stability.

II. THE MODEL

Production Y is described by the equation:

$$Y \dot{\phi} = a [(R, Y) + X(Y, Z) - S(Y, Z)] a > 0 \quad (1)$$

Equation (1) simply expresses the difference between aggregate demand and aggregate supply. Aggregate demand is equal to $C + I + E$ where C , I , E are investment, consumption and exports, respectively, and aggregate supply is equal to $C +$

$S + M$ where C , S , M , are consumption, savings and imports, respectively. Subtracting aggregate supply from aggregate demand we get $I + X - S$ where $X = E - M$ denotes net export [3]. The difference between aggregate demand and supply causes the increase of production. If the difference is positive, this implies an increase in production and if the difference is negative this implies a decrease in production [4]. Dividing equation (1) by Y we get:

$$\frac{Y \dot{\phi}}{Y} = a \left[\frac{\dot{\phi}(Y, R)}{Y} + \frac{X(Y)}{Y} - \frac{S(Y)}{Y} \right] \quad (2)$$

The investment function has the form:

$$I = (i_0 - i_2 R) Y, \quad i_0, i_2 > 0 \quad (3)$$

The net exports function has the form:

$$X = x_0 Y, \quad x_0 > 0 \quad (4)$$

The savings function has the form:

$$S = (s_0 + s_1 \ln Y) Y, \quad s_0, s_1 > 0 \quad (5)$$

Also, let:

$$y = \ln Y \quad (6)$$

$$x = \ln X \quad (7)$$

Substituting equations (3)-(7) into equation (2) we get:

$$y \dot{\phi} = a [i_0 - i_2 R + x_0 - (s_0 + s_1 y)] \quad (8)$$

For the money market we assume that:

$$e^{R\phi} = \frac{\dot{\phi}(Y, R)}{\dot{\phi}} \frac{b}{M}, b > 0 \quad (9)$$

Or:

$$R\phi = b[l_0 + l_1 y - l_2 R - m] \quad (10)$$

Where M and L denote money stock and demand, respectively.

Finally, the dependence of the demand for money on production and nominal interest rate is given by the following function:

$$L(Y, R) = l_0 \frac{Y^{l_1}}{(1+R)^{l_2}}, l_0, l_1, l_2 > 0 \quad (11)$$

The final model consists of equations (8) and (10):

$$y\dot{\phi} = a[l_0 - i_2 R + x_0 - (s_0 + s_1 y)]$$

$$R\dot{\phi} = b[l_0 + l_1 y - l_2 R - m]$$

The model is linear and stable for each economically admissible value of the parameters.

III. EQUILIBRIUM AND STABILITY OF THE LINEAR MODEL

The equilibrium of dynamical systems is defined as the situation where the variables do not evolve in time. So our system in equilibrium conditions is [5]:

$$y\dot{\phi} = a[l_0 - i_2 R + x_0 - (s_0 + s_1 y)] = 0$$

$$R\dot{\phi} = b[l_0 + l_1 y - l_2 R - m] = 0$$

Next we examine the stability of the system by reference to the well known Ruth – Hurwitz criterion. So, the Jacobian of the original system is as follows [6]:

$$A = \begin{pmatrix} as_1 & -ai_2 \\ bl_1 & -bl_2 \end{pmatrix}$$

The eigenvalues of the matrix are computed as roots of the following equation:

$$|A - lI| = \begin{vmatrix} -as_1 - l & -ai_2 \\ bl_1 & -bl_2 - l \end{vmatrix} =$$

$$l^2 + (as_1 + l_2 b)l + ab(s_1 l_2 + i_2 l_1) = 0$$

We construct the Ruth-Hurwitz matrices:

$$H^1 = as_1 + l_2 b > 0$$

$$H^2 = \begin{vmatrix} as_1 + l_2 b & 1 \\ 0 & ab(s_1 l_2 + i_2 l_1) \end{vmatrix} > 0$$

According to the Ruth-Hurwitz rule the necessary and sufficient condition for a linear system to be asymptotically stable $[\text{Re}(\lambda^i) < 0]$ is $H^i > 0$ for all i . Given that $H^1, H^2 > 0$ this result implies that the system is asymptotically stable [7]. Consequently, small open economies operating in the euro area, i.e. without exchange rate dynamics are asymptotically stable.

A. Numerical Example:

Let us introduce a numerical example by using the following numerical values which are typically relevant for a small open economy without exchange rate dynamics:

$$i_0 = 0.048, i_2 = 0.16, x_0 = 0.26, s_0 = 0.1, s_1 = 0.07, s_2 = 0.16, l_0 = 0.25, l_1 = 0.12, l_2 = 0.6, M = 0.48$$

The behavior of the linear system is depicted in Figs.1-2 where the evolution in time of production and interest rate are shown.

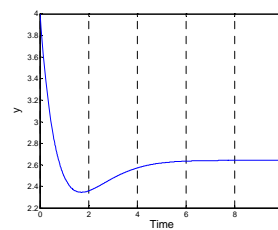


Figure 1

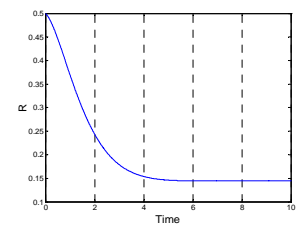


Figure 2

IV. SIMPLE NON – LINEAR SYSTEM

Typically, the dependence of investment on product is non-linear. If we consider a typical non-linear investment function of the logistic form:

$$I = \left(\frac{k}{1 + e^{a \cdot y}} - i_2 R \right) Y, \quad i_2 > 0$$

Instead of (8) we get:

$$y \dot{\phi} = a \left(\frac{k}{1 + e^{a \cdot y}} - i_2 R + x_0 - (s_0 - s_1 y) \right) \dot{\phi}$$

A. Numerical Example:

We use the same numerical values as in the previous example. Additionally, we assume that $k=0.4$ and $a=4$. The Jacobian, the determinant and the eigenvalues of the system can be computed routinely. The behavior of the non-linear system is shown in Figs. 3-4 where the evolution in time of production and interest rate are shown.

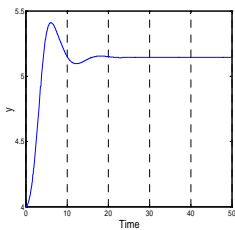


Figure 3

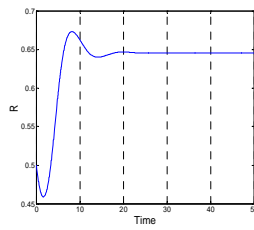


Figure 4

V. GENERAL NON – LINEAR SYSTEM

If we consider a more general non-linear investment function of the form:

$$I = \left(\frac{1}{1 + R} \frac{k}{1 + e^{b \cdot ay(t)}} - i_2 R \right) Y, \quad i_2 > 0$$

Instead of (8) we get:

$$y \dot{\phi} = a \left(\frac{1}{1 + R} \frac{k}{1 + e^{b \cdot ay(t)}} - i_2 R + x_0 - (s_0 - s_1 y) \right) \dot{\phi}$$

A. Numerical Example:

We use the same numerical values as in the previous example. Additionally, we assume that $b=1.0$ and $a=4$. The Jacobian, the determinant and the eigenvalues of the system can be computed routinely. The behavior of the non-linear system is shown in Figs. 5-6 where the evolution in time of production and interest rate are shown.

VI. CONCLUSIONS

Microeconomic models deal with the behavior and the decisions of individuals, households and firms and the way their behavior determines prices and quantities [8]. In this context some authors have presented models of a small open

economy from a microeconomic perspective based on the idea that a representative consumer chooses his equilibrium by solving inter-temporal optimization problems [9]. In this paper, we have introduced a macroeconomic model which deals with the performance and behavior of the national economy as a whole [10]. Macroeconomic models are typically used by governments and corporations in the formulation of business strategy and policy rules.

The macroeconomic linear system of the Small Open Economy model for a country operating in the Euro area without exchange rate dynamics was examined. The linear system was stable for any economically admissible values of the parameters. Also, non-linear perturbations were applied in two cases which both led to a stable system. From a theoretical perspective in economics this implies that for any small open economy operating in the Euro area without exchange rate dynamics under the specific conditions, regardless of any possible non-linearity in the investment function, the resulting economic system is stable.

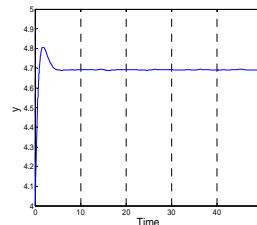


Figure 5

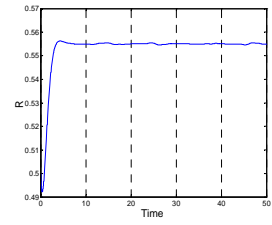


Figure 6

REFERENCES

- [1] Tobin, J. (1975), "Keynesian Models of Recession and Repression", *American Economic Review*, 65 (2), pp. 195–202.
- [2] Mundell, R.A.(1962), "The Appropriate Use of Monetary and Fiscal Policy for Internal and External Balance", *IMF Staff Papers*, March, pp. 70-79.
- [3] Dornbusch, R. (1980), *Open Economy Macro-Economics*, New York: Basic Books, 1980.
- [4] Flaschel, P., Franke R., and Demmler, W. (1997), *Dynamic Macroeconomics*, MIT Press, Cambridge, MA 1997
- [5] Guckenheimer, J. and Holmes, P. (1986), *Non-Linear Oscillation, Dynamical Systems and Bifurcations of Vector Fields*, Springer-Verlag, New York.
- [6] Takayama, A. (1994), *Analytical Methods in Economics*, Harvester, Hertfordshire.
- [7] Tu, P. N.V. (1994), *Dynamical Systems*, Springer-Verlag, Berlin-Heidelberg.
- [8] Varian, H. (1992), *Microeconomic Analysis*, New York: W.W. Norton.
- [9] Schubert, S. and Turnovsky, S. (2002), "The Dynamics of Temporary Policies in a Small Open Economy", *Review of International Economics* 10 (4), pp. 604–622.
- [10] Blaug, M. (1985), *Economic theory in retrospect*, Cambridge, UK: Cambridge University Press.

Panayotis Michaelides is Lecturer in Economics (407/80) at National Technical University of Athens (NTUA), Greece. He received the Diploma Degree in Mechanical Engineering from NTUA. Then, he earned an MSc in Economics, followed by an MBA in Business Administration and an MSc in Mathematics. Dr. Michaelides completed his PhD on a full scholarship. In total, he has conducted studies or research in three (3) institutions including Athens University of Economics and Business and University of Groningen, The Netherlands. He has given lectures in Greek and foreign universities at international conferences and speaks English, French and German fluently. Dr. Michaelides has authored one textbook, two scholarly books, a lot of teaching material and serves as reviewer for scholarly journals. Also, he has authored or co-authored more than sixty (60) papers published or forthcoming in refereed journals or appearing in refereed international conferences and collective volumes, including *Cambridge Journal of Economics*, *History of Political Economy*, *History of Economics Review*, *Review of Political Economy*, *European Journal of the History of Economic Thought*, *Applied Economics*, *Energy Economics*, *Journal of Economics and Business*, *Economics Letters*, *The Journal of Technology Transfer*, *East-West Journal of Economics and Business*, *Journal of Transport and Shipping*, *IEEE Trans. Neural Networks*, *SPOUDAI*, etc. Dr. Michaelides was recipient of three (3) scholarships for academic excellence and has received the NTUA award for the promotion of Sciences. Also, he has supervised numerous Diploma Theses and has participated in numerous research projects with an active role. His research relates to many fields of economics, econometrics and applied mathematics. He is member of a variety of scientific organizations.

Angelos Vouldis is a Researcher at National Technical University of Athens (NTUA), Greece, since 2001. He received the Diploma degree in Electrical and Computer Engineering in 2000 and the PhD degree in 2007 both from NTUA. He has authored or co-authored papers published or forthcoming in international refereed journals such as *Review of Political Economy*, *Journal of Economics and Business*, *Economics Letters*, *IEEE Trans. Neural Networks*, *IEEE Trans. Instrumentation and Measurement*, *Journal of the Optical Society of America A* or appearing in refereed international conferences. Also, he has participated in several research projects. His research interests include economics, econometrics, applied mathematics and the development of computational algorithms.

Self-organized optimization and synchronization of material flow networks with decentralized control

Reik Donner and Stefan Lämmer
 Institute for Transport and Economics
 Dresden University of Technology
 Andreas-Schubert-Str. 23
 01062 Dresden, Germany
 Email: donner,laemmer@vwi.tu-dresden.de

Dirk Helbing
 Department of Humanities and Social Sciences
 ETH Zurich
 Universitätsstr. 41
 8192 Zurich, Switzerland
 Email: dhelbing@ethz.ch

Abstract—The efficient and reliable operation of material flows in transportation networks is a subject of broad economic interest. Important applications include the control of signalized intersections in urban road systems and the planning and scheduling of logistic processes. Traditional approaches to operating material flow networks are however known to have severe disadvantages: centralized controllers suffer from their high computational demands that make an on-line control hardly possible in larger networks, whereas a decentralized control using clearing policies leads under rather general conditions to instabilities. As an alternative approach that may help to overcome these problems, a self-organization mechanism of conflicting flows is proposed that is inspired by oscillatory phenomena of pedestrian and animal flows at intersections or bottlenecks. For this purpose, a permeability function is introduced that allows to sequentially serve the different possible flow directions at an intersection in a fully demand-dependent way.

The self-organized optimization achieved by the presented approach is demonstrated to be closely linked to synchronization of the oscillatory service dynamics at the different intersections in the network. For regular grid topologies, different synchronization regimes are present depending on the inertia of the switching from one service state to the next one. The dependence of this observation on the regularity of the considered network is tested. The reported results contribute to an improved understanding of the conditions that have to be present for efficiently operating material flow networks by a decentralized control, which is of major importance for future implementations in real-world traffic or production systems.

I. INTRODUCTION

Many real-world complex systems have (among others) the function of transportation of material and/or information from one place to the other. Examples include systems in technology (including vehicular traffic [1], [2], [3], production, logistics, supply networks [4], or telecommunication) as well as biology (for example, the nervous and cardio-vascular system, intracellular transport using the cytoskeleton [5], [6], and nutrient transport in amoeboid organisms [7] or fungal mycelia [8]). One may distinguish continuous-flow systems (for example, power grids, water supply networks, nutrient or blood transport systems in organisms) from such systems which are characterized by a large number of individual and mutually interacting transportation processes (which is the case for most information flow networks, road, railway, pedestrian or animal traffic, production and logistics systems).

In the case of systems characterized by discrete flows, the aim of an efficient organization is to minimize the time required for all individual transportation processes. Typically, this optimization is difficult and demanding, since the topology of the underlying networks is composed of a potentially large number of merges and intersections at which there are conflicts between the flows on different routes. To avoid physical collisions, these flows have to be controlled by devices like traffic lights. The operation strategy of these devices is decisive for the optimization of the system performance.

Whereas in the case of a low network load, the individual service of transportation units is beneficial, due to the necessary safety headways between individual services, it becomes inefficient if the traffic volume in a material flow network exceeds a certain threshold. Hence, in the presence of substantially high traffic volumes, a coordinated operation of the conflicting flows leads to better results. Such a coordinated operation is achieved by bundling material or vehicles into platoons, which is performed in urban road networks by the action of traffic lights, or in logistics by transporting heavy loads on railways instead of roads.

In a coordinated service of conflicting material flows, the switching between flows from and/or in different directions leads to an accumulation of material (like vehicles or products) on the links which are currently not served. The corresponding effects are mathematically described in terms of queueing theory. In switched queueing systems, every intersection of conflicting material flows is characterized by the amount of delayed material on all of the incoming links, which is determined by the lengths $N(t)$ of the associated queues. The arrival and departure rates of material, $A(t)$ and $O(t)$, are bounded by the maximum capacity \hat{Q} that is an intrinsic property of the transportation route and the used devices. Regarding the state of the different queues (which determine the current service state of the intersection point), one may distinguish different states of the queue: a “no service” state and a service period, which itself is composed of a “setup” state, a “clearing” state, and a possible “extension” state with free-flow conditions on the served routes (see Fig. 1). In the context of vehicular traffic control, a “setup” state of duration τ is essential for a safe operation making sure that all vehicles

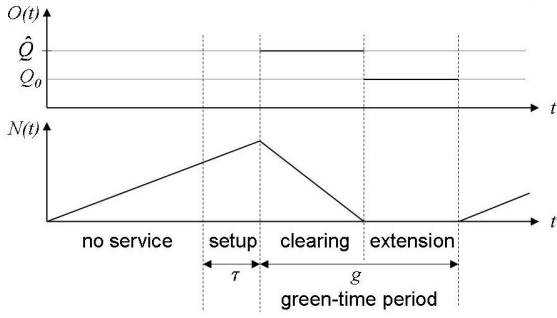


Fig. 1. Evolution of the departure flow (outflow) $O(t)$ and the amount of queued material (vehicles) $N(t)$ for one incoming link with a constant inflow rate $A(t) \equiv Q_0 < \hat{Q}$. The different states of the queue are schematically shown.

have left the conflict area before the considered traffic stream enters, whereas “clearing” and “extension” states combine to the total green time g during a service period.

Each of the states mentioned above is associated with different dynamical regimes of the queueing process, which are characterized by the relationship between the arrival flow and the change in the amount of queued material:

$$\frac{dN}{dt} = \begin{cases} A(t), & \text{“no service” and “setup” states,} \\ A(t) - \hat{Q}, & \text{“clearing” state,} \\ 0, & \text{“extension” state.} \end{cases} \quad (1)$$

In a similar way, one may write for the departure flow:

$$O(t) = \begin{cases} 0, & \text{“no service” and “setup” states,} \\ \hat{Q}, & \text{“clearing” state,} \\ A(t), & \text{“extension” state.} \end{cases} \quad (2)$$

Present day, material flow networks are typically subjected to a global control. Beside the high computational demands of such a control in the case of larger networks, the systems become very inflexible with respect to their reactions to random fluctuations of the transportation volume and extraordinary events like traffic accidents, machine failures, or attacks. Despite these disadvantages, for example, typical traffic lights are mainly operated by traffic-adaptive fixed-time controllers, which means that the average service period is fixed and can only be varied within small intervals [9]. The natural alternative of a decentralized control is very appealing in terms of computational demands and flexibility. However, the traditional approach to such a control using clearing policies has been shown to lead to severe instabilities in networks [10]: even if a corresponding policy is stable and optimal for a single intersection, it may not be used for controlling acyclic networks which are commonly present in traffic, production, and logistics. In this work, an alternative strategy is proposed for a decentralized control of conflicting material flows in networks, which is motivated by empirical observations of self-organized oscillations of pedestrian motion at bottlenecks [11]. Using the resulting concept of a oscillating permeability function that is controlled by the net pressure difference

between the conflicting flows, the self-organized optimization and synchronization of the flows in a simple network configuration is studied in some detail.

This paper is organized as follows: In Sec. II, the basic ingredients of a model for an efficient decentralized control and its generalization to arbitrary network configurations are described. The resulting switching dynamics at an isolated merge or intersection of two flows is considered in Sec. III. If it is applied to regular grid networks, the proposed control leads to a system-wide coordination with a phase coherent, mutually lagged switching dynamics of the individual intersection, which is studied in some detail in Sec. IV. Finally, the major results of this study are summarized and completed by an outlook on possible modifications of the presented approach that appear to be necessary for a practical implementation in real-world material flow networks.

II. DESCRIPTION OF THE MODEL

The model behind the decentralized control strategy used in this work is motivated by empirical findings from the field of pedestrian dynamics. Suppose there are two flows of pedestrians in opposite directions which have to pass a common bottleneck. Using simulations with the social force model assuming interactions between individuals due to physical and “social” pressure terms, Helbing *et al.* [11], [12] have been able to explain the empirical observation of an oscillatory switching between different flow directions by a varying net pressure difference. Corresponding findings have also been experimentally reported for ant traffic [13]. In addition, related effects have been found both empirically and by means of simulations in terms of self-organized lane formation in intersecting pedestrian flows [14] and pedestrian counter-flows [15] as well as for intersecting and bottleneck flows of pedestrian and vehicular traffic [16], [17], [18].

The above mentioned results suggest that the oscillatory switching between traffic in different directions is induced by the variations of the mutual (physical as well as social) pressure of the waiting and moving pedestrians. Mathematically, this phenomenon can be formulated by a cost function $C(t)$ which controls the permeability of the bottleneck in both directions. For the sake of simplicity, this function will be firstly specified for the case of two merging or intersecting flows. In the presented model, there are two main factors entering the cost function [19]:

- 1) a net “pressure” force of the waiting material, which is proportional to the difference between the amounts of material still waiting to cross the intersection in both possible directions;
- 2) a net “drain” force that corresponds to the natural inertia of a flow that is currently served; it will be assumed that this drain is proportional to the difference of the departure flows in both directions.

As an additional factor, one may also penalize the total waiting time $T(t)$ of the delayed material waiting on the incoming links. In the pedestrian analogy, this additional factor may be

reasonable as pedestrians waiting for a relatively long time become impatient and, as a consequence, enhance their pressure on the crowd with increasing waiting time. Summarizing, one may formulate the following cost function:

$$\begin{aligned} C(t) = & \alpha_N(N_2(t) - N_1(t)) \\ & + \alpha_O(O_2(t) - O_1(t)) \\ & + \alpha_T(T_2(t) - T_1(t)), \end{aligned} \quad (3)$$

where the indices $i = 1, 2$ correspond to the incoming links, and $\alpha_{N,O,T}$ are proper weights. For simplicity, in the following the specific choice $\alpha_T = 0$, $\alpha_N = 1$ and $\alpha_O = \alpha$ will be considered.

Having specified the cost function, the next step is to define a permeability function $\gamma_i(t)$ for the whole set of incoming links i at a given intersection point. In the formalism used in this work [19], the possible choice of this function will be restricted by some general properties: First, $\gamma_i(t)$ is a multiplicative “factor” entering the dynamic equation for the outflows $O_i(t)$, i.e., there is no outflow from link i if $\gamma_i(t) = 0$. Second, $\gamma_i(t)$ has to be normalized, that is, $\gamma_i(t) \leq 1$. Third, $\gamma_i(t)$ should be a function of the current value of the cost function $C(t)$ exclusively. Fourth, $\gamma_2(t) = 1.0 - \gamma_1(t)$, i.e., in the case of a simple merge or intersection of two flows, the permeability for both incoming directions have to add to one. With this setting, it is possible to fully describe a self-organized oscillatory switching between flows in different directions.

In the case of pedestrian motion where simultaneous flows in both directions (and, hence, collisions between different pedestrians) are still possible, a logistic function [19]

$$\gamma_{1,2}(t) = \frac{1}{1 + \beta e^{\pm \eta C(t)}} \quad (4)$$

can be used as a specification for $\gamma_i(t)$ (see Fig. 2). A similar continuous parametrization may be used for describing transport processes in biological systems like the cardio-vascular system or related biological transportation networks, where a simultaneous service of different directions is possible under the action of pressure gradients or incorporating diffusive processes between the different flows. In contrast to such situations, in technological systems such as vehicular traffic, material transport in production systems by automatically guided vehicles or conveyors, or baggage handling networks at airports, a continuous parametrization with $0 \leq \gamma_i(t) \leq 1$ would allow for potential collisions between objects transported in different directions. However, in the mentioned systems, such collisions have to be avoided to reduce the occurrence of accidents and the resulting damages of the transported objects. For this purpose, it is beneficial to replace the logistic function by a piecewise constant function that can only approach binary values (corresponding to “stop” and “go” commands for the respective flows) [20], [21], [22]. An example for such a function is shown in Fig. 2. As a particular advantage, this choice allows a sharp switching between both states. In order to avoid losses of efficiency due to finite times required for accelerating and decelerating, an

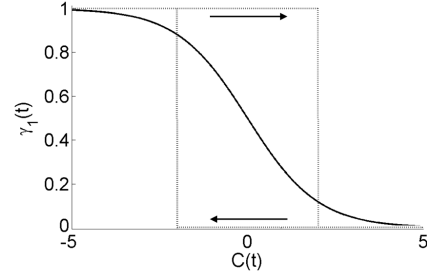


Fig. 2. Two specific parametrizations for the permeability function in dependence on the value of the cost $C(t)$. The solid line shows a logistic function (see Eq. (4)) that may be used for describing intersecting pedestrian or biological flows, whereas the dotted line corresponds to the hysteretic piecewise constant model used for controlling material flows in technological systems within the framework of this study.

additional hysteresis effect may be introduced into the model, which causes the service state to remain the same if the traffic conditions in the operated and stopped directions are comparable and thus introduces a preferred switching interval at given traffic conditions.

In situations where the material flows can be operated in a two-phase mode (e.g., merges or intersections without turning conflicts), the resulting dynamics of the system is described by a small set of equations relating the amounts of waiting material $N_i(t)$, the arrival flows $A_i(t)$, the departure flows $O_i(t)$, and the permeability $\gamma_i(t)$ of the different directions (service phases) at the “intersection”. In addition to the above considerations, one has to specify the relationship between the change of the queue lengths and the associated arrival and departure flows (which is rather trivial) and an explicit expression for the departure flows. Following the considerations from Sec. I, in the case of a complete permeability of the intersection in direction i (i.e., $\gamma_i(t) = 1$), the departure flow $O_i(t)$ from the respective queue occurs with maximum rate \hat{Q}_i if there is material left in the queue, or otherwise with the arrival rate $A_i(t)$ of new material which is instantaneously processed. Summarizing, one finds the following set of equations:

$$\frac{d}{dt}N_i(t) = A_i(t) - O_i(t) \quad (5)$$

$$O_i(t) = \gamma_i(t) \times \begin{cases} A_i(t), & N_i(t) = 0 \\ \hat{Q}_i, & N_i(t) > 0 \end{cases} \quad (6)$$

$$\gamma_1(t) = \begin{cases} 1, & C(t) < -\Delta C/2, \\ 0, & C(t) > \Delta C/2 \end{cases} \quad (7)$$

$$\gamma_2(t) = 1 - \gamma_1(t) \quad (8)$$

$$C(t) = \left(\sum_{i \in \mathcal{L}_2} - \sum_{i \in \mathcal{L}_1} \right) (N_i(t) + \alpha O_i(t)), \quad (9)$$

where the permeability functions show a bistable behavior in the interval $[-\Delta C/2, \Delta C/2]$ of the cost function, \mathcal{L}_s are the sets of compatible flows that can be served in a joint phase s , and \hat{Q}_i are the maximally possible flows in the direction corresponding to the queue i . In order to give

different priorities to different queues, it is also possible to use an asymmetric window $[C_{min}, C_{max}]$ (or, under more general conditions, route-specific thresholds C_i) for defining the switching thresholds of the permeability function. Note that the above set of equations neglects finite setup times τ required for a safe operation of real-world material flows. However, such setup times may be easily incorporated into the model, such that it is general enough to describe network flows in a variety of situations, including urban road traffic, transportation of goods in factories (e.g., by automatically guided vehicles), logistics, biological systems, or even the routing of data packages in certain kinds of information networks.

If the operation of a node in a material flow network requires more than two disjoint service phases (for example, in case of intersections in urban road networks where left-hand turning needs to be taken into account), the above formalism can be generalized in a straightforward way [22], yielding a control of the dynamics by assigning a priority index

$$P_s(t) := \sum_{i \in \mathcal{L}_s} (N_i(t) + \alpha O_i(t)) \quad (10)$$

to each service phase \mathcal{L}_s , operating the phase with the highest priority index until the cost function

$$C_s(t) := P_s(t) - \frac{1}{S-1} \sum_{s' \neq s} P_{s'}(t). \quad (11)$$

falls below a certain threshold, and then switching to the next phase. Again, in order to avoid extraordinarily high waiting times on connections with a low load, it is possible to additionally penalize the total waiting time $T_i(t)$ of the material stored on each link by an additional term proportional to $T_i(t)$ in the definition of the priority index.

III. DYNAMICS OF ISOLATED INTERSECTIONS

In the case of an isolated merge or turning-free intersection of two conflicting material flows, the main properties of the switching dynamics can be analyzed analytically. In order to have stable flow conditions without a successive congestion of any of the links, the average outflow \bar{O}_i over one service period must equal the average inflow \bar{A}_i on every link. Assuming the link capacity being the same on every incoming link ($\hat{Q}_i = \hat{Q}$), there are only two dynamically relevant parameters remaining: the total intersection load defined as $u = (A_1 + A_2)/\hat{Q}$, and the inflow ratio $r := A_2/A_1$ [22].

A. Constant Inflows

If the corresponding arrival flows $A_i(t)$ are assumed to be constant with sub-critical values (that is, the sum of all inflows is beyond the capacity limit of the intersection¹, it is possible to derive exact expressions for the switching periods, the duration of eventual extension periods, and the minimum and maximum amounts of material stored on the different transportation routes.

¹In general, $u < 1 - f(\tau)$ where f is a monotonously increasing function of the incorporated setup time τ , which is neglected in the considered model.

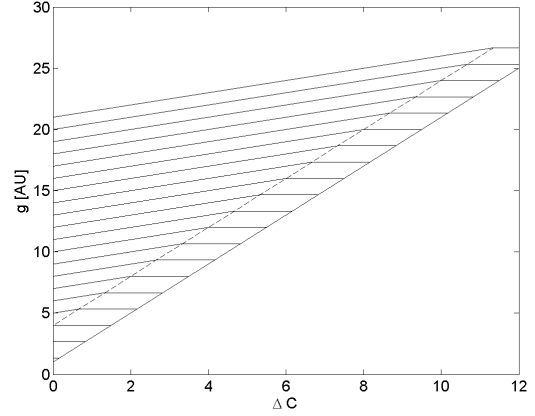


Fig. 3. Dependence of the green time g (in arbitrary units (AU)) on the switching threshold ΔC for $A_1 = A_2 = 0.25$ and $\alpha = 1.0$ in the regimes of incomplete clearing, complete clearing, and complete clearing with extension phase. While the second queue j is assumed to be completely cleared at the beginning of the service period, the different lines correspond to initial queue lengths of $N_i = 20, 19, 18, \dots$ (from top to bottom). The dashed line indicated the transition between incomplete and complete clearing.

Using a piecewise constant permeability function as described in Sec. II with equal switching thresholds $\Delta C/2$ for all possible service states, one may easily convince oneself that for an initial queue length N_i^0 , a complete clearing requires a time

$$T_{C,i} = \frac{N_i^0}{\hat{Q}_i - A_i}. \quad (12)$$

However, this complete clearing takes only place if the choice of the switching threshold $\Delta C/2$ is large enough, in particular,

$$\Delta C \geq 2 \left[\frac{A_j N_i^0}{\hat{Q}_i - A_i} + N_j^0 - \alpha \hat{Q}_i \right]. \quad (13)$$

Otherwise, the switching to a service of the remaining link j occurs already after a time

$$T_{I,i} = \frac{\alpha \hat{Q}_i + N_i^0 - N_j^0 + \Delta C/2}{\hat{Q}_i - (A_i - A_j)}. \quad (14)$$

If this threshold is sufficiently large to allow a complete clearing of the queue i , there may be eventually another extension phase with a duration of

$$T_{E,i} = \frac{\alpha A_i - N_j(T_{C,i}) + \Delta C/2}{A_j} \quad (15)$$

with $N_j(T_{C,i}) = N_j^0 + A_j T_{C,i}$. Following these arguments, in all cases the duration of the service period for link i , T_i , increases linearly with the switching threshold $\Delta C/2$. Hence, ΔC may be thought of as a characteristic scale determining the cycle time T of the traffic light for fixed traffic volumes described by the incoming flows A_1 and A_2 .

Fig. 3 illustrates the above analytical findings for two symmetric inflows with a road utilization of 0.5. In the dependence of the green time on the switching threshold, two regimes can

be distinguished: complete clearing and extension (lowest line with a constant slope) and incomplete clearing (shifted lines with smaller slope). Both regimes are separated by a region where a complete clearing of the queue without an extension phase takes place. The width of this transitional regime is determined by the value of α , and the corresponding time increases linearly with the initial queue length N_i^0 . For small values of N_i^0 (here: $N_i^0 < 4$, there is always a complete clearing of the queue within one service period due to the drain force realized by the parameter α . In contrast to this, for larger initial queues, the green time required for complete clearing increases linearly with both switching threshold ΔC and initial queue length N_i^0 as expected.

The above results suggest that for sufficiently large ΔC , extension phases can be found on both incoming links for a wide range of arrival rates (see [22]). In general, the switching dynamics of an isolated intersection can be qualitatively classified by considering whether the service period of one or both queues leads to an incomplete (I) or complete (C) clearing and even an eventual extension (E) phase. The decision which of the possible combinations (II, IC, IE, CC, CE, or EE) is realized is determined by the inflows A_1 and A_2 (or, alternatively, the quantities u and r), the switching threshold $\Delta C/2$ of the permeability function, and the weight α quantifying the impact of the net drain. Previous investigations [22] have revealed that concerning the qualitative switching dynamics, there are two striking features: First, the presence of an incomplete clearing requires a rather low traffic volume on the considered link, whereas there is much more traffic on the second one (i.e., for low values of r and high values of u). Such a phase can only affect the less frequently used link. Second, extension states can be found at almost all traffic conditions, except of such with a sufficiently high intersection load u . Moreover, as one would expect, there is a strong correlation between long green times and the presence of extension phases. Note, however, that the presence of an extension phase must not necessarily correspond to optimal traffic conditions in terms of usage of the total node capacity, which is related to the freedom in defining the switching threshold ΔC .

Summarizing, the switching threshold parameter ΔC determines (together with the arrival flow rates and initial queue lengths) the typical durations of a service period g in terms of a monotonously increasing piecewise linear function. In addition, the parameter α weighting the influence of the net drain due to the current departure flows is responsible for a complete clearing of the queue within a finite interval of ΔC . Choosing parameter combinations within this range, the self-organized control strategy leads to an instantaneous switching to the next service period as the queue has been completely cleared. If $\alpha \rightarrow 0$, the switching period is exclusively determined by the net “pressure” difference $N_2(t) - N_1(t)$, such that for arbitrary initial conditions, there is no guarantee that any of the involved queues will be completely cleared. If in contrast $\alpha \gg 1$, the drain will dominate the dynamics, which means that a switching can only take place when the presently served queue is empty. From this perspective, this case has a

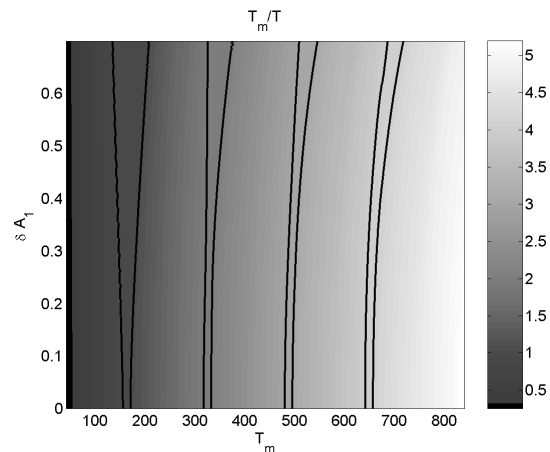


Fig. 4. Emergence of phase-locked states in the case of a periodic arrival flow $A_1(t) = \langle A_1 \rangle (1 + \delta A_1 \sin(2\pi t/T_m))$ on link 1 and a constant arrival flow on link 2. The results are shown for arrival flows with $\langle A_1 \rangle = A_2 = 0.25$ (all values are normalized with respect to the link capacity Q), $\Delta C = 20$ and $\alpha = 1.0$. Gray-scale colors correspond to the ratio between arrival flow period T_m and switching period T , the black lines indicate parameter regions where the deviation from a perfect 1:1 to 4:1 frequency locking (from left to right) is smaller than 5%.

strong similarity to one of the standard clearing policies, “clear largest buffer” (CLB).

B. Periodic Inflows

The case of constant arrival flows of material discussed above is rather artificial. For example, in an urban road network, vehicles are usually bundled to platoons by the action of traffic lights. Since these traffic lights operate in a periodic way, the outflow on a link i and, hence, the inflow to the queue at the downstream end of this link is described by a periodic function, too. If the arrival flows are determined by a periodic function with period T_m , for some distinct interval of these periods (which depends on ΔC), the switching period T of the self-organized control locks to this external demand period [20]. If the amplitude of the periodic arrival flow increases, the width of this locking window increases as well. Moreover, there are other windows of higher-order frequency locking with a similar behavior, which are indicated in Fig. 4. The detailed position and width of the corresponding Arnold tongues is determined by the parameters α and ΔC of the permeability function $\gamma_i(t)$ and the average inflows $\langle A_1 \rangle$ and $\langle A_2 \rangle$. In general, the choice of these parameters again yields a naturally preferred switching frequency in the case of constant inflows, whose existence gives rise to the non-trivial locking intervals.

It has to be mentioned that the existence of various phase-locked states can be observed independently of the shape of the periodic functions. In particular, under certain situations, non-trivial $m:n$ locking states can be found [20]. One may speculate that the appearance and width of such states can be enhanced by different modifications of the scenario studied in this work, for example, a) by decreasing the critical switching

threshold ΔC (i.e., allowing for a complete clearing of all queues with extension phases under almost all conditions) or adjusting it in a way that the preferred switching time is close to the modulation period, b) by changing from “positive” to “negative” hysteresis in the permeability function (i.e., choosing a *negative* value of ΔC), which would correspond to an anticipative switching regime, c) by choosing continuous instead of piecewise constant permeability functions, or d) by considering periodic arrival flows with more pronounced temporal variability profiles (for example, arrival flows described by rectangular (on-off) functions instead of sinusoids). It should be noted that options b) and c) have been used in a recent study [20], revealing a much larger variety of locking windows than in the scenario shown in Fig. 4. A detailed examination of the corresponding dynamic effects is however outside the scope of the presented study.

IV. DYNAMICS OF COUPLED INTERSECTIONS

Whereas the dynamics of isolated intersections can be (under certain assumptions) treated analytically, the practically more relevant case of controlling networks of intersecting flows is more challenging. In the following, this problem is hence addressed by means of simulations.

A. Specification of the Scenario

In order to keep the number of variables as low as possible, in the following, some simplifications will be made:

- 1) For avoiding an unlimited congestion of the incoming links, which would finally affect the whole network, it is required that the sum of the maximum inflows for all necessary service phases of a given intersection is sufficiently smaller than the maximum link capacity \hat{Q} , which is assumed to be equal for all links.
- 2) The studied networks consist only of nodes of degree $k = 4$ (i.e., with four pairs of ingoing and outgoing links which connect neighboring pairs of nodes). A consideration of nodes with $k = 3$ (i.e., a merge or diverge) is also possible, however, the case of $k > 4$ is not considered here. All links are assumed to allow a bi-directional traffic.
- 3) Motivated by the problem of vehicular traffic in networks with right-hand driving policy, for every intersection and every incoming link, only right-hand turning is permitted with a given probability $p \in [0, 1]$. In contrast to this, direct left-hand turning will remain forbidden, as the corresponding possibility would call for two additional turning phases at least if the arrival flows are sufficiently large. Moreover, in the case of road networks with bi-directional traffic, left-hand turning may be effectively achieved by a sequence of right-hand turnings.

Under these assumptions, the cycle of successive service periods consists of only two phases. The dynamic coupling of different intersection points in a material flow network requires to represent the inflows at a given node by the outflows from neighboring nodes at an earlier time. In a zeroth-order

approximation, the corresponding time delay is assumed to equal the free-flow travel time τ_i^{free} on the respective link,

$$A_i(t) = \sum_{j \neq i} \alpha_{ji} O_j(t - \tau_i^{free}), \quad (16)$$

where α_{ji} is the fraction of the flow on link j which is turning to link i ($\alpha_{ji} = p$ for right-hand turning, $\alpha_{ji} = 0$ for left-hand turning, and $\alpha_{ji} = 1 - p$ otherwise). As a necessary condition of material conservation, $\sum_i \alpha_{ji} = 1$ for all links j . To approach more realistic conditions, the free-flow travel time has to be replaced by a load-dependent travel time, i.e., a time-dependent travel time which is determined by the amount of material waiting on the link. A very simple way for doing this would be setting

$$\tau_i(t) = \frac{l_i - N_i(t)\Delta l}{v_{free}}, \quad (17)$$

where l_i is the total length of the road between two neighboring intersections and Δl the space occupied by one of the queued objects.

Using the described coupling between neighboring nodes, the switching dynamics has been studied for regular grid networks with 25 nodes where the material flows are operated the same way (i.e., with the same parameters of the permeability function) at all intersections. In a simplified setting without load-dependent travel times and left-hand turning, it has been observed that a network-wide self-organization of the flows takes place that leads to a certain minimization of the total amount of waiting material [21]. As one increases the preferred switching threshold determined by the parameter ΔC , the total capacity of the network, but also the amount of delayed material successively increase.

B. Phase Coherence Analysis

In order to better understand the dynamics of the self-organization process due to the proposed decentralized control, a detailed phase coherence analysis has been performed. For evaluating the presence of phase coherence in this context, the appropriate definition of a monotonously increasing phase variable is necessary. Without loss of generality, the initial phase of node j has been defined in a way that $\phi_j = 0$ corresponds to the time of the first switching of its permeability function. In a similar way, $\phi_j = (n - 1)\pi$ then corresponds to the time of the n -th switching at this node. Between these switching times, the phase variable $\phi(t)$ is defined by linear interpolation. Although this definition leads to an increase of the phase which may be periodically modulated if the “on” and “off” times for one specific direction are not symmetric, in the long-term limit, these variables may be used for a phase coherence analysis.

In order to quantify the phase coherence in a multivariate way, different approaches based on the mean resultant length

$$r_{jk} = \left| \left\langle e^{i\Delta\phi_{jk}(t)} \right\rangle_t \right| = \frac{1}{T} \left| \sum_{t=1}^T e^{i\Delta\phi_{jk}(t)} \right| \quad (18)$$

(with $\Delta\phi_{jk}(t) = \phi_k(t) - \phi_j(t)$) as a particularly useful bivariate measure for phase coherence have been considered [21]: a) global or neighbor-based averages of this pairwise phase coherence index, b) average mean resultant length of all intersections with respect to their mean-field, c) the synchronization cluster strength computed using the synchronization cluster analysis algorithm of Allefeld and Kurths [23], d) eigenvalue statistics obtained from the matrix of pairwise indices in terms of the generalized synchronization cluster analysis [24], and e) the LVD dimension density method [20], [21] which describes the average exponential scaling of the residual variances obtained from the eigenvalues.

Whereas all mentioned measures yield comparable results for model systems like a network of Kuramoto phase oscillators with long-range interactions [21], they show a quantitatively different behavior when applied to the switching dynamics in the considered material flow model, which is most likely explained by their different sensitivity to heterogeneity effects. In particular, the global and neighbor-based averages and the average coherence with the mean-field quantify only the mean degree of phase coherence, but are not sensitive to detect effects of spatial heterogeneity. The synchronization cluster strength assumes implicitly the presence of a unique synchronization cluster², which is under general conditions a too strong assumption, especially during the transition from non-coherent to phase-coherent dynamics. The number and average strength of synchronization clusters based on the generalized synchronization cluster analysis allow a better characterization of heterogeneity effects, but yield rather coarse measures. Finally, the phase coherence parameter based on the LVD dimension density approach is well suited to quantify heterogeneities, but is only a coarse and uncertain measure for the strength of phase synchronization. In summary, a combined consideration of different approaches is here helpful to distinguish information about the average phase coherence and its heterogeneity.

Looking at the dynamics of the material flow model in some more detail, it turns out that the probability $\alpha_{ji} = p$ of right-hand turning serves as a coupling parameter between neighboring intersections (at least as long as possible sources or sinks along the links of the network are neglected): If p is large, only a lower amount of material crossing one intersection arrives also the next one, which corresponds to a low coupling of the dynamics, and vice versa. In a two-parameter study in dependence on both p and the switching threshold ΔC , multivariate phase coherence analysis reveals pronounced Arnold tongues that correspond to different phase coherent regimes in the system (see Fig. 5). These tongues are separated by parameter regions that correspond to an incoherent switching at the different nodes. The presence of multiple

²Note that the measures used here for quantifying phase coherence have been introduced in the context of phase synchronization analysis, while the notation of phase synchronization is doubtful in the context considered here since the intersecting material flows subjected to decentralized control do not represent self-sustained oscillators, which are a prerequisite for phase synchronization in the standard definition [25].

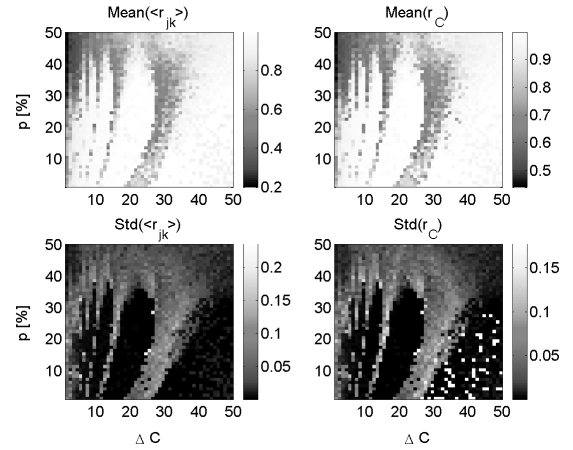


Fig. 5. Mean values (upper panels) and standard deviations (lower panels) of the mean pairwise mean resultant length $\langle r_{jk} \rangle$ (left) and synchronization cluster strength r_C (right), obtained from different parts of a set of long simulation runs for a regular 5×5 grid network with constant travel times $\tau = 30s$, fixed randomly chosen inflows A_i on the links entering from outside the network, and $\alpha = 0.1$. Whereas in the phase coherent regimes, this coherence is found to be stable in time (low standard deviations), in the incoherent parts, the considered measures fluctuate also significantly in time (high standard deviations). Note that the results concerning the synchronization cluster strength r_C may be less reliable, as the corresponding algorithm does not necessarily converge correctly in all cases.

regimes appears to be a consequence of the presence of two disjoint time scales in the dynamics: the preferred switching period described by the threshold ΔC in the permeability functions $\gamma_i(t)$, and the free-flow travel times τ_i^{free} that are equal for all links in the considered grid-like topology.

C. Synchronization Analysis

In the previous paragraphs, evidence has been reported for different regimes with a coherent switching at different nodes. As the notation of phase synchronization cannot be used in this context without criticism due to the missing of well-defined self-sustained oscillators, it is of interest how the above findings may be interpreted in a synchronization context. In order to avoid systematic errors in the estimation of phase coherence indices due to the piecewise linear phase definition applied in the context of switching dynamics, it may be beneficial to use alternative synchronicity concepts instead that refer to the isochronicity (or fixed-lag synchronicity) of switching events. Similar approaches are already used for quantifying synchronization of events, for example, in neurophysiological systems.

Consider the switching dynamics of two individual intersections in the network, which consist of two distinct phases under the assumptions described above. In the case of a phase coherent dynamics, the cycle length at all intersections must be the same. Then, for every pair of oscillations, the following quantities are constructed:

- For the second last switching event at intersection j , the switching event at intersection k is identified which has a minimum time lag with respect to this event. This time lag

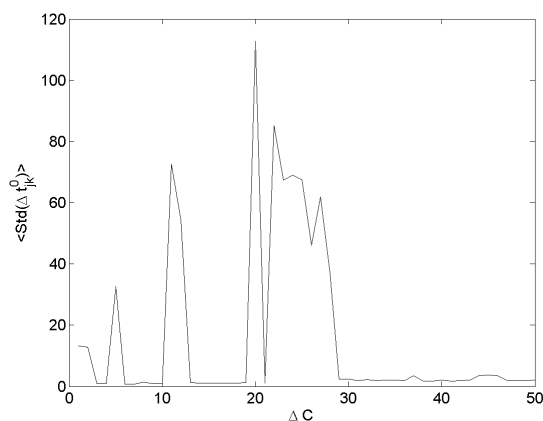


Fig. 6. Mean standard deviations of the switching-time differences at different intersections as a function of the switching threshold parameter ΔC for $\alpha = 0.1$ and $p = 0.05$.

is computed. After this, the sequences of switching events are traced backwards in time for both intersections event-by-event, leading to a series of time differences $\Delta t_{jk}^{(0)}$.

- In a similar way, a sequence of time differences $\Delta t_{jk}^{(1)}$ is constructed where the reference event at intersection k is replaced by its predecessor.

In the case of (almost) isochronous switching, the values of $\Delta t_{jk}^{(0)}$ will be centered around zero with a narrow distribution. If the switching is synchronous with a certain lag, $\Delta t_{jk}^{(0)}$ and/or $\Delta t_{jk}^{(1)}$ are characterized by a small standard deviation with non-zero mean (depending on the symmetry of the switching dynamics). Following this idea, the mean value of $\Delta t_{jk}^{(0)}$ can be used as a measure of isochronicity, whereas the minimum of the standard deviations of both sequences yields a measure for the presence of (lagged) event synchronicity, and the corresponding mean value determines the average lag. The concept of event synchronization analysis can be further refined, however, this is outside of the scope of the presented work. For example, in the case of delays covering more than one switching cycle, an optimal lag could be inferred by considering the standard deviations of all event sequences that are shifted with respect to each other by $\pm k$ events and identifying the minimum of the resulting function.

The results of this event synchronization analysis (see Fig. 6) are in good qualitative agreement with those obtained from the phase coherence analysis [21]. In particular, for a fixed turning probability p , there are distinct values of the switching threshold for which the standard deviations of the mutual event-time differences between different intersections approach values near zero, indicating a possibly lagged synchronization of the switching.

D. Heterogeneity Effects

The structural properties of the system studied so far have been fully homogeneous in space. In order to understand

the impact of corresponding heterogeneities to the coherent switching dynamics and, hence, the optimal self-organization of the network, it has been studied how distributed travel times corresponding to a deviation from the regular grid structure influence the degree of synchronization in the switching dynamics of the network. In a recent paper [21], it has been demonstrated that the measures of phase coherence discussed above decay only slowly as the disorder of the system increases. In general, this disorder is reflected in an increasing amount of delayed material and a systematic tendency towards shorter service intervals. From this, one may argue that the presence of heterogeneities limits the capability of material flow systems to optimally self-organize in terms of the local control strategy used in this work.

It is likely that also an uneven spatial distribution of other parameters (in particular, turning probabilities, switching thresholds, or the mutual weights of the different force terms entering the cost function $C(t)$) will lead to similar consequences. Of more fundamental interest, however, is the question how a consideration of dynamically adjusted travel times incorporating queued road sections as well as acceleration and deceleration effects may affect the resulting material flow dynamics. This question will be further addressed in future studies.

V. CONCLUSIONS

In many socio-economic systems, in particular in the fields of production and logistics, there has already been a paradigm shift from a centralized control towards a decentralized self-organization of material flows [26]. In the special case of urban traffic networks, the situation is however still quite different, as local control strategies have so far not been very successful in practical implementations. A particular reason for this is that “traditional” decentralized control approaches based on clearing policies may lead to unstable traffic conditions due to the presence of dynamic feedbacks. The results reported in this contribution may be an important step in overcoming these problems. However, for specific practical applications, there may be a need for incorporating additional mechanisms for stabilizing the large-scale dynamics, for example, by including demand anticipation over a finite time horizon [9], [27] or by implementing additional heuristic strategies for avoiding local deadlocks [9], [28].

In the presented work, a general concept has been discussed for serving conflicting material flows in general networks in a fully demand-dependent way. Apart from the potential applicability of this approach to controlling material flows in real-world networks, it may also be used for modelling and understanding flows in a variety of other (in particular, biological) systems. The key ingredient of a permeability function which is determined by gradient forces like net pressures or drains can be specified in such systems for describing discrete as well as continuous flows.

It has been shown that an appropriate specification of the permeability function leads to a fully self-organized and synchronized dynamics of the traffic at intersections, which is

significantly more flexible than traditional approaches using a centrally enforced cyclic traffic light control. Hence, using the presented approach for implementing a decentralized control strategy at all intersections of a material flow network, the time-delayed local coupling between the flows at neighboring nodes leads to the emergence of a network-wide phase coherent switching dynamics that can be understood in the context of event synchronization. As a particularly interesting feature, the presence of multiple disjoint synchronization regimes in networks has been revealed, which is a so far not yet fully understood dynamical phenomenon possibly related to the presence of two intrinsic time scales of the dynamics, corresponding to the preferred switching intervals prescribed by the parameter ΔC of the considered model and the typical travel times τ_i on the different links.

Although in the presented considerations, a continuous flow approximation has been used for describing all material flows, theoretical investigations [29] as well as simulations not discussed here in detail suggest that the resulting dynamics on the network is very similar if the individual transportation units or agents are explicitly considered. Moreover, in this study, a variety of simplifications have been made, which are necessary for a detailed analytical treatment of the dynamical properties of the permeability model. Additional effects have to be explicitly taken into account in future studies, including the influence of spatial heterogeneity and distributed parameters, the dynamical feedback between queue lengths and travel times, the definition of setup phases, acceleration effects leading to a delayed clearing of queues, etc. It will be of particular interest how these effects influence the emergence of a synchronized switching and, as a consequence, the efficiency of a self-organized traffic light control within the network.

The question how the observed self-organization processes are related to an optimization of network flows has not been discussed in much detail in this paper. From the perspective of temporal variability, synchronization introducing regularity of material flows on large spatial scales can be considered as a particular optimization goal. However, regarding the minimization of throughput (or, alternatively, waiting) times in the network, one has to recall that the duration of service periods increases monotonously with the switching threshold ΔC . However, when tuning this parameter in a way that corresponds to a transition from a non-synchronous to a synchronous switching, the corresponding increase of delayed material is significantly reduced. These preliminary results have so far only been verified for switching intervals without setup times. Recent results in the field of urban traffic networks [28] however suggest that the transition to a synchronized, not necessarily phase-coherent service could lead to a significant decrease in the total waiting times. The further validation of this hypothesis within a more general framework of arbitrary material flow networks will be an important topic of future research.

ACKNOWLEDGMENT

The authors would like to thank the German Research Foundation (DFG projects He 2789/5-1,8-1), the Volkswagen foundation, and the Daimler-Benz foundation for their partial support of this study. Discussions with Mamen Romano and Marco Thiel are gratefully acknowledged.

REFERENCES

- [1] D. Chowdhury, L. Santen, and A. Schadschneider, *Statistical physics of vehicular traffic and some related systems*, Phys. Rep. 329 (2000), 199–329
- [2] D. Helbing, *Traffic and related self-driven many-particle systems*, Rev. Mod. Phys. 73 (2001), 1067–1141
- [3] B.S. Kerner, *The Physics of Traffic: Empirical Freeway Pattern Features, Engineering Applications, and Theory*, Berlin: Springer, 2004
- [4] D. Helbing, *Modelling supply networks and business cycles as unstable transport phenomena*, New J. Phys. 5 (2003), 90.1–90.28
- [5] J. Howard, *Mechanics of Motor Proteins and the Cytoskeleton*, Sunderland, MA: Sinauer Associates, 2001
- [6] B. Alberts, D. Bray, J. Lewis, M. Raff, K. Roberts, and J.D. Watson, *Molecular Biology of the Cell*, 3rd ed., New York: Garland, 2004
- [7] T. Nakagaki, R. Kobayashi, Y. Nishiura, and T. Ueda, *Obtaining multiple separate food sources: behavioural intelligence in the Physarum plasmodium*, Proc. R. Soc. Lond. B 271 (2004), 2305–2310
- [8] D.P. Bebber, J. Hynes, P.R. Darrach, L. Boddy, and M.D. Fricker, *Biological solutions to transport network design*, Proc. R. Soc. B 274 (2007), 2307–2315
- [9] S. Lämmer, *Reglerentwurf zur dezentralen Online-Steuerung von Lichtsignalanlagen in Straßennetzwerken*, PhD thesis, Dresden University of Technology, 2007
- [10] P.R. Kumar and T.I. Seidman, *Dynamic instabilities and stabilization methods in distributed real-time scheduling of manufacturing systems*, IEEE Trans. Automat. Contr. 35 (1990), 289–298
- [11] D. Helbing and P. Molnár, *Social force model for pedestrian dynamics*, Phys. Rev. E 51 (1995), 4282–4286
- [12] D. Helbing, A. Johansson, J. Mathiesen, M.H. Jensen, and A. Hansen, *Analytical approach to continuous and intermittent bottleneck flows*, Phys. Rev. Lett. 97 (2006) 168001
- [13] A. Dussutour, J.-L. Deneubourg, and V. Fourcassié, *Temporal organization of bi-directional traffic in the ant Lasius niger (L.)*, J. Exp. Biol. 208 (2005), 2903–2912
- [14] D. Helbing, L. Buzna, A. Johansson, and T. Werner, *Self-Organized Pedestrian Crowd Dynamics: Experiments, Simulations, and Design Solutions*, Transp. Sci. 39 (2005), 1–24
- [15] C. Burstedde, K. Klauck, A. Schadschneider, and J. Zittartz, *Simulation of pedestrian dynamics using a two-dimensional cellular automaton*, Physica A 295 (2001), 507–525
- [16] D. Helbing, R. Jiang, and M. Treiber, *Analytical investigation of oscillations in intersecting flows of pedestrian and vehicle traffic*, Phys. Rev. E 72 (2005), 046130
- [17] R. Jiang and Q.-S. Wang, *Interaction between vehicle and pedestrians in a narrow channel*, Physica A 368 (2006), 239–246
- [18] R. Jiang, D. Helbing, P. Kumar Shukla, and Q.-S. Wang, *Inefficient emergent oscillations in intersecting driven many-particle flows*, Physica A 368 (2006), 567–574
- [19] D. Helbing, J. Siegmeyer, and S. Lämmer, *Self-organized network flows*, Netw. Heterog. Med. 2 (2007), 193–210
- [20] R. Donner, A. Hofleitner, J. Höfener, S. Lämmer, and D. Helbing, *Dynamic stabilization and control of material flows in networks and its relationship to phase synchronization*, Proc. 3rd Int. Conf. Physics and Control (PhysCon 2007), 1188
- [21] R. Donner, *Multivariate analysis of spatially heterogeneous phase synchronisation in complex systems: Application to self-organised control of material flows in networks*, Eur. Phys. J. B, in press, doi:10.1140/epjb/e2008-00151-8
- [22] R. Donner, S. Lämmer, A. Hofleitner, and D. Helbing, *Decentralised control of traffic flows in urban networks*, in: J.J. Schneider (ed.), *Lectures on Socio- and Econophysics*, Springer, Berlin (2008), in press
- [23] C. Allefeld and J. Kurths, *An approach to multivariate phase synchronization analysis and its application to event-related potentials*, Int. J. Bifurcation Chaos 14 (2004), 417–426

- [24] C. Allefeld, M. Müller, and J. Kurths, *Eigenvalue decomposition as a generalized synchronization cluster analysis*, *Int. J. Bifurcation Chaos* 17 (2007), 3493–3497
- [25] A. Pikovsky, M. Rosenblum, and J. Kurths, *Synchronization - A Universal Concept in Nonlinear Sciences*, Cambridge: Cambridge University Press, 2001
- [26] M. Hülsmann and K. Windt, *Understanding Autonomous Cooperation and Control in Logistics*, Berlin: Springer, 2008
- [27] S. Lämmer, R. Donner, and D. Helbing, *Anticipative control of switched queueing systems*, *Eur. Phys. J. B*, in press, doi:10.1140/epjbe2007-00346-5
- [28] S. Lämmer and D. Helbing, *Self-Control of Traffic Lights and Vehicle Flows in Urban Road Networks*, *J. Stat. Mech. Theor. Exp.* (2008), P04019
- [29] D. Helbing, S. Lämmer, and J.-P. Lebacque, *Self-organized control of irregular or perturbed network traffic*, in: C. Deissenberg and R.F. Hartl, *Optimal Control and Dynamic Games*, Dordrecht: Springer, 2005, pp 239–274



Reik Donner studied physics and mathematics at the University of Potsdam, where he obtained his diploma degree in 2002 for a thesis on the dynamics of a simple conceptual model of the Earth dynamo. From 2002 to 2006, he worked as a research assistant at the nonlinear dynamics group at the University of Potsdam. In his Ph.D. thesis defended in early 2007, he developed novel concepts of multivariate time series analysis for applications to short noisy data from geological records.

In 2006, Reik Donner joined the Chair of Traffic Modeling and Econometrics at Dresden University of Technology as a post-doctoral research scientist. In 2007, he received a postdoctoral fellowship of the Japanese Society for the Promotion of Science (JSPS). His main research interests include the self-organized dynamics in traffic, production, logistics, and biological networks, the emergence of coherent macroscopic behavior through synchronization phenomena, and the development and application of complex systems based methods of time series analysis to interdisciplinary problems.



Stefan Lämmer obtained his master in electrical engineering from Dresden University of Technology, where he specialized in control theory. In his Ph.D. thesis, which has been successfully defended in 2007, he developed innovative solutions for the self-control of traffic lights in urban road networks.

Stefan Lämmer is currently appointed as a post-doctoral research scientist at the Chair of Traffic Modeling and Econometrics at Dresden University of Technology. His research interests are focussed on the self-organization processes in material flow systems and the dynamics of traffic and production networks.



Dirk Helbing studied physics and mathematics at the Georg-August University Göttingen. His master thesis finished in 1990 dealt with the nonlinear modeling and multi-agent simulation of observed self-organization phenomena in pedestrian crowds. Two years later, he received his Ph.D. at the University of Stuttgart with a thesis on modelling social interaction processes by means of game-theoretical approaches, stochastic methods and complex systems theory, which was awarded two research prizes.

After having completed his habilitation on traffic dynamics and optimization at the University of Stuttgart in 1996, Dirk Helbing received a Heisenberg scholarship. He worked at the Weizmann Institute in Israel, at Xerox PARC in Silicon Valley, at INRETS in Paris and the Collegium Budapest - Institute for Advanced Study in Hungary, where he is now a member of the external faculty. In 2000, he was appointed full professor and Managing Director at the Institute for Transport & Economics at Dresden University of Technology. Since 2007, Dirk Helbing is Professor of Sociology, in particular of Modeling and Simulation at ETH Zurich. His main research interests include the modeling and analysis of material flows in networks and cooperative dynamics in socio-economic and traffic systems.

Multiple-Model Seismic Structural Control

Alexandar Ichtev

Technical University of Sofia
Faculty of Automatics, System and Control Group
8 Kliment Ochridsky Blvd.
1000, Sofia, Bulgaria
ichtev@tu-sofia.bg

Svetla Radeva

University of Architecture
Civil Engineering and Geodesy
1 Hristo Smirnensky Blvd.
1046 Sofia, Bulgaria
svetla_fce@abv.bg

Abstract— the aim of this research is to develop an approach for seismic protection of high-risk structures with multiple-model structural control. Structural control provide opportunity to realize measures for reduction of seismic vulnerability of high risk structures, like nuclear power plants, bridges, lifelines, dams, high rise buildings etc. In this paper is proposed an approach for multiple-model for active and semi-active structural control realised with removable cross-braces control systems, where each system corresponds to different actuator or combination of actuators for structural control. After determination of frequencies characteristics, resonances and anti-resonances, is made decision about reconfiguration of the system. The semi-active structural control is realised by engaging a subset of all possible actuators. The choice of the actuator subset, made on the base of frequency response and magnitude characteristics leads to reconfiguration of the structural control system. The active bracing structural control system is realized with acceleration feedback strategies. An algorithm for multiple-model real-time control is proposed. The simulation results for active and semi-active bracing experiments provided with a model of three storey building are shown.

Keywords— *Structural Control; Multiple-Model Approach; Simulation and Modeling of Seismic Signals; Strong Motion Seismic Waves; Controllers; Sliding Mode Control.*

I. INTRODUCTION

The aim of this research is to develop an approach for seismic protection of high-risk structures with multiple-model structural control. Structural control provide possibility to realize measures for reduction of seismic vulnerability of high risk structures, like nuclear power plants, bridges, lifelines, dams, high rise buildings [5]. Displacements and velocities of the structures during earthquake are not absolute but depend upon inertial reference frame in which they are taken. As it is not always possible to provide structural response measurements during strong motion earthquakes their modelling by computer simulation enable earthquake engineers to compare and study the behaviour of structures during earthquakes, regarding their overall characteristics and potential of structural damages [5]. The structural control theory methods and their applications in state space, allow almost complete elimination of the negative motions in the

structure, by employing active or semiactive control [4]. The active control strategies have been developed as one means by which to minimize the effects of seismic loads. The active control systems operate by external energy supplied by actuator to impart forces on the structure. The main drawback of this approach is that in order to achieve this effect it is required to apply control actions with magnitude, similar with the seismic one [7]. This is difficult to accomplish in practice. Actually, full elimination of the seismic effect on the structure is not needed. It is sufficient enough to reduce this effect to a degree to which it can be guaranteed that the structure will not sustain damage or at least will not fail [2]. Due to the possibility of the extreme force of the seismic signal, even this reduction is sometimes difficult to achieve. In order to accomplish this task it is required to take into account specific characteristics of the structure as well as of the seismic signal.

In this paper is proposed an approach for active/semiactive control for structures. It is applicable for both open loop and close loop control systems realizations. Determination of the seismic signals characteristics is from great importance. Due to the fact, that the response spectrum of the seismic signal varies in time it is proposed that it, or its components can be estimated online. The main goal of the control is accomplished, i.e. sufficient reduction of the structures movement, by combine usage of the modelled seismic signals with the structure, controllers and control realization scheme. This is done by minimizing the effect not to the whole seismic signal, but only to the most dangerous components of it – resonance frequencies or close to them.

II. CONTROL SYSTEM

In this paper is proposed an approach for multiple-model active and semi-active structural control realized with active bracing control systems, where each system corresponds to different device or combination of devices for structural control. After determination of frequencies characteristics, resonances and anti-resonances, is made decision about including different subsystems into the overall control system. This leads to reconfiguration of the structural control system – sliding mode control.

The control system consists from two main parts - controller and controlled structure (Fig.1). It is assumed that many actuators a_1, a_2, \dots, a_n , can be switched on in the

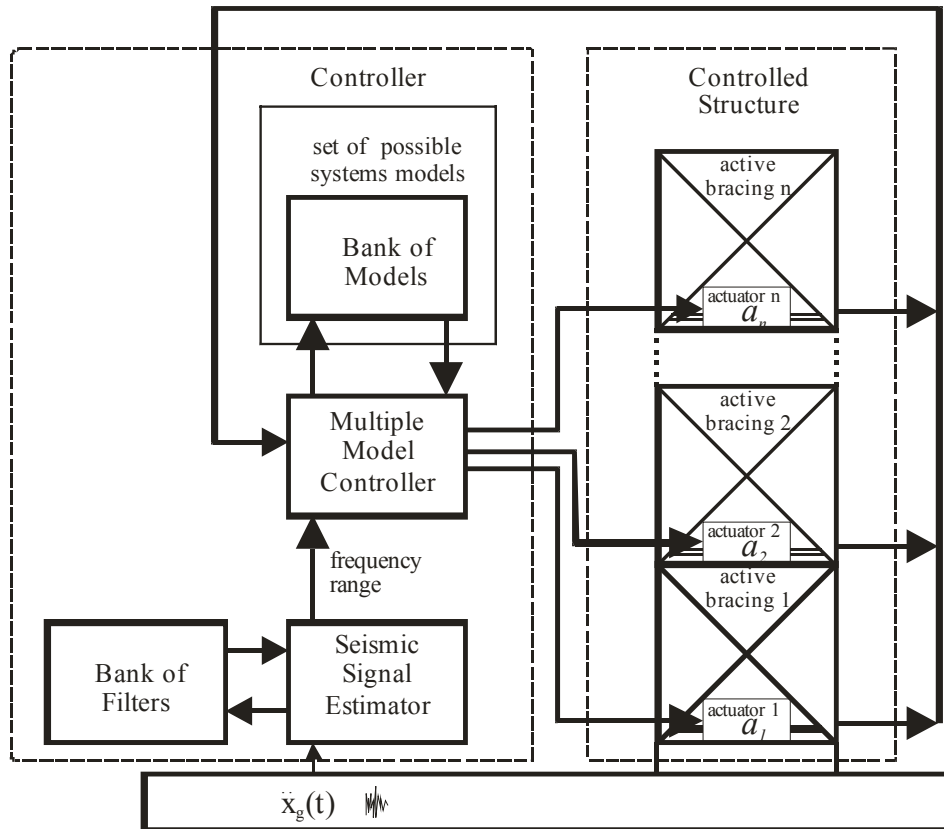


Figure 1 Multiple model seismic structural control system

structure for accomplishment of the control aim. A *set of possible system models* are designed. Each of these models corresponds to a different system's configurations - with one actuator or with different combinations of actuators. Frequency responses, and especially resonance and anti-resonance frequencies and ranges for system models are analyzed.

From the set of all possible models, a subset is selected. This set will be referred as *Bank of Models*. Each model from the model bank corresponds to a particular working regime of the system or to a different system scheme – system in different control configuration. The *Seismic Signal Estimator* determines the seismic resonance range. In order to accomplish this task, a bank of digital filters is set up. This step is performed off-line

During the active faze of the earthquake on-line estimation of the seismic signal resonance is performed. This information is used for *Multiple Model Controller* reconfigurations. The reconfiguration task is performed by choosing such control configuration from the model bank that ensures best suppression of the momentary earthquake resonance. In accordance with this selected model, the controller switch on, or switch off the corresponding actuators. By doing so the controller is realizing *sliding mode control* for the system with a variable in time structure. In this way, an adaptation of the control system to the seismic signal is accomplished.

III. STRUCTURE MODELS AND CONTROLLERS

The following matrix differential equation is assumed for a mathematical model of the structure, presented as (1)

$$\mathbf{M} \frac{d^2 \mathbf{Y}}{dt^2} + \mathbf{C} \frac{d\mathbf{Y}}{dt} + \mathbf{K}\mathbf{Y} = \mathbf{F}\mathbf{V} + \mathbf{B}\mathbf{U}. \quad (1)$$

Here \mathbf{Y} is n dimensional vector of the movements in the main points of the structure, \mathbf{V} is vector representation of the external seismic forces, \mathbf{U} is n dimensional vector of the control signals (it is assumed that control action can be applied to all n basic points of the structure), \mathbf{M} , \mathbf{C} , \mathbf{K} , \mathbf{F} and \mathbf{B} are matrixes, which represent mass, damping, stiffness, input and control correspondingly.

The feedback principle can be applied for control purpose of this structure. Control vector \mathbf{U} is computed using information from the vectors of the movements \mathbf{Y} , velocities $d\mathbf{Y}/dt$, accelerations $d^2\mathbf{Y}/dt^2$, as well as combination of these vectors at the structure's basic points. The most general description of the controller can be written in the form (2)

$$\mathbf{U} = -\mathbf{R}_a \frac{d^2 \mathbf{Y}}{dt^2} - \mathbf{R}_v \frac{d\mathbf{Y}}{dt} - \mathbf{R}_y \mathbf{Y}. \quad (2)$$

Here \mathbf{R}_a is the feedback matrix in respect to accelerations, \mathbf{R}_v is the feedback matrix in respect to velocities, and \mathbf{R}_y if the feedback matrix in respect to position's movements.

The equation for the closed loop system can be obtained, by substituting the expression (2) into equation (1) as (3)

$$(\mathbf{M} + \mathbf{BR}_a) \frac{d^2 \mathbf{Y}}{dt^2} + (\mathbf{C} + \mathbf{BR}_v) \frac{d\mathbf{Y}}{dt} + (\mathbf{K} + \mathbf{BR}_y) \mathbf{Y} = \mathbf{FV}. \quad (3)$$

By comparison between equations (3) and (1), can be observed that components \mathbf{R}_a , \mathbf{R}_v and \mathbf{R}_y of the control signal are modifying the plants matrixes \mathbf{M} , \mathbf{C} and \mathbf{K} independently. The role of the matrixes \mathbf{M} , \mathbf{C} and \mathbf{K} over the dynamics of the structures is well studied. This makes equation (3) suitable for analysis of the controls signal impact on the systems dynamics (in particular the effect on the discussed below resonance and antiresonance frequencies). This will significantly contribute to the controller design.

From equation (3) it can be analyzed the impact of the controllers matrixes over the properties of the closed loop system: the matrix \mathbf{R}_v of the velocity feedback modifies the damping matrix of the structure \mathbf{C} . This means that through it, it is possible to be increased the overall damping of the system, i.e. to decrease the resonances. The matrix \mathbf{R}_y of the position feedback modifies the structure's stiffness matrix \mathbf{K} . This means that with it the resonance frequencies of the system can be changed. Acceleration feedback \mathbf{R}_a has similar impact on the system. It can be stated that the negative acceleration feedback stiffens the system, i.e. it increases its natural frequency. The negative acceleration feedback has the opposite effect – it lowers the plants frequency, i.e. it is equivalent to the increase of the elements of the \mathbf{M} matrix. The seismic signals are high frequency signals and this will going to produce positive results for the control.

IV. QUALITY CRITERIA AND CONTROLLER CHOICE

It is convenient to perform system analysis and controller design in accordance to the frequency response approach, due to the clear physical relation between the frequency response and characteristics of the structures movement. Significant danger (during the earthquake) of a structural failure presents coincidence of any natural frequency of the structure with the resonance frequency of the seismic signal. This hazard is increased when the structures has small damping, i.e. with large resonance picks in the magnitude-frequency response.

In this paper is proposed to control the structure's natural frequencies. For controller design purposes it is proposed to be used following quality criteria: *maximum distance between basic natural frequencies of the structure and resonance basic frequencies of the seismic signal*. Of course, in order to apply these criteria, it is essential to have information about the seismic signals. For the spectral composition of the seismic signals or at least his resonance frequencies, some effect can be obtain by the controller if it is tuned in such way that antiresonance of the structure neutralize some of the main resonances of the bedrock.

V. FREQUENCY RESPONSE, RESONANCE AND ANTIRESONANCE

The paper considers acceleration feedforward and feedback strategies for reduction of structural response during seismic activity with active bracing structural control. Used methods for experimental determination of frequency response function break down into two fundamental types: swept-sine and the broadband approaches using fast Fourier transforms. Both methods can produce accurate frequency response functions estimates.

The swept-sine approach is rather time-consuming, because it analyzes the system one frequency at a time. The broadband approach estimates the frequency response function simultaneously over a band of frequencies. The first step is to independently excite each of the system's inputs over the frequency range of interest.

Exciting the system at frequencies outside this range is typically counter productive; thus the excitation should be bound limited (e.g., pseudo-random). Assuming the two continuous signals (input $u(t)$ and output $y(t)$) are stationary, the frequency response function is determined by dividing the cross spectral density of the two signals S_{uy} by the auto-spectral density of the of the input signal S_{uu} .

More precise investigation of the control effect, natural frequencies and antiresonance as well as controller design can be performed by system's transfer function. By applying the Laplas transform to the equation (3) was received (4)

$$[(\mathbf{M} + \mathbf{BR}_a)s^2 + (\mathbf{C} + \mathbf{BR}_v)s + (\mathbf{K} + \mathbf{BR}_y)]\mathbf{Y}(s) = \mathbf{FV}(s). \quad (4)$$

The transfer function can be obtained as (5).

$$\begin{aligned} W(s) &= \frac{\mathbf{Y}(s)}{\mathbf{V}(s)} = \\ &= [(\mathbf{M} + \mathbf{BR}_a)s^2 + (\mathbf{C} + \mathbf{BR}_v)s + (\mathbf{K} + \mathbf{BR}_y)]^{-1} = \mathbf{F}, \end{aligned} \quad (5)$$

from which it is easy to compute the resonance frequencies – roots of the polynomial in the denominator and antiresonance frequencies – roots of the polynomial (polynomials) in the nominator. From the transfer function the frequency response of the system can be easily obtained as well.

In cases of high order models of the system, some concerns, regarding the inverse of the polynomial matrix in (5), may rise. In such case a state space model of the closed loop system can be obtained and applied for control purposes. Using the following notations:

$$\mathbf{M}_a = \mathbf{M} + \mathbf{BR}_a, \quad \mathbf{C}_v = \mathbf{C} + \mathbf{BR}_v, \quad \mathbf{K}_y = \mathbf{K} + \mathbf{BR}_y,$$

equation (3) is transformed to(6).

$$\frac{d^2 \mathbf{Y}}{dt^2} + \mathbf{M}_a^{-1} \mathbf{C}_v \frac{d\mathbf{Y}}{dt} + \mathbf{M}_a^{-1} \mathbf{K}_y \mathbf{Y} = \mathbf{M}_a^{-1} \mathbf{FV}. \quad (6)$$

Then, by introduction of the $2n$ dimensional state vector $\mathbf{X}^T = [\mathbf{Y}^T (d\mathbf{Y}^T / dt)]$, the model of the closed loop system in state space becomes (7).

$$\dot{\mathbf{X}} = \begin{bmatrix} \mathbf{0} & \mathbf{I} \\ -\mathbf{M}_a^{-1}\mathbf{K}_y & -\mathbf{M}_a^{-1}\mathbf{C}_v \end{bmatrix} \mathbf{X} + \begin{bmatrix} \mathbf{0} \\ \mathbf{M}_a^{-1}\mathbf{F} \end{bmatrix} \mathbf{V} \quad (7)$$

The resonance and antiresonance frequencies can be obtained from it as well (for example with Matlab[®] 6.5).

VI. SEMI-ACTIVE STRUCTURAL CONTROL

The feedback from the control structure to the controller (Fig.1) creates a possibility for application of active control strategy. This kind of control allows almost complete elimination of the structures movements. However in order to achieve such control, large control action is required.

Multiple model control can be realized without feedback. In this case the controller is working in open loop. The controller determines the control action only on the base on the information for the seismic signal, obtained from the seismic signal estimator. The control is very similar to the gain scheduling. Of course, in such case the control will not be effective as in the closed loop scheme (with the feedback), but still it can be archived significant reduction in the structures movement. The main advantage of the semi-active control is that the control strategy requires significantly less energy for control purposes. Such control can be achieved for example by switching on and off by an actuator (actuators) additional structural elements – removable cross-braces.

On Fig.2 is shown an experimental setup of a model of three degrees of freedom structure with only one actuator. By switching on and off the removable cross-braces the stiffness of the structure is altered. On Fig.3 are presented magnitude characteristics of the structure in nominal regime (without switching the removable cross-braces), as well as in other regime – in which all removable cross-braces are switched on. It can be observed that only these two models are sufficient for damping the seismic signal in the important frequency range. This means that for each frequency at least one of the two characteristic is with negative values. The shown values are expectable the whole range, which guaranties sufficient damping of the seismic signal. This proves that only these two systems models (with switched off and all removable cross-braces switched on) are sufficient to form the model set (Fig.1). Each of the model is preferred than the other one in two frequency ranges. This means that four filters are required for frequency range separation. They form the filter bank of the Seismic Signal Estimator. In that way the crucial frequency range (the range around the resonance frequency of the seismic signal) can be estimated for each time instant. The proposed digital filters are eight orders Butterworth filters. The chosen characteristics of the filters are presented in Fig. 4. During the earthquake the Seismic Signal Estimator detects the presence of the strong signal and estimates his main frequency range. Depending on the predominant magnitude of the corresponding filter the model is chosen. The removable cross-braces system is

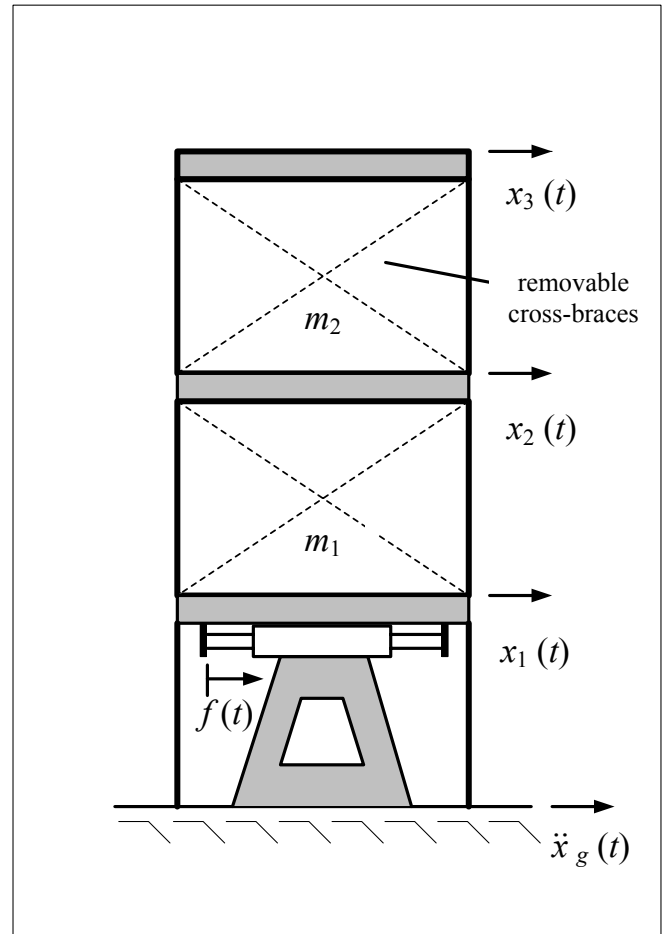


Figure 2 Experimental setup of active bracing control system

switched on and off according to the chosen model, thus the sliding mode control is realized.

On the base on the above discussion an algorithm for control is proposed. It consists from two parts. The first one is design of banks of filters and controllers. The next step is performed in real-time and it is on the base of the obtained from the previous step system.

A. System design

1. Design of a set from possible models for the closed loop system. Each of the models consist of the controlled structure and a controller (or a combination of controllers), which can perform the control tasks without exceeding predefined boundaries of the necessary additional energy for control purposes.
2. Determination of (for each of the closed loop system models) the frequencies response, resonance and antiresonance ranges.
3. Selection of model's bank from a multiple model set. The selection is made in such a way that the antiresonance frequency range overlaps whole possible frequency ranges of the seismic signal.

- Design of bank from digital filters. Each of the filters corresponds to the important frequency range of the seismic signal. For the particular model it can be more than one filter.

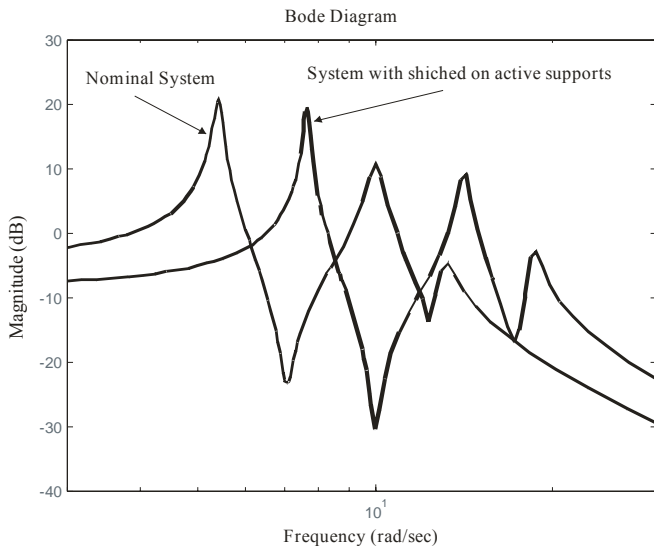


Figure 3 Frequency - magnitude characteristics of the nominal system with removable cross braces.

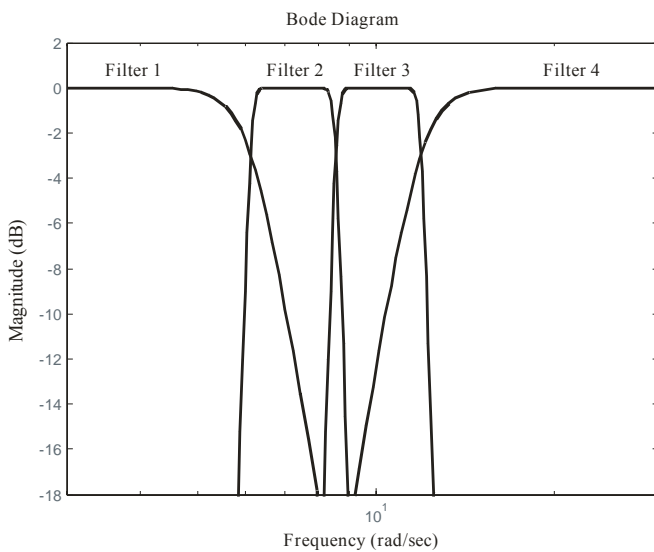


Figure 4 Frequency - magnitude characteristics of the proposed Butterworth filters.

B. Real-time control

- Probability analysis for the arrival moment of the destructive phase of the seismic signal, based on the initial phase of the earthquake (P wave).
- Estimation of the current resonance frequency of the seismic signal.
- Model selection from the multiple models set. This is done in such a way that the antiresonance frequencies of the

chosen model have the best overlap of the resonance range of the seismic signal.

- Switch on the chosen controller.

The step 2 of the algorithm is evaluated for each time instant and in case of significant change of the seismic signal resonance frequency the new model selection (steps 3) is selected and new controller configuration is engaged (Step 4).

VII. EXPERIMENTAL RESULTS

In this chapter are presented experimental results for the closed loop system. The simulator used for this investigation consists of a hydraulic actuator servo/valve assembly that drives a 122cm × 122 cm aluminium slip table mounted on high-precision, low-friction linear bearings. The capabilities of simulator are: maximum displacement ±5 cm, maximum velocity ±90 cm/sec, and maximum acceleration ±4 g/s with a 450 kg test load. The operational frequency range of the simulator is nominally 0-50 Hz. The test structure, shown on Fig.5, was a model of a three-storey single-bay scale model building. The building frame was constructed on steel with a height of 160 cm. the floor masses of the model weighted a total of 230 kg, distributed evenly between the three floors. The time scale factor was 0,2 making the natural frequencies of the model approximately five times those of the prototype.

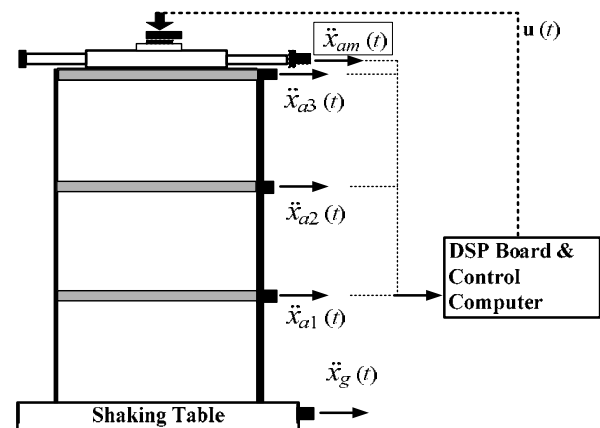


Figure 5. Experimental setup of a three degree of freedom model

As shown in Fig. 5 accelerometers positioned on the each floor of the structure measured the absolute accelerations of the model, and an accelerometer located on the base measured the ground excitation.

To develop a high quality, control-oriented model, an eight channel data acquisition system consisted of eight Syminex XFM82 3 decade programmable anti-aliasing filters were employed. The data acquisition system consists as well of an Analogical CTRTM-05 counter-timer board and the Snap-Master software package. The XFM82 offer programmable pre-filter gains to amplify the signal into the filter, programmable post-filter gains to adjust the signal so that it falls in the correct range for the A/D converter, and analog anti-aliasing filters which are programmable up to 25 kHz.

Implementation of the digital controller was performed using the Spectrum Signal Processing Real-Time Signal Processor (DSP) System. The on-board A/D system has two channels with 16 bit precision and a maximum sampling rate of 200 kHz. The two D/A channels, also with 16 bit precision, allow for even greater output rates so as not to be limiting.

Typically, times the closed-loop system bandwidth, as was the case in this experiment, the discrete equivalent system will adequately represent the behaviour of the emulated continuous-time system over the frequency range of interest.

Two series of experimental tests were provided to evaluate the performance of the controllers that were designed. First a broadband signal (0-50 Hz) was used to excite the structure and root mean square responses were calculated. In the second series of the tests an earthquake-type excitation was applied to the structure and peak responses were determined.

The results include responses for the relative displacement of the actuators, the absolute accelerations of the three floors, \ddot{x}_{a_1} , \ddot{x}_{a_2} , \ddot{x}_{a_3} , and the applied control force f . The *zeroed-control* case corresponds to the case in which the actuator is attached, but the command signal is set equal to zero (i.e., $u=0$). From the response of the zeroed configuration it is shown that the "stiffness" of the actuator has a significant effect on the displacement (97,4%) and a moderate effect on the accelerations. Notice that with control, the absolute accelerations of the three floors are reduced by 37,8%, 56,4% and 61,0%, respectively, over the uncontrolled responses, and the first floor displacement is reduced by 95,6%. The controlled responses are achieved by using less force than the zeroed-control case.

Comparison of the uncontrolled, zeroed and controlled transfer functions for the ground acceleration to the first floor absolute acceleration is shown on Fig. 6. Notice that the peaks of the controlled transfer functions from the ground acceleration to the structural responses are significantly smaller those of the zeroed transfer functions. Only the controlled transfer function from the ground acceleration to the actuator displacement is larger in magnitude than the zeroed response, because in the zeroed configuration the actuator attempts to remain in the locked position.

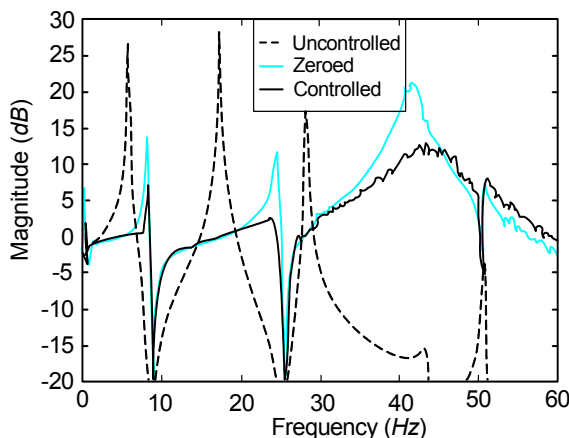


Figure 6. Comparison of uncontrolled zeroed and controlled transfer functions: ground acceleration to the first floor absolute acceleration.

Comparison of the uncontrolled, zeroed and controlled transfer functions for the ground acceleration to the second floor absolute acceleration is shown on Fig. 7.

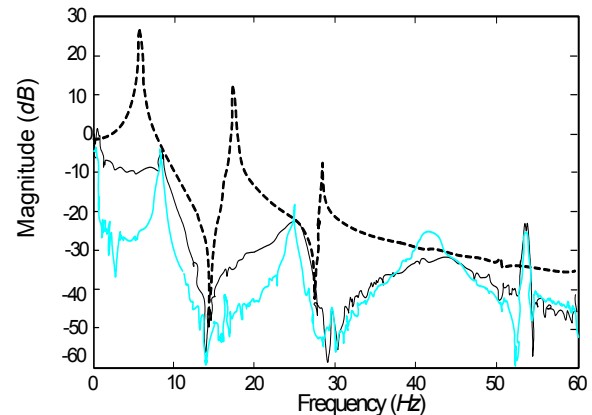


Figure 7. Comparison of uncontrolled zeroed and controlled transfer functions: ground acceleration to the second floor absolute acceleration.

VIII. CONCLUSIONS

An approach for seismic protection of high-risk structures with multiple-model structural control has been proposed and evaluated. The effects on actuator dynamics and control structure interaction were incorporated into the system identification procedure, where each control system corresponds to different device or combination of devices for structural control. After determination of the frequencies characteristics, resonances and anti-resonances, a decision about including or not some parts of the system into the total control system is made. This leads to reconfiguration of the structural control system.

Under the broadband excitation on the experimental setup was achieved in total approximately 78% reduction of acceleration responses and a significant response reduction were achieved in different modes of the system. When excited by an earthquake disturbance, the peak response reduction of the top floor acceleration was 68%. The received results show that proposed approach should be regarded as viable and effective for mitigation of structural response due to seismic excitations.

ACKNOWLEDGMENT

This work is a part of the international NATO research project Science for Peace PDD(TC)-ESP.EAP.SFP.983238 Forecast and Reduction of Seismic Vulnerability of High Risk Structures and the research project of Bulgarian science fund TH1511/05.

REFERENCES

- [1] Gluck, J., Ribakov, Y., Dancygier, A. (2000). Predictive Active Control of MDOF Structures, *Earthquake Engineering and Structural Dynamics*, 29(1), 109-125.

- [2] He, W., Agarwal, A., Yang, J. (2003). Novel Semiactive Friction Controller for Linear Structures Against Earthquakes. *ASCE Journal of Structural Engineering*, 129(7), 931-941.
- [3] Nasu, T., Kobori, T., Takahashi, M., Niwa, N., Ogasawara, K. (2001). Active Vibrate Stiffness System with Non-Resonant Control, *Earthquake Engineering and Structural Dynamics*, 30(7), 1594-1614.
- [4] Nishitani, A., Nitta, Y., Ikeda, Y. (2003). Semiactive Structural Control Based on Variable Slip-Force Level Dampers. *ASCE Journal of Structural Engineering*, 129(7), 933-940.
- [5] Radeva, S., Paskaleva, I., Radev, D., Panza. (2006). Site Dependent Estimation of the Seismic Strong Motion: Case Study for Sofia Region, *Acta Geodaetica et Geophysica Hungarica*, Vol. 41, No 3 - 4, pp. 395 - 407.
- [6] Radeva, S., Scherer, R., Radev, D. (2005). Strong Motion Waves Estimation for Seismic Control of Nuclear Power Plant. *Journal of Nuclear Engineering and Design*, NED vol.235, Issues 17-19, Elsevier, 1977-1988.
- [7] Scruggs, J. T., Iwan, W. D. (2003). Control of a Civil Structure Using an Electric Machine with Semiactive Capability. *ASCE Journal of Structural Engineering*, 129(7), 951-959.
- [8] Yuen, K., and Beck, J. (2003). Reliability-Based Control of Uncertain Dynamical Systems Using Feedback of Incomplete Noisy Response Measurements. *Earthquake Engineering and Structural Dynamics*, 32(5), 751-770.
- [9] Zhang, Y., and Iwan, W. (2002). Active Interaction Control of Civil Structures. Part 2: MDOF Systems, *Earthquake Engineering and Structural Dynamics*, 31(1), 179-194.

BIOGRAPHY

ALEXANDAR ICHTEV, PhD is Assistant Professor at Department of Automatics, Systems and Control Group, Technical University of Sofia. His main research interests are in Control Theory, Adaptive Control, Fuzzy Systems, Robust Control, Fault detection, Fault Tolerant Control; ichtev@tu-sofia.bg

SVETLA RADEVA, PhD is Associate Professor at Department of Computer Aided Engineering at University of Architecture Civil Engineering and Geodesy, Sofia, Bulgaria. Her main research interests are Structural Control, Simulation and Modelling of Earthquake Processes, and Seismic Response Reduction; svetla_fce@abv.bg

Self-Organising Sync in a Robotic Swarm

Vito Trianni and Stefano Nolfi

Institute of Cognitive Sciences and Technology - CNR

via S. Martino della Battaglia, 44, 00185 Rome, Italy

Email: {vito.trianni,stefano.nolfi}@istc.cnr.it

Abstract—Self-organised synchronisation is a common phenomenon observed in many natural and artificial systems: simple coupling rules at the level of the individual components of the system result in an overall coherent behaviour. Owing to these properties, synchronisation appears particularly interesting for swarm robotic systems, as it allows to robustly coordinate through time the activities of the group while keeping a minimal complexity of the individual controllers. The goal of the experiments presented in this paper is the study of self-organising synchronisation for robots that present an individual periodic behaviour. In order to design the robot controllers, we make use of artificial evolution, which proves capable of synthesising minimal synchronisation strategies based on the dynamical coupling between robots and environment. The obtained results are analysed under a dynamical systems perspective, which allows us to uncover the evolved mechanisms and to predict the scalability properties of the self-organising synchronisation with respect to varying group size.

I. INTRODUCTION

Synchrony is a pervasive phenomenon: examples of synchronous behaviours can be found in the inanimate world as well as among living organisms [1], [2]. The discovery of the basic mechanisms behind self-organised synchronisation aroused research for many years, until the appropriate analytical methods were developed [3], [4]. Self-organising synchronisation phenomena can be modelled as systems of multiple coupled oscillators. Consider for example the synchronous flashing of fireflies [5]. Fireflies can be modelled as a population of pulse-coupled oscillators with equal or very similar frequencies. These oscillators can influence each other by emitting a pulse that shifts or resets their oscillation phase. The numerous interactions among the individual oscillator-fireflies are sufficient to explain the synchronisation of the whole population (for more details, see [5]–[7]).

The synchronisation behaviours observed in Nature can be a powerful source of inspiration for the design of robotic systems. Synchronisation is an important mean to achieve coordination. This holds true particularly for swarm robotic systems [8], where emphasis is given to the emergence of coherent group behaviours from simple individual rules. Much work takes inspiration from the self-organised behaviour of fireflies or similar synchronisation behaviours observed in Nature [9]–[13]. The goal of the experiments presented in this paper is the study of self-organising synchronisation in a group of robots based on minimal behavioural and communication strategies. We follow the basic idea that if an individual displays a periodic behaviour, it can synchronise with other (nearly) identical individuals by temporarily modifying its

behaviour in order to reduce the phase difference with the rest of the group. In other robotic studies, synchronisation is based on the entrainment of the individual internal dynamics through some form of communication. In this paper, instead, we do not postulate the need of internal dynamics. Rather, the period and the phase of the individual behaviour are defined by the sensory-motor coordination of the robot, that is, by the dynamical interactions with the environment that result from the robot embodiment. We show that such dynamical interactions can be exploited for synchronisation, allowing to keep a minimal complexity of both the behavioural and the communication level. In order to define a robot controller able to exploit such dynamical agent-environment interactions, we use artificial evolution [14], [15]. The obtained results are analysed under a self-organising perspective, evaluating their scalability to large groups of robots.

The main contribution of this paper consists in the analysis of the evolved behaviours, which is brought forth exploiting a dynamical systems approach [16]. In this paper, we introduce a dynamical system model of the robots interacting with the environment and among each other. This model offers us the possibility to deeply understand the evolved behaviours, both at the individual and collective level, by uncovering the mechanisms that artificial evolution synthesised to maximise the user-defined utility function. Moreover, we show how the developed model can be used to predict the ability of the evolved behaviour to efficiently scale with the group size. We believe that such predictions are of fundamental importance to quickly select or discard obtained solutions without performing a time-demanding scalability analysis, as well as to engineer swarm robotic systems that present the desired properties.

II. EVOLUTION OF SELF-ORGANISING SYNCHRONISATION

In this section, we present the experimental scenario defined for the evolution of synchronisation behaviours. The task requires that each robot in the group displays a simple periodic behaviour, which should be entrained with the periodic behaviour of the other robots present in the arena. The individual periodic behaviour consists in oscillations along the y direction of the rectangular arena (see Figure 1). Oscillations are possible through the exploitation of a symmetric gradient in shades of grey painted on the ground, which can be perceived by the robots through the infrared sensors placed under their chassis. The gradient presents a black stripe for $|y| > 1$, in which the robots are not supposed to enter. Collisions with

walls or other robots are avoided using the infrared proximity sensors placed around the cylindrical body of the robots. Finally, synchronisation of the movements can be achieved by exploiting a binary communication system: each robot can produce a continuous tone with fixed frequency and intensity. When a tone is emitted, it is perceived by every robot in the arena, including the signalling one. The tone is perceived in a binary way, that is, either there is someone signalling in the arena, or there is no one.

The robots used in this experiments are the *s-bots*, which are small autonomous robots with a differential drive system [17]. The evolutionary experiments presented in this paper are performed in simulation, using a simple kinematic model of the *s-bots*, and the results are afterwards validated on the physical platform. Artificial evolution is used to set the connection weights and the bias terms of a fully connected, feed forward neural network—a perceptron network. The evolutionary algorithm is based on a population of 100 genotypes, which are randomly generated. This population of genotypes encodes the connection weights of 100 neural controllers. Each connection weight is represented with a 8-bit binary code mapped onto a real number ranging in $[-10, +10]$. Subsequent generations are produced by a combination of selection with elitism and mutation. Recombination is not used. At each generation, the 4 best individuals—i.e., the *elite*—are retained in the subsequent generation. The remainder of the population is generated by mutation of the 20 best individuals. Each genotype reproduces at most 5 times by applying mutation with 3% probability of flipping a bit. The evolutionary process runs for 500 generations.

The evolved genotype is mapped into a control structure that is cloned and downloaded onto all the *s-bots* taking part in the experiment (i.e., we make use of a homogeneous group of *s-bots*). The performance of a genotype is evaluated by a 2-component function: $F = 0.5 \cdot F_M + 0.5 \cdot F_S \in [0, 1]$. The movement component F_M simply rewards robots that move along the y direction within the arena at maximum speed. The oscillatory behaviour derives from the fact that the arena is surrounded by walls, so that oscillations during the whole trial are necessary to maximise F_M . The second fitness component F_S rewards synchrony among the robots as

the cross-correlation coefficient between the distance of the robots from the x axis. In this way, synchronous oscillations are rewarded also when robots are in perfect anti-phase. In addition to the fitness computation described above, two indirect selective pressures are present. First of all, a trial is stopped when an *s-bot* moves over the black-painted area, and we assign to the trial a performance $F = 0$. In this way, robots are rewarded to exploit the information coming from the ground sensors to perform the individual oscillatory movements. Secondly, a trial is stopped when an *s-bot* collides with the walls or with another robot, and also in this case we set $F = 0$. In this way, robots are evolved to efficiently avoid collisions.

III. EVOLUTIONARY RESULTS

We performed 20 evolutionary replications, each starting with a different population of randomly generated genotypes. Each replication produced a successful synchronisation behaviour, in which robots display oscillatory movements along the y direction and synchronise with each other, according to the requirements of the fitness function. The individual ability to perform oscillatory movements is based on the perception of the gradient painted on the arena floor, which gives information about the direction parallel to the y axis and about the point where to perform a U-turn and move back towards the x axis. In order to produce self-sustained oscillations, signalling is exploited. The main role of the evolved communication strategy is to provide a coupling between the oscillating *s-bots*, in order to achieve synchronisation. In fact, each evolved controller produces a signalling behaviour that varies while the robots oscillate. In this way, the signal emitted by a robot carries information about its position (or *phase*), which can be exploited by other robots for synchronisation. In summary, the evolved synchronisation behaviours are the results of the dynamical relationship between the robot and the environment, modulated through the communicative interactions among robots. No further complexity is required at the level of the neural controller: simple and reactive behavioural and communication strategies are sufficient to implement effective synchronisation mechanisms.

A qualitative analysis of the obtained controllers reveals that the behaviours produced are quite similar one to the other. In general, it is possible to distinguish two phases in the evolved behaviours: an initial transitory phase during which robots achieve synchronisation, and a subsequent synchronised phase. The transitory phase may be characterised by physical interferences between robots due to collision avoidance, if robots are initialised close to each other. The collision avoidance behaviour performed in this condition eventually leads to a separation of the *s-bots* in the environment, so that further interferences to the individual oscillations are limited and synchronisation can be achieved. During the synchronous phase, collision avoidance is therefore less probable, but still possible due to the environmental noise, which may let robots deviate from their normal movements and approach other robots. Otherwise, this phase is characterised by stable synchronous oscillations of all *s-bots*, and small deviation from synchrony are immediately compensated.

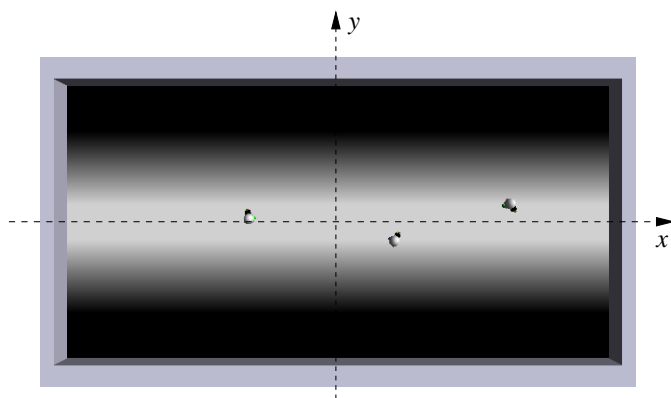


Fig. 1. Snapshot of a simulation showing three robots in the experimental arena. The dashed lines indicate the reference frame used in the experiments.

IV. DYNAMICAL SYSTEM MODELLING

We want to analyse the behaviour of a group of robots that synchronise their periodic oscillations. Our main interest is the understanding of both the individual behaviour and the synchronisation mechanism. Such understanding may be useful to predict some features of the evolved behaviour, e.g., scalability. To do so, we model the behaviour of the single robot looking only at the relevant features of the agent-environment dynamics. In particular, we ignore physical interactions among robots and between robots and walls. Moreover, we neglect the environmental noise and second order dynamics in the robot motion. As a consequence of such simplifications, the oscillatory behaviour of the robot r can be modelled as follows:

$$\langle y_r, \theta_r, S_r \rangle|_{t+1} = \mathcal{B}_c(y_r, \theta_r, s)|_t. \quad (1)$$

where y_r is the y coordinate of robot r at time t , θ_r its orientation, s is the binary communication signal perceived at time t and S_r is the signal emitted by robot r at time t . The function \mathcal{B}_c encodes the fundamental features of the individual behaviour, as it is produced by the parameters c of the evolved controller. In other words, given the above simplification and considering the features of the gradient painted on the arena floor, it is possible to neglect the x coordinate of a robot, as it does not influence the individual behaviour. The latter can be described as a trajectory in the 3D space $\langle y, \theta, s \rangle$, which is determined by \mathcal{B}_c . Notice that when only one robot is present, the perceived sound s corresponds to the self-emitted signal S_r . With R interacting robots, the communication channel determines the following coupling rule:

$$s(t) = \max_r S_r(t) \in \{0, 1\}, \quad (2)$$

which specifies that a binary signal is perceived if and only if it exists at least one s -bot r that is signalling. Notice that the sound perception s is equal for all robots in the environment, because communication is global and binary. What happens with R robots? The only interaction among s -bots is a communicative one, given by the coupling introduced in equation (2). It is therefore possible to define the following discrete-time dynamical system of $3R + 1$ equations:

$$\begin{cases} \langle y_1, \theta_1, S_1 \rangle|_{t+1} = \mathcal{B}_c(y_1, \theta_1, s)|_t \\ \vdots \\ \langle y_R, \theta_R, S_R \rangle|_{t+1} = \mathcal{B}_c(y_R, \theta_R, s)|_t \\ s|_{t+1} = \max_r S_r|_{t+1} \end{cases}. \quad (3)$$

In the following, we make use of this model to discuss about the behaviour of a single s -bot and the evolved synchronisation mechanism.

V. BEHAVIOURAL ANALYSIS

The behaviour of the individual s -bot can be studied looking at how position y , orientation θ and perceived sound s vary through time. We analyse the behaviour produced by the best evolved controller among the 20 evolutionary replications, namely the controller evolved in the 8th replication, which will be referred to as c_8 . To do so, we numerically integrate equation (3) for $R = 1$ to compute a *vector field* showing

the instantaneous direction and magnitude of change for each point in the state space $\langle y, \theta, s \rangle$ (see the top-left plot in Figure 2). This is a 3-dimensional space where y and θ are continuous variables that vary respectively in the range $[-1, 1]$ and $[0, 2\pi]$, while s is a binary variable. The plot suggests how the state of an s -bot starting at any point in its space evolves through time. Together with the vector field, the continuous line indicates the limit cycle attractor to which every trajectory converges. Notice that the continuous line is actually a closed trajectory, due to the 2π -periodic boundary conditions of θ . The existence of such a limit cycle attractor indicates that the individual behaviour is actually periodic, and defines the dynamics of convergence toward a stable motion of the robot.

Another important information can be extracted from the vector field: the signalling behaviour. For each point in the plane $\langle y, \theta \rangle$, it is possible to distinguish 4 different signalling behaviours:

- **no signalling:** the robot never emits a signal when placed at position $\langle y, \theta \rangle$.
- **environment-driven signalling:** the robot always emits a continuous signal when placed at position $\langle y, \theta \rangle$, no matter what signal is perceived. Signalling depends entirely on the position of the s -bot in the environment.
- **signal-driven signalling:** the robot emits a continuous signal when placed at position $\langle y, \theta \rangle$, but only in response to a perceived signal. Otherwise, no signal production is observed.
- **alternate signalling:** the robot emits a signal when placed at position $\langle y, \theta \rangle$ if no signal is perceived, and signalling is stopped in response to a perceived signal. As a consequence, the s -bot continuously switches on and off its loudspeaker.

We show the signalling behaviour of the best evolved controller in the top-right plot of Figure 2. Different signalling behaviours are indicated by circles filled with varying grey-level. It is possible to notice that the limit cycle traverses areas of the state space characterised by varying signalling behaviour. A signal is produced when the s -bot enters the “environment-driven” area, and it is stopped when the s -bot exits from the “signal-driven” area. Notice that entering in the signal-driven area having $s = 0$ does not lead to the production of a signal, while entering with $s = 1$ maintains the previous signalling status.

In order to describe the individual behaviour, notice that the limit cycle attractor jumps between the planes characterised by $s = 0$ and $s = 1$. In other words, the system switches between two different dynamics. The vector fields for these two conditions determine the quality of the individual oscillations, as shown in the bottom plots of Figure 2. When $s = 0$, the robot follows the left vector field, moving straight until it enters in the environment-driven signalling area. At this point, the production of a signal corresponds to a switch to the dynamics described by the right vector field, which presents a limit cycle attractor displayed by a dotted line. It is possible to notice how the normal limit cycle approaches this attractor when $s = 1$ (see the grey segments of the limit cycle in Figure 3). However, before converging onto this attractor, the limit cycle enters the

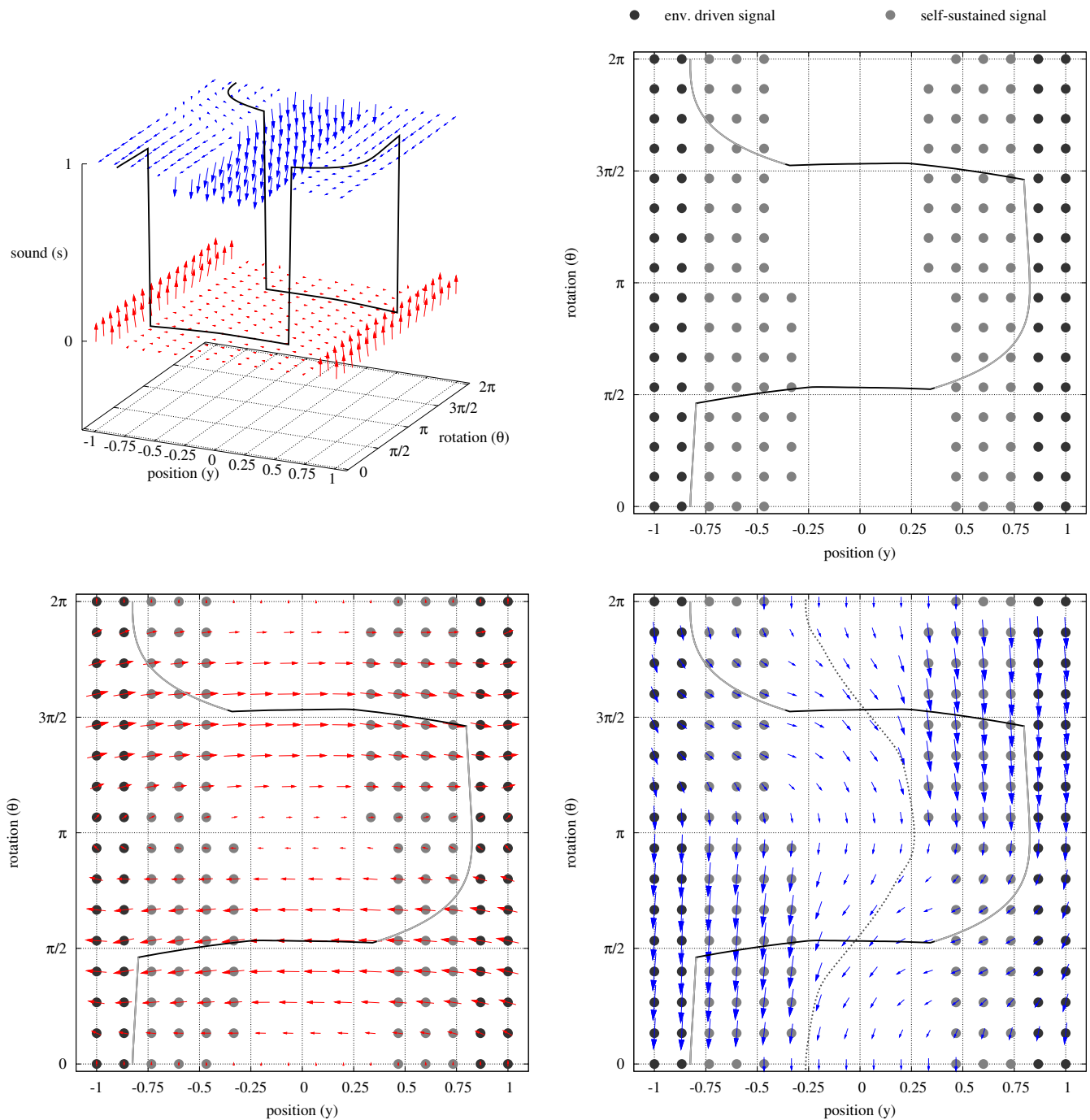


Fig. 2. Individual behaviour produced by controller c_8 . Top-Left: 3D vector field showing for each point in the state space the direction of variation and its magnitude. The θ dimensions is characterised by 2π -periodic boundary conditions. The continuous line represents the limit cycle attractor. Top-Right: signalling behaviour of the controller for each position and orientation (see text for details). The continuous line represents a projection of the limit cycle on the $y\theta$ plane: a black line colour indicates that the trajectory belongs to the plane $s = 0$, while the grey colour corresponds to the portion of trajectory that belongs to the plane $s = 1$. Bottom-Left/Right: projection on the $y\theta$ plane of the vector fields for a perceived signal $s = 0$ and $s = 1$. The dotted line in the bottom-right vector field represents the limit cycle for a constant perceived signal forced to 1, despite the individual behaviour.

“no signalling” area, and therefore the s -bot switches back to movements dictated by the vector field for $s = 0$.

Once decoded the individual behaviour, we analyse the system (3) with $R = 2$ robots. In this case, the dimensionality of the system does not allow an easy visualisation of the trajectories. However, we observed that the s -bots’ movements are governed solely by the individual behaviour \mathcal{B}_c and by

the coupling rule (2), which states that a signal is perceived whenever some s -bot emits a signal. As a consequence, it is possible to describe the behaviour of synchronising s -bots by looking at how the individual movements change with respect to incoming signals. Figure 3 presents various plots that represent different phases of the synchronisation. In the upper part, the position y for the two robots is plotted

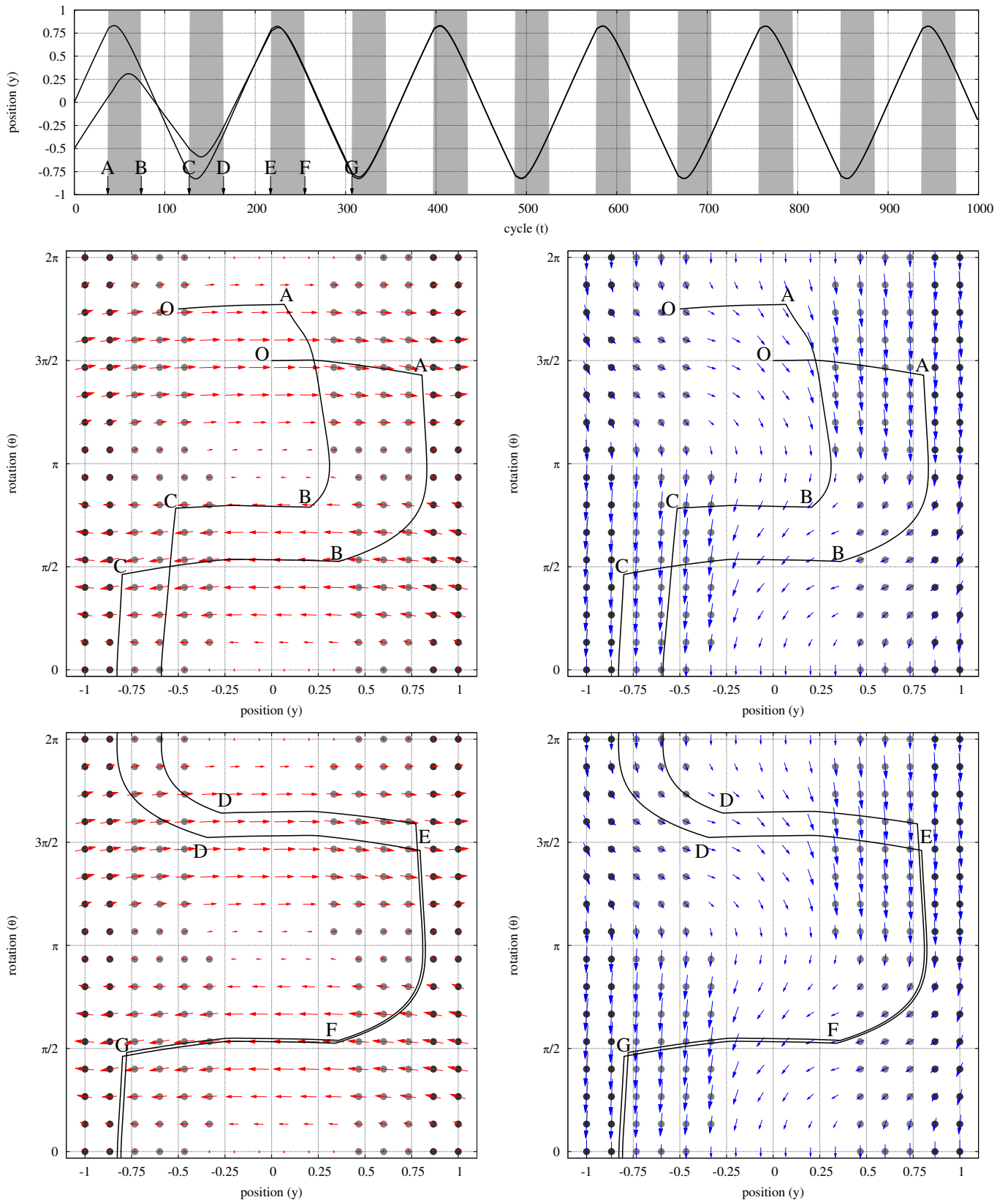


Fig. 3. Synchronisation behaviour of controller c_8 . Top: the position y of two s -bots that synchronise is plotted through time. The gray band in the background indicate that a signal is being perceived. Centre and bottom: vector fields for the condition $s = 0$ (left) and $s = 1$ (right). For each point, the individual signalling behaviour is displayed as a dot with varying grey level (see also Figure 2). The trajectories of the two synchronising robots are shown, and relevant events are marked with capital letters. The same letters indicate the time of the corresponding events in the top graph.

with respect to time. It is possible to observe that after an initial transitory phase, the robots converge towards coordinated movements. In particular, the position y is “modulated” through communicative interactions: the robot that signals first influences the behaviour of the other robot, which anticipates the turnabout in response to the perceived signal (see the gray bands in the background that indicate a continuous perceived signal). A better idea on how synchronisation is achieved is given by plotting the trajectories of the two robots over the vector fields for $s = 0$ and $s = 1$ (see the central and bottom plots of Figure 3). The two s -bots start in the points indicated by ‘O’, and none of them is signalling. As a consequence, the s -bots follow the top-left vector field, until they reach the point indicated by an ‘A’. Here, one of the robot enters the environment-driven signalling area, and therefore emits a signal, that triggers a behavioural change in both robots. The robots now follow the top-right vector field and both perform a clockwise turn, as indicated by the arrows. However, this turn is not performed at the same speed by the two robots: the one at larger y moves faster than the other, as indicated by the size of the arrows of the vector field. Consequently, the difference in distance among the two robots is consistently reduced in this phase, which ends with the robots reaching the points indicated with ‘B’. In the interval from points ‘B’ to points ‘C’ no robot is signalling and no interaction is present. The same interaction characterises the phases between points ‘C’ and ‘D’ and between ‘E’ and ‘F’, until synchronisation is achieved. This synchronisation mechanism is therefore based on the modulation of the position y during the oscillation: the first robot that reaches the environment-driven signalling area triggers a U-turn in the other robot, which is however performed at a lower speed, allowing the trajectories to approach and eventually converge into synchronous oscillations.

VI. SCALABILITY ANALYSIS

The analysis of the synchronisation behaviour for two s -bots is accompanied by a scalability analysis in which we test all evolved behaviours with groups of 3, 6, 12, 24, 48 and 96 s -bots. We first test the evolved behaviour in simulation, and we found that physical interactions may prevent the system from scaling to very large number of robots (data not shown). In fact, physical interactions occur with a higher probability per time step as the group size increases. Every collision avoidance provokes a temporary de-synchronisation of at least two robots, which have to adjust their movements in order to re-gain synchronous oscillations with other robots. As a consequence, the performance of the group as a whole is negatively affected. Still, the evolved synchronisation mechanism may scale well if there are no physical interactions. To prove so, we performed a further scalability analysis by ignoring collisions among robots (see Figure 4). We found that many controllers present perfect scalability, with only a slight decrease in performance due to the longer time required by larger groups to perfectly synchronise. However, other controllers present poor performance for large groups. By observing the actual behaviour produced by these controllers, we realised that the absence of scalability is caused by a

communicative interference problem: the signals emitted by different s -bots overlap in time and are perceived as a constant signal (recall that the sound signals are global and that they are perceived in a binary way, preventing an s -bot from recognising different signal sources). If the perceived signal does not vary in time, it does not bring enough information to be exploited for synchronisation. This problem is the result of the fact that we used a “global” communication form in which the signal emitted by an s -bot is perceived by any other s -bot everywhere in the arena. Moreover, from the perception point of view, there is no difference between a single s -bot and a thousand signalling at the same time. The lack of locality and of additivity is the main cause of failure for the scalability of the evolved synchronisation mechanisms. However, as we have seen, this problem affects only some of the analysed controllers. In the remaining ones, the evolved communication strategies present an optimal scalability that is only weakly influenced by the group size.

Is it possible to predict whether a given evolved behaviour will scale or not with increasing group size? We try to give an answer by exploiting the mathematical model introduced in Section IV. We start from the observation that, if a synchronisation mechanism does not scale with the group size R , there exist an alternative attractor to the synchronous one, in which robots move incoherently. In other words, the dynamical system (3) undergoes a bifurcation with varying parameter R , so that two attractors are observable for large R : the coherent, synchronous one, and the incoherent one. In order to predict from the individual behaviour whether such a bifurcation exists, it is necessary to understand which are the conditions for the existence of an incoherent attractor. Recall that, whenever an evolved synchronisation mechanism does not scale, the perceived signal does not vary in time. In such a situation, in fact, the s -bots do not receive information about the position and orientation of other robots. If an s -bot r perceives a constant signal, its behaviour can be predicted as follows:

$$\langle y_r, \theta_r, S_r \rangle|_{t+1} = \mathcal{B}_c(y_r, \theta_r, f(s))|_t, \quad (4)$$

where $f(s)|_t$ indicates the constant perceived signal. It is therefore possible to plot the vector field for the above behaviour, and analyse possible attractors—be they fixed points or limit cycles—towards which all trajectories of the s -bot converge. We claim that, if such attractors exist and if they entirely lay out of the portion of state space in which $S_r(y_r, \theta_r, f(s))|_{t+1} = f(s)|_{t+1}$ —which we refer to as the *non-interaction area*—then the evolved synchronisation mechanism is scalable, no matter the group size R .

To prove the above claim, simply observe that the incoherent attractor exists contextually to a perceived signal that does not vary in time. Given that the s -bots themselves are responsible for signal production, the existence of the incoherent attractor requires that all s -bots participate in the signal production, so that:

$$\forall t \exists r \in \{1, \dots, R\} : S_r(y_r, \theta_r, f(s))|_{t+1} = f(s)|_{t+1}. \quad (5)$$

However, this requires that the attractor for the system (4) is contained at least partially within the *non-interaction area*,

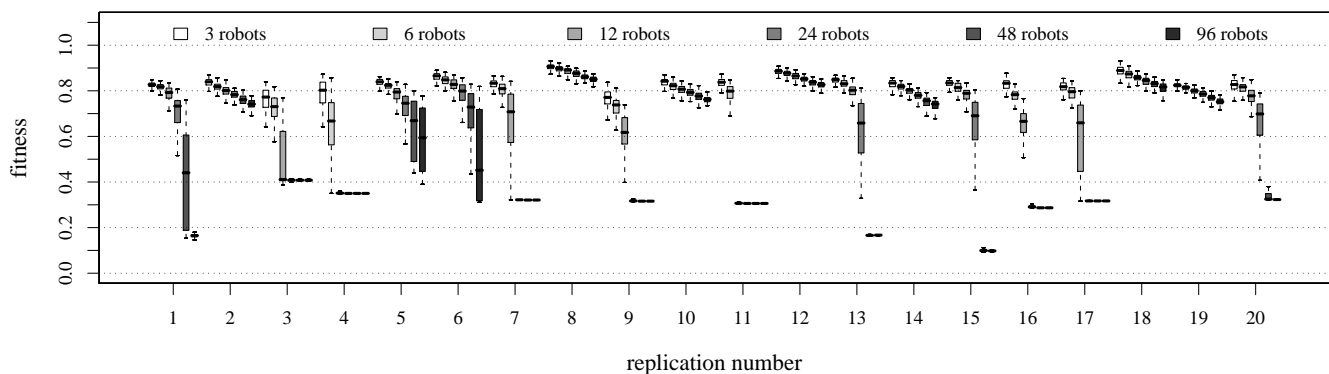


Fig. 4. Scalability of the synchronisation mechanism. The boxplot shows, for each evolved controller, the performance obtained in tests with 3, 6, 12, 24, 48, and 96 *s-bots*. Each box represents the inter-quartile range of the data, while the black horizontal line inside the box marks the median value. The whiskers extend to the most extreme data points within 1.5 times the inter-quartile range from the box. Outliers are not shown.

which contradicts our hypothesis.

The controller c_8 analysed in Section V produces a scalable behaviour, as shown in Figure 4. In fact, it presents a limit cycle attractor shown as a dotted line in the bottom-right vector field of Figure 2, which is completely contained within the no-signalling area. On the contrary, controller c_{13} does not present scalability (see Figure 4). The evolved behaviour can be appreciated and analysed with the 3D vector field of Figure 5 that shows the individual behaviour under normal conditions. The right vector field in Figure 5 corresponds to the behaviour of the *s-bot* when a continuous signal $s = 1$ is constantly perceived. It is possible to notice that the limit cycle attractor for this condition traverses the environment-driven signalling area. As a consequence, with a sufficiently large number of *s-bots* the evolved synchronisation mechanism does not scale, as can be appreciated in Figure 4.

A further prediction from the mathematical model consists in the minimum group size R_m for which the incoherent attractor exists (i.e., the bifurcation point). This group size depends on the time each robot spends in the *non-interaction area* while moving over the limit cycle. In fact, in order to satisfy condition (5), it is necessary that while a robot moves within the *non-interaction area*, another robot prepares to enter in it. In other words, R_m robots should be evenly spaced over the limit cycle so that, when one *s-bot* exits the *non-interaction area*, another one enters in it, therefore sustaining the production of the constant signal. As a consequence, the minimum group size R_m is given by:

$$R_m = \left\lceil \frac{T}{T_n} \right\rceil, \quad (6)$$

where T is the period of a single oscillations, and T_n is the fraction of this period spent within the *non-interaction area*. For controller c_{13} , we experimentally obtained $R_m = 6$, which is to be considered a theoretical lower bound for the minimum group size. We actually observed the appearance of the incoherent attractor for a minimum group size of 9 (data not shown).

VII. CONCLUSION

Much as natural evolution produced swarms of fireflies able to self-organise to achieve coherent group behaviour, artificial evolution can synthesise self-organising swarms of robots that accomplish complex tasks. In this respect, swarm intelligence can benefit from the study and analysis of natural as well as artificial systems: in both cases, a deep understanding of the dynamics that govern the individual behaviour and the social interactions can underpin novel developments in the engineering of swarm intelligent systems. In this paper, we have presented an artificial evolutionary process that has shaped the behaviour of a robotic system to display self-organised synchronisation. We have also shown how the dynamical system analysis can explain the evolved mechanisms and predict the behaviour of the robotic system for varying group size. We believe that this analysis can bring useful insights on how to build—through automatic techniques or hand-design—swarm robotics systems that are capable of self-organised synchronisation and that scale to large number of robots. In fact, we have given a clear description of the building blocks necessary to produce synchronised behaviours, and, most importantly, we have decoded the individual behaviour to find the conditions that allow the system as a whole to synchronise, no matter the group size. In conclusion, we believe that studies about synchronisation such as the one presented in this paper, notwithstanding the explicitly simplified experimental setup, can have a strong impact on future studies in swarm robotics.

REFERENCES

- [1] S. H. Strogatz, *Sync: The Emerging Science of Spontaneous Order*. Hyperion Press, New York, NY, 2003.
- [2] A. Pikovsky, M. Rosenblum, and J. Kurths, *Synchronization: A Universal Concept in Nonlinear Sciences*. Cambridge University Press, Cambridge, UK, 2001.
- [3] Y. Kuramoto, "Phase dynamics of weakly unstable periodic structures," *Progress of Theoretical Physics*, vol. 71, no. 6, pp. 1182–1196, 1984.
- [4] S. H. Strogatz, "From kuramoto to crawford: exploring the onset of synchronization in populations of coupled oscillators," *Physica D: Nonlinear Phenomena*, vol. 143, no. 14, pp. 1–20, 2000.
- [5] J. Buck and E. Buck, "Mechanism of rhythmic synchronous flashing of fireflies," *Science*, vol. 159, no. 3821, pp. 1319–1327, 1968.
- [6] R. E. Mirollo and S. H. Strogatz, "Synchronization of pulse-coupled biological oscillators," *SIAM Journal on Applied Mathematics*, vol. 50, no. 6, pp. 1645–1662, 1990.

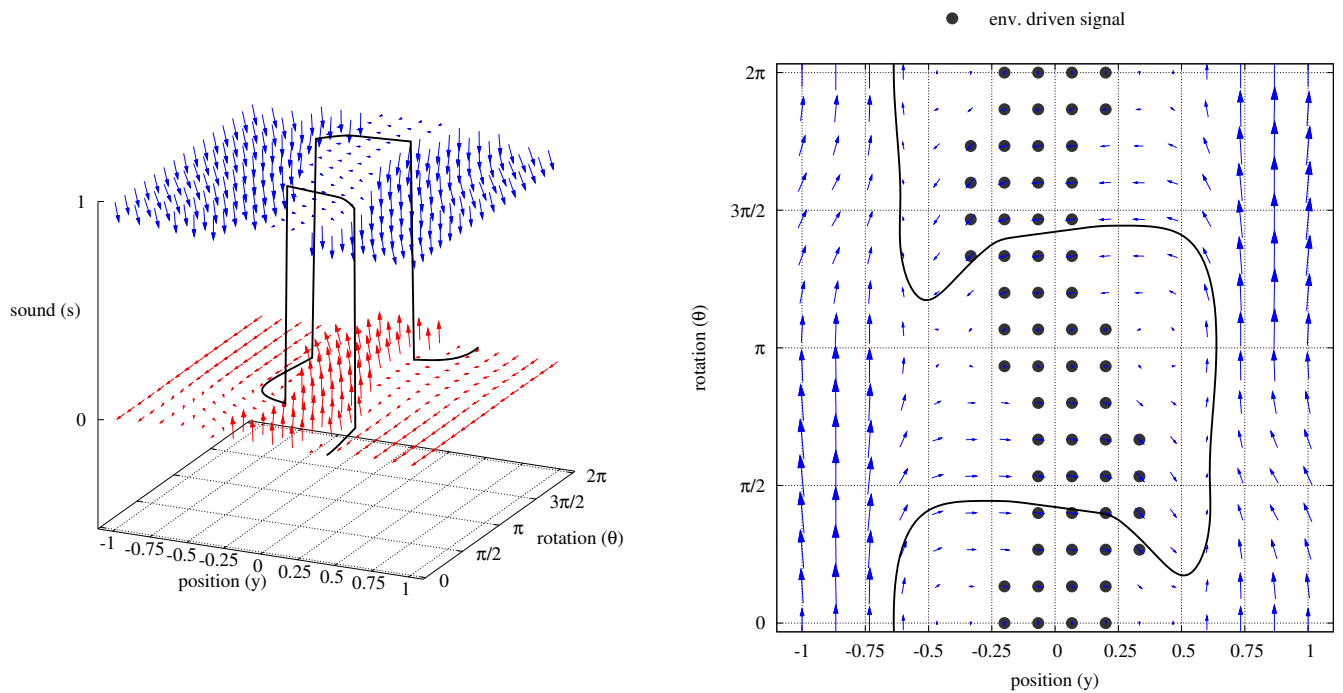


Fig. 5. Individual behaviour of controller c_{13} . Left: the 3D vector field shows for each point in the state space the direction of variation and its magnitude. Right: projection on the $y\theta$ plane of the vector field for a constant perceived signal $s = 1$. The black line represent the limit cycle for this condition. The black dots represent the *non-interaction area*.

- [7] S. H. Strogatz and I. Stewart, "Coupled oscillators and biological synchronization," *Scientific American*, vol. 269, no. 6, pp. 102–109, 1993.
- [8] M. Dorigo and E. Şahin, "Swarm robotics — special issue editorial," *Autonomous Robots*, vol. 17, no. 2–3, pp. 111–113, 2004.
- [9] O. Holland and C. Melhuish, "An interactive method for controlling group size in multiple mobile robot systems," in *Proceedings of the 8th International Conference on Advanced Robotics (ICAR '97)*. IEEE Press, Piscataway, NJ, 1997, pp. 201–206.
- [10] C. Melhuish, O. Holland, and S. Hoddell, "Convoying: using choring to form travelling groups of minimal agents," *Robotics and Autonomous Systems*, vol. 28, pp. 207–216, 1999.
- [11] S. Wischmann, M. Huelse, J. F. Knabe, and F. Pasemann, "Synchronization of internal neural rhythms in multi-robotic systems," *Adaptive Behavior*, vol. 14, no. 2, pp. 117–127, 2006.
- [12] M. Hartbauer and H. Römer, "A novel distributed swarm control strategy based on coupled signal oscillators," *Bioinspiration and Biomimetics*, vol. 2, pp. 42–56, 2007.
- [13] S. Wischmann and F. Pasemann, "The emergence of communication by evolving dynamical systems," in *From animals to animats 9: Proceedings of the Ninth International Conference on Simulation of Adaptive Behaviour*, ser. LNAI, S. N. et al., Ed., vol. 4095. Springer Verlag, Berlin, Germany, 2006, pp. 777–788.
- [14] S. Nolfi and D. Floreano, *Evolutionary Robotics: The Biology, Intelligence, and Technology of Self-Organizing Machines*. MIT Press/Bradford Books, Cambridge, MA, 2000.
- [15] I. Harvey, E. A. Di Paolo, R. Wood, M. Quinn, and E. Tuci, "Evolutionary robotics: A new scientific tool for studying cognition," *Artificial Life*, vol. 11, no. 1–2, pp. 79–98, 2005.
- [16] S. H. Strogatz, *Nonlinear Dynamics and Chaos: With Applications to Physics, Biology, Chemistry, and Engineering*. Westview Press, Cambridge, MA, 1994.
- [17] F. Mondada, G. C. Pettinaro, A. Guignard, I. V. Kwee, D. Floreano, J.-L. Deneubourg, S. Nolfi, L. M. Gambardella, and M. Dorigo, "SWARM-BOT: A new distributed robotic concept," *Autonomous Robots*, vol. 17, no. 2–3, pp. 193–221, 2004.

isti



Dr. Vito Trianni received the Laurea (Master of Technology) degree in computer science engineering from Politecnico di Milano, Milan, Italy, in 2000, the Master in Information Technology from the ICT Center of Excellence For Research, Innovation, Education and Industrial Labs Partnership (CEFRIEL), Milan, Italy, in 2001, and the Diplôme d'Études Approfondies and the Ph.D. in Applied Sciences from the Université Libre de Bruxelles, Brussels, Belgium, in 2003 and in 2006, respectively. Currently, he is a Research Fellow at the Laboratory of Autonomous Robotics and Artificial Life, Institute of Cognitive Sciences and Technologies of the Italian National Research Council (LARAL-ISTC-CNR) in Rome, Italy. His research interests span over the field of evolutionary robotics, swarm intelligence, and self-organisation.



Dr. Stefano Nolfi is a research director at the Institute of Cognitive Sciences and Technologies of the Italian National Research Council (ISTC-CNR), where he heads the Laboratory of Autonomous Robotics and Artificial Life (LARAL). He is also coordinator of the RTD European Integrated Project ECAGents: Embodied and Communicating Agents. His research interests are in the field of neuro-ethological studies of adaptive behaviour in natural and artificial agents and include: evolutionary robotics, artificial life, complex systems, neural networks, and genetic algorithms. He is the author of the book S. Nolfi and D. Floreano, *Evolutionary Robotics: The Biology, Intelligence, and Technology of Self-Organizing Machines* (MIT Press/Bradford Books, 2000) and of more than 100 peer-reviewed articles.

Adaptive frequency oscillators and applications

Ludovic Righetti*, Jonas Buchli† and Auke Jan Ijspeert*

*School of Communication and Computer Science
Ecole Polytechnique Fédérale de Lausanne
Lausanne, CH-1015 Switzerland
email: ludovic.righetti@epfl.ch, auke.ijspeert@epfl.ch

†Computational Learning and Motor Control Lab
University of Southern California
Los Angeles, CA 90089, USA
email: jonas@buchli.org

Abstract—In this contribution we present a generic mechanism to transform an oscillator into an adaptive frequency oscillator, which can then dynamically adapt its parameters to learn the frequency of any periodic driving signal. Adaptation is done in a dynamic way: it is part of the dynamical system and not an offline process. This mechanism goes beyond entrainment since it works for any initial frequencies and the learned frequency stays encoded in the system even if the driving signal disappears. Interestingly, this mechanism can easily be applied to a large class of oscillators from harmonic oscillators to relaxation types and strange attractors. Several practical applications of this mechanism are then presented, ranging from adaptive control of compliant robots to frequency analysis of signals and construction of limit cycles of arbitrary shape.

I. INTRODUCTION

Nonlinear oscillators are very important modeling tools in biological and physical sciences and these models have gained a particular attention in engineering fields over the last decades. These models are interesting because of their synchronization capabilities with other oscillators or with external driving signals. However their synchronization capabilities are limited and it is not always an easy task to correctly choose their parameters to ensure proper synchronization with external driving signals. Indeed, an oscillator has a finite entrainment region that depends on many parameters, such as coupling strength and frequency difference between the oscillator and the driving signal.

Some recent work, however, showed that it is possible to modify oscillators such that they can overcome these

synchronization limitations, by adding some dynamics to the parameters of the oscillator such that it can learn the frequency of an input signal. But these attempts are often limited to simple classes of oscillators, equivalent to phase oscillators [1], [2] or to simple classes of driving signal (pulses) [3].

Recently we designed a learning mechanism for oscillators which adapts their frequency to the frequency of any periodic input signal [4], [5]. The parameter with the strongest influence on the frequency of the oscillator is turned into a new state variable of the system. Interestingly this mechanism appears to be generic enough to be applied to many different types of oscillators, from phase oscillators to relaxation types, and to strange attractors. The frequency adaptation process goes beyond mere entrainment because if the input signal disappears, the learned frequency stays encoded in the oscillator. Moreover, it is independent of the initial conditions, thus working beyond entrainment basins (i.e. it has an infinite basin of attraction). We called this adaptation mechanism *dynamic Hebbian learning* because it shares similarities with correlation-based learning observed in neural networks [6].

In this contribution, we present this generic adaptation mechanism. Then we show several applications, ranging from adaptive control for legged robots with passive dynamics [4], [7], where the adaptive oscillators find the resonant frequency of the robot to frequency analysis with systems of coupled adaptive oscillators [8] and construction of limit cycles with arbitrary shape [9].

II. ADAPTIVE FREQUENCY OSCILLATORS

A. A generic rule for frequency adaptation

We consider general equations for an oscillator perturbed by a periodic driving signal

$$\begin{aligned}\dot{x} &= f_x(x, y, \omega) + KF(t) \\ \dot{y} &= f_y(x, y, \omega)\end{aligned}$$

where f_x and f_y are functions of the state variables that produce a structurally stable limit cycle and of a parameter ω that has a monotonic relation with the frequency of the oscillator when unperturbed, $K = 0$ (we do not require this relation to be linear). $F(t)$ is a time periodic perturbation and $K > 0$ the coupling strength.

In order to make the oscillator learn the frequency of $F(t)$, we transform the ω parameter into a new state variable, that will have its own dynamics. The generic rule that allows us to transform this oscillator into an adaptive frequency one is as follows

$$\dot{\omega} = \pm KF(t) \frac{y}{\sqrt{x^2 + y^2}}$$

where the sign depends on the direction of rotation of the limit cycle in the (x, y) plane.

B. Properties of the adaptation mechanism

We proved in [5] that the adaptation mechanisms made the frequency converge to the frequency of any periodic input signal for phase and Hopf oscillators. In the case of several frequencies in the spectrum of $F(t)$, the frequency converges to one of the frequency component, depending on the initial frequency of the oscillator.

Moreover, the higher the coupling strength K is, the faster the convergence. It can be shown that for suitable coupling strength, the convergence is exponential (of order e^{-t}). Examples of frequency adaptation for the Hopf oscillator, with several different inputs is shown in Figure 1. The corresponding equations for the adaptive Hopf oscillator are

$$\begin{aligned}\dot{x} &= (\mu - x^2 - y^2)x - \omega y + KF(t) \\ \dot{y} &= (\mu - x^2 - y^2)y + \omega x \\ \dot{\omega} &= -KF(t) \frac{y}{\sqrt{x^2 + y^2}}\end{aligned}$$

We can notice in Figure 1(d) that the adaptation mechanism works also for time-varying signals (i.e. with a time-varying frequencies). This tracking is however

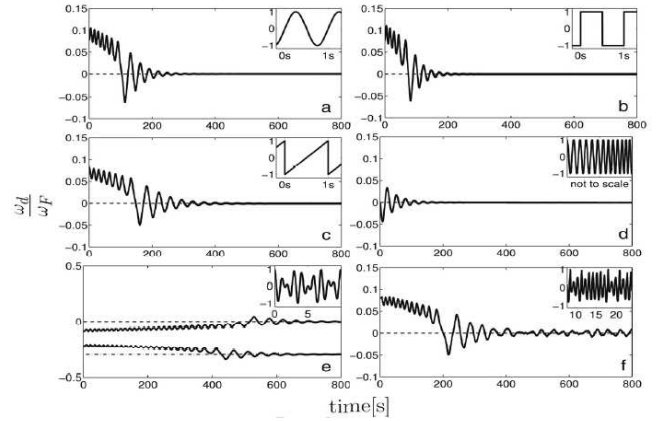


Fig. 1. (a) Typical convergence of an adaptive frequency Hopf oscillator driven by a harmonic signal ($F(t) = \sin(2\pi t)$). The frequencies converge towards the frequency of the input (indicated in dashed line). After convergence the frequency oscillates with a small amplitude around the frequency of the input. In all figures, we plot in the main graph the time evolution of the difference between ω and the input frequency, normalized by the input frequency. The top right panel shows the driving signals (note the different scales). (b) Square pulse $I(t) = \text{rect}(\omega_F t)$, (c) Sawtooth, $I(t) = \text{st}(\omega_F t)$, (d) Chirp $I(t) = \cos(\omega_c t)$, where $\omega_c = \omega_F(1 + \frac{1}{2}(\frac{t}{1000})^2)$. (Note that the graph of the input signal is illustrative only since changes in frequency takes much longer than illustrated). (e) Signal with two non-commensurate frequencies $I(t) = \frac{1}{2}[\cos(\omega_F t) + \cos(\frac{\sqrt{2}}{2}\omega_F t)]$, i.e. a representative example how the system can evolve to different frequency components of the driving signal depending on the initial condition $\omega_d(0) = \omega(0) - \omega_F$. (f) $I(t)$ is the non-periodic output of the Rössler system. The Rössler signal has a $1/f$ broad-band spectrum, yet it has a clear maximum in the frequency spectrum. In order to assess the convergence we use $\omega_F = 2\pi f_{\max}$, where f_{\max} is found numerically by FFT. The oscillator converges to this frequency.

limited by the exponential convergence rate of the adaptation mechanism. Further examples of such tracking and limitations can be found in [8] for pools of oscillators.

Moreover, extensive numerical simulations show that this adaptation mechanism works also for many different types of non-harmonic oscillators. Some examples are shown in Figure 2, with an adaptive Rayleigh oscillator, an adaptive Fitzhugh-Nagumo one and a Rössler system in chaotic mode. For the first two oscillators there is no linear relation between ω and the frequency of oscillations but the adaptive mechanism is able to find a suitable value for ω such that the frequency of the oscillator is the same as the frequency of the input signal. For the Rössler system, the frequency of the system is not well defined since the system is not periodic, but we can define a pseudo-frequency and the system can adapt it to the frequency of a periodic input.

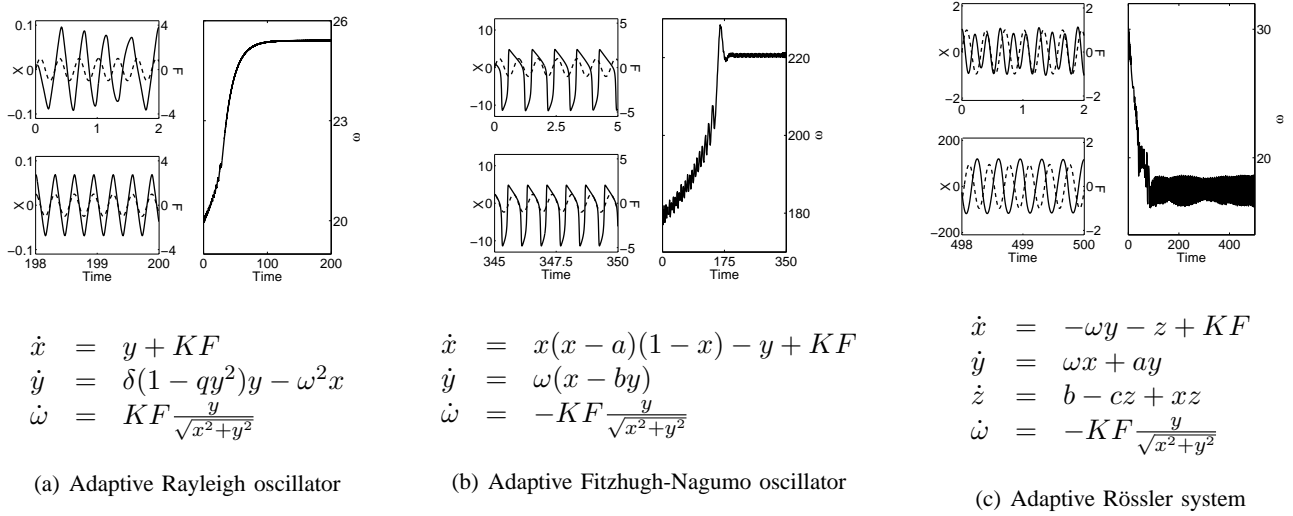


Fig. 2. For each oscillator, ω corresponds to the adaptive parameter. Each figure is composed of 3 plots. The right one shows the evolution of ω . The left ones are plots of the oscillations (the x variable) and of the input signal F (dashed line), before (upper figure) and after (lower figure) adaptation.

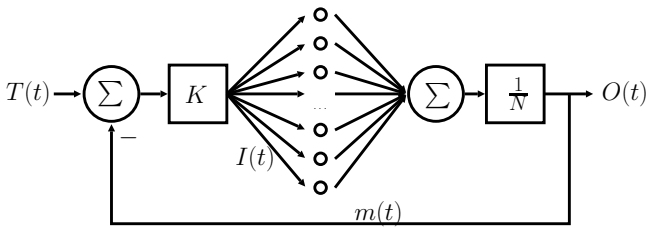


Fig. 3. Structure of the pool of adaptive frequency oscillators that is able to reproduce a given teaching signal $T(t)$. The mean field produced by the oscillators is fed back negatively on the oscillators.

III. APPLICATIONS

We now present several applications for the adaptation mechanism, ranging from robot control to frequency analysis and automatic construction of limit cycles of arbitrary shape.

A. Robot with passive dynamics

The adaptation mechanism can be used to find the resonant frequencies of legged robots with passive elements (i.e. springs) [4], [7], [10]. The developed controller, based on adaptive frequency oscillators, can tune itself to the resonant frequency of the robot via a simple feedback loop from sensors on the robot (e.g. position or inertial sensors). The locomotion thus becomes very efficient by exploiting the intrinsic dynamics of the robot. Another advantage of this type of control is that one does not need to tune the controller to specific robot and the controller can track any change in this frequency automatically, for example if this frequency change due to mass or spring

stiffness changes or to a gait transition (if the robot is stepping on 2 feet or 4 feet, its resonant frequency changes).

B. Frequency analysis

Another application is the use of a pool of adaptive frequency Hopf oscillators to perform frequency analysis of an input signal [8]. The oscillators are coupled via a negative mean field with the input signal to analyze as is shown in Figure 3. The oscillators converge to the frequencies present in the spectrum of the teaching signal and due to the negative feedback, each time an oscillator finds a correct frequency, this one loses its amplitude. Thus, the other oscillators only *feel* the remaining frequencies to learn.

This pool of oscillators is able to approximate the frequency spectrum of any signal. This works for signals with discrete spectra, but also for continuous spectra and time-varying spectra. The spectrum is approximated by the distribution of the frequencies of the oscillators and thus, the resolution of the approximation can be made arbitrary good by increasing the number of oscillators present in the pool.

Figure 4 shows how the system can approximate the spectrum of a broad-band chaotic signal from the Rössler system. As can be seen, the important features of the spectrum are caught by the system, especially the broad spectrum and the major peaks of frequency.

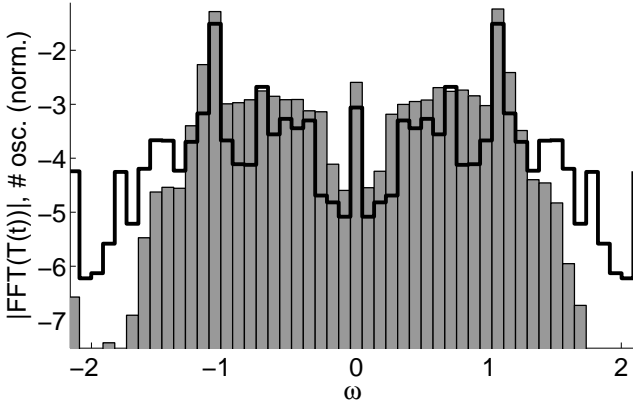


Fig. 4. FFT of the Rössler signal (black line) in comparison with the distribution of the frequencies of the oscillators (gray bars normalized to the number of oscillators, $N = 10000$). The spectrum of the signal has been discretized into the same bins as the statistics of the oscillators in order to allow for a good comparison with the results from the full-scale simulation.

C. Construction of limit cycles with arbitrary shape

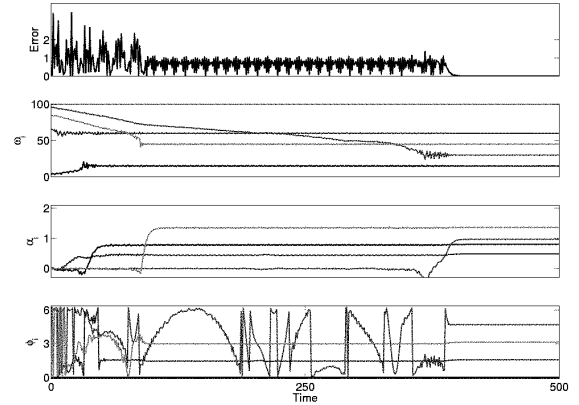
The previous pool of oscillators can be extended by adding a weight to each oscillator in the mean field sum and coupling between the oscillators to ensure stability of the constructed pattern. Then an oscillator will be able to fully match the energetic content of a frequency in the spectrum of the teaching signal. Moreover the coupling will ensure that the system exhibits a stable limit cycle. The amplitudes and phase differences become also state variables of the system as for the frequencies. The governing differential equations of the system are then

$$\begin{aligned}\dot{x}_i &= (\mu - r_i^2)x_i - \omega_i y_i + KF(t) + \tau \sin(\theta_i - \phi_i) \\ \dot{y}_i &= (\mu - r_i^2)y_i + \omega_i x_i \\ \dot{\omega}_i &= -KF(t) \frac{y_i}{r_i} \\ \dot{\alpha}_i &= \eta x_i F(t) \\ \dot{\phi}_i &= \sin\left(\frac{\omega_i}{\omega_0} \theta_0 - \theta_i - \phi_i\right)\end{aligned}$$

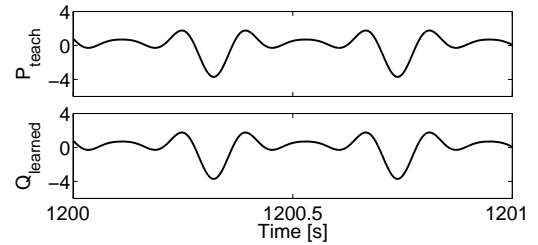
with

$$\begin{aligned}\theta_i &= \text{sgn}(x_i) \cos^{-1}\left(-\frac{y_i}{r_i}\right) \\ F(t) &= P_{\text{teach}}(t) - Q_{\text{learned}}(t) \\ Q_{\text{learned}}(t) &= \sum_{i=0}^N \alpha_i x_i\end{aligned}$$

where τ , K and η are positive constants. The output of the system, Q_{learned} , is the weighted sum of the outputs of each oscillator. $F(t)$ represents the negative feedback, which in average is the remaining of the teaching signal



(a) Evolution of the state variables of the system



(b) Result of learning

Fig. 5. Construction of a limit cycle by learning an input signal ($P_{\text{teach}} = 0.8 \sin(15t) + \cos(30t) - 1.4 \sin(45t) - 0.5 \cos(60t)$). Figure 5(a) shows the evolution of the state variables of the system during learning. The upper graph is a plot of the error ($\|P_{\text{teach}} - Q_{\text{learned}}\|$). The 3 other graphs show the evolution of the frequencies, ω_i , the amplitudes, α_i and the phases, ϕ_i . We clearly see that the system can learn perfectly the teaching signal, the frequencies, amplitudes and phase differences converge to the correct values and the error become zero. Figure 5(b) shows the result of learning (teaching signal in upper graph, output of the system in lower one), we notice the perfect reconstruction of the signal.

$P_{\text{teach}}(t)$ the network still has to learn. α_i represents the amplitude associated to the frequency ω_i of oscillator i . Its equation of evolution maximizes the correlation between x_i and $F(t)$, which means that α_i will increase only if ω_i has converged to a frequency component of $F(t)$ (the correlation will be positive in average) and will stop increasing when the frequency component ω_i will disappear from $F(t)$ because of the negative feedback loop. ϕ_i is the phase difference between oscillator i and 0. It converges to the phase difference between the instantaneous phase of oscillator 0, θ_0 , scaled at frequency ω_i and the instantaneous phase of oscillator i , θ_i . Each adaptive oscillator is coupled with oscillator 0, with strength τ to keep correct phase relationships between oscillators.

Figure 5 shows an example of convergence of the network of oscillators with amplitudes and coupling together with the resulting learned signal. We see that the frequencies first converge to the different frequency components present in the signal, the amplitudes increase when the associated frequency matches one frequency of the input signal. At the end, the phase differences stabilize and we see that the error is zero, which means that the system perfectly reconstructed the teaching signal. Moreover, it is now encoded into a structurally stable limit cycle and it is easy to smoothly modulate its frequency and amplitude by changing $\vec{\omega}$ and $\vec{\alpha}$. These properties can be very useful, together with sensory feedback, for robotics control (see for example [9]). This system can be viewed as a dynamic Fourier series decomposition where there is not need of explicit definition of a time window or any preprocessing of the signal to analyze.

IV. CONCLUSION

In this contribution we presented a generic mechanism to build adaptive frequency oscillators from a given existing oscillator. We showed that it could be applied to many different types of oscillators, that the system was able to learn the frequencies of any periodic input signal. Interestingly there is no need to preprocess the signal and no external optimization procedures are needed to get the correct frequency. All the learning is embedded into the dynamics of the adaptive oscillators. Moreover it goes further than entrainment, since the learned frequency is kept into the system even if the external drive disappears and the basin of attraction is infinite (the system can start from any initial frequency). Finally we discussed some applications of this mechanism, ranging from adaptive control for compliant robots, to frequency analysis and construction of limit cycles of arbitrary shape.

ACKNOWLEDGMENT

This work was supported by the European Commission's Cognition Unit, project no. IST-2004-004370: RobotCub (L.R.) and by a grant from the Swiss National Science Foundation (L.R., J.B. and A.I.)

REFERENCES

- [1] R. Borisyuk, M. Denham, F. Hoppensteadt, Y. Kazanovich, and O. Vinogradova, "Oscillatory model of novelty detection," *Network: Computation in neural systems*, vol. 12, pp. 1–20, 2001.
- [2] J. Nishii, "A learning model for oscillatory networks," *Neural networks*, vol. 11, pp. 249–257, 1998.
- [3] E. Large and J. Kolen, "Resonance and the perception of musical meter," *Connection science*, vol. 6, pp. 177–208, 1994.

- [4] J. Buchli and A. Ijspeert, "A simple, adaptive locomotion toy-system," in *From Animals to Animals 8. Proceedings of the Eighth International Conference on the Simulation of Adaptive Behavior (SAB'04)*, S. Schaal, A. Ijspeert, A. Billard, S. Vijayakumar, J. Hallam, and J. Meyer, Eds. MIT Press, 2004, pp. 153–162.
- [5] L. Righetti, J. Buchli, and A. Ijspeert, "Dynamic hebbian learning in adaptive frequency oscillators," *Physica D*, vol. 216, no. 2, pp. 269–281, 2006. [Online]. Available: <http://dx.doi.org/10.1016/j.physd.2006.02.009>
- [6] R. Kempter, W. Gerstner, and J. van Hemmen, "Hebbian learning and spiking neurons," *Physical Review E*, vol. 59, pp. 4498–4514, 1999.
- [7] J. Buchli, F. Iida, and A. Ijspeert, "Finding resonance: Adaptive frequency oscillators for dynamic legged locomotion," in *Proceedings of the IEEE/RSJ International Conference on Intelligent Robots and Systems (IROS)*, 2006, pp. 3903–3909.
- [8] J. Buchli, L. Righetti, and A. Ijspeert, "Frequency analysis with coupled nonlinear oscillators," *Physica D*, 2008. [Online]. Available: <http://dx.doi.org/10.1016/j.physd.2008.01.014>
- [9] L. Righetti and I. A.J., "Programmable central pattern generators: an application to biped locomotion control," in *Proceedings of the 2006 IEEE International Conference on Robotics and Automation*, 2006, pp. 1585–1590.
- [10] J. Buchli, L. Righetti, and A. Ijspeert, "A dynamical systems approach to learning: a frequency-adaptive hopper robot," in *Proceedings of the VIIIth European Conference on Artificial Life ECAL 2005*, ser. Lecture Notes in Artificial Intelligence. Springer Verlag, 2005, conference, in press.



Ludovic Righetti is doing a PhD at the Biologically Inspired Robotics Group (BIRG) at the Ecole Polytechnique Fédérale de Lausanne (EPFL). He has a BS/MS in Computer Science from EPFL (March 2004). He is particularly interested in the theoretical aspects of locomotion, both in animals and legged robots, and more generally in control theory and dynamical systems.



Jonas Buchli is currently a Post-doctoral Fellow at the Computational Learning and Motor Control Lab at the University of Southern California in Los Angeles. He received a Diploma in Electrical Engineering from the ETHZ (the Swiss Federal Institute of Technology, Zürich) in 2003 and a Doctorate from the EPFL (the Swiss Federal Institute of Technology, Lausanne) in 2007. His research interests include self-organization and emergent phenomena in complex systems, the theory of nonlinear dynamical systems and information concepts. And, especially the applications of these topics to the intersecting field of engineering and biology.



Auke Ijspeert is a SNF (Swiss National Science Foundation) assistant professor at the EPFL (the Swiss Federal Institute of Technology at Lausanne), and head of the Biologically Inspired Robotics Group (BIRG). He has a BSc/MSc in Physics from the EPFL, and a PhD in artificial intelligence from the University of Edinburgh (with John Hallam and David Willshaw as advisors). He carried

out postdocs at IDSIA and EPFL (LAMI) with Jean-Daniel Nicoud and Luca Gambardella, and at the University of Southern California (USC), with Michael Arbib and Stefan Schaal. Before returning to the EPFL, he was a research assistant professor at USC, and an external collaborator at ATR (Advanced Telecommunications Research institute) in Japan. He is still affiliated as adjunct faculty to both institutes. His research interests are at the intersection between robotics, computational neuroscience, nonlinear dynamical systems, and adaptive algorithms (optimization and learning algorithms). He is interested in using numerical simulations and robots to get a better understanding of the functioning of animals (in particular their fascinating sensorimotor coordination abilities), and in using inspiration from biology to design novel types of robots and adaptive controllers. He is regularly invited to give talks on these topics. With his colleagues, he has received the Best Paper Award at ICRA2002, the Industrial Robot Highly Commended Award at CLAWAR2005, and the Best Paper Award at the IEEE-RAS Humanoids 2007 conference. He is/was the Technical Program Chair of 5 international conferences (BioADIT2004, SAB2004, AMAM2005, BioADIT2006, LATSIS2006), and has been a program committee member of over 35 conferences.

Controlling EMI with A Chaotic Peak Current-mode Boost Converter

H. Li, Z. Li and W.A. Halang
 Faculty of Electrical and
 Computer Engineering
 Fernuniversität in Hagen
 58084 Hagen, Germany
 Email: zhong.li@fernuni-hagen.de

Juan Gonzalo Barajas Ramirez
 Division de Matematicas Aplicadas y
 Sistemas Computacionales -DMASC IPICYT

Abstract—In this paper, a novel boost converter is designed where its current mode control is dependent on two reference currents and an external clock. A detailed study on its dynamics is carried out based on its corresponding current mapping function. As demonstrated in both simulations and experiments, by operating the proposed boost converter in its chaotic mode, the electromagnetic interference can be reduced and the ripples of the converter's output are greatly suppressed.

I. INTRODUCTION

The dynamics of DC-DC converters, either boost or buck converters, have been extensively studied in the last few decades. The recent observation of chaotic dynamics in these converters, have also opened a new direction of research, while its distinct effect on reducing electromagnetic interference (EMI) has widely been reported [1] - [10].

The innovative work by Deane and Hamill [1] in 1996 may be the first design that utilized chaos for the improvement of the electromagnetic compatibility (EMC) of power supplies. Their idea was later reformulated in [2] and modified by applying some other control schemes [3]. From all the reported works, it can be concluded that EMC is effectively improved by the introduction of chaos via current mode control of a power converter.

In [4], a detailed study on the parametric design of a chaotic DC-DC converter was carried out based on its periodic spectral components. Similarly, but focusing on chaos control and utilization of chaos, design improvement were suggested in [5], while a low-EMI chaotic peak current-mode controlled boost converter was experimentally reported in [6].

However, despite of the success of EMI suppression using chaos, there are two opened problems to be tackled with. As observed in the previous designs, ripples of the output current are usually much greater than those operated in periodic mode [7]. Recognizing that a DC-DC converter is mainly used as a power supply of a system, large ripples simply imply a degradation of performance. Although an explicit relationship between ripples and spectral spreading of the current has been obtained in [11], it is still a difficult task to design a suitable control in order to suppress the ripples to a desirable level.

In addition, it is found that the power of the background spectra will also be increased, although the peak values of the

power spectrum is reduced. This hence will result in a larger power consumption, becoming another major disadvantage of these designs.

It should be emphasized that these two disadvantages are also found in other chaotic power converters [8], [9], and in turns, seriously impeded their popularity. Therefore, it is the objective of this paper to address the questions of how to improve the control method for chaos-based DC-DC converters so that low EMI and small output ripples can be achieved, and to verify the relationship between the ripples and background spectrum.

The rest of the paper is organized as follows. In Sect. II, a new design of peak current-mode boost converter is proposed and its corresponding chaotic mapping function is derived. Based on the mapping function, the dynamical characteristics of the converter, including spectrum analysis, bifurcating and chaotic behaviors, are analyzed in Sect. III. Its performance in terms of EMI reduction and ripple suppression are also verified and demonstrated with simulation results in the same section. The design is then further confirmed based on the experiments described in Sect. IV. Finally, concluding remarks are given in Sect. V.

II. A NEW DESIGN OF CURRENT-MODE BOOST CONVERTER

Figure 1 depicts a new design of current mode converter, which is considered as an enhanced version of that proposed in [4]. It consists of a current-mode boost converter (see Fig. 1 (a)), and a switch control generated by a simple circuit shown in Fig. 1 (b). In the followings, its dynamics will be studied, which contributes its attractive performance on EMI and ripple suppression.

Referring to Fig. 1 (b), the switch S is now controlled by three elements, namely a clock with period T_C , a lower reference current signal I_1 and an upper one I_2 .

Depending on the value of T_C , three different cases can be categorized:

$$\text{Case I: } t_2 \geq T_C,$$

$$\text{Case II: } T_A \geq T_C > t_2, \text{ and}$$

$$\text{Case III: } T_C \geq T_A,$$

where t_1 is the rising time of $i(t)$ from I_1 to I_2 , t_2 is the falling time of $i(t)$ from I_2 to I_1 , and $T_A = t_1 + t_2$.

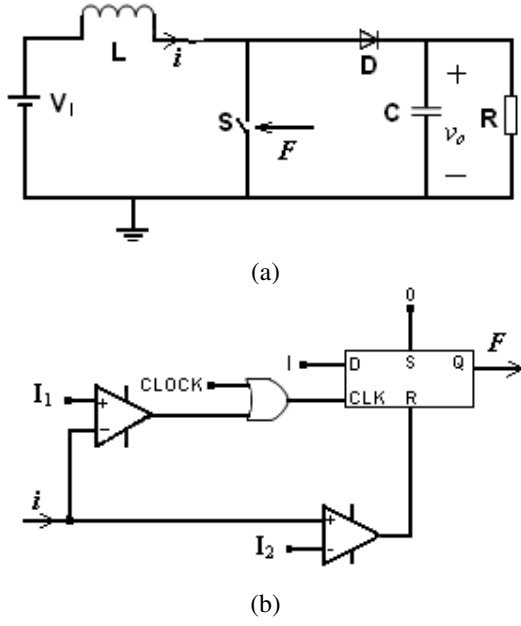


Fig. 1. (a) Current-mode boost converter (b) Switch control

For each case, the corresponding inductor current waveforms can be obtained as shown in Fig. 2.

According to Fig. 2, i_n is only sampled at the moment when S opens in Case I, however, there appears a new kind of i_n for Cases II and III which can be sampled at the some clock cycles even when S is closed.

Similar to [4], the analysis of the proposed converter is carried out based on a discrete-time mapping of $i(t)$. Let i_n be the inductor current sampled at the instants of the clock pulses as $i(t)$ is decreasing, and we will focus on the time interval when $i(t)$ changes from i_n to i_{n+1} . For clarity, a time mapping is assumed, such that $i(\tau_n) = i_n$ when $\tau_n = 0$. Referring to Fig. 2, S is closed at $\tau_n = 0$, and hence

$$\begin{cases} \frac{di}{d\tau_n} = \frac{V_I}{L}, \\ i(\tau_n) = i_n + \frac{V_I}{L}\tau_n, \end{cases} \quad (1)$$

where V_I is input voltage and L is the inductance.

Let t_n be the time required for the current from i_n to reach I_2 . Based on (1), we have

$$t_n = \frac{(I_2 - i_n)L}{V_I}. \quad (2)$$

The switch S is then opened and $i(\tau_n)$ is governed by

$$\frac{di}{d\tau_n} = \frac{(V_I - \bar{V}_O)}{L}, \quad (3)$$

where \bar{V}_O is the mean output voltage. Therefore,

$$i(\tau_n) = I_2 + \frac{V_I - \bar{V}_O}{L}(\tau_n - t_n) \quad (4)$$

until the next clock pulse arrives or $i(\tau_n) = I_1$.

The mean output voltage \bar{V}_O can then be approximated by equating the mean of the aperiodic inductor current with a

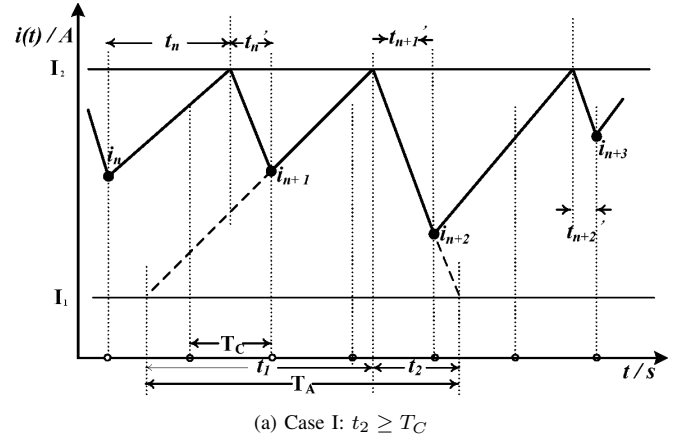
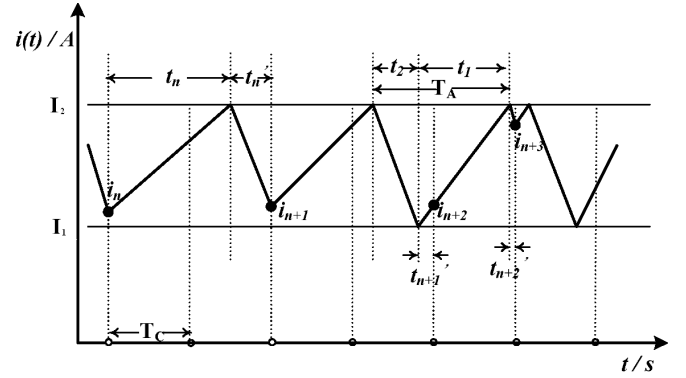
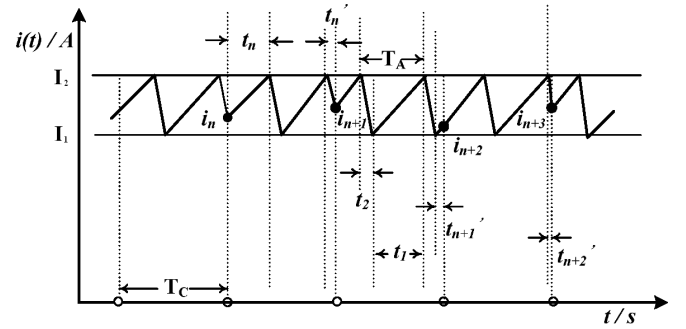

 (a) Case I: $t_2 \geq T_C$

 (b) Case II: $T_A \geq T_C > t_2$

 (c) Case III: $T_C \geq T_A$

 Fig. 2. Different current waveforms $i(t)$ obtained from the boost converter

periodic one. Therefore, one obtains the following input-output relationship:

$$\bar{V}_O^3 + \bar{V}_O \left(\frac{V_I T_p}{2L} - I_2 \right) R V_I - R \frac{T_p V_I^3}{2L} = 0. \quad (5)$$

In [4], T_p is set to be T_C . However, in our Cases II and III, T_p is also dependent on I_2 and I_1 . As shown in Fig. 2, T_p is proportional to I_2 but inversely proportional to I_1 . Therefore, T_p can be determined as:

$$T_p = \left(a \frac{I_2}{I_1} + b \right) T_C, \quad (6)$$

using first order approximation and a and b are some constants.

According to our experimental results, it is found that $a = 2.0499$ and $b = 1.5455$, while the relative errors of \bar{V}_O are well within 2%, much better than reported in [4].

Let t'_n be the time interval from the last action of S within a clock period to the next clock pulse, it can be derived that

$$t'_n = \begin{cases} \varepsilon & \text{if } \varepsilon \leq t_2, \\ \varepsilon - t_2 & \text{otherwise,} \end{cases} \quad (7)$$

where $\varepsilon = [T_C - (t_n \bmod T_C)] \bmod T_A$.

Referring to Fig. 2, one has

$$i_{n+1} = \begin{cases} I_2 + \frac{(V_I - \bar{V}_O)\varepsilon}{L} & \text{if } \varepsilon \leq t_2, \\ I_1 + \frac{V_I}{L}(\varepsilon - t_2) & \text{otherwise.} \end{cases} \quad (8)$$

Defining

$$x_n = \frac{t_n}{T_C} = \frac{(I_2 - i_n)L}{V_I T_C} \quad \text{and} \quad \alpha = \frac{\bar{V}_O}{V_I} - 1,$$

based on (8) a discrete mapping can be constructed as

$$x_{n+1} = \begin{cases} \alpha x'_n, & \text{if } x'_n \leq \gamma, \\ \rho + \gamma - x'_n, & \text{otherwise,} \end{cases} \quad (9)$$

where

$$x'_n = \beta \left\{ \left[\frac{1}{\beta} (1 - (x_n \bmod 1)) \right] \bmod 1 \right\},$$

$$\gamma = \frac{t_2}{T_C}, \quad \beta = \frac{T_A}{T_C} \quad \text{and} \quad \rho = \frac{(I_2 - I_1)L}{V_I T_C}.$$

It is remarked that, for Case I or $t_2 > T_C$, (9) becomes

$$x_{n+1} = \alpha [1 - (x_n \bmod 1)],$$

which is equivalent to the chaotic mapping obtained in [4], and hence can be considered as a special case for the proposed design.

III. CHARACTERISTICS OF THE CURRENT MAPPING FUNCTION

The characteristics of the mapping function (9) are to be studied, while their dependence on I_1 is focused. Referring to Fig. 1, it is assumed that that $V_I = 10V$, $L = 1mH$, $C = 12\mu F$, $T_C = 100\mu s$, and $R = 30\Omega$, onwards.

A. Spectrum analysis

The three possible cases given in Sect. II are investigated. Figures 3, 4 and 5 show the time evolutions of the inductor currents $i(t)$, the phase portrait of i_n against i_{n+1} and the corresponding spectra of each case, base on $I_1 = 1A$, $2.25A$, and $3.7A$, respectively and $I_2 = 4A$.

Comparing the waveforms in Figs. 3 (a), 4 (a) and 5 (a), it is noticed that the ripples of $i(t)$ can greatly be reduced when a larger I_1 is applied. On the other hand, as indicated by the corresponding phase portraits and the power spectrum, a complicate dynamics are observed. The power is well spread over the entire frequency band, while it is interesting to notice that, instead of having a maximum peak of a magnitude close to the clock frequency T_C as in Cases I and II, the peak is

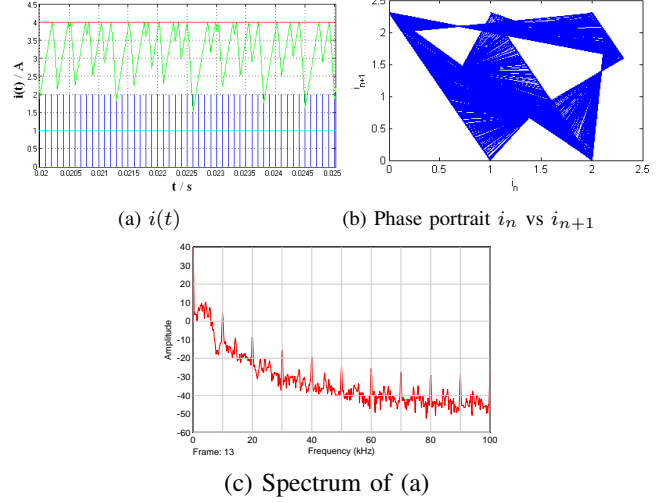


Fig. 3. Case I: $t_2 \geq T_C$

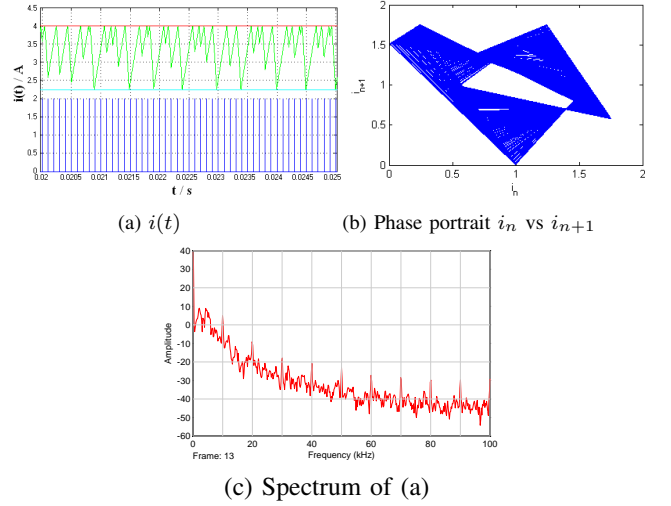


Fig. 4. Case II: $T_A \geq T_C > t_2$

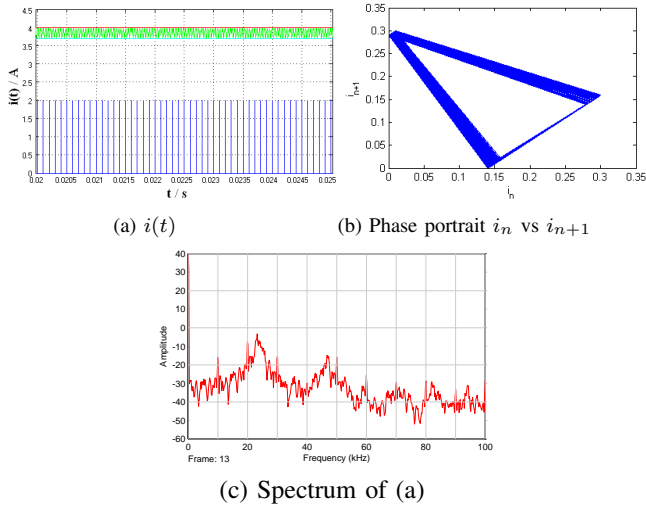
shifted to a frequency of approximately $\frac{1}{T_A} = 23.5$ KHz in Case III.

In all cases, the low frequency components of $i(t)$ are suppressed and a better spectrum distribution is obtained. However, it is also noticed that the background spectrum is not significantly improved, even though the ripples are suppressed.

B. Bifurcation and the Lyapunov exponents

As indicated by the broadband spectrum obtained in the previous section, the boost converter (9) possesses an interesting chaotic nature. In the sequel, this nature is further investigated based on its bifurcation diagrams and Lyapunov exponents.

Figure 6 depicts the bifurcation diagram of x_n versus I_1 , and the corresponding maximum Lyapunov exponents (LEs). The existence of positive LEs confirms the chaotic mode of the system and some periodic windows are also noticed in between. It can be explained by the fact that (9) can be


 Fig. 5. Case III: $T_C \geq T_A$

rewritten as $x_{n+1} = \beta(1 - \frac{1}{\beta}x'_n)$ when $\rho + \gamma = \beta$, giving $LE = 0$ and hence the system is in a periodic mode.

Similarly, the bifurcation diagrams of x_n versus V_I and x_n versus T_C are obtained and shown in Figs. 7 and 8. It is remarked that Case III (it is also our main interest) is assumed.

In Fig. 7, a route from period to chaos is clearly observed when the input voltage V_I is decreased, while some periodic windows exist. Similar conclusion is drawn from the bifurcation diagram given in Fig. 8. Therefore, the mapping (9) exhibits rich dynamical behavior like bifurcation and chaos, which constitutes the corner stone of our design to reduce EMI and improve EMC.

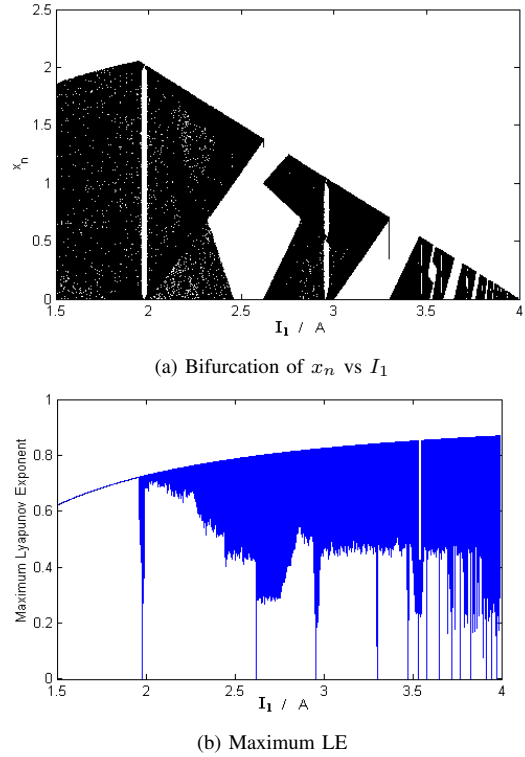
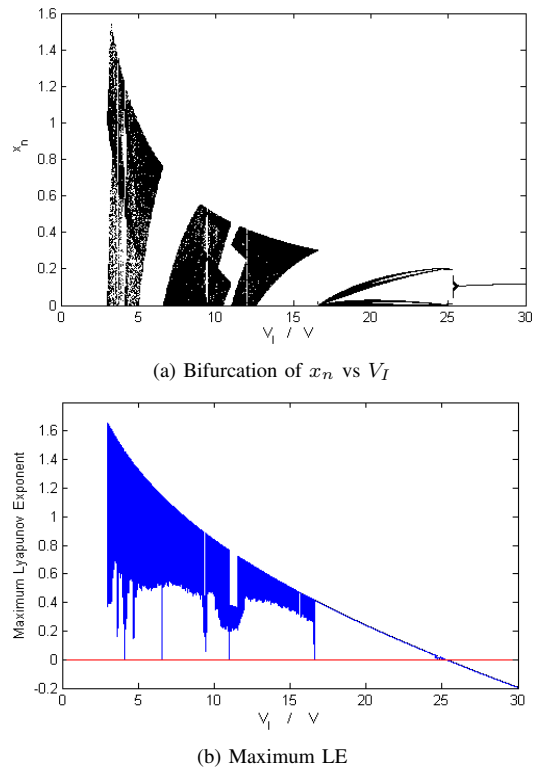
C. EMC performance

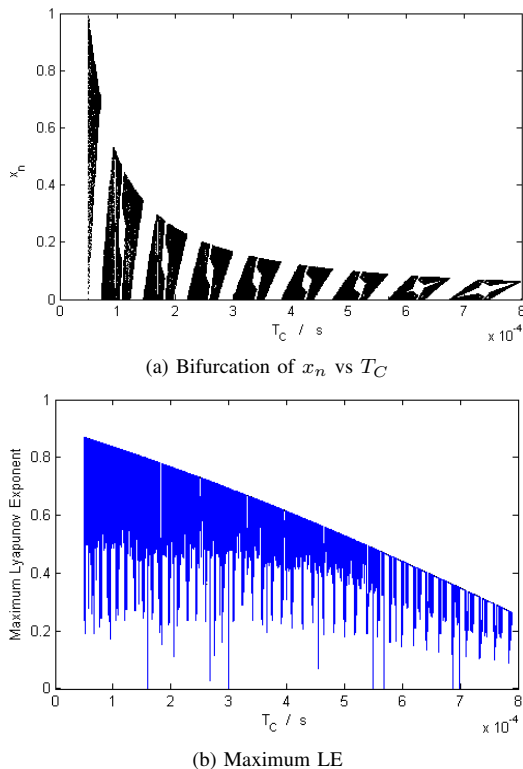
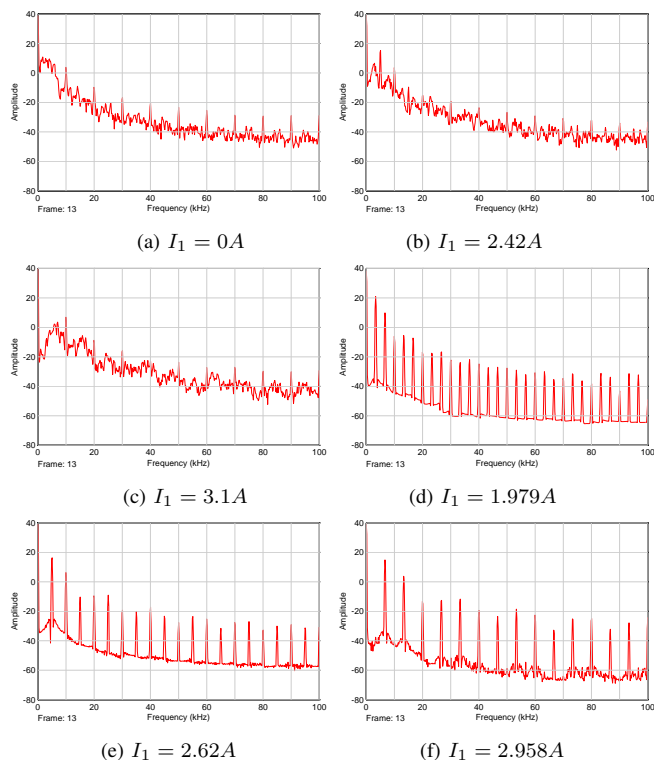
In order to design a good DC/DC converter, its EMC performance is critical. As shown in the bifurcation diagram obtained in the previous section, the proposed converter operates either in chaotic or periodic mode. In the followings, simulations are conducted to compare which operating mode will provide better EMI suppression.

Figure 9 (a)–(c) depict the spectra when the boost converter operates in chaotic modes with $I_1 = 0A$, $2.42A$, and $3.1A$ ($I_2 = 4A$) for the three specified cases. A smaller maximum peak value is obtained when $I_1 = 3.1A$, as compared with the case of $I_1 = 0A$ (Note: $I_1 = 0A$ is equivalent to the original design given in [4]), and a slight shift of the dominant frequency is observed.

For periodic cases, the the power spectra of the corresponding inductor currents with $I_1 = 1.979A$, $2.62A$, and $2.958A$ ($I_2 = 4A$) are shown in Fig. 9 (d)–(f). The peak amplitude remains the same with the base frequency shifting to higher frequencies when I_1 is increased (Note: an increase of I_1 results in a decrease of ripple amplitudes).

Therefore, by operating the designed converter in chaotic mode, the switch control strategy in Fig. 1 (b) not only suppresses the ripples, but also improves EMC.


 Fig. 6. Bifurcation of x_n against I_1 and the corresponding maximum LE

 Fig. 7. Bifurcation of x_n against V_I and the corresponding maximum LE


 Fig. 8. Bifurcation of x_n against T_C and the corresponding maximum LE

 Fig. 9. Spectra with different I_1 : (a)–(c) chaotic mode and (d)–(e) periodic mode

IV. EXPERIMENTAL VERIFICATION

The design in Fig. 1 is realized with discrete components, while the major components are tabulated in Table I. In addition, it is set that $V_I = 10V$, $T_C = 100\mu s$, $L = 0.56mH$, $C = 47\mu F$, and $R = 30\Omega$.

TABLE I
THE LIST OF MAIN COMPONENTS

Component	Device
diode	MBR2045CT
switch	IRFZ234N
current sensor	LA-55-P
flip-flop	74HC74N
comparator	LM393
driver	34152P

Figures 10 (a), (c) and (e) show the current waveforms for the three cases with the boost converter operating in periodic mode with the corresponding spectra given in Figs. 10 (b), (d) and (f). As compared with the simulations presented in Sect. III-C, a close match is confirmed. The maximum peak of the frequency are also unchanged, even though the ripples have been greatly reduced (the peak-to-peak ripples are 2.4A, 1.4A, and 0.9A, respectively).

When the boost converter is operated in chaotic mode, as shown in Fig. 11, an improvement of EMI suppression is clearly demonstrated with an increase of I_1 , while a large reduction of ripples can be achieved at the same time. It should be emphasized that $I_1 = 0A$ is equivalent for the design presented in [4]. The experimental results are also consistent to the observations in Sect. III-A and no obvious relationship between the ripple magnitude and the background spectrum is found.

V. CONCLUSION

In this paper, a new peak current-mode boost converter is proposed and studied. The current control is dependent on two reference currents and an external clock, which can be realized in a simple circuit.

By deriving its current mapping function, it is found that the boost converter can exhibit complicated dynamics. Bifurcations and chaotic dynamics are easily obtained by the introduction of I_1 as compared with the design given in [4].

The performance of the proposed design is confirmed both in simulations and experiments, and it shows that the current ripples and also the EMI are suppressed. It is also noticed that there is a shift of the dominant frequencies in the power spectrum when I_1 is increased, for which further studies will be carried out for identifying the causes.

REFERENCES

- [1] J.H.B. Deane, D.C. Hamill, "Improvement of power supply EMC by chaos", *Electronics Letters*, vol. 32, no. 12, pp. 1045, 1996.
- [2] D.C. Hamill, J.H.B. Deane, and P.J. Aston, "Some applications of chaos in power converters", *IEE Colloquium on New Power Electronic Techniques (Digest No: 1997/091)*, pp. 5/1–5/5, May 1997.
- [3] A. Grial, A. El Aroudi, L. Martinez-Salamero, R. Leyva and J. Maixe, "Current control technique for improving EMC in power converters", *Electronics Letters*, vol. 37, no. 5, pp. 274–275, March 2001.

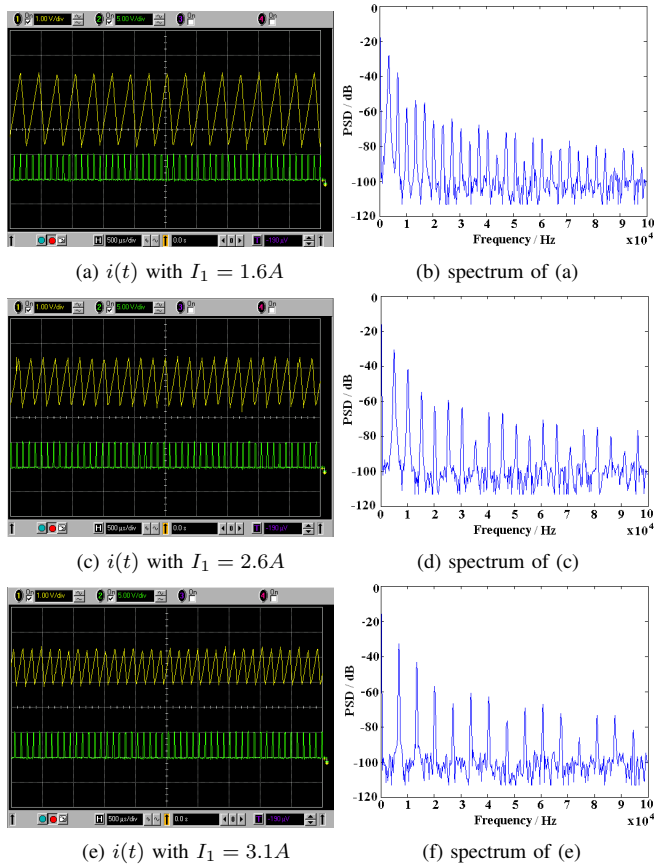


Fig. 10. Current waveforms and corresponding spectra in periodic mode for Cases I-III

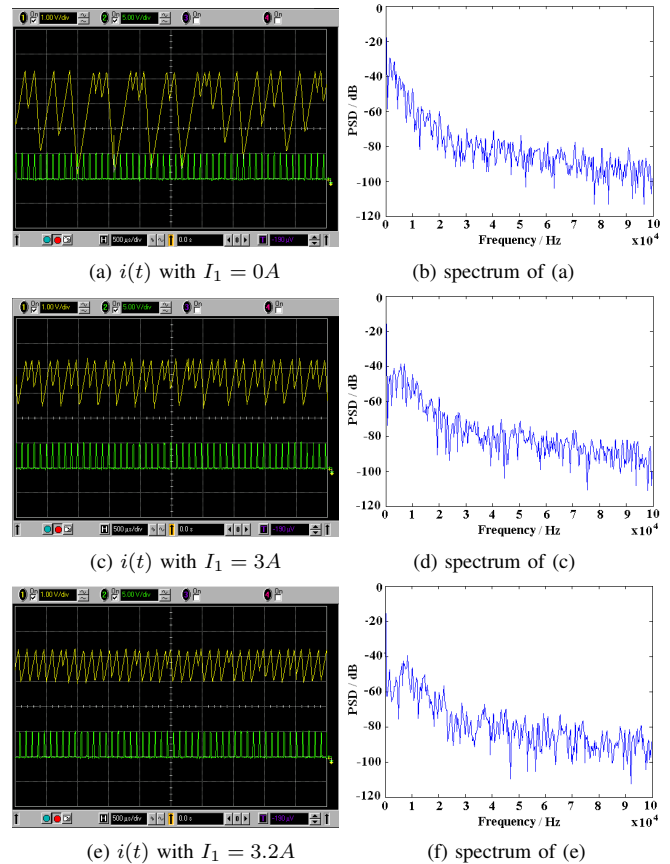


Fig. 11. Current waveforms and corresponding spectra in chaotic mode for Cases I-III

- [4] J.H.B. Deane, P. Ashwin, D.C. Hamill and D.J. Jefferies, "Calculation of the periodic spectral components in a chaotic DC-DC converter", *IEEE Transactions on Circuits and Systems I*, vol. 46, no. 11, pp. 1313-1319, 1999.
- [5] A.L. Baranovski, A. Mogel, W. Schwarz and O. Woywode, "Chaotic control of a DC-DC converter", *IEEE Int. Symp. Circuits and Systems*, pp. II/108-II/111, May 2000.
- [6] M. Balestra, M. Lazzarini, G. Setti, and R. Rovatti, "Experimental performance evaluation of a low-EMI chaos-based current-programmed DC-DC Boost converter", *IEEE Int. Symp. Circuits and Systems*, vol. 2, pp. 1489-1492, May 2005.
- [7] S. Banerjee, D. Kasha and S. SenGupta, "Minimising EMI problems with chaos", *Int. Conf. Electromagnetic Interference and Compatibility*, pp. 162-167, February 2002.
- [8] R. Mukherjee, S. Nandi and S. Banerjee, "Reduction in spectral peaks of DC-DC converters Using chaos-modulated clock", *IEEE Int. Symp. Circuits and Systems*, vol. 4, pp. 3367-3370, May 2005.
- [9] R. Yang, B. Zhang, F. Li, and J.J. Jiang, "Experiment research of chaotic PWM suppressing EMI in converter", *IEEE 5th Int. Conf. Power Electronics and Motion Control*, vol. 1, pp.1-5, August 2006.
- [10] S. Banerjee, A.L. Baranovski, J.L.R. Marrero, and O. Woywode, "Minimizing electromagnetic interference problems with chaos", *IEICE Trans. Fundamentals*, vol. E87-A, no. 8, pp. 2100-2109, 2004.
- [11] A.L. Baranovski, H. Gueldner, W. Schwarz, J. Weber and O. Woywode, "On the trade-off of ripple and spectral properties of chaotic DC-DC converters", *Int. Symp. Nonlinear Theory and Its Applications*, October 2002.

BIOGRAPHIES



applications.



cryptography, fuzzy control and its applications, and coordinated control of networked multi-agent systems

Hong Li received her BS and MS from Taiyuan University of Technology and South China University of Technology, in 2002 and 2005, respectively. She is now a Ph.D. student at the FernUniversitaet in Hagen, Germany. Her research interests include power electronics, electromagnetic interference and chaos control and its ap-

Zhong Li received his BS, MS and Ph.D. from Sichuan University, Jinan University, and South China University of Technology, in 1989, 1996, and 2000, respectively. He is now a junior professor at the FernUniversitaet in Hagen, Germany. His research interests include chaos theory and chaos control, application of chaos in



Wolfgang A. Halang, born 1951 in Essen, Germany, received a doctorate in mathematics from Ruhr-Universität Bochum in 1976, and a second one in computer science from Universität Dortmund in 1980. Since 1992 he holds the Chair of Computer Engineering in the Faculty of Electrical and Computer Engineering at Fernuniversität in Hagen, Germany. His research interests comprise all major areas of hard real-time computing with special emphasis on safety-related systems.



Dr. Barajas Ramírez graduated in 1995, with the degree Ingeniero Industrial en Electrónica (Industrial Engineering majoring in Electronics) from the Instituto Tecnológico de Tijuana. In 1997 he received the degree of Maestro en Ciencias en Electrónica y Telecomunicaciones con especialidad en Instrumentación y Control (Masters in Science, Electronics and Telecommunications, majoring in Instrumentation and Control) from CICESE in Ensenada México. In 2002, received the Doctor of Philosophy on Electrical Engineering degree from the University of Houston. Since 2004 he is a member of the National System of Researchers (SNI) of México, currently SNI-1.

Application of Asynchronous Channels Method to the W-CDMA Systems

Etsushi Nameda^{*†}, Hideaki Terai^{*†}, Minghui Kao^{*†} and Ken Umeno^{*†}

^{*}ChaosWare Inc.,

Bldg.135, Nukui-kitamachi 4-2-1, Koganei, Tokyo 184-8795, Japan

[†]Next Generation Mobile Communications Laboratory, RIKEN

Hirosawa 2-1, Wako, Saitama 351-0198, Japan

E-mail:{nameda, terai, kao, chaosken}@chaosware.com

Abstract—We evaluate here an interfering suppression method that utilizes the effect of asynchronous accesses. The method called as asynchronous channels (ACL) can be applied to one of the present third generation standards, wideband code division multiple access (W-CDMA) systems. Applying together with auto-correlation controlling filters, called as Lebesgue spectrum filter (LSF), the system capacity gains up by 154% in band-unlimited situations. On the other hand, in practical band-limited situation, the asynchronous channel method can effectively halve the system chiprate. Because the next generation mobile communication system allows wider bandwidth, the mobile transmitter need to accelerate its chiprate, which induces more electricity power consumption. The asynchronous channel method can be one of solution to the electric power consumption problem of mobile communication equipment.

I. INTRODUCTION

Wideband code division multiple access (W-CDMA), also known as universal mobile telecommunications system (UMTS), is one of third generation wireless mobile communication standards, subscribed over 2 billion today and expected 3 billion by 2010 [1]. The significant feature of W-CDMA is the tolerance of asynchronous multiple access in the uplink, the connection from user equipment (UE) transmitters to the Base Station (BS) receiver. One reason for the asynchronous uplink support is that it was easier to realize continuous system deployment, from outdoors to indoors, with no requirement of any external timing source such as global positioning system [2]. The another reason, relatively not so widely known, is that the asynchronous access suppresses interfering noise between multiple mobile stations, revealed by the pioneering analysis of direct sequence CDMA systems by Pursley in 1970's [3].

Though the estimation of interfering suppression effects in asynchronous accesses is affected by chip

shapes [4], we remark that the asynchronous access is important to design highly efficient mobile communication systems. Asynchronous channels (ACL) is a method that aims to utilize such interfering suppression effect of the asynchronous access by staggering multiple channels of a user [5].

In this paper, we report simulation results of ACL applied to W-CDMA systems. ACL demonstrates highly interfering suppression effects as expected, decreasing bit error rates (BER) and increasing the system capacity. In band-unlimited situations, ACL attain the same bitrate only in half of original chiprate without loss of BER. We also demonstrate the Lebesgue spectrum filter (LSF) that controls optimal auto-correlations of scrambling sequences. ACL and LSF can work together in proper settings and situations.

The organization of the paper is as follows. In section II, we introduce the W-CDMA systems and two proposal method, ACL and LSF. In section III, we show the simulation results of ACL applied to W-CDMA systems. In section IV, we discuss the effects of ACL. Finally, in section V, we draws some conclusions and complete the paper.

II. PRELIMINARIES

A. W-CDMA

W-CDMA is based on DS-SS systems where transmitted symbols are scrambled and spread by pseudo-noise codes. Fig.1 shows a simplified block diagram of the W-CDMA uplink. W-CDMA utilize two types of code spreading. The first is the channelization operation, which transforms every data symbol into a number of chips, thus increasing the bandwidth of the signal. The number of chips per data symbol is called as the spreading factor (SF). The second operation is the scrambling operation, which spread signal broadly to the

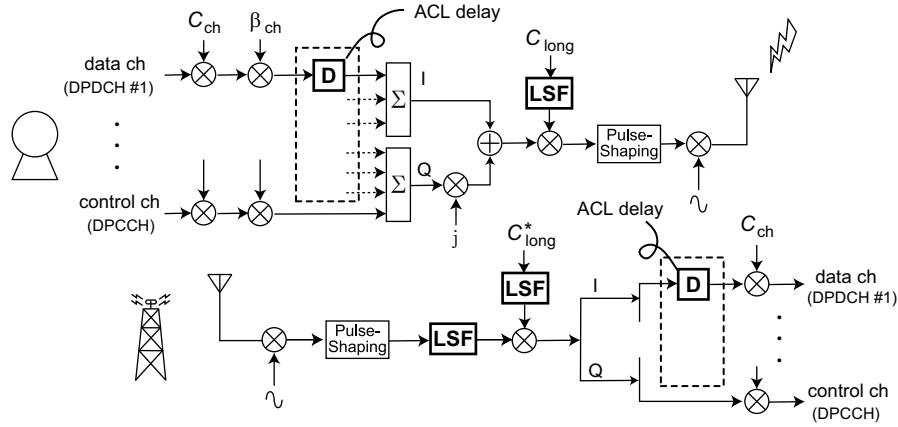


Fig. 1. A simplified block diagram of a user equipment transmitter (upper) and a base station receiver (lower) in the W-CDMA reverse link. Delay blocks and LSF filter blocks are also inserted for our proposed extension.

bandwidth by pseudo-random complex codes denoted as C_{long} in Fig.1.

The code used in channelization operation is called as Orthogonal Variable Spreading Factor (OVSF) code. The OVSF code $C_{\text{ch,SF},k}$ is defined by recursively substitutions into the Walsh function such as

$$C_{\text{ch},1,0} = 1,$$

$$\begin{bmatrix} C_{\text{ch},2,0} \\ C_{\text{ch},2,1} \end{bmatrix} = \begin{bmatrix} C_{\text{ch},1,0} & C_{\text{ch},1,0} \\ C_{\text{ch},1,0} & -C_{\text{ch},1,0} \end{bmatrix} = \begin{bmatrix} 1 & 1 \\ 1 & -1 \end{bmatrix},$$

$$\begin{bmatrix} C_{\text{ch},2^{(n+1)},0} \\ C_{\text{ch},2^{(n+1)},1} \\ \vdots \\ C_{\text{ch},2^{(n+1)},2^{(n+1)}-2} \\ C_{\text{ch},2^{(n+1)},2^{(n+1)}-1} \end{bmatrix} = \begin{bmatrix} C_{\text{ch},2^n,0} & C_{\text{ch},2^n,0} \\ C_{\text{ch},2^n,0} & -C_{\text{ch},2^n,0} \\ \vdots & \vdots \\ C_{\text{ch},2^n,2^{n-1}} & C_{\text{ch},2^n,2^{n-1}} \\ C_{\text{ch},2^n,2^{n-1}} & -C_{\text{ch},2^n,2^{n-1}} \end{bmatrix},$$

where k is the code number in $0 \leq k \leq \text{SF} - 1$ [6]. The OVSF codes preserve their orthogonality even in different lengths as far as avoiding their parents and children of recursive generations. Hence, the OVSF codes realize multiple physical channels of various bitrates [7], [8].

Among the codes of length SF, we often refer the particular number k of codes which has simple characteristics listed as follows.

- If $k = 0$ then all symbols are value 1.
- If $k = \text{SF}/2$ then symbol signs alternate every chips.
- If $k = \text{SF}/4$ then symbol signs alternate every 2 chips.

In W-CDMA systems, there are two kinds of major physical channels, namely, a control channel and data channels. The dedicated physical control channel (DPCCH)

is multiplied by the code $C_{\text{ch},256,0}$ that every symbol repeats sequential value 1 such as $\{1 \ 1 \ 1 \ 1 \ 1 \dots\}$. The dedicated physical data channels (DPDCHs) are typically used only one channel, DPDCH#1, multiplied by the code number SF/4 that symbols alternate signs every 2 chips such as $\{1 \ 1-1-1 \ 1 \ 1-1-1 \dots\}$.

B. Asynchronous channels

ACL is a method to stagger a control channel and data channels on purpose. As illustrated in Fig.1, we apply ACL to W-CDMA system by inserting delay blocks to DPDCHs. The delaying duration are set within a chip duration i.e. $0.26\mu\text{sec}$ at the W-CDMA default chiprate of 3.84Mcps, the W-CDMA default chiprate. Fig.2 illustrates schematic timing of spreading and scrambling of ACL applied DPDCH. The timings of multiplying channelization and scrambling codes are off to the side, consequently output sequences are chopped narrower than the default chip duration. Meanwhile, the DPCCH synchronizes with the scrambling code, so it remains as is.

C. Lebesgue spectrum filter

LSF is a kind of finite impulse response filter, designed to fit ideal autocorrelation coefficient of spreading codes on generic DS-CDMA systems. As illustrated in Fig.3, LSF adds up each delayed codes multiplied by $(-r)^n$ at n -th order. In practically, it is known that the filter order is sufficient at two [9]. The coefficient $(-r)$ has minus sign because it emphasize that the average coefficient of the optimal autocorrelation tends to register minus value. The optimal value for r is analytically estimated as $2 - \sqrt{3}$ when using pseudo-random codes such as

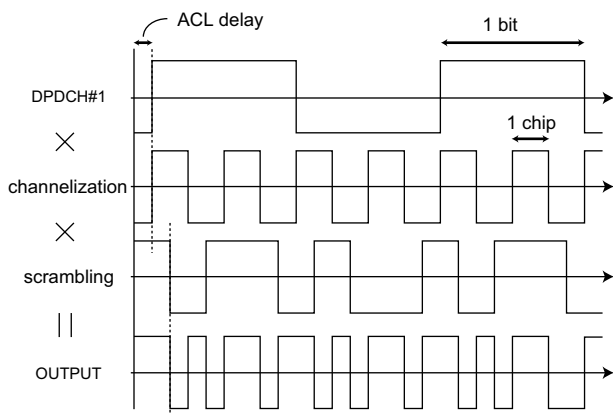


Fig. 2. Schematic chart of spreading and scrambling with ACL.

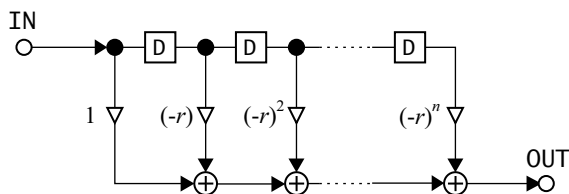


Fig. 3. Block diagram of LSF.

gold sequences or Chebychev chaotic sequences, which makes the system capacity up by 15% ideally [9].

In W-CDMA systems, LSF can be applied to scrambling or de-scrambling sequences as illustrated in Fig.1. In addition, LSF can also be applied to all the received signals. In this paper, the inserted positions of LSF are shortly denoted as ue , bs and air , respectively. Each places can be combined individually. For example, applying LSF to both scrambling and de-scrambling sequences will be denoted as $ue+bs$. It is reported by the authors that W-CDMA system applied LSF can gain its capacity up by 13% in band-unlimited situation with the code number zero of the channelization code and LSF applied to $ue+bs$ [10].

III. SIMULATIONS

We evaluate effects of ACL by Monte-Carlo simulations. In the following simulations, we assume all users adopt a fixed duration for asynchronous channel delay and generic noises or fading are not concerned. First, we investigate band unlimited situation to reveal the basic capability of ACL, and then, we apply the ACL in band-unlimited situations.

A. asynchronous channel delay and OVSF codes

Fig.4 shows raw BER performances of ACLs against delay of DPDCH#1, where the number of user equip-

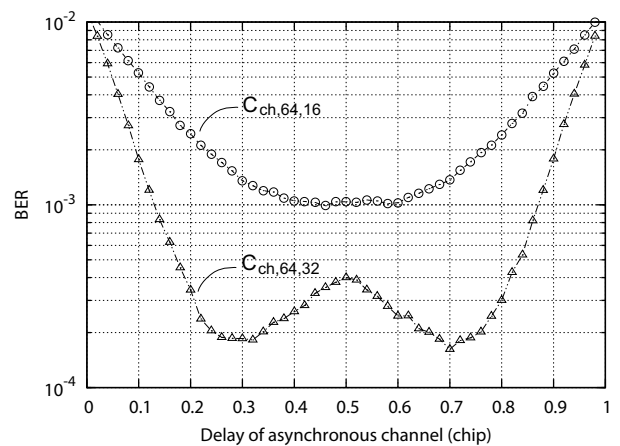


Fig. 4. BER performances against delay of DPDCH#1 ($U_e=30$, $SF=64$).

ments is 30 and the spreading factor is fixed to 64. When applying the W-CDMA default channelization code $C_{ch,64,16}$, BERs decrease along the asynchronous channel delay, reaching the minimum at the half of chip duration. This is the same result as the analysis on a simple DS-CDMA model [11]. However, when applying the code $C_{ch,64,32}$ that alternates signs every chips such as $\{1-1 1-1 \dots\}$, BERs show twin valleys, reaching the minimum at both 0.3 and 0.7 chip duration.

Fig.5 show BERs against numbers of user equipments in 60Kbps. Comparing the number of U_e that achieve $BER=10^{-3}$, we can measure the system capacity gains. The left most plotted lines are the W-CDMA default. In Fig.5, the maximum capacity is achieved when we delay 0.3 chip duration and also apply LSF to both scrambling and de-scrambling codes, which gains up by 154% relative to the W-CDMA default plotted on the left most lines.

Fig.6 shows the system capacity gains by ACL and LSF on various bitrates from 60Kbps ($SF=64$) to 960Kbps ($SF=4$). The combination of the code $C_{ch,SF,SF/2}$, 0.3 (or 0.7) chip delay and LSF applied to $ue+bs$ always performs the highest system capacity gains.

B. band-unlimited situation

In practice, all radio transmitters are regulated within a given bandwidth. For the case of the present W-CDMA systems, the occupied bandwidth is limited in 5MHz. To evaluate the realizability the ACL, we have to simulate the performance in band-unlimited situations.

Fig.7 shows the BER along with bandwidths limited by ideal low-pass filters. Unfortunately, BER of both 0.3 and 0.5 chip delay at 5MHz is less than that of

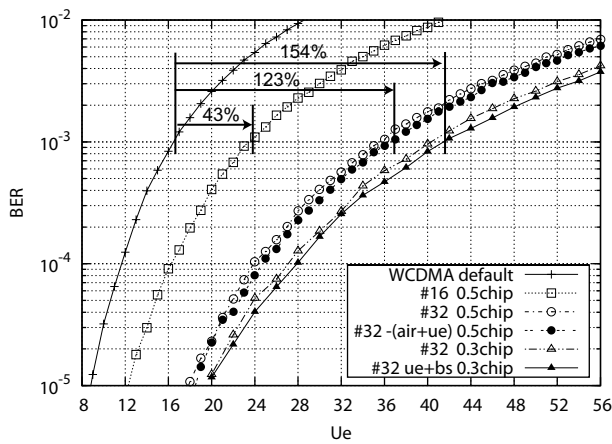


Fig. 5. Comparisons of system capacities (SF=64).

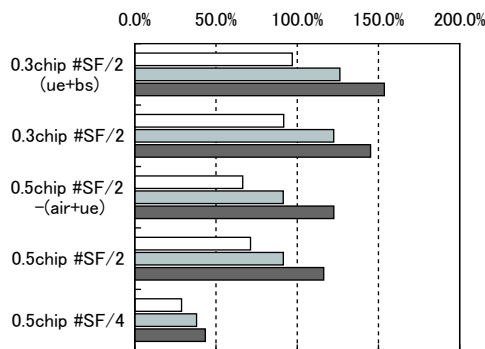
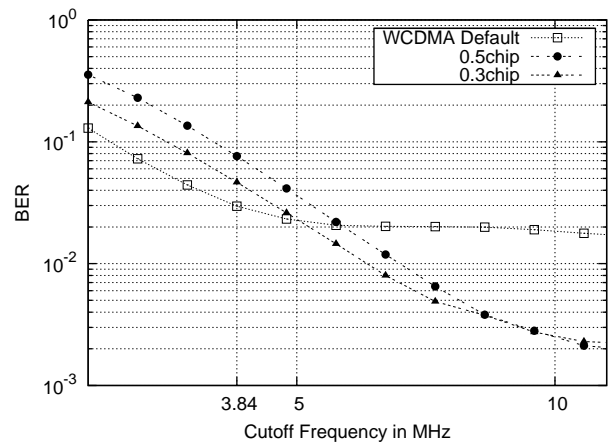
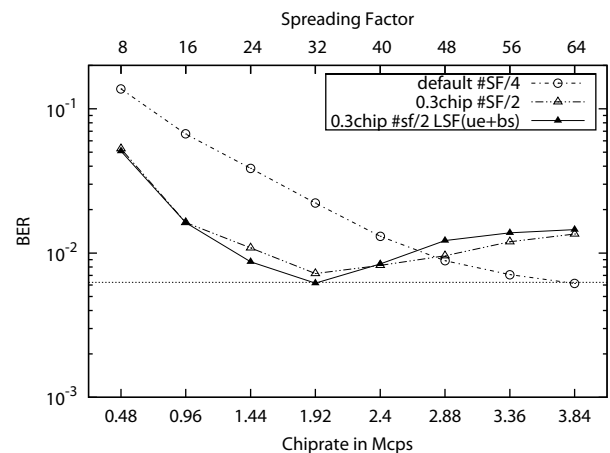


Fig. 6. System capacity gains relative to the W-CDMA default.

W-CDMA default feature. This implies that the ACL method broaden the occupied bandwidth than the original, which is the reason for getting significant system capacity gains relative to the default. Because the descending lines are not floored until 10MHz or more, the occupied bandwidth of 0.3 or 0.5 chip ACL will be widen by the double or triple compared to the default W-CDMA. However, it is possible to narrow the occupied bandwidth by decreasing the chiprate.

Fig.8 shows the another comparison of BERs where chiprates and spreading factors change under the same bandwidth limitation. The adopted low-pass filter here is the root raised cosine (RRC) filter, a well known pulse-shaping digital filter. The RRC filter has a characteristic parameter α , called as roll-off factor, which regulates the system bandwidth in $(1 + \alpha) \times R$ where R is the system chiprate. In accordance with the regulation [12], the roll-off factor of the W-CDMA systems is defined as 0.22, so the bandwidth is restricted to $3.84\text{Mcps} \times (1 + 0.22) = 4.6848\text{MHz}$. In the simulation, we alter the chiprate and the spreading factor but stay their ratio constant to $R /$


 Fig. 7. Comparison of BER under band-unlimited by ideal LPF ($U_e=30$, $R=3.84\text{Mcps}$, $SF=64$).

 Fig. 8. Comparison of BER according to chiprates and spreading factors under the fixed bandwidth ($U_e=16$ and bitrate = $R / SF = 60\text{Kbps}$, bandwidth = 4.6848MHz). The dashed horizontal line indicate the BER of the default W-CDMA of $U_e=16$, $R=3.84\text{Mcps}$ and $SF=64$.

$SF = 60\text{Kbps}$ and also alter the sampling rate of the RRC filter so that the limited bandwidth is fixed to the above regulation, in other words, varying chiprate without changing the spectrum efficiency defined by bitrate per hertz. From the definition, the channelization code length is originally restricted to involution of two, but we relax the code length to arbitrary multiple of four with limiting the particular code number, $SF/2$ and $SF/4$, re-defined by the characteristics listed in section II-A. As in Fig.8, we achieve just the same bitrate and BER at the half of the default chiprate, 1.92Mcps , by delaying 0.3 chip duration and applying LSF to both scrambling and de-scrambling codes. Hence, the chiprate can be halved at the maximum application of ACL and LSF.

IV. DISCUSSION

The ACL method can significantly increase the system capacity in band-unlimited situations. This is because the asynchronous summation of physical channels duplicates their chips, which increases seeming chiprates and widens the occupied bandwidth as shown in Fig. 7. However, the system of the half chiprate can accomplish the same BER performance without losing bitrate and broadening bandwidth as shown in Fig. 8, this intends that the ACL method can effectively halve the system chiprates. In the next generation mobile communications, the system bandwidth broadens as to 100MHz, so the mobile transmitter needs to accelerate its chiprate by twenty times in simple calculation, which induces serious electricity power consumption. In general, the electricity power consumption of radio system increases linearly by its chiprates, the problem will be critical especially for mobile transmitters. The ACL method could be one of solutions to the electric power consumption problem of mobile communication equipments.

The reason why 0.3 (or 0.7) chip delay is the optimum is still unknown. It should relate to the channelization code spreading but further analysis of the channel delay and channelization code will be our future works.

V. CONCLUSION

We evaluate the performance of asynchronous channels method adopted to W-CDMA systems. The ACL method employs the interfering suppression effect of asynchronous access in DS-CDMA systems. Applying together with ACL and LSF, the system capacity gains up by 154% relative to the default W-CDMA system in band-unlimited situations. In practical band-unlimited situation of the present regulation, we achieved the same bitrate and BER at the only half of the default chiprate by synergy effects of ACL and LSF. The advantage of the ACL method is that it can halve the chiprate, and it will be another solution to the electric power consumption problem of the next generation mobile communication equipments.

REFERENCES

- [1] P. Rysavy, "EDGE, HSPA & LTE," 3G Americas," White Paper, Sep. 2006. [Online]. Available: http://www.3gamericas.org/English/Technology_Center/WhitePapers/
- [2] F. Adachi, M. Sawahashi, and H. Suda, "Wideband DS-CDMA for next-generation mobile communications systems," *IEEE Commun. Mag.*, vol. 36, no. 9, pp. 56–69, Sep. 1998.
- [3] M. B. Pursley, "Performance evaluation for phase-coded spread-spectrum multiple-access communication-part I: System analysis," *IEEE Trans. Commun.*, vol. 25, pp. 795–599, 1977.
- [4] R. Kohno, R. Meidan, and L. B. Mislstein, "Spread spectrum access methods for wireless communication," *IEEE Commun. Mag.*, vol. 33, no. 1, pp. 58–67, Jan. 1995.
- [5] K. Umeno, JP patent 3650821; filed May 28 2003; awarded Oct. 21 2004.
- [6] 3GPP, "Spreading and modulation (Release 6)," TS 25.213," Technical Specification, March 2006.
- [7] F. Adachi, M. Sawahashi, and K. Okawa, "Tree-structured generation of orthogonal spreading codes with different lengths for forward link of DS-CDMA mobile radio," *Electronics Letters*, vol. 33, pp. 27–28, Jan. 1997.
- [8] K. Okawa and F. Adachi, "Orthogonal forward link using orthogonal multi-spreading factor codes for coherent DS-CDMA mobile radio," *IEICE Trans. Commun.*, vol. E81-B, no. 4, pp. 777–784, April 1998.
- [9] K. Umeno and A. Yamaguchi, "Construction of optimal chaotic spreading sequence using lebesgue spectrum filter," *IEICE Trans. Fundamentals*, vol. E85-A, no. 4, pp. 849–852, April 2002.
- [10] E. Nameda, H. Terai, M. Kao, and K. Umeno, "Dependency of asynchronous channels (ACL) and Lebesgue spectrum filter," in *22nd SIP SYMPOSIUM*. IEICE, 2007, pp. 532–537, (in Japanese).
- [11] K. Umeno and R. Takahashi, "Optimal asynchronous channel (ACL) method for multi-carrier communication systems," in *22nd SIP SYMPOSIUM*. IEICE, 2007, pp. 538–541, (in Japanese).
- [12] 3GPP, "User Equipment (UE) radio transmission and reception (Release 1999)," TS 25.101," Technical Specification, Dec. 2006.



Etsushi Nameda graduated from the University of Tokyo, Japan in 1998 and received the Ph.D. degree from the same University in 2007. In 2007, He joined ChaosWare Inc. and also joined the Next Generation Mobile Communications Laboratory, RIKEN as an invited researcher.



Hideaki Terai graduated from Fukuoka Institute of Technology, Japan and received B.E. degrees in 2002. He joined the Chaos-CDMA project team of JST and he joined ChaosWare Inc. in 2003. He also joined the Next Generation Mobile Communications Laboratory, RIKEN as an invited technician since 2006. He has been engaged in the research of chaos CDMA and online ICA algorithm.



Ming-hui Kao received her MSc degree from the Tokyo Institute of Technology in 1989. She joined Motorola from 1991-2000, worked with strong interest in CDMA communications. She was the subleader of the Chaos-CDMA project team of JST during the term 2000-2003. She is co-founder of ChaosWare Inc.



Ken Umeno received his BSc degree in electronic communication from Waseda University, Japan, in 1990. He received his MSc and PhD degrees in physics from University of Tokyo, Japan, in 1992 and 1995, respectively. From 1995 to 1998, he was a special postdoctoral fellow of RIKEN, Japan. He joined the National Institute of Information and Communications Technology (NICT), Japan, in 1998. He led the Chaos-CDMA project team of JST during the term 2000-2003. Currently, he is the president of ChaosWare Inc. and a senior researcher of NICT. His research interests include chaos-based computation and chaos-based communication networks as well as the fundamental theory of dynamical systems and computer science. He received LSI IP Award in 2003.

Recursive Backstepping for Synchronization of Chaotic Systems

Ashraf A. Zaher

Physics Department, Science College, Kuwait University
P. O. Box 5969, Safat 13060, Kuwait
a.zaher@kuniw.edu

Abstract— A recursive technique based on the backstepping approach is introduced to build fast state observers for chaotic systems using the drive-response mechanism. A single scalar time series of the output is used to construct the synchronization algorithm that can perform as a nonlinear states observer as well. The proposed technique relies on using virtual states while employing control parameters that can adjust the convergence rate of the observed states. In addition, these control parameters can be used to improve the transient performance of the response system to accommodate small and large variations of the initial conditions, thus achieving superior performance to conventional synchronization techniques. The permissible range of the control parameters is estimated using Simple Lyapunov functions. Two benchmark chaotic systems are considered for illustration, namely the Lorenz and Chua systems. Tuning the control parameters and resolving the conflict between stability and agility are addressed while comparing a comparison with conventional synchronization methods. Implementation of the proposed technique in both analog and digital forms is also considered and experimental results are reported ensuring feasibility and real-time applicability.

Keywords— *Chaos Synchronization; Nonlinear Observers*

I. INTRODUCTION

Since the early introduction of chaos synchronization [1,2], many techniques were reported in the literature with a wide variety of applications in different fields in science and engineering. Because of sensitivity to initial conditions, two trajectories emerging from two different closely initial conditions separate exponentially in the course of the time. As a result, chaotic systems defy synchronization [3]. Using a coupling or a forcing (periodical or noisy), two identical (or different) chaotic systems can adjust a given property of their motion to a common behavior. The most widely used types of synchronization, currently reported in the literature include complete synchronization [4], lag synchronization [5], generalized synchronization [6], phase synchronization [7], Q-S synchronization [8], and impulsive synchronization [9].

When performing complete synchronization of identical chaotic systems, a combination of drive and response systems is often utilized. The drive system represents the original chaotic system while the response system can represent a full or reduced states observer. In this type of synchronization both the drive and response systems have the same structure and dynamics except that the response system is driven by one of

the signals of the drive systems. In this particular type of synchronization there is an interaction between one system and the other, but not vice versa, and synchronization can be achieved provided that all real parts of the Lyapunov exponents of the response system, under the influence of the driver, are negative [2]. Because both the drive and response systems follow the same chaotic trajectory over the course of time, the response system can be used to generate estimates of the immeasurable states of the drive system [10,11]. Therefore synchronization of dynamical systems and the design of state observers can be considered analogous [12] where many notations and terminologies are being shared between the two. In addition, Lyapunov functions play an important role in both synchronization of chaotic systems (originating from physics) and the design of states observers (originating from control engineering) as it is often used to prove the stability of the overall system as well as finding good estimates for the permissible range of the control parameters [13]. The drive-response synchronization scheme is essentially a control problem as the drive signal is used as a feedback signal for the response system such that the synchronization error is continuously attenuated. The error dynamics governing the difference between the driver and the response (observer) states are required to be globally stable while approaching zeros to ensure complete synchronization. This configuration found useful applications in both secure communication applications [14] and the construction of parameter identification algorithms [15].

When using the drive-response synchronization scheme the same set of parameters appears in both systems and consequently no control is done over the speed of convergence that is now strongly dependent on initial conditions. In this paper, a recursive procedure based on the backstepping approach is used such that, instead of observing the drive system states directly, virtual states are introduced in an intermediate stage that is characterized by having fast convergence rate via employing additional control parameters in either linear or nonlinear framework. This has the effect of speeding up the synchronization process resulting in better performance in applications such as secure communications.

Backstepping, a recursive technique, relies on introducing virtual reference models in designing model-based control systems and has proven to be very efficient for both regulation and tracking problems [16]. When using virtual reference models, it is possible to prescribe a target behavior for some or all of the system states and then use some of them as virtual

controls to the output. This idea seems to be very appealing, especially when combined with Lyapunov-energy-like functions to design the control law for both linear and nonlinear systems [17]. In addition, backstepping designs are flexible and do not force the designed system to appear linear and can also avoid cancellation of useful nonlinearities and often introduce additional nonlinear terms to improve transient performance [18].

The need to develop faster states observers for chaotic systems for demanding applications such as secure communication and chaos control under the assumption that a single scalar time series, from the drive system, is available for measurement is the main motivation for the work presented in this paper. It is intended to use the drive-response synchronization method as a framework for the design of the fast states observer with the exception that both systems have non-identical structures. In addition, a feasible hardware-realizable implementation of the response system that can be easily tuned to achieve a fast synchronization with the drive system is introduced. This modified response system has an adjustable convergence rate, in contrast to the conventional synchronization mechanism in [2] where there are no control parameters to adjust the decay rate of the synchronization errors.

The rest of this paper is organized as follows: Sec. II introduces a detailed analysis of the design methodology by considering the Lorenz system as a chaotic benchmark model. Both simulations as well as experimental results are being reported to demonstrate the effectiveness of the proposed design. Extending the results to other chaotic systems is addressed in Sec. III where the Chua's model is considered. Comments regarding the practicality, advantages, and limitations of the proposed design are highlighted in Sec. IV as well as a brief comparison with other techniques reported in the literature and suggestions for future extensions.

II. THE LORENZ SYSTEM

The mathematical model of the Lorenz system, originally introduced in [19], is given by:

$$\begin{aligned}\dot{x}_1 &= -\alpha x_1 + \alpha x_2 \\ \dot{x}_2 &= \rho x_1 - x_2 - x_1 x_3 \\ \dot{x}_3 &= -\beta x_3 + x_1 x_2\end{aligned}\quad (1)$$

where the nominal values of the parameters are 10.0, 28.0 and 8/3 corresponding to σ , ρ , and β respectively. These values are known to produce chaos for the free running case as illustrated in Fig. (1). Assuming that only x_1 is observable, the following two virtual states are now introduced:

$$f_i = x_i - k_{i1}x_1 - k_{i3}x_1^3, \quad i = 2, 3 \quad (2)$$

where k_{21} , k_{23} , k_{31} , and k_{33} are design parameters. It is now required to use both f_2 and f_3 to recursively control the states x_2 and x_3 of the response system in order to continuously minimize the synchronization error while ensuring fast convergence rate. In addition, a deliberate cubic nonlinearity is introduced in Eq. (2) to increase the sensitivity of the virtual states to large synchronization errors; thus minimizing the effect of initial condition.

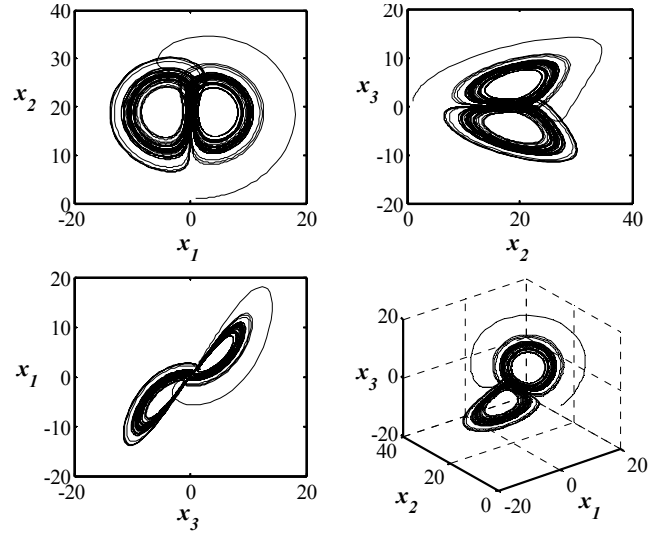


Figure 1. Chaotic behavior of the Lorenz system.

Differentiating Eq. (2), while using Eq. (1) for substituting for the states' derivatives, yields:

$$\begin{aligned}\dot{f}_2 &= [\rho x_1 - (f_2 + k_{21}x_1 + k_{23}x_1^3) - x_1(f_3 + k_{31}x_1 + k_{33}x_1^3)] \\ &\quad - (k_{21} + 3k_{23}x_1^2)[- \alpha x_1 + \sigma(f_2 + k_{21}x_1 + k_{23}x_1^3)] \\ &= -f_2 - x_1 f_3 - \sigma k_{21} f_2 - 3\sigma k_{23} x_1^2 f_2 + \varphi_2(x_1)\end{aligned}\quad (3)$$

where

$$\begin{aligned}\varphi_2(x_1) &= +x_1[\sigma k_{21}(k_{21} - 1) + \rho - k_{21}] \\ &\quad - x_1^2[k_{31}] \\ &\quad + x_1^3[k_{23}(\sigma k_{21} - 1) + 3\sigma k_{23}(k_{21} - 1)] \\ &\quad - x_1^4[k_{33}] \\ &\quad + x_1^5[3\sigma k_{23}^2]\end{aligned}\quad (4)$$

and

$$\begin{aligned}\dot{f}_3 &= [-\beta(f_3 + k_{31}x_1 + k_{33}x_1^3) + x_1(f_2 + k_{21}x_1 + k_{23}x_1^3)] \\ &\quad - (k_{31} + 3k_{33}x_1^2)[- \alpha x_1 + \sigma(f_2 + k_{21}x_1 + k_{23}x_1^3)] \\ &= x_1 f_2 - \beta f_3 - \sigma k_{31} f_2 - 3\sigma k_{33} x_1^2 f_2 + \varphi_3(x_1)\end{aligned}\quad (5)$$

where

$$\begin{aligned}\varphi_3(x_1) &= -x_1[\sigma k_{31}(k_{21} - 1) + \beta k_{31}] \\ &\quad + x_1^2[k_{21}] \\ &\quad - x_1^3[3\sigma k_{33}(k_{21} - 1) + \sigma k_{31}k_{23} + \beta k_{33}] \\ &\quad + x_1^4[k_{23}] \\ &\quad - x_1^5[3\sigma k_{23}k_{33}]\end{aligned}\quad (6)$$

Introducing the following virtual errors:

$$e_i = f_i - \hat{f}_i, \quad i = 2, 3 \quad (7)$$

results in:

$$\begin{aligned}\dot{e}_2 &= -(1 + \sigma k_{21})e_2 - x_1 e_3 - 3\sigma k_{23} x_1^2 e_2 \\ \dot{e}_3 &= x_1 e_2 - \beta e_3 - \sigma k_{31} e_2 - 3\sigma k_{33} x_1^2 e_2\end{aligned}\quad (8)$$

The following Lyapunov function is used to test for the global stability of the synchronization process:

$$L = 0.5(e_2^2 + e_3^2) \quad (9)$$

From which, we have:

$$\begin{aligned} \dot{L} &= e_2 \dot{e}_2 + e_3 \dot{e}_3 \\ &= -[(1 + \sigma k_{21})e_2^2 + \sigma k_{31}e_2e_3 + \beta e_3^2] - 3\sigma k_{23}x_1^2e_2^2 - 3\sigma k_{33}x_1^2e_2e_3 \end{aligned} \quad (10)$$

which can be made negative definite via the following selection of the design parameters:

$$\begin{aligned} k_{33} &= 0 \\ k_{23} &\geq 0 \\ k_{21} &\geq \frac{\sigma k_{31}^2}{4\beta} - \frac{1}{\sigma} \end{aligned} \quad (11)$$

as Eq. (10) now reduces to:

$$\dot{L} \leq -(1 + \sigma k_{21} - \frac{\sigma^2 k_{31}^2}{4\beta})e_2^2 - (\frac{\sigma k_{31}}{2\sqrt{\beta}}e_2 + \sqrt{\beta}e_3)^2 - 3\sigma k_{23}x_1^2e_2^2 \quad (12)$$

thus ensuring that as the synchronization errors will decay to zero.

A. Resolving the Conflict between Stability and Agility

Equation (11) illustrates that a wide range of gains exist to satisfy the stability requirement. In addition, it is clear that the analysis of Eq. (10) can be greatly simplified by setting the terms corresponding to the cubic nonlinearity of Eq. (2) to zero; thus minimizing the tuning effort of the control parameters.

When setting all the control parameters to zero, the designed observer reduces to the conventional drive-response synchronization method illustrated in [2] for which the dynamics for both systems are identical. In such case the synchronization speed is solely dependant on initial conditions.

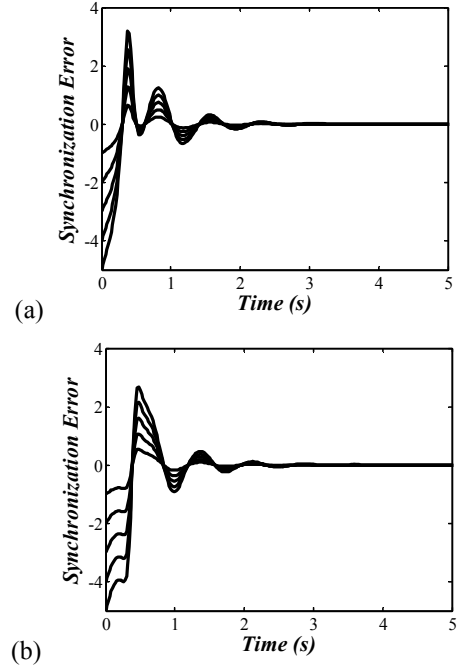


Figure 3. Initial conditions effect using conventional synchronization.

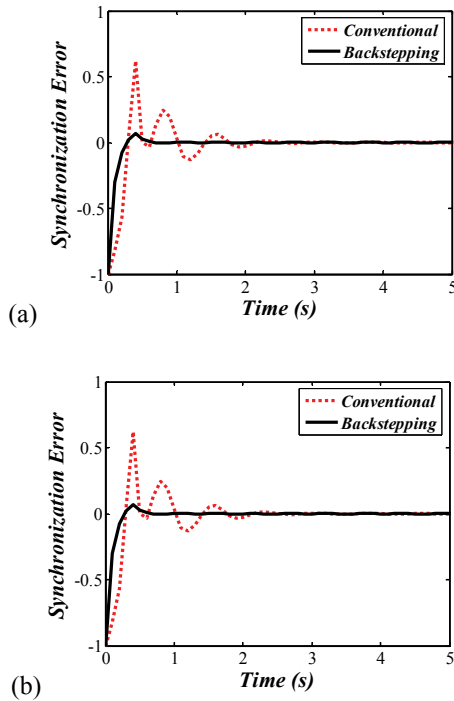


Figure 2. Synchronization errors for the two states x_1 in (a) and x_2 in (b).

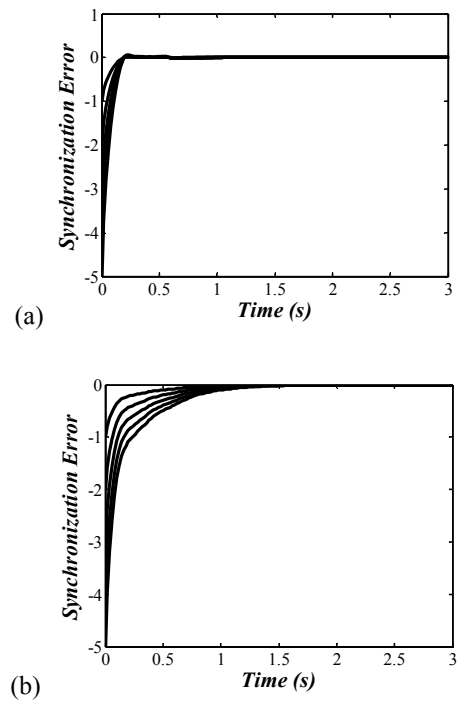


Figure 4. Initial conditions effect using backstepping synchronization.

Figure (2) illustrates the difference between the fast and smooth backstepping approach versus the slow and sluggish conventional approach where the gains for the backstepping case were adjusted to $k_{21} = k_{31} = 1.0$ and $k_{23} = k_{33} = 0.0$, while for the conventional case they were all set to zero. The effect of initial conditions on the transient performance of the synchronization process is shown in Figs. (3) and (4) illustrating the conventional and the backstepping methods respectively. The control parameters were all set to zero in Fig. (3) that clearly demonstrates the strong dependence for both x_2 and x_3 in (a) and (b) respectively on initial conditions. In contrast to the conventional synchronization method [2], Fig. (4) illustrates the superior transient performance for the backstepping case, where the control parameters were adjusted to $k_{21} = k_{31} = 1.0$, $k_{23} = 0.1$, and $k_{33} = 0.0$ for both x_2 and x_3 in (a) and (b) respectively.

B. Implementing the Proposed Technique

The proposed design, given by Eqs. (3-6), can be easily implemented using both analog and digital hardware. To verify this, a simplified version of the synchronization system is now illustrated for the case where only one design parameter is used, namely $k_{21} = 1$, while cancelling all other parameters.

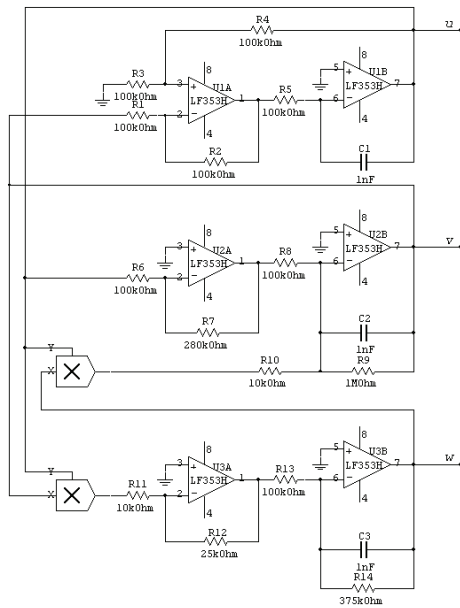


Figure 5. The drive circuit of the modified Lorenz system.

Figures (5) and (6) exemplifies one possible analog design, where the analog multipliers represent AD633AD, operational amplifiers are LF353, the supply was $V^+ = +15.0$, $V^- = -15.0$, and all resistors and capacitors have 1% tolerance. To meet the linearity constraints of the analog circuit, a linear transformation was applied such that the new states $u = 0.2 x_1$, $v = 0.2 x_2$, $w = 0.1 x_3$, $g_2 = 0.2 f_2$, and $g_3 = 0.1 f_3$ were used instead of the original ones. Equation (13) illustrates the new system where a time scaling $\tau = 1$ ms was introduced to simplify the analog implementation.

$$\begin{aligned}
 \dot{u} &= -\sigma u + \sigma v \\
 \dot{v} &= \rho u - v - 10uw \\
 \dot{w} &= 2.5uv - \beta w \\
 \dot{\hat{g}}_2 &= \rho u - \hat{g}_2 - 10u\hat{g}_3 - u - \sigma\hat{g}_2 \\
 \dot{\hat{g}}_3 &= 2.5u\hat{g}_2 - \beta\hat{g}_3 + 2.5u^2 \\
 \hat{v} &= \hat{g}_2 + u \\
 \hat{w} &= \hat{g}_3
 \end{aligned} \tag{13}$$

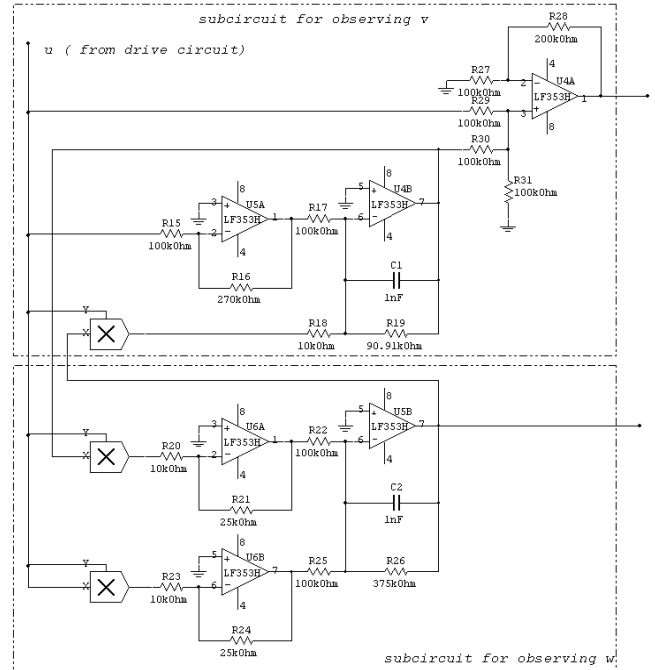


Figure 6. The response circuit of the modified Lorenz system.

The observed signals of the response circuit were measured using FLUKE 199C scopemeter and the analog data were converted to their digital equivalent and interfaced to the MATLAB environment using FLUKE SCC190. Figures (7) and (8) show the synchronization results for both v and w respectively reflecting the accurate convergence from the random initial conditions.

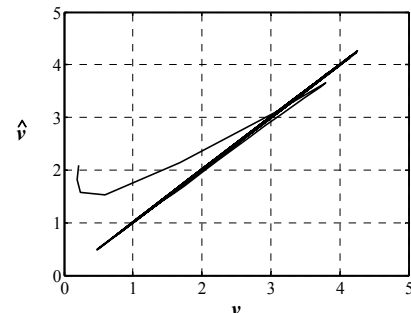
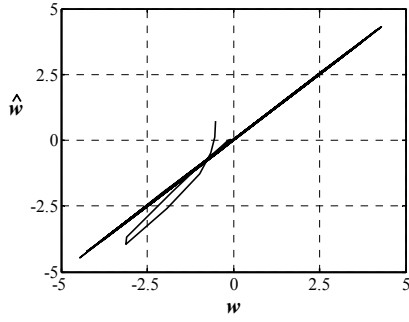


Figure 7. The synchronization performance for v .


 Figure 8. The synchronization performance for w .

III. THE CHUA'S SYSTEM

The next illustrative example is the Chua's system with smooth cubic nonlinearity for which the dynamical model is given in Eq. (14). This system is known to be a variant of the famous Chua's system with piecewise linear characteristics [20] that is easily implementable in both analog and digital hardware with typical applications in secure communications and synchronization-based systems.

$$\begin{aligned}\dot{x}_1 &= \alpha(x_2 - x_1^3 + cx_1) \\ \dot{x}_2 &= x_1 - x_2 + x_3 \\ \dot{x}_3 &= -\beta x_2\end{aligned}\quad (14)$$

where the nominal values of the parameters are $\alpha = 10$, $\beta = 16$, and $c = 0.2$. Figure (9) illustrates the response of the system.

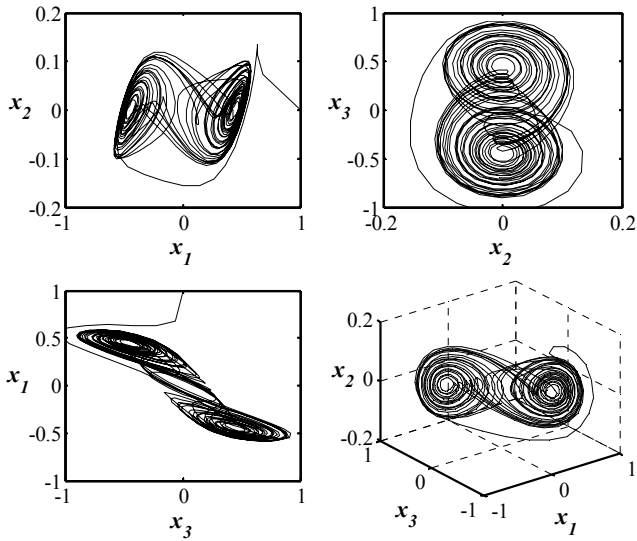


Figure 9. Chaotic behavior of the Chua's system.

Following the same methodology, outlined in the previous section, and assuming that only x_1 is available, the following virtual states can be introduced:

$$f_i = x_i - k_{i1}x_1, \quad i = 2, 3 \quad (15)$$

from which we have:

$$\begin{aligned}\dot{f}_2 &= -f_2 + f_3 - \alpha k_{21}f_2 + \varphi_2(x_1) \\ \dot{f}_3 &= -\beta f_2 - \alpha k_{31}f_2 + \varphi_3(x_1)\end{aligned}\quad (16)$$

where

$$\begin{aligned}\varphi_2(x_1) &= x_1(1 - k_{21} + k_{31} - \alpha k_{21}^2 - \alpha c k_{21}) + \alpha k_{21}x_1^3 \\ \varphi_3(x_1) &= -x_1(\beta k_{21} + \alpha k_{21}k_{31} + \alpha c k_{31}) + \alpha k_{31}x_1^3\end{aligned}\quad (17)$$

Introducing the following Lyapunov function:

$$L = 0.5(\mu e_2^2 + e_3^2), \quad \mu > 0 \quad (18)$$

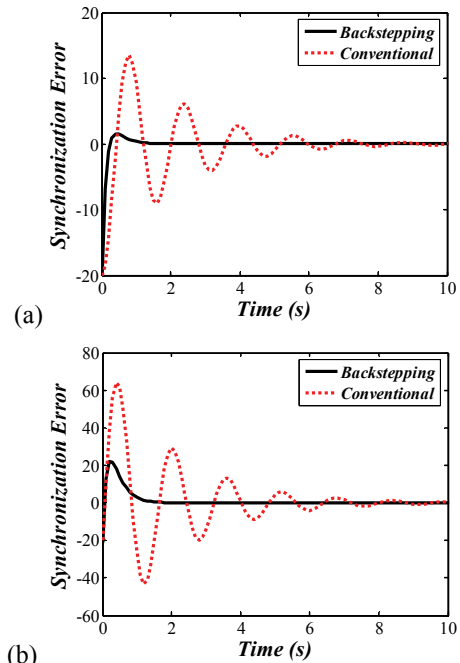
results in:

$$\begin{aligned}\dot{L} &= \mu e_2 \dot{e}_2 + e_3 \dot{e}_3 \\ &= -\mu(1 + \alpha k_{21})e_2^2 + e_2 e_3(\mu - \beta - \alpha k_{31})\end{aligned}\quad (19)$$

which can be made negative definite by the following choice of the control parameters:

$$\begin{aligned}k_{21} &\geq \frac{-1}{\alpha} \\ k_{31} &= \frac{\mu - \beta}{\alpha} \geq \frac{-\beta}{\alpha}\end{aligned}\quad (20)$$

Equation (20) verifies the flexibility of the proposed design as a wide range of the control parameters exist to resolve any conflicts between ensuring stability while maintaining fast response. In addition, Fig. (10) illustrates the improvement in the speed of convergence between the observed states (the response system) and their counterparts (the drive system). The backstepping gains were adjusted to $k_{21} = k_{31} = 1$, and the value of μ was set to 26, while for the conventional case they were set to zero


 Figure 10. Synchronization errors for the two states x_1 in (a) and x_2 in (b).

IV. DISCUSSION AND CONCLUSION

The proposed technique was first exemplified by the Lorenz system and it was shown that the observed states do converge to their true values, thus completely synchronizing both the drive and response systems. The strategy of introducing virtual states to indirectly observe the true states of the drive system proved to have two advantages; first using one or more control parameters to adjust the speed of convergence, and second to have an overparameterized structure that allows introducing deliberate useful nonlinearities such that the transient performance of the synchronization errors is improved. The many possible implementations of the virtual system add both flexibility and versatility to the proposed design as depicted by the comparative analysis when the virtual system was reset to directly represent the response system. Tuning the control parameters requires the knowledge of the range for which the system representing the virtual synchronization errors is stable. This was seen to be an easy task via using a suitable Lyapunov function. In addition, it was further demonstrated that sensitivity to initial conditions was greatly reduced as the response system produced satisfactory results despite starting from different initial conditions in contrast to the conventional synchronization method where the results reflect large variance and strong dependence on initial conditions. This suggests that the proposed technique is well suited to applications in both chaos control and chaos synchronization, e.g. secure communications. Extending the application of the proposed technique to the Chua's system proved to be straight forward. For this particular case, and because of the existence of smooth cubic nonlinearity in the original drive system, there was no need to introduce more nonlinearities in the virtual model and only a simple linear model was proposed. This verifies the flexibility of the design and how it can be easily tailored to meet the structure of different systems and/or constraints imposed by the physical dynamic model. Also the choice of the suitable Lyapunov function can be a bottleneck in the design process as tuning the control parameters to achieve stable performance requires the proper choice of which output to be considered to construct the states observer, e.g. it was not possible to use x_3 to observe both x_1 and x_2 for the Lorenz system. Thus, which state is used for feedback and which states are to be observed, crucially affect the design process. Although the range of the control parameters is derived from the Lyapunov stability criteria, their maximum values should be constrained to ensure proper implementation of the design. This is due to the fact that overdriving the states observer can cause saturation in both the analog and digital implementations that can lead to instability as the observer dynamics are no longer valid.

Finally, the case when some or all of the drive system parameters are uncertain or unknown can be resolved by using a single control parameter during the implementation phase and consequently performing simple fine tuning for adjusting the gains. Another possible solution to this problem is to incorporate adaptive parameters' estimators; however, this will come at the expense of sacrificing the simplicity of the design and the increased order of the overall system.

REFERENCES

- [1] L. M. Pecora and T. L. Carroll, "Synchronization in Chaotic Systems," *Phys. Rev. Lett.*, vol. 64, pp. 821-825, 1990.
- [2] L. M. Pecora and T. L. Carroll, "Driving systems with chaotic signals," *Phys. Rev. A*, vol. 44, pp. 2374-2284, 1991.
- [3] S. Boccaletti, J. Kurths, G. Osipov, D. Valladares, and C. Zhou, "The synchronization of chaotic systems," *Phys. Rep.*, vol. 366, pp. 1-101, 2002.
- [4] K. Murali and M. Lakshmanan, "Drive-response scenario of chaos synchronization in identical nonlinear systems," *Phys. Rev. E*, vol. 49, pp. 4882-4885, 1994.
- [5] M. G. Rosenblum, A. S. Pikovsky, and J. Kurths, "From Phase to Lag Synchronization in Coupled Chaotic Oscillators," *Phys. Rev. Lett.*, vol. 78, pp. 4193-4196, 1997.
- [6] A. E. Hramov and A. A. Koronovskii, "Generalized synchronization: A modified system approach," *Phys. Rev. E*, vol. 71, 067201, 2005.
- [7] M. G. Rosenblum, A. S. Pikovsky, and J. Kurths, "Phase Synchronization of Chaotic Oscillators," *Phys. Rev. Lett.*, vol. 76, pp. 1804-1807, 1996.
- [8] Z. Yan, "Chaos Q-S synchronization between Rössler system and the new unified chaotic system," *Phys. Lett. A*, vol. 334, pp. 406-412, 2005.
- [9] T. Yang, L. Yang, and C. Yang, "Impulsive synchronization of Lorenz systems," *Phys. Lett. A*, vol. 226, pp. 349-354, 1997.
- [10] Ashraf A. Zaher, "Design of model-based controllers for a class of nonlinear chaotic systems using a single output feedback and state observers," *Phys. Rev. E*, vol. 75, 056203, 2007.
- [11] Ashraf A. Zaher, "A nonlinear controller design for PM motors using a synchronization-based technique inspired from the Lorenz System," *J. Chaos*, vol. 18, 013111, 2008.
- [12] H. Nijmeijer and I. Mareels, "An Observer Looks at Synchronization," *IEEE Trans. Circuits Syst. I*, vol. 44, pp. 882-890, 1997.
- [13] C. W. Wu, L. O. Chua, "A unified framework for synchronization and control of dynamical systems," *Int. J. Bif. Chaos*, vol. 4, pp. 979-998, 1994.
- [14] T. L. Liao and N. S. Huang, "An Observer-Based Approach for Chaotic Synchronization with Applications to Secure Communications," *IEEE Trans. Circuits Syst. I*, vol. 46, pp. 1144-1150, 1999.
- [15] T. L. Carroll, "Chaotic control and synchronization for system identification," *Phys. Rev. E*, vol. 69, 046202, 2004.
- [16] L. Alexander, *Nonlinear and adaptive control of complex systems*, Kluwer Academic Publishers, 1999.
- [17] Ashraf A. Zaher, "Nonlinear Control of Systems with Multiple Equilibria and Unknown Sinusoidal Disturbance," *J. Nonlin. Sci. Numerical Sim.*, vol. 12, pp. 1518-1533, 2007.
- [18] M. Krstic, I. Kanellakopoulos and P. Kokotovic, *Nonlinear and Adaptive Control Design*, John Wiley & sons Inc., 1995.
- [19] E. N. Lorenz, "Deterministic nonperiodic flow," *J. Atmos. Sci.*, vol. 20, pp. 130-141, 1963.
- [20] L. O. Chua, "Chua's circuit - An overview ten years later," *J. Circuits, Syst. Comp.*, vol. 4, pp. 117-159, 1994.



Ashraf A. Zaher was born in Egypt in 1966. He received both his B.Eng. in Electronics and Communication Engineering in 1988 and his M.Phil. in Automatic Control Engineering in 1994 from Mansoura University, Egypt. He received his first Ph.D. in Systems Engineering from Oakland University, Michigan, USA in 2001, and his second Ph.D. in Control Engineering from Oakland /Mansoura Universities (joint supervision) in 2004.

He was a research scholar and a visiting professor at Oakland University, Electrical and Systems Engineering department and is currently working as an assistant professor at Kuwait University, Science College, Physics department. His research interests include virtual engineering, DSP, nonlinear dynamics and chaos. He is a member of IEEE, ISCA and AACCC.

Cumulant Analysis of Rössler Attractor

Luis A. Beltrán*, V. Kontorovich* and Z. Lovtchikova**

*Electrical Engineering Department, Telecommunications Section, CINVESTAV-IPN.

Av. IPN 2508, Col. San Pedro Zacatenco, C.P. 07360, México D.F.

Phone (52)+55 50613764, Fax (52)+55 50613977, Email:valeri@cinvestav.mx

**Interdisciplinary Professional Unit in Engineering and Advanced Technologies UPIITA -IPN
Ticomán, C.P. 07340, D.F. México. Telephone: (52)+5557296000, Email: alovtchikova@ipn.mx

Abstract—This paper is dedicated to the cumulant analysis of the Rössler attractor, based on the so-called “degenerate cumulant equations” method. The approach is illustrated by the calculus of the first cumulants, which are necessary to create an approximation of the probability density function (PDF), applying the Gramm-Charlier series, the model distribution method, etc. An approximate method for the variance calculation at the output of the Rössler strange attractor is shown. The latter is based on the Kolmogorov-Sinai entropy that is defined by the Lyapunov exponents for a statistically linearized chaotic system and by the differential Kolmogorov entropy.

Index Terms—Cumulants, cumulant brackets, attractor, kurtosis, variance, Kolmogorov-Sinai entropy.

I. INTRODUCTION

Nowadays, the number of chaos applications has grown considerably [1], but there are still a lack of the effective tools for the statistical analysis of the chaotic behavior for strange attractors, particularly in the electrical engineering field.

Recently it was proposed a so-called “degenerate cumulant equations method” [2-4] for applied statistical analysis of the strange attractors, based on the parameters of the corresponding dynamic systems¹. It was shown [2-4], that by means of the proposed approach not only the expressions for the cumulants can be found, but also the so-called “model distributions” for each component of the attractors under analysis, etc.

The “attractive” features of the cumulants (instead of moments) for engineering purposes was explained in detail at [3], [5] and also a comprehensive and adequate method for the cumulant calculus was presented: the cumulant brackets.

Note, that the “weight” of cumulants diminish as its order grows [5], so for engineering analysis it is sufficient to consider only the first four cumulants: $\chi_1 - \chi_4$, and

This work was supported by Intel C. through the grant “Intel-VK”

¹Certainly, all statistical properties of the attractor can be obtained through statistical computer simulation, but it is not the case here.

corresponding shape coefficients for PDF: γ_3 is the asymmetry coefficient and γ_4 is the kurtosis coefficient [5].

It was also shown recently, that chaotic models are adequate to model several natural phenomena, related to the communication field. For example, output signals of some components of the well known attractors: Lorenz, Chua, etc, can successfully describe the PDF’s of the interferences from some digital interconnects, and the cumulant analysis provides a very good coincidence with the measurement data.

The improvement of the characteristics of the modern digital communications from mobile to mobile PC’s users, etc is so important, that it is highly encouraging to continue with the statistical research of other attractors, for example, Rössler attractor.

It is worth to notice here, that any cumulant analysis of the dynamic system is not only qualitative, but also quantitative.

As it was stated from the very beginning of its applications, the cumulant method presents a “general view” of the statistical system behavior due to system parameters [6], [7].

As it follows from the title, this paper is dedicated to the cumulant analysis of the Rössler attractor from the engineering point of view. The paper is organized as follows. Section II contains the basics of the degenerate cumulant method and the concept of cumulant brackets. Section III is dedicated to the analytical cumulant analysis of the Rössler attractor. In section IV some of the numerical results for Rössler attractor, their comparison with analytical predictions and the concept of equations for cumulants and cumulant brackets are presented. Section V presents the analytical approximate method for the variance evaluation of the Rössler attractor. Section VI is dedicated to some comments to the section V. Conclusions are presented in section VII.

II. DEGENERATE CUMULANT EQUATIONS

It is well known [8], that each dissipative continuous time dynamic system (strange attractor) can be defined with the following equation:

$$\dot{\mathbf{x}} = \mathbf{f}(\mathbf{x}(t)), \quad \mathbf{x} \in \mathbf{R}^n, \quad \mathbf{x}(t_0) = \mathbf{x}_0, \quad (1)$$

where $\mathbf{f}(\cdot) = [f_1(\mathbf{x}), \dots, f_n(\mathbf{x})]^T$ is a differentiable vector function.

Following the principles for the ergodic theory of the equation (1) [8], one has to annex the external weak noise at (1) (idea of Kolmogorov) in order to obtain the meaningful concept for the physical measure of $\mathbf{x}(t)$ – $W_{st}(\mathbf{x})$. $W_{st}(\mathbf{x})$ is a stationary PDF for $\mathbf{x}(t)$ (see details in [8] and in [3], [4] as well).

Note, that $W_{st}(\mathbf{x})$, as well as its characteristic function, is totally defined by the complete set of cumulants [5].

Let us consider in the following only the one dimensional PDF $W_{st}(\mathbf{x})$ as:

$$\begin{aligned} W_{st}(x) &= F^{-1}\{\theta_m(j\mathcal{U})\}, \\ \theta(j\mathcal{U}) &= \exp\left\{\sum_{s=1}^{\infty} \frac{(j\mathcal{U})^s}{s!} \chi_s\right\} \end{aligned} \quad (2)$$

where χ_s is the cumulant of the s – th order.

If one assumes that cumulants for all $s > m$ are equal to zero, then for the finite set of cumulants $\{\chi_s\}_1^m$, we can introduce the “model distribution” $\hat{W}_{st}(\mathbf{x})$ of the m – th order and its characteristic function is defined by $\theta_m(j\mathcal{U})$.

It is clear that $F\{\cdot\}$ and $F^{-1}\{\cdot\}$ are direct and inverse Fourier transforms respectively.

The distribution $\hat{W}_{st}(\mathbf{x})$ is only an approximation of the true PDF and the model distributions ([11], and references therein) provide an accuracy, better than the orthogonal series expansions for the case $\gamma_4 < 0$, and can also be applied for $\gamma_4 > 0$.

Another option for analytical approximation are the orthogonal representations, for example, Gramm-Charlier, Laguerre series, etc. [5]. For example, the Gramm-Charlier series are defined by:

$$W(x) = W_G(x) \left[1 + \frac{\gamma_3}{3!} H_3(x) + \frac{\gamma_4}{4!} H_4(x) \right], \quad (3)$$

where

$$H_n(x) = (-1)^n \exp\left(\frac{x^2}{2}\right) \frac{d^n}{dx^n} \exp\left\{-\frac{x^2}{2}\right\};$$

$H_n(\cdot)$ is a Hermitian polynomial of n -order,

$$W_G(x) = \frac{1}{\sqrt{2\pi}} \exp\left\{-\frac{x^2}{2}\right\}$$

is a Gaussian distribution,

$$\gamma_3 = \frac{\chi_3}{\sigma^3}$$

is the skewness coefficient and

$$\gamma_4 = \frac{\chi_4}{\sigma^4}$$

is the kurtosis coefficient.

It is important to mention that for a symmetrical PDF the above coefficients satisfy:

$$\gamma_3 = 0, \mu_3 = \chi_3, \mu_4 = \chi_4 + 3(\sigma^2)^2$$

with χ_3 and χ_4 being the third and fourth cumulants; $\gamma_4 \geq -2$.

Now (1) can be rewritten in the form of the stochastic differential equation (SDE):

$$\dot{\mathbf{x}} = \mathbf{f}(\mathbf{x}(t)) + \varepsilon \xi(t), \quad (4)$$

where $\xi(t)$ is a vector of a weak external white noise with the related positive defined matrix of “intensities” $\varepsilon = [\varepsilon_{ij}]^{n \times n}$, [3], [5].

In other words $\mathbf{x}(t)$ is a continuous n -dimensional Markov process with kinetic coefficients, given by $\mathbf{K}_1(\mathbf{x}) = \mathbf{f}_i(\mathbf{x})$ and $\mathbf{K}_2 = [\varepsilon_{ij}]^{n \times n}$, [3], [5].

For the SDE representation of the attractor the approach, named as cumulant equations for the SDE with the given $\mathbf{K}_1(\mathbf{x})$ and \mathbf{K}_2 [5], can be successfully applied.

For the moment we assume (as it was proposed above), that $W_{st}(x)$ exists, and that it is a reasonable physical measure for (1) and (4) [13]; although there exists all cumulants that adequately represent $W_{st}(x)$. Those cumulants can be found from the following equations for the stationary cumulants (the interested reader can find all necessary developments in details and with examples at [5, ch. 4]):

$$\begin{aligned} \langle \mathbf{K}_{ij}(\mathbf{x}) \rangle &= 0, \\ 2\langle \langle x_i, \mathbf{K}_{1i}(\mathbf{x}) \rangle \rangle_s + \langle \mathbf{K}_{2ij} \rangle &= 0, \\ 3\langle \langle x_i, x_j, \mathbf{K}_{1\beta}(\mathbf{x}) \rangle \rangle_s + 3\langle \langle x_1, \mathbf{K}_{2j\beta} \rangle \rangle_s &= 0, \\ &\vdots \\ \sum_{l=1}^n C_n^l [\langle \langle x_1, x_2, \dots, x_{n-l}, \mathbf{K}_{1n-l+1}(\mathbf{x}) \rangle \rangle_s \dots \\ &+ \langle \langle x_1, x_2, \dots, x_{n-l}, \mathbf{K}_{2n-l+1,l} \rangle \rangle = 0] \end{aligned} \quad (5)$$

where $i \neq j, \beta = \overline{1, n}$.

We can evidently see from (5), that if $\forall \varepsilon_{ij} \rightarrow 0$, then the second summand in (5) tends to zero and the equations in (5) tend to the so-called “degenerate cumulant equations”.

Hence, the degenerate cumulant equations have the following form:

²Here we apply the definition for kinetic coefficients in Stratonovich form.

$$\begin{aligned}
 \langle \mathbf{K}_{1_i}(\mathbf{x}) \rangle &= 0, \\
 2\langle \{x_i, \mathbf{K}_{1_j}(\mathbf{x})\}_s \rangle &= 0, \\
 3\langle \{x_i, x_j, \mathbf{K}_{1_\beta}(\mathbf{x})\}_s \rangle &= 0, \\
 &\vdots
 \end{aligned} \tag{6}$$

where $i, j, \beta = \overline{1, n}$, and $\langle x_i, x_j, \dots, x_\beta \rangle$ are the so-called “cumulant brackets” - abbreviated representation for any cumulant [5].

$A\{x, y, \dots, z\}_s$ is an abbreviation of the Stratonovich symmetrization brackets (A is an integer) and represents the sum of all possible permutations in times of the arguments inside the brackets [5] (see Appendix).

Essentially equations (5) and (6) represent a set of non-linear algebraic equations and this set, in general, is not closed, but it is always possible to cut the set of cumulants by neglecting all cumulants with order $s > m$.

The equations (6) have to be sequentially solved first for each component of $\mathbf{x} = [x_1, x_2, \dots, x_n]^T$ (first line); next for couples of components $\{x_i, x_j\}_{i,j=1}^n$ (second line), and then for triplets $\{x_i, x_j, x_\beta\}_{i,j,\beta=1}^n$ (third line), etc.

The way to do it is to “open” the cumulant brackets as shown in Appendix A2 at chapter 4 at [5].

To illustrate the procedure described above, we apply this material to the analysis of the Rössler attractor.

III. RÖSSLER ATTRACTOR

Equation (1) for Rössler attractor has the following form:

$$\begin{aligned}
 \dot{x} &= -y - z \\
 \dot{y} &= x + ay \\
 \dot{z} &= b + zx - zc
 \end{aligned} \tag{7}$$

where a, b, c are the parameters of the attractor, $\mathbf{x} = [x, y, z]^T$.

Thus, the first kinetic coefficients for (6) are:

$$\begin{aligned}
 \mathbf{K}_{1,1}(x) &= -y - z \\
 \mathbf{K}_{1,2}(x) &= x + ay \\
 \mathbf{K}_{1,3}(x) &= b + zx - zc.
 \end{aligned} \tag{8}$$

Introducing (7) and (8) into (6) for the first component “x”, one gets:

$$\left. \begin{aligned}
 \chi_1^y &= \langle y \rangle = -\langle z \rangle = -\chi_1^z \\
 \chi_{1,1}^{x,z} &= -\chi_{1,1}^{x,y} \\
 \chi_{2,y}^{x,y} &= -\chi_{2,1}^{x,z} \\
 \chi_{3,1}^{x,y} &= -\chi_{3,1}^{x,z} \\
 \chi_{4,1}^{x,y} &= -\chi_{4,1}^{x,z}
 \end{aligned} \right\} \tag{9}$$

For the second component “y”:

$$\left. \begin{aligned}
 \chi_1^x &= \langle x \rangle = -a\langle y \rangle = -a\chi_1^y \\
 \chi_2^y &= -\frac{1}{a}\chi_{1,1}^{x,y} \\
 \chi_3^y &= -\frac{1}{a}\chi_{2,1}^{y,x} \\
 \chi_4^y &= -\frac{1}{a}\chi_{3,1}^{y,x}
 \end{aligned} \right\} \tag{10}$$

For the third component “z”:

$$\left. \begin{aligned}
 \chi_{1,1}^{x,z} &= \chi_{1,1}^{z,x} = c\langle z \rangle = -\langle z \rangle \langle x \rangle \\
 \chi_2^y &= \frac{c\langle z \rangle - a\langle z \rangle^2}{a}
 \end{aligned} \right\} \tag{11}$$

Then, going on with two components $\{x, y\}$, one can get: $\chi_3^y = \frac{2\chi_{1,2}^{y,x}}{1+a} \neq 0$, i.e PDF of $y(t)$ is asymmetrical.

With two components $\{x, z\}$ it follows: $\chi_3^z \neq 0$, i.e PDF of $z(t)$ is asymmetrical as well, and

$$\chi_2^y = \frac{\chi_2^x}{\langle z \rangle} \tag{12}$$

Please note, that notations for cumulants described in this section are considered in the Appendix.

In the same way all necessary cumulants of the higher order can be found.

IV. NUMERICAL RESULTS AND DISCUSSIONS

The results were obtained using Matlab. It is pretty simple to carry out numerical simulations of any strange attractor, especially Rössler attractor, and find all the cumulants (moments) necessary to make analytical approximation of the PDF for each component, etc.

Let us consider the results of simulations of the Rössler attractor with the following parameters: $a = 0.2$, $b = 0.2$, $c = 5.7$ [6], [7].

Note, that obviously each component of the attractor achieves its stationary conditions with different time constant. At this step of the research it was empirically found (from simulations), that the “x” components reach their stationary state faster than “y and z” components. Therefore for comparison with the analytical results it is

reasonable to apply data from the simulations, when the PDF's clearly achieve their stable shapes.

Keeping this in mind, let us make brief comparisons between analytical and simulation results. Based on the analytical results, which were presented in section II, we'll consider mainly the comparisons of the first two cumulants, as they are very important for practice.

From simulations it was found:

$$\langle x \rangle = 0.17, \quad \langle y \rangle = -0.76, \quad \langle z \rangle = 0.75.$$

One can see from (9) and (10) an almost exact coincidence with theory.

It is important to mention that all the components of the Rössler attractor are normalized before realizing the calculations.

Then, from (11) it follows, $\chi_2^y = 17.8$ and simulation gives $\chi_2^y = 18.9$ (error is about 5.8%).

From (10) $\langle x \rangle = 0.13$ and $|\langle x \rangle| < \langle y \rangle$: and $\langle x \rangle = 0.17$, from (12) it comes: when $\chi_2^x = 13.3$, $\chi_2^y = 17.8$ (simulation gives almost the same.)

Both PDF's for components "y" and "z" are not symmetrical. From (10) it follows, that PDF's for "x" and "y" are oppositely asymmetric, in contrary to Lorenz attractor (see [3]).

It can be seen, that besides of a good accuracy of the analytical prediction for cumulants, for complete calculus of the cumulants it is mandatory to provide the calculus of the variances: $\chi_2^x, \chi_2^y, \chi_2^z$, as high order cumulants depend to them.

In Figure (1-3) are represented the histograms for PDF's of the "x", "y" and "z" components of the Rössler attractor.

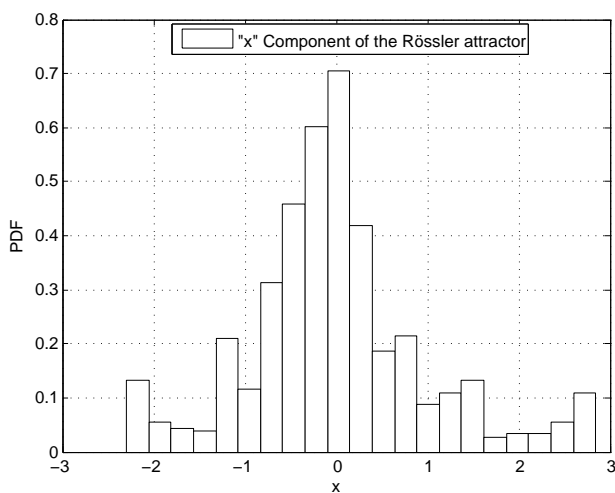


Fig. 1. "x" component of the Rössler attractor

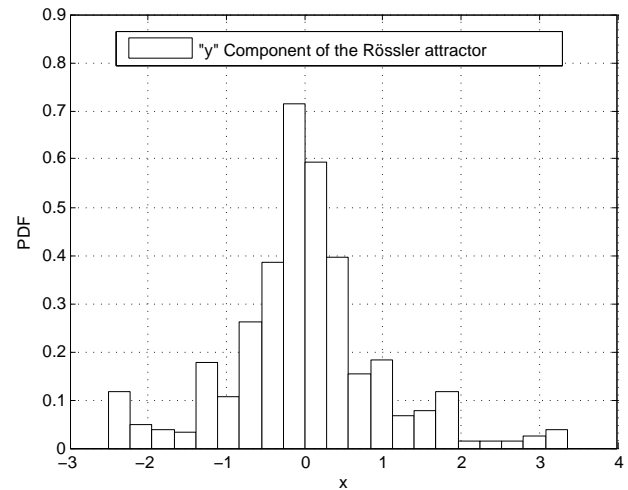


Fig. 2. "y" component of the Rössler attractor

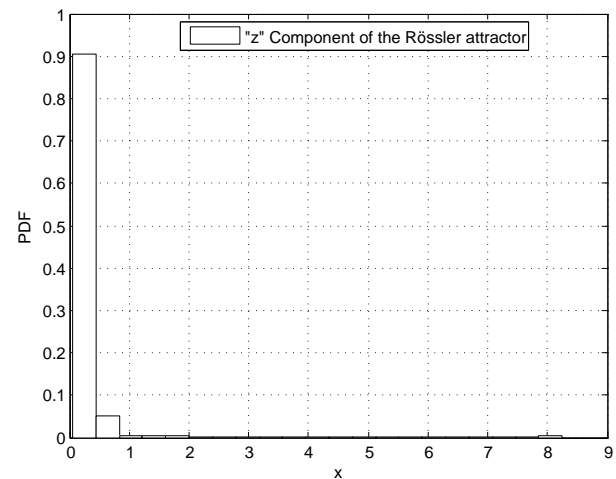


Fig. 3. "z" component of the Rössler attractor

One can see, that the components "x" and "y" are "oppositely" symmetric (see also (8)), and have unimodal PDF'S with $\gamma_4 > 0$, i.e. the vertices of the distributions are "sharper", than the Gaussian ones.

We can see that the component z can be approximated by means of a delta- function.

For "x" and "y" components we describe the PDF histograms by means of the Laplace distribution defined by:

$$f(x) = \frac{1}{2\lambda} \exp\left\{-\frac{|x - \mu|}{\lambda}\right\}.$$

This distribution is characterized by location μ (any real number) and scale λ (has to be greater than a 0) parameters. The use of Laplace distribution allows to make a right description for the “x” component and “y” components of the Rössler attractor as it is observed in Figures 4 and 5.

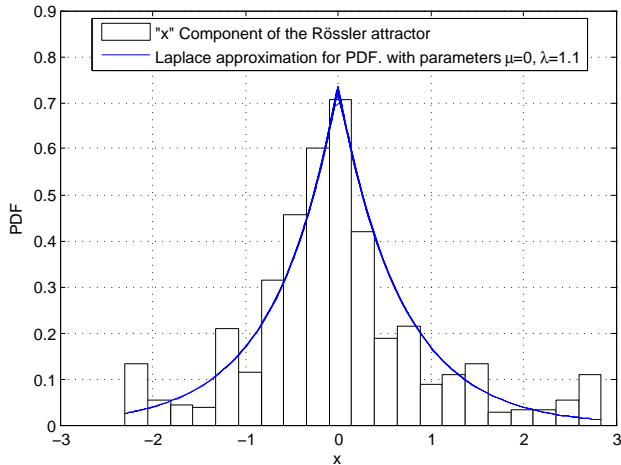


Fig. 4. “x” component of the Rössler attractor

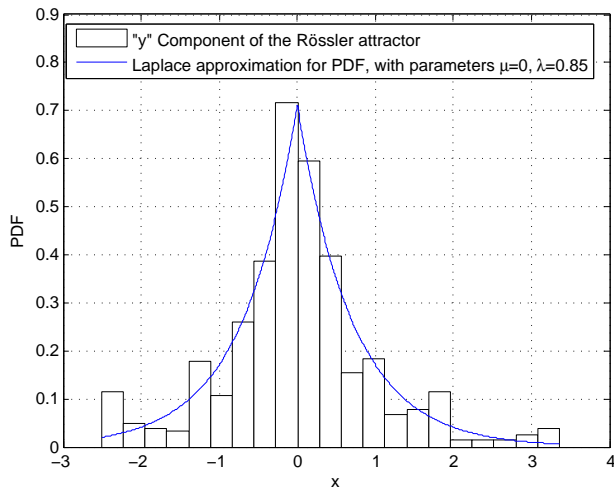


Fig. 5. “y” component of the Rössler attractor

Then, as it follows from Figures 4 and 5, the (PDF), for the “x” component of the Rössler attractor is approximated by a Laplace distribution with the local parameter $\mu = 0$ and scale parameter $\lambda = 1.1$ and for the “y” component with local parameter $\mu = 0$ and scale parameter $\lambda = 0.85$.

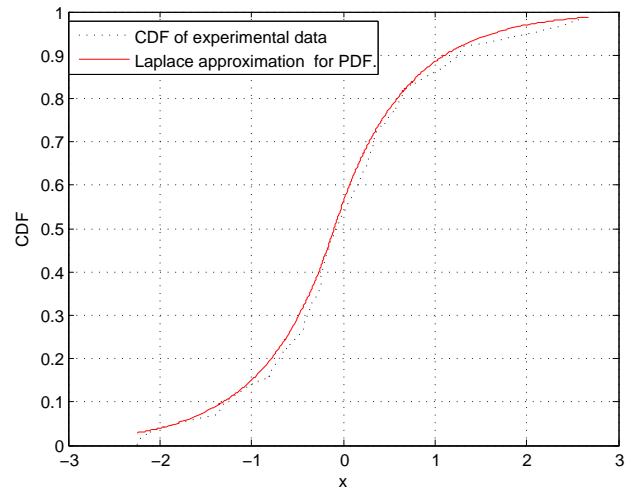


Fig. 6. CDF of the “x” component using the Laplace approximation

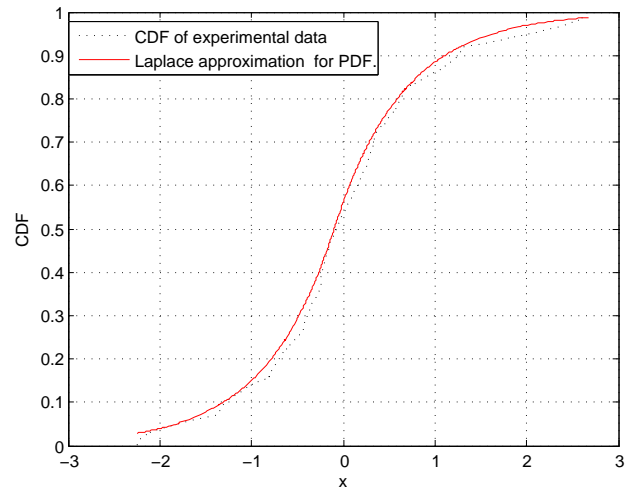


Fig. 7. CDF of the “y” component using the Laplace approximation

In Figures 6 and 7, we apply the Kolmogorov-Smirnov goodness of fit test with a significance level $\alpha = 0.05$, in order to examine whether the accuracy of the PDF of the “x” and “y” components of the Rössler attractor and its approximation using the Laplace distribution are adequate or not. As it can be seen from the figures 6 and 7, the approximation can be considered as acceptable.

In Figures 8 and 9, the results of the approximation of the PDF for the “x” and “y” components of the Rössler attractor by means of the Gram-Charlier series and the model distribution (2) (both with $\gamma_2 > 0$), are represented.

One can see, that, as it was commented before, the Gram-Charlier approximation is more precise, than the expression (2), because of $\gamma_2 > 0$.

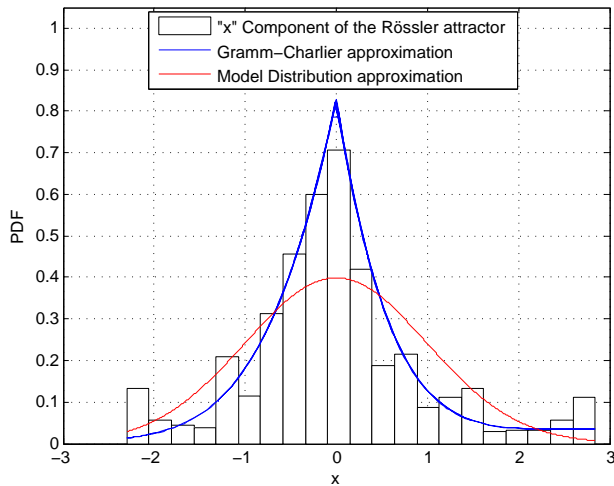


Fig. 8. The “x” component of the Rössler attractor with the Laplace and model distribution approximations.

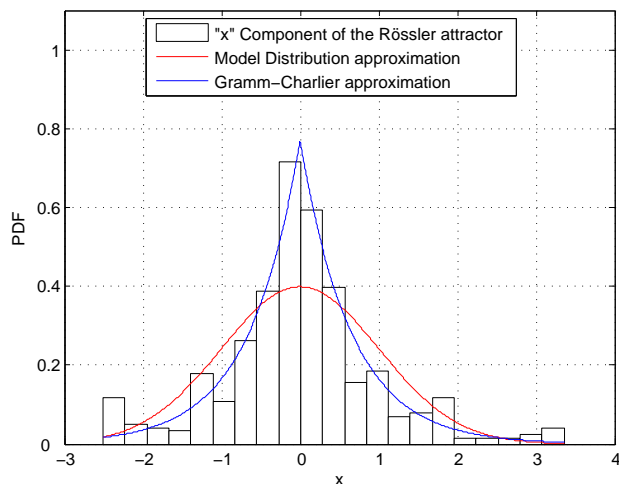


Fig. 9. The “y” component of the Rössler attractor with the Laplace and model distribution approximations.

V. APPROACH FOR VARIANCE CALCULATION

By considering the results presented in previous sections we realize that the approximations obtained by applying the cumulant method are really good.

As it is emphasized above, the first four cumulants for the Rössler attractor depend on the evaluation of the variance χ_2 that is based on the Kolmogorov-Sinai H_{k-s} entropy.³ The H_{k-s} entropy is defined by the sum of the Lyapunov exponents for a non-linear system [9, page

³Considering that K-S entropy can't be exactly calculated, it is impossible by using this method to obtain an exact result for variance. Nevertheless, assuming that for practical purposes an error about 10-20% is acceptable, we are able to apply this method.

122]. For a linear matrix the Lyapunov exponents are defined by its eigen-values [9, pages 542-543].

In the proposed methodology we compare the differential entropy obtained from the PDF approximation for a component of the Rössler attractor, with the H_{k-s} entropy computed through the parameters of the attractor (Lyapunov exponents).

Note, (see in the following) that in the framework of this analysis H_{k-s} coincides with the Kolmogorov differential entropy of the PDF [9, pages 542-543, 839].

The proposed methodology can be summarized as follows.

- 1) The non-linear system describing the chaotic behavior of the Rössler attractor has to be statistically linearized [9, p 760].
- 2) The eigen-values must be found from the coefficients matrix formed by the linearized system.
- 3) Once the eigen-values have been obtained, the H_{k-s} for the dynamic system can be estimated as follows:

$$\log|\lambda_{max}| < H_{k-s} \leq \sum_{j=1}^m \log|\lambda_j|, \quad (13)$$

where, $j = \overline{1, m}$, λ_j - is the j -th eigen-value of the linear matrix and $\log|\lambda_j|$ - is the j -th Lyapunov exponent for the linear matrix [9, p 542].

- 4) On the other hand the Kolmogorov differential entropy is:

$$h_{dif} = - \int_{-\infty}^{\infty} W(x) \log[W(x)] dx, \quad (14)$$

where $W(x)$ is the PDF of the output signals whose parameters have to be represented through χ_2 .

- 5) Then, we create an algebraic equation depending on the variance according to steps 3 and 4.
- 6) Solving equation from steps 3 and 4, we can have now a solution for variance.

It is worth mentioning, that as the whole Kolmogorov-Sinai entropy is addressed to the given component of the Rössler attractor the value of the variance obtained from the approach is actually its upper bound. The lower bound can be found applying the left hand side of the inequality (12).

Here we present the results of the application of this method for the Rössler attractor considering only the x component. From equation (5) we can obtain a linearized system as it was mentioned in step 1. From step 2, we obtain the coefficient matrix \mathbf{A} of this linearized system as:

$$\mathbf{A} = \begin{vmatrix} 0 & -1 & -1 \\ 1 & a & 0 \\ 0 & 0 & -c \end{vmatrix}$$

Matrix \mathbf{A} has a determinant different from zero, for this reason we can obtain eigen-values, considering $a = 0.2$ and $c = 5.7$. The characteristic equation becomes:

$$\lambda^3 - (a - c)\lambda^2 - (ac - 1)\lambda + c = 0,$$

where $\lambda_1 = -5.7$, $\lambda_2 = 0.1 + j$ and $\lambda_3 = 0.1 - j$.

Note, that the main eigen-value λ_1 is equal to the parameter c .

Having the results for the eigen-values, and substituting λ_1 into (12), we can obtain a numeric value for the entropy as $H_{k-s} \approx 1.74$.

And for steps 3 and 6 it follows:

$$\chi_2^x = \frac{\exp(3.48)}{2e^2} = 2.1.$$

From the Fig. 4 it follows, that $\chi_2^x \approx 2$ and the error is 5%.

A. Some Modifications

In the previous material it was assumed that the parameters of the Rössler strange attractor are predefined as well as the PDF's for the output signals.

Here we'll consider a more general case. Let us suppose, that the set of parameters of the strange attractor and the PDF's are not predefined, but the chaotic regime of the attractors is established.

Then one can apply for the PDF choice the so-called "Maximun Entropy Method (MEM)" [10]. If the attractor of interest can be characterized by the symmetric PDF's, then it can be applied as a MEM distribution Gaussian PDF.

From the MEM principle it follows, that for the given H_{k-s} for Gaussian PDF, the evaluated χ_2 has to be a lower boundary for its true value.

As it was mentioned before if one of the positive Lyapunov exponents predominates it is possible to apply for the lower boundary for χ_2 the inequality $H_{k-s} > \log|\lambda_{max}|$. If all values for positive Lyapunov exponents are comparable, then for the lower boundary evaluation it is possible to assume $\frac{1}{3}H_{k-s} \leq \sum_i \log|\lambda_i|$, if the strange attractor consists of three equations and we assume that all components are statistically independent.

It follows from (12), that the variance χ_2 obeys the following inequality:

$$\chi_2 \geq \frac{10^{2H_{k-s}}}{2\pi e} \quad (15)$$

For the Rössler attractor $\chi_2^x \geq 1.8$ (true value is 2)

VI. SOME COMMENTS OF THE SECTION V

The material of the section V shows that through the ordinary equations of strange attractors and their statistical linearization it is possible to obtain analytical estimations of the Lyapunov exponents of the non-linear dissipative system describing the attractor. After the Lyapunov exponents are found it is possible to get a well known approximation for the Kolmogorov-Sinai entropy H_{k-s} .

On the other side, applying the attractors PDF's for the components of interest (from computer simulations) together with its analytical approximation, it is possible to find the Kolmogorov differential entropy (h_{dif}) wich practically coincides with H_{k-s} for the strange attractors under consideration. Finally, by solving a simple quadratic algebraic equation one can find $\chi_2 \geq 0$.

The approach shows acceptable accuracy for engineering evaluation of χ_2 (less than 20%) and it is completely analytical. Why it happened?

This means that it has to depend on the details of the stochastic set, dimension of the phase space, etc. (see [9,12], etc. for details) of the attractor.

For example if the dimension of the stochastic set D for the strange attractor is more that two, almost all phase trajectories, that constitute the strange attractor are localized in a very thin layer, i.e. it can be approximately represented by a one dimensional Poincare mapping (details can be found in [12]). It is actually true for Chua, Lorenz, Rössler etc. strange attractors as well (see [12], [14], etc).

So, any non-linear dissipative system with a dimension D equal or more than two represents a one-dimensional Poincare mapping (one dimensional dynamics) and one of the consequences of this is the similarity between H_{k-s} and the Kolmogorov differential entropy. Therefore, the acceptable accuracy of the proposed approach might be, in some sense, predicted.

Next, please, note that the dependence of χ_2^x on the parameters of the strange attractors (even in the framework of the predefined chaotic regime) is not trivial and it depends on the attractor's type. As it was shown above, the χ_2^x for the Rossler attractor clearly shows the dependence on the unique parameter c (see also [10]).

VII. CONCLUSIONS

- 1) A rather simple method for statistical analysis of the Rössler attractor, based on the "degenerate cumulant equations" was presented.
- 2) It was shown, that application of the cumulant analysis gives not only a qualitative picture of

the stochastic behavior of the attractor, but also a quantitative evaluation for cumulants.

- 3) Cumulants can be useful to obtain an approximation of the plot of PDF's of output signals for Rössler attractor.
- 4) The solution for variance for Rössler strange attractors presented in Section V results to be appropriate as a prediction for this parameter. The error in the calculation is considered permissible in the estimation approach as well.

ACKNOWLEDGMENT

The authors are pleased to pass their gratitude to Fernando Ramos for his help in the preparation of this paper.

APPENDIX

The concept of cumulant brackets was introduced as an abbreviated representation for any cumulant, i.e.

$$\begin{aligned} \chi_{m_1, m_2, \dots, m_n}^{\xi_1, \xi_2, \dots, \xi_n} &= \langle \xi_1, \dots, \xi_2, \xi_2, \dots, \xi_2, \dots, \\ \xi_n, \dots, \xi_n \rangle &\equiv \langle \xi_1^{[m_1]}, \xi_2^{[m_2]}, \dots, \xi_n^{[m_n]} \rangle \quad ; \end{aligned} \quad (16)$$

where ξ_1 appears inside the brackets m_1 times, ξ_2 appears m_2 times, and so on; for example, the third cumulant is $K_{1,2}^{\xi_1, \xi_2} = \langle \xi_1, \xi_2, \xi_2 \rangle$. Some useful features for cumulant brackets can be found in [5,11].

The relations between moments and cumulants as well as the relations between moment and cumulant brackets were discussed in an exhaustive way in [5,11]; the fact that by means of cumulants brackets it is possible to formalize the operations between random variables and their transformations (linear and nonlinear, inertial and non-inertial), in an easy way, was presented in [11] (see also [5] for some generalizations).

For the above presented material some features for cumulant brackets need to be taken into account [5,11]:

- 1) $\langle \xi, \eta, \dots, \omega \rangle$ is a symmetric function of its arguments.
- 2) $\langle a\xi, b\eta, \dots, g\omega \rangle = a \cdot b \cdot \dots \cdot g \langle \xi, \eta, \dots, \omega \rangle$, where a, b, \dots, g are constants.
- 3) $\langle \xi, \eta, \dots, \theta_1 + \theta_2, \dots, \omega \rangle = \langle \xi, \eta, \dots, \theta_1, \dots, \omega \rangle + \langle \xi, \eta, \dots, \theta_2, \dots, \omega \rangle$.
- 4) $\langle \xi, \eta, \dots, \theta, \dots, \omega \rangle = 0$, if θ is independent of $\{\xi, \eta, \dots, \omega\}$.
- 5) $\langle \xi, \eta, \dots, a, \dots, \omega \rangle = 0$.
- 6) $\langle \xi + a, \eta + b, \dots, \omega + g \rangle = \langle \xi, \eta, \dots, \omega \rangle$.

In addition to cumulant brackets it is necessary to introduce here the concept of Stratonovich symmetrization brackets: symmetrization brackets together with the

integer number in front of the brackets represent the sum of all possible permutations of the arguments inside the brackets. For example, the operator $3\{\langle \xi_1 \rangle \cdot \langle \xi_2, \xi_3 \rangle\}_s$ means that

$$\begin{aligned} 3\{\langle \xi_1 \rangle \cdot \langle \xi_2, \xi_3 \rangle\}_s &= \langle \xi_1 \rangle \cdot \langle \xi_2, \xi_3 \rangle \dots \\ &+ \langle \xi_2 \rangle \cdot \langle \xi_1, \xi_3 \rangle + \langle \xi_3 \rangle \cdot \langle \xi_1, \xi_2 \rangle \quad , \end{aligned} \quad (17)$$

where $\{\}_s$ is the notation for the Stratonovich symmetrization brackets. Rules for manipulations with cumulant brackets can be found in A2[5].

The relations between moments and cumulants for the same distribution $W(x)$ are well known (see, for instance, references [5,11]).

The following notation is also quite known: $\langle g(x) \rangle$, $\langle \xi_1 \cdot \xi_2 \rangle$, which denotes the operator of statistical average for $g(x)$ and for the product of two random variables ξ_1 and ξ_2 , respectively.

Following [5] we call this operator $\langle \cdot \rangle$ as moment brackets. The formal difference between moment and cumulant brackets is, that the first one contains a 'dot' between random variables (usually it is skipped), and the second one contains a 'comma' between variables.

REFERENCES

- [1] M. Hasler, G. Mazzini, M. Ogorzalek, afal (ed). "Applications of Nonlinear Dynamics to Electronics and Information Engineering", Proceedings of the IEEE (Special Issue), vol. 90, 2002.
- [2] M. Mijangos, V. Kontorovich. "Non-Gaussian perturbation modeling through Chua's attractor". XVI Int. Conference on Electromagnetic Disturbances, (EMD 2006). (Special Issue), vol. 90, 2002.
- [3] V. Kontorovich. "Applied Statistical analysis for strange attractors and related problems". Mathematical Methods in Applied Science. vol. 30, pp. 1705-1717, 2007.
- [4] M. Mijangos, V. Kontorovich, J. Aguilar-Torrenera. "Some Statistical Properties of Strange Attractors: Engineering View" Journal of Physics: conference series 96 012147, March 2008.
- [5] S. Primak, V. Kontorovich, V. Lyandres; "Stochastic Methods and their Applications to Communications. Stochastic Differential Equations Approach". John Wiley & Sons, Ltd. 2004
- [6] R. Radev "Full State Observer for Rossler's System". Int. IEEE symp. "Intelligent systems", 2002.
- [7] B. G. Kukharenco "Detecting orbits of high periods from numerical solutions of the Rossler system". Int. IEEE symp. "Phys Com.", 2005.
- [8] Eckman J.P., D. Ruelle. "Ergodic theory and Strange Attractors". Review of Modern Physics 1985;. vol. 57, (3 part 1), pp. 617-656.
- [9] A. Scott (ed). "Encyclopedia of non-linear sciences", N.Y. Rontledge, 2005.
- [10] A. Popoulis. "Probability, Random Variables, and Stochastic Processes", 3er. ed Boston, M.A, McGraw- Hill, 1991.
- [11] Malakhov AN. "Cumulant analysis of Random Non-Gaussian Process and their Transformation". Sovetskoe Radio: Moscow, 1975 (in Russian).
- [12] A. Nayfeh and B. Balanchandra "Applied non-linear dynamics". John Wiley & Sons, Ltd, 1995.
- [13] M. Rabinovich and D. Trubetskov. "Introduction to Oscillation Theory". "Nauka", Moscow, 1984. (In Russian):. pp. 617-656.

- [14] R. Badit, A. Politi "Statistical Description of Chaotic Attractors: The Dimension function". "Journal of statistical Physics. vol.40, (5/6) 1985, pp.725-749.



Luis Alberto Cruz Beltrán was born in Tehuantepec City, México, in 1983. He received B.Sc. in Communications and Electronic Engineering from Instituto Politécnico Nacional in 2005 and currently is working toward the M.Sc. degree in Telecommunications in the area of communications at Instituto Politécnico Nacional. Since 2007 he works at the Research and Advanced Studies Center (CINVESTAV-IPN) campus México City.



Valeri Kontorovitch was born in Sverdlovsk, Rusia. He received the M.S.E.E. (1963), Ph. D. (1968) and Dc. Sc. (1987) degrees all from St. Petersburg State University of Telecommunications (St. Pt. UT). From 1964 to 1965 he was Technical Staff member of the State Radio Institute. In 1965, he joined the St. Pt. UT, where in 1976 he founded the Laboratory of Electromagnetic Compatibility (EMC lab). In 1984 the laboratory was transformed into branch lab of the ministry of telecommunications of the former USSR. Since 1988 he is full professor and was head of department of radio receivers and EMC form 1992 to 1995. Since 1993 he is full professor at the Research and Advanced Studies Center (CINVESTAV) of the National Polytechnic Institute (IPN) in México. His present interest are electromagnetic compatibility of radio communication systems, interference analysis, channel modeling and statistical theory of communications. He has published six books and more than 200 journal and conference papers. He holds 17 patents. He is member of the Mexican Academy of Sciences and Fellow of the IEEE.



Zinaida Lovtchikova obtained her Ms. degree from Leningrad State University in 1972 and her Ph.D degree from Leningrad "LenSovet" Technological Institute in 1983. Currently she is full professor of UPIITA-IPN (México) and her research activities are dedicated to stochastic methods in bioelectronics.

Detecting dynamical interdependence and generalised synchronisation using the Lorenz method of analogues.

Erik Casagrande

Neural Computing Research Group
School of Engineering and Applied Science
Aston University
Email: casagrae@aston.ac.uk

David Lowe

Neural Computing Research Group
School of Engineering and Applied Science
Aston University
Email: d.lowe@aston.ac.uk

Avgis Hadjipapas

The Wellcome Trust Laboratory
School of Life and Health Sciences
Aston University
Email: hadjipaa@aston.ac.uk

Abstract— We provide results comparing two new methods based on different embedding space approaches to infer directional interdependence between bivariate time series, such as the transition to synchronisation. Both methods share a common identification stage which models the underlying generator of each single observable data. This consists of two parts: state space reconstruction, and local model fitting using a class of kernel density estimation methods which is an extension of Lorenz Analogues techniques. The mutual information derived from the density estimation is used to compare the two approaches and is tested on coupled dynamical systems for which the interdependence is controlled.

I. INTRODUCTION

Identifying dynamical directional interdependence among multivariate time series is an important problem in many scientific fields such as engineering, econometrics, biology and biomedical analysis. Generally, the mathematical formulation of the underlying generator of the observed signals is not known a priori and their coupling needs to be inferred using observational data. This latent generator can be represented by a composite interplay of many subsystems which can result in a global complex collective behaviour. Instead of the complete statistical description of hidden systems, it can be sufficient to estimate information about the relationship between observed signals. An accurate analysis of these relationships can bring about useful inference regarding the hidden connections inside the underlying generator.

The nonlinearity of the system is a further complication which is common in nature and can make the generator dynamics more difficult to analyse. Linear tools such as correlation or Fourier analysis have limitations for uncovering nonlinear couplings. Instead, in the literature, nonlinear interdependence concepts such as causality or synchronisation are being used to construct a framework which, in this work, we use as the motivational background for our study.

Causality has been the subject of debate due to different views around its nature and interpretation. While an empirical idea of cause and effect is relatively easy to comprehend, its practical translation can lead to an algorithmic representation providing many issues (see [1] for a discussion). Granger [2]

based on ideas from Wiener, studied a particular class of linear stochastic systems where a plausible definition of causality proposed a statistical framework of analysis. Given two observable time series x and y from systems \mathcal{X} and \mathcal{Y} , if a k -step ahead predictor of x_i using the past observable of x_i and y_i together increases the predictability likelihood over a predictor using only x_i , then we can say that \mathcal{Y} and \mathcal{X} are causally related. Depending on the flow of information in predicting \mathcal{Y} from \mathcal{X} or \mathcal{X} from \mathcal{Y} allows us to infer directionality of coupling. From a different point of view, we can express the same concept in a probabilistic way,

$$\text{If } P(x_{i+k}|x_i^-, y_i^-) \neq P(x_{i+k}|x_i^-) \quad \mathcal{Y} \text{ causes } \mathcal{X} \quad (1)$$

where x_i^- and y_i^- are the past time series of the systems prior to the time i and x_{i+k} is the k -step ahead predictor. Using a linear stochastic system, a totally admissible algorithmic choice [2] which has been largely used, based on (1) uses the conditional variance of the prediction error, i.e., $\sigma(x_{i+k}|x_i^-, y_i^-)$ and $\sigma(x_{i+k}|x_i^-)$. The Granger implementation was based on ARMA modelling and has been employed in many data analysis domains, including, econometrics [3] [4] and recently neuroscience [5]. Since for a linear system the autocorrelation and Fourier spectrum are related by the Wiener-Khinchin theorem, we can find implementations of causality measures based on coherence [2]. Recent studies have addressed the nonlinear analysis issue using an extension of Granger causality based on nonlinear predictor modelling [6], [7], [8]. Other approaches using entropy (for a review see [9]) have been developed. In [10] (1) has been called the *measure of deviance from the Markov property* which leads to the concept of Transfer Entropy.

Most of the methods we have listed above for causality discovery containing nonlinear systems make use of a preprocessing stage based on State Space Reconstruction [11]. This approach has become a popular solution in order to learn the underlying dynamical structure which generates the observable time series. We use this technique in this paper to build the

reconstructed state space in which we run the modified Lorenz analogues approaches.

Defining *synchronisation* has been less empirical due its historical focus on periodic system such as relaxation oscillators in which phase contains the information needed to infer interdependence and synchronisation. In the last two decades, it has been shown [12] that chaotic systems can identically synchronise and other levels of definition needed to be introduced [13]. One of the reasons was the query of how to define the phase of a chaotic signal. There are different measures of synchronisation and we refer to the literature [14], [15]. In this work, we focus on a class of methods which are related to the concept of *Generalised Synchronisation* [16]. Two systems are synchronised if it is possible to find a smooth function Ψ which relates the two state-spaces of the underlying generators of \mathcal{X} and \mathcal{Y} , i.e., $\mathbf{Y} = \Psi(\mathbf{X})$, where \mathbf{X} and \mathbf{Y} are the state spaces of \mathcal{X} and \mathcal{Y} . A set of possible measures of generalised synchronisation have been explored using the concept of mutual neighbours in the reconstructed or embedding state spaces which we denote here as $\hat{\mathbf{X}}$ and $\hat{\mathbf{Y}}$. In [17], the author projects the local structure of one reconstructed state space, i.e. $\hat{\mathbf{X}}$, on the other, i.e. $\hat{\mathbf{Y}}$ in order to search for generalised synchronisation. Other similar measures can be found in [18] and [19] in which the *Synchronisation Likelihood* is defined. In [20] the procedure of mutual neighbours is used to build a simple nonlinear predictor in state space.

In this paper, we compare two nonlinear approaches to interdependence analysis motivated by a local nonlinear mapping version of the Lorenz method of analogues. The Lorenz technique was originally a simple way to build a predictor in the reconstructed space. We first consider here a novel version of the Lorenz algorithm which uses a kernel density estimation techniques in order to compensate nonlinearity of the underlying generator of the data. This particular predictor models the conditional distributions required in (1) which we employ to check, using the deviation of the Markov property, the information flow between the two time series generators. In the second part, we investigate two possible ways we found in literature, to obtain the joint information of the past sets x_i^- and y_i^- on the left hand side of (1). The causality literature suggests approaches based on joining the sets x_i^- and y_i^- obtaining a larger dimensionality set $x_i^- \oplus y_i^-$ based on a 'direct sum' generator space. Instead, using an approach emphasized for example in [20] [19], we use a method based on mutual mappings between local neighbours in the two spaces which we denote by $P(x_{i+1}|x_i^-, y_i^-) = P(x_{i+1}|x_i^- \star y_i^-)$ with \star the notation that we use to define the mutual neighbours mapping operator, to be discussed later.

In the following section, we define the approach we use to construct nonparametric predictors in embedding space using the Lorenz method of analogues. We define in the second part the mutual predictors using the two different approaches using \oplus , \star operators. We employ a Granger like statistic to check the deviance to the Markov property in (1) as our measure of directed interdependence. We illustrate the approach using

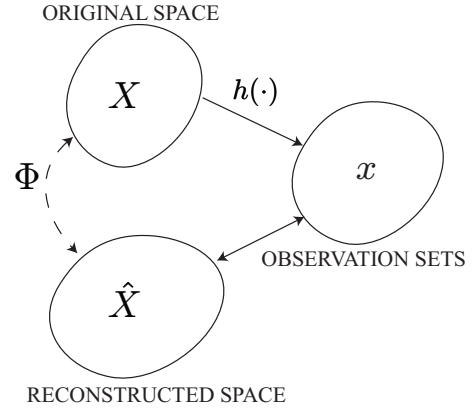


Fig. 1. The dynamics of the underlying generator described by the space \mathbf{X} are projected to the observable subspace x by the function $h(\cdot)$. A space Reconstruction algorithm uses the time series point in x to build an equivalent space $\hat{\mathbf{X}}$ of \mathbf{X} up to a diffeomorphic function $\Phi(\cdot)$.

synthetic examples where we have control over the coupling.

II. METHODS

A. Nonlinear modelling

We consider two finite dimensional dynamical systems \mathcal{X} and \mathcal{Y} which describe our underlying generators of the data. Using the state space representations in (2-3), we assume the dynamics of the system is described by stochastic differential equations $f_{\mathcal{X}}(\cdot)$, $f_{\mathcal{Y}}(\cdot)$ and the measure functions $h_{\mathcal{X}}(\cdot)$, $h_{\mathcal{Y}}(\cdot)$ which defines the observable time series x_i and y_i .

$$\mathcal{X} = \begin{cases} \mathbf{X}_{i+1} & = f_{\mathcal{X}}(\mathbf{X}_i, \mathbf{Y}_i) + \xi_{\mathcal{X}} \\ x_i & = h_{\mathcal{X}}(\mathbf{X}_i) + \nu_{\mathcal{X}} \end{cases} \quad (2)$$

$$\mathcal{Y} = \begin{cases} \mathbf{Y}_{i+1} & = f_{\mathcal{Y}}(\mathbf{Y}_i, \mathbf{X}_i) + \xi_{\mathcal{Y}} \\ y_i & = h_{\mathcal{Y}}(\mathbf{Y}_i) + \nu_{\mathcal{Y}} \end{cases} \quad (3)$$

where ξ and ν are general stochastic terms which we consider additive and uncorrelated with each other. The observable time series are the quantities between which we want to infer interdependence which we consider here to be one-dimensional. As we introduced in the previous section, we use the bold notation, i.e. \mathbf{X} , to define a vector space while the indexed bold one, i.e. \mathbf{X}_i , to specify an element. The lower notation, i.e. x , indicates the corresponding observable time series.

We proceed to the nonlinear modelling of x and y using a two stage identification procedure. In the first part, we use a *State Space Reconstruction* which we described (1). For each time point i of the time series, we construct an M -dimensional space from the vectors $\hat{\mathbf{X}}_i = (x_i, x_{i+\tau}, \dots, x_{i+(M-1)\tau})$ and $\hat{\mathbf{Y}}_i = (y_i, y_{i+\tau}, \dots, y_{i+(M-1)\tau})$ where τ is the delay parameter [21]. In order to simplify the analysis, in this paper we assume that both \mathcal{X} and \mathcal{Y} are embedded in the same dimension M and have common delay τ . For a linear stochastic system, the dimension of the spaces $\hat{\mathbf{X}}_i$ and $\hat{\mathbf{Y}}_i$ are related by the order of the model which can be retrieved for autoregressive representations by the AIC criterion [22], for

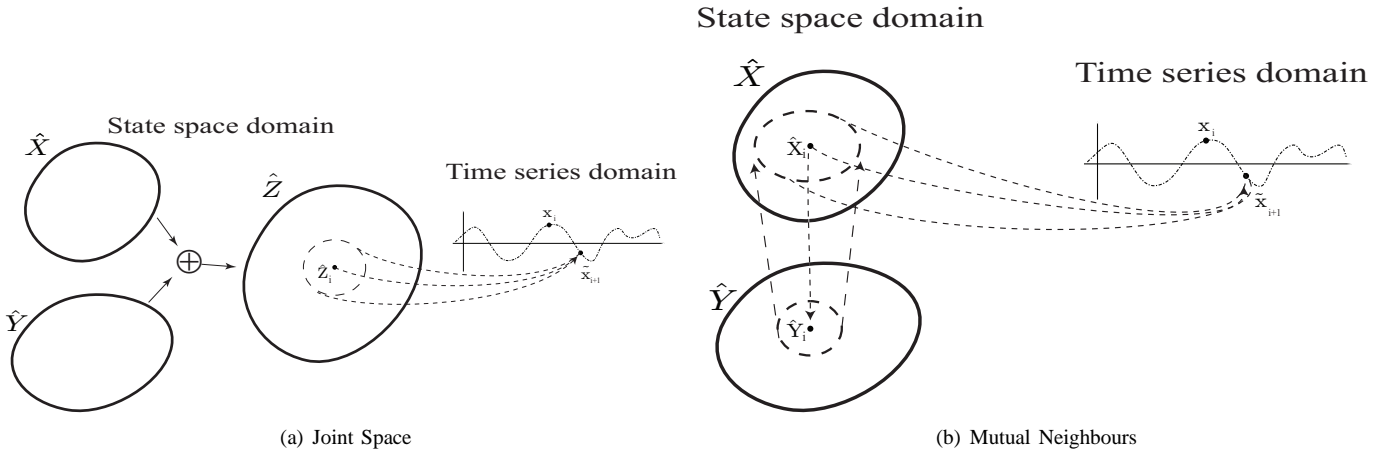


Fig. 2. Graphical comparison between the two approaches we use to extract the conditional joint distribution between the two reconstructed spaces.

instance. In nonlinear time series analysis, Takens [11] showed that under the sufficient condition that $M \geq D + 1$, the space $\hat{\mathbf{X}}$ and the space of the vectors \mathbf{X} are an *embedding*, i.e., they are related by a diffeomorphic map Φ . We have that D is the dimension of the limit set of \mathbf{X} or the attractor of (2-3).

The previous property leads to a useful fact for the purpose of building a prediction model which we consider as the second identification stage. The projection over the observable space x of the true joint distribution of the data $p(\mathbf{X}, x)$ can be retrieved using $p(\hat{\mathbf{X}}, x)$ instead, thanks to the diffeomorphic condition between $\hat{\mathbf{X}}$ and \mathbf{X} . In this work, we model $p(\hat{\mathbf{X}}, x)$ (the same for $p(\hat{\mathbf{Y}}, y)$) using a class of kernel density estimation methods based on Parzen estimators from which we can derive the following conditional expectation (see [23] for details):

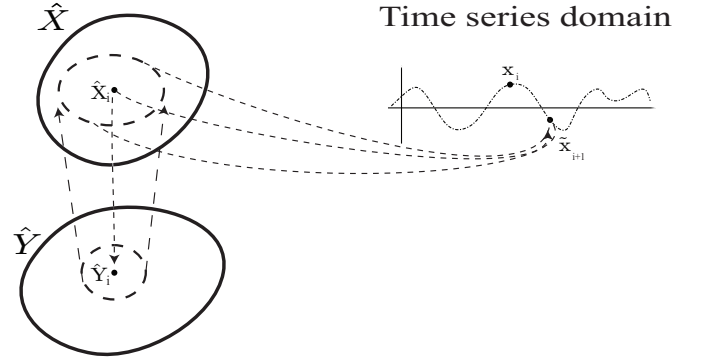
$$\tilde{x}_{i+k} = E(x|\hat{\mathbf{X}}) = \sum_{j=1}^N w(\hat{\mathbf{X}}_i, \hat{\mathbf{X}}_j) x_j \quad (4)$$

where \tilde{x}_{i+k} is the k -step ahead predictor of the time series point x given by the N -nearest points $\hat{\mathbf{X}}_j$ to $\hat{\mathbf{X}}_i$. The kernel function $w(\hat{\mathbf{X}}_i, \hat{\mathbf{X}}_j)$ is imposed to satisfy the summation constraint $\sum_{j=1}^N w(\hat{\mathbf{X}}_i, \hat{\mathbf{X}}_j) = 1$. If we choose the simplest kernel function as a constant, i.e., $w(\hat{\mathbf{X}}_i, \hat{\mathbf{X}}_j) = 1/N$, the approach is equivalent to the well-known *Lorenz method of Analogues* [21] or the *zero-th order predictor* [20].

A different choice of the kernel $w(\cdot, \cdot)$ can be used in order to increase the performance and the complexity of the predictor model. In this paper we continue with the Lorenz method, since the main goal is the comparison between the mutual predictors approaches defined by the operators \oplus and \star which we describe in the next section. We leave the performance analysis for causality discovery using different kernels as future development.

The approach we describe is an example of a *memory-based* method in the pattern recognition literature [23]. From the technique we use to build the reconstructed space, we have a one-to-one relationship between the spaces $\hat{\mathbf{X}}$ and

State space domain



(b) Mutual Neighbours

the observable space x that can be considered as a database. We further divided this database in two parts: a training set and a test set. Normally, the training set is used to learn the conditional probability $p(\hat{\mathbf{X}}, x)$ using a minimization algorithm which is then used on the test set to produce the predicted value \tilde{x} . Memory-based methods do not learn during the training stage but at each new embedding vector $\hat{\mathbf{X}}_i$ the algorithm needs to find the neighbours $\hat{\mathbf{X}}_j$ and project the neighbourhood structure on the correspond time series points x_j . Computationally, we have that memory based methods are fast in training, since they require only to build the set, but slow in prediction. In order to increase the performance of the algorithm, we need to build the training set using an optimal procedure. Algorithms which build the embedding space using K-D trees [24] can compute the neighbours problem in $O(K \log K)$ time compared to an unstructured solution. The complexity of the neighbours problem is $O(dK^2)$ if we need to compute the pairwise distance of K embedding d dimensional vectors.

The analogues algorithm requires parameters to be tuned such as the dimension of the embedding, the delay parameter and the number of neighbours. Using a different kernel function $w(\cdot, \cdot)$ could result in further parameters to choose. In the literature [21], there are several procedures developed to tune the embedding parameters M and τ . In this work, since the purpose of the predictor methods is not forecasting, but method comparison, we can use the available test set to drive the choice of the optimal parametrization of the algorithm. As described in the results section, we collect the time series for an offline interdependence analysis. The test set is known a priori and we consider a *Cross-Validation-Procedure* to choose the parameters which minimise the out-of-sample prediction errors in this set. The choice of using the test set in order to compute the prediction errors avoids the problem of model overfitting of the training data. We define the prediction errors as e_x, e_y .

B. Mutual Predictors

Following (1) and the Granger paradigm, considering one time series, i.e. x , we want to examine if the information gained by incorporating the other time series, i.e., y improves the nonlinear predictability of x . In the section above we modelled the conditional distribution of the right hand side of (1). In this part we are interested in devising a mutual predictor of x which takes into account the information of both embedding spaces $\hat{\mathbf{X}}, \hat{\mathbf{Y}}$ in order to model the left hand side of (1) and quantify the deviation from the Markov property.

As described in the introduction, in this paper we investigate two different approaches to gather mutual information from the reconstructed spaces $\hat{\mathbf{X}}$ and $\hat{\mathbf{Y}}$. The first one, which we refer to as the *Joint space approach* is depicted in Fig. (2) and it uses the direct sum space $\hat{\mathbf{Z}} = \hat{\mathbf{X}} \oplus \hat{\mathbf{Y}}$ where $z_i = (x_i, x_{i+\tau}, \dots, x_{i+(M-1)\tau}, y_i, y_{i+\tau}, \dots, y_{i+(M-1)\tau})$ is a double-dimensional concatenated embedding space. Using the space $\hat{\mathbf{Z}}$ we model the conditional probabilities $p(\hat{\mathbf{Z}}, x)$ and $p(\hat{\mathbf{Z}}, y)$ using the kernel analogues approach we discussed in the previous section. This mutual predictor for the case of $p(\hat{\mathbf{Z}}, x)$ assumes the following expression

$$(\tilde{x}|xy)_{i+k} = \sum_{j=1}^N w(\hat{\mathbf{Z}}_i, \hat{\mathbf{Z}}_j) x_j \quad (5)$$

where $\hat{\mathbf{Z}}_j$ are the N -nearest neighbours of $\hat{\mathbf{Z}}_i$.

For the second approach, the *Mutual neighbours approach*, we employ an alternative notation using the operator $\hat{\mathbf{X}} \star \hat{\mathbf{Y}}$ to extract mutual information from the two reconstructed spaces $\hat{\mathbf{X}}$ and $\hat{\mathbf{Y}}$. Figure (2) depicts this approach. We consider the embedding vector $\hat{\mathbf{X}}_i$ at time point i and we search for the corresponding counterpart $\hat{\mathbf{Y}}_i$ in the partner space. We then obtain the N -nearest neighbours of $\hat{\mathbf{Y}}_i$ in the partner space and we gather the respective set of time points, i.e. $\hat{\mathbf{Y}}(j)$. We choose the mutual set of neighbours back in the original $\hat{\mathbf{X}}$ space corresponding to the $\hat{\mathbf{Y}}$ -space neighbours $\hat{\mathbf{Y}}(j)$ and we build the following mapping predictor

$$(\tilde{x}|xy)_{i+k} = \sum_{j=1}^N w(\hat{\mathbf{X}}_i, \hat{\mathbf{X}}_{\hat{\mathbf{Y}}(j)}) x_{\hat{\mathbf{Y}}(j)} \quad (6)$$

As in the previous section, we compute for (6) and (5) the k -th step prediction out-of-sample errors on the test set. We denote this error as $e_{x|xy}$ and $e_{y|xy}$, respectively.

From the construction of the algorithms, we emphasise that the mutual neighbours approach is computationally faster than the joint space approach. Joining the two spaces needs an additional searching procedure for neighbours in the new higher dimensional space $\hat{\mathbf{Z}}$. Instead, the mutual neighbours technique can re-use the local structure which has been computed for each $\hat{\mathbf{X}}$ and $\hat{\mathbf{Y}}$ separately.

C. Interdependence Analysis

In the final step, we need to employ a measure of interdependence which quantifies the deviation away from the Markov property in (1). As discussed in the introduction, the

conditional probabilities are usually substituted by the variances of the prediction errors which in this case are estimated from (4) and (5) or (6) for the conditional probabilities. This choice is valid if we consider the system has been generated by a linear stochastic component. In this work, we model the underlying generator of the data using a local linear kernel mapping which is consistent with this assumption.

The Granger literature, for example [3] [25], has largely discussed different statistical significance tests in order to check the difference between single and mutual predictability. A comparison of significance tests can be found in [26]. In this work we employ the following measure which has been used in [6]:

$$G_{y \rightarrow x} = \ln \left(\frac{\sigma_x^2}{\sigma_{x|xy}^2} \right). \quad (7)$$

where σ_x^2 and $\sigma_{x|xy}^2$ are respectively the variance of the single and the mutual prediction errors. Similarly, we compute the term $G_{x \rightarrow y}$ using σ_y^2 and $\sigma_{y|xy}^2$ to check for the inverse link. A potential difference between $G_{y \rightarrow x}$ and the equivalent $G_{x \rightarrow y}$ therefore provides a test for directionality of the coupling which we define as the *differential Granger measure* $\Delta G = G_{x \rightarrow y} - G_{y \rightarrow x}$. In [7], the authors proposed another index for bidirectional coupling $D = \frac{c_2 - c_1}{c_1 + c_2}$ where $c_1 = \sigma_x^2 - \sigma_{x|xy}^2$ and $c_2 = \sigma_y^2 - \sigma_{y|xy}^2$ but we leave this index for future comment.

III. RESULTS

We consider two numerical experiments of nonlinear systems common in the literature to compare interdependence behaviour. We consider here a quantitative study of the two approaches introduced previously. During the simulation, we discard the first 10^4 synthetically generated samples (the 'burn-in' samples) and we divide the rest into 20 sets of 1000 points. On each set we construct the models discussed previously. We further partitioned each set into two subsets of 700 samples for the training and 300 for the test procedures. In the following discussion, we compute the mean and standard deviation of the differential Granger measure ΔG computed over the 20 sets for one-step ahead predictors.

A. Logistic map

We consider first a unidirectional coupled logistic map which has been described in [7]:

$$\begin{aligned} \mathcal{X}: \quad x_{i+1} &= ax_i(1 - x_i) + s\eta_{i+1} \\ \mathcal{Y}: \quad y_{i+1} &= (1 - C)ay_i(1 - y_i) + Cax_i(1 - x_i) + s\xi_{i+1} \end{aligned} \quad (8)$$

where η and ξ are unit variance Gaussian distributed noise and s controls the strength of the noise terms. The parameter $a = 3.8$ has been chosen. The coupling can vary between $C = 0$ and $C = 0.5$ for the noiseless case. In Fig (7), we plot the synchronisation pattern for different coupling strengths

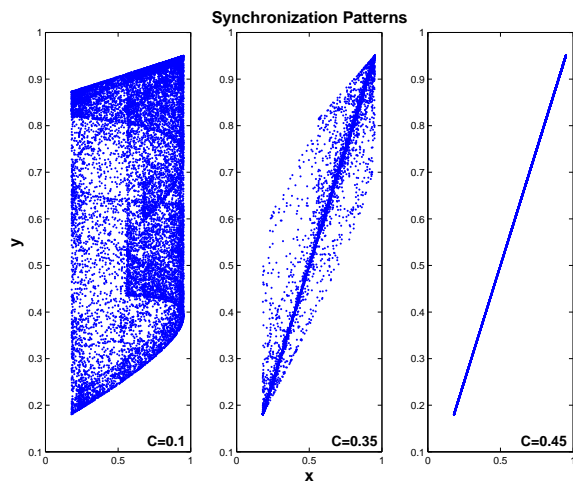


Fig. 3. Synchronisation patterns x vs y for the noiseless coupled logistic map for different values of coupling C . We notice perfect synchronisation for $C = 0.45$

of the map. The case of identical ('perfect') synchronisation occurs for $C > 0.35$, is evident in the figure.

In Fig (4), we consider the measure of ΔG for the two different embedding space treatments. For this particular map we perform a cross validation procedure and we choose $M = 1$ and $\tau = 1$. Moreover, we establish that two neighbours are sufficient to build the optimal predictor model. Both of the methods find directional interdependence from \mathcal{Y} to \mathcal{X} without any particular difference in terms of value. In fact in Fig. (4) the positive value of ΔG indicates the direction of the information flow from \mathcal{Y} to \mathcal{X} . Both measures fail to find any directionality when the two systems are in perfect synchronisation, which is intuitively correct. In this situation it should be impossible to distinguish any directional information flow between the systems.

We repeat the analysis for the coupled logistic map including a nonzero $s = 0.01$ random noise contribution. This value has been chosen so as not to distort the convergent evolution of the systems in (8-9). In Fig (5) we do not have, as in the previous case, perfect synchronisation but instead a 'noisy synchronisation' for $C = 0.45$. From the interdependence analysis in Fig (6) we can still find evidence for directionality in both approaches. Different from the zero-noise case, both methods find a non zero directional values for all studied couplings. However, the values of the two methods settle down to a different ΔG for high values of coupling. In the noisy synchronisation stage their behaviours are different.

B. Henon map

Next, we take the case of a 2D discrete system using the numerical simulations of two unidirectionally coupled Hénon maps which has been studied in several papers [20] [27] [18].

$$\mathcal{X} \begin{cases} x_{i+1} = 1.4 - x_i^2 + 0.3u_i \\ u_{i+1} = x_i \end{cases} \quad (10)$$

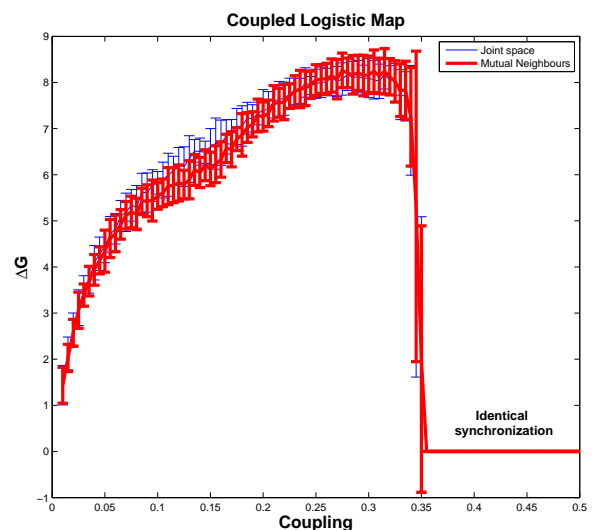


Fig. 4. Values of the directional Granger measure ΔG for different values of the coupling. The bold line is the mutual neighbours approach and the thin the joint space approach. $\Delta G > 0$ indicates the correct information flow from \mathcal{Y} to \mathcal{X}

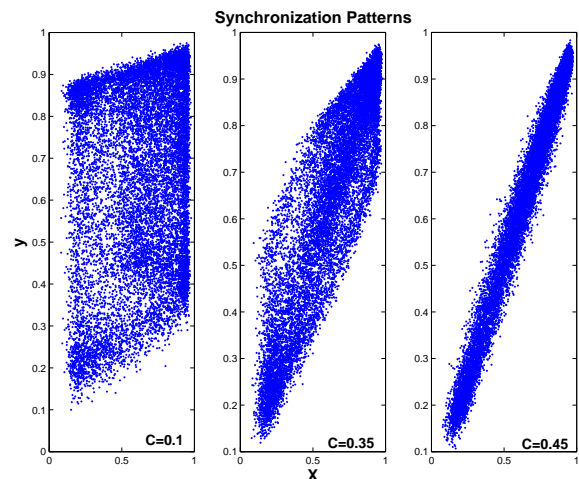


Fig. 5. Same plot of Fig (4) for the case of coupled logistic maps with noise level $s = 0.01$

$$\mathcal{Y} \begin{cases} y_{i+1} = 1.4 - (Cx_i + (1-C)y_i)y_i + Bv_i \\ v_{i+1} = y_i \end{cases} \quad (11)$$

Following the literature, the parameter $B = 0.3$ imposes two identical system while $B = 0.1$ is used for non-identical systems [20]. Here, we assume two identical systems. We vary the coupling parameter C between 0 and 1. For $C \simeq 0.8$ we observe the coupled system switching to perfect synchronisation. In Fig. (7) we show the synchronisation pattern for this example.

Using the values $M = 3$, $\tau = 1$ and we construct a predictor using 4 neighbours. These values were selected based on

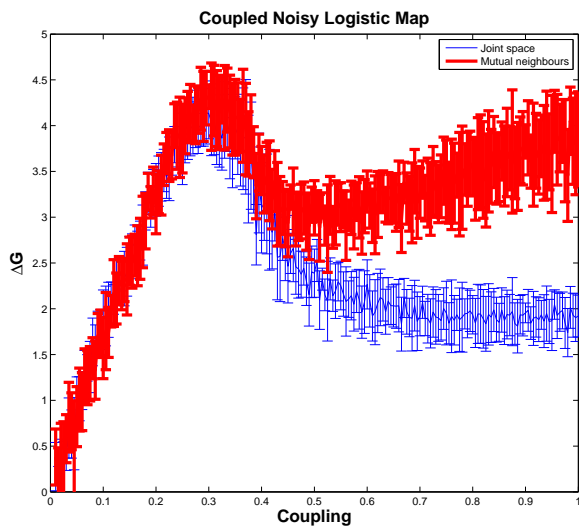


Fig. 6. Granger measure ΔG in the case of coupled logistic noisy map. Directionality can be found in the range of coupling we study. However in this case we notice a difference in the two approaches for high value of coupling.

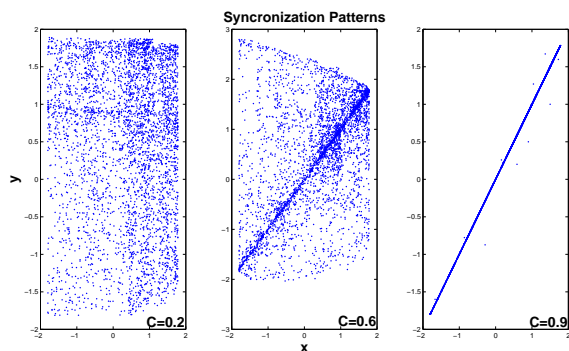


Fig. 7. Henon map Synchronisation pattern x vs y

cross validation. In Fig. (8) we show the differential Granger measure ΔG with respect to the two approaches. In this case, the higher complexity of the map even in the noiseless case, drives a difference in the two approaches for the value reached by ΔG . Importantly, for both cases we can find the correct directionality of the flow.

C. Chain of Tent maps

Our final example of increasing complexity is a chain of L one-dimensional tent maps. The coupling scheme has been studied in [10] and is given by

$$x_{i+1} = f(Cx_i^{l-1} + (1-C)x_i^l), \quad (12)$$

where l indicates the index of the chosen map in the chain. The tent map is given by

$$f(x) = \begin{cases} 2x & x < 0.5 \\ 2 - 2x & x \geq 0.5. \end{cases} \quad (13)$$

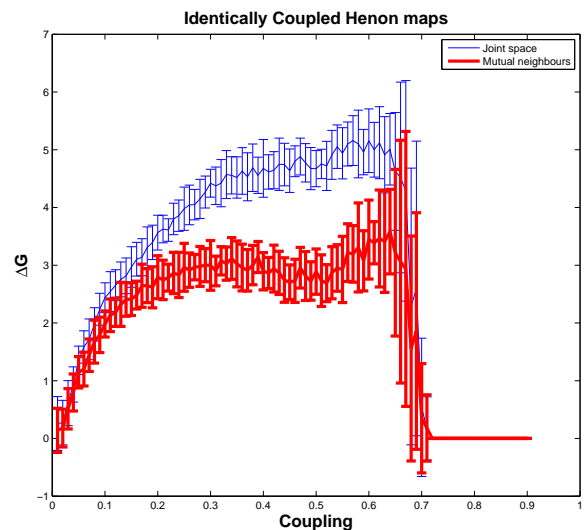


Fig. 8. Directional Granger measure ΔG

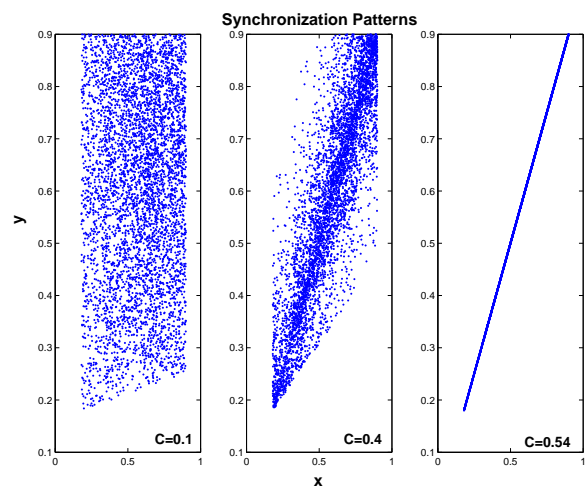


Fig. 9. Chain of tent maps with 2 elements. Synchronisation patterns x vs y .

In the following analysis, we consider the case where the number of maps L is increased from 2 to 5. Using the same paradigm as in the two previous examples, for each value of L we compute the joint space and the mutual neighbours Granger indices between the first and the last elements in the chain. We use $M = 1$, $\tau = 1$ and we construct the Lorenz analogues predictor using 4 neighbours. In Fig. (9), we plot the synchronization patterns between the first and the last element of a chain of $L = 2$ tent elements. We observe a transition to complete synchronization at the value of $C = 0.45$. In Fig. (10), we plot the synchronization pattern for $L = 4$. The transition to the complete synchronization stage is the same for $L = 2, 4$. From the plots in Fig. (9)(10), we notice that the results are less 'sparse' for $L = 2$, prior to complete synchronization.

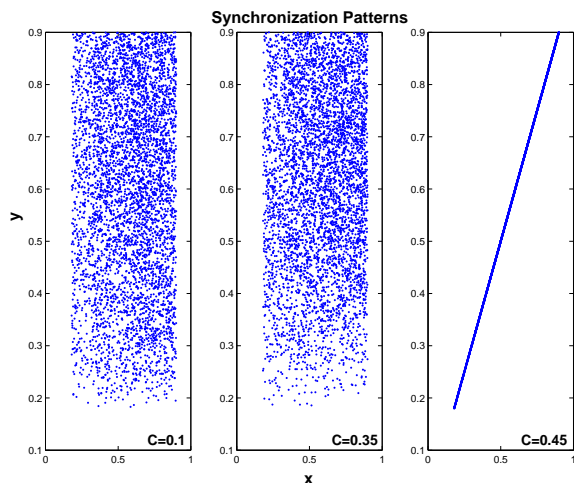


Fig. 10. Chain of tent maps with 4 elements. Synchronisation patterns x vs y .

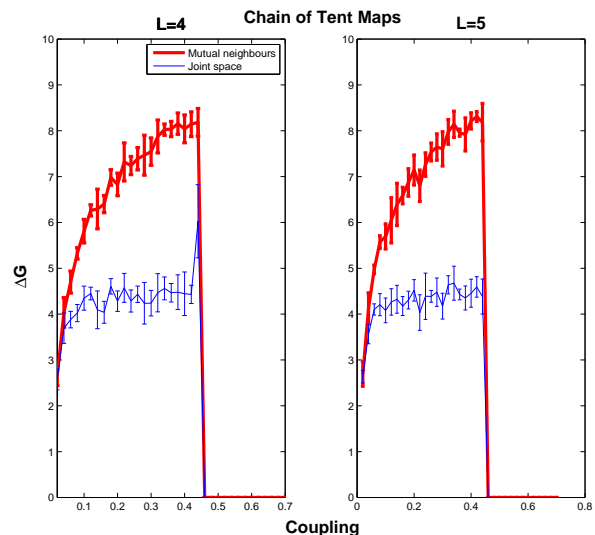


Fig. 12. Same plot as in Fig. (11) with $L = 4$ and $L = 5$.

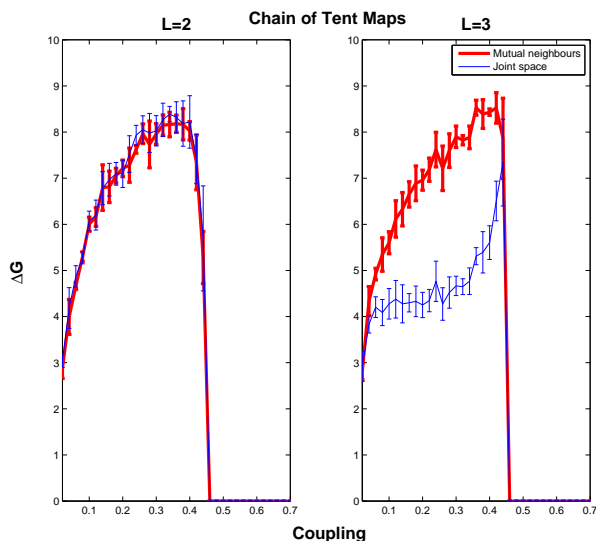


Fig. 11. Directional Granger measure ΔG for the case of $L = 2$ and $L = 3$ tent map elements. Increasing the number of elements results in a decreasing value of the joint space approach Granger index.

In Fig. (11), we show the results of the two differential Granger indices using $L = 2$ and $L = 3$ while Fig. (12) depicts the indices for $L = 4$ and $L = 5$. We notice that the behaviour of the mutual neighbours index does not modify its qualitative behaviour under an increase of the number of tent map elements. On the other hand, the joint space index decreases its value as the length L is changed. Nevertheless, both measures correctly find the true directional interaction in the chain.

IV. CONCLUSION

The goal of this work was to investigate two different state space approaches to infer dynamical directional interdependence between nonlinear time series of a latent complex sys-

tem. We based our comparison on the Granger approach given by the mutual predictability using (1). The two techniques we considered were the joint space approach, which is used in the causality literature and the mutual neighbours approach, which has been studied mainly for generalised synchronisation purposes.

In order to check predictability, in this work we employed a model which was equivalent to the Lorenz method of analogues based on a particularly simple form of interpolation of the conditional density estimation. For more general problems, the kernel model will need to be expanded to incorporate more useful kernels leading to an alternative formulation of the analogues approach. We are currently investigating different choices of kernels and their spatial extension in order to study local and global modelling of the reconstructed manifold.

From our qualitative investigation, based on synthetic examples, we conclude that the mutual neighbours approach performs as well as the joint space approach in finding directional interactions but with less computational load. The computational load is due to the choice of the density estimation algorithm which needs a procedure to search for analogues in the reconstructed space. From the examples we studied we have observed differences between the two approaches when the complexity of the underlying system is increased, although both methods correctly estimated the directionality of information flow. An analytical study of the difference between these two approaches is left for a future investigation.

ACKNOWLEDGMENT

The authors wish to acknowledge EPSRC project EP/D00036X/1 “Exploiting emergent collective behaviours in complex large MEMS systems”, for funding

REFERENCES

- [1] C. W. J. Granger, "Testing for causality : A personal viewpoint," *Journal of Economic Dynamics and Control*, vol. 2, no. 1, pp. 329–352, May 1980.
- [2] ———, "Investigating causal relations by econometric models and cross-spectral methods," *Econometrica*, vol. 37, no. 3, pp. 424–38, July 1969.
- [3] C. A. Sims, "Money, income, and causality," *American Economic Review*, vol. 62, no. 4, pp. 540–52, September 1972.
- [4] Z. A. Ozdemir and E. Cakan, "Non-linear dynamic linkages in the international stock markets," *Physica A: Statistical Mechanics and its Applications*, vol. 377, no. 1, pp. 173–180, Apr. 2007.
- [5] B. Gourevitch, R. Bouquin-Jeannes, and G. Faucon, "Linear and non-linear causality between signals: methods, examples and neurophysiological applications," *Biol. Cybern.*, vol. 95, no. 4, pp. 349–369, 2006.
- [6] Y. Chen, G. Rangarajan, J. Feng, and M. Ding, "Analyzing multiple nonlinear time series with extended granger causality," *Physics Letters A*, vol. 324, pp. 26–35, Apr. 2004.
- [7] N. Ancona, D. Marinazzo, and S. Stramaglia, "Radial basis function approach to nonlinear granger causality of time series," *Physical Review E (Statistical, Nonlinear, and Soft Matter Physics)*, vol. 70, no. 5, p. 056221, 2004.
- [8] W. A. Freiwald, P. Valdes, J. Bosch, R. Biscay, J. C. Jimenez, L. M. Rodriguez, V. Rodriguez, A. K. Kreiter, and W. Singer, "Testing non-linearity and directedness of interactions between neural groups in the macaque inferotemporal cortex," *Journal of Neuroscience Methods*, vol. 94, no. 1, pp. 105–119, Dec. 1999.
- [9] K. Hlavackova-Schindler, M. Palus, M. Vejmelka, and J. Bhattacharya, "Causality detection based on information-theoretic approaches in time series analysis," *Physics Reports*, vol. 441, no. 1, pp. 1–46, Mar. 2007.
- [10] T. Schreiber, "Measuring information transfer," *Phys. Rev. Lett.*, vol. 85, no. 2, pp. 461–464, Jul 2000.
- [11] F. Takens, "Detecting strange attractors," in *Lecture Notes in Mathematics*, D. Rand and L. Yang, Eds. Springer, 1981, vol. 898.
- [12] L. M. Pecora and T. L. Carroll, "Synchronization in chaotic systems," *Phys. Rev. Lett.*, vol. 64, no. 8, pp. 821–824, Feb 1990.
- [13] S. Boccaletti, J. Kurths, G. Osipov, D. Valladares, and C. Zhou, "The synchronization of chaotic systems," *Physics Reports*, vol. 366, pp. 1–101(101), August 2002.
- [14] R. Quiroga, A. Kraskov, T. Kreuz, and P. Grassberger, "Performance of different synchronization measures in real data: A case study on electroencephalographic signals," *Phys. Rev. E*, vol. 65, no. 4, p. 041903, Mar 2002.
- [15] A. Pikovsky, M. Rosenblum, and J. Kurths, *Synchronization : A Universal Concept in Nonlinear Sciences*. Cambridge University Press, April 2003.
- [16] N. F. Rulkov, M. M. Sushchik, L. S. Tsimring, and H. D. I. Abarbanel, "Generalized synchronization of chaos in directionally coupled chaotic systems," *Phys. Rev. E*, vol. 51, no. 2, pp. 980–994, Feb 1995.
- [17] J. Arnold, P. Grassberger, K. Lehnertz, and C. Elger, "A robust method for detecting interdependences: application to intracranially recorded eeg," *Physica D*, vol. 134, pp. 419–430(12), 1999.
- [18] R. Quiroga, J. Arnold, and P. Grassberger, "Learning driver-response relationships from synchronization patterns," *Phys. Rev. E*, vol. 61, no. 5, pp. 5142–5148, May 2000.
- [19] C. J. Stam and B. W. van Dijk, "Synchronization likelihood: an unbiased measure of generalized synchronization in multivariate data sets," *Phys. D*, vol. 163, no. 3, pp. 236–251, 2002.
- [20] S. J. Schiff, P. So, T. Chang, R. E. Burke, and T. Sauer, "Detecting dynamical interdependence and generalized synchrony through mutual prediction in a neural ensemble," *Phys. Rev. E*, vol. 54, no. 6, pp. 6708–6724, Dec 1996.
- [21] H. Kantz and T. Schreiber, *Nonlinear Time Series Analysis*. Cambridge University Press, November 2003.
- [22] P. J. Brockwell and R. A. Davis, *Time series: theory and methods*. New York, NY, USA: Springer-Verlag New York, Inc., 1986.
- [23] C. M. Bishop, *Pattern Recognition and Machine Learning*, ser. Information Science and Statistics, Springer, Ed. Springer-Verlag New York Inc., 2006.
- [24] T. H. Cormen, C. E. Leiserson, R. L. Rivest, and C. Stein, *Introduction to Algorithms, Second Edition*. The MIT Press, September 2001.
- [25] J. Geweke, "Measurement of linear dependence and feedback between multiple time series," *Journal of the American Statistical Association*, vol. 77, no. 378, pp. 304–313, 1982.
- [26] J. Geweke, R. Meese, and W. Dent, "Comparing alternative tests of causality in temporal systems : Analytic results and experimental evidence," *Journal of Econometrics*, vol. 21, no. 2, pp. 161–194, Feb. 1983.
- [27] T. Kreuz, F. Mormann, R. G. Andrzejak, A. Kraskov, K. Lehnertz, and P. Grassberger, "Measuring synchronization in coupled model systems: A comparison of different approaches," *Physica D: Nonlinear Phenomena*, vol. 225, no. 1, pp. 29–42, Jan. 2007.

Erik Casagrande received a MSc in control engineering in 2003 from Padova university. He completed his studies visiting Lund University and working in image processing and computer vision areas. He then received an MPhil in numerical modelling in 2005 from Padova university. He is currently working towards the PhD degree at Aston university focusing on causality and synchronisation identification analysis. Recent research interest has been in nonlinear time series, dynamical systems, machine learning techniques for biomedical data.

David Lowe had an early background in theoretical physics in the analysis and modelling of extremely small many particle systems at the quantum and semiclassical level, obtaining BSc and PhD degrees from Warwick University, UK. He then worked in signal processing areas in the Defence Research Agency UK and then in statistical pattern processing in areas such as speech, and generic sensor processing. In recent years he has developed expertise in the invention, analysis and application of nonlinear inference machines such as artificial and biological neural networks. He is coinventor of the Radial Basis Function neural network architecture and NeuroScale visualisation machine learning models, and the Shadow Targets optimisation algorithm. Recent research has been in stochastic control, steganography, bioinformatic and biomedical data analysis, brain signal processing, and emergent behaviour in coupled MEMS sensor arrays. He has held a Chair at Aston University, UK since 1994.

Avgis Hadjipapas obtained a Medical Degree from the University of Kiel, Germany in 2000, an MS degree in Cognitive Science/Electroencephalography from the Central and Eastern European Center in Cognitive Science (Sofia, Bulgaria) in 2002 and a PhD degree in neuroscience/Magnetoencephalography from the Wellcome Trust Laboratory for MEG studies (Aston University, UK) in 2005. He has held an appointment as a Research Fellow with the Wellcome Trust Laboratory for MEG studies Aston University, since January 2005. His research interests are in the field of functional neuroimaging in humans, mostly focused in the time series analysis of magneto- and -electroencephalographic (MEG/EEG) signals, the modeling of the underlying network generators of these macroscopic brain signals and the identification of such generators from measured time series both in health and disease. Avgis Hadjipapas has developed expertise in the noninvasive characterization of local cortical dynamics underlying basic functions of human visual cortex and the assessment of functional /dysfunctional long-range coordination the brain.

Instabilities driven by dipole resonances in cold atoms

Hugo Terças

CFIF, Instituto Superior Técnico Portugal
Av. Rovisco Pais, 1049-001, Lisbon (Portugal)
email: htercas@cfif.ist.utl.pt

José Tito Mendonça

IPFN, Instituto Superior Técnico Portugal
Av. Rovisco Pais, 1049-001, Lisbon (Portugal)
email: titomend@ist.utl.pt

Abstract— We present a model for the coupling between the recently predicted hybrid wave modes and the well-established dipole resonances observed in a cloud of cold atoms. We show that such oscillations are described by a forced oscillator equation in the form of a generalized Mathieu equation. We report on the stability conditions. A feedback control scheme is discussed in order to control the unstable solutions of the homogenous system.

I. INTRODUCTION

In the last years, special attention has been given to the low temperature physics [3]. The advent of laser cooling techniques, essentially because of the growing interest in the Bose-Einstein condensation, has envisaged the possibility to explore, both theoretic and experimentally, new exciting features in the field. Many fundamental aspects of low temperature physics, which have recently been reported, arise from several disciplines and may compromise the actual boundaries between them. As example, one should emphasize the studies developed in cold atoms and Bose-Einstein condensation, and very exciting theoretical works in quantum plasmas.

In this work, we explore the nonlinear coupling between the recently predicted hybrid waves and the dipole resonance due to the trapping potential, in a system of cold atoms [6]. The hybrid modes in cold atoms are formally similar to the Langmuir plasma waves [1], [2], but they present an acoustic nature. Therefore, such modes consist on sound oscillations that exhibit a lower cut-off when $k \rightarrow 0$.

II. BASIC EQUATIONS AND DERIVATION OF THE MODEL

A system of cold atoms is achieved by mean of a magneto-optical trapping (MOT), which results of the combination of Doppler cooling techniques with the spatial confinement potential due to the magnetic field. In the low density Doppler model, the effective external force $\vec{F}_{MOT} = -\alpha\vec{v} - \kappa\vec{r}$ depends on the experimental parameters $\kappa = \alpha\mu/k_L$, which represents the spring constant of the trap, and α , the friction coefficient, given by $\alpha = -8\hbar^2 s\Delta/\Gamma/(1 + 4\Delta^2/\Gamma^2)$. Here, $s = I_0/I_{sat}$ is the incident on-resonance saturation parameter per beam, I_0 is the incident laser intensity, Γ the natural line width of the transition used in the cooling process and $\Delta = \omega_L - \omega_a$ the frequency detuning between the laser frequency $\omega_L = k_L c$ and the atomic transition frequency ω_a . The spring constant κ defines the natural time scale, the dipole

frequency $\omega_D = \sqrt{\kappa/M}$, where M represents the mass of a single atom. The validity of this model is known to be limited to only a moderate number of atoms (typically $10^5 - 10^6$). For larger number of atoms, additional forces need to be taken into consideration. Therefore, the second force to be considered is the shadow force, or absorption force, \vec{F}_A , and was first discussed by Dalibard [4]. This is associated with the gradient of the incident laser intensity due to laser absorption by the atomic cloud. It is an attractive force which can be determined by $\nabla \cdot \vec{F}_A = -\sigma_L^2 I_0 c^{-1} n(\vec{r})$, where σ_L represents the laser absorption cross section and $n(\vec{r})$ is the atom density profile. The third force to be included in this model is the repulsive force between the atoms due to the radiation pressure, \vec{F}_R , and can be given by $\nabla \cdot \vec{F}_R = \sigma_L \sigma_R I_0 c^{-1} n\vec{r}$, where σ_R represents the scattering cross section. This allows us to describe the dynamics with an effective force $\vec{F}_T = \vec{F}_{MOT} + \vec{F}_c$, where $\vec{F}_c = \vec{F}_A + \vec{F}_R$ may be regarded as a collective self-consistent force, which is given by $\nabla \cdot \vec{F}_c = Qn$, $Q = \sigma_R(\sigma_L - \sigma_R)I_0 c$. Here Q stands for the effective charge and allows us to regard the system of cold atoms as a one-component plasma, confined in an external potential. The natural time scale associated with this effective fluid description is given by the generalized plasma frequency $\omega_P = \sqrt{Qn_0/M}$, where n_0 is the unperturbed density profile, such that $\nabla \cdot \vec{F}_T(n = n_0) = 0$.

By taking the zeroth and first order momenta in the Fokker-Planck equation, we can write down the system of equations that effectively describe an amount of cold atoms as a fluid,

$$\frac{\partial n}{\partial t} + \nabla \cdot (n\vec{v}) = 0, \quad (1)$$

$$\frac{\partial \vec{v}}{\partial t} + (\vec{v} \cdot \nabla)\vec{v} = \frac{\vec{F}_T}{M} - \frac{\vec{\nabla}P}{Mn}, \quad (2)$$

$$\nabla \cdot \vec{F}_T = Q(n - n_0). \quad (3)$$

This system has been also used by other authors to describe Coulomb explosions in optical molasses [5]. The principal aim of this work is to describe the coupling between the two time scales given by ω_D and ω_P , which respectively represent the typical time scales of the oscillations of the center-of-mass and the acoustic waves that may be excited in the system. To proceed with this task, we will use the linear response theory techniques by separating each relevant physical quantity into its equilibrium and perturbation components, such as

$n = n_0 + \tilde{n}$, $\vec{v} = \vec{v}_0 + \delta\vec{v}$, $\vec{F}_T = \vec{F}_{MOT} + \delta\vec{F}_c$. Setting the equilibrium velocity field $\vec{v}_0(t) = \vec{u}_0 \sin \omega_D t + \phi$, basic algebra calculations yield

$$\frac{\partial^2 \tilde{n}}{\partial t^2} + n_0 \frac{\partial}{\partial t} \nabla \cdot \delta\vec{v} + \vec{u}_0 \cdot \nabla \left[\frac{\partial \tilde{n}}{\partial t} \sin(\omega_D t + \phi) + \tilde{n} \omega_D \cos(\omega_D t + \phi) \right] = 0, \quad (4)$$

where he have retained only the terms in first order of perturbation. We will later devote some attention to the question of how higher orders in the perturbative analysis could originate qualitatively different results. In particular, we will explain the origin of the saturation in the stability observed by di Stefano *et al.* in Ref. [7]. One of the problems that may arise in this effective model is concerned with the equation of state for the hydrodynamical pressure $P = P_0 + \tilde{P}$. In the present derivation, we will assume that the cloud of cold atoms is described by adiabatic law $P \propto n^\gamma$, where γ represents the adiabatic constant. Therefore, we can define the sound velocity $u_S = \gamma \frac{P_0}{M}$ for the equilibrium system. Regarding that the wave number k of the sound waves is small enough compared to the size of the system, such that it can be regarded as an infinite medium, the following relation holds

$$\frac{\nabla^2 \tilde{P}}{P_0} \approx -\gamma \frac{k^2 \tilde{n}}{n_0}. \quad (5)$$

By putting eqs. (4)-(5) together, we should obtain

$$\frac{\partial^2 \tilde{n}}{\partial t^2} + (\omega_P^2 + u_S^2 k^2) \tilde{n} + \vec{u}_0 \cdot \nabla \left[\frac{\partial \tilde{n}}{\partial t} \sin(\omega_D t + \phi) + \omega_D \tilde{n} \cos(\omega_D t + \phi) \right] = 0, \quad (6)$$

and assuming that $\tilde{n}(\vec{r}, t) = \tilde{B}(\vec{r}) \tilde{A}(t)$, we may finally write

$$\frac{\partial^2 \tilde{A}}{\partial \tau^2} + [\Delta + 2\epsilon \cos(2\tau)] \tilde{A} + 2\epsilon \sin(2\tau) \frac{\partial \tilde{A}}{\partial \tau} = 0, \quad (7)$$

where we defined $2\tau = \omega_D t + \phi$, $\Delta = 4(\omega_P^2 + u_S^2 k^2)/\omega_D^2$ and $\epsilon = 2\vec{u}_0 \cdot \nabla \ln \tilde{B}/\omega_D$. Equation (7) belongs to the family of Hill equations and is formally similar to the Mathieu equation, whose properties are already well-known. The interest of this work thus remain in the numerical exploration of the homogeneous system in order to understand how to design a feedback system to control the instabilities.

In order to conclude the discussion of the main features of this model, we point out some remarks concerning the first order perturbation used in its derivation. One of the reasons for such an assumption has to deal with the approximation of parabolic potential, related to the confinement force $-k\vec{r}$ discussed in the introduction. In that case, the linear response theory holds. This obviously does not correspond to the experimental reality, since the potential is not perfectly parabolic, leading the instabilities to saturate, as observed in Ref. [7]. Such saturation would be explained by taking higher order of

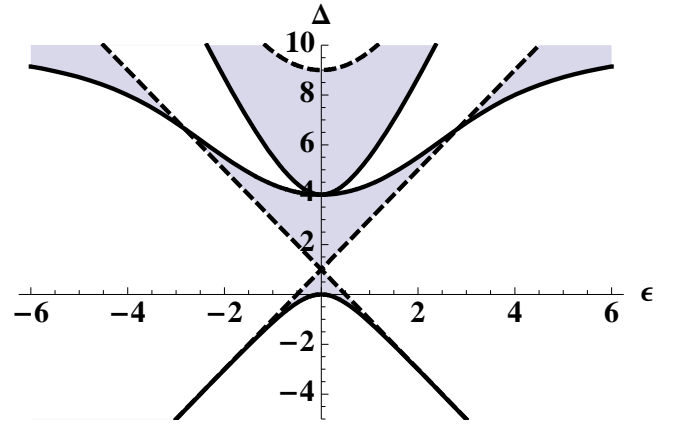


Fig. 1. Characteristic curves separating the stable and the unstable regimes computed numerically by using the Floquet's theory. The shadowed zones correspond to the first three stable zones. The full lines represent the π -periodic solutions and the dashed lines represent the 2π -periodic ones.

perturbation in Eq. (7), which would introduce anharmonicity to the system and thus an amplitude dependent frequency, leading to the detuning between the natural and the forcing frequencies, saturating the instability. For that reason, this model illustrates the "worse case scenario" of the instabilities that may occur in a magneto-optical trap and so the design of a robust control system may be required. In the future, we may think of extending this techniques to saturated instabilities which, under the experimental point of view, would represent the more interesting problem.

III. STABILITY AND FREE RESPONSE OF THE GENERALIZED MATHIEU EQUATION

By using the Floquet theory, it is possible to verify that the general solution to eq. (7) is a linear combination of two periodic functions, whose frequencies are given by ω_D and the imaginary part of the characteristic exponent, say γ [8]. Depending on the sign of the $\Re(\gamma)$, one of the solutions is either bounded or unbounded, and so defining the the stability of the general solution. Therefore, if $\Re[\gamma(\epsilon, \Delta)] > 0$ (< 0), the system is said to be unstable (stable). In fig. (1) we plot the first stability regions in the Strutt chart of (7), for the case of π and 2π -periodic solutions.

Under the physical and experimental point of view, there are three cases of major interest: (a) the wave frequency is much lower than the dipole frequency, $\Delta \ll \omega_D$; (b) the wave and dipole frequencies have the same order of magnitude, $\Delta \approx \omega_D$; and (c) the wave frequency is much higher than the dipole frequency, $\Delta \gg \omega_D$. However, given the nature of this work, only one case may be enough to motivate a feedback control problem, so we decide to explore the resonant case $\Delta = 2$.

IV. DESIGN OF A FEEDBACK CONTROL SYSTEM

Equation (7) does not envisage the usual PID methods [9] used to control linear systems. Therefore, we should adopt solutions which are typical of time-dependent or even nonlinear analysis. Depending on the design goals, there are several

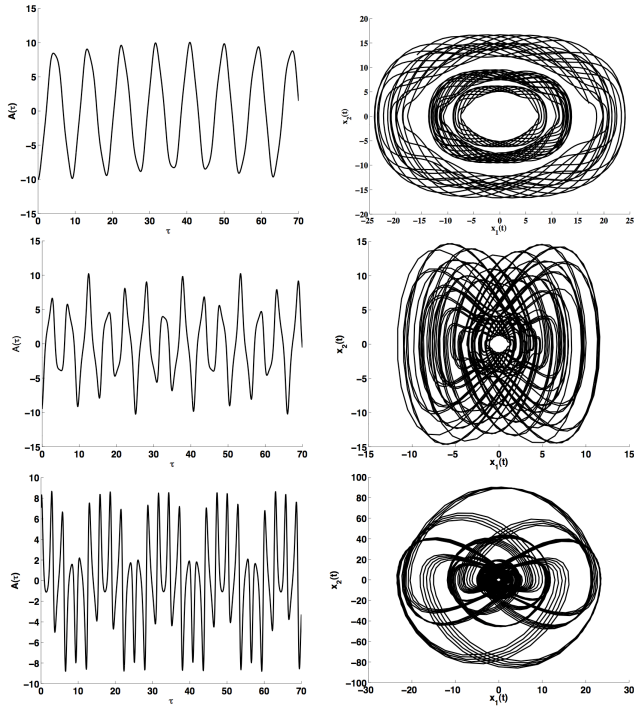


Fig. 2. Time evolution (left) and phase-space portraits (right) of the stable (bounded) solutions of Eq. (7) plotted for different stability zones. From top to bottom: $\Delta = 0.5$, $\epsilon = 0.2$; $\Delta = 2.0$, $\epsilon = 1.0$; $\Delta = 8.0$, $\epsilon = 2.0$.

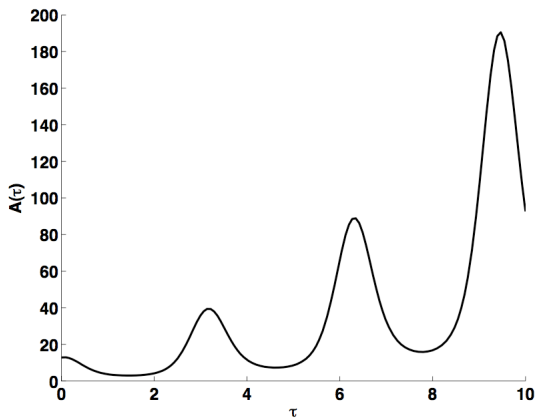


Fig. 3. Unstable solution of eq. (7) plotted for $\Delta = 2$ and $\epsilon = 2.1$.

formulations of the control problem. The tasks of stabilization, tracking and disturbance rejection or attenuation (or even combinations of them) lead to a large number of choices [12]. In each one, one may have a state feedback version where all state variables can be measured or an output feedback version where only few variables can be measured. Other solutions are related rather with stochastic than deterministic methods, like fuzzy-logic control [10]. In a typical control problem, there are additional tasks for the design, like meeting certain requirements on the transient response or certain constraints on the control input, recurrently related to hardware or software limitations. When model uncertainty is taken into account, issues of sensitivity and robustness play an important role.

Therefore, the attempt to design a feedback control system to cope with a wide range of uncertainty models leads to either robust or adaptive control systems.

In this work, we will limit our discussion to the case of a disturbance rejection problem. At the end of this section, we devote some attention to the main reasons for that choice.

If we define the output vector $\mathbf{x}(\tau) \equiv (x_1(\tau), x_2(\tau)) = (\tilde{A}(\tau), \dot{\tilde{A}}(\tau))$, we can rewrite (7) in the form

$$\dot{\mathbf{x}}(\tau) = \mathbf{A}(\tau) \cdot \mathbf{x}(\tau), \quad (8)$$

where $\mathbf{A}(\tau)$ represents the matrix of the time-dependent dynamical system

$$\mathbf{A}(\tau) = \begin{bmatrix} 0 & 1 \\ -\Delta - 2\epsilon \cos(2\tau) & -2\epsilon \sin(2\tau) \end{bmatrix}. \quad (9)$$

The stabilization problem is generally given by

$$\dot{\mathbf{x}}(\tau) = f(\tau, \mathbf{x}, \mathbf{u}), \quad (10)$$

where $\mathbf{u} = g(\tau, \mathbf{x})$ is the control law. Such a control law is usually called "static feedback", because is memoryless in respect to the state vector \mathbf{x} . Sometimes $\mathbf{u}(\tau - \tau_0)$ is a time-delayed control function, since the attempt of designing a state feedback control that depends on the measurement of a set of output variables often introduces a certain delay τ_0 on the response [11]. In that cases, it is common to design a dynamic feedback control $\mathbf{u} = g(\tau, \mathbf{x}, \mathbf{z})$, where \mathbf{z} is the solution of a dynamical system driven by \mathbf{x} , given by $\dot{\mathbf{z}} = h(\tau, \mathbf{x}, \mathbf{z})$.

We are interested in a disturbance rejection problem, so we should design a feedback control law \mathbf{u} such that the origin $\mathbf{x} = 0$ is an asymptotically stable equilibrium point of the closed-loop (10), regardless the fact that a more general solution could be adopted to stabilize the system in respect to an arbitrary steady-state point \mathbf{x}_{ss} . Since the system is linear, and assuming the possibility of making a continuous reading of the state variables at each time τ , the closed-loop system can be written in the form

$$\dot{\mathbf{x}}(\tau) = \mathbf{A}(\tau) \cdot \mathbf{x}(\tau) - K\mathbf{B} \cdot \mathbf{x}(\tau - \tau_0), \quad (11)$$

where the control law $\mathbf{u} = -K\mathbf{x}(\tau - \tau_0)$ preserves the linearity of the open-loop system. Here, \mathbf{B} is a matrix of parameters. In the case of no delay, $\tau_0 = 0$, we know that the origin is an asymptotically stable point if, and only if, $\mathbf{A} - K\mathbf{B}$ is Hurwitz, i.e., if the real part of the 1st eigenvalues are negative. For the general case $\tau_0 \neq 0$, we should use numerical calculations.

Although the parameters Δ and ϵ are time independent, it is expected that they contain a certain error, since they depend upon the experimental conditions, in a more realistic control system presented in (11) should be tested. For the sake of illustration, in fig. (IV) we present several situation of stabilization for an unstable solution of (7). First, we set either the delay time τ_0 and the errors associated to the parameters to zero. Second, we assume the existence of a finite time-delay in the response of the control law function. Finally, we

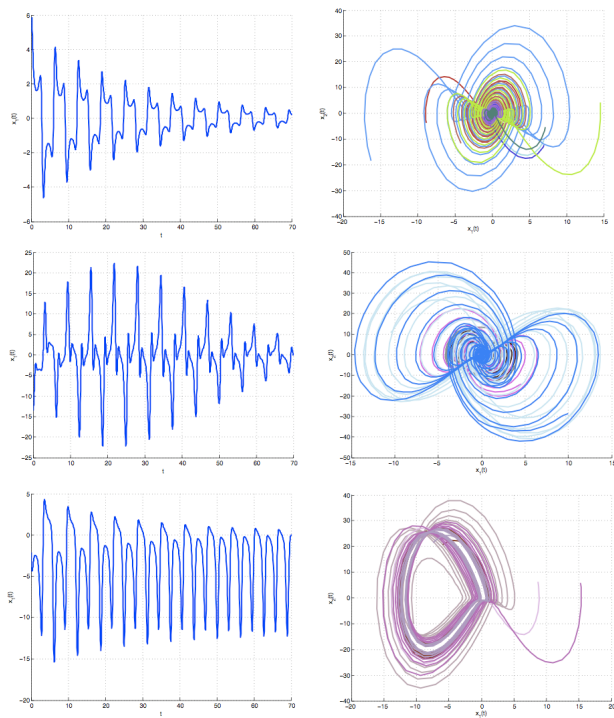


Fig. 4. (Color Online) Examples of control of the unbounded solution presented in fig. (3). Solutions obtained in the time domain (left) and in the phase-space domain (right) for five different orbits. From top to bottom: Simple negative feedback; negative feedback with time delay of $\tau_0 = 0.3$, and negative feedback with gaussian noise ($\sigma_\Delta = 2$, $\sigma_\epsilon = 2$).

assume that the errors on the parameters follow a gaussian distribution with zero mean value and variances σ_Δ and σ_ϵ .

In the case where $\tau_0 = 0$ and $\sigma_\Delta = \sigma_\epsilon = 0$, the unstable solution of the open-loop system is stabilized at the origin, without exhibiting any transient regime. In the second stabilization scheme, the time delay is set to 0.3, the solution tends to zero after a transient regime around $\tau_{trans} = 20$. In the last case, we can observe that the introduction of a bandwidth of $\sigma_\Delta = \sigma_\epsilon = 2$ in the parametric noise lead to a quasi-periodic stable solution, in opposition to the previous situations. However, because our aim is to avoid the occurrence of instabilities rather than zero-point stabilization, the later simulation suggests that this control system is robust to the noise.

We have restricted our discussion to the disturbance rejection problem for reasons that have to deal with the experimental conditions. In a typical MOT experiment, we are interested in cooling down the atoms, by decreasing their kinetic energy to zero. Instabilities obviously bring the system out of such configuration, preventing the atoms to be cooled and trapped. The design of a control system based on a defined steady-state configuration would also lead to similar results, since the disturbance rejection problem is only a particular case of the later.

V. CONCLUSION

The description of a cold Bose gas with a set of effective fluid equations opens place to the occurrence of plasma-like waves. Because of the trapping used in the typical experimental setups, the system oscillates at the dipole frequency, which is roughly defined by the magnetic field conditions. In such conditions, it is possible to predict the couple between the waves and the dipole oscillations. This system of coupled modes is described by a time-dependent model that generalizes the well-known Mathieu equation. It is shown that this equation exhibits unstable solutions, which may result in a source of instabilities that should be stabilized in the context of experimental work. Hence, the design of a negative feedback control system is of great interest. In the present work, we show that a simple time-dependent control law, based on the measurement of the open-loop state variables, should be considered as an efficient way of stabilizing the system. We propose an extension of the usual techniques in control of linear time-dependent systems by including delaying and noise in the response functions.

ACKNOWLEDGMENT

One of the authors (H. Terças) would like to thank professor Paulo Oliveira, from the electrical engineering department of Instituto Superior Técnico, for helpful discussions and advices concerning the control system solutions.

REFERENCES

- [1] J.V. Parker, J.C. Nickel and R.W. Gould, *Phys. Fluids*, **7**, 1489 (1964).
- [2] R. Guerra and J.T. Mendonça, *Phys. Rev. E*, **62**, 1190 (2000).
- [3] S. Chu, *Rev. Mod. Phys.* **70**, 685 (1998); C. Cohen-Tannoudji, *Rev. Mod. Phys.* **70**, 707 (1998); W. D. Phillips, *Rev. Mod. Phys.* **70**, 721 (1998).
- [4] J. Dalibard, *Opt. Commun.*, **68**, 203 (1988).
- [5] L. Pruvost et al., *Phys. Rev. A*, **61**, 053408 (2000).
- [6] J.T. Mendonca et al, *Phys. Rev. A* (submitted to PRA) (2008).
- [7] Andre di Stefano et al., *Phys. Rev. A* **67**, 033404 (2003).
- [8] A. Nayfeh and D. Mook, *Nonlinear Oscillations*, 1979.
- [9] Joseph J. DiStefano et al, *Feedback and Control Systems*
- [10] Ling Hong and Jian-Qiao Sun, *Chaos, Solitons and Fractals*, **27**, 895-904 (2006).
- [11] T. Insperger and G. Stepan, *Proceedings-Royal Society Mathematica, Physical and Engineering sciences*, ISSN 1364-5021.
- [12] H. Kahlil, *Nonlinear Systems*, Prentice Hall.

Ultrasonic Sensor Data Processing using Support Vector Machines

D.Isa, R.Rajkumar

School of Electrical and Electronic Engineering

University Of Nottingham, Malaysia Campus, Jalan Broga, 43500, Semenyih, Selangor, Malaysia

Dino.Isa@nottingham.edu.my.

Abstract— Ultrasonic sensors are ideal for non-destructive testing due to its many advantages over conventional sensors. Oil and gas pipelines are an area which uses ultrasonic sensors for monitoring and detecting the presence corrosion and defects. The proposed techniques ultimately aims at providing a continuous monitoring system using an array of ultrasonic sensors strategically positioned on the surface of the pipeline to predict the occurrence of defects rather than just monitoring. The sensors used are piezoelectric ultrasonic sensors. The raw sensor signal will be first processed using the Discrete Wavelet Transform (DWT) as a feature extractor and then classified using the powerful learning machine called the Support Vector Machine (SVM). Preliminary tests show that the sensors can detect the presence of wall thinning in a steel pipe by classifying the attenuation and frequency changes of the propagating lamb waves. The SVM algorithm was able to classify the signals as abnormal in the presence of wall thinning.

Key-Word- Ultrasonic Sensor, Pipeline, Support Vector Machines, Discrete wavelet transform

I. INTRODUCTION

Ultrasonic waves have been used in detecting defects in pipes, tubes and metal plates in many applications [1][2]. In the area of oil and gas pipelines, ultrasonic sensors are incorporated in many commercial products for monitoring corrosion and defects [3]. Ultrasonic waves propagate through the pipeline as Lamb waves thus picking up critical information on the condition of the pipe. Ultrasonic sensors enable detection without any contact with the object regardless of its material, nature, color and degree of transparency. The advantages of ultrasound detection include:

- No physical contact with the object to be detected, therefore, no wear and detection possible of fragile or freshly painted objects, etc.
- Detection of any material, irrespective of color, at the same distance, without adjustment or correction factor.
- Very good resistance to industrial environments (robust products entirely encapsulated in resin). Tough environments such as fumes, dust, noisy.
- Solid-state units: no moving parts in the sensor, therefore, service life independent of the number of operating cycles.

Currently, an established form of pipeline inspection uses smart pigs in a process called pigging [4]. These smart pigs travel within the pipeline recording critical information like corrosion levels, cracks and structural defects using its numerous sensors. Pigs can give pinpoint information on the location of defects using techniques like magnetic flux leakage and ultrasonic detection [5]. However, using smart pigs in pipeline inspection has a few disadvantages. The cost of implementing a pigging system can be expensive. More importantly, pigs measure the pipeline condition only at the instance it is deployed and does not provide continuous measurements over time. The proposed techniques aim at providing a continuous monitoring system using an array of different sensors strategically positioned on the external surface of the pipeline. The raw sensor signal will be first processed using the Discrete Wavelet Transform (DWT) and then classified using the powerful learning algorithm called the Support Vector Machines (SVM).

The DWT is used here as a feature extraction tool in order to single out any unique features in the sensor data. A useful property of the DWT is that it compresses signals and by doing so, it has the tendency to eliminate high frequency noise. The DWT is used here to eliminate noise in the sensor signals and also to compress large amounts of real-time sensor data for faster processing. The compressed data or the DWT coefficients are then used as inputs to the SVM classifier, which will fuse the different sensor data together and then perform the classification task. The SVM has been widely used lately for numerous applications due to its excellent generalization ability with small training samples. The SVM will be trained with normal and simulated defect conditions using an experimental pipeline rig in the laboratory.

II BACKGROUND

A. Support Vector Machines

SVM functions by creating a hyperplane that separates a set of data containing two classes. According to the SRM principle, there will just be one optimal hyperplane, which has the maximum distance (called maximum margin) to the closest data points of each class as shown in Fig. 1[6]. These points, closest to the optimal hyperplane, are called Support Vectors (SV). The hyperplane is defined by the equation

$\mathbf{w} \cdot \mathbf{x} + b = 0$, and therefore the maximal margin can be found by minimizing (1).

$$\frac{1}{2} \|\mathbf{w}\|^2 \quad (1)$$

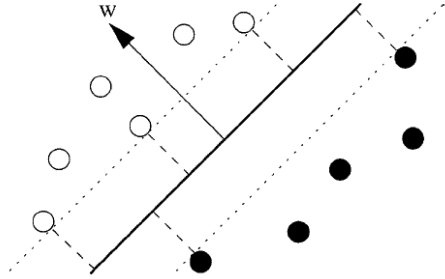


Fig. 1: Optimal Hyperplane and maximum margin for a two class data.

The Optimal Separating Hyperplane can thus be found by minimizing Eq. (1) under the constraint Eq.(2) that the training data is correctly separated [7].

$$y_i \cdot (\mathbf{x}_i \cdot \mathbf{w} + b) \geq 1, \forall i \quad (2)$$

The concept of the Optimal Separating Hyperplane can be generalized for the non-separable case by introducing a cost for violating the separation constraints Eq.(2). This can be done by introducing positive slack variables ξ_i in constraints Eq.(2), which then become:

$$y_i \cdot (\mathbf{x}_i \cdot \mathbf{w} + b) \geq 1 - \xi_i, \forall i \quad (3)$$

If an error occurs, the corresponding ξ_i must exceed unity, so $\sum_i \xi_i$ is an upper bound for the number of classification errors. Hence a logical way to assign an extra cost for errors is to change the objective function Eq.(1) to be minimized into:

$$\min \left\{ \frac{1}{2} \|\mathbf{w}\|^2 + C \cdot (\sum_i \xi_i) \right\} \quad (4)$$

C is a tuning parameter which allows the user to control the trade off between maximizing the margin (first term in the objective) and classifying the training set without error. Minimizing Eq.(4) under constraint in Eq.(3) gives the *Generalized Optimal Separating Hyperplane*. This is a Quadratic Programming (QP) problem which can be solved here using the method of Lagrange multipliers [8].

After performing the required calculations [7], [9], the QP problem can be solved by finding the LaGrange multipliers, α_i , that maximizes the objective function in Eq.(5),

$$W(\alpha) = \sum_{i=1}^n \alpha_i - \frac{1}{2} \sum_{i,j=1}^n \alpha_i \alpha_j y_i y_j (\mathbf{x}_i^T \mathbf{x}_j) \quad (5)$$

Since the input vectors enter the dual only in form of dot products the algorithm can be generalized to non-linear classification by mapping the input data into a high dimensional feature space via an a priori chosen non-linear mapping function Φ . Constructing a separating hyperplane in this feature space leads to a non-linear decision boundary in the input space. Expensive calculation of dot products in a high-dimensional space can be avoided by introducing a kernel function, K in Eq. (6).

$$K(x_i, x_j) = \Phi(x_i) \cdot \Phi(x_j) \quad (6)$$

By introducing the kernel function, it is not necessary to explicitly know $\Phi(\cdot)$. So that the optimization problem in Eq.(5) can be translated directly to the more general kernel version in Eq. (7),

$$W(\alpha) = \sum_{i=1}^n \alpha_i - \frac{1}{2} \sum_{i,j=1}^n \alpha_i \alpha_j y_i y_j K(x_i, x_j) \quad (7)$$

subject to

$$C \geq \alpha_i \geq 0, \sum_{i=1}^n \alpha_i y_i = 0$$

The equation for the indicator function, used to classify new data (from sensors) is given in Eq.(11) where the new data \mathbf{z} is classified as class 1 if $i > 0$, and as class 2 if $i < 0$ [10].

$$i_f(x) = \text{sign} \left[\sum_{i=1}^l y_i \alpha_i K(x, x_i) + b \right] \quad (8)$$

Note that the summation is not actually performed over all training data but rather over the support vectors, because only for them do the Lagrange multipliers differ from zero. Fig. 2 illustrates the SVM data flow, from input data point to the final decision value [11].

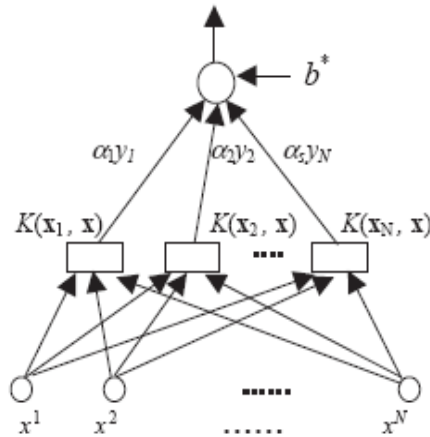


Fig 2: Diagram of SVM data flow

As such, using the support vector machine we will have good generalization and this will enable an efficient and accurate classification of the sensor signals. It is this excellent generalization that we look for when analyzing sensor signals due to the small samples of actual defect data obtainable from field studies. In this work, we simulate the abnormal condition and therefore introduce an artificial condition not found in real lie applications.

B. Discrete Wavelet Transform

A discrete wavelet transform (DWT) is basically a wavelet transform for which the wavelets are sampled in discrete time. The DWT of a signal x is calculated by passing it through a series of filters. First the samples are passed through a low pass filter with impulse response g , resulting in a convolution of the two (9). The signal is also decomposed simultaneously using a high-pass filter h (10).

$$y_{low}[n] = \sum_{k=-\infty}^{\infty} x[k]g[2n - k] \quad (9)$$

$$y_{high}[n] = \sum_{k=-\infty}^{\infty} x[k]h[2n - k] \quad (10)$$

The output of the equations 9 and 10 gives the detail coefficients (from the high-pass filter) and approximation coefficients (from the low-pass). It is important that the two filters are related to each other for efficient computation and they are known as a quadrature mirror filter [12].

However, since half the frequencies of the signal have now been removed, half the samples can be discarded according to Nyquist's rule. The filter outputs are then down sampled by 2 as illustrated in Fig. 3. This decomposition has halved the time resolution since only half of each filter output characterizes the signal. However, each output has half the frequency band

of the input so the frequency resolution has been doubled. The coefficients are used as inputs to the SVM [13].

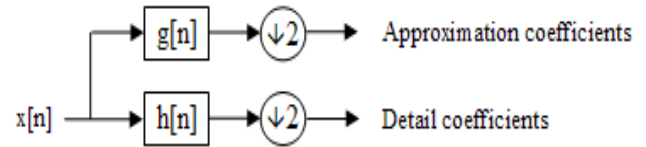


Fig. 3: DWT filter decomposition

C. Corrosion Measurement

A pipe failure and leakage of crude oil in Winchester, Kentucky on January 2000, was one of the biggest accidents that occurred and it incurred the owner Marathon Ashland Pipe Line LLC a clean up cost of \$7.1 million. The crack was due to a small dent in the pipe that might have been caused by stone particles flowing along the path, in addition to the fluctuating pressure of the pipe wall [14]. An example of such a failure is shown in Fig. 4.

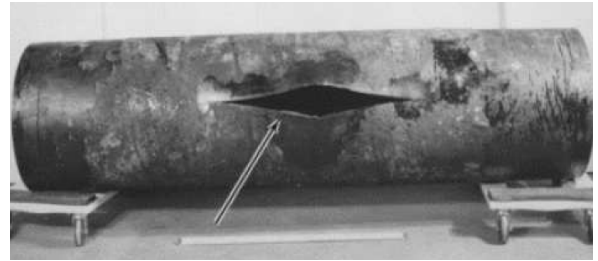


Fig. 4: The rupture pipe due to fatigue cracking [14].

Wall thinning, a common occurrence in the oil piping industry, is characterized by metal loss caused by surface erosion due to high temperature, high pressure and high flowing velocity of the flowing commodity [15]. The pipes are also subjected to combined loading by internal pressure, bending moment, and longitudinal forces. The internal wall thinning of a pipe cannot be observed from the outside of the pipe, hence a method of condition monitoring using ultrasonic waves as a non-destructive test of the metal loss can help to determine when the pipe may be at risk for leaks or failure. Ultrasonic sensor enables detection without any contact with the object regardless of its material, nature, color and degree of transparency.

The detection technology used here lies within the concepts of nonlinear acoustics. This basically states that when sound waves travels through a material, frequency and attenuation changes occur to the sound waves. The changes in the frequency and amplitude must be detected and analyzed to give precise information on the state of the material. Ultrasonic transmitters can be used to send ultrasonic waves and ultrasonic receivers can be used to detect the propagating

waves. These sensors are very accurate as they can produce and detects high frequency sound wave based on Piezoelectricity [16]. Piezoelectric transducers have solid-state pressure sensitive elements that will expand and contract in step with input signals.

Demma [17] examined the effect of defect size with frequency on the reflection from notches and was able to show the relation between the value of reflection coefficient and the defect sizing. The cylindrical ultrasonic waves propagate along the pipe and are partially reflected when met with defects thus providing a fast screening technique to determine the presence of defects. Similar results and observation are recorded by Lin [18] by using guided waves and electromagnetic acoustic transducers (EMATs) to measure the wall thickness precisely. Wave propagation is performed for a specimen with thickness of 10mm, where different artificial defects are introduced to model local wall thinning. As shown in Fig.5, when transmitted waves impinge the wall thinning, they are reflected and the intensity of the reflected waves varies.

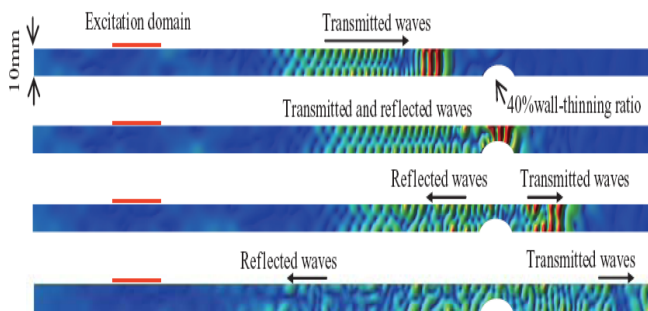


Fig. 5: The energy carried by the transmitted waves passes through the wall thinning and some reflected back as echoes. [18]

It is therefore a well known phenomenon, both theoretically and experimentally that defects in pipes can be detected by ultrasonic transducers [15].

III METHODOLOGY

This section details the experimental setup that will be used to simulate pipeline conditions and also defect conditions. The aim is to create a scaled down version of an actual section of pipeline in the laboratory using commonly available materials. Fig. 6 shows the experimental setup. A motor pump is used to pump hydraulic oil in the reservoir through the pipeline section. A flow rate of around $5 \text{ m}^3/\text{h}$ was achieved through a 1 m section of pipe (outer diameter of 48.30 mm and inner diameter of 42 mm). Two experiments will be carried out. The first experiment is to compare a defective pipe and a normal pipe.

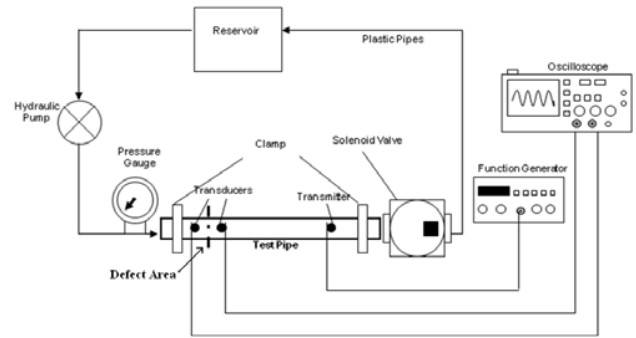


Fig. 6: Pipeline Experimental Setup.

A lathe is used to clear an area of 1mm wide and 1mm deep all around the circumference at the inner surface of the pipe. This is to simulate a crack or corrosion at the inner surface of the pipe. An ultrasonic transmitter is used to transmit a signal across the flowing pipe and through the defect area to see changes in the ultrasound signal. Ultrasonic receivers, placed at the other end of the pipe, will be able to pick-up the waveform that is vibrating in the pipe and can be used to monitor the condition of the pipe. The changes in the ultrasound signal will be used to determine the presence of any defects. The experiment was repeated on a pipe without any defects.

Ultrasonic sensors used are Murata analogue ultrasonic sensors which is an open structure type of sensor that has a range of up to 6 m and they will be attached to the outer surface of the pipe using epoxy. MA40B8S have the nominal frequency of 40 kHz with the maximum input voltage of 40V peak to peak. The stationary sensors can avoid any disturbance from the environment and will be able to transmit ultrasound along the length of the pipe by ringing the surface of galvanized steel pipe.

The second experiment is to simulate progressive defects or corrosion as seen in real pipelines. Therefore, a simulation was carried out to corrode the interior of the test pipe. In order to perform this, the test pipe is removed from the setup. Stones and rocks of different sizes are passed through the pipe for 5 hours a day to speed up the corrosion process. This is done by recycling stones and rocks by using a conveyor belt and clamping the pipe vertically. This process is repeated daily in order to cause random metal loss in the interior of the pipe.

IV RESULTS

The results of from the experimental rig will ultimately be used to ascertain whether SVM can detect the presence of cracks and whether DWT helps in the decision making. DWT is performed on raw time domain samples and the coefficients of the resulting DWT are inputted into the SVM for classification. Various wavelets can be tested including the Haar and Daubechies wavelets. A popular SVM algorithm called LIBSVM [19] is used to perform the SVM calculation. LIBSVM includes for kernel functions: linear, polynomial,

radial basis function (RBF), and sigmoid. To train an SVM, the user must select the proper C value as well as any required kernel parameters.

Time domain samples before and after the defect area are first broken down into frames where the number of samples within the frame is a variable. Each frame will represent one instance or sample needed for the SVM and the frame size is the number of attributes or dimensions. Table 1 show the results of the first experiment where the SVM accuracy is shown as a percentage. The signals are decomposed into two frame sizes, 25 and 50 and inputted into the LIBSVM algorithm. 10,000 data points from the defective pipe and 10,000 data points from the normal pipe are used to obtain the results. This is therefore is a binary classification problem where the two classes are defective and non-defective.

Table 1: Classification accuracy (%) for pipeline data using LIBSVM for various kernel functions.

Wavelet	Kernel Func.	Frame Size	
		25	50
-	Poly	73.68	67.74
	RBF	75.44	70.97
	Sig	73.68	67.74
DB2	Poly	83.87	61.11
	RBF	80.64	72.22
	Sig	80.64	61.11
Haar	Poly	89.65	75.00
	RBF	89.65	75.00
	Sig	86.21	75.00

As can be seen from Table 1, the smaller frame size provides better classification accuracy than the bigger frame size. The radial basis function (RBF) kernel shows the highest classification rates among the kernel functions tested. The Haar wavelet also shows better classification accuracy as compared to the DB2 wavelet. Fig. 7 shows the results of the second experiment where the defects are progressively increased over time. The results shown are taken at weekly intervals with results for 5 weeks shown.

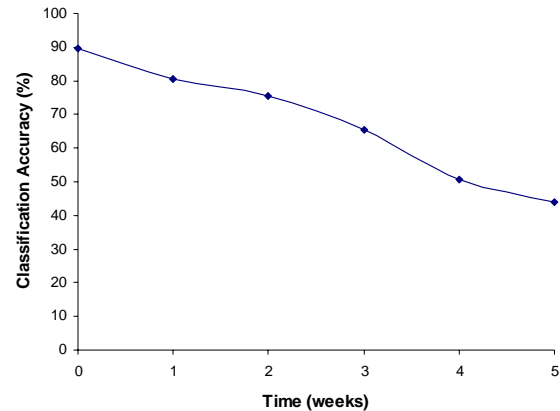


Figure 7: SVM classification accuracy as defect size increased over time.

As can be seen from the data from Fig 7, as the defects are increased over time, the SVM classification accuracy decreases. This trend can be used to predict the occurrence of defects.

CONCLUSION

Monitoring hundreds of kilometers of pipelines is a difficult task due to the high number of unpredictable variables involved. Rapidly changing weather conditions, pressure changes and erosion due to gas or oil flow and ground movement are a few variables that can have direct impact on the pipelines. There variables can cause defects like corrosion, dents and cracks which will lead to loss of the valuable commodity and not to mention the series affects on the surrounding environment.

The use of an array of sensors with help of support vector machine processing intends to solve these problems in two ways. Firstly the array of sensors provides a continuous monitoring platform along the entire distance of the pipeline. Secondly the use of artificial intelligence tools like support vector machines, makes it possible to monitor and ultimately predict the occurrence of defects. Support vector machines are ideal for applications like these where there are high number of dimensions of data (sensors) and also the small number of samples for defect scenarios. SVM have been used widely in many such applications and has provided excellent generalization performance.

An experimental miniature pipeline rig provided the setting to examine the initial performance of the SVM on pipeline-like data. For now, no correlation study is made between the simulated and real situation. Ultrasonic sensors were used and the corrosion defect was simulated using human manipulation. The results of the first experiment showed good performance by the SVM using an RBF kernel function. Results with other kernels indicate that these other kernels do not accurately represent the inner product of feature vectors of that data set. The use of DWT further improved the performance of the SVM accuracy to 89.65%. This is due to the DWT compressing the data and filtering away unwanted noise from the high frequency acoustic signals. The second experiment show that as the defects are increased, the SVM

classification accuracy decreases. The reason for this is that the signal attenuation and phase are changing as the defects are increased. So the ultrasonic signals are looking more and more dissimilar to that of the pipe at the beginning causing the SVM algorithm to classify more points to the defective class.

The conclusion is reached that a combination DWT and SVM algorithm can predict, to a high accuracy the presence of defects and also progressive defects in small pipes. The results of this paper will be used in future research where multiple sensors resulting in multiple time series signals need to be analyzed on bigger diameter pipes. Multiple defect scenarios will also be studied resulting in multiclass classification problems. The ultimate aim of the research will be to predict defects before they occurs thereby conserving the precious commodity and environment.

REFERENCES

- [1] Tua P S, Quek S T and Wang Q, Detection of cracks in cylindrical pipes and plates using piezo-actuated Lamb waves, *Smart Mater. Struct.*, Vol.14, 2005, 1325-1342
- [2] Demma, A., Cawley, P., Low, M., Roosenbrand, A.G. and Pavlakovic, B., 2004, The reflection of guided waves from notches in pipes, *NDT&E International*, 37, 167-180.
- [3] World Centre For Materials Joining Technolog, 'Long Range Ultrasonic Technologies' Part of TWI's Non-Destructive Testing Technology Group. URL: www.twi.co.uk
- [4] Lebsack, S., 2002, Non-invasive inspection method for unpiggable pipeline sections, *Pipeline & Gas Journal*, 59.
- [5] Bickerstaff, R., Vaughn, M., Stoker, G., Hassard, M. and Garrett M. 2002. Review of sensor technologies for in-line inspection of natural gas pipelines, Sandia National Laboratories.
- [6] Müller K., Mika S., Rättsch G., Tsuda K., and Schölkopf B., "An Introduction To Kernel-Based Learning Algorithms, *IEEE Transactions On Neural Networks*, Vol. 12, No. 2, March 2001, 181
- [7] Burges, Christopher J.C. "A Tutorial on Support Vector Machines for Pattern Recognition". Bell Laboratories, Lucent Technologies. Data Mining and Knowledge Discovery, 1998.
- [8] Haykin, Simon. "Neural Networks. A Comprehensive Foundation", 2nd Edition, Prentice Hall, 1999
- [9] V. Vapnik. The Nature of Statistical Learning Theory, 2nd edition, Springer, 1999
- [10] Kecman, Vojislav, "Support Vector Machines Basics", School Of Engineering Report 616, The University of Auckland, 2004. URL: http://genome.tugraz.at/MedicalInformatics2/Intro_to_SVM_Report_616_V_Kecman.pdf
- [11] Ming Ge, R. Du, Guicai Zhang, Yangsheng Xu, 'Fault diagnosis using support vector machine with an application in sheet metal stamping operations, *Mechanical Systems and Signal Processing* 18 (2004) 143-159.
- [12] Mallat, S. *A Wavelet Tour of Signal Processing*, 1999, Elsevier.
- [13] Lee, K. and Estivill-Castro, V., Classification of ultrasonic shaft inspection data using discrete wavelet transform. In: *Proceedings of the Third IASTED International Conferences on Artificial Intelligence and application*, ACTA Press. pp. 673-678
- [14] National Transportation Safety Board Washington, D.C. 20594, Pipeline Accident Brief. URL: www.ntsb.gov/publicntm/2001/PAB0102.pdf
- [15] Koji Takahashi, Kotoji Andoa, Masakazu Hisatsune, Kunio Hasegawa, "Failure behavior of carbon steel pipe with local wall thinning near orifice", *Nuclear Engineering and Design*, No. 237, April 2006, pg 335-341
- [16] P S Tua, S T Quek and Q Wang, Detection of cracks in cylindrical pipes and plates using piezo-actuated Lamb waves, *Smart Mater. Struct.*, Vol.14, 2005 1325-1342
- [17] Demma, A., Cawley, P., Low, M., Roosenbrand, A.G. and Pavlakovic, B., 2004, The reflection of guided waves from notches in pipes, *NDT&E International*, 37, 167-180.
- [18] S. Lin, et.al., 2006, "Development of Measuring Method of Pipe Wall Thinning Using Advanced Ultrasonic Techniques", CRIEPI Report Q05006
- [19] Chang C, Lin C., 'LIBSVM : A Library for Support Vector Machines', 2001. Software available at: <http://www.csie.ntu.edu.tw/~cjlin/libsvm/>



Dino Isa is an Associate Professor at the University of Nottingham, Malaysia Campus attached to the Faculty of Engineering and Computer Science. His current interest is in applying the support vector machine in various domains in order to further understand its mechanisms. Dr Isa obtained his BSEE (Hons) in Electrical Engineering from the University of Tennessee, Knoxville in 1986 and his PhD from the University of Nottingham, University Park, Nottingham, England in 1991. He was employed in Motorola Seremban as Engineering Section Head after he completed his PhD, and moved to Crystal Clear Technology in 1996 as Chief Technology Officer prior to joining the University of Nottingham in 2001.



R RajKumar is currently a PhD student in the School of Electrical and Electronic Engineering, Faculty of Engineering and Computer Science, University of Nottingham, Malaysia Campus. He obtained his Masters from the same University in 2005 and his main interest is in using the Support Vector Machine to predict failures in oil and gas pipelines.

System Identification using Symbolic Chaotic Sequence

Ajeesh P. Kurian and Henry Leung
 Dept. of Electrical and Computer Engineering
 University of Calgary
 Calgary, Alberta, Canada T2N 1N4
 E mail - leungh@ucalgary.ca

Abstract—In this paper, the problem of system identification using chaotic symbolic sequence is presented. We will consider the parameter estimation of linear moving average systems driven by chaotic sequences and formulate it as a semiblind identification scheme. The only knowledge that needs to be assumed at the estimator is about the dynamics of underlying chaotic system that generates the input sequence. To implement this estimator, we utilize expectation maximization (EM) algorithm. The sufficient statistics in the E-step is obtained with an unscented Kalman smoother (UKS). This intermediate step in system identification has similarity with chaos synchronization and hence we extend this idea to the synchronization of two chaotic systems under multipath. The estimation and synchronization performance of the proposed algorithm is evaluated using computer simulations.

I. INTRODUCTION

Chaotic sequences have found many applications in secure communications, cryptography and digital watermarking due its wide-band nature. Synchronization of chaotic systems/maps is the backbone of many of these methods. The objective of any chaotic synchronization scheme is to get the trajectories of two systems with arbitrary initial conditions close to each other. Following the drive-response system suggested by Pecora and Carrol [1], various schemes have been proposed for the synchronization of chaotic systems [2]–[6]. One of the key issues in chaos synchronization is the presence of channel noise. Although many of these schemes can result in an acceptable level of synchronization, intermittent bursts of desynchronization is observed when channel noise is present [7]. A detailed account of the effect of the noise on synchronization is presented in [8]–[10]. One of the solutions suggested to synchronize chaotic systems when there is noise is the Kalman filter and its variants. Extended Kalman filter (EKF) has been shown to be successful in synchronizing chaotic systems/maps in stochastic environments. This ability of the EKF initiated a significant research interest [11], [12]. The EKF based scheme can be considered as a scheme which is capable of estimating the coupling strengths adaptively. Similarly, other variants of Kalman filters are also studied for chaotic synchronization hoping to improve the approximation errors introduced by EKF [13], [14].

Perturbation signal design for linear system identification is one of the key task [15]. For the persistent excitation, the input signal should have an impulse like auto correlation function.

Filtered Gaussian noise is widely used as input sequence for system identification [16]. Random binary sequence, especially pseudo-random binary sequence (PRBS) are used as the input signal for system identification since it has desirable crest factor¹. Chaos has been found to be an effective way to drive linear system for identification [17]–[19]. Chaotic time series is characterized by its noise like appearance and wide-band spectrum. Unlike white Gaussian noise, chaotic sequences are deterministic. It has been shown that the chaotic dynamics can act as a source of information and thus these sequences can be used as an alternative to the pseudo random noise signal. Chaotic sequences can be used either as an un-quantized sequence (i.e. the chaotic numeric sequences) or as chaotic symbolic sequences (Symbolic dynamics (SD) is the coarse-grain description of the chaotic dynamics and has been used for the analysis of chaotic systems/maps [20]). In any case, the potential of chaotic sequence for system identification still remain unexplored by the industry to a large extent. We believe it is due to the sensitive dependence of chaotic systems on its initial conditions and the difficulty in synchronizing noisy chaotic signals.

The method proposed in this paper attacks the problem of system identification and synchronization in a single framework. We formulate a semiblind system identification method which can be used for the synchronization of two chaotic systems. In system identification literature, semiblind estimation is used to emphasize that the estimator has only partial knowledge about the input signal. For example, in this case, only the dynamics of the chaotic that generates the input sequence is available at the estimator. We formulate the system identification problem as maximum likelihood estimation (MLE). Expectation maximization (EM) [21] is used for the recursive implementation of the MLE. Since the dynamics that generate perturbation signal is highly nonlinear, we use unscented Kalman smoother (UKS) for obtaining sufficient statistics in the expectation step (E-Step). This situation is very similar to the chaotic synchronization methods, where a estimate of the trajectory that generated the observation is estimated from the received signals. Thus, the problem is formulated as a joint estimation and synchronization problem, where we will estimate the channel coefficient and recover the

¹Crest factor is the ratio of the peak value of a signal to its root mean square value. A lower crest factor represent more effective energy transfer to the system which results in enhanced signal to noise ratio.

transmitted chaotic trajectories recursively.

The current work is a continuation of the EM-EKS (extended Kalman smoother) based system identification presented in Ref. [22]. Though the proposed estimator is not restricted to any particular class of linear systems, we adopt a generic FIR system for simulation and performance comparison. For the second case, we run numerical simulations to study the estimation and synchronization performance. We have found that the performance of the proposed scheme is noticeable even at low SNR values. The rest of this paper is organized as follows. In section II, the problem of semi-blind identification is formulated for linear systems. We provide the numerical simulation results in section III. Finally, conclusions are drawn in section IV.

II. PROBLEM FORMULATION

A. Parameter Estimation and Synchronization

We will consider a situation where a linear system excited by a chaotic sequence z_n and it could be a chaotic numerical sequence c_n or a chaotic symbolic sequence s_n . We observe the output of the system which is corrupted by noise. i.e.

$$y_n = \mathbf{h}^T \mathbf{z}_n + w_n. \quad (1)$$

where $\mathbf{z}_n = [z_n, \dots, z_{n-p+1}]$ is the input to the system with $\mathbf{h} = [h_1, \dots, h_p]$ and w_n is zero mean additive white Gaussian noise with variance σ_w^2 . The sequence $c_n, n = 1, \dots, N$ with N as the total length of the input sequence is obtained by

$$c_{n+1} = f(c_n, \eta) \quad (2)$$

where $f(c_n, \eta)$ is a chaotic function parameterized on η . The symbolic sequence s_n is generated by

$$s_n = g(c_n) = \begin{cases} +1 & \text{if } c_n \geq \eta \\ -1 & \text{otherwise} \end{cases} \quad (3)$$

We need to estimate \mathbf{h} by using only the observations and knowledge about the chaotic generator. Since we assume that the dynamics of the sequence generator is available, this method falls under semiblind identification. In our formulation, if the initial condition of the chaotic generator, c_0 , is known the entire symbolic sequence can be reconstructed. This step has similarities with chaotic synchronization where the trajectories of one system are forced to follow the other. i.e the mean square of the error

$$e_n = c_n - \hat{c}_n, \quad (4)$$

should be minimal (\hat{c}_n is the estimated chaotic sequence).

The estimation problem becomes estimating \mathbf{h} and σ_w^2 in addition to the initial condition. Let $\boldsymbol{\theta} = \{c_0, \sigma_w^2, \mathbf{h}\}$ are the set of parameters we need to estimate. This procedure can be treated as a batch approach for joint parameter estimation and synchronization.

B. The Proposed EM-UKS Estimator

In this section we formulate EM-UKS algorithm for system identification. EM is a standard tool for iterative maximum likelihood estimation [23]. It is a two stage algorithm which involves an expectation step (E-Step) and a maximization step (M-Step) in each iteration. After randomly initializing the unknown parameters, the algorithm performs E-Step using the current parameter estimates and M-Step by maximizing the expectation. In the next subsection, these two steps are explained.

1) *E-Step*: In the EM algorithm, missing variables are introduced as a part of the estimation process. In certain situation this variable is introduced as an artifact to make the problem tractable. In many other situations, this missing variable will be a part of the estimation problem [23]. In our problem, the state variables of the chaotic system are unobserved and it will naturally become the missing variable. We formulate an augmented state space model for our application. The three unknowns ($\boldsymbol{\theta}$) we try to estimate here is \mathbf{h} , σ_w^2 and c_0 . We form the state vector $\mathbf{z}_n = [z_n, z_{n-1}, \dots, z_{n-(p-1)}]$ which is the missing variable and has the dynamics

$$\mathbf{z}_{n+1} = \begin{bmatrix} f(z_n) \\ \mathbf{0} \end{bmatrix} + \begin{bmatrix} \mathbf{0} & 0 \\ \mathbf{I}_{p-1} & \mathbf{0} \end{bmatrix} \mathbf{z}_n \quad (5)$$

where \mathbf{I}_{p-1} is an identity matrix of order $p-1$. In the E-Step we construct the complete statistics, $\mathcal{P}(\mathbf{Z}, \mathbf{y})$, with hidden variable $\mathbf{Z} = [\mathbf{z}_1, \dots, \mathbf{z}_N]$ which is an estimate of c_n and observances $\mathbf{y} = [y_1, \dots, y_N]$. Then the probability density function is given by

$$\mathcal{P}(\mathbf{Z}, \mathbf{y}) = \mathcal{P}(\mathbf{z}_1) \prod_{n=2}^N \mathcal{P}(y_n | \mathbf{z}_n), \quad (6)$$

since due to the deterministic nature, $\mathcal{P}(\mathbf{z}_{n+1} | \mathbf{z}_n) = 1$. We have

$$\begin{aligned} \mathcal{P}(\mathbf{z}_1) &= \mathcal{N}(0, \sigma_c^2 \mathbf{I}) \\ \mathcal{P}(y_n | \mathbf{z}_n) &= \mathcal{N}(\mathbf{h}^T \mathbf{z}_n, \sigma_w^2) \end{aligned} \quad (7)$$

Once this is obtained, the next step is to get the expectation Q as

$$\begin{aligned} Q &= \mathbb{E}[\mathcal{L}(\mathbf{Z}, \mathbf{y}) | \mathbf{y}, \boldsymbol{\theta}] \\ &= -\frac{1}{2} \ln(2\pi\sigma_c^2) - \frac{N}{2} \ln(2\pi\sigma_w^2) - \frac{1}{2\sigma_c^2} \mathbb{E}[\mathbf{x}_1^2 | \mathbf{y}, \boldsymbol{\theta}] \\ &\quad - \sum_{n=1}^N y_n^2 - 2 \sum_{n=1}^N y_n \mathbf{h}^T \mathbb{E}[\mathbf{z}_n | \mathbf{y}, \boldsymbol{\theta}] \\ &\quad + \sum_{n=1}^N \mathbf{h}^T \mathbb{E}[\mathbf{z}_n \mathbf{z}_n^T | \mathbf{y}, \boldsymbol{\theta}] \mathbf{h}. \end{aligned} \quad (8)$$

In order to compute the above expectation, we need to find the individual expectations

$$\begin{aligned} \mathbf{x}_n^s &= \mathbb{E}[\mathbf{z}_n | \mathbf{y}, \boldsymbol{\theta}] \\ \mathbf{P}_n^s &= \mathbb{E}[\mathbf{z}_n \mathbf{z}_n^T | \mathbf{y}, \boldsymbol{\theta}] \end{aligned} \quad (9)$$

A smoother can give these individual expectation values. Since the sequence generated from a nonlinear system, Unscented Kalman Smother (UKS) is used for its advantage over the

traditional EKS [24]. We use UKS based on the Rauch–Tung–Striebel smoothing [25].

2) *M-Step*: In the M-Step, we use the result from the previous steps to do the maximization using the following steps.

$$\begin{aligned}\hat{\mathbf{h}} &= \left[\sum_{n=1}^N \mathbf{P}_n^s \right]^{-1} \sum_{n=1}^N y_n \mathbf{x}_n^s \\ \hat{\sigma}_w^2 &= \frac{1}{N} \sum_{n=1}^N (y_n - \hat{\mathbf{h}}^T \mathbf{x}_n^s) \\ \hat{\sigma}_c &= c_0^s\end{aligned}\quad (10)$$

These results are used in the next E-Step. This process is repeated until the iterations converge. The schematic of the proposed method is shown in figure 1.

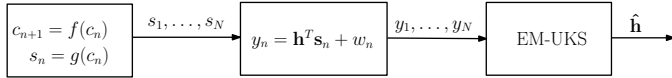


Fig. 1. Parameter estimation of a linear system using EM-UKS.

One of the motivations for this work is the interplay between the E-step and M-step. In the E-step, it is assumed that the estimated parameters are true and is used to obtain a smooth estimate of the state of the chaotic map from the observations. This is essentially similar to synchronization method where, system trajectories are estimated from observations. Once the smoothed states are obtained, this will be used for the parameter estimation. Thus, the overall procedure results in synchronized trajectories once the algorithm is converged.

III. RESULTS AND DISCUSSION

In this section, we will discuss the result of the numerical simulations. The chaotic map we used for all the simulation is given by

$$c_{n+1} = \frac{\gamma c_n (1 - c_n^2)}{1 + \rho c_n^2} \quad (11)$$

where $\gamma = 5$ and $\rho = 2$. The chaotic attractor of the map is shown in Fig. 2. We set the threshold value $\eta = 0$. We analyze the parameter estimation as well as synchronization qualities of the proposed method.

A. Performance of the Proposed System on Parameter Estimation

For the analysis, we define the estimation error in the linear channel \mathbf{h} , $\text{MSE}_{\mathbf{h}}$ as

$$\text{MSE}_{\mathbf{h}} = \frac{1}{N} \sum_{i=1}^N \frac{\|\mathbf{h} - \hat{\mathbf{h}}\|}{P} \quad (12)$$

where N is the number of iteration carried out in each SNR values². We compare this with both filtered Gaussian noise and PRBS based non-blind identification systems.

²Here, the SNR is defined as the power of the signal after threshold operation divided the power of the noise. This is identical to the typical formulation communication systems.

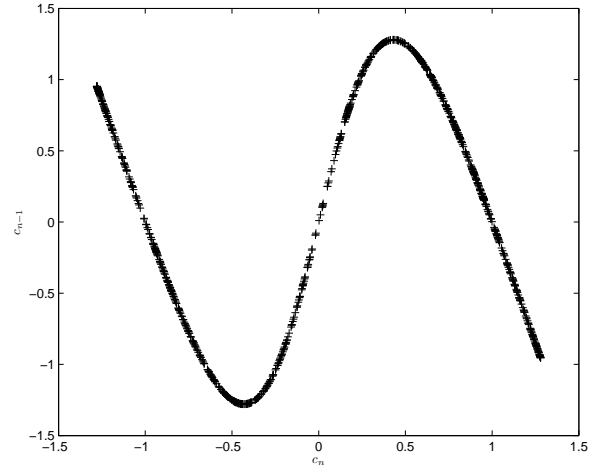


Fig. 2. Original Attractor.

We consider the system identification problem in a general settings with FIR coefficients $\mathbf{h} = [1, 0.6, 0.3]$. We run numerical simulations to study the effectiveness of the proposed scheme. $\text{MSE}_{\mathbf{h}}$ is calculated according to Eq. (12) with $N = 16$. The result is plotted in figure 3. For comparison purpose, we have also plotted the non-blind identification schemes based on the white Gaussian noise and PRBS. Clearly, chaotic symbolic sequence based estimation scheme closely follows the training sequence based non-blind identification scheme at all SNR values. Compared to the chaotic numeric sequence, it is clearly an advantage. We will see the reason for this in the next subsection when we study the synchronization performance.

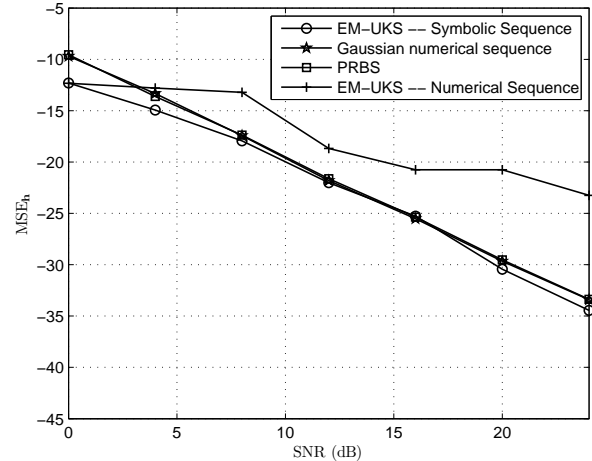


Fig. 3. SNR vs $\text{MSE}_{\mathbf{h}}$.

As we know from general statistical signal processing, it is desirable to have a large number of observations to improve the accuracy of the estimate. Next, we will study the effect of the number of sample N on the MSE performance. Figure 4 shows relationship between the length of the observations and $\text{MSE}_{\mathbf{h}}$. We change the value of N from 16 to 512 by

keeping channel noise at 20dB. For both chaotic symbolic and numerical sequences, the dependence of MSE on N is obvious. The chaotic symbolic sequence outperforms the numerical sequence in all the SNR values. Also, the rate of decrease in MSE is more prominent in the case of the symbolic sequence based identification. Since the increase in N increase the computational complexity, this information can be used for designing the receiver.

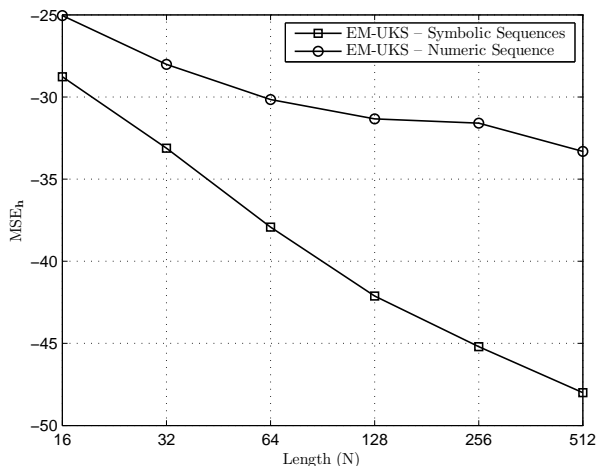


Fig. 4. Length vs MSE_h.

As an iterative algorithm, computational power requirement for EM algorithm is very high. It is desirable to achieve convergence with minimum iterations. To study effect of noise on the convergence of the EM algorithm, we consider two SNR values and performed a number simulations. The number of iterations required for convergence is plotted as histogram in figures 5 and 6. It can be seen that there is a strong dependency on the convergence of EM-UKS and noise. For chaotic symbolic sequences, at 20dB most of the iterations converge within seven or eight iterations while at 10dB EM-UKS takes at least 8 iterations. We observe few simulations takes close to 30 iterations to converge. Similar observations are made on the chaotic numeric sequence; however, compared to chaotic symbolic sequence it takes more number of iterations to converge. From all these studies, we can see that chaotic symbolic sequence based system identification scheme has very attractive performance measures despite the heavy computational load.

B. Performance of the Proposed System on Chaotic Synchronization

In this section we present the results of the proposed technique for the synchronization of chaotic sequences. We will start the analysis with un-quantized chaotic sequence. We consider a situation where, strong multipath and channel noise exists. We use the same channel as in the previous section for these simulations. The state space of the received signal (when the channel noise is 10dB) is given figure 7 and the corresponding reconstructed state-space is shown in figure 8. Clearly, even at 10dB noise, the attractor of the chaotic system

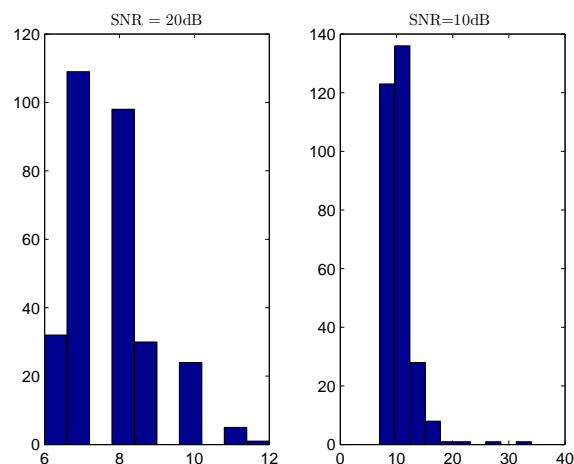


Fig. 5. Histogram of number of iterations taken for convergence: (a) 20dB and (b) 10dB.

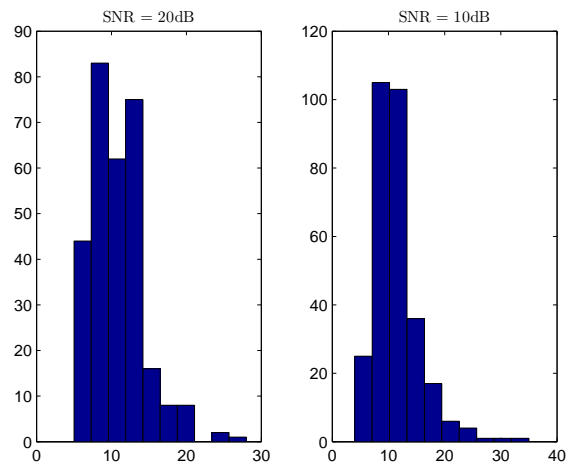


Fig. 6. Histogram of number of iterations taken for convergence: (a) 20dB and (b) 10dB.

is reconstructed very closely to the original one. For the higher SNR, qualitatively, the reconstructed attractor matches closely with the original one (figure 9). The original, received and reconstructed waveforms, when the channel noise is 10dB are shown in figure 10. We have observed no transient in our simulations which implies a quick synchronization.

Next, we will study when symbolic sequences are used for the transmission. From figure 11, we can see that the estimated and original sequence does not follow one to one. This is due to the approximation we used in the execution step. i.e. instead of finding the exact trajectory, its coarse representation estimated. Figure 12 shows the original and estimated symbolic sequences. The estimated symbolic sequence closely follows the corresponding symbolic sequence entering the channel. This method can be used with other symbolic sequence based synchronization schemes [26] in order to estimate the corresponding numeric sequence.

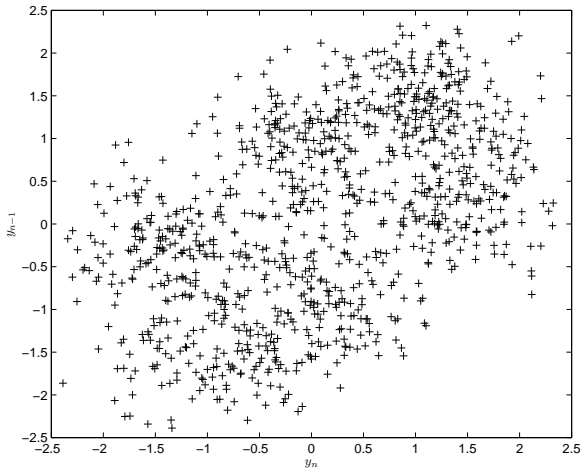


Fig. 7. State-space of the received signal when the channel noise is 10dB.

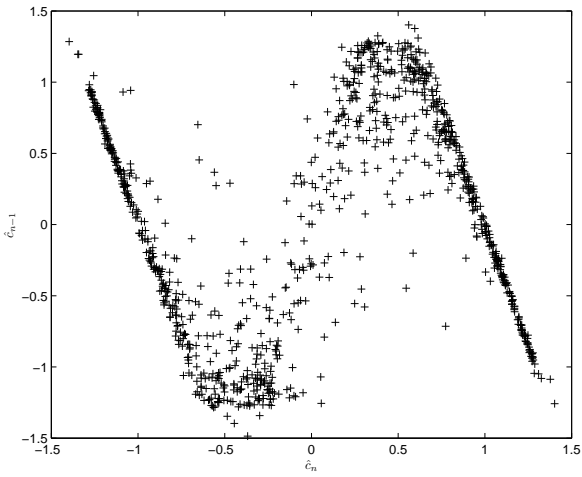


Fig. 8. Recovered state-space when the channel noise is 10dB.

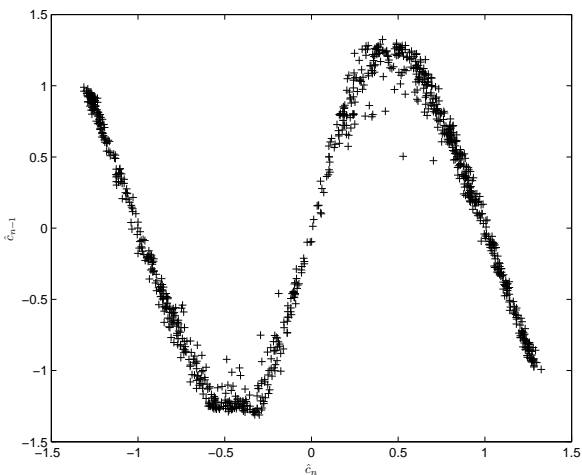


Fig. 9. Recovered state-space when the channel noise is 20dB.

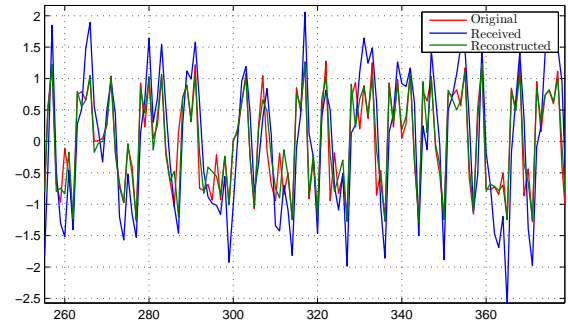


Fig. 10. Portion of the original, received, and recovered signals: Chaotic numeric sequence with channel noise 10dB.

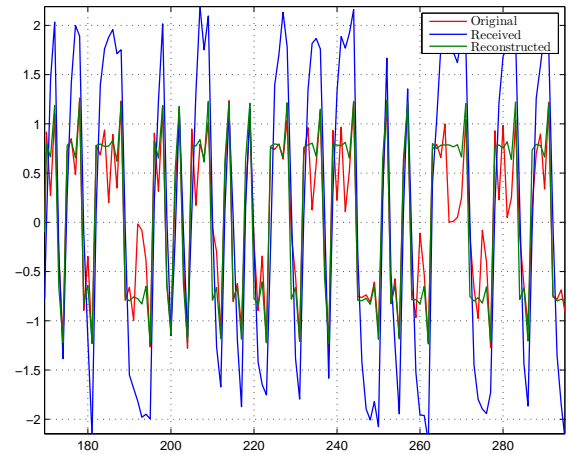


Fig. 11. Portion of the original, transmitted, and recovered signals: Chaotic symbolic sequence with channel noise 10dB.

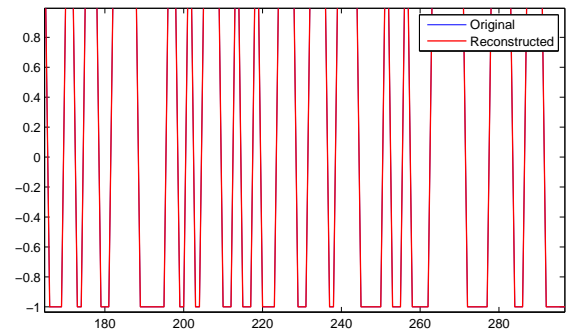


Fig. 12. Original and estimated symbolic sequence with channel noise 10dB.

IV. CONCLUSION

In this paper, the problem of chaotic synchronization is formulated as joint estimation and synchronization. By combining EM with UKS we form EM-UKS estimator for system identification. With this, the E-step acts as synchronization step and M-step acts as parameter estimation step. We compared the estimation and synchronization performance using numerical simulations. We found that the estimation performance of the

proposed system is close to training based Gaussian white noise and PRBS in all SNRs when symbolic sequence is used. Similarly, at low and high SNRs, the proposed scheme was able to synchronize well.

REFERENCES

- [1] L. M. Pecora and T. L. Carroll, "Synchronization in chaotic systems," *Phys. Rev. E*, vol. 64, no. 8, pp. 821–824, Feb 1990.
- [2] L. M. Pecora, T. L. Carroll, G. A. Johnson, D. J. Mar, and J. F. Heagy, "Fundamentals of synchronization in chaotic systems, concepts, and applications," *Chaos*, vol. 7, pp. 520–543, Dec. 1997.
- [3] H. Nijmeijer and I. Mareels, "An observer looks at synchronization," *IEEE Trans. Circuits Syst. I*, vol. 44, no. 10, pp. 882–890, 1997.
- [4] Z. He, K. Li, L. Yang, and Y. Shi, "A robust digital secure communication scheme based on sporadic coupling chaos synchronization," *IEEE Trans. Circuits Syst. I*, vol. 47, no. 3, pp. 397–403, Mar 2000.
- [5] H. Leung and Z. Zhu, "Performance evaluation of EKF-based chaotic synchronization," *IEEE Trans. Circuits Syst. I*, vol. 48, no. 9, pp. 1118–1125, Sept. 2001.
- [6] G. Jiang, W. X. Zheng, W. K.-S. Tang, and G. Chen, "Integral-observer-based chaos synchronization," *IEEE Trans. Circuits Syst. II*, vol. 53, no. 2, pp. 110–114, 2006.
- [7] J. F. Heagy, T. L. Carroll, and L. M. Pecora, "Desynchronization by periodic orbits," *Phys. Rev. E*, vol. 52, no. 2, pp. R1253–R1256, Aug 1995.
- [8] R. Brown, N. F. Rulkov, and N. B. Tufillaro, "Synchronization of chaotic systems: the effects of additive noise and drift in the dynamics and driving," *Phys. Rev. E*, vol. 50, pp. 4488–4508, 1994.
- [9] R. Brown and N. F. Rulkov, "Synchronization of chaotic systems: Transverse stability of trajectories in invariant manifolds," *Chaos*, vol. 7, pp. 395–413, Sept. 1997.
- [10] Z. Zhu, H. Leung, and Z. Ding, "Optimal synchronization of chaotic systems in noise," *IEEE Trans. Circuits Syst. I*, vol. 46, no. 11, pp. 1320–1329, 1999.
- [11] K. Cuomo, A. Oppenheim, and S. Strogatz, "Synchronization of lorenz-based chaotic circuits with applications to communications," *IEEE Trans. Circuits Syst. II*, vol. 40, no. 10, pp. 626–633, 1993.
- [12] C. Cruz and H. Nijmeijer, "Synchronization through filtering," *Intl. J. Bifurc. Chaos*, vol. 10, pp. 763–775, 2000.
- [13] M. Luca, S. Azou, G. Burel, and A. Serbanescu, "On exact kalman filtering of polynomial systems," *IEEE Trans. Circuits Syst. I*, vol. 53, no. 6, pp. 1329–1340, 2006.
- [14] A. P. Kurian and S. Puthusserypady, "Unscented kalman filter and particle filter for chaotic synchronization," *Circuits and Systems, 2006. APCCAS 2006. IEEE Asia Pacific Conference on*, pp. 1830–1834, 2006.
- [15] H. A. Barker, D. E. Rivera, A. H. Tan, and K. R. Godfrey, "Perturbation signal design," in *14th IFAC Symp. System Identification*, 2006.
- [16] L. Ljung, *System Identification: Theory for the users*. Prentice Hall, 1999.
- [17] H. Papadopoulos and G. Wornell, "Optimal detection of a class of chaotic signals," in *IEEE Intl Conf. Acoust., Speech, Signal Processing, 1993. ICASSP-93*, vol. 3, 27-30 April 1993, pp. 117–120vol.3.
- [18] N. Xie and H. Leung, "A nonlinear prediction approach for system identification using chaos symbolic dynamic," *IEEE Intl. Conf. Systems, Man and Cybernetics, 2003.*, vol. 2, pp. 1365–1370, Oct. 2003.
- [19] —, "Blind identification of autoregressive system using chaos," *IEEE Trans. Circuits Syst. I*, vol. 52, no. 9, pp. 1953–1964, Sept. 2005.
- [20] H. Bailin, *Elementary Symbolic Dynamics and Chaos in Dissipative Systems*. World Scientific, Singapore, 1989.
- [21] A. P. Dempster, N. M. Laird, and D. B. Rubin, "Maximum likelihood from incomplete data via the *em* algorithm," *J. Royal Stat. Soc. Series B (Methodological)*, vol. 39, no. 1, pp. 1–38, 1977.
- [22] V. Venkatasubramanian and H. Leung, "Chaos based semi blind identification of nonlinear systems," in *IEEE Intl. Workshop on Nonlinear Signal and Image Processing*, May 2005.
- [23] R. H. Shumway and D. S. Stoffer, "An approach to time series smoothing and forecasting using the *em* algorithm," *J. Time Series Analysis*, vol. 3, no. 4, pp. 253–264, 1982.
- [24] E. A. Wan, R. van der Merwe, and A. T. Nelson, "Dual estimation and the unscented transformation," *Neural Information Processing Systems*, vol. 12, pp. 666–672, 2000.
- [25] S. Särkkä, "Unscented Rauch–Tung–Striebel smoother," *IEEE Trans. Automat. Contr.*, 2007 (Expected).
- [26] A. Dmitriev, G. Kassian, and A. Khilinsky, "Information viewpoint on chaotic synchronization," *Control of Oscillations and Chaos, 2000. Proceedings. 2000 2nd International Conference*, vol. 2, pp. 335–338, 2000.



Ajeesh P. Kurian received the B.Tech. degree in Instrumentation and Control Engineering from University of Calicut, Kerala, India in 1999 and PhD in Electrical and Computer Engineering from the National University of Singapore, Singapore in 2006. He was with Panasonic Singapore Laboratories from 2005 to 2006 working as an R&D Engineer. Currently he is a Postdoctoral fellow at the University of Calgary, Canada. His research interests are nonlinear dynamics, chaos, statistical signal processing, and sensor networks.



Henry Leung received the Ph.D. degree in electrical and computer engineering from McMaster University, Hamilton, ON, Canada.

He is now a Professor at the Department of Electrical and Computer Engineering, University of Calgary, Calgary, AB, Canada. Before that he was with the Defense Research Establishment Ottawa, Canada, where he was involved in the design of automated systems for air and maritime multisensor surveillance. His research interests include chaos,

computational intelligence, data mining, nonlinear signal processing, multimedia, radar, sensor fusion, and wireless communications.

Models of Oscillatory Nonlinear Mappings

Wieslaw Citko, Wieslaw Sienko

Department of Electrical Engineering

Gdynia Maritime University

81-225 Gdynia, Morska 83, Poland

emails: sienko@am.gdynia.pl, wcitko@am.gdynia.pl

Abstract— In this paper we present how to design very large scale oscillatory nonlinear mappings by using orthogonal filters which, due to spectrum based information processing, can be seen as implementations of holographic-like structures.

Keywords— nonlinear mappings, oscillatory neural networks

I. INTRODUCTION

A number of experiments show that some cognitive functions of biological brains could be seen as holographic processes (see for example [1]). Hence, we believe that biologically motivated structures of artificial neural networks cannot rely on dissipative dynamical networks, with their different type of attractors, (e.g. chaotic attractors) or on multilayer feedforward neural networks trained by backpropagation algorithms. It seems that, at least for very large scale associative memories needed to implement cognition functions in great projects like Ersatz-Brain [2] and Cognitive Memory [3], the types of neural networks mentioned above are not adequate, as the attractor objects are too ‘fragile’. Moreover, multilayer neural networks, seen as implementations of nonlinear mappings, are not suitable for large scale problems. It is, however, worth noting, that the implementation of nonlinear mappings proposed in [4] and known as Regularized Least Squares Classification (RLSC), could be used for realization of very large scale associative memories. Relying on an RLSC approach, some novel structures of classifiers have been considered [5, 6, 7]. These structures are specific to using the Hamiltonian Neural Networks (HNN) based spectrum analysis, recognition and memorization, giving rise to the mapping of implementations with skew-symmetric kernels, as well. In this paper we present how to design very large scale nonlinear mappings of oscillator type, by using HNN, which, due to spectrum based information processing, can be seen as an implementation of holographic-like structures.

II. ON MODELLING OF THE OSCILLATORY NEURAL NETWORKS

To our knowledge, the fundamental research in the field of oscillatory implementation of neural networks has been done by Hoppenstead [9, 10, 11, 12]. Let us briefly review that an oscillator can be described by the following state equation:

$$\dot{\mathbf{x}} = \mathbf{f}(\mathbf{x}), \mathbf{x} \in \mathbb{R}^m, \quad (1)$$

and it is a nonlinear dynamical system with a limit cycle. Hence, a net of weakly coupled oscillators is given by:

$$\dot{\mathbf{x}}_i = \mathbf{f}_i(\mathbf{x}_i) + \varepsilon \mathbf{g}_i(\mathbf{x}_1, \dots, \mathbf{x}_n, \varepsilon), \varepsilon \ll 1, i = 1, \dots, n \quad (2)$$

Synchronization phenomenon in such a network is one of the most challenging mathematical and engineering problems. According to [11], the sufficient conditions for synchronization in the net (2) can be formulated as follows:

Transform the state space equation (2) onto phase equations:

$$\dot{\varphi}_i = \Omega_i + \varepsilon h_i(\varphi_1, \dots, \varphi_n, \varepsilon), \varphi_i \in \mathbb{S}^1 \quad (3)$$

where: Ω_i – natural frequency of i -th oscillator (i.e. for $\varepsilon = 0$).

Assuming a weak coupling of oscillators, the state equation and phase equation can be simplified, as follows:

$$\dot{\mathbf{x}}_i = \mathbf{f}_i(\mathbf{x}_i) + \varepsilon \sum_{j=1}^n \mathbf{g}_{ij}(\mathbf{x}_i, \mathbf{x}_j) \quad \mathbf{x}_i \in \mathbb{R}^m \quad (4)$$

and

$$\dot{\varphi}_i = \Omega_i + \varepsilon \sum_{j=1}^n h_{ij}(\varphi_i, \varphi_j) \quad i = 1, \dots, n. \quad (5)$$

Introducing a phase deviation Ψ_i of i -th oscillator i.e.:

$$\varphi_i = \Omega_i t + \Psi_i \quad (6)$$

and averaging over a period $T = 2\pi/\Omega$, the phase equation (5) can be formulated as:

$$\dot{\Psi}_i = \varepsilon \sum_{j=1}^n H_{ij}(\Psi_i - \Psi_j), \quad i = 1, \dots, n \quad (7)$$

where nonlinear functions H_{ij} ; $i, j = 1, \dots, n$ determine time evolution of momentary frequency of coupled oscillators in the net. It is clear, that state of synchronization is given by equilibria of differential equations (7), i.e. :

$$\varepsilon \sum_{j=1}^n H_{ij}(\Psi_i - \Psi_j) = 0, \quad i = 1, \dots, n \quad (8)$$

or

$$\Delta\omega_i + \sum_{j=1}^n H_{ij}(\Psi_i - \Psi_j) = 0; \quad \forall i \quad (9)$$

where: $\Delta\omega_i = H_{ii}(0)$ is a deviation of natural frequency Ω_i .

For steady state of synchronization the equilibria have to be asymptotically stable. Unfortunately, the general solution of Eq.(9) is a nontrivial task, for $n \gg 1$. In special case, under assumption that $H_{ij}(\bullet)$ has a form:

$$H_{ij}(\Psi_i - \Psi_j) = H(\Psi_i - \Psi_j) = -\sin(\Psi_i - \Psi_j) \quad (10)$$

the solution of equation (9) can be analytically found. The above case is known and celebrated as Kuramoto model [11, 13]. For example, for $n=2$, Kuramoto model is given by:

$$\begin{aligned} \frac{d\Psi_1}{d\tau} &= \Delta\omega_1 - \sin(\Psi_1 - \Psi_2) \\ \frac{d\Psi_2}{d\tau} &= \Delta\omega_2 + \sin(\Psi_1 - \Psi_2) \end{aligned} \quad (11)$$

where: $\tau = \varepsilon t$.

It is worth noting that, assuming equation (1) as a model of an oscillatory neuron, state equation (4) describes an oscillatory neural network, which can be synchronized, as shown above. But, it seems that synchronization alone insufficiently determines a neural network as an information processor. We claim that neural networks, to be treated as information processors, have to function as orthogonal filters.

III. ON OSCILLATORY IMPLEMENTATION OF ORTHOGONAL-FILTERS

The models of nonlinear mappings described in this paper rely on using Hamiltonian Neural Networks (HNN) based orthogonal filters. Let us note that HNN are nonlinear,

dynamical structures composed of elementary lossless neurons. A basic d.c. model of a lossless neuron is shown in Fig.1 and its state space description is as follows:

$$\begin{bmatrix} \dot{z}_1 \\ \dot{z}_2 \end{bmatrix} = \begin{bmatrix} 0 & w \\ -w & 0 \end{bmatrix} \begin{bmatrix} \Theta(z_1) \\ \Theta(z_2) \end{bmatrix} + \begin{bmatrix} x_1 \\ x_2 \end{bmatrix} \quad (12)$$

where activation function $\Theta(z)$ is passive and fulfills:

$$\mu_1 \leq \frac{\Theta(z_i)}{z_i} \leq \mu_2; \mu_1, \mu_2 \in [0, \infty), i = 1, 2$$

x - input data

z - state vector

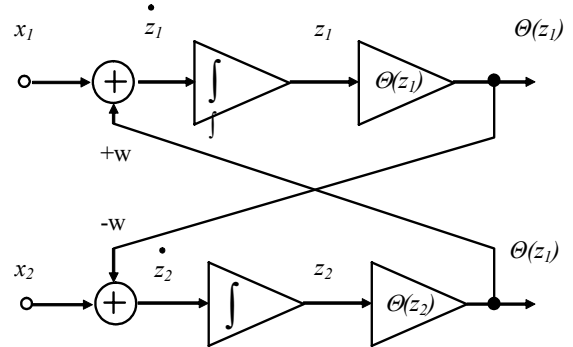


Figure 1. D.C. model of lossless neuron.

This model gives rise to the following notes:

1. From the point of view of circuit theory, a lossless neuron can be treated as a loop connection of a nonlinear inductor and capacitor, forming a passive nonlinear oscillator. Moreover, looking for an analogy between circuit theory and mechanics, one could consider the above mentioned oscillator as an energy model of a relativistic particle. Indeed, taking into consideration the following classical relationships:

$$F = \dot{p} \quad (13)$$

$$v(p) = \frac{p}{m_0 \sqrt{1 + \left(\frac{p}{m_0 c}\right)^2}} \quad (14)$$

where: F - external force

p - momentum

c - absolute velocity

m_0 - rest mass

v - velocity (activation function)

for free particle ($F = 0$), one obtains the basic model of a Hamiltonian particle, as shown in Fig.2

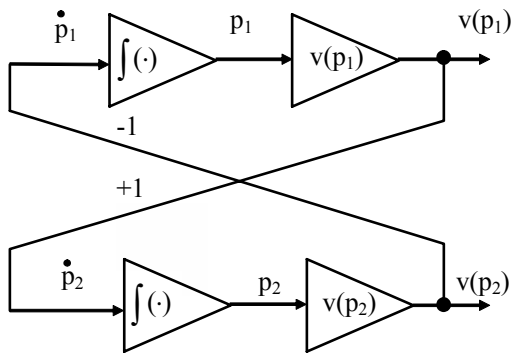


Figure 2. Model of Hamiltonian particle ("fermion")

Thus, Eq. (12) takes the following form:

$$\begin{aligned} \dot{p}_1 &= v(p_2) \\ \dot{p}_2 &= -v(p_1) \end{aligned} \quad (15)$$

Assuming, $p_1 = p_2 = p$, the whole internal energy stored in the particle shown in the Fig. 2. is given by Hamiltonian:

$$H = E = 2 \int_{-\infty}^t \dot{p} v(p) dt = \frac{2}{m_0} \int_0^{p_{max}} \frac{p}{\sqrt{1 + \left(\frac{p}{m_0 c}\right)^2}} dp = 2m_0 c^2 \left(\sqrt{1 + \left(\frac{p_{max}}{m_0 c}\right)^2} - 1 \right) \quad (16)$$

Considering a linearization of function $v(p)$, as shown in Fig.3.

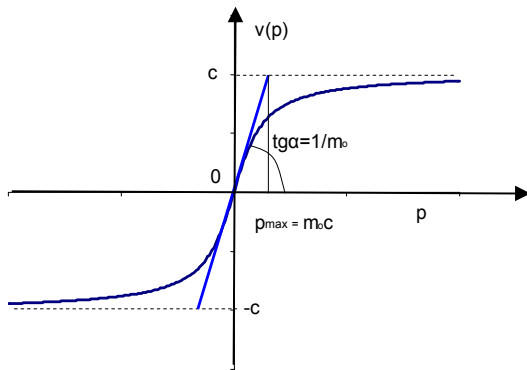


Figure 3. Velocity in SRT.

equation (16) takes the following form:

$$\begin{aligned} \text{for } p_{max} &= m_0 c \text{ (see Fig.3.)} \\ E &= 2 \cdot 0.41 \cdot m_0 c^2 = 0.82 \cdot m_0 c^2 \end{aligned} \quad (17)$$

The classical amount of rest energy i.e., $E_0 = m_0 c^2$, is obtained only under the assumption that function $v(p)$ is piecewise linear. The model of particle used in this consideration can be seen as a Hamiltonian oscillator. Solutions of Eq.(15) are periodical and are dependent on initial values of momentum. Thus, for example, a numerical solution for initial values: $|p_{01}| = m_0 c$, $p_{02} = 0$ or $|p_{02}| = m_0 c$, $p_{01} = 0$ is presented in Fig. 4.

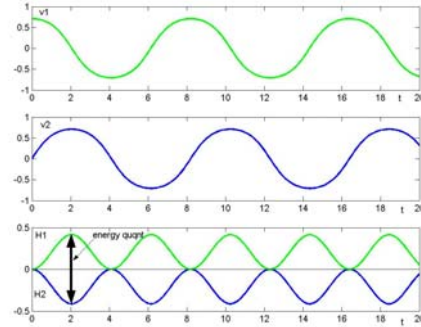


Figure 4. A numerical solution of dynamical system Eq (15) for $p_{01} = 1$, $p_{02} = 0$, $m_0 = 1$, $c = 1$

$$H_{1max} + H_{2max} = 0.82 \cdot m_0 c^2$$

where

$$H_{imax} = \max \left| \int_0^t \dot{p}_i v_i dt \right|$$

It can be seen, that the internal energy of a particle-oscillator has a form of quanta. For external observers, this energy is not visible. In the case of Eq.(15), force field is skew-symmetric, i.e., the internal forces are of "electromagnetic" type. However, this skew-symmetry can be easily changed into symmetry. Hence, the particle-oscillator is a "connection", via an internal "gravitation field" (symmetric), of matter ($m > 0$) and antimatter ($m < 0$). It is worth noting, that, by adequate interpretation of solutions (Fig.4.), one could easily obtain such objects like "spin" and "uncertainty". But, such interpretation would guide us to exotic physics.

2. A D.C. model of a lossless neuron can be, one-to-one, transformed into an oscillatory model, using two phase-locked-loops (PLLs). Such a PLL based model is shown in Fig. 5

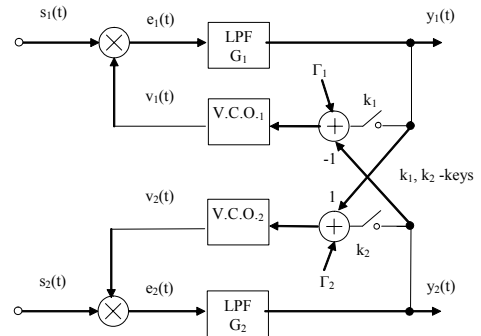


Figure 5. Oscillatory model of lossless neuron.

It is easy to see that the model in Fig. 5 (PLL model) consists of two antisymmetrically coupled sinusoidal phase oscillators. Input signals $s_i(t)$, $i = 1, 2$ are sinusoidal carriers. Thus:

$$s_i(t) = A_{C_i} \sin(\Omega_i t + \Psi_{s_i}), \quad (18)$$

$$v_i(t) = A_{V_i} \cos(\Omega_i t + \Psi_i); \quad i = 1, 2. \quad (19)$$

Assuming ideal transmittances of loop filters, i.e., $G_1 = G_2 \equiv 1$, the mean phase equation (Adler equation) of this model is as follows (keys k_1, k_2 open):

$$\frac{d}{dt} \begin{bmatrix} \Psi_{s_1} - \Psi_1 \\ \Psi_{s_2} - \Psi_2 \\ \vdots \\ \Psi_{s_n} - \Psi_n \end{bmatrix} = 2\pi \begin{bmatrix} 0 & \pm k_{v_1} k_{m_2} A_{C_2} A_{V_2} \\ \mp k_{v_2} k_{m_1} A_{C_1} A_{V_1} & 0 \\ \vdots & \vdots \\ \mp k_{v_n} k_{m_1} A_{C_1} A_{V_1} & \mp k_{v_n} k_{m_2} A_{C_2} A_{V_2} \\ \vdots & \vdots \\ \mp k_{v_n} k_{m_1} A_{C_1} A_{V_1} & \mp k_{v_n} k_{m_2} A_{C_2} A_{V_2} \\ \vdots & \vdots \\ -k_{v_n} k_{m_1} A_{C_1} A_{V_1} & -k_{v_n} k_{m_2} A_{C_2} A_{V_2} \end{bmatrix} \begin{bmatrix} \sin(\Psi_{s_1} - \Psi_1) \\ \sin(\Psi_{s_2} - \Psi_2) \\ \vdots \\ \sin(\Psi_{s_n} - \Psi_n) \end{bmatrix} + \begin{bmatrix} \Delta\omega_1 \\ \Delta\omega_2 \\ \vdots \\ \Delta\omega_n \end{bmatrix} - 2\pi \begin{bmatrix} k_{v_1} \Gamma_1 \\ k_{v_2} \Gamma_2 \\ \vdots \\ k_{v_n} \Gamma_n \end{bmatrix} \quad (20)$$

where: $\Delta\omega_i$ - frequency deviations of input $s_i(t)$ signal
 k_{v_i} , k_{m_i} - sensitivity of VCO and phase-detector, respectively
 Γ_i - input d.c. signal ($i = 1, 2$)

The similarity between equation (20) and Kuramoto model is worth noting. Closing k_1, k_2 - keys in model from Fig. 5. one obtains an elementary PLL orthogonal filter described by:

$$\frac{d}{dt} \begin{bmatrix} \Psi_{s_1} - \Psi_1 \\ \Psi_{s_2} - \Psi_2 \\ \vdots \\ \Psi_{s_n} - \Psi_n \end{bmatrix} = 2\pi \begin{bmatrix} -k_{v_1} k_{m_1} A_{C_1} A_{V_1} & k_{v_1} k_{m_2} A_{C_2} A_{V_2} \\ -k_{v_2} k_{m_1} A_{C_1} A_{V_1} & -k_{v_2} k_{m_2} A_{C_2} A_{V_2} \\ \vdots & \vdots \\ -k_{v_n} k_{m_1} A_{C_1} A_{V_1} & -k_{v_n} k_{m_2} A_{C_2} A_{V_2} \end{bmatrix} \begin{bmatrix} \sin(\Psi_{s_1} - \Psi_1) \\ \sin(\Psi_{s_2} - \Psi_2) \\ \vdots \\ \sin(\Psi_{s_n} - \Psi_n) \end{bmatrix} + \begin{bmatrix} \Delta\omega_1 \\ \Delta\omega_2 \\ \vdots \\ \Delta\omega_n \end{bmatrix} - 2\pi \begin{bmatrix} k_{v_1} \Gamma_1 \\ k_{v_2} \Gamma_2 \\ \vdots \\ k_{v_n} \Gamma_n \end{bmatrix} \quad (21)$$

where assumed that connection matrix has a form:

$$\mathbf{W}_c = \mathbf{W} - w_0 \mathbf{1} \quad (22)$$

$$\text{with } \mathbf{W}^2 = -\mathbf{1}, \mathbf{W}^T = \mathbf{W}^{-1} = -\mathbf{W} \quad (23)$$

and $w_0 > 0$ (\mathbf{W} -skew-symmetric, orthogonal)

Let us note that PLL implementation of the elementary orthogonal filter from Fig.5. can be easily scaled up to n-dimensional space. Such a generalization is shown in Fig.6. [7].

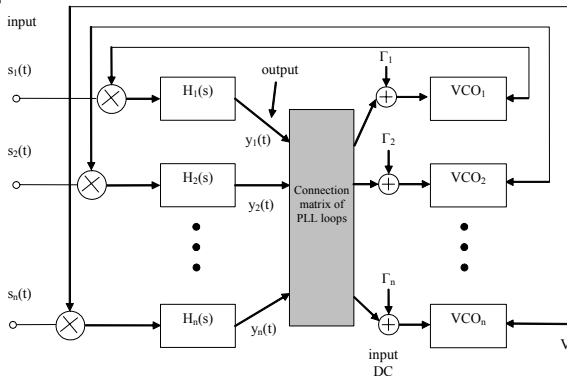


Figure 6. PLL model of n-dim neural network

The Adler equation of this model is given by:

$$\frac{d}{dt} \begin{bmatrix} \Psi_{s_1} - \Psi_1 \\ \Psi_{s_2} - \Psi_2 \\ \vdots \\ \Psi_{s_n} - \Psi_n \end{bmatrix} = 2\pi \begin{bmatrix} -k_{v_1} k_{m_1} A_{C_1} A_{V_1} & \pm k_{v_1} k_{m_2} A_{C_2} A_{V_2} & \cdots & \pm k_{v_1} k_{m_n} A_{C_n} A_{V_n} \\ \mp k_{v_2} k_{m_1} A_{C_1} A_{V_1} & \cdots & \cdots & \pm k_{v_2} k_{m_n} A_{C_n} A_{V_n} \\ \vdots & \vdots & \vdots & \vdots \\ \mp k_{v_n} k_{m_1} A_{C_1} A_{V_1} & \mp k_{v_n} k_{m_2} A_{C_2} A_{V_2} & \cdots & -k_{v_n} k_{m_n} A_{C_n} A_{V_n} \end{bmatrix} \begin{bmatrix} \sin(\Psi_{s_1} - \Psi_1) \\ \sin(\Psi_{s_2} - \Psi_2) \\ \vdots \\ \sin(\Psi_{s_n} - \Psi_n) \end{bmatrix} + \begin{bmatrix} \Delta\omega_1 \\ \Delta\omega_2 \\ \vdots \\ \Delta\omega_n \end{bmatrix} - 2\pi \begin{bmatrix} k_{v_1} \Gamma_1 \\ k_{v_2} \Gamma_2 \\ \vdots \\ k_{v_n} \Gamma_n \end{bmatrix} \quad (24)$$

where : $s_i(t) = A_{C_i} \sin(\Omega_i t + \Psi_{s_i})$
 $v_i(t) = A_{V_i} \cos(\Omega_i t + \Psi_i)$
 $\Delta\omega_i$ - frequency deviation
 Γ_i - input d.c. signal
 $i = 1, \dots, n$

Equation (24) can be rewritten as:

$$\dot{\mathbf{z}} = \mathbf{W}_c \sin \mathbf{z} + \Delta\omega - \Gamma \quad (25)$$

where: $\mathbf{z} = [z_1, \dots, z_n]^T = [\Psi_{s_1} - \Psi_1, \dots, \Psi_{s_n} - \Psi_n]^T$

\mathbf{W}_c - matrix of connections.

It is worth noting that:

1. The hold range of a PLL network is determined by the stable equilibrium of Eq.(25). It means that, for a given $\Delta\omega$ and Γ , one can find such loop gains ($k_v k_m A_c A_v$) that PLL network attains synchronization in point: $|\sin z_i| < 1, i = 1, \dots, n$.
2. Under synchronization, the steady-state output of PLL network is given by:

$$\mathbf{y} = \sin \mathbf{z} = \mathbf{W}_c^{-1} (\Gamma - \Delta\omega). \quad (26)$$

Taking connection matrix \mathbf{W}_c as weight matrix in orthogonal filter, output \mathbf{y} gives the Haar spectrum of the input vector. Moreover, the PLL network from Fig.6 can be treated as a n-dimensional F.M. signal demodulator.

3. The PLL network from Fig. 6. can be seen as a model of a neural network with dynamical connections. The weight of connections can be changed by parameter k_v (i.e. sensitivity of VCO).

IV. ORTHOGONAL FILTERS BASED NONLINEAR MAPPINGS

Nonlinear functions or mappings approximation can be implemented by using HNN-based orthogonal filters, which perform spectrum analysis and memorization. Function approximation, as known from machine learning, starts with training data $(\mathbf{x}_i, \mathbf{y}_i)_{i=1}^m$, where input vectors $\mathbf{x}_i \in X \subset \mathbb{R}^n$ and $\mathbf{y}_i \in Y \subset \mathbb{R}$. One synthesizes a multivariate function that

optionally represents the relation between the input \mathbf{x}_i and y_i . We use here a kernel representation, i.e.:

$$f(\mathbf{x}) = \sum_{i=1}^m c_i \mathbf{K}_{\mathbf{x}_i}(\mathbf{x}) \quad (27)$$

where: $\mathbf{c} = [c_1, c_2, \dots, c_m]^T$, $c_i \in \mathbb{R}$

and kernels $\mathbf{K}_{\mathbf{x}_i}(\mathbf{x})$ are definite functions continuous on $X \times X$. The weights c_i are such, to minimize the error on the training set, i.e., they can be found from the equation:

$$\mathbf{K} \mathbf{c} = \mathbf{y} \quad (28)$$

where: \mathbf{K} is the square matrix with elements $K_{ij} = \mathbf{K}_{\mathbf{x}_i}(\mathbf{x}_j)$ and \mathbf{y} is the vector with coordinates y_i .

For implementation of $f(\mathbf{x})$, equation (28) has to be well-posed. One of the most important positive-definite kernels is the Gaussian:

$$\mathbf{K}_{\mathbf{x}_i}(\mathbf{x}) = e^{-\|\mathbf{x}_i - \mathbf{x}\|^2 / 2\sigma^2}$$

giving structure known as RBF.

Generally, taking kernels as positive-definite functions, matrix \mathbf{K} in Eq.(28) is positive-definite and hence Eq.(28) is well-posed. Moreover, taking into account the Tikhonov regularization, Eq.(28) can be reformulated as a key algorithm for RLSC structure, as follows [4]:

$$(\gamma \mathbf{1} + \mathbf{K}) \mathbf{c} = \mathbf{y} \quad (29)$$

where: $\gamma > 0$ and $(\gamma \mathbf{1} + \mathbf{K})$ is strictly positive.

The purpose of this paper is to show, how mappings, classifiers and associative memories can be implemented using HNN based orthogonal filters, which perform spectrum analysis. Spectrum analysis can be treated as a transform from input signal space into a feature space. Relying on RLSC approach, we propose to define here a skew-symmetric kernel $\mathbf{K}_{\mathbf{u}_i}(\mathbf{v})$:

$$\mathbf{K}_{\mathbf{u}_i}(\mathbf{v}) := \Theta(\mathbf{u}_i^T \mathbf{v}) \quad (30)$$

where: $\mathbf{u}_i = (\mathbf{W} - \mathbf{1}) \mathbf{x}_i$

$\mathbf{v} = -(\mathbf{W} + \mathbf{1}) \mathbf{x}$

$\Theta(\cdot)$ is an odd function (e.g. sigmoid)

$\mathbf{W}^2 = -\mathbf{1}$, $\mathbf{W}^T \mathbf{W} = \mathbf{1}$

$w_0 > 0$

\mathbf{u}_i, \mathbf{v} – Haar spectrum of input \mathbf{x}_i and \mathbf{x} , respectively

Thus:

$$\mathbf{K}_{\mathbf{u}_i}(\mathbf{v}_j) = \Theta(\mathbf{u}_i^T \mathbf{v}_j) = \Theta(2\mathbf{x}_i^T \mathbf{W} \mathbf{x}_j)$$

and

$$\mathbf{K}_{\mathbf{v}_j}(\mathbf{u}_i) = -\mathbf{K}_{\mathbf{u}_i}(\mathbf{v}_j)$$

Hence, matrix

$\mathbf{K}_a = \{\mathbf{K}_{i,j}\} = \{\mathbf{K}_{\mathbf{u}_i}(\mathbf{v}_j)\}$ is skew-symmetric

As mentioned above, the key problem in design of the approximation is the solvability of linear equation:

$$\mathbf{K}_a \mathbf{c} = \mathbf{y} \quad (31)$$

Since \mathbf{K}_a is skew-symmetric, it needs to be regularized, making equation (31) well-posed.

Hence, we propose the following regularization of matrix \mathbf{K}_a :

$$\mathbf{K}_r = (\gamma \mathbf{1} + \mathbf{K}_a) \quad (32)$$

where: $\gamma \neq 0$

Then, the following design equation is well-posed for any $m < \infty$ (number of training vectors):

$$\mathbf{K}_r \mathbf{c} = \mathbf{y} \quad (33)$$

One of possible architectures, implementing equation (27) with skew-symmetric kernels K_{ij} is shown in Fig.7.

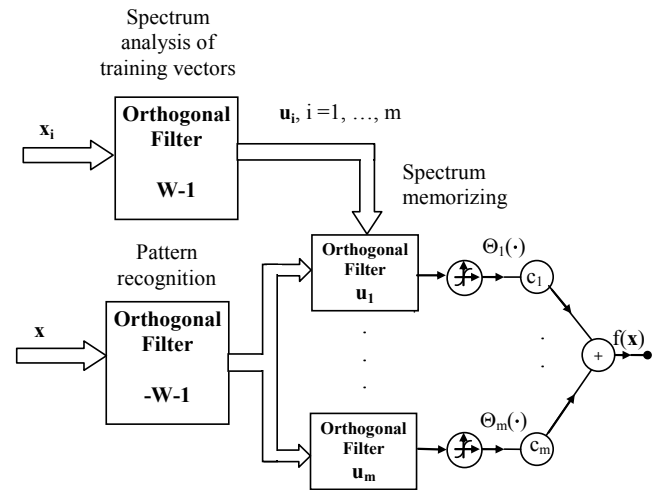


Figure 7. Structure of function $f(\mathbf{x})$ approximator.

Thus, the unknown function $f(\mathbf{x})$ can be approximated by the structure from Fig.7. consisting of two HNN based spectrum analyzers and a set of m orthogonal filters memorizing the spectrum of m training points. It is easy to see that the activation functions $\Theta(\cdot)$ of neurons should be endowed with a “superconducting impulse” γ , as shown in Fig. 8.

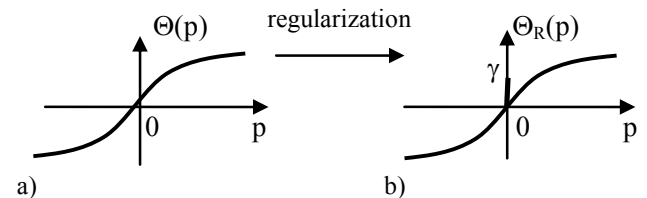


Figure 8. Activation function of neurons.

Hence, one obtains:

the overall structure from Fig.7. can be implemented by connection of oscillatory (PLL) octonionic modules.

VI. SIMULATIONS

As mentioned above, Eq.(24) and (25) describe the mean equation of a PLL network. But, in real implementations, the loop filters have to be taken into consideration. In other words, one has to pose a question: Is it possible to find such loop filters where full phase equation and Adler equation for PLL network are approximately the same? From an analytical point of view such a possibility exists, since a PLL network has a stable integral manifold [8]. This possibility has been experimentally proven by simulations using the makro-models of PLL, offered by Matlab-Simulink.

Some simulations of octonionic modules have been performed by using a general PLL model from Fig.6.. Full analysis using Matlab-Simulink macro-models of phase-locked loops, endowed with different loop filters, showed that algebraic transformation given by Eq. 36. can be, under synchronization, exactly performed by oscillatory structure. Moreover, this structure sets up an oscillatory memory cell, according to solution presented in Fig. 9.

VII. CONCLUSION

The main issue considered in this paper is the design of mappings. Mappings designed here rely on multivariate function approximations with skew-symmetric kernels, giving rise to very large scale classifiers and associative memories. Due to regularization, such classifiers and memories can be implemented for any even n (dimension of input vector space) and any $m < \infty$ (number of training patterns). Accuracy of classification depends on phase-space geometry of mappings. It can be changed by appropriate covering of the neighborhood of the approximation points. Kernels utilized in function and mapping approximation are implemented by using HNN based orthogonal filters. Thus, classifiers and memories, here designed, can exist as numerically stable algorithms or physical devices, performing their functions in real-time. Moreover, we have proposed oscillatory (PLL) implementation of mappings. Presented in this paper PLL neural networks can be seen as a special problem in the theory of coupled oscillators. To our knowledge, orthogonal filters based information processing can be considered as inspired by biological systems.

REFERENCES

- [1] K. H. Pribram, "Free Will: The Brain as an Anticipatory System", *Proceedings of Third International Conference on Computing Anticipatory Systems*, AIP Conference Proceedings No 517, Liege, Belgium, 1999.
- [2] J. A. Anderson, P. Allopenna, "The Ersatz Brain Project: Neural Inspiration, Cognitive Application", *Proceedings of IEEE International Joint Conference on Neural Networks*, Vancouver, Canada, 2006.
- [3] B. Widrow, J. C. Aragon, "Cognitive Memory", *Computational Intelligence: Principles and Practice*, Edited by G.Y. Yen and D.B.

Fogel, *IEEE World Congress on Computational Intelligence*, Vancouver, Canada, 2006.

- [4] T. Poggio, S. Smale, "The Mathematics of Learning: Dealing with Data", *Notices of the AMS*, vol. 50, no. 5, pp. 537-544, 2003.
- [5] W. Sienko, D. Zamojski, "Hamiltonian Neural Networks Based Classifiers and Mappings", *Proceedings of IEEE International Joint Conference on Neural Networks*, Vancouver, Canada, 2006.
- [6] W. Sienko, D. Zamojski, "On Geometry of Hamiltonian Neural Networks Based Classifiers", *Proceedings of IEEE International Conference on Signals and Electronic Systems*, Łódź, Poland, pp. 471-474, 2006.
- [7] W. Sienko, W. Citko, "Orthogonal Filter-Based Classifiers and Associative Memories", *Proceedings of International Joint Conference on Neural Networks (IJCNN)*, Orlando, USA, 2007.
- [8] J. Kudrewicz, "Dynamics of Phase Loop" WNT, Warszawa 1991(in polish)
- [9] F. C. Hoppensteadt, E. M. Izhikevich, "Weakly Connected Neural Network", *Springer*, New York 1997.
- [10] E. M. Izhikevich, "Weakly connected quasiperiodic oscillators, FM interactions, and multiplexing in the brain", *SIAM Journal on Applied Mathematics* 59, pp.. 2193-2223, 1999.
- [11] E. M. Izhikevich, "Dynamical Systems in Neuroscience: The Geometry of Excitability and Bursting", *Cambridge, MA: The MIT Press*, 2006.
- [12] F. C. Hoppensteadt, E. M. Izhikevich, "Pattern Recognition Via Synchronization in Phase-Locked Loop Neural Networks", *IEEE Transactions on Neural Networks*, vol. 11, No.2, May 2000.
- [13] S. H. Strogatz, "From Kuramoto to Crawford exploring the onset of synchronization in populations of coupled oscillators", *Physica D* 143: p. 1-20, 2000.
- [14] W. Sienko, "Quantum Aspect of Passive Neural Networks", *Proc. of Third International Conference on Computing Anticipatory Systems*, Liege, Belgium, Sym. 2, p.18, 1999.
- [15] B. Eckmann, "Topology, Algebra, Analysis-Relations and Missing Links", *Notices of the AMS*, vol. 46, no. 5, pp. 520-527, 1999.

Wieslaw Citko received his Ph.D. degree in electrical engineering from Technical University of Lodz in 2000. Currently he is an Associate Professor at the Telecommunications Department of the Electrical Engineering Faculty of Gdynia Maritime University. His research interests include nonlinear circuits, neural networks and signal processing.



Wieslaw Sienko received his Ph.D. and D.Sc. degrees in electrical engineering from the Technical University of Gdansk. Currently he is a Professor at the Telecommunications Department of the Electrical Engineering Faculty of Gdynia Maritime University. His research interests include circuits theory, neural networks, quantum algorithms and signal processing.



Generation and Circuitry Implementation of N -double Scroll Delayed Chaotic Attractors

Lidan Wang, Shukai Duan

School of Electronics and Information Engineering
Southwest University
Chongqing 400715, China
lidanwang@yahoo.cn, duansk@swu.edu.cn

Xiaofan Yang

College of Computer Science
Chongqing University
Chongqing 400044, China
xf_yang1964@yahoo.com

Abstract—A first-order delayed chaotic model with n -double scroll attractors is investigated. The associated piecewise-linear activation function requires only a few operational amplifiers, which can easily be realized by an electronic circuit. The typical waveforms and phase portraits are plotted to illustrate n -double scroll chaotic oscillations.

Keywords—delay; chaotic attractor; n -double scroll; circuitry implementation; chaotic oscillation

I. INTRODUCTION

The theoretical study and circuitry implementation of more complex chaotic systems have been a key issue in various technological and engineering applications. Indeed, there were reported many multi-scroll, n -double scroll oscillators, which are produced with ODEs [1-2], where the activation function assumes a sine function, a piecewise linear function, or a hysteresis series, etc. Due to additional breakpoints owned by such activation functions, these systems exhibit hyperchaotic oscillations with multiple positive Lyapunov exponents.

On the other hand, chaotic behaviors have been found in various simple first-order systems with delayed feedback. This implies the evolution of state of such a system inherently depends on its history as well as its present state [3]. A diversity of delayed systems stemming from biology, ecology and engineering can be considered as models to analyze and implement hyperchaos [4-8].

In this pursuit, we study a novel delayed chaotic model capable of generating n -double scroll chaotic oscillations, where the nonlinear activation function is mathematically a PWL function and its circuitry implementation requires only several operational amplifiers. Experimental results show that the proposed attractor can exhibit mono-scroll, one- two-, three- or four-double scroll chaotic oscillations by adjusting the value of a single parameter.

The rest of this paper is organized as follows. In Section 2, the mathematical model of the proposed n -double scroll system is described. In Section 3, the electronic circuitry implementation of this system is discussed and analyzed in detail. Finally, some concluding remarks are given in Section 4.

II. MATHEMATICAL MODEL

In this paper, we propose an n -double scroll delayed chaotic model:

$$\frac{dx}{dt} = -x(t) + g[x(t - \tau)] \quad (1)$$

where τ is a delay time, g is a piecewise-linear activation function of the form:

$$g_{2n}(x) = m_n x + \frac{1}{2} \sum_{i=1}^n (m_{i-1} - m_i) (|x + c_i| - |x - c_i|) \quad (2)$$

n denotes number of double scrolls, m_i ($i = 1, \dots, n$) and c_i ($i = 1, \dots, n$) represent the slopes and values in the abscissa corresponding inflexions of the piecewise-linear activation function, respectively. As an example, when $n = 4$, $m_0 = m_2 = m_4 = -6.5$, $m_1 = m_3 = -8.5$, $c_1 = 0.8$, $c_2 = 2.4$, $c_3 = 4$, $c_4 = 5.6$, $\tau = 10$, the activation function is shown in Fig. 1, and the system (1) shows a four-double scroll chaotic oscillations, plotted in Fig. 2.

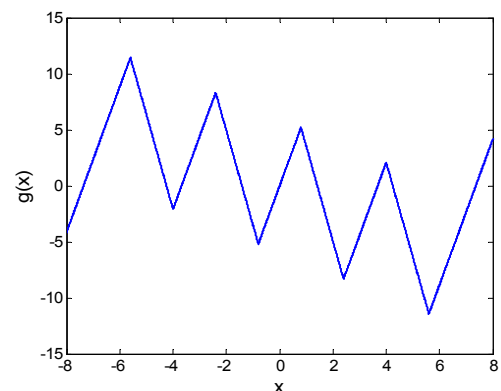


Fig. 1. Waveform diagram of a piecewise-linear function.

III. CIRCUITRY IMPLEMENTATION

In this section, an electronic circuit is designed to realize an n -double scroll delayed system. The circuit consists of a

piecewise-linear activation function circuit unit, a time delay circuit unit, an integration circuit unit and a low-pass filter. Common resistors, capacitors, inductances and operational amplifiers are employed to realize these circuit units. DC voltage sources supply energy of the circuit system.

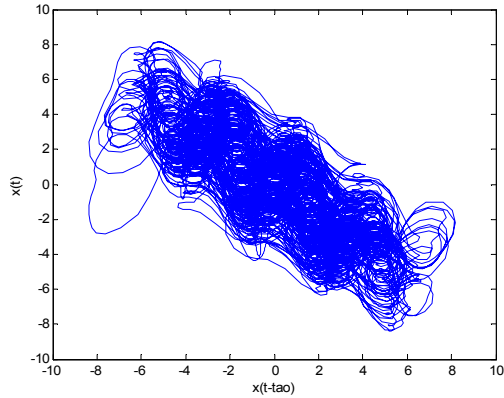


Fig. 2. Phase trajectories of the *four-double scroll* chaotic attractor.

A. Circuit Implementation of the Piecewise-linear Activation Function

To facilitate the circuitry design, piecewise-linear activation function (6) for four-double scroll oscillator is reformulated as follows:

$$\begin{aligned}
 g_8(x) = & m_4 x + \frac{1}{2}(m_0 - m_1)(|x + c_1| - |x - c_1|) \\
 & + \frac{1}{2}(m_1 - m_2)(|x + c_2| - |x - c_2|) \\
 & + \frac{1}{2}(m_2 - m_3)(|x + c_3| - |x - c_3|) \\
 & + \frac{1}{2}(m_3 - m_4)(|x + c_4| - |x - c_4|)
 \end{aligned} \quad (3)$$

Obviously, the waveform diagram of the piecewise-linear function (3) can easily be varied by adjusting the values of m_i and c_i , $i = 1, \dots, n$. Let

$$\begin{cases} m_0 = m_2 = m_4 = ka \\ m_1 = m_3 = kb \end{cases} \quad (4)$$

where $k > 0$ is a common scaling factor of all the slopes, $a > 0$ and $b < 0$ are initial slopes of the line segments involved in the function (3). Hence, we can adjust all slopes synchronously by changing the value of k .

The function (3) can be circuitry implemented by a combination of six operational amplifiers and assistant circuits, as shown in Fig. 3.

The operational amplifiers ($\mu A741$ U_1-U_6) are employed to realize the gain control, subtraction and reversion operations.

The values of the resistors are: $R_1 = R_3 = R_5 = R_7 = R_{15} = R_{16} = 1k\Omega$, $R_2 = R_4 = R_6 = R_8 = 15k\Omega$, $R_9 = R_{10} = R_{11} = R_{12} = 2k\Omega$, $R_{13} = 307\Omega$, $R_{14} = 2k\Omega$. The constant voltage sources are: $V_1 = 1.4V$, $V_2 = -1.4V$, $V_3 = 4.2V$, $V_4 = -4.2V$. The voltages of the electronic sources are $\pm 12V$. All of the slopes in (3) are changed synchronously by adjusting the value of resistor R_{14} .

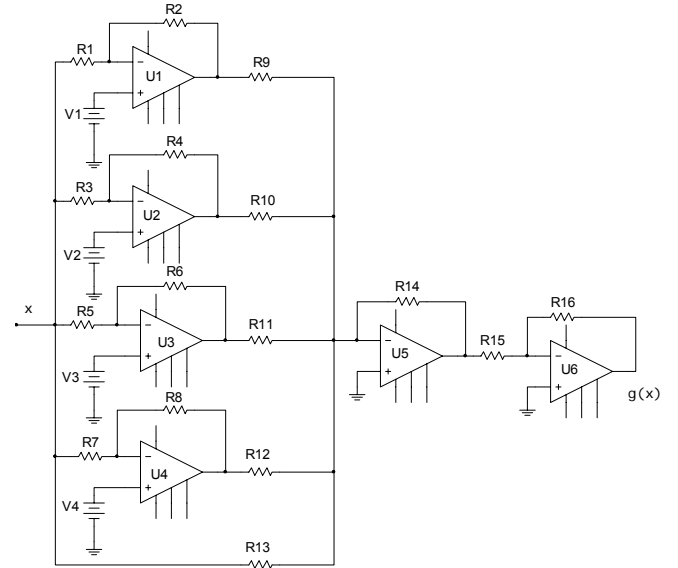


Fig. 3. A circuitry implementation of $g_8(x)$.

The DC sweep analysis result of the piecewise-linear activation function circuit unit is given in Fig. 4.

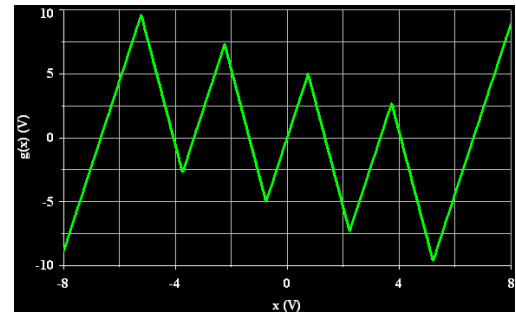


Fig. 4. The DC sweep analysis result of the piecewise-linear function circuit.

B. Circuit Implementation of the Time Delay Unit

A circuit implementation for the delay unit is plotted in Fig. 5. This is a network of T -type LCL filters with matching resistors at the input and the output. The time delay can be approximated by

$$T_{Delay} = n\sqrt{2LC}, \quad n \geq 1, \quad (5)$$

where n is the number of the LCL filter. From (5), it can be seen that the value of the time delay can be tuned by changing the values of the inductances and capacitors in circuit unit, or changing the number of the LCL filter. Notably, the time delay unit will somewhat bring a little attenuation of the circuit gain. To eliminate this hurdle, two additional operational amplifiers

(U_7 and U_8) are used to adjust the circuit gain. Inductances $L_i = 9.5mH$ ($i = 1, 2, \dots, 20$), capacitors $C_i = 525 nF$ ($i = 1, 2, \dots, 10$) and resistors $R_{17} = R_{18} = R_{21} = 10k\Omega$, $R_{19} = R_{20} = 1k\Omega$, $R_{22} = 30k\Omega$ are chosen, respectively. The effectiveness of the time delay unit is demonstrated by observing the output of the circuit unit when a sine wave with frequency $1kHz$ and amplitude $1.35V$ is given, as shown in Fig. 6.

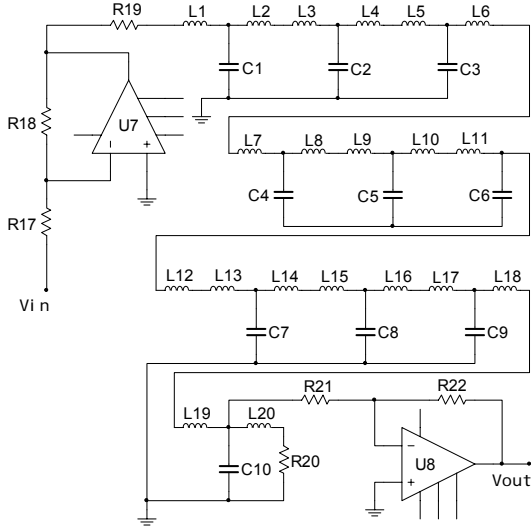


Fig. 5. Circuit implementation of the time delay unit.

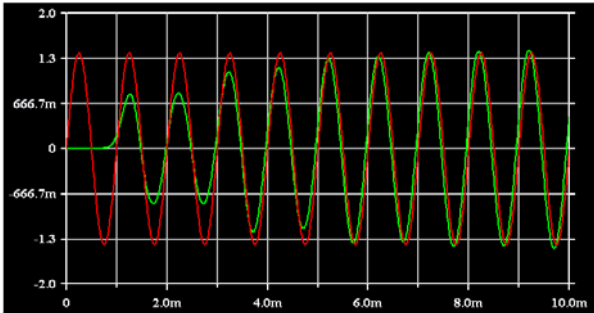


Fig. 6. Input (red waveform) and output (green waveform) of the proposed time delay unit when a sine wave is given.

C. Circuit Implementation of the N -double Scroll Delayed Chaotic Model

Now, the proposed n -double scroll chaotic system can be implemented by a piecewise-linear activation function circuit unit, a time delay circuit unit, an integration circuit unit and a low-pass filter ($R_0 C_0$), as shown in Fig. 7. For simplification, we use block diagrams to replace those already designed circuit units.

The dimensionless delay parameter τ is calculated according to the rule

$$\tau = T_{Delay} / R_0 C_0 \quad (6)$$

A standard node analysis of the circuit shows that the state equation that governs the dynamical behavior of the circuit is

$$\frac{dx(t)}{dt} = -\frac{1}{R_{24}C_{11}}x(t) + \frac{1}{R_{23}C_{11}}g[x(t-\tau)] \quad (7)$$

when $R_{23} = R_{24} = 10k\Omega$, $R_0 = 1k\Omega$, $C_{11} = 10nF$, $C_0 = 100nF$, Eq. (6) is equivalent to system (1) with activation function (3) and $\tau = 10$. In addition, the coefficients of $x(t)$ and $g[x(t-\tau)]$ can be varied independently by adjusting the values of resistors R_{24} and R_{23} .

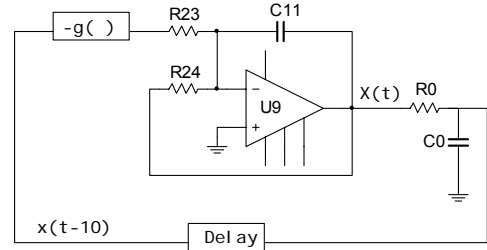
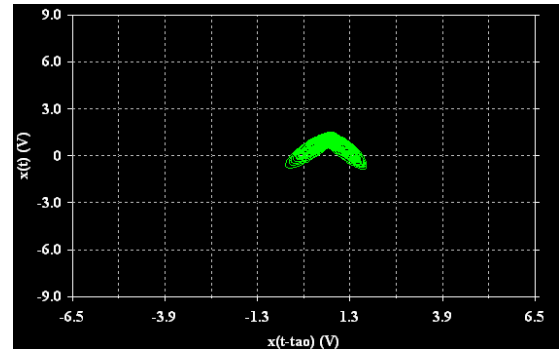
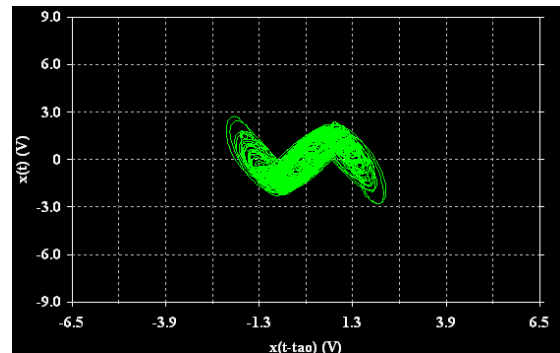


Fig. 7. Circuit implementation of the n -double scroll chaotic model.

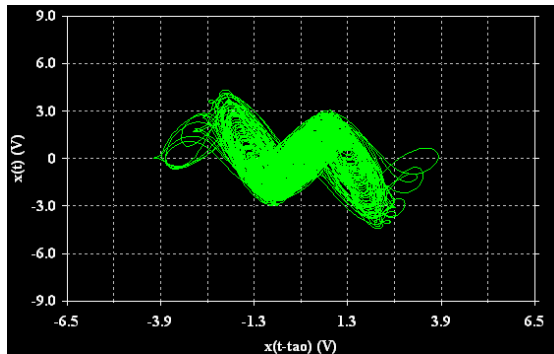
Through experimental observation, we find that the proposed n -double scroll circuit can exhibit mono-, two- or three-double-scroll chaotic oscillations with the change of the value of resistor R_{14} . The respective phase plane diagrams of the chaotic double scroll circuits are given in Fig. 8. A comparison between Fig. 2 and Fig. 8 (e) indicates a qualitative agreement between the numerical simulation and the experimental measurement.



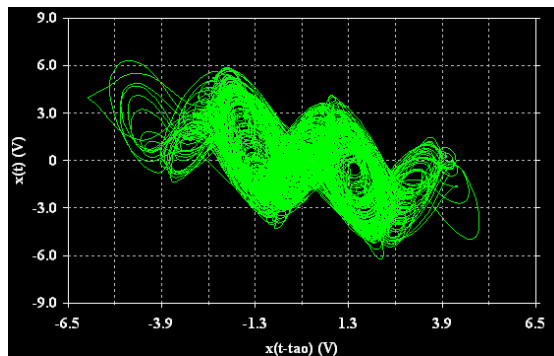
(a)



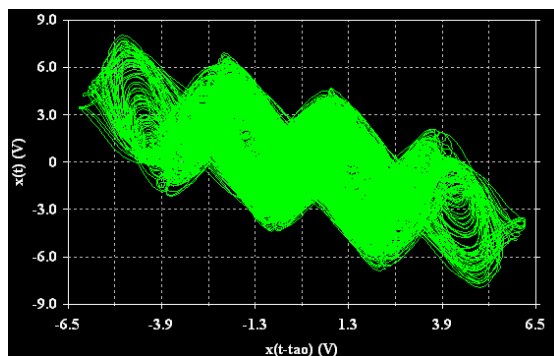
(b)



(c)



(d)



(e)

Fig. 8. Phase portraits of the n -double scroll chaos generator: (a) a mono-scroll oscillation when $R_{14} = 620\Omega$; (b) a one-double scroll oscillation when $R_{14} = 1.0k\Omega$; (c) a two-double scroll oscillation when $R_{14} = 1.3k\Omega$; (d) a three-double scroll oscillation when $R_{14} = 1.8k\Omega$; (e) a four-double scroll oscillation when $R_{14} = 2.0k\Omega$.

IV. CONCLUSION

We have presented a first-order delayed model with PWL activation function that displays double scrolls chaotic behavior, and have proposed a scheme for its circuit implementation. By adjusting the value of a single resistor, this simple circuit exhibits complex chaotic behaviors such as (a) a mono-scroll chaotic oscillation and (b) one-, two-, three- or four-double scroll chaotic oscillations.

The proposed chaotic circuit may be used as a delayed multi-scroll chaos generator, a chaotic neuron circuit unit, or

even a cell for delayed cellular neural network. It has potential applications to secure communication and signal processing.

ACKNOWLEDGMENT

This work was supported by the Natural Science Foundation of Chongqing CSTC (2007BB2331), the Doctorate Foundation of the Southwest University (104180-20710907) and Natural Science Foundation of China (10771227).

REFERENCES

- [1] G. Chen and T. Ueta, *Chaos in circuits and systems*, World Scientific, Singapore, 2002.
- [2] J. Lü and G. Chen, "Multi-scroll chaos generation: theories, methods and applications," *Int. J. Bifurc. Chaos*, vol. 16, pp. 775-858, 2006.
- [3] P. Thangavel, K. Murali and M. Lakshmanan, "Bifurcation and controlling of chaotic delayed cellular neural networks," *Int. J. Bifurcation Chaos*, vol. 8, pp. 2481-2492, 1998.
- [4] J. D. Farmer, "Chaotic attractor of an infinite-dimensional dynamical system," *Physica D*, vol. 4, pp. 366-393, 1982.
- [5] K. Ikeda and M. Matsumoto, "Study of a high dimensional chaotic attractor," *J. Stat. Phys.*, vol. 44, pp. 955-983, 1986.
- [6] M. C. Mackey and L. Glass, "Oscillation and chaos in physiological control system," *Science*, vol. 197, pp. 287-289, 1977.
- [7] A. Tamaševičius, G. Mykolaitis and S. Bumelienė, "Delayed feedback chaotic oscillator with improved spectral characteristics," *Electron. Lett.*, vol. 42, pp. 736-737, 2006.
- [8] A. Tamaševičius, T. Pyragiene and M. Meskauskas, "Two-scroll attractor in a delay dynamical system", *Int. J. Bifurcation and Chaos*, vol. 17, pp. 3455-3460, 2007.

Ultra Fast Object Counting Based-on Cellular Neural Network

Alireza Fasih

Transportation Informatics Group
fasih@qazviniau.ac.ir

Jean Chedjou

Transportation Informatics Group
University of Klagenfurt
Klagenfurt-Austria
jean.chedjou@uni-klu.ac.at

Kyandoghene Kyamakya

Transportation Informatics Group
University of Klagenfurt
Klagenfurt-Austria
kyandoghene.kyamakya@uni-klu.ac.at

Abstract— Vision based counter systems are very important tools in industries. Movement of objects on conveyer systems at a high speed requires an accordingly very fast processing. Therefore, traditional methods for object counting are not efficient due to the fact that they are generally slow. In this paper a CNN based method for counting objects. Simulation results for this method shows that this system is very applicable for object counting at very high speed conveyers. By just a few reconfigurations in CNN templates coefficients, we are able to modify this system for other similar applications.

Keywords— Cellular Neural Network; Image Processing; Object counting; Simulation.

I. INTRODUCTION

Some of the main applications of object counting in industrial systems are packaging, quality control, and so on. Object counting in conveyor in traditional method is based on a simple digital camera and a central processing unit. In the first step, by an external trigger mechanism, camera starts to grab a picture immediately. By some new CMOS cameras we are able to grab pictures very fast and accurate. The main topic and bottleneck is processing time. A blob finding algorithm for labeling and indexing objects is very time consuming. After applying preprocessing algorithm on image for increasing the quality we need to segment the important parts of the picture. For this we use a threshold or dynamic threshold method. This part is our Region of Interest (ROI) for next step. By a connection method that is very time consumer we can index and label or parts and objects. In our approach that we will introduce in this paper, we will shows a CNN based method for counting object without passing this time consuming steps. Cellular Neural Networks (CNN), proposed by Leon Chua in 1988. The main aim of CNN technology is designing of an ultra fast Universal Machine for signal processing purposes.

II. CELLULAR NEURAL NETWORKS (CNN)

Cellular Neural Network were introduced by Leon O. Chua and Yang from university of California at Berkeley in 1988. This type of neural networks is a somehow reduced version of Hopfield Neural Network. One of the most

important features of CNN is locally connectivity, in this technology each cells is connect only to neighbor cells. Due to locally connection between a cell and the neighbors, implementation of this type of neural network on chip is easily feasible. The mathematical model of a CNN cell is a first-order equation like the following state equation:

State Equation

$$C \frac{dv_{xij}(t)}{dt} = -\frac{1}{R_x} v_{xij}(t) + \sum_{C(k,l) \in N_r(i,j)} A(i, j; k, l) v_{ykl}(t) + \sum_{C(k,l) \in N_r(i,j)} B(i, j; k, l) v_{ukt} + I$$

$$1 \leq i \leq M; 1 \leq j \leq N$$

In this equation 'A' is a template for feedback operator and 'B' is a template for control. Output Equation is a linear sigmoid function for limiting output state value. In some note sigmoid function enumerate by $f(\cdot)$.

Output Equation :

$$v_{yij}(t) = \frac{1}{2} (|v_{xij}(t) + 1| - |v_{xij}(t) - 1|)$$

$$1 \leq i \leq M; 1 \leq j \leq N$$

III. OBJECT COUNTING BASED ON CNN

In this section we will describe algorithm for object counting based on CNN. A block diagram that shows the system algorithm is showed in figure 1. After picture grabbing, and picture enhancement unit, this algorithm begins. A selected image for simulate and testing of algorithm is a 64×64 pixel image with 256 level gray level depths that is shown in figure 2. Subsequently, by applying first step of algorithm, image converts to a binary image black and white.

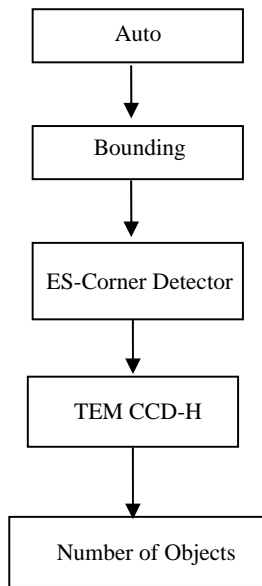


Figure-1, Diagram of object counting algorithm based on CNN technology

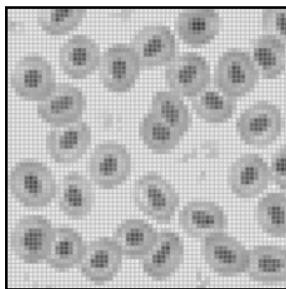


Figure-2, Original Image, 64x64 pixel and 256 gray level bitmap.

The first step of this algorithm shows the auto threshold unit. This unit is a unique and valuable operation that can select opaque region and remove noise on around of image. Traditionally, for designing this operator, designer had to combine many low level operators, like threshold, median filter and noise remover. Auto threshold consists of below templates:

$$A = \begin{bmatrix} 0 & 1 & 0 \\ 1 & 4 & 1 \\ 0 & 1 & 0 \end{bmatrix}, B = \begin{bmatrix} 0 & 0 & 0 \\ 0 & -1 & 0 \\ 0 & 0 & 0 \end{bmatrix}, I = 1$$

Effect of feedback template (A) is very important. Another alternative for this template for having a smoothed result is an 8 value in center and 1 value in around.

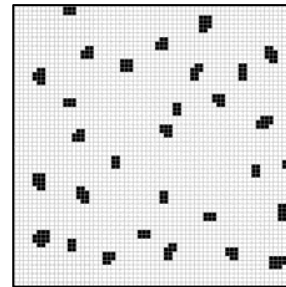


Figure 3, Auto Threshold Template Result.

After this step, system runs the Bounding Box Template.

$$A = \begin{bmatrix} 0 & 1 & 0 \\ 1 & 2 & 1 \\ 0 & 1 & 0 \end{bmatrix}, B = \begin{bmatrix} 0 & 0 & 0 \\ 0 & 0 & 0 \\ 0 & 0 & 0 \end{bmatrix}, I = -2$$

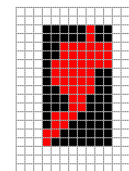


Figure-4, Bounding Box Template Result after converge time, Red region is the initial state.

This operator is very sensitive, and we must consider to something. Applying Bounding Box template on below red region shows that, system converges to a rectangular shape. But it cause to problem when a region is connect to a boundary margin in CNN chip. This problem cause to grow-up of bounding box in an unenviable manner. This problem shows in figure 5.

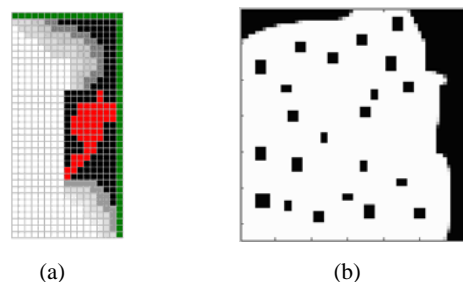


Figure 5, (a) Bounding Box Template fails when a region is connected to margin. (b) Step=10, simulation result

To solve this problem, we must remove margin by an AND template. Figure 6, shows the result of bounding box template after removing margin boundary.

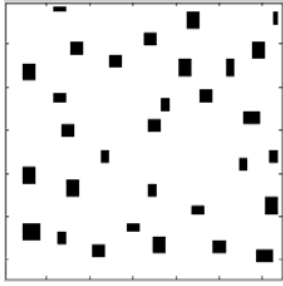


Figure 6, Bounding Box Result

There is an effective South-East Corner finder template that can select the S-E Corner of each rectangle.

$$A = \begin{bmatrix} 0 & 0 & 0 \\ 0 & 0 & 0 \\ 0 & 0 & 0 \end{bmatrix}, B = \begin{bmatrix} 0 & 0 & 0 \\ 0 & -1 & -1 \\ 0 & -1 & 3 \end{bmatrix}, I = 5$$

By this method, we are able to convert each rectangle to a pixel. Notice that some pixels are located on the right margin of frame. Therefore for the next step, we must apply left to right (Connected Component Detector) CCD template. Otherwise it will draw a shadow, and cause to fail.

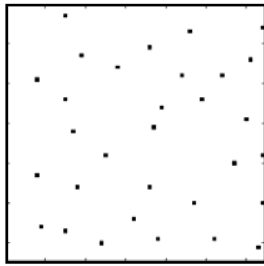


Figure 7, SE Corner Detector Result

Figure 8, shows the connected component detector template result. Now by counting of pixels, the number of objects will obtain. It should be mentioned that this algorithm couldn't distinguished two objects that have an overlap. For distinguishing overlap object we need to use shape based matching algorithms.

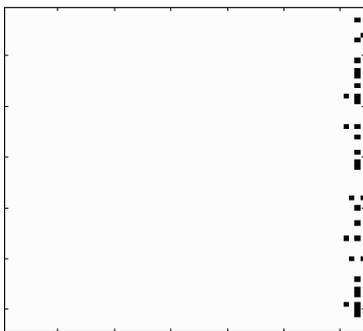


Figure 8, Connected Component Detector (CCD) Result

IV. CONCLUSION

The simulation results for this method show that this algorithm with reduced operators based on CNN technology is very effective and reliable for ultra fast object counting. Extensions of this system are very simple and all template values that used in this simulation are in regular range of VLSI technology CNN chips [-5 ~ +5]. For the future work, we are going to improve this system for detecting and distinguishing of overlapped objects.

REFERENCES

- [1] Chua, L. O. and L. Yang (1988). "Cellular neural networks: applications." *Circuits and Systems, IEEE Transactions on* 35(10): 1273-1290.
- [2] L. Bertucco, G. Nunnari, c. Randieri, V. Rizza, A. Sacco, "A cellular neural network based system for cell counting in culture of biological cells" *Control Applications, 1998. Proceedings of the 1998 IEEE International Conference on* Volume 1, Issue , (1-4 Sep 1998) Pages 341 – 345.
- [3] W. Shitong, K. F. L. Chung, Fu Duan, "Applying the improved fuzzy cellular neural network IFCNN to white blood cell detection", *Neurocomputing, Volume 70 , Issue 7-9 (March 2007) table of contents* Pages 1348-1359.
- [4] T. Matsumoto, L. O. Chua, R. Furukawa, "CNN Cloning Template: Hole-Filter".
- [5] T. MATSUMOTO, L. O. CHUA, T. YOKOHAMA, "Image Thinning with a Cellular Neural Network".
- [6] T. Matsumoto, T. Yokohama, H. Suzuki, R. Furukawa, A. Oshimoto, T. Shimmi, Y. Matsushita, "Several Image Processing Examples By CNN".
- [7] A. Zarandy, A. Stoffls, Tamas Roska, Leon O. Chua, "Morphological Operators On the CNN Universal Machine".
- [8] A. Zarandy, A. Stoffls, Tamas Roska, Leon O. Chua, "Implementation of Binary and Gray-Scale Mathematical Morphological on the CNN Universal Machine".
- [9] P. Julian, Radu Dogaru, Leon O. Chua, "a piecewise-linear simplicial coupling cell for cnn gray-level image processing".
- [10] D. Monnin, A. Koneke, J. Hérault, "Boolean Design of Binary Initialized and Coupled CNN Image Processing Operators".

A linear path towards self-synchronization: Analysis of the fully locked transition of the Kuramoto model

David C. Roberts

Theoretical Division and Center for Nonlinear Studies
Los Alamos National Laboratory
Los Alamos, NM 87545
Email: dcr@lanl.gov

Razvan Teodorescu

Theoretical Division and Center for Nonlinear Studies
Los Alamos National Laboratory
Los Alamos, NM 87545
Email: razvan@lanl.gov

Abstract— We present a linear reformulation of the Kuramoto model describing a self-synchronizing phase transition in a heterogeneous system of globally coupled oscillators that in general have different characteristic frequencies. While this approach can also be applied to systems with a finite number of oscillators, discussion here will focus on the reformulated model in the continuum limit, the regime of validity of the original Kuramoto solution. This new approach allows one to solve explicitly for the synchronization order parameter and the critical point for a new class of continuum systems that have no solution through the traditional approach to the Kuramoto model. Furthermore, the synchronization order parameter will be shown to exhibit anomalous scaling in the vicinity of the critical point. This novel linear approach appears to be a promising way to extend the applicability of the Kuramoto model, which is the paradigm of spontaneous synchronization. Although discussion here will be restricted to systems with global coupling, the formalism of the linear approach also lends itself to solving systems that exhibit local or asymmetric coupling.

I. INTRODUCTION

The Kuramoto model of self-synchronizing coupled phase oscillators is recognized as important for being able to describe diverse synchronization phenomena such as collective atomic recoil lasing, the behavior of Josephson junction arrays, and neural firing patterns [1][2][3]. In a broader sense, however, the Kuramoto model is an exactly solvable model that exhibits behavior reminiscent of a nonequilibrium phase transition. As such, it is a useful medium through which we can develop a better comprehension of nonequilibrium systems and, to this end, in this paper we seek to extend the Kuramoto solution. Certainly, a more general Kuramoto solution will also broaden the applicability of the Kuramoto model as a paradigm of spontaneous synchronization.

To generalize the Kuramoto solution we will take a linear approach, which will phrase this nonlinear problem in terms of eigenvalues and eigenvectors, opening it up to spectral theory and other tools and powerful techniques developed for solving linear problems. Note that only the fully locked transition will be considered here.

We shall begin by presenting a linear model that maps onto the Kuramoto model and deriving the general solution it yields for the synchronization order parameter and the critical point of a continuum system of oscillators. We then focus on a system with a particular coupling scheme, which

cannot be solved using the traditional approach. We present the solution for this case, demonstrate that the synchronization order parameter has anomalous scaling about the critical point, and apply this linear approach to oscillator systems with different characteristic frequency distributions.

While the discussion here will cover only the continuum limit and global coupling, which is the regime of validity of the traditional Kuramoto solution, the linear approach presented can also be used to solve systems populated by a finite number of oscillators [5] as well as systems with local or asymmetric coupling. For further details of these results, see [5] and [6].

II. LINEAR REFORMULATION FOR GENERALIZED COUPLING

For a system of coupled oscillators in the continuum limit, the linear reformulation of the Kuramoto model to be discussed here can be expressed as

$$\dot{\psi}(\omega, t) = (i\omega - \gamma)\psi(\omega, t) + \int_{-\infty}^{\infty} \Omega(\omega, \omega')g(\omega')\psi(\omega', t)d\omega', \quad (1)$$

where $\Omega(\omega, \omega')$ describes the coupling between pairs of oscillators with characteristic frequencies ω and ω' respectively, the phases of the complex variable $\psi(\omega, t)$ correspond to those of the system's oscillators whose synchronization properties we investigate, and $g(\omega)$ is the distribution of their characteristic frequencies. γ is a parameter fixed according to the system parameters such that the amplitude of $\psi(\omega, t)$ goes to a steady state in the long-time limit. This allows the linear model to be mapped onto the original Kuramoto model in the synchronized region, since with the nonlinear transformation $\psi(\omega) = R(\omega)e^{i\theta(\omega)}$ we can write the real and imaginary parts of eq. (1) as

$$\dot{R}(\omega) = -\gamma R(\omega) + \int_{-\infty}^{\infty} \Omega(\omega, \omega')g(\omega')R(\omega') \cos[\theta(\omega') - \theta(\omega)]d\omega' \quad (2)$$

$$\dot{\theta}(\omega) = \omega + \int_{-\infty}^{\infty} \Omega(\omega, \omega')g(\omega') \frac{R(\omega')}{R(\omega)} \sin[\theta(\omega') - \theta(\omega)]d\omega', \quad (3)$$

and, if $R(\omega)$ goes to a steady state in the long-time limit, eq. (3) is simply the Kuramoto model with a generalized coupling

$$K(\omega, \omega') = \Omega(\omega, \omega') \frac{R(\omega')}{R(\omega)}. \quad (4)$$

Note that the variable $R(\omega)$ is introduced simply to carry out the mapping, and has no physical significance. γ is set such that $R(\omega)$ will reach a steady state.

Having reformulated the Kuramoto model in terms of linear dynamics, we can proceed to analyze and solve it using tools from the linear repertoire. Indeed, the synchronization problem can be discussed in terms of the spectrum of the linear operator on the RHS of eq. (1). More precisely, let $\mathcal{K}(\omega, \omega') = \Omega(\omega, \omega')g(\omega') - i\omega\delta(\omega - \omega')$ and assume that the Fredholm integral equation

$$\int_{\mathbb{R}} d\omega' \mathcal{K}(\omega, \omega') \phi_{\sigma}(\omega') = \mu_{\sigma} \phi_{\sigma}(\omega), \quad \sigma \in \mathbb{Z}, \mathbb{R} \quad (5)$$

has a mixed, discrete-continuum spectrum $\{\mu_n, \mu_{\sigma}\}$. Then a generic solution of (1) is given by

$$\psi(\omega, t) = \sum_{n \in \mathbb{Z}} a_n \phi_n(\omega) e^{(\mu_n - \gamma)t} + \int_{\sigma \in \mathbb{R}} b(\sigma) \phi_{\sigma}(\omega) e^{(\mu_{\sigma} - \gamma)t} d\sigma, \quad (6)$$

with coefficients $\{a_n\}_{n \in \mathbb{Z}}, \{b(\sigma)\}_{\sigma \in \mathbb{R}}$ determined by initial conditions.

The spectrum $\{\mu_n, \mu_{\sigma}\}$ determines the appropriate value of γ , which we set equal to the real part of the eigenvalue with the largest real part. It becomes evident that this spectrum dictates the synchronization behavior of the system. If there is only one eigenvalue whose real part equals γ then in the long-time limit contributions from all other eigenvalues die away, $R(\omega)$ goes to a steady state, the linear model maps onto the Kuramoto model with time-independent coupling, and there is full phase locking and synchronization (as defined below). Otherwise, more than one eigenvalue remains, $R(\omega)$ does not reach a steady-state value, and the phases of ψ do not converge.

As mentioned earlier, we will restrict our discussion to systems with no partial population of drifting oscillators, i.e. the incoherent-to-partially locked (usually referred to as the synchronization transition) and the partially locked-to-fully locked phase transitions occur at the same point [4]. We say our system is synchronized if the synchronization order parameter given by

$$r = \left| \int_{-\infty}^{\infty} d\omega g(\omega) e^{i\theta(\omega)} \right| = \left| \int_{-\infty}^{\infty} d\omega g(\omega) \frac{\psi(\omega, t)}{|\psi(\omega, t)|} \right| \quad (7)$$

goes to a nonzero steady-state value [2][3]. As mentioned above, this happens at the critical point where the real part of more than one eigenvalue becomes equal to γ . So in the synchronized region where the real part of only one eigenvalue equals γ ,

$$r = \left| \int_{-\infty}^{\infty} d\omega g(\omega) \frac{b(\omega)}{|b(\omega)|} \right| \quad (8)$$

where $b(\omega)$ is the eigenfunction corresponding to that differentiated eigenvalue, λ_N .

III. SOLUTION FOR SPECIFIC COUPLING

A. Solution of the synchronization order parameter

Let us consider now one type of global coupling in the linear model, $\Omega(\omega, \omega') = \Omega$. The linear model describes this

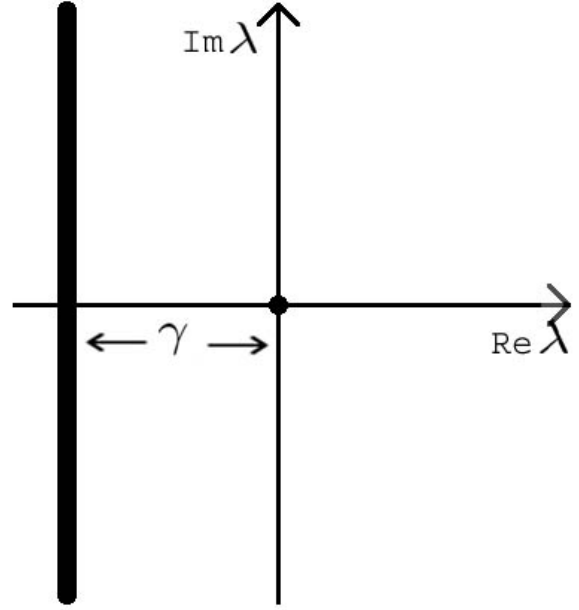


Fig. 1. The spectrum of eigenvalues associated with the RHS of eq. (9) when $\Omega > \Omega_c$. The spectrum comprises a continuum of eigenvalues along $-\gamma$ and a single eigenvalue at the origin. As $\Omega \rightarrow \Omega_c^+$, $\gamma \rightarrow 0$, and the continuum approaches the imaginary axis and the eigenvalue at the origin. When $\Omega \leq \Omega_c$, $\gamma = 0$, and the continuum of eigenvalues sits on the imaginary axis and the eigenvalue at the origin becomes indistinguishable from the continuum.

system as

$$\dot{\psi}(\omega, t) = (i\omega - \gamma)\psi(\omega, t) + \Omega \int_{-\infty}^{\infty} g(\omega') \psi(\omega', t) d\omega', \quad (9)$$

which maps onto the original Kuramoto model with the following coupling constant:

$$K(\omega, \omega') = \Omega \sqrt{\frac{(\omega - \omega_r)^2 + \gamma^2}{(\omega' - \omega_r)^2 + \gamma^2}}, \quad (10)$$

where ω_r is the collective frequency of the synchronized state and is given by the imaginary part of λ_N , $\Im(\lambda_N)$. With this coupling scheme, we can solve the spectrum of the RHS of eq. (9) exactly.

With γ set as described above, the spectrum comprises a continuous line of eigenvalues λ in the complex plane along $\Re[\lambda] = -\gamma$ ($\Re[\lambda]$ denoting the real part of λ) for any value of Ω and one eigenvalue λ_N at the origin, which stands apart from the continuum of eigenvalues if $\Omega > \Omega_c$. As $\Omega \rightarrow \Omega_c^+$, $\gamma \rightarrow 0$, and for $\Omega \leq \Omega_c$ the continuum of eigenvalues lies along the imaginary axis and λ_N becomes indistinguishable from the continuum, as shown in Figure 1; since, in the steady state, the entire spectrum remains, it is clear that $r = 0$ for $\Omega \leq \Omega_c$.

Setting the collective frequency $\Im[\lambda_N]$ to zero, γ to $\Re[\lambda_N]$, and assuming $g(\omega)$ is an even function and nowhere increasing for $\omega \geq 0$, we arrive at the following formula that determines

γ :

$$1 = \Omega \int_{-\infty}^{\infty} \frac{g(\omega)\gamma}{\gamma^2 + \omega^2} d\omega \quad (11)$$

By taking $\gamma \rightarrow 0^+$ and assuming $g(\omega)$ has a finite width, it becomes clear from eq. (11) that

$$\Omega_c = \frac{1}{\pi g(0)}. \quad (12)$$

From eq. (8), for $\Omega > \Omega_c$, we can determine the following explicit expression for r :

$$r = \int_{-\infty}^{\infty} d\omega g(\omega) \frac{1}{\sqrt{1 + \left(\frac{\omega}{\gamma}\right)^2}}. \quad (13)$$

where γ can be determined from eq. (11). So, for a given distribution $g(\omega)$, eqns (11), (12), and (13) completely specify $r(\Omega)$ and Ω_c for $K(\omega, \omega')$, eq. (10). (For details, see [6].)

It is interesting to note that about $\Omega = \Omega_c$ the behavior of r resembles a second-order phase transition in that r grows continuously from zero as the coupling increases. Where $\Omega \rightarrow \Omega_c^+$, $r \rightarrow 0$ because, although the oscillators are phase locked, the phases of the oscillators are evenly distributed from zero to 2π , i.e. the system is in a splay state [7]. Below, we investigate the scaling behavior about $\Omega = \Omega_c$, where this second-order “phase transition” occurs.

B. Anomalous scaling

If one assumes $g(\omega)$ to be such that $\int_{-\infty}^{\infty} d\omega g'(\omega)/\omega$ is nonzero and finite (where $g'(\omega) \equiv \partial_\omega g(\omega)$), then perturbatively the behavior of γ as $\Omega \rightarrow \Omega_c$ becomes

$$\gamma = -\frac{\pi g(0)}{\int_{-\infty}^{\infty} d\omega g'(\omega)/\omega} \left(\frac{\Omega - \Omega_c}{\Omega_c} \right) + O \left[\left(\frac{\Omega - \Omega_c}{\Omega_c} \right)^2 \right]. \quad (14)$$

As $\gamma \rightarrow 0$, the behavior of $r(\gamma)$ can be described by

$$r(\gamma) = -2g(0)\gamma \log[g(0)\gamma] + O[g(0)\gamma]. \quad (15)$$

This behavior of r can be seen as anomalous with respect to the usual square-root scaling behavior of the traditional Kuramoto solution. One might venture that the anomalous scaling is due to the bicritical nature of the critical point. For derivation and explanations of this behavior, see [6].

C. Specific examples of characteristic frequency distributions

With these general solutions for the parameters of any system with global coupling $\Omega(\omega, \omega') = \Omega$, we can solve for a specific system given its characteristic frequency distribution. Take for instance the Lorentzian distribution about ω_r , i.e. $g(\omega - \omega_r) = \frac{\Delta}{\pi[\Delta^2 + (\omega - \omega_r)^2]}$. From eq. (12) we find $\Omega_c = \Delta$, and from eq. (11), $\gamma_{lor} = \Omega - \Delta$. Using these in eq. (13), we obtain

$$r_{lor} = \frac{2 \cos^{-1} \left(\frac{\Omega_c - \Omega}{\Omega - \Omega_c} \right)}{\pi \sqrt{1 - \left(\frac{\Omega_c - \Omega}{\Omega - \Omega_c} \right)^2}} \quad (16)$$

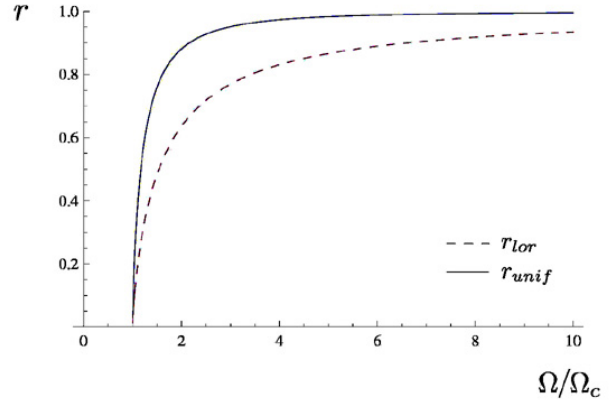


Fig. 2. The synchronization order parameter as a function of the normalized coupling constant for a uniform and Lorentz distribution of characteristic frequencies

for $\Omega > \Omega_c$, as shown in Figure 2. $r = 0$ for $\Omega \leq \Omega_c$ as discussed above. The scaling for this distribution is then

$$r_{lor} \approx \frac{2}{\pi} \frac{\Omega - \Omega_c}{\Omega_c} \log \left(\frac{\Omega_c}{\Omega - \Omega_c} \right). \quad (17)$$

This agrees with eqns (14) and (15) knowing that, for this Lorentzian distribution, $g(0) = \frac{1}{\pi\Delta}$ and $\int_{-\infty}^{\infty} d\omega g'(\omega)/\omega = -\frac{1}{\Delta^2}$.

Similarly, for a uniform distribution about ω_r , i.e. $g(\omega - \omega_r) = \frac{1}{\pi\Delta}$ for $|\omega - \omega_r| < \pi\Delta/2$ and 0 otherwise, the above equations give $\Omega_c = \Delta$, $\gamma_{unif} = \frac{\Delta\pi}{2} \cot \left(\frac{\pi\Delta}{2\Omega} \right)$, and

$$r_{unif} = \cot \left(\frac{\pi}{2} \frac{\Omega_c}{\Omega} \right) \sinh^{-1} \left[\tan \left(\frac{\pi}{2} \frac{\Omega_c}{\Omega} \right) \right] \quad (18)$$

for $\Omega > \Omega_c$ (see Figure 2). As above, $r = 0$ for $\Omega \leq \Omega_c$. The scaling for the uniform distribution is

$$r_{unif} \approx \frac{\pi}{2} \frac{\Omega - \Omega_c}{\Omega_c} \log \left(\frac{\Omega_c}{\Omega - \Omega_c} \right). \quad (19)$$

Again, there is agreement with eqns (14) and (15) as $g(0) = \frac{1}{\pi\Delta}$ and $\int_{-\infty}^{\infty} d\omega g'(\omega)/\omega = -\frac{4}{(\pi\Delta)^2}$.

IV. CONCLUSION

The linear reformulation presented here of the Kuramoto model constitutes a fresh take on the problem of self-synchronization of a heterogeneous population of coupled phase oscillators, opening it to solution through established linear approaches such as spectral theory. This alternative treatment of spontaneous synchronization can give new insight into the mechanics underlying the phenomenon. In addition, this method allows for analytical solutions of systems with finite oscillator populations. Although we have restricted ourselves to the fully locking transition with global coupling, this method holds great promise for solving partial synchronization states and for synchronization problems in complex topologies.

ACKNOWLEDGMENT

D.C.R. would like to thank Steven Strogatz for many insightful comments over the course of this research.

REFERENCES

- [1] Y. Kuramoto. International Symposium on Mathematical Problems in Theoretical Physics, Lecture Notes in Physics. 39, 420 (1975)
- [2] S. H. Strogatz. *Physica D*. 143, 1 (2000)
- [3] J. Acebron *et al.*. *Rev. Mod. Phys.* 77, 137 (2005)
- [4] R. Mirollo and S. H. Strogatz. *J. Nonlinear Sci.* 17, 309 (2007)
- [5] D. C. Roberts. *Phys. Rev. E*. 77, 031114 (2008)
- [6] D. C. Roberts and R. Teodorescu. Accepted to *Eur. Phys. J.* arXiv:0801.3449v1
- [7] K. Y. Tsang, R. E. Mirollo, S. H. Strogatz and K. Wiesenfeld. *Physica D*, 48(1), 102 (1991)



David Roberts concurrently received the B.Sc. degree in engineering physics and the M.Sc. degree in environmental geophysics from Cornell University, Ithaca, NY, in 1999. He received the D.Phil. degree in physics from Oxford University, Oxford, in 2003 as a Marshall Scholar. He was then a Marie Curie Fellow at the Ecole Normale Supérieure from 2004 to 2006 and was a research associate at the Lewis-Sigler Institute at Princeton University. He has been with the Center for Nonlinear Science and the Theoretical Division at Los Alamos National Laboratory

since 2006, first as a Director-funded Postdoctoral Fellow and presently as a Feynman Fellow. His current research interests are in superfluidity, synchronization of coupled oscillators, and quantitative genetics. More information can be found at <http://cnls.lanl.gov/dcr/>.



Razvan Teodorescu received his Ph.D. in Theoretical Physics from the University of Chicago, in 2004. He also holds undergraduate degrees from Ecole Polytechnique - Palaiseau, France and University "Al. I. Cuza", Romania. He is currently a postdoctoral fellow in the Theory Division at Los Alamos National Laboratory. Previously, he was a postdoctoral research officer in the Physics department at Columbia University, NY. His research interests cover non-equilibrium stochastic processes, strongly correlated systems, multi-scale optimization and advanced approximation techniques.

Ragged Synchronizability and Clustering in a Network of Coupled Oscillators

Przemyslaw Perlikowski, Andrzej Stefanski
and Tomasz Kapitaniak

Division of Dynamics, Technical University of Lodz,
Stefanowskiego 1/15, 90-924 Lodz, Poland
Email: przemyslaw.perlikowski@p.lodz.pl

Abstract—We show the phenomenon of complete synchronization in an network of coupled oscillators. We confirm that non-diagonal coupling can lead to the appearance or disappearance of synchronous windows (ragged synchronizability phenomenon) in the coupling parameter space. We also show the appearance of clusters (synchronization in one or more group) between coupled systems. Our numerical studies are confirmed by an electronic experiment.

I. INTRODUCTION

Over the last decade, chaotic synchronization in the networks of coupled dynamical systems has been intensively investigated, e.g., [1-4]. An issue, the most often appearing during the study of any synchronization problem, is to determine a synchronization threshold, i.e. the strength of coupling which is required for the appearance of synchronization. In the case of identical systems (the same set of ODEs and values of the system parameters) a complete synchronization [3] can be obtained. The first analytical condition for the complete synchronization of regular sets (all-to-all or nearest-neighbour types of coupling) of completely diagonally coupled identical dynamical systems has been formulated in [5-7]. A complete diagonal (CD) coupling is realized by all diagonal components of output function (see Eq. (2)) for each pair of subsystems. Such a type of coupling induces a situation, when the condition of synchronization is determined only by the largest Lyapunov exponent of a node system and the coupling coefficient [5-9]. This property of CD coupling causes, that a synchronous range of a coupling parameter for time-continuous subsystems is only bottom-limited (Fig.1a) by a value of coupling coefficient being a linear function of the

largest Lyapunov exponent [8]. If the coupling is partly diagonal (PD, i.e. realized by not all diagonal components of output function - see Eq. (3)) or non-diagonal (ND - also or only non-diagonal components of output function are used in the coupling - see Eqs (4) and (5)), then more advanced techniques like a concept called Master Stability Function (Sec. II) have to be applied [10]. This approach allows to solve the networks synchronization problem for any set of coupling weights, connections or number of coupled oscillators. Generally, in the literature dealing with PD or ND coupling problems dominate the works, where the synchronization ranges of a coupling parameter are only bottom-limited (like in the case of CD coupling - see Fig.1b) or they are double-limited (Fig.1c), i.e. there exists one window of synchronization (interval) in desynchronous regime [5-15]. In the previous work [16], we presented an example of ND coupled oscillators array, in which more than one separated ranges of synchronization occur when the coupling strength increases. We observe the appearance or disappearance of desynchronous windows in coupling parameter space, when the number of oscillators in the array or topology of connections changes. This phenomenon has been called the ragged synchronizability (RSA). This work describes the RSA phenomenon in an array of coupled van der Pol's oscillators. Our numerical studies are supported by a simple electronic experiment.

II. SYNCHRONIZABILITY OF COUPLED OSCILLATORS

In order to estimate the synchronization thresholds of a coupling parameter, we apply the idea

of the MSF [10]. Under this approach, the synchronizability of a network of oscillators can be quantified by the eigenvalue spectrum of the connectivity matrix, i.e. the Laplacian matrix representing the topology of connections between the network nodes. The dynamics of any network of N identical oscillators can be described in block form:

$$\dot{\mathbf{x}} = \mathbf{F}(\mathbf{x}) + (\sigma \mathbf{G} \otimes \mathbf{H}) \mathbf{x} \quad (1)$$

where $\mathbf{x} = (\mathbf{x}_1, \mathbf{x}_2, \dots, \mathbf{x}_N) \in \mathbf{R}^m$, $\mathbf{F}(\mathbf{x}) = (\mathbf{f}(\mathbf{x}_1), \dots, \mathbf{f}(\mathbf{x}_N))$, \mathbf{G} is the connectivity matrix (e.g. Eq. (13)), σ is the overall coupling coefficient, \otimes is a direct (Kronecker) product of two matrices and $\mathbf{H} : \mathbf{R}^m \rightarrow \mathbf{R}^m$ is an output function of each oscillator's variables that is used in the coupling (it is the same for all nodes). Taking under consideration the classification of couplings mentioned in Sec. I we can present the following instances of output function for 3-D node system:

$$\mathbf{H} = \begin{bmatrix} 1 & 0 & 0 \\ 0 & 1 & 0 \\ 0 & 0 & 1 \end{bmatrix}, \quad (2)$$

$$\mathbf{H} = \begin{bmatrix} 1 & 0 & 0 \\ 0 & 1 & 0 \\ 0 & 0 & 0 \end{bmatrix}, \quad (3)$$

$$\mathbf{H} = \begin{bmatrix} 1 & 0 & 0 \\ 1 & 0 & 0 \\ 0 & 0 & 1 \end{bmatrix}, \quad (4)$$

$$\mathbf{H} = \begin{bmatrix} 0 & 0 & 0 \\ 1 & 0 & 0 \\ 0 & 0 & 1 \end{bmatrix}. \quad (5)$$

The \mathbf{H} matrices exemplify CD (Eq. (2)), PD (Eq. (3)) and ND (Eqs (4) and (5)) coupling respectively. Eq. (5) defines the exemplary case of pure ND coupling, because all the diagonal components are equal to zero. In accordance with the MSF concept, a tendency to synchronization of the network is a function of the eigenvalues γ_k of connectivity matrix \mathbf{G} , $k = 0, 1, 2, \dots, N - 1$. After block diagonalization of the variational equation of Eq. (1) there appear $N - 1$ separated blocks $\dot{\gamma}_k = [D\mathbf{f} + \sigma\gamma_k D\mathbf{H}]$, (for $k = 0$, $\gamma_0 = 0$ is corresponding to the longitudinal mode), where γ_k represents different transverse modes of perturbation from synchronous state [10-13]. Substituting $\sigma\gamma = \alpha + i\beta$, where

$\alpha = \text{Re}(\gamma)$, $\beta = \text{Im}(\gamma)$ and γ represents an arbitrary value of γ_k , we obtain generic variational equation

$$\dot{\zeta} = [D\mathbf{f} + (\alpha + i\beta)D\mathbf{H}] \zeta, \quad (6)$$

where ζ symbolizes an arbitrary transverse mode. The connectivity matrix $\mathbf{G} = \{G_{ij}\}$ satisfies $\sum_{j=1}^N G_{ij} = 0$ (zero row sum) so the synchronization manifold $\mathbf{x}_1 = \mathbf{x}_2 = \dots = \mathbf{x}_N$ is invariant and all the real parts of eigenvalues γ_k associated with transversal modes are negative ($\text{Re}(\gamma_{k \neq 0}) < 0$). Hence, we obtain the following spectrum of the eigenvalues of \mathbf{G} : $\gamma_0 = 0 \geq \gamma_1 \geq \dots \geq \gamma_{N-1}$. Now, we can define the MSF as a surface representing the largest transversal Lyapunov exponent (TLE) λ_T , calculated for generic variational equation, over the complex numbers plane (α, β) . If all the eigenmodes corresponding to eigenvalues $\sigma\gamma_k = \alpha_k + i\beta_k$ can be found in the ranges of negative TLE then the synchronous state is stable for the considered configuration of the couplings. If an interaction between each pair of nodes is mutual and symmetrical there exist only real eigenvalues of matrix \mathbf{G} ($\beta_k = 0$). In such a case, which is called the real coupling [12-13], the matrix \mathbf{G} is symmetrical (see Eq. (13)) and the MSF is reduced to a form of a curve representing the largest TLE in function of a real number α fulfilling the equation

$$\alpha = \sigma\gamma. \quad (7)$$

In Figs 1a–c typical examples of the MSF for CD coupling (Fig. 1a) and for PD or ND coupling (Figs 1b,c) are shown.

If the real coupling is applied to a set of oscillators with the MSF providing a single range of negative TLE as it is shown in Figs 1a, 1b and 1c, then the synchronous interval of a coupling parameter σ is simply reflected from the synchronous α -interval according to Eq. (7). For the case of MSF with double-limited α -interval of negative TLE (Fig. 1c) two transverse eigenmodes have an influence on the σ -limits of the synchronous regime: the longest spatial-frequency mode, corresponding to the largest eigenvalue γ_1 , and the shortest spatial-frequency mode, corresponding to the smallest eigenvalue γ_{N-1} . These both eigenvalues determine the width of synchronous σ -range and two types of desynchronizing bifurcations can

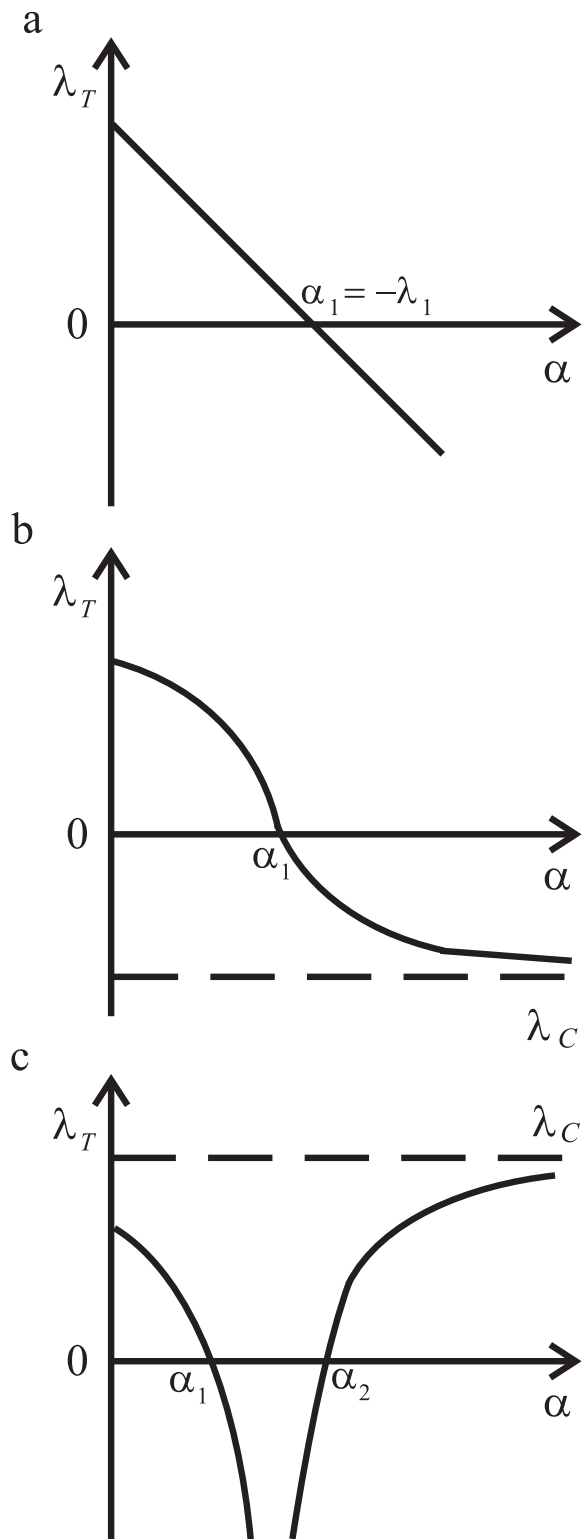


Fig. 1. Typical examples of MSF - $\lambda_T(\alpha)$ in the case of real coupling: (a, b) bottom-limited synchronous range (α_1, ∞) , (c) double-limited synchronous interval (α_1, α_2) .

occur when the synchronous state loses its stability [11]. Decreasing σ leads to a long wavelength bifurcation (LWB), because the longest wavelength mode γ_1 becomes unstable. On the other hand, the increase of the couplin strength causes the shortest wavelength mode γ_{N-1} to become unstable, thus a short wavelength bifurcation (SWB) takes place [11-13]. Another, characteristic feature of the coupled systems with double-limited synchronous interval is the array size limit, i.e. a maximum number of oscillators in an array which are able to synchronize. For the number of oscillators, which is larger then the size limit, the synchronous σ -interval does not exist. Such an interval exists if $\gamma_{N-1}/\gamma_1 < \alpha_2/\alpha_1$, where α_1 and α_2 are the boundaries of synchronous $-\alpha$ -interval (see Fig. 1c) [10-13]. If the synchronous range is only bottom-limited as it is depicted in Figs 1a and 1b, then the boundary (the smallest) value of σ , required for the appearance of synchronization, is determined only by the value of γ_1 and then desynchronizing LWB occurs with the decrease of σ . A type of single synchronous range appearing in the systems with PD coupl g depends on conditional Lyapunov exponents (CLEs) [4] of the remaining, uncoupled sub-block of node system. This property results from the asymptotic effect of the PD coupling [12-13]. An essence of this effect, depicted in Figs 1b and 1c, is that the largest TLE (MSF) tends asymptotically to the value of the largest CLE (λ_C) for strong coupling. Therefore, for negative λ_C the synchronous range is only bottom-limited (Fig. 1b) and for positive λ_C such a range is double-limited (Fig. 1c).

In numerical studies van der Pol's oscillator

$$\dot{x} = z \quad (8a)$$

$$\dot{z} = d(1 - x^2)z - x + \cos(\Omega\tau), \quad (8b)$$

where d and Ω are constant, has been taken as an array node. Ω represents the frequency of the external excitation. The evolution of each oscillator coupled in 3-dimensional array is given by

$$\dot{x}_1 = z_1, \quad (9a)$$

$$\dot{z}_1 = d(1 - x_1^2)z_1 - x_1 + \cos(\Omega\tau) + \sigma(x_2 - x_1), \quad (9b)$$

$$\dot{x}_2 = z_2, \quad (9c)$$

$$\dot{z}_2 = d(1 - x_2^2)z_2 - x_2 + \cos(\Omega\tau) + \sigma(x_1 + x_3 - 2x_2), \quad (9d)$$

$$\dot{x}_3 = z_3, \quad (9e)$$

$$\dot{z}_3 = d(1 - x_3^2)z_3 - x_3 + \cos(\Omega\tau) + \sigma(x_2 - x_3), \quad (9f)$$

where σ is a constant coupling coefficient and $i = 1, 2, 3$.



Fig. 2. The model of an open array of van der Pol's oscillators.

In the numerical analysis we assumed $d = 0.401$ and considered Ω and σ as control parameters. Eqs. (8) model, for example, a chain (the nearest-neighbor configuration of couplings) of 3 van der Pol's oscillators coupled in the open chain shown in Fig. 2. Such a connection of oscillators can be classified as the case of pure (diagonal components are equal to zero) ND coupling due to the form of output function

$$\mathbf{H} = \begin{bmatrix} 0 & 0 \\ 1 & 0 \end{bmatrix}. \quad (10)$$

The structure of the nearest-neighbor connections of array nodes is described by the following connectivity matrix

$$\mathbf{G} = \begin{bmatrix} -1 & 1 & 0 \\ 1 & -2 & 1 \\ 0 & 1 & -1 \end{bmatrix}. \quad (11)$$

Matrix \mathbf{G} has the following eigenvalues $\gamma_0 = 0, \gamma_1 = -1, \gamma_2 = -3$. Since nonzero eigenvalues are not equal to each other one can expect the appearance of RSA. Substituting the analyzed system (Eqs (8) and (10)) in Eq. (6) we obtain the generic

variational equation for calculating the MSF, i.e., $\lambda_T(\alpha)$ in the form

$$\dot{\zeta} = \psi, \quad (12a)$$

$$\dot{\psi} = d(1 - x^2)\zeta - 2dx\psi\zeta - \psi + \alpha\psi. \quad (12b)$$

III. NUMERICAL AND EXPERIMENTAL RESULTS

Figure 3 presents the value of the synchronization error

$$e = \sum_{i=2}^3 \sqrt{(x_1 - x_i)^2 + (z_1 - z_i)^2}, \quad (13)$$

versus the coupling coefficient σ and the frequency of external excitation Ω .

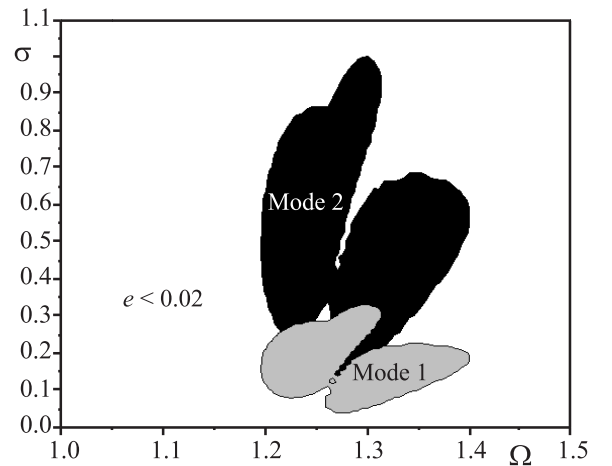


Fig. 3. The synchronization error $e = \sum_{i=2}^3 \sqrt{(x_1 - x_i)^2 + (z_1 - z_i)^2}$ versus coupling coefficient σ and the frequency of external excitation Ω for Eqs. (9): $d = 0.401$.

In the white region $e < 0.02$ so we assumed that the systems are synchronized, grey and black regions denote desynchronization connected with the modes associated with eigenvalues γ_1 and γ_2 respectively. The calculations have been performed according to the idea of MSF for the probe of two oscillators [12-13]. One can expect RSA to appear for $\Omega \in (1.2, 1.5)$.

As an example consider $\Omega = 1.22$, i.e., in the absence of coupling each oscillator shows periodic behavior with the period equal to the period of excitation. In Fig. 4(a,b) we present the bifurcation diagrams of MSF versus the coupling coefficient σ . The diagram shown in Fig. 4(a) is based on the

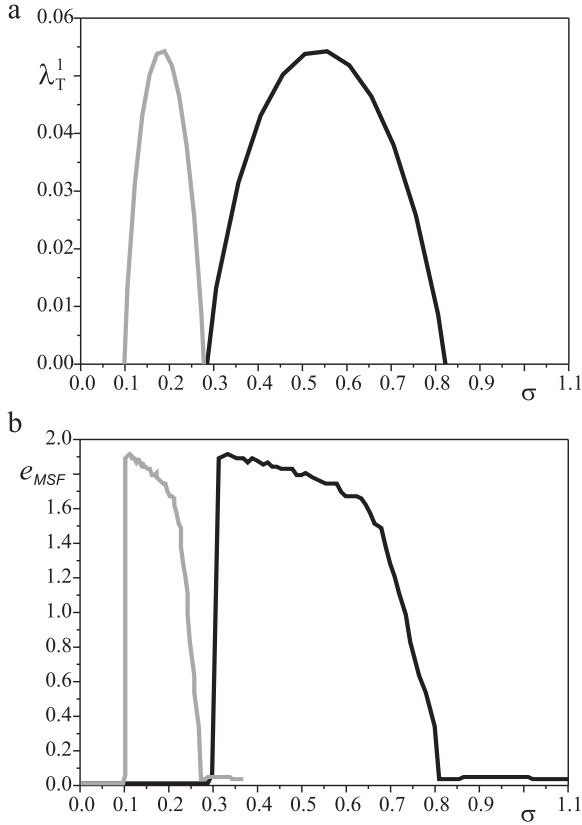


Fig. 4. Bifurcation diagrams of MSF versus coupling coefficient σ : $d = 0.401$, $\Omega = 1.22$; (a) diagram based on the transverse Lyapunov exponent λ_T^1 , desynchronization intervals connected with eigenvalues γ_1 and γ_2 are shown in grey and black respectively, (b) diagram based on the synchronization error e_{MSF} calculated according to two oscillators probe.

transverse Lyapunov exponent λ_T^1 (desynchronization intervals connected with eigenvalues γ_1 and γ_2 are shown in grey and black respectively), while the one in Fig. 4(b) on the synchronization error e_{MSF} calculated according to two oscillators probe [12,13]. In both diagrams the ragged synchronizability is visible as the 'windows' of synchronization and desynchronization can be observed, before the final synchronous state is achieved due to the increase of the coupling strength at $\sigma = 0.8$.

To confirm the existence of RSA in the real systems we have performed an experiment in which van der Pol's oscillator has been implemented as an electronic circuit [17]. We have considered dynamics of three circuits coupled in the way described in Sec. 3. An example of typical experimental results is shown in Fig. 5, where we plot the synchronization error e versus σ . These results have been obtained

for the same parameter values as the numerical results of Fig. 4(a,b).

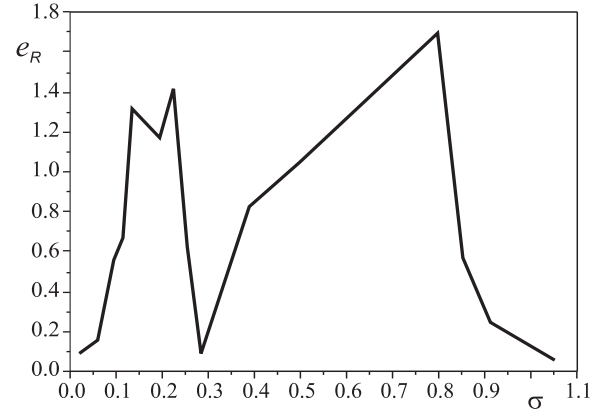


Fig. 5. Experimental synchronization error e versus σ : $d = 0.401$, $\Omega = 1.22$.

It should be mentioned here that in the experiments it is impossible to avoid parameter mismatches so the complete synchronization is replaced by the imperfect complete synchronization in which synchronization error is sufficiently small but not equal to zero. One can see a good agreement in both results. The details of this experiment will be reported elsewhere [18].

In considered network one can observe the phenomenon of clustering [19,20]. Such behaviour corresponding to existence one or more groups of synchronized oscillators although the whole network is in the desynchronized state. In our case we can obviously observe only (2,1) cluster, i.e. two nodes have common behaviour and one node is independent. We defined the synchronization errors between first and second ($e_{1-2} = \sqrt{(x_1 - x_2)^2 + (z_1 - z_2)^2}$) and first and third ($e_{1-3} = \sqrt{(x_1 - x_3)^2 + (z_1 - z_3)^2}$) oscillator. In Figure 6 we present results of numerical calculation of synchronization error e_{1-2} (black line) and e_{1-3} (grey line).

As it easy to see in range $\sigma = (0.1, 0.27)$ one can observed a cluster between fist and third oscillator, while second system is in the desynchronized state with them. This phenomenon is confirmed by calculation of eigenvectors [21] of connectivity matrix G . The synchroniation in range $\sigma = (0.1, 0.27)$ is governed by eigenvalue $\gamma_2 = -3$ with corresponding eigenvector $v_2 = [1, -2, 1]$. This values of v_2

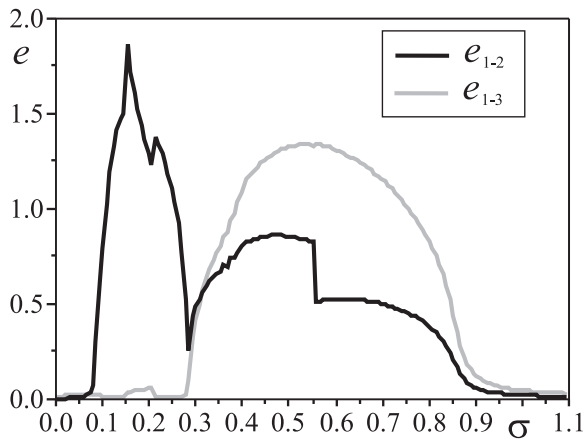


Fig. 6. Experimental synchronization error e versus σ : $d = 0.401$, $\Omega = 1.22$.

leads to existence of cluster shown in Figure 6.

IV. CONCLUSIONS

To summarize, we have confirmed and explained the phenomenon of the ragged synchronizability (RSA) in the networks of van der Pol's oscillators with ND coupling between the nodes. Its occurrence is independent of the motion character (periodic or chaotic) of an isolated node system. We have shown the mechanism responsible for the appearance or disappearance of the windows of synchronizability is the same as the previously studied network of Duffing oscillators [16]. It seems that the phenomenon of RSA is common for the systems with non-diagonal coupling and not sensitive for the small parameter mismatch, i.e., can be observed in real experimental systems.

REFERENCES

- [1] V. S. Afraimovich, N. N. Verichev, and M. Rabinovich, *Izv. Vusov. Radiofizika* 28(9) (1985)1050.
- [2] Blekhman I., *Synchronization in Science and Technology* (ASME Press, New York, 1988);
- [3] L.M. Pecora, T.L. Carroll, *Phys. Rev. Lett.* 64 (1990) 821.
- [4] S. Boccaletti, J. Kurths, D. Osipov, D.L. Valladares, and C.S. Zhou, *Physics Reports* 366 (2002) 1.
- [5] H. Fujisaka and T. Yamada, *Prog. Theor. Phys.* 69 (1983) 32.
- [6] T. Yamada and H. Fujisaka, *Prog. Theor. Phys.* 70 (1983) 1240.
- [7] A. Pikovsky, *Zeitschrift Phys. B* 55 (1984) 149.
- [8] A. Stefanski, J. Wojewoda, T. Kapitaniak, S. Yanchuk S., *Phys. Rev. E* 70, 026217 (2004).
- [9] S. Dmitriev, M. Shirokov and S. O. Starkov, *IEEE Trans. Circuits Syst. I. Fund. Th. Appl.* 44(10) (1997) 918.
- [10] L. M. Pecora and T. L. Carroll, *Phys. Rev. Lett.* 80(10) (1998) 2109.
- [11] L. M. Pecora, *Phys. Rev. E* 58(1) (1998) 347.

- [12] L. M. Pecora and T. L. Carroll, G. Johnson, D. Mar, K. Fink, *Int. J. Bifurcation Chaos* 10(2) (2000) 273.
- [13] K. Fink, G. Johnson, T. L. Carroll, D. Mar, and L. M. Pecora, *Phys. Rev. E* 61 (2000) 5080.
- [14] M. Barahona and L. M. Pecora, *Phys. Rev. Lett.* 89 (2002) 054101.
- [15] T. Nishikawa, A. E. Motter, Y.-C. Lai, and F. C. Hoppensteadt, *Phys. Rev. Lett.* 91(1) (2003) 014101.
- [16] A. Stefanski, P. Perlikowski and T. Kapitaniak, *Phys. Rev. E* 58(1) (2007) 347.
- [17] B. Nana, P. Wofo, *Phys. Rev. E*, 74, (2006), 046213.
- [18] P. Perlikowski, A. Stefanski and T. Kapitaniak, in preparation.
- [19] Belykh V. N., Belykh I. V., Mosekilde E.: Cluster synchronization modes in an ensemble of coupled chaotic oscillators. *Phys. Rev. E*, 63(3):036216, 2001.
- [20] Kaneko K.: Clustering, coding, switching, hierarchical ordering, and control in network of chaotic elements. *Physica D*, 41:137172, 1990.
- [21] Yanchuk S., Maistrenko Y., Mosekilde E.: Partial synchronization and clustering in a system of diffusively coupled chaotic oscillators. *Math. Comp. Simul.* 54, (2000), 491.

Designing Couplings for Synchronization

Ioan Grosu

Bioengineering Department
University of medicine and Pharmacy Gr.T.Popa, UMF
Iasi, Romania
e-mail address: ioan.grosu@instbi.umfiasi.ro

Servilia Oancea

Biophysics Department
University of Agricultural Science and Veterinary
Medicine, USAMV
Iasi, Romania
e-mail address: liaoancea@yahoo.com

Master-slave synchronization and mutual synchronization of two identical oscillators respectively are presented. We believe that this method could be adopted for the teaching of the topic. Numerical results are given for the synchronization of two Sprott's chaotic electric circuits.

Keywords: synchronization, Sprott's circuits

I. INTRODUCTION

In biology, medicine and agriculture many systems can be modelled as oscillators or vibratory systems and those systems show a tendency towards synchronous behaviour. From the control point of view, the controlled synchronization is the most interesting. That means to design a controller or interconnections that guarantee synchronization of the multi-composed systems with respect to certain desired functional. Jackson and Grosu [1] developed a powerful method of control: the open-plus-closed-loop (OPCL) method. This method is very general and is mathematically based. It offers a driving in order to determine a general system to reach a desired dynamics. If the goal dynamics is the dynamics of an identical system (master system) then the driving is simpler. The driving term contains an arbitrary Hurwitz matrix. Choosing with care this matrix the driving term can be even simpler. This method was used for Chua systems [2], for neural systems [3] and for Sprott's collection [4]. A similar strategy can be used for mutual synchronization [5]. More than this it can be extend to 3 systems [6] and very recent to several systems. This method can be used for Parameter Estimation [7]. Sprott 's collection can be rewritten into third-order ODE in a single variable [8]. In addition the author in [9] presents some chaotic electronic circuits which can be described in the same manner, by the equation:

$$\ddot{x} + A\dot{x} + x = G(x) \quad (1)$$

These circuits contain resistors, capacitors, diodes and operational amplifiers. Here we present one method for master-slave synchronization and one for mutual synchronization of identical oscillators. We apply these methods to the synchronization (master-slave and mutual respectively) of two identical oscillators from Sprott's circuits.

II. MASTER-SLAVE SYNCHRONIZATION

A general master system is of the form:

$$\frac{dX}{dt} = F(X), X \in R^n \quad (2)$$

and the slave system coupled to the master is:

$$\frac{dx}{dt} = F(x) + \left(H - \frac{dF(X)}{dX} \right)_{x=X} \quad (3)$$

where H is a constant Hurwitz matrix (a matrix with negative real part eigenvalues). The matrix H should be chosen in such a manner in order that the coupling to be as simple as possible. If the characteristic equation of the matrix H is:

$$\lambda^3 + a_1\lambda^2 + a_2\lambda + a_3 = 0 \quad (4)$$

then the Ruth-Hurwitz conditions are

$$a_1 > 0; a_1a_2 - a_3 > 0; a_3 > 0 \quad (5)$$

One big disadvantages of this general method is that the coupling term could be complicated and hard to be implemented in practical/engineering applications [4].

III. MUTUAL SYNCHRONIZATION

Let's consider two identical general oscillators:

$$\frac{dx}{dt} = F(x) \quad (6)$$

and

$$\frac{dy}{dt} = F(y) \quad (7)$$

In order to obtain synchronization it is necessary to couple the two systems. The coupled systems are:

$$\frac{dx}{dt} = F(x) + u(x,y) \tag{8}$$

$$\frac{dy}{dt} = F(y) + u(x,y) \tag{9}$$

where

$$u(x,y) = (H - \frac{dF(s)}{ds})_{(x-y)/2} \tag{10}$$

and $s=(x+y)/2$ and H a Hurwitz matrix.

We use the notations: $s=(x+y)/2$ and $r=(x-y)/2$ and the Taylor expansions:

$$F(s+r) = F(s) + \frac{dF(s)}{ds} r + \dots$$

$$F(s-r) = F(s) + \frac{dF(s)}{ds} (-r) + \dots \tag{11}$$

Subtracting (8) from (7) we obtain

$$\frac{dr}{dt} = Hr \tag{12}$$

IV. COMPARISON BETWEEN MASTER-SLAVE SYNCHRONIZATION AND MUTUAL SYNCHRONIZATION

For the simplest choice of $G(x)$ in (1) of the form

$$G(x) = 0.58x^2 - 1,$$

the master system:

$$\begin{aligned} \dot{X}_1 &= X_2 \\ \dot{X}_2 &= X_3 \\ \dot{X}_3 &= -AX_3 - X_2 + 0.58x^2 - 1 \end{aligned} \tag{13}$$

The Routh-Hurwitz conditions (4) give:

$$p \in (-0.6;0)$$

for $A=0.6$

The strange attractor for this system is:

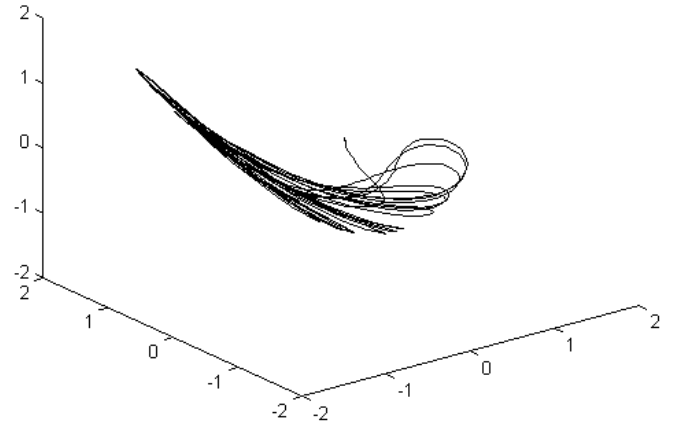


Fig.1. The strange attractor for the system 13

The slave system:

$$\begin{aligned} \dot{x}_1 &= x_2 \\ \dot{x}_2 &= x_3 \\ \dot{x}_3 &= -0.6x_3 - x_2 + 0.58x_1^2 - 1 + (-0.5 - 1.16x_1)(x_1 - X_1) \end{aligned} \tag{14}$$

In Fig. 2 the numerical results are shown for master slave synchronization for initial conditions $X_1(0)=X_2(0)=X_3(0)=0.1$ and $x_1(0)=x_2(0)=x_3(0)=-0.1$

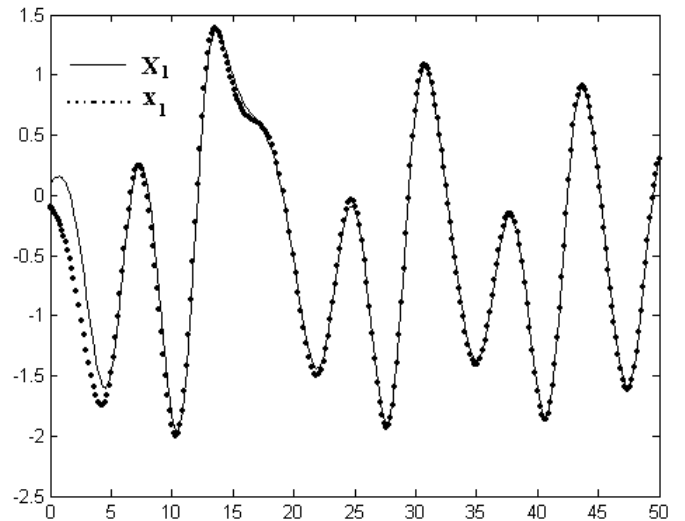


Fig.2. $X_1(t), x_1(t)$ from (13) and (14) and $p=-0.5$

The systems (5), (6) for the system (11) are:

$$\begin{aligned}
\dot{x}_1 &= x_2 \\
\dot{x}_2 &= x_3 \\
\dot{x}_3 &= -0.6x_3 - x_2 + 0.58x_1^2 - 1 + \\
&(-0.5 - 0.58(x_1 + y_1)/2)(x_1 - y_1)/2 \\
\dot{y}_1 &= y_2 \\
\dot{y}_2 &= y_3 \\
\dot{y}_3 &= -0.6y_3 - y_2 + 0.58y_1^2 - 1 + \\
&(-0.5 - 0.58(x_1 + y_1)/2)(-x_1 + y_1)/2
\end{aligned} \tag{15}$$

Numerical results are shown in Fig. 3 with $p=-0.5$, $x_1(0)=1$; $x_2(0)=0.1$; $x_3(0)=0.01$ and $y_1(0)=1$; $y_2(0)=0.1$; $y_3(0)=-0.01$

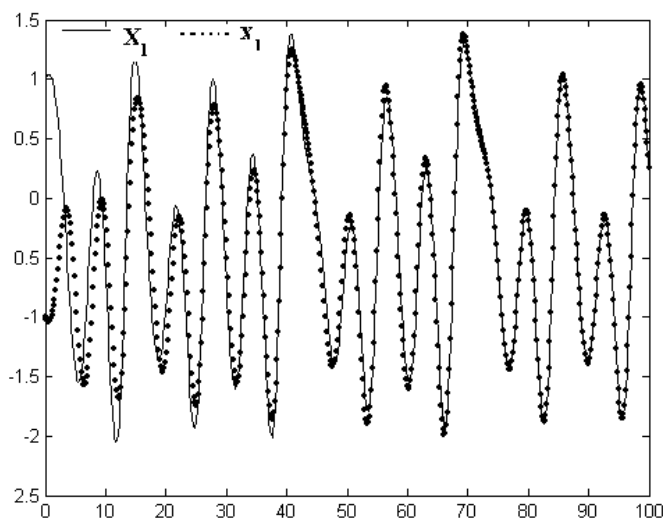


Fig.3. $x_1(t)$, $y_1(t)$ from (15) and $p=-0.5$

V. CONCLUSIONS

Figures 1 and 2 showed that the synchronization is faster for master-slave synchronization than the mutual synchronization ($t \approx 25$ time unities in the first case and $t \approx 50$ time unities for the second case, this means is obtained two times rapidly). Formulation of the Sprott's oscillator chaotic presented in [8], using a jerk function, is simple as form and the synchronization is simpler and easily to learn.

REFERENCES

- [1] E.A. Jackson, and I. Grosu, "An Open-Plus-Closed-Loop (OPCL) Control of Complex Dynamic Systems," *Physica D*, vol. 85, pp. 1-9, 1995.
- [2] E.A. Jackson, and I. Grosu, "Toward Experimental Implementation of Migration Control," *Int. J. of Bifurcation and Chaos*, vol. 5, pp. 1767-1772, 1995.
- [3] V.Dragoi, and I.Grosu, "Synchronization of Locally Coupled neural Oscillator," *Neural Processing Letters*, vol. 7, pp. 199-210, 1998.
- [4] A.I. Lerescu, N.Constandache, S. Oancea, and I. Grosu, "Collection of master-slave synchronized chaotic systems," *Chaos, Solitons and Fractals*, vol. 22(3), pp. 599-604, 2004.
- [5] A.I. Lerescu, S. Oancea, and I. Grosu, "Collection of Mutually Synchronized Chaotic Systems," *Physics Letters A*, vol. 352, pp. 222-228, 2006.
- [6] I.Grosu, "General Coupling for Synchronization of 3 Identical Oscillators," *Int. J. of Bifurcation and Chaos*, vol. 17(10), pp. 3519-3522, 2007.
- [7] I.Grosu, "Parameter Estimation from time series using OPCL autosynchronization," *Int. J. of Bifurcation and Chaos*, vol. 14(6), pp. 2133-2141, 2004.
- [8] J.C. Sprott, "Some simple chaotic jerk functions," *Am. J. Phys.*, vol. 65(6), pp. 537-543, 1997.
- [9] J.C. Sprott, "A new class of chaotic circuits," *Phys.Lett A*, vol. 266, pp. 19-23, 2000.

Adaptive Synchronization of Lorenz System and Its Uses in Cryptanalysis

Ying Liu and Wallace K.S. Tang
Department of Electronic Engineering,
City University of Hong Kong,

Tat Chee Avenue, Kowloon, Hong Kong, P.R. China

Email: yingliu2@student.cityu.edu.hk, kstang@ee.cityu.edu.hk

Abstract—This paper addresses the adaptive synchronization problem of Lorenz system even when its system structure is imprecise and some of its parameters are unknown. With only a single observable state, this is accomplished by a newly designed adaptive observer based on linear feedback control, where the estimated parameters are adaptively updated by some dynamical minimization algorithms. As illustrated with the numerical simulations, the observer's states can asymptotically synchronize with the targeted system, while the unknown parameters can be identified simultaneously in a fast convergence rate. Furthermore, the proposed observer is applied for providing the cryptanalysis of some Lorenz-based chaotic modulation communication systems. It is demonstrated that the covered messages can be easily estimated by such an adaptive attack. Hence, the securities of those systems are challenged.

Keywords—Adaptive observer; adaptive synchronization; cryptanalysis; minimization algorithm; secure communication

I. INTRODUCTION

The importance of chaos synchronization [1] has aroused a lot of interests, not only because of its theoretical importance, but also its wide applications, such as secure communications and data encryption.

In the last two decades, a large number of chaos-based cryptosystems have been suggested based on the concept of synchronization, see Refs. [2]–[7] for example. The success of these cryptosystems is largely dependent on how resistive they are for different kinds of attacks. In additions, as pinpointed in [2], the in-use chaotic systems must also be *anti-adaptive* in order to prevent intruder from retrieving the system states and/or the parameters based on the observability of the transmitted output.

The concept of *anti-adaptiveness* is closely related with *adaptive synchronization*, which implies the

synchronization of a targeted system without knowing its exact model. Currently, a variety of adaptive synchronization approaches have been reported, such as, Refs. [8]–[15], where Lorenz system is of particular interest. Lorenz system has been commonly used in practical communication system designs, as it is a well-known difficult synchronization problem when some unknown parameters are resided in all the three state equations and only the first state is measurable. As a general remark, this problem is manageable if the second state is observed [11], [12].

Recently, some static minimization approaches [16], [17] have been explored to tackle with this difficult synchronization problem. Evolutionary computation technique [18], namely particle swarm optimization, has also been successfully applied for the parameter estimations in chaotic systems. However, these methods do not serve the needs for real-time estimation as a set of fixed record is generally required.

On the other hand, designs based on adaptive rules [13], [14], [15] provide some possible solutions. In [13], an adaptive rule for parameter estimation, driven by the synchronization error, has been suggested for observer design based on the concept of system control. However, detailed design procedure is missed, and the time for synchronization is very long as presented. Similarly, a local adaptive Lyapunov function has been established in [14], where parameter adaptive control loops are designed to synchronize a given system as well as to estimate its unknown parameters. Although the construction of this local Lyapunov function is rather complex, it is considered to be a practical means to justify the design of the parametric update rules.

In this paper, a new observer based on the linear feedback control and dynamical minimization algorithm [11] is proposed to achieve the adaptive synchronization of Lorenz system. In addition, the designed observer will also be applied for the cryptanalysis of some chaos-synchronization based secure communication systems.

[†]Corresponding author: Ying Liu, Email: yingliu2@student.cityu.edu.hk

As shown from our simulations, the suggested design serves as an effective means for challenging the anti-adaptiveness of those systems.

The rest of the paper is organized as follows. In Sect. II, a design of observer system proposed for adaptive synchronization of Lorenz system is described. The design is then verified and some simulation results are also given in the same section. In Sect. III, the proposed observer system is adopted for the cryptanalysis of some Lorenz-based chaotic modulation communication systems, supported with various simulation examples. Finally, conclusions are drawn in Sect. IV.

II. ADAPTIVE SYNCHRONIZATION OF LORENZ SYSTEM

In this section, the adaptive synchronization of Lorenz system is described. To formulate a more challenging problem, it is assumed that the exact form of Lorenz equation is unknown while the following generalized form is considered:

$$M : \begin{cases} \dot{x}_1 = p_1(x_2 - x_1) \\ \dot{x}_2 = p_2x_1 - p_3x_2 - x_1x_3 \\ \dot{x}_3 = x_1x_2 + p_4x_2 - p_5x_3 \end{cases} \quad (1)$$

where $\mathbf{x} = [x_1 \ x_2 \ x_3]^T$ is the state vector and $\mathbf{p} = [p_1 \ p_2 \ p_3 \ p_4 \ p_5]^T$ are unknown parameters but linearly depend on the system states.

In (1), an addition term p_4x_2 is included in the third equation. It is expected that the exact form of the equation can be recovered if p_4 can be correctly estimated as zero.

It is also letting that the output is:

$$y = \mathbf{C}\mathbf{x} \quad (2)$$

where $\mathbf{C} = [1 \ 0 \ 0]$ and hence $y = x_1$ is observable. Similar to all the identification problem, the condition of persistently excitation is assumed (Note: This is generally true when the system M is in its chaotic mode).

In order to achieve adaptive synchronization, another system, known as an observer system S , is to be designed such that the states and unknown parameters can be simultaneously estimated. Motivated by a recent work [15], a new design of S is proposed as follows:

$$S : \begin{cases} \dot{\hat{x}}_1 = q_1(\hat{x}_2 - \hat{x}_1) + k_1e_y \\ \dot{\hat{x}}_2 = q_2\hat{x}_1 - q_3\hat{x}_2 - \hat{x}_1\hat{x}_3 + k_2e_y \\ \dot{\hat{x}}_3 = \hat{x}_1\hat{x}_2 + q_4\hat{x}_2 - q_5\hat{x}_3 + k_3e_y \\ \dot{q}_i = \delta_i h_i(\hat{\mathbf{x}}, e_y) \mu_i(\hat{\mathbf{x}}) \quad \text{for } i = 1, \dots, 5 \end{cases} \quad (3)$$

where $\hat{\mathbf{x}} = [\hat{x}_1 \ \hat{x}_2 \ \hat{x}_3]^T$ is the observer state vector; $e_y = y - \hat{y}$ and $\hat{y} = \mathbf{C}\hat{\mathbf{x}}$; $\mathbf{q} = [q_1 \ q_2 \ q_3 \ q_4 \ q_5]^T$

is the estimator for unknown parameter \mathbf{p} ; $\mathbf{K} = [k_1 \ k_2 \ k_3]^T$ is the feedback gain to stabilize the linear part of the original system; $\delta_i > 0, i = 1, \dots, 5$ are some stiffness constants; h_i and μ_i are functions to ensure the minimization of the synchronization errors and to allow the unknown parameters converging with a similar rate, respectively.

The detailed design procedures are given as follows:

- 1) Design \mathbf{K} to stabilize the linear part of the system: Rewrite (1) as

$$M : \dot{\mathbf{x}} = \mathbf{A}(\mathbf{p})\mathbf{x} + \varphi(\mathbf{x}) \equiv \mathbf{F}(\mathbf{x}, \mathbf{p}) \quad (4)$$

where $\mathbf{F} = F_i(i = 1, 2, 3)$, $\mathbf{A}(\mathbf{p}) = \begin{bmatrix} -p_1 & p_1 & 0 \\ p_2 & -p_3 & 0 \\ 0 & p_4 & -p_5 \end{bmatrix}$ and the only nonlin-

earity $\varphi(\mathbf{x}) = \begin{bmatrix} 0 \\ -x_1x_3 \\ x_1x_2 \end{bmatrix}$ is Lipschitzian, i.e. there exists a positive constant $L < \infty$, such that

$$\|\varphi(\mathbf{x}) - \varphi(\hat{\mathbf{x}})\| \leq L \|\mathbf{x} - \hat{\mathbf{x}}\|, \quad \forall \mathbf{x}, \hat{\mathbf{x}} \in \mathcal{R}^n \quad (5)$$

Since $\mathbf{A}(\mathbf{p})$ is unknown, for the best estimation, \mathbf{K} is chosen to have all the eigenvalues of $(\mathbf{A}(\mathbf{q}^0) - \mathbf{K}\mathbf{C})$ being negative, where \mathbf{q}^0 is the initial guess of the parameter \mathbf{p} . For example, let $\mathbf{q}^0 = [12.0 \ 30.0 \ 2.0 \ 2.0 \ 2.5]^T$, one has the feedback gain $\mathbf{K} = [60 \ 120 \ 0]^T$, where the eigenvalues of $(\mathbf{A}(\mathbf{q}^0) - \mathbf{K}\mathbf{C})$ are $\lambda_{1,2,3} = -49.04, -24.96, -2.50$, respectively.

- 2) Design the function $h_i, i = 1, \dots, 5$:

The updating equations for unknown parameters are designed based on the dynamical minimization of the synchronization error e_y and the dependence of parameter q_i on the observable state. Details can be referred to [11], while the concept is briefly explained as follows.

The major idea is to design the dynamical equations for unknown parameters q_i so that the synchronization error:

$$E(q_i, t) = \min \left\{ (y - \hat{y})^2 \right\} \quad (6)$$

is to be minimized. With an analogy to an equation in mechanics, where an overdamped particle goes to a minimum of a potential, the following design rules are obtained:

- a) if q_i appears in the dynamical evolution of \hat{x}_1 , we have

$$h_i \propto \frac{\partial F_1(\hat{\mathbf{x}}, \mathbf{q})}{\partial q_i} e_y, \quad (7)$$

b) if q_i appears in \hat{x}_i , $i \neq 1$ and the evolution of \hat{x}_1 depends on state \hat{x}_i directly, then

$$h_i \propto \frac{\partial F_1(\hat{\mathbf{x}}, \mathbf{q})}{\partial \hat{x}_i} \frac{\partial F_i(\hat{\mathbf{x}}, \mathbf{q})}{\partial q_i} e_y, \quad (8)$$

c) if q_i appears in \hat{x}_i , $i \neq 1$ but the dynamical function F_1 does not depend on state \hat{x}_i explicitly, then a further dependence according to the dynamical evolution of the system should be considered as follows:

$$h_i \propto \left\{ \sum_k \frac{\partial F_1(\hat{\mathbf{x}}, \mathbf{q})}{\partial \hat{x}_k} \frac{\partial F_k(\hat{\mathbf{x}}, \mathbf{q})}{\partial \hat{x}_i} \right\} \frac{\partial F_i(\hat{\mathbf{x}}, \mathbf{q})}{\partial q_i} e_y \quad (9)$$

Hence, for the Lorenz system (1) and the proposed observer (3), the functions h_i can be derived as:

$$\begin{aligned} h_1 &= \text{sgn}(\hat{x}_2 - \hat{x}_1) e_y \\ h_2 &= \text{sgn}(\hat{x}_1) e_y \\ h_3 &= -\text{sgn}(\hat{x}_2) e_y \\ h_4 &= -\text{sgn}(\hat{x}_1 \hat{x}_2) e_y \\ h_5 &= \text{sgn}(\hat{x}_1 \hat{x}_3) e_y. \end{aligned} \quad (10)$$

It should be noticed that a sign function is now introduced for performance improvement. As demonstrated in later simulation, not only that (10) provides a more simple structure, its convergence speed is also found to be faster. The dependence of q_1 in original functions h_i , $i = 2, 3, 4, 5$ is further omitted as it is always positive.

3) Design μ_i such that the convergence rates of the estimation errors are similar [15]:

The error convergence rate of each parameter is approximated by the case that it is the sole unknown. For example, if only p_1 is unknown, by linearizing the error dynamics of the targeted system (1) and the observer (3) evaluated on a typical trajectory, one obtains:

$$\begin{cases} \dot{\mathbf{e}} &= J_{11(i)} \mathbf{e} + J_{12(i)} r \\ \dot{r} &= J_{21(i)} \mathbf{e} \end{cases} \quad (11)$$

where $\mathbf{e} = \mathbf{x} - \hat{\mathbf{x}}$, $r = p_1 - q_1$,

$$\begin{aligned} J_{11(i)} &= \begin{bmatrix} -q_1 - k_1 & q_1 & 0 \\ p_2 - \hat{x}_3 - k_2 & -p_3 & -\hat{x}_1 \\ \hat{x}_2 - k_3 & p_4 + \hat{x}_1 & -p_5 \end{bmatrix} \\ J_{12(i)} &= [\hat{x}_2 - \hat{x}_1 \quad 0 \quad 0]^T \\ J_{21(i)} &= [-\delta_1 \mu_1(\hat{\mathbf{x}}) \text{sgn}(\hat{x}_2 - \hat{x}_1) \quad 0 \quad 0]. \end{aligned} \quad (12) \text{ Lyapunov functions.}$$

The convergence rate of (11) is then governed by:

$$\begin{aligned} \Gamma_1 &= -J_{21(i)} J_{11(i)}^{-1} J_{12(i)} \\ &= -\frac{\delta_1}{|J_{11(i)}|} \mu_1 (p_3 p_5 + \hat{x}_1 (p_4 + \hat{x}_1)) |\hat{x}_2 - \hat{x}_1| \end{aligned} \quad (13)$$

Similarly, for having other parameters p_i , $i = 2, 3, 4, 5$ as the unknown, we have

$$\Gamma_2 = -\frac{\delta_2}{|J_{11(2)}|} \mu_2 p_1 p_5 |\hat{x}_1| \quad (14)$$

$$\Gamma_3 = -\frac{\delta_3}{|J_{11(2)}|} \mu_3 p_1 p_5 |\hat{x}_2| \quad (15)$$

$$\Gamma_4 = -\frac{\delta_4}{|J_{11(4)}|} \mu_4 p_1 |\hat{x}_1 \hat{x}_2| \quad (16)$$

and

$$\Gamma_5 = -\frac{\delta_5}{|J_{11(5)}|} \mu_5 p_1 |\hat{x}_1 \hat{x}_3| \quad (17)$$

where $|J_{11(i)}| = (p_1 + k_1)[p_3 p_5 + \hat{x}_1 (p_4 + \hat{x}_1)] - p_1 [p_5 (p_2 - \hat{x}_3 - k_2) - \hat{x}_1 \hat{x}_2 + k_3 \hat{x}_1]$, in which p_i is taken place by q_i .

Obviously, the choice of \mathbf{K} should also make $|J_{11(i)}|_{i=1, \dots, 5} > 0$, implying k_1 and k_2 are large but k_3 is small.

By reviewing the Eqns. (13)–(17), it is noticed that the convergence of the parameter estimation is related with the estimated states \hat{x}_i . It can also be observed that Γ_i , $i = 1, 4, 5$ are dependent on higher order terms, while Γ_i , $i = 2, 3$ in (14) and (15) are of first order.

Therefore, in order to force all the Γ_i to have similar dynamics and convergence rate, we have $\mu_i = 1$, for $i = 1, 4, 5$ and $\mu_i = |\hat{x}_2|$ for $i = 2, 3$.

Remark 1: When there are multiple unknown parameters appearing in the dynamical equation of the non-observable states, the design solely based on the minimization algorithm [11] may not be successful. It is due to the fact that the unknown parameters may converge in different rates, causing a failure of estimation. Therefore, auxiliary functions μ_i are now introduced. It will also be shown in the later section that this design is valid by verifying some of its local

The final adaptive observer is then constructed as:

$$S : \begin{cases} \dot{\hat{x}}_1 &= q_1(\hat{x}_2 - \hat{x}_1) + k_1 e_y \\ \dot{\hat{x}}_2 &= q_2 \hat{x}_1 - q_3 \hat{x}_2 - \hat{x}_1 \hat{x}_3 + k_2 e_y \\ \dot{\hat{x}}_3 &= \hat{x}_1 \hat{x}_2 + q_4 \hat{x}_2 - q_5 \hat{x}_3 + k_3 e_y \\ \dot{q}_1 &= \delta_1 \text{sgn}(\hat{x}_2 - \hat{x}_1) e_y \\ \dot{q}_2 &= \delta_2 |\hat{x}_2| \text{sgn}(\hat{x}_1) e_y \\ \dot{q}_3 &= -\delta_3 |\hat{x}_2| \text{sgn}(\hat{x}_2) e_y \\ \dot{q}_4 &= -\delta_4 \text{sgn}(\hat{x}_1 \hat{x}_2) e_y \\ \dot{q}_5 &= \delta_5 \text{sgn}(\hat{x}_1 \hat{x}_3) e_y \end{cases} \quad (18)$$

A. Design Justification

As mentioned in many reports, it is impossible to construct a global Lyapunov stability function for Lorenz system if \mathbf{p} in (1) is unknown and only x_1 is observed.

To justify our design, the local Lyapunov function approach suggested in [14] is adopted. As pointed out in [14], it is possible to construct some local Lyapunov functions based on the information of a control surface if the observer system is sufficiently robust to parameter mismatches. It is required that the time average of control functions must be smooth with respect to the parameter \mathbf{q} near the true value of \mathbf{p} , and converge to zero when $\mathbf{p} = \mathbf{q}$.

These criteria can provide a guideline for the design of the observer S , in turns, become a method to evaluate whether it can achieve adaptive synchronization. For multiple parameters identification, the parameter adaptive control functions (i.e. \dot{q}_i) must not only be smooth, but also converge to zero with similar rates when \mathbf{q} deviates slightly from \mathbf{p} . This also explains why additional function μ_i has to be introduced.

Consider local Lyapunov functions $U_i, i = 1, \dots, 5$ defined as follows:

$$U_i(\tau_0, T) = \frac{1}{T} \int_{\tau_0-T}^{\tau_0} \dot{q}_i d\tau \quad (19)$$

where $q_i \in [p_i - \Delta p_i, p_i + \Delta p_i]$, assuming that the other unknown parameters are set as their nominal values.

Consider the case of $\mathbf{p} = [16.0 \ 45.6 \ 1.0 \ 0.0 \ 4.0]^T$ while the system (1) is in its chaotic mode, Fig. 1 depicts the time average of $U_i(\tau_0, T)$ chosen from each state variable with $T = 250$ (denoted as U_i). For clarity, only the functions $U_{1,2,5}$ are given, and similar results can be obtained for $U_{3,4}$.

From Fig. 1, it can be observed that U_i varies smoothly when the parameter deviation Δp_i is small. Also, as illustrated by the slope of the functions, the time average of all parametric updating functions converge to zero approximately the same in each individual dimension, agreeing with our design concept.

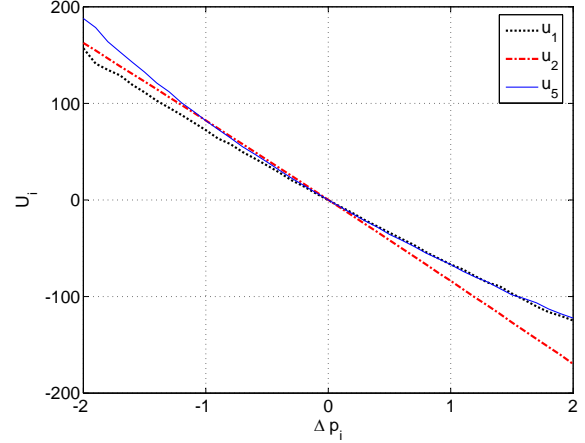


Fig. 1. $U_i, i = 1, 2, 5$ as a function of the relative deviation of the parameter error for q_i

B. Simulation Results

Now, consider a Lorenz system (1) with unknown parameter $\mathbf{p} = [16.0 \ 45.6 \ 1.0 \ 0.0 \ 4.0]^T$ and follow the procedures described in Sect. II, one obtains the observer (3).

Let $\delta_{1,4,5} = 12$, $\delta_{2,3} = 2$, and assume that the initial conditions are:

$$\begin{aligned} \mathbf{x}^0 &= [1 \ 1 \ 1]^T, \\ \hat{\mathbf{x}}^0 &= [2 \ 2 \ 2]^T \quad \text{and} \\ \mathbf{q}^0 &= [12.0 \ 30.0 \ 2.0 \ 2.0 \ 2.5]^T, \end{aligned}$$

Fig. 2 (a) shows the evolutions of the synchronization errors based on adaptive synchronization (denoted as '2'). For comparison, the same error based on identical synchronization (i.e. with \mathbf{p} known) is also given and denoted as '1'.

Obviously, it takes longer time for the synchronization error to reduce to a small value when parameters are unknown. However, as illustrated in Fig. 2 (a), the error drops exponentially and reaches the order of 10^{-4} within about 120s, which is considered to be very fast. In fact, a shorter synchronization time is possible when fewer parameters are unknown. For example, if only the common system parameters $p_{1,2,5}$ are unknown, it will only takes about 40s for the synchronization error to reach the order of 10^{-4} , which is much faster than that presented in [13], [14].

The estimated parameters q_i against time are given in Fig. 2 (b). It clearly shows that all the estimators converge to their true values, and the exact Lorenz equation is identified.

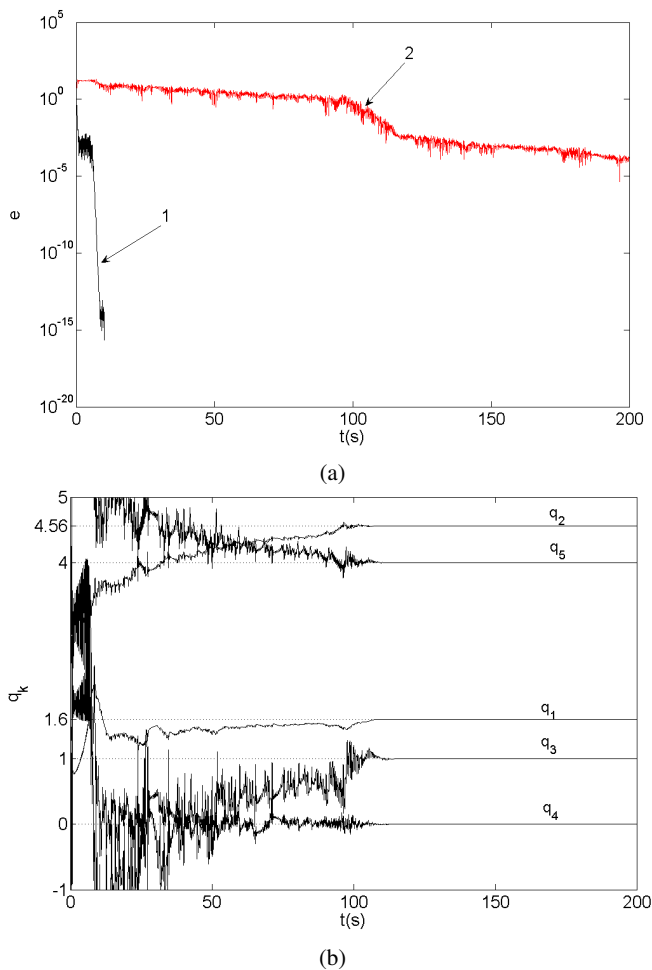


Fig. 2. (a) Synchronization errors $\sqrt{\sum e_i^2}$ vs t , where '1' and '2' indicate the synchronization errors with normal identical synchronization and adaptive synchronization, respectively ; (b) Convergence of the recovered parameter values $q_{1,2}/10$ and $q_{3,4,5}$ of the observer (3) correspond to the true values in the master system (1)

III. CRYPTANALYSIS OF SOME CHAOTIC MODULATION SYSTEMS

In this section, it is to suggest an adaptive attack using the proposed adaptive observer, serving as the cryptanalysis of some chaos-based secure communication systems. We will only focus on those systems using Lorenz attractor as their basic units, such as [6], [7], although some other chaotic systems with unknown parameters can also be adaptively synchronized with the similar approach.

The cryptanalysis is based on the assumption that the structure of the cryptosystem is known while the system parameters, which are probably the users' specific keys, are kept secret.

A. System I

Recall the system proposed in [7], which can be expressed as:

$$M_1 : \begin{cases} \dot{x}_1 = p_1(x_2 - x_1) \\ \dot{x}_2 = p_2x_1 - x_2 - x_1x_3 \\ \dot{x}_3 = x_1x_2 - \tilde{p}_3x_3 \end{cases} \quad (20)$$

where $\tilde{p}_3 = p_3 + m(t) \times \Delta$, $m(t) = \pm 1$ and Δ is a constant.

The parameters p_i , $i = 1, 2, 3$ are considered to be the secret keys. The message $m(t)$ is used to modulate p_3 and the signal x_1 is transmitted.

1) *Case I:* In our simulation, the same parameters given in [7] and [14] are used. They are: $p_1 = 16$, $p_2 = 45.6$, $p_3 = 4.2$ and $\Delta = 0.2$. As shown in Fig. 3, the two chaotic attractors corresponding to $m(t) = \pm 1$ look very similar.

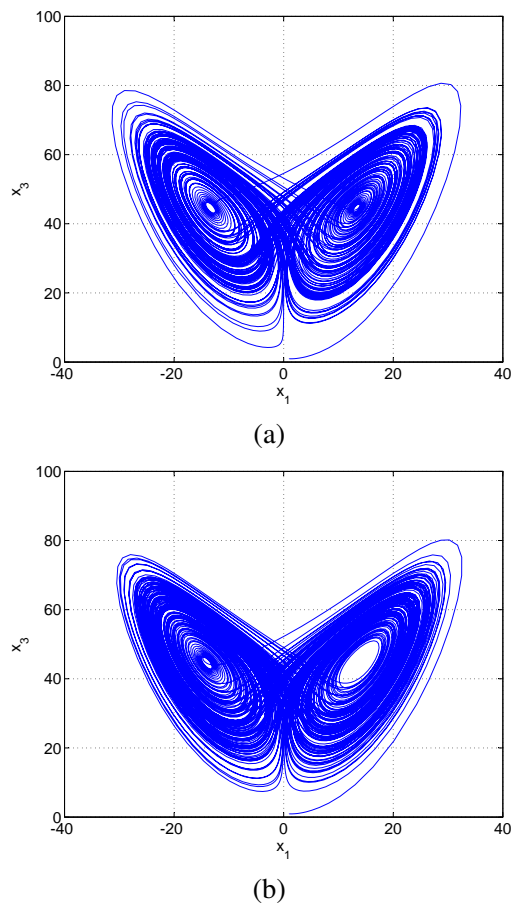


Fig. 3. (a) The chaotic attractor of Lorenz circuit for encoding (a) '-1' and (b) '1'

It should be noticed that the realization of Lorenz system in electronic circuit involves a particular time constant, and hence a transformation of time-scale is needed. As determined in [14], the new time-scale $t =$

τ/T_0 , where τ is the time-scale used in simulation and $T_0 = 2505$.

When the bit duration time of $m(t)$ is sufficiently long (say 16ms), as shown in Fig. 4, the parameter q_3 can correctly follow the modulated value \tilde{p}_3 , and the original message $m(t)$ can be obtained by estimating the medium value of q_3 . Due to the transient effect, some errors are noticed in the first few milliseconds, which can be improved with the use of a moving average filter. In our simulation, a moving average filter with a length 1ms is adopted for the first 2ms.

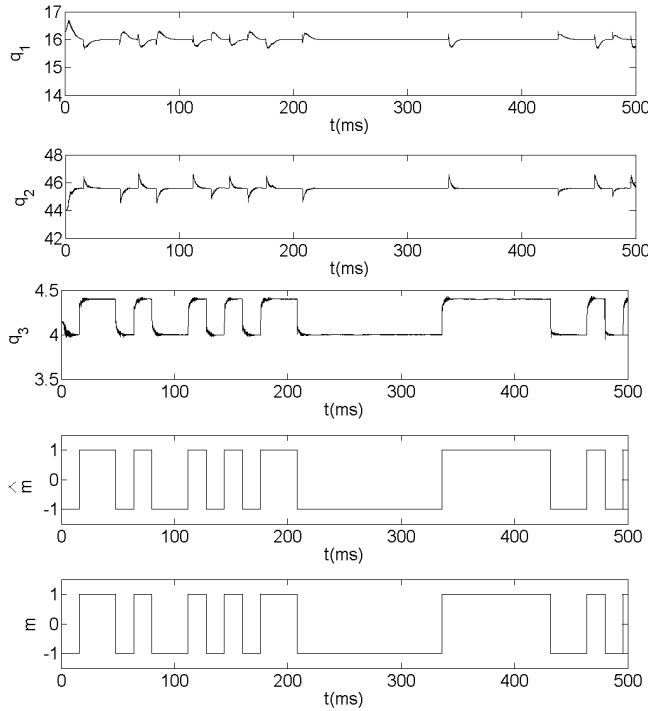


Fig. 4. Parameters q_i , recovered message $\hat{m}(t)$ and the plaintext $m(t)$ vs t

2) *Case II*: In the second case, the bit duration time is reduced to 4ms which is much smaller than the synchronization transient time. As compared with the attack suggested in [14] in which a wrong estimation of \tilde{p}_3 is obtained, the value of q_3 obtained with the proposed observer design is more accurate. By taking the average of the maximum and minimum values of q_3 after the initial transient time (in our example, 2ms), we get a coarse estimate $p_3 \approx 4.2$, which is further employed as the threshold to recover the message $m(t)$. Note that the value of the threshold is not exclusive and strict. Generally, it can be chosen as the mean of the maximum and the minimum of the modulated parameters (after the initial transient time). The simulation result is shown in Fig. 5. Again, to avoid errors caused by the initial synchronization process, a moving average filter with

length of 1ms has been used for the first 2ms.

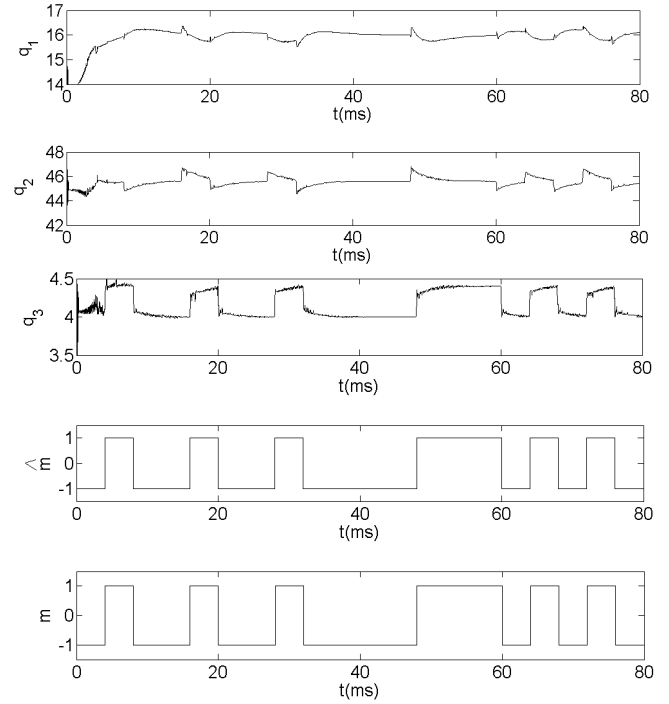


Fig. 5. Parameters q_i , recovered message $\hat{m}(t)$ and the plaintext $m(t)$ vs t

B. System II

In our second example, the system described in [6] is studied. The message is used to modulate the parameter p_2 in the cryptosystem (20), which can be described as follows:

$$M_1 : \begin{cases} \dot{x}_1 = p_1(x_2 - x_1) \\ \dot{x}_2 = \tilde{p}_2 x_1 - x_2 - x_1 x_3 \\ \dot{x}_3 = x_1 x_2 - p_3 x_3 \end{cases} \quad (21)$$

where $\tilde{p}_2 = p_2 + m(t) \times \Delta$, $m(t) = \pm 1$ and Δ is a constant. Again, the state x_1 is used as the output signal.

1) *Case I*: Now, it is letting that the system true values are: $p_1 = 10$, $p_2 = 30$, $p_3 = 8/3$, and $\Delta = 2$. The same message as in the Case I of System I is to be transmitted, with the bit duration period of 16ms (again, it is based on the new time-scale). Figure 6 depicts the estimators for the unknown parameters and the decoded message from the system parameters. From the result, it can be observed that the estimator q_2 closely follows the modulation \tilde{p}_2 , while the other two parameters also reflect the switch of the message from one value to the other. By using a simple threshold test, i.e. $p_2 = 30$ (it is determined by taking the mean of the maximum and the minimum values of q_2 after the initial transient time of 2ms.), one can easily decode the message signal $m(t)$. In

this example, a moving average filter with a length 1ms is employed in the whole process for message recovery, in order to reduce the transients. Therefore, there exists a time delay, less than 1ms, in the recovered signal.

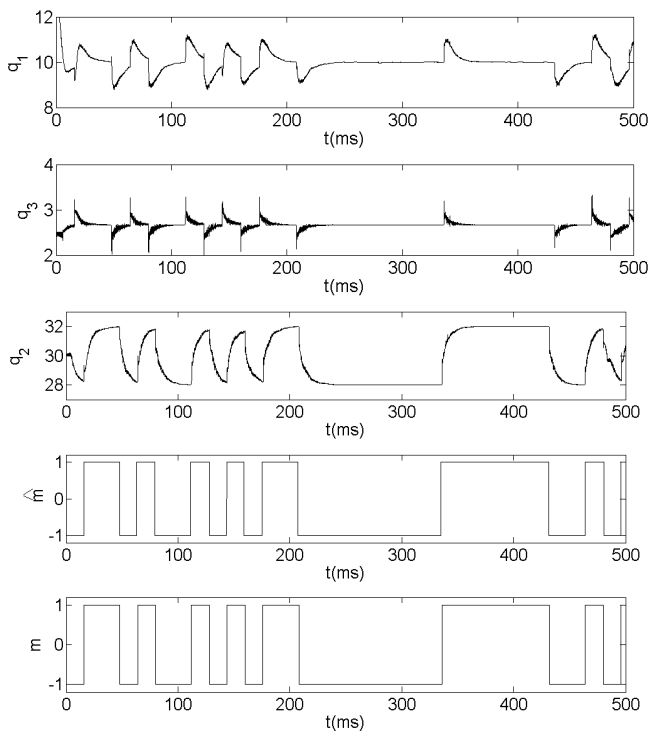


Fig. 6. Parameters q_i , recovered message $\hat{m}(t)$ and the plaintext $m(t)$ vs t

2) *Case II:* In this case, the bit rate of the message is increased, and the bit duration time is set as 4ms. As the bit duration time is very short, the convergence speed of the adaptive observer should be fast enough to correctly reveal the message. Therefore, in this example, a large feedback gain and stiffness constants are used.

The simulation results are shown in Fig. 7 with parameter settings: $\delta_{1,3} = 24$, $\delta_2 = 30$ and the feedback gain $\mathbf{K} = [120 \ 300 \ 0]^T$. It is noticed that the transient time for the System II is much longer than the System I, yet the message can still be correctly recovered by the use of a moving average filter with a length of 1ms and a simple threshold test after about 10ms.

IV. CONCLUSIONS

In this paper, the adaptive synchronization of Lorenz system with total five unknown parameters is achieved. An adaptive observer is designed for this difficult task, based on the concept of feedback control and dynamical minimization algorithm. The design is verified by the use of a local Lyapunov function approach. As shown in the simulation results, both state synchronization errors

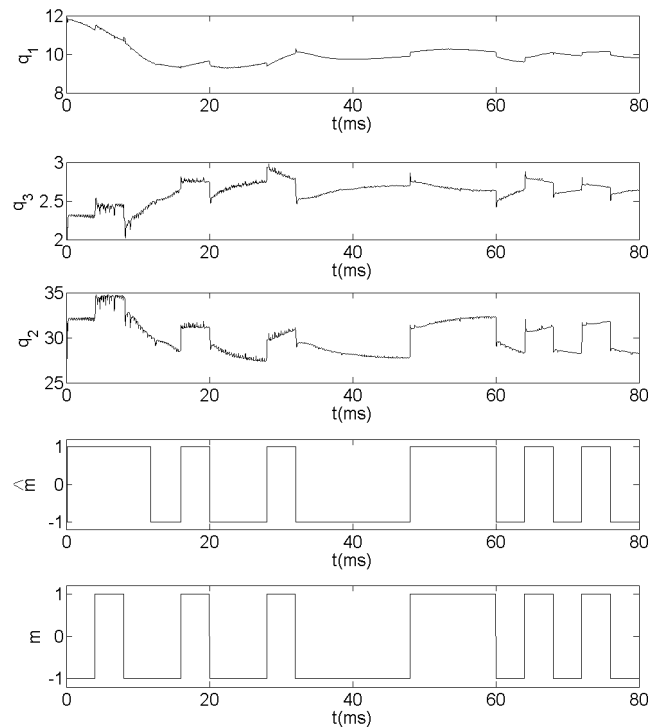


Fig. 7. Parameters q_i , recovered message $\hat{m}(t)$ and the plaintext $m(t)$ vs t

and parameter estimation errors converge to zero within a short transient, achieving the adaptive synchronization with good quality.

In addition, the adaptive observer is used as a means to perform the cryptanalysis of some chaos-synchronization based secure communication systems, in which one of the system parameters is used as carrier to transmit the information signal. From the view point of system adaptive control, the securities of those systems are questionable. Simulation results have shown that the transmitted message of different bit rates can be correctly extracted by an intruder, even though the exact parameter values in the transmitter are unknown.

ACKNOWLEDGMENT

The work described in this paper was fully supported by a grant from the Research Grants Council of the Hong Kong Special Administrative Region, China [CityU 120407].

REFERENCES

- [1] L.M. Pecora and T.L. Carroll, "Synchronization in chaotic systems," *Phys. Rev. Lett.*, vol. 64, pp. 821–824, 1990.
- [2] S.Čelikovský and G.R.Chen, "Secure synchronization of a class of chaotic systems from a nonlinear observer approach," *IEEE Trans on Automatic Control*, vol. 50, pp. 76–82, 2005.

- [3] L. Kocarev, K.S. Halle, K. Eckert, L.O. Chua and U. Parlitz, "Experimental demonstration of secure communication via chaotic synchronization," *Int. J. Bifurc. Chaos* vol. 2, pp. 709–713, 1992.
- [4] C.K. Tse and F.C.M. Lau, *Chaos-Based Digital Communication Systems: Operating Principles, Analysis Methods, and Performance Evaluation*, (Springer Verlag, Berlin, 2003).
- [5] M. Boutayeb, M. Darouach and H. Rafaralahy, "Generalized state-space observers for chaotic synchronization and secure communication," *IEEE Trans. Circuits Syst. I*, vol. 49, no. 3, pp. 345–349, Mar. 2002.
- [6] Y. Song and X. Yu, "Multi-parameter modulation for secure communication via Lorenz chaos," *Proc. IEEE Conf. Decision and Control*, pp. 42–45, 2000.
- [7] K.M. Cuomo and A.V. Oppenheim, "Circuit implementation of synchronized chaos with applications to communications," *Phys. Rev. Lett.*, vol. 71, pp. 65–68, 1993.
- [8] M. Feki, "An adaptive chaos synchronization scheme applied to secure communication," *Chaos, Solitons and Fractals*, vol. 18, pp. 141–148, 2003.
- [9] X.J. Wu, "A new chaotic communication scheme based on adaptive synchronization," *Chaos*, vol. 16, no. 4, 043118, 2006.
- [10] T. Liao and S. Tsai, "Adaptive synchronization of chaotic systems and its application to secure communications," *Chaos, Solitons and Fractals*, vol. 11, no. 9, pp. 1387–1396, 2000.
- [11] A. Maybhate and R.E. Amritkar, "Use of synchronization and adaptive control in parameter estimation from a time series," *Phys. Rev. E* vol. 59, pp. 284–293, 1999.
- [12] D.B. Huang, G.J. Xing and D.W. Wheeler, "Multiparameter estimation using only a chaotic time series and its applications," *Chaos*, vol. 17, no. 2, 023118, 2007.
- [13] U. Parlitz, "Estimating model parameters from time series by auto-synchronization," *Phys. Rev. Lett.*, vol. 76, pp. 1232–1235, 1996.
- [14] C.S. Zhou and C.H. Lai, "Decoding information by following parameter modulation with parameter adaptive control," *Phys. Rev. E*, vol. 59, no. 6, pp. 6629–6636, 1999.
- [15] Y. Liu, W.K.S. Tang and L. Kocarev, "An adaptive observer design for the auto-synchronization of Lorenz system," *Int. J. Bifurc. Chaos*, scheduled on Aug. 2008.
- [16] R. Konnur, "Synchronization-based approach for estimating all model parameters of chaotic systems," *Phys. Rev. E*, vol. 67, no. 4, 027204, 2003
- [17] D.L. Xu and F.F. Lu, "An approach of parameter estimation for non-synchronous systems," *Chaos, Solitons and Fractals*, vol. 25, no. 2, pp. 361–366, 2005
- [18] Q. He, L. Wang and B. Liu, "Parameter estimation for chaotic systems by particle swarm optimization," *Chaos, Solitons and Fractals*, vol. 34, pp. 654–661, 2007



Wallace Tang obtained his BSc from the University of Hong Kong in 1988, and both MSc and PhD from the City University of Hong Kong in 1992 and 1996, respectively. He is currently an Associate Professor in the Department of Electronic Engineering, City University of Hong Kong. He has published over 60 journal papers and four book chapters, and co-authored two books, focusing on genetic algorithms and chaotic theory. He is a member of Nonlinear Circuits and Systems Technical Committee in IEEE Circuits and Systems Society, IEEE SMCS Technical Committee on Soft Computing, and a member of technical committee on Optimal Control of IFAC. He was the Associate Editor for IEEE Transactions on Circuits and Systems Part II in 2004-2005 and is now an associate editor of Dynamics of Continuous, Discrete & Impulsive Systems, Series B. He is also the Distinguished Lecturer of IEEE Circuits and Systems Society in 2007/08.



Ying Liu received her BSc and MSc from the College of Information Engineering at Dalian Maritime University, China, in 2003 and the Department of Electrical Engineering at Shantou University, China, in 2006, respectively. She is now pursuing PhD degree from Department of Electronic Engineering of City University of Hong Kong. Her research interest is adaptive observer design and nonlinear signal processing.

Ensemble Learning for Time Series Prediction

Abdelhamid Bouchachia
 Dept. of Informatics-Systems
 University of Klagenfurt, Austria
 Email: hamid@isys.uni-klu.ac.at

Saliha Bouchachia
 Group of Integrated Systems and Circuits Design
 University of Applied Sciences, Villach, Austria
 Email: sbouchachia@fh-kaernten.ac.at

Abstract—This paper introduces a novel ensemble learning approach based on recurrent radial basis function networks (RRBFN) for time series prediction with the aim of increasing the prediction accuracy. Standing for the base learner in this ensemble, the adaptive recurrent network proposed is based on the nonlinear autoregressive with exogenous input model (NARX) and works according to a multi-step (MS) prediction regime. The ensemble learning technique combines various MS-NARX-based RRBFNs which differ in the set of controlling parameters. The evaluation of the approach which uses two known benchmark time series, Sunspot and chaotic Mackey-Glass, includes a discussion on the performance of the individual predictors and their combination.

I. INTRODUCTION

A temporal sequence is a set of finite set of discrete items linked or correlated in time. Items may be scalars or vectors. Essentially time series can be classified into 3 types: deterministic, stochastic, chaotic [1]. In deterministic time series, the items and their order are specified with 100% certainty. Typically, stochastic time series result from measuring the behavior of some dynamic systems for which the observed variability has random noise as a basic component. On the other hand, while similar to stochastic time series, in chaotic time series the observed variability is not due to noise, but to nonlinear interaction among the variables of the underlying deterministic system.

In learning temporal (and spatial) sequences for predictions purposes, recurrent neural networks have attracted a lot of attention. There exist a number of studies showing different neural architectures and relying on different learning models, i.e., supervised, unsupervised and with reinforcement. While supervised learning recurrent algorithms seem to be the most popular ones [2], [3], unsupervised learning (i.e, clustering) has witnessed increasing attention especially with the advent of self-organized maps and vector quantization networks [4]. Reinforcement on the other hand has been applied for time series in a smaller number of studies [5].

Temporal relationship often are captured using feedback connection in neural networks. This has resulted in a number of architectures and have been classified in 3 main groups [6]. globally recurrent networks [2], locally recurrent networks [3] and nonlinear autoregressive with exogenous input networks (NARX networks) [7]. In the first class, hidden nodes provide a context (hidden states) and are globally fed back as new input. In locally recurrent networks, the feedback connections

are allowed only from neurons to themselves (looped neurons). In the NARX architecture, the output of the network are fed back to the input layer.

In this paper we use a new adaptive NARX recurrent radial basis function network as a prototypical base learner for an ensemble learning approach. This neural network is called a MS-NARX-RRBFN standing for multi-step NARX-based recurrent radial basis function network. As will be described in Sec. II, the aim is to construct parsimonious and flexible radial basis function networks. To achieve such a goal, the proposed neural network is equipped with multi-step-ahead prediction mechanisms and is totally self-adaptive in the sense that most of the parameters defining its architecture are learned too.

In addition to the multi-step-ahead prediction strategy endowing the radial basis function network during training, to further enhance the prediction accuracy, a neural ensemble (committee) predictor is devised. This ensemble is generated by varying the MS-NARX-RRBFN allotting different settings.

Ensemble learning has recently attracted much attention due to its ability to perform better than single learning model and to discover regularities in dynamic and non-stationary data. Ensemble methods aim at leveraging the performance of a set of models to achieve better prediction accuracy than that of the individual models. While in some literature sources, authors refer to individual models as weak learners, it is however necessary to have them as competent as possible [8]. This is the approach taken in this paper. We aim at obtaining a set of competent complementary decision makers. It is worth stressing here to note that due to the non-stationarity characterizing time series, prediction by means of committee learners is indeed a very appealing approach.

The rest of this paper is organized as follows. Section II describes the base learner used in this ensemble predictor. Section. III introduces the ensemble predictor. In Sec. IV, the evaluation of the proposed approach is discussed.

II. RECURRENT MULTI-STEP RBFN

Like multilayer perceptron, RBF neural networks are function approximators [9] able of learning to map a given input set to its corresponding output set. In a RBF network, the hidden units form a set of functions that compose a random basis for the input patterns, hence the name of radial basis functions [10]. They serve to perform a nonlinear transformation of the patterns into a high-dimensional space in order

to tackle the problem of pattern separability. An interesting development stage of RBFNs is regularization that allows to enhance the generalization of the network via interpolation mechanisms in the high-dimensional space [11].

This generalization capability, however, depends largely on the appropriateness of the model's parameters, i.e. centers, number, form, and width of the radial basis functions and the learning algorithm used to train the network. As to this latter aspect, several RBFN training schemes have been developed. The known ones include gradient descent [10] and orthogonal least square optimization [12]. Such training schemes may involve learning the RBF parameters also. In fact, the centers of the radial basis functions can be determined either by clustering (and vector quantization) [13] or can along with the radial basis widths be part of the training stage [10].

The number of radial basis functions depends on the data and should be carefully selected. It can either a priori fixed and remains static or dynamically set (i.e., centers are added or deleted) in the course of training. To avoid such a problematic, a criterion that defines the optimum number of basis functions for the RBF networks has been introduced in [14]. Such a criterion relies on Steins unbiased risk estimator to derive an analytical criterion for assigning the appropriate number of basis functions.

Moreover, there exists a set of basis functions that can be used and for which the interpolation can be achieved. These include multi-quadratic, Gaussian, inverse multi-quadratic, thin-plate spline, cubic and linear. These functions have been compared on time series in [15]. The authors recommend to try various basis functions with their range of widths to find an optimal solution.

Motivated by these considerations about the network's architecture and the diversity of heuristics used to estimate the network's parameters as discussed earlier, it seems very appealing to use ensemble learning to face such diversity and tuning problems. The ensemble method we propose in this paper relies on the NARX architecture of recurrent neural networks. Compared to globally recurrent networks, in NARX-based recurrent networks the states of the network are obtained from the output layer not from the hidden layer. In terms of complexity, NARX models are less dense since the size of hidden layer is larger than that of the output layer. In the case of time series, the output layer consists of only one neuron.

NARX-RRBFN relies on the nonlinear autoregressive model with exogenous inputs that is described by:

$$\hat{y}(t+1) = F(x(t+1), \dots, x(t-D_x), y(t), \dots, y(t-D_y)) \quad (1)$$

where $x(t)$ and $y(t)$ are the input and output of the nonlinear system at time t , F is a nonlinear function, D_y and D_x represent the order of the model. For time series, this model is reduced to:

$$\hat{y}(t+1) = F(y(t), y(t-1), \dots, y(t-D)) \quad (2)$$

where D is the size of a time window. In other terms, the time series behavior can be captured by expressing the value $y(t+1)$

as a function of the D previous values of the time series, $(y(t) \cdots (y(t-D)))$. Syntactically such behavior corresponds to one-step prediction which "fits" the last D samples to estimate the current value at time t . However, such a prediction scheme may not provide enough information especially if one wants to anticipate the behavior of the time series evolution.

To overcome this, NARX-RRBFN can be enhanced by embedding a multi-step predictive model that offers the possibility to handle complex dynamics over a long period of time. The idea underlying multi-step predictive model, as a generalization of the one-step model, is that predicting at time $t+1$ requires to perform p prediction steps ahead into the future, i.e. $\hat{y}(t+1), \dots, \hat{y}(t+p+1)$. Hence, the goal is to approximate the function F such that the model given by Eq. 2 can be used as a multi-step prediction scheme.

The mathematical formulation of multi-step prediction is as follows:

$$\hat{y}(t+p+1) = F(\hat{y}(t+p), \dots, \hat{y}(t+1), y(t), \dots, y(t-D+p)) \quad (3)$$

where p is called prediction horizon. Basically this formulation can be unfolded as follows:

$$\begin{cases} \hat{y}(t+1) = F(y(t), \dots, y(t-D)) \\ \hat{y}(t+2) = F(\hat{y}(t+1), y(t), \dots, y(t-D+1)) \\ \dots = \dots \\ \hat{y}(t+p+1) = F(\hat{y}(t+p), \dots, \hat{y}(t+1), y(t), \dots, y(t-D+p)) \end{cases} \quad (4)$$

which suggests that at any time t , predictions have to be made based on the time interval $[t+1, t+p+1]$ taking D samples as input. Such input is split into two parts: context input and external input. The context input stands for the internal states of the network which are obtained from the delayed network output. They memorize the context of the current input by recalling information about the past. This context provides the network the ability to handle long-term predictions. Indeed for the sake of long-term predictions, the multi-step approach adopted here allows the network to take future sample change over a prediction horizon into account. The external input represents the last samples seen by the network preceding the current time t . Initially these samples act as a window that represents the historical trend obtained directly from the data. This means that the predicted network output $\hat{y}(t+1)$ at instant $t+1$ is sent back as input for the next step prediction. The remaining input part corresponds to the input values shifted ahead by one sample.

Graphically the multi-step NARX-RBFN is portrayed in Fig. 1 and its unfolding architecture is portrayed as a cascade of RBFNs in Fig. 2.

Basically the function F in Eq. 3 has the form of

$$\hat{y}(t+p+1) = F(\hat{y}(t+p), \dots, \hat{y}(t+1), y(t), \dots, y(t-D+p), \Theta) \quad (5)$$

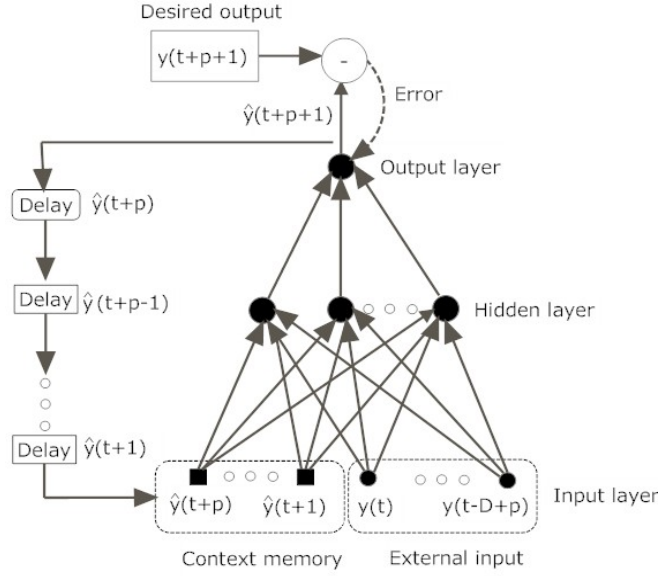


Fig. 1. Recurrent radial basis function with multi-step learning

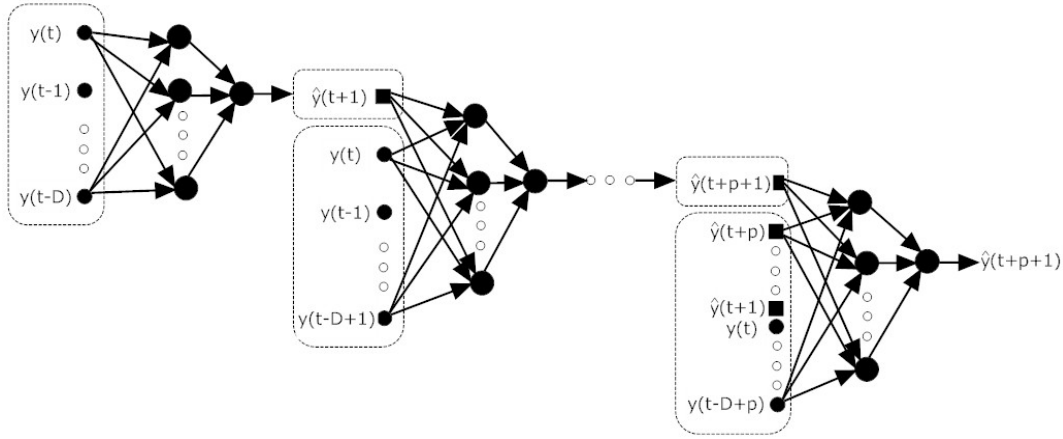


Fig. 2. Unfolding the multi-step NARX-RRBFN

where Θ is the parameter set of the model (C_i, Σ_i, W) which stands for the centers and widths of the radial basis functions and the weights between the hidden and the output layers.

To define $\Theta = \{v_j, \sigma_j, w_j\}$, the following performance index has to be minimized:

$$Q(t+1) = \frac{1}{2} \sum_{i=1}^p (y(t+i+1) - \hat{y}(t+i+1))^2 \quad (6)$$

standing for the multi-step prediction error.

Since, the present work is about adaptive recurrent radial basis function network, the weights, centers, and widths of the radial basis functions are updated using the following gradient descent rules:

$$\frac{\partial Q}{\partial \Theta} : \frac{\partial Q}{\partial v_j}, \frac{\partial Q}{\partial \sigma_j}, \frac{\partial Q}{\partial w_j} \quad (7)$$

Recall that the output node is a linear combination of a set of basis functions:

$$\hat{y}(x_i) = \sum_{j=1}^H w_j \phi_j(x_i) \quad (8)$$

where x_i is the input vector with elements x_{im} (where m is the dimension of the input vector); v_j is the center vector of the basis function $\phi_j(\cdot)$ with elements v_{ji} ; w_j are the output layer's weights. The hidden nodes equipped with the basis function $\phi_j(x_i)$ are nonlinear, while those of the output are linear.

The radial basis function takes different forms which we will use in ensemble learning approach intended in this study. These forms are shown in Tab. I. For the sake of simplicity we omit the index $(t+1)$ from Eq. 7. Therefore, $\hat{y}(t+1+i)$ (resp.

TABLE I
 RADIAL BASIS FUNCTIONS

Function	Form
Gaussian	$e^{-\frac{\ y-v_j\ ^2}{2\sigma_j^2}}$
Multiquadratic	$(\ y-v_j\ ^2 + \sigma_j^2)^{\frac{1}{2}}$
Inverse multiquadratic	$(\ y-v_j\ ^2 + \sigma_j^2)^{-\frac{1}{2}}$
Cubic	$\ y-v_i\ ^3$

$y(t+1+i)$ will be written \hat{y}_i (resp. y_i). Then the following holds:

$$\frac{\partial Q}{\partial w_j} = \frac{\partial Q}{\partial \hat{y}_i} \frac{\partial \hat{y}_i}{\partial w_j} = -(y_i - \hat{y}_i) \phi_j \quad (9)$$

Hence, the weight can be updated as follows:

$$w_j = w_j - \eta_1 \frac{\partial Q}{\partial w_j} = w_j + \eta_1 (y_i - \hat{y}_i) \phi_j \quad (10)$$

To update the centers we need to compute:

$$\frac{\partial Q}{\partial v_j} = \frac{\partial Q}{\partial \hat{y}_i} \frac{\partial \hat{y}_i}{\partial \phi_j} \frac{\partial \phi_j}{\partial v_j} = -w_j (y_i - \hat{y}_i) \frac{\partial \phi_j}{\partial v_j} \quad (11)$$

leading to the following update rule:

$$v_j = v_j - \eta_2 \frac{\partial Q}{\partial v_j} = v_j + \eta_2 w_j (y_i - \hat{y}_i) \frac{\partial \phi_j}{\partial v_j} \quad (12)$$

The last update operation is that of the width which requires:

$$\frac{\partial Q}{\partial \sigma_j} = \frac{\partial Q}{\partial \hat{y}_i} \frac{\partial \hat{y}_i}{\partial \phi_j} \frac{\partial \phi_j}{\partial \sigma_j} = -w_j (y_i - \hat{y}_i) \frac{\partial \phi_j}{\partial \sigma_j} \quad (13)$$

leading to the following update rule:

$$\sigma_j = \sigma_j - \eta_3 \frac{\partial Q}{\partial \sigma_j} = \sigma_j + \eta_3 w_j (y_i - \hat{y}_i) \frac{\partial \phi_j}{\partial \sigma_j} \quad (14)$$

The MS-NARX-RRBF learning algorithm consists of the steps shown in Alg. 1. For a particular base learner, the architecture of the RRBF is kept fixed but the input layer is dynamic. Just recall that at time t , the algorithm must predict the time series values at instants $t+1, \dots, t+p+1$ during which the number of external input nodes decreases from $D+1$ to $D+1-p$ while the number of context neurones increases from 0 to p . Thus, initially the number of context nodes is 0 and the external nodes correspond to the input indexed by $t, \dots, t-D$. Generally, at time $t+i$ to predict the future $t+i+1^{th}$ time series sample, the context nodes receive output corresponding to the predictions realized in interval $[t+1, t+1+i-1 = t+i]$ (i.e, the number of context nodes is $(t+i) - (t+1) = i-1$, whereas the external input nodes correspond to the time series samples indexed by time interval $[t-D+i-1, t]$ (since the window is of length $D+1$). Note that to learn the last p training samples of the time series, the number of context nodes will not exceed $T-i$ (since $t+i \leq T$ must hold, where T is the size of the training data). On the other hand, in this study p is set to value less $D+1$, so that we have at least one external input, otherwise all neurons in the input layer will be context nodes.

Algorithm 1 : Training the multi-step NARX-RRBFN

- 1: - Initialize η_1, η_2, η_3 , the size of the hidden layer H , the prediction horizon p , the window D (such that $p \leq D$ to avoid learning exclusively from future predictions).
 - 2: **repeat**
 - 3: - Set the initial input window $[y_1, \dots, y_D]$
 - 4: - Initialize the network: radial basis function type, initial centers (V), width (σ) and the weights (W)
 - 5: **for** $t = D+1$ to $T-1$ **do**
 - 6: - Compute $\hat{y}(t+1) = F(y(t), \dots, y(t-D))$
 - 7: **for** $i = 1$ to p **do**
 - 8: - Recursively predict the output $\hat{y}(t+i+1)$ of the current configuration of the NARX-RRBFN using:

$$\hat{y}(t+i+1) = F(\hat{y}(t+i), \dots, \hat{y}(t+1), y(t), \dots, y(t-D+i-1))$$
 - 9: - Update the parameter set $\Theta = \{V, \Sigma, W\}$ according to Eqs. 12,14, 10 respectively
 - 10: - Update the input sequence at the input layer
 - 11: **end for**
 - 12: **end for**
 - 13: **until** Stopping criterion is met
-

III. ENSEMBLE LEARNING

Radial basis function neural networks are universal non-linear function approximators with a controllable complexity. They are known for their prediction power. However, due to the diversity and the definition range of their parameters, the performance of these neural networks may vary strongly. To alleviate the effect of parameter setting, it seems appealing to combine in a symbiotic way several predictors. The idea is that even if the performance of one or few neural networks may not be that much satisfactory, the ensemble of the algorithms can still predict the correct output. Usually, when the task is relatively hard, multiple predictors are used following the conquer-and-divide principle [16].

Ensemble learning has been mostly applied for classification problems. However, recently a certain number of studies propose their application for time series forecasting problems. For instance, an ensemble learning based on feedforward neural networks has been proposed in [17] for time series forecasting. In [18], the ensemble combines radial basis function networks and the Box-Jenkins models. In [19], a combination genetic classifiers is proposed for predicting stock indexes, while in [20], a hybrid combination of neural networks and the ARIMA model is applied for time series forecasting. In [21], an ensemble of Elman networks combined by Adaboost is proposed for predicting drug dissolution profiles. Similar work has been investigated in [22] relying on Adaboost and its variants such as Adaboost.R proposed in [23].

It is important to note that most of the studies rely on one scheme that is classifier combination trained on different data sets. In this scheme several classifiers, each trained on randomly generated sets (re-sampling from a larger training set)

TABLE II
 DIVERSITY CRITERIA

Parameter	Value set
1- Learning	{Gradient descent}
2- Number of RBFs	{Fitting mixture of Gaussians using EM}
3- Type of RBFs	{Multi-quadratic, Gaussian, inverse multi-quadratic, cubic}
4- Width of RBFs	{Gradient descent}
5- Center of RBFs	{Gradient descent}
6- RBFN Architecture	{Globally recurrent}

 TABLE III
 COMBINATION RULES

Rule	Expression
Average Rule	$O^j(x) = \frac{1}{N} \sum_{i=1}^N O_i^j(x)$
Max Rule (optimistic)	$O^j(x) = \max_{i=1}^N O_i^j(x)$
Min Rule (pessimistic)	$O^j(x) = \min_{i=1}^N O_i^j(x)$

are combined to perform the classification or regression task. These include stacking [24], bagging [25] and boosting [23].

In this study we rather focus on a different scheme that is *combination of different classifiers* [16], [26]. According to this scheme, the classifier ensemble contains several classifiers of different types (neural networks, decision trees, etc.), of different parameters (e.g. in multi-layer neural networks: different number of hidden layers, different number of hidden neurons, etc.), or trained using different initial conditions (e.g. weight initialization in neural networks, etc.). The application of such scheme is not well studied in the context of time series. For instance, in [26], an ensemble learning model using the fuzzy k-nearest neighbor classifier as a base classifier is proposed. K-nearest neighbor classifier is also used in [27] but combined with multi-layer perceptron, nearest trajectory models and some polynomial models.

In our study we focus on recurrent radial basis functions adapted to the NARX architecture and working in a multi-step prediction regime shown in Alg. 1. This ensemble of recurrent neural networks are mainly diversified according to the architecture, type of radial basis function, the initialization of the weights, and the initial position of the radial basis functions (see Tab. II). As already mentioned, there exist many ways the individual NARX-RBFN can be combined. In the present study, we consider the rules shown in Tab. III.

IV. NUMERICAL SIMULATIONS

A. Benchmarks

In this study, we will rely on two major data sets to evaluate the proposed approach. These are the sunspots and the chaotic Mackey-Glass time-series datasets. The former contains the yearly number of dark spots on the sun from 1700 to 1979. The time series has a pseudo-period of 10 to 11 years. In many studies, the training set includes the time series from

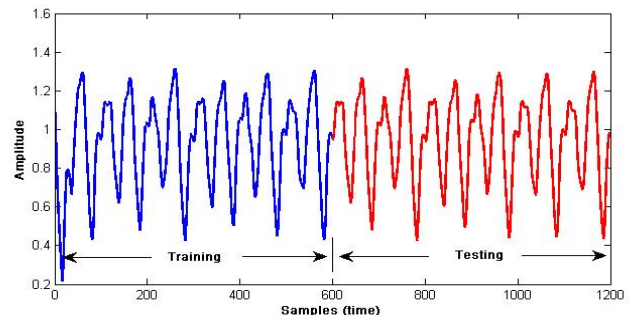


Fig. 3. Mackey-Glass time series

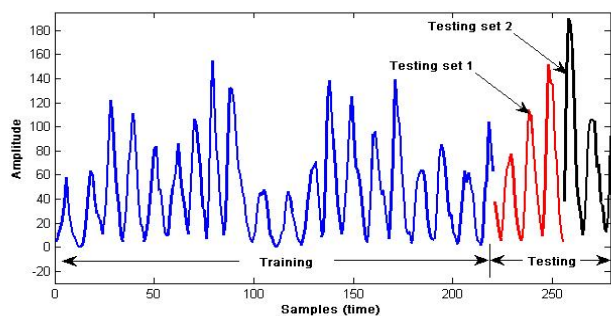


Fig. 4. Sunspot time series

1700 to 1920, while the testing set consists of two subsets, 1921-1955 (test1) to be used here and 1956-1979 (test2). The chaotic Mackey-Glass time-series are generated by the following nonlinear differential equation:

$$\frac{dx(t)}{dt} = -0.1 * x(t) + \frac{0.2 * x(t - \tau)}{1 + x^{10}(t - \tau)} \quad (15)$$

The initial conditions used in our test bench are set as $x(0) = 0.8$ and $t = 17$. These are set so in order to conduct a comparative study against other approaches using the same benchmarks.

B. Experiments

To assess the proposed approach, we study two aspects: (i) the prediction accuracy of the individual networks, (ii) the accuracy of their combination following the the four types of radial basis functions on both data sets: the sunspots and the chaotic Mackey-Glass time-series. For the sake of the evaluation, the root mean squared error (RMSE) measure is used to quantify the goodness-of-fit. It is given by:

$$RMSE = \sqrt{\frac{\sum_{i=1}^N (y(i) - \hat{y}(i))^2}{N}} \quad (16)$$

Before starting the evaluation of each of the individual NARX-RBFN, it is important to check the effect the key parameters that characterize the proposed NARX architecture. Basically, these parameters include the time window size (D)

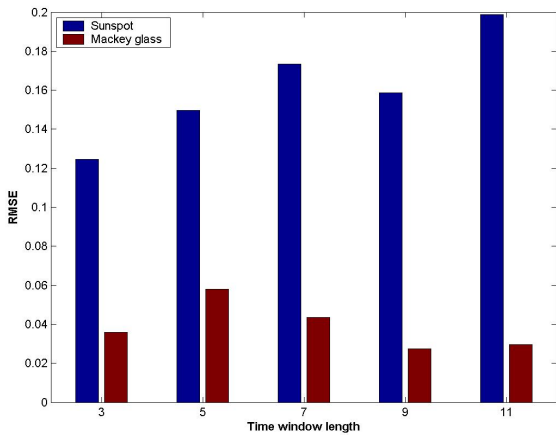


Fig. 5. The effect of window size

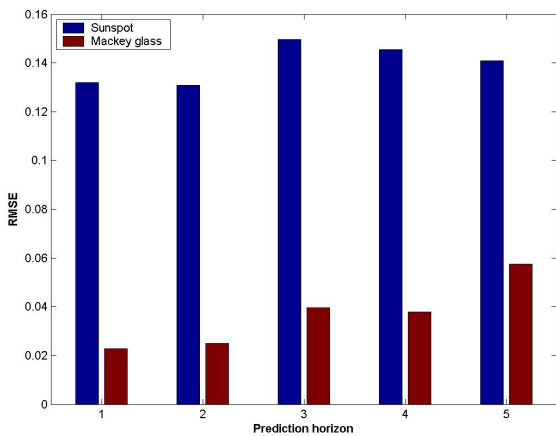


Fig. 6. The effect of the prediction horizon

used for training the networks and the prediction horizon (p), and the number of radial basis functions. Figures 5 and 6 show the effect of the two parameters on the prediction root mean square error for both data sets.

The observed trend from these figures is that for the sunspot time series, small window size is preferred. In fact, when $D = 3$, a least root mean square error is obtained. In the case of Mackey glass data set, there is no clear trend window size, though larger sizes seem to be preferred. On the other hand, small size of the prediction horizon is preferred for both data sets. These results are consistent with the variability of time series. Indeed, the variability of Mackey-glass, that is 0.0556, is far smaller than that of sunspot (1554.20). Therefore, it is important to set the window time in the case of sunspot also smaller than that applied to the Mackey-glass time series.

This experiment has allowed to estimate the near-optimum D and p (in a certain range of values). In the next experiments, we will consider $D_{sunpot} = 3$, $D_{Mackey} = 9$, $p_{sunpot} = 2$,

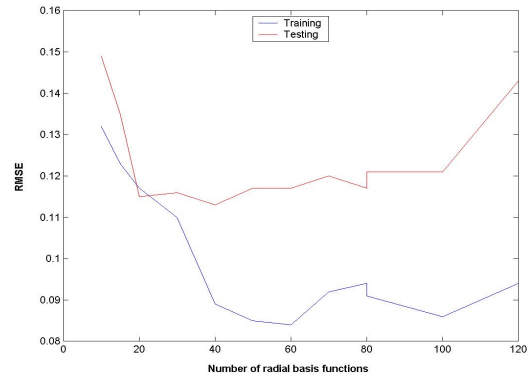


Fig. 7. The effect of cluster number - sunspot

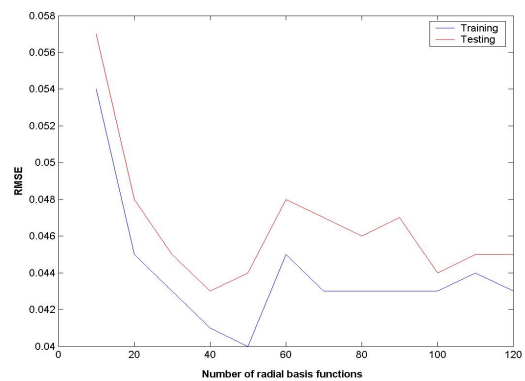


Fig. 8. The effect of the cluster number - Mackey glass

and $p_{Mackey} = 2$.

On the other hand, to find the optimal number of radial basis functions used by the neural networks, we have used the Bayesian Information Criterion (BIC) to judge the statistical significance of a number of inspected finite mixture models. We do that by relying on the expectation maximization algorithm. The highest BIC value corresponds to the optimal number of radial basis function.

As expected, the BIC increases as the number of clusters increases. However, a significant increase is obtained after setting the number of clusters to 48 in the case of Mackey glass data and 56 for the sunspot data. This has also been noticed when computing the root mean square error as shown in Figs. 7 and 8 for the case of Gaussian radial basis function as an illustrative example. Therefore, we have considered 60 and 50 clusters for sunspot and Mackey glass respectively.

Applying the set of NARX-RBFNNs under the optimal conditions (i.e., optimal number of radial basis functions, size of the time window, size of the prediction horizon) on the training and testing data of both data sets, we obtain Figs. 9, 10, 11, and 12. These show how good the fit is.

TABLE IV
 COMBINING THE NARX-RBFNNs (RMSE)

		Sunspot		Mackey Glass	
		Train	Test	Train	test
Radial basis functions	Gaussian	1.2613	0.2603	0.5119	0.6782
	Multiquadratic	1.3660	0.2653	0.6636	1.0302
	Inverse multiquadratic	1.3350	0.2643	0.7696	1.1985
	Cubic	1.4385	0.2654	0.6590	1.2293
Combination rules	Max rule	1.3551	0.2399	0.7277	1.1631
	Min Rule	1.4010	0.2784	0.7240	1.1866
	Average	1.2401	0.2231	0.5040	0.5999

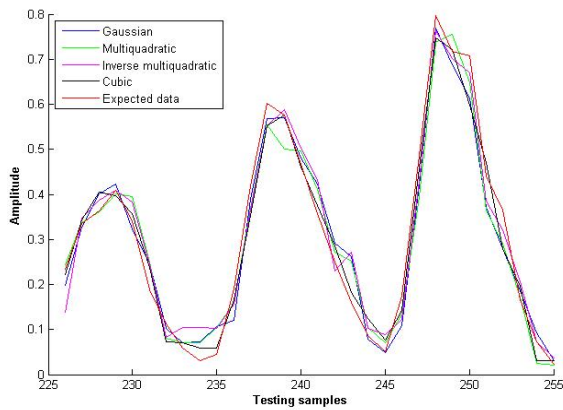


Fig. 10. Testing the individual NARX-RBFNNs - sunspot

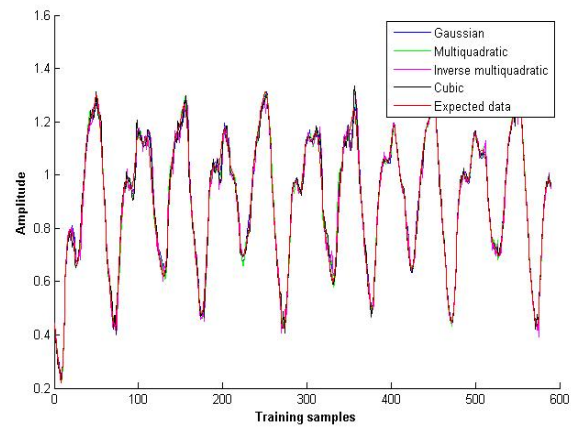


Fig. 11. Training the individual NARX-RBFNNs - Mackey glass

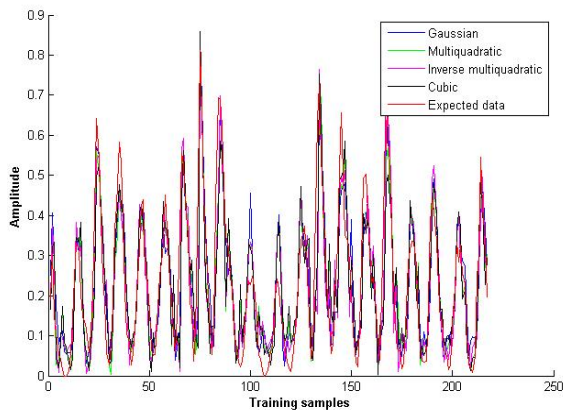


Fig. 9. Training the individual NARX-RBFNNs - sunspot

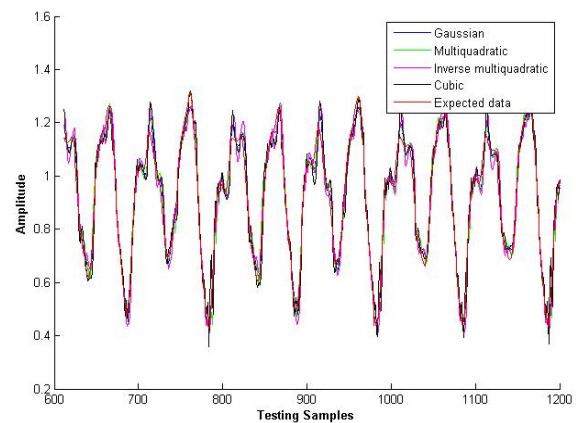


Fig. 12. Testing the individual NARX-RBFNNs - sunspot

The combination of the four NARX-RBFNNs according to the combination rules portrayed in Tab. III yields the results shown in Tab. IV with respect to both data sets. The accuracy of the ensemble is much higher compared to each of the individual predictor. The average rule is the best combination rule. Comparing the individual NARX-RBFNNs on these two particular time series, it seems that the Gaussian radial basis

function produces more accurate fitting.

V. CONCLUSION

The present paper deals with a new method of time series predictions based on multiple predictors. Each of these is a multi-step nonlinear autoregressive with exogenous input model (NARX) radial basis function network. Relying on two time series, the experiments have shown that the combination improves the prediction accuracy. However, it is still necessary to conduct further experiments with a larger sets of time series in order to thoroughly assess the approach suggested in this study.

REFERENCES

- [1] A. Barreto, A. A. Araujo, and S. Kremer, "A taxonomy for spatiotemporal connectionist networks revisited: the unsupervised case," *Neural Computation*, vol. 15, pp. 1255–1320, 2003.
- [2] S. Kremer, "Spatiotemporal connectionist networks: A taxonomy and review," *Neural Comput.*, vol. 13, no. 2, pp. 249–306, 2001.
- [3] P. Frasconi, M. Gori, and G. Soda, "Local feedback multilayered networks," *Neural Comput.*, vol. 4, no. 1, pp. 120–130, 1992.
- [4] A. Araújo and G. Barreto, "Context in temporal sequence processing: A self-organizing approach and its application to robotics," *IEEE Transactions on Neural Networks*, vol. 13, no. 1, pp. 45–57, 2002.
- [5] F. Liu, G. Ng, and C. Quek, "Rlde: A novel reinforcement learning-based dimension and delay estimator for neural networks in time series prediction," *Neurocomput.*, vol. 70, no. 7-9, pp. 1331–1341, 2007.
- [6] T. Lin, B. Horne, P. Tiño, and C. Giles, "Learning long-term dependencies in NARX recurrent neural networks," *IEEE Transactions on Neural Networks*, vol. 7, no. 6, pp. 1329–1338, 1996.
- [7] J. Menezes and G. A. Barreto, "A new look at nonlinear time series prediction with narx recurrent neural network," in *SBRN '06: Proceedings of the Ninth Brazilian Symposium on Neural Networks*, 2006, p. 28.
- [8] A. Bouchachia, "Learning with partly labeled data," *Neural Computing and Applications*, vol. 16, no. 3, pp. 267–293, 2007.
- [9] J. Park and I. Sandberg, "Universal approximation using radial-basis-function networks," *Neural Comput.*, vol. 3, no. 2, pp. 246–257, 1991.
- [10] S. Haykin, *Neural Networks: A Comprehensive Foundation*. Prentice Hall, 1999.
- [11] T. Poggio and F. Girosi, "Networks for approximation and learning," *Proceedings of the IEEE*, vol. 78, pp. 1481–1497, 1990.
- [12] G. Fasshauer, *Mathematical Methods for Curves and Surfaces*. Vanderbilt Univ. Press, 1995, ch. Adaptive least squares fitting with radial basis functions on the sphere, pp. 141–150.
- [13] J. Moody and C. Darken, "Fast learning in networks of locally tuned processing units," *Neural Comput.*, vol. 1, pp. 281–294, 1989.
- [14] A. Ali Ghodsi and D. Schuurmans, "Automatic basis selection techniques for rbf networks," *Neural Networks*, vol. 16, no. 5-6, pp. 809–816, 2003.
- [15] C. Harpham and C. Dawson, "The effect of different basis functions on a radial basis function network for time series prediction: A comparative study," *Neurocomputing*, vol. 69, no. 16–18, pp. 2161–2170, 2006.
- [16] L. Kuncheva, J. Bezdek, and R. Duin, "Decision templates for multiple classifier fusion: An experimental comparison," *Pattern Recognition*, vol. 34, no. 2, pp. 299–314, 2001.
- [17] D. Karunasinghea and S. Liong, "Chaotic time series prediction with a global model: Artificial neural network," *Journal of Hydrology*, vol. 323, no. 1-4, pp. 92–105, 2006.
- [18] D. Wedding II and K. Cios, "Time series forecasting by combining rbf networks, certainty factors, and the box-jenkins model," *Neurocomputing*, vol. 10, no. 2, pp. 149–168, 1996.
- [19] G. Armano, M. Marchesi, and A. Murru, "A hybrid genetic-neural architecture for stock indexes forecasting," *Inf. Sci.*, vol. 170, no. 1, pp. 3–33, 2005.
- [20] O. Valenzuela, I. Rojas, F. Rojas, H. Pomares, L. Herrera, A. Guillen, L. Marquez, and M. Pasadas, "Hybridization of intelligent techniques and arima models for time series prediction," *Fuzzy Sets Syst.*, vol. 159, no. 7, pp. 821–845, 2008.
- [21] W. Goh, C. Lim, and K. Peh, "Predicting drug dissolution profiles with an ensemble of boosted neural networks: a time series approach," *IEEE Transactions on Neural Networks*, vol. 14, no. 2, pp. 459–463, 2003.
- [22] M. Assaad, R. Boné, and H. Cardot, "A new boosting algorithm for improved time-series forecasting with recurrent neural networks," *Inf. Fusion*, vol. 9, no. 1, pp. 41–55, 2008.
- [23] Y. Freund and R. Schapire, "A decision-theoretic generalization of on-line learning and an application to boosting," in *Proceedings of the Second European Conference on Computational Learning Theory*, 1995, pp. 23–37.
- [24] D. Wolpert, "Stacked generalization," *Neural Networks*, vol. 5, no. 2, pp. 241–259, 1992.
- [25] L. Breiman, "Bagging predictors," *Machine Learning*, vol. 24, no. 2, pp. 123–140, 1996.
- [26] C. Christian Dietrich, G. Palm, and F. Schwenker, "Decision templates for the classification of bioacoustic time series," *Information Fusion*, vol. 4, no. 2, pp. 101–109, 2003.
- [27] J. Wichard and M. Ogorzalek, "Time series prediction with ensemble models applied to the cats benchmark," *Neurocomputing*, vol. 70, no. 13-15, pp. 2371–2378, 2007.



Abdelhamid Bouchachia is affiliated with the group of Software Engineering and Soft Computing, Dept. of Informatics, University of Klagenfurt, Austria, as Associate Prof. His current research interests cover a range of soft computing and machine learning techniques encompassing data and information processing, incremental learning, semi-supervised learning, prediction systems, nature-inspired computing, processing and modeling of uncertainty in pattern recognition and rule based systems.

Saliha Bouchachia, is affiliated as a research assistant with the Group of Integrated Systems and Circuits Design, University of Applied Sciences, Villach, Austria. Her research interests cover mobile multicas receivers, microwaves, transmission lines and analog design.

Feature extraction for the prognosis of electromechanical faults in electrical machines through the DWT

J.A. Antonino-Daviu, M. Riera-Guasp, M. Pineda-Sánchez, J. Pons-Llinares, R. Puche-Panadero

Instituto de Ingeniería Energética
 Universidad Politécnica de Valencia
 Camino de Vera s/n, 46022 Valencia
 joanda@die.upv.es

Abstract—Recognition of characteristic patterns is proposed in this paper in order to diagnose the presence of electromechanical faults in induction electrical machines. Two common faults in this type of machines are considered; broken rotor bars and mixed eccentricities. The presence of these faults leads to the appearance of frequency components following a very characteristic evolution during the startup transient and other transients through which the machine operates. The identification and extraction of these characteristic patterns through the Discrete Wavelet Transform (DWT) has been proven to be a reliable methodology for diagnosing the presence of these faults, showing certain advantages in comparison with the classical FFT analysis of the steady-state current. In the paper, a compilation of healthy and faulty cases are presented; they confirm the validity of the approach for the correct diagnosis of a wide range of electromechanical faults.

Keywords—*electric machines, fault diagnosis, wavelet transform, broken bars, eccentricities*

I. INTRODUCTION

Electrical induction machines are of extensive use in many industrial processes. An unexpected fault in these machines can lead to high expenses in terms of time and costs, since most of the times they are critical elements in those processes in which they are involved. Due to this fact, the diagnosis of the possible faults taking place in these devices has become a topic of special interest and concern in the industrial environment [1-2]. The development and optimization of techniques being able to detect the possible failures in an earlier stage have been the motivation of many works during these last few years.

Statistical studies [1] on the occurrence of electromechanical faults in asynchronous machines show a significant percentage of faulty events related to the rotor, such as rotor bar breakages and various modalities of eccentricities; they have been deeply analyzed in the literature due to their particular hazard caused by the progressive

propagation or the possibility of rotor to stator rub [3-5].

Most of these faults lead to some effects in the different electromechanical quantities of the machine (currents, vibrations, fluxes, torque...) which may help to diagnose the presence of the corresponding failure. Indeed, some studies have investigated the effect that each particular fault provokes on the different electrical quantities, trying to obtain the most suitable for diagnosing the presence of each failure, according to its sensitivity, non-invasive nature and other criteria.

In the industrial environment, the most common approach for the diagnosis of most of the faults (for instance, rotor asymmetries or different types of eccentricities) is based on the analysis of the current demanded by the machine; this is a quantity easy to be measured in a non-invasive way, this is, without interference on the usual operation of the machine. The equipment required for capturing the current signal is very simple and also the software needed for its computation.

The classical diagnosis method based on current analysis, is focused on applying the Fourier transform to the current of the machine during its steady-state operation. Under ideal operation and healthy condition, this should be a pure sinusoidal signal, so the Fourier analysis would reveal the presence of a single frequency component at the supply frequency. However, even under healthy condition, this spectrum is usually polluted by other frequencies caused by the slotting, non-ideal winding distribution, perturbations in the operation of the machine, noises, transient oscillations or even rotor imperfections due to the manufacturing process [6-7].

In the case of a faulty machine, for instance a machine with rotor asymmetries or a machine with certain level of eccentricity, some particular frequency components appear in the Fourier spectrum of the steady-state current. Many authors have studied the frequencies amplified by the presence of these faults; these works have led to expressions that have become very common in the industrial environment for diagnosis purposes; for instance, in the case of rotor bar breakages, the main frequencies amplified by the presence of

the fault are given by (1) (with s =slip and f =supply frequency) and they are known as sideband components [4]. These components are shown in Figure 1, corresponding to a loaded machine with two broken bars. Analogue expressions are obtained for the case of static, dynamic or mixed eccentricities.

$$f_s = f \cdot (1 \pm 2 \cdot s) \quad (1)$$

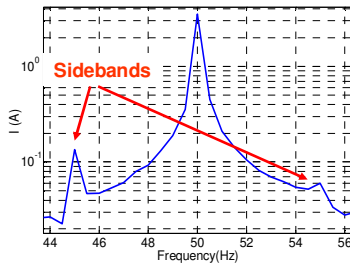


Figure 1. FFT of the steady state current for a loaded machine with two broken bars.

This classical approach based on the steady-state analysis of the current, has some drawbacks reported by several authors [6-7]; for instance, when the machine is unloaded or lightly loaded, the diagnosis of rotor asymmetries or even eccentricities can become specially difficult due to the low value of the slip [6-7], causing that the frequency components used for the diagnosis overlap the frequency of supply (Figure 2(a)). Moreover, other common phenomena such as load fluctuations or voltage oscillations can introduce frequencies very close to those amplified by the previous faults, leading to confusion or even to a wrong diagnosis (Figure 2(b)).

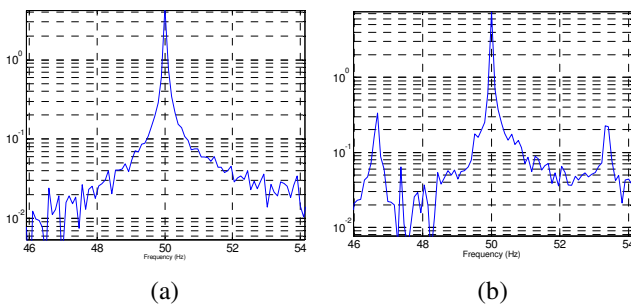


Figure 2. FFT of the steady state current fo: (a) unloaded machine with two broken bars (b) healthy machine with fluctuating load torque .

Due to all these facts, some authors have proposed the study of the transient processes of the machine as an alternative way to obtain additional information which could complement that provided by the steady-state methods. In this context, the study of the current during the connection process of the machine (startup transient) has drawn most of the attention [7-12]. The implicit common basis of these methods is the detection of the evolution during that transient of certain characteristic components created by the corresponding fault.

In this context, a new methodology based on the application of the Discrete Wavelet Transform (DWT) to the startup current, and the subsequent study of the wavelet signals resulting from the transform was proposed recently [8-12]; these signals enable not only the mere detection, but also the extraction of the evolution during the transient of the components created by each fault, arising characteristic patterns that could be used for the reliable diagnosis of the fault. The further automatic recognition of these patterns, using modern image recognition algorithms would enable the on-line diagnosis of the corresponding fault as well as the quantification of the degree of severity.

The aim of this paper is to review the proposed diagnosis methodology, presenting a compilation of different cases. These experimental cases are referred to a 1.1 kW machine operating under various conditions and with different faults. In some of the presented cases, the classical diagnosis method, currently used in the industrial environment and based on the application of the FFT to the steady-state current, is not suitable or leads to a confusing diagnostic. The results show the validity of the method for the reliable diagnosis of the failure. This might lead to the possible future implementation of portable condition monitoring devices based on this methodology.

II. ELECTROMECHANICAL FAULTS DURING THE STARTUP

Two main faults are considered in the paper; broken rotor bars and dynamic eccentricities:

A. Broken Rotor Bars

The presence of broken rotor bars introduces, in the steady-state current spectrum, two sideband components around the supply frequency, with frequencies given by (1). During the startup transient, the slip s changes from 1 to a value very close to 0. As the slip varies, the frequency of the component with negative sign in (1) (left sideband component) also changes; it decreases firstly from a value equal to the supply frequency to 0 Hz and it increases again up to reaching a value very close to the supply frequency [7]. Its amplitude also evolves in a very characteristic way [8]. The extraction of that characteristic transient waveform has revealed as a reliable way for diagnosing the presence of the asymmetry in the machine.

B. Dynamic eccentricities

Some authors [3] have provided a general expression for the frequencies amplified by mixed eccentricities:

$$f_{ecc} = f_1 \left[1 \pm m \left(\frac{1-s}{p} \right) \right] \quad (2)$$

where p = number of pole pairs and $m=1,2,3\dots$

As it was proven in previous works [9], the slip variation during the startup leads to a particular evolution of the frequency components created by the eccentricity. For $m=p/2$, considering $f=50$ Hz, two frequency components with very

characteristic evolutions appear; one of them evolving during the transient from 50 Hz to 25 Hz and the second changing from 50 Hz to 75 Hz [9]. This variation, totally different from that of the broken bars, can be also used for the diagnosis of the eccentricity.

III. DISCRETE WAVELET TRANSFORM

The main idea that underlies the application of the DWT is the dyadic band pass filtering process carried out by this transform. Provided a certain sampled signal $s = (i_1, i_2, \dots, i_N)$, the DWT decomposes it onto several wavelet signals (an approximation signal a_n and n detail signals d_j) [7, 13]. A certain frequency band is associated with each wavelet signal; the wavelet signal reflects the time evolution of the frequency components of the original signal s which are contained within its associated frequency band [7, 14].

More concretely, if f_s (samples/s) is the sampling rate used for capturing s , then the detail d_j contains the information concerning the signal components with frequencies included in the interval:

$$f(d_j) \in [2^{-(j+1)} f_s, 2^{-j} f_s] \text{ Hz.} \quad (3)$$

The approximation signal a_n includes the low frequency components of the signal, belonging to the interval:

$$f(a_n) \in [0, 2^{-(n+1)} f_s] \text{ Hz} \quad (4)$$

Therefore, the DWT carries out the filtering process shown in Figure 1. Note that the filtering is not ideal, a fact leading to a certain overlap between adjacent frequency bands [7, 12, 15]. This causes some distortion if a certain frequency component of the signal is close to the limit of a band.

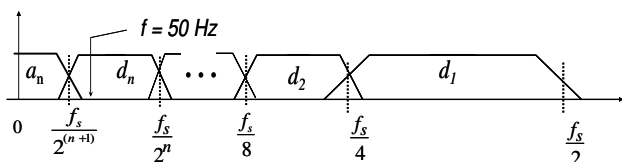


Figure 3. Filtering process performed by the DWT.

Due to the automatic filtering performed by the wavelet transform, the tool provides a very attractive flexibility for the simultaneous analysis of the transient evolution of rather different frequency components present in the same signal. At the same time, in comparison with other tools, the computational requirements are low. In addition, the DWT is available in standard commercial software packages, so no special or complex algorithm is required for its application.

IV. EXPERIMENTAL RESULTS

In this section the presented methodology is applied to the diagnosis of several machines under different fault and operation conditions. The tests were performed in the laboratory, using commercial cage motors with 4 poles, 28 rotor bars, rated 1.1 kW, 400V, 50 Hz, coupled to two different DC machines acting as loads (load 1 (direct coupling) and load 2 (coupling through straps)). Figure 4(a) shows the motor under test.

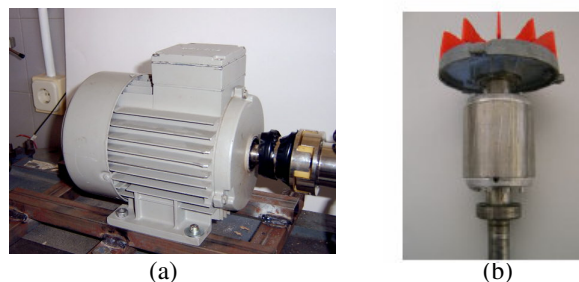


Figure 4. (a) 1.1 kW motor under test (b) Rotor with one broken bar.

A phase current was used as diagnostic signal; this current was captured using a 15/5, class 0.5 current transformer and a 1A, 60 mV shunt; the resulting voltage signal was captured by means a digital oscilloscope with a sampling frequency $f_s = 5000$ samples/s, and finally transferred to a PC for the analyses. The standard MATLAB Wavelet Toolbox was used for performing the DWT of the signals; Daubechies-44 was selected as mother wavelet. Figures in the next sections show the wavelet signals resulting from the transform, as well as their associated frequency bands.

A. Unloaded healthy machine

Figure 5 shows the DWT of the startup current for the healthy motor coupled to load 1. The wavelet signals resulting from the analysis (approximation and detail signals) do not show any significant oscillations once the electromagnetic transient, occurring at the beginning of the startup in every machine, is finished. This shows the absence of any fault component, confirming the healthy condition of the machine.

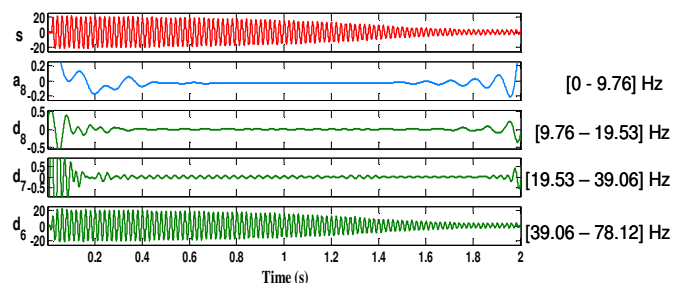


Figure 5. 8-level DWT of the startup current for the unloaded healthy machine.

B. Unloaded machine with one broken bar

A bar breakage was artificially forced in the laboratory, by drilling a hole in the selected rotor bar. Figure 4 (b) shows the rotor after the breakage. Figure 6 shows the application of the DWT for the case of a machine with 1 broken bar and coupled to load 1. Clear oscillations appear in the wavelet signals resulting from the analysis. Moreover, they are arranged in such a way that they reflect the evolution of the left sideband component created by the breakage (first decreasing from the supply frequency towards 0 Hz and later increasing towards the supply frequency again).

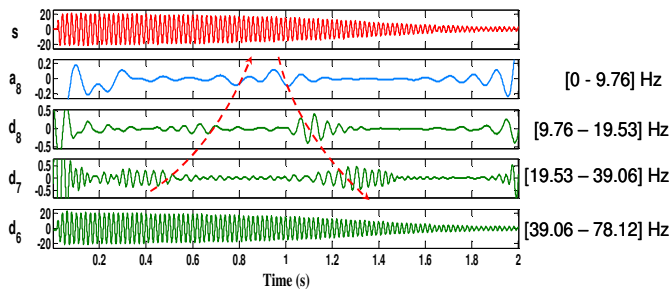


Figure 6. 8-level DWT of the startup current for the unloaded machine with one broken bar.

If the classical diagnosis methodology, based on the FFT of the steady-state current, is applied in this case the diagnosis conclusion could not be reached. This is due to the fact that the machine is unloaded and, therefore, the slip s is very low, so the sideband components given by (1) overlap the supply frequency. This is shown in Figure 7, where the sidebands are not detectable due to this fact.

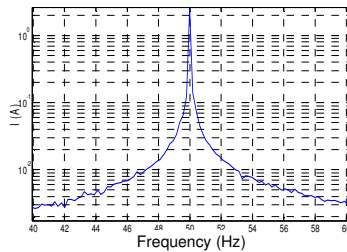


Figure 7. FFT of the steady state current for the unloaded machine with one broken bar.

C. Unloaded machine with two broken bars

Figure 8 shows the application of the diagnosis methodology to an unloaded machine with two broken bars and coupled to load 1. The conclusion is similar to that of the previous case; the characteristic pattern caused by the evolution of the left sideband is clear in the wavelet signals resulting from the DWT. Moreover, the oscillations within the signals a_8 , d_8 and d_7 have higher amplitudes, due to the higher degree of severity of the fault, in comparison with the previous case. This indicates the possibility of introducing parameters for quantifying the degree of severity of the fault based on the energy of the wavelet signals.

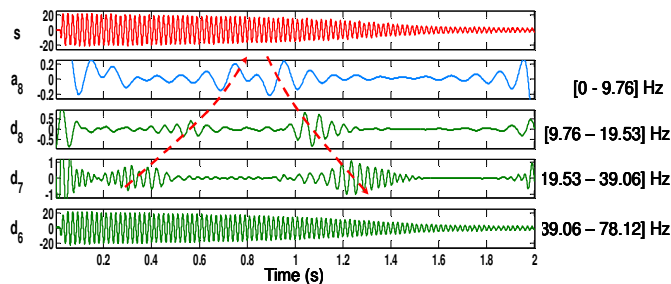


Figure 8. 8-level DWT of the startup current for the unloaded machine with two broken bars.

D. Unloaded machine started through soft-starter.

This test was carried out using the unloaded machine with one broken bar, coupled to load 2 and started by means of a soft starter. The soft starter controls the voltage supplied to the motor during the startup, increasing it progressively during the transient. This starting method is also common in the industrial environment. Figure 9 shows schematically the test-bed for the experiment.

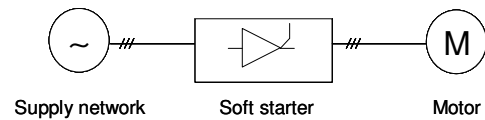


Figure 9. Simplified scheme for the test.

Figure 10 shows the DWT analysis of the startup current for this case. The characteristic pattern caused by the evolution of the left sideband appears clearly, confirming also the validity of the approach in this situation.

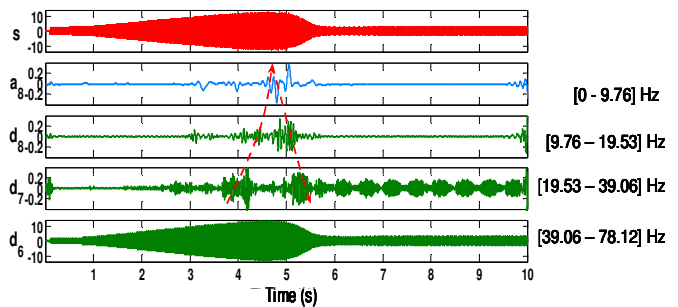


Figure 10. 8-level DWT of the startup current for the unloaded machine with one broken bar started through soft-starter.

E. Machine with mixed eccentricity

Figure 11 shows the application of the methodology for a machine with mixed eccentricity, considering now 6 decomposition levels. The evolution of the aforementioned fault components is clearly noticed; there is one component whose frequency evolves from 50 Hz to 25 Hz during the transient and a second one evolving from 50 Hz to 75 Hz. Therefore, a characteristic pattern really different from that associated with the bar breakage arises.

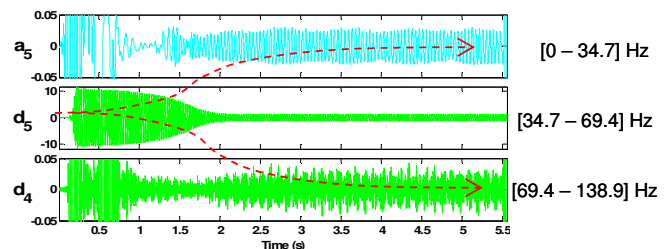


Figure 11. 6-level DWT of the startup current for the machine with mixed eccentricity.

V. INTRODUCTION OF QUANTIFICATION PARAMETERS

Once the condition of the machine has been preliminarily diagnosed, using the qualitative identification of characteristic patterns, it is necessary to compute the quantification parameter defined for the corresponding fault, in order to quantify the degree of failure in the machine.

In the case of rotor asymmetries, a quantification parameter γ_{asym} was defined in previous works [16]. It was based on the energy of the wavelet signal with the next level higher than the signal containing the fundamental. This parameter is given by (5).

$$\gamma_{asym}(dB) = 10 \cdot \log \left[\frac{\sum_{j=N_b}^{N_s} i_j^2}{\sum_{j=N_b}^{N_s} [d_{nf+1}(j)]^2} \right] \quad (5)$$

where i_j is the value of the j th sample of the startup current signal $i(t)$; $d_{nf+1}(j)$ is the j element of the detail with level $nf+1$ (nf =level of the signal containing the fundamental); N_s is the number of samples of the signal, until reaching the steady-state and N_b is the number of samples between the origin of the signals and the extinction of the oscillations due to border effect.

According to the experience achieved by tests carried out in motors with this range of powers (few kW), a value for γ_{asym} higher than 40 dB is indicative of a healthy condition in the machine. Values between 30 dB and 40 dB mean that a partial breakage or one broken bar is present in the machine. Values around 30 dB or lower are usually obtained when at least two bars are broken.

Table I shows the results obtained when computing this indicator for different cases tested, as well as the deviations with respect the healthy condition for each machine. The values obtained confirm the ranges commented above.

In the case of mixed eccentricities, a quantification parameter γ_{mecc} could be also defined, based on the energy of the approximation signal with the next level higher than that containing the fundamental component. This parameter would be according to (6).

$$\gamma_{mecc}(dB) = 10 \cdot \log \left[\frac{\sum_{j=N_b}^{N_s} i_j^2}{\sum_{j=N_b}^{N_s} [a_n(j)]^2} \right] \quad (6)$$

where i_j is the value of the j sample of the current signal; $a_n(j)$ is the j element of the order n approximation signal; N_s is the number of samples of the signal, after finishing the first 10 cycles in the steady-state regime and N_b is the number of samples between the origin of the signals and the extinction of the oscillations due to border effect.

Machine	Condition	γ_{asym}	$\Delta\gamma_{asym}$
1.1 kW motor coupled to load 1	Healthy	47.1	-
1.1 kW motor coupled to load 1	1 broken bar, unloaded	37	-10.1
1.1 kW motor coupled to load 1	1 broken bar, 80% load	36.2	-10.9
1.1 kW motor coupled to load 1	1 broken bar, full-load	35.2	-11.9
1.1 kW motor coupled to load 1	2 broken bars, unloaded	30.6	-16.5
1.1 kW motor coupled to load 1	2 broken bars, 60% load	30.0	-17.1
1.1 kW motor coupled to load 1	2 broken bars, full load	30.1	-17
1.1 kW motor coupled to load 2	Healthy	44.4	-
1.1 kW motor coupled to load 2	1 broken bar, unloaded	35.6	-8.8
1.1 kW motor coupled to load 2	1 broken bar, 80% load	35.4	-9
1.1 kW motor coupled to load 2	1 broken bar, full-load	35.1	-9.3
1.1 kW motor coupled to load 2	2 broken bars, unloaded	30.7	-13.7
1.1 kW motor coupled to load 2	2 broken bars, full load	31.8	-12.6

VI. ADDITIONAL CONSIDERATIONS FOR THE APPLICATION OF THE METHOD

The different experiments performed showed the suitability of the method for the diagnosis of electromechanical faults introducing slip-dependant components. Nevertheless, additional considerations need to be done regarding the different parameters of the DWT decomposition, such as the type of mother wavelet, the order of the mother wavelet or the number of decomposition levels.

With regards to the type of mother wavelet, the Daubechies family was well suited for the application of this method, due to its inherent properties, although other families (symlet, biorthogonal, Gaussian, and specially dmeyer) also enable a clear detection of the patterns, despite their different mathematical characteristics. As an example, Figures 12 (a) and (b) show the application of the method for the case of unloaded machine with one broken bar and coupled to load 2, using symlet-30 and dmeyer, respectively. The similarities between both figures are obvious, appearing the characteristic pattern caused by the sideband.

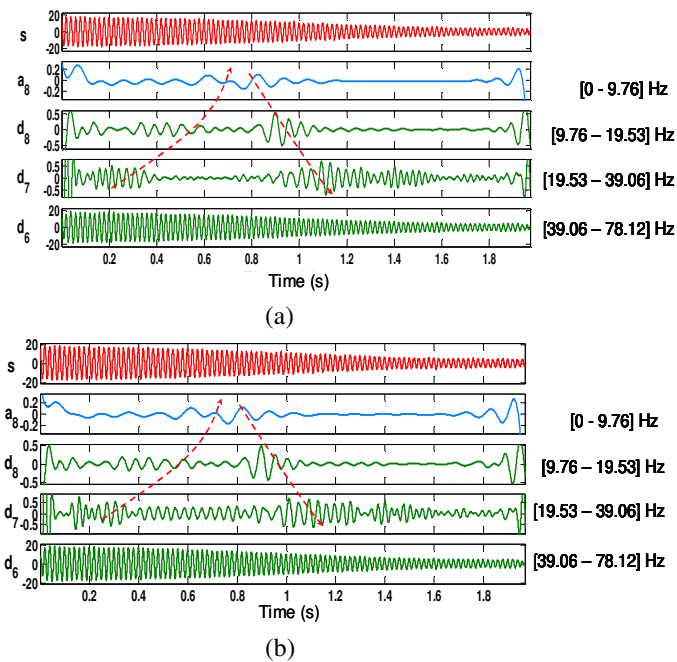


Figure 12. 8-level DWT of the startup current for the unloaded machine with one broken bar using: (a) symlet-30, (b) dmeyer.

When using the Daubechies family, an important fact observed was the overlapping between the frequency bands associated with successive wavelet signals resulting from the DWT of the current. This is due to the fact that the wavelet signals act as non-ideal filters, extracting the components of the signal included within a certain frequency band that can overlap partially with the adjacent band [7, 15]. In this sense, it was observed that, when using a high-order Daubechies wavelet for signal decomposition, the overlapping was smaller than when using a low-order one. In other words, high-order wavelets behave as more ideal filters, a fact that helps to avoid partially the overlapping between frequency bands.

Finally, the number of decomposition levels (n_d) is related to the sampling frequency of the signal being analysed (f_s). This parameter has to be chosen in such a way that the DWT supplies at least three high-level signals (two details and an approximation) with frequency bands below the supply frequency f ; this condition implies:

$$n_d \geq n_f + 2 \quad , \quad (7)$$

being n_f the level of the detail which contains the supply frequency, that can be calculated using (8).

$$2^{-(n_d+1)} \cdot f_s < f \quad (8)$$

This condition means that the lower limit of the frequency band of the n_f level detail is lower than the supply frequency.

Thus:

$$n_d > \frac{\log(f_s / f)}{\log(2)} + 1 \quad (\text{integer}) \quad (9)$$

VII. CONCLUSIONS

A diagnosis methodology is presented in this paper to diagnose the presence of electromechanical faults in electrical machines. It is based on the application of the DWT to the stator startup current and the further recognition of characteristic patterns created by each fault.

Several faulty cases are presented in the paper, all them confirming the validity of the approach, even in some cases in which the classical methodology, currently used in the industrial environment, might not lead to correct results.

The method admits the quantification of the degree of failure using parameters based on the energy of the wavelet signals resulting from the analysis.

Further step would be the application of image recognition algorithms for the automatic identification of these characteristic patterns, which could be the basis of the implementation of portable diagnosis devices.

ACKNOWLEDGMENT

The authors thank 'Vicerrectorado de Investigación, Desarrollo e Innovación de Universidad Politécnica de Valencia' for financing a part of this research through the program 'Programa de Apoyo a la Investigación y Desarrollo (PAID-06-07).

REFERENCES

- [1] W.T. Thomson, M. Fenger, "Current signature analysis to detect induction motor faults" IEEE Industry Applications Magazine, July/August 2001, pp. 26-34.
- [2] D.B.Durocher, G.R. Feldmeier, "Predictive versus preventive maintenance" IEEE Industry Applications Magazine, Vol. 10, No.5, October 2004, pp. 12-21.
- [3] M. H. Benbouzid, "A review of induction motors signature analysis as a medium for faults detection" IEEE Transactions on Industrial Electronics, Vol. 47, No. 5, October 2000.
- [4] G.B Kliman, J Stein, and R.D. Endicott, "Noninvasive Detection of Broken Rotor Bars in Operating Induction Motors," IEEE Transactions on Energy Conversion, vol. 3, no. 4, pp. 873-879, December 1988.
- [5] J.R Cameron et W.T. Thomson and A.B. Dow, "Vibration and current monitoring for detecting airgap eccentricity in large induction motors," IEE Proceedings, vol. 133, pt. B, no. 3, May 1986, pp. 155-163.
- [6] R.R. Schoen and T.G. Habetler. "Evaluation and Implementation of a System to Eliminate Arbitrary Load Effects in Current-Based Monitoring of Induction Machines," IEEE Transactions on Industry Applications, Vol. 33, No. 6, November/December 1997, pp. 1571-1577.
- [7] J.A. Antonino-Daviu, M.Riera-Guasp, J.Roger-Folch and M.P. Molina, "Validation of a New Method for the Diagnosis of Rotor Bar Failures via Wavelet Transform in Industrial Induction Machines". IEEE Transactions on Industry Applications, vol. 42, no. 4, July/August 2006, pp.990-996.
- [8] M. Riera-Guasp, J. Antonino-Daviu, J. Roger-Folch and M.P. Molina, "The Use of the Wavelet Approximation Signal as a Tool for the Diagnosis and Quantification of Rotor Bar Failures," IEEE Transactions on Industry Applications (In press).
- [9] J. Antonino-Daviu, P. Jover, M. Riera-Guasp, J. Roger-Folch and A. Arkkio, "DWT Analysis of Numerical and Experimental Data for the Diagnosis of Dynamic Eccentricities in Induction Motors", Mechanical Systems and Signal Processing, Elsevier, Vol. 21, No. 6, August 2007,

pp. 2575-2589.

- [10] H. Douglas, P. Pillay and A. Ziarani, "Broken rotor bar detection in induction machines with transient operating speeds", IEEE Transactions on Energy Conversion, Vol. 20, No.1, March 2005, pp.135-141.
- [11] Z. Zhang and Z. Ren, "A novel detection method of motor broken rotor bars based on wavelet ridge," IEEE Transactions on Energy Conversion, Vol. 18, No. 3, September 2003, pp. 417-423.
- [12] J. Antonino-Daviu, M. Riera-Guasp, J. Roger-Folch, F. Martínez-Giménez, A. Peris, "Application and Optimization of the Discrete Wavelet Transform for the Detection of Broken Rotor Bars in Induction Machines". Applied and Computational Harmonic Analysis, Elsevier, Vol. 21, September 2006, pp. 268-279.
- [13] C.S. Burrus, R.A. Gopinath and H. Guo, Introduction to Wavelets and Wavelet Transforms. A primer, Prentice Hall, 1998.
- [14] R.Polikar, 'The wavelet tutorial'
<http://engineering.rowan.edu/~polikar/WAVELETS/WTtutorial.html>
- [15] T. Tarasiuk, "Hybrid wavelet-Fourier Spectrum Analysis," IEEE Transactions on Power Delivery, vol. 19, no. 3, pp. 957-964, July 2004.
- [16] M. Riera, J. A. Antonino, J. Roger-Folch, and M.P. Molina, "Definition of DWT-based parameters for the quantification of rotor bar breakages in industrial induction machines", Proc. XII Internacional Symposium on Electromagnetic Fields in Mechatronics, Electrical and Electronic Engineering, ISEF 2005, Baiona, Spain, September 17-19, 2005.



Jose. A. Antonino-Daviu received the M.Sc. degree in Electrical Engineering from the Polytechnic University of Valencia in 2000 and the Ph.D. degree in Electrical Engineering in 2006. He worked in the private sector, being involved in several international projects. Currently, he is Associate Professor in the School of Industrial Engineering of the mentioned University, where he develops his docent and research work. His primary research interests are condition monitoring of electric machine, wavelet theory and its application to fault diagnosis and design and optimization of electrical installations and systems.



M. Riera-Guasp received the M.Sc. degree in Industrial Engineering and the Ph.D. degree in Electrical Engineering from the Universidad Politecnica de Valencia (Spain) in 1981 and 1987, respectively. Currently he is an Associate Professor in the Department of Electrical Engineering of the Polytechnic University of Valencia. His research interests include condition monitoring of electrical machines, applications of the Wavelet Theory to electrical engineering and efficiency in electric power applications.



M. Pineda-Sanchez was born in 1962 in Albacete (Spain). He received his Dipl. Ing. and Dr. Ing. degrees in electrical engineering from the Universidad Politécnica de Valencia (Spain) in 1985 and 2004, respectively. He joined the faculty of the Universidad Politécnica de Valencia in 1987 as Professor in the Department of Electrical Engineering, in the area of theory and control of electrical machines. His interests include electrical machines and drives, numerical simulation of electromagnetic fields and software development.



Joan Pons Llinares received the M.Sc. degree in Industrial Engineering (Electrical Speciality) from the Universitat Politècnica de València (UPV, Spain) in 2007. In 2005, he started working as a researcher in the Department of Electrical Engineering of the UPV. At first, he worked in the domain of Distribution losses. He did some research works about Overvoltages and Space Phasors too and had a short time period work in the private sector. After obtaining the M.Sc. degree, he focused his research interests in the Wavelet Theory and its applications to fault diagnosis of electrical machines. He is currently pursuing the Ph.D. degree.



Ruben Puche-Panadero obtained his MSc. in Automatic and Electronic Engineering in 2003 from the Universidad Politécnica de Valencia. From 2003 to 2006 he worked in a Innovate European Project of Automation as Developer of Plc's Program, Scada, Panels, etc. Since 2006 he joined the Universidad Politécnica de Valencia and he is currently Professor of Machines Control. His research interests focus in induction motor diagnostics and maintenance, numerical modeling and automation of industrial installations.

Networks of Mixed Canonic-Dissipative Systems and Dynamic Hebbian Learning

Julio Rodriguez

École Polytechnique Fédérale de Lausanne
STI / IMT / LPM1
Lausanne 1015
Switzerland
Email: julio.rodriguez@epfl.ch

Max-Olivier Hongler

École Polytechnique Fédérale de Lausanne
STI / IMT / LPM1
Lausanne 1015
Switzerland
Email: max.hongler@epfl.ch

Abstract— We consider a collection $\{\mathcal{O}_k\}_{k=1}^N$ of interacting parametric mixed canonical-dissipative systems, (MCD). Each individual \mathcal{O}_k , exhibits, in absence of interaction, a limit cycle \mathcal{L}_k on which the orbit circulation is parameterized by $\omega_k(t)$. The underlying network defining the interactions between the \mathcal{O}_k 's is assumed to possess a diffusive Laplacian matrix. For each \mathcal{O}_k , we construct a class of position- and velocity-dependent interactions which lead to a dynamic learning process of the Hebbian type (DHL). More precisely, the interactions affect the circulation parameterization $\omega_k(t)$ and the DHL mechanisms manifests itself by asymptotically driving the system towards a consensual (oscillatory) global state in which all \mathcal{O}_k share a common circulation parameterization ω_c . It is remarkable that for our class of interactions, we are able to analytically calculate ω_c which, in our case, is independent of the topology of the connecting network. However, the coupling network topology explicitly controls the relaxation rate via the spectral gap of the underlying adjacency matrix (i.e. the so called *Fiedler number* of the associated graph). Finally, we report several numerical illustrations which enable to observe the DHL mechanisms at work and confirm our theoretical assertions.

Keywords— mixed canonic-dissipative systems, limit cycles oscillators, dynamic Hebbian learning, consensual states, diffusive coupling, Laplacian matrix, algebraic connectivity.

I. INTRODUCTION

In a recent paper [1], L. Righetti et al. show how to implement what they call a Dynamic Hebbian Learning (DHL) process by coupling nonlinear parametric oscillators with an external time-dependent signal. As a paradigmatic illustration, they consider an non-autonomous parametric Hopf oscillator (HO), defined, in its phase space, by the system of equations:

$$\text{HO} \begin{cases} \dot{x} &= +\omega y + (1 - x^2 - y^2) x + \epsilon \sin(\Omega t), \\ \dot{y} &= -\omega x + (1 - x^2 - y^2) y, \\ \dot{\omega} &= \epsilon \sin(\theta(t)) \sin(\Omega t), \end{cases} \quad (1)$$

where ϵ is a small positive constant, $\sin(\Omega t)$ externally perturbs the basic dynamics of the HO (Ω is a positive constant) and where $\theta(t) := \arctan(\frac{y(t)}{x(t)})$. The DHL process manifests itself by the fact that the circulation parameterization (i.e. here the basic frequency of the underlying HO) $\omega(t)$ does, asymptotically converge, to Ω , the frequency of the external input signal. In other words, the external signal "plastically" deforms the original limit cycle dynamics. We speak about

plasticity to reflect the fact that, once this deformation is realized, it definitely subsists even if the external input is removed. This generic behavior can be qualitatively understood by the fact that the external perturbing signal gradually affects the circulation parameterization ω on the limit cycle \mathcal{L} , (for Eqs.(1), $\mathcal{L} := \{(x, y) \in \mathbb{R}^2 | x^2 + y^2 = 1\}$), but leaves the shape of \mathcal{L} essentially invariant.

The core of the present paper is to substitute in Eqs.(1) the role played by the external signal by the dynamics delivered by other limit cycle oscillators and then, to study the resulting mutual DHL process. More generally, we will consider a collection $\{\mathcal{O}_k\}_{k=1}^N$ of independent mixed canonical-dissipative systems (MCD) as introduced in [2] and [3], which exhibit limit cycles \mathcal{L}_k and different individual $\omega_k(t)$, $k = 1, 2, \dots, N$ on \mathcal{L}_k . The action of dissipative mechanism is to stabilize the orbits on \mathcal{L}_k and the canonic part of the vector field (i.e. its Hamiltonian part) is responsible for the circulation on the limit cycles. In our class of models, the mutual interactions between the \mathcal{O}_k 's are characterized by:

- a) a network \mathcal{N} of diffusively coupled \mathcal{O}_k 's - i.e. the row elements of the associated Laplacian coupling matrix of the network add to zero.
- b) a dynamic Hebbian learning mechanism (DHL). We allow the $\omega_k(t)$ to behave as additional variables and we implement couplings between these variables with the whole dynamics. Qualitatively speaking, the DHL coupling rule essentially affects the circulation parameterization on the limit cycles \mathcal{L}_k while keeping the shape of \mathcal{L}_k approximately unchanged.

The DHL process and the resulting "plasticity" of the dynamics confers a fundamentally different perspective compare to the yet abundantly studied synchronization networks of limit cycle oscillators. Indeed, interactions of the DHL type offer the possibility to drive the dynamics into a global (identical for all \mathcal{O}_k 's), stable oscillatory state which, once reached, remains "frozen" even when the interactions are removed. This final oscillatory behavior shared by all \mathcal{O}_k 's will be called the *consensual oscillatory state*. In this context, a (non-exhaustive) list of natural issues, to be addressed in this paper, will be:

- 1) How to calculate the circulation parameterization $\omega_c(t)$

characterizing the final consensual state ?

2) How does the consensual circulation parameterization depend on the Laplacian matrix associated to network ?

3) How does the network influence the convergence rate towards the the final consensual state?

In this contribution, we propose, in section II, the construction of an analytically soluble class of coupled oscillators with mutual interactions leading to a DHL rule. A paradigmatic illustration of this class of dynamics is thoroughly studied in section III where explicit and fully analytical answers to questions 1) to 3) can be given. Future research perspectives and conclusion will be found in section V.

II. CONSTRUCTION OF A DHL DYNAMICAL NETWORK

The collection $\{\mathcal{O}_k\}_{k=1}^N$ of oscillators will be chosen to belong to the class of mixed canonical-dissipative systems which we briefly expose in II-A.

A. Mixed Canonic-Dissipative systems

A member of our collection $\{\mathcal{O}_k\}_{k=1}^N$ will be defined as:

$$\mathcal{O}_k \begin{cases} \dot{x}_k &= +\omega_k \frac{\partial H_k}{\partial y_k} + g_k(H_k) \frac{\partial H_k}{\partial x_k}, \\ \dot{y}_k &= \underbrace{-\omega_k \frac{\partial H_k}{\partial x_k}}_{\text{conservative evolution}} + \underbrace{g_k(H_k) \frac{\partial H_k}{\partial y_k}}_{\text{dissipative evolution}}, \end{cases} \quad (2)$$

where $H_k : \mathbb{R}^2 \rightarrow \mathbb{R}^+$ and $g_k : \mathbb{R}^+ \rightarrow \mathbb{R}$. The H_k 's functions are C^2 and positive definite and play the role of Hamiltonians (i.e. energy). In the sequel, we shall assume that $H_k(x_k, y_k) = \mathcal{E}_k$ uniquely defines a set of closed (concentric) curves $\mathcal{L}_k(\mathcal{E}_k)$ in \mathbb{R}^2 that surrounds the origin. The g_k 's functions are C^1 and $g_k(H_k(x_k, y_k))$ are non-conservative terms which, according to the value of H_k , feeds or dissipates energy from the Hamiltonian system. In particular, if $g_k(H_k(x_k, y_k))$ vanishes for $H_k(x_k, y_k) = \mathcal{E}_k$, the dynamics is purely conservative (i.e. only the *canonical* part drives the dynamics) and we therefore have:

$$H_k(x_k, y_k) = \mathcal{E}_k \text{ defines the limit cycle } \mathcal{L}_k(\mathcal{E}_k)$$

with

$$\mathcal{L}_k(\mathcal{E}_k) := \{(x, y) \in \mathbb{R}^2 \mid H_k(x, y) = \mathcal{E}_k\}.$$

The stability of the $\mathcal{L}_k(\mathcal{E}_k)$'s will be determined by:

$$\begin{aligned} g_k(H_k) > 0 \text{ in } \mathcal{A}_k & \Rightarrow \mathcal{L}_k(\mathcal{E}_k) \text{ is stable,} \\ g_k(H_k) < 0 \text{ in } \mathbb{R}^2 \setminus \bar{\mathcal{A}}_k & \end{aligned} \quad (3)$$

$$\begin{aligned} g_k(H_k) < 0 \text{ in } \mathcal{A}_k & \Rightarrow \mathcal{L}_k(\mathcal{E}_k) \text{ is unstable,} \\ g_k(H_k) > 0 \text{ in } \mathbb{R}^2 \setminus \bar{\mathcal{A}}_k & \end{aligned}$$

where \mathcal{A}_k stands for the interior of $\mathcal{L}_k(\mathcal{E}_k)$, (i.e. $\mathcal{A}_k := \{(x, y) \in \mathbb{R}^2 \mid H_k(x, y) < \mathcal{E}_k\}$). Therefore, for $g_k(\mathcal{E}_k) = 0$ and when $\mathcal{L}_k(\mathcal{E}_k)$ is stable, the energy-type control $g_k(H_k(x_k, y_k))$ drives all orbits towards the stable limit cycle $\mathcal{L}_k(\mathcal{E}_k)$ which is hence an attractor. The system defined by Eqs.(2) belongs to the general class of mixed canonical-dissipative dynamics

(MCD) (c.f [2], [3] and [4]). In the sequel, we shall make use of the short hand notation:

$$\begin{aligned} P_k(x_k, y_k, \omega_k) &:= +\omega_k \frac{\partial H_k}{\partial y_k}(x_k, y_k) + g_k(H_k(x_k, y_k)) \frac{\partial H_k}{\partial x_k}(x_k, y_k), \\ Q_k(x_k, y_k, \omega_k) &:= -\omega_k \frac{\partial H_k}{\partial x_k}(x_k, y_k) + g_k(H_k(x_k, y_k)) \frac{\partial H_k}{\partial y_k}(x_k, y_k). \end{aligned}$$

Observe that in Eqs.(2), we restrict our study to non-parametric MCD for which ω_k are constant.

Having defined the individual dynamics, it is now time to characterize the interactions.

B. Network of diffusively coupled oscillators

The interactions between the MCD's given by Eqs.(2) will be realized via a simply connected network \mathcal{N} with N edges without loop (i.e. its adjacent matrix A is such that, for the j^{th} edge, $A_{j,j} = 0$, $j = 1, 2, \dots, N$ and $A_{i,j} \in \{0, 1\}$ for $j \neq i$). Let L be the associated Laplacian matrix, namely $L = A - D$, where D is the diagonal matrix with $D_{j,j}$ being the degree of edge j . Accordingly, we now consider the dynamics:

$$\mathcal{O}_k \begin{cases} \dot{x}_k &= P_k(x_k, y_k, \omega_k) + C_k x \\ \dot{y}_k &= \underbrace{Q_k(x_k, y_k, \omega_k)}_{\text{MCD}} + \underbrace{C_k y}_{\text{diffusive coupling}} \end{cases} \quad (4)$$

with $C_k x$ and $C_k y$ reading as:

$$C_k x := \epsilon_1(x, y) \sum_{j=1}^N L_{k,j} x_j \quad \text{and} \quad C_k y := \epsilon_2(x, y) \sum_{j=1}^N L_{k,j} y_j,$$

where $0 \leq \epsilon_l(x, y) < \epsilon$, $l = 1, 2$ not simultaneously vanishing and $x := (x_1, \dots, x_N)$, $y := (y_1, \dots, y_N)$.

Finally, we now introduce the DHL process into the dynamics.

C. Dynamic Hebbian learning for Mixed Canonic-Dissipative systems

Directly inspired from Eqs.(1), we now propose our generalized DHL in the context of Eqs.(4). The dynamical system is given by:

$$\mathcal{O}_k \begin{cases} \dot{x}_k &= P_k(x_k, y_k, \omega_k) + C_k x, \\ \dot{y}_k &= Q_k(x_k, y_k, \omega_k) + C_k y, \\ \dot{\omega}_k &= \underbrace{\mathcal{K}_k [Dy C_k x - Dx C_k y]}_{\text{DHL mechanism}}, \end{cases} \quad (5)$$

where

$$Dy := \eta_1(x, y) \sum_{j=1}^N \frac{\partial H_j}{\partial y_j},$$

$$Dx := \eta_2(x, y) \sum_{j=1}^N \frac{\partial H_j}{\partial x_j}.$$

with $0 \leq \mathcal{K}_k \leq \kappa$ is a set of learning coupling strengths and $0 \leq \eta_l(x, y) \leq \eta$, $l = 1, 2$ are not simultaneously vanishing.

Observe at this point that the dynamics defined by Eqs.(5) exhibit the salient features of the basic model given by Eqs.(1). We namely have:

- when $C_k x = C_k y = 0$ and for appropriate choices of the $g_k(H_k(x_k, y_k))$ terms, (see Eq.(3)), the dynamics exhibits a stable limit cycle \mathcal{L}_k ,
- on the limit cycle \mathcal{L}_k , the dynamics obeys a (conservative) canonical Hamiltonian motion,
- a DHL type mechanism explicitly affects the circulation parameterization $\omega_k(t)$ of the orbits on \mathcal{L}_k .

For simplicity and without lost of generality, in what follows we shall systematically take $\epsilon_1(x, y) = \epsilon_2(x, y) = 1$ and $\eta_1(x, y) = \eta_2(x, y) = 1$ in Eqs.(5).

Proposition 1: Let $K_k > 0$, for all k in the system defined by Eqs. (5). Then:

$$J := \sum_{k=1}^N \frac{\omega_k(t)}{K_k} \quad (6)$$

is a constant of the motion.

Proof:

$$\begin{aligned} \sum_{k=1}^N \frac{\dot{\omega}_k}{K_k} &= \sum_{k=1}^N Dy C_k x - \sum_{k=1}^N Dx C_k y \\ &= Dy \sum_{k=1}^N \sum_{j=1}^N L_{kj} x_j - Dx \sum_{k=1}^N \sum_{j=1}^N L_{kj} y_j \\ &= Dy \sum_{j=1}^N x_j \sum_{k=1}^N L_{kj} - Dx \sum_{j=1}^N y_j \sum_{k=1}^N L_{kj} \\ &= 0. \end{aligned}$$

where the last equality identically vanishes due to the diffusive character of the coupling matrix L . ■

Proposition 2: Assume that we have a collection of identical MCD systems (i.e. $H_k \equiv H$ for all k) admitting, in absence of coupling, the same stable limit cycle $\mathcal{L}_c := \mathcal{L}_k(\mathcal{E}_c)$ for all k (i.e. for a fixed energy level \mathcal{E}_c common to all oscillators, we suppose that $g_k(\mathcal{E}_c) = 0$ for all k). Then, the synchronized orbit given by $\mathcal{S}(t) := (x_s(t), y_s(t), \omega_c, \dots, x_s(t), y_s(t), \omega_c) \in \mathbb{R}^{3N}$, with $\omega_c = \text{constant}$ and with:

$$g(H(x_s(t), y_s(t))) = g(\mathcal{E}_c) = 0, \quad (7)$$

is an exact solution of the dynamical system defined by Eqs.(5).

Proof: For the synchronized orbit, we have $x_k(t) = x_s(t)$, $y_k(t) = y_s(t)$ and $\omega_k(t) = \omega_c(t)$ for all k . The diffusive nature of the coupling, implies that the terms $C_k x = C_k y = 0$ and therefore $\dot{\omega}_k(t) = 0$. Hence, the $\omega_c(t)$ are identically a constant written as ω_c . ■

So far, we have introduced a globally non-conservative dynamical system \mathbb{R}^{3N} given by Eqs.(5) for which an explicit

orbit $\mathcal{S}(t)$ is known. In addition, our dynamics possesses one constant of the motion J given by Eq.(6). One therefore may now question whether the orbit $\mathcal{S}(t)$ corresponds to a stable solution of the globally non-conservative dynamics. As usual, by linearizing the dynamics around $\mathcal{S}(t)$ produces information regarding its stability - this will be explicitly performed in section III for systems with an underlying circular symmetry. At this stage and to make head on, assume that $\mathcal{S}(t)$ is indeed a stable solution of the dynamics given by Eqs.(5) and that we have $\lim_{t \rightarrow \infty} \omega_k(t) = \omega_c$ for all k . Hence, ω_c corresponds to the **consensual circulation parameterization on the common limit cycle \mathcal{L}_c** . In this case, Proposition 1 and 2 provide explicit answers to questions 1) and 2) raised in the introduction. Indeed, Eq.(6) enables us to write:

$$\text{if } \lim_{t \rightarrow \infty} \omega_k(t) = \omega_c \text{ then } \sum_{k=1}^N \frac{\omega_c}{K_k} = \sum_{k=1}^N \frac{\omega_k(0)}{K_k}$$

and therefore, we end with:

$$\omega_c = \frac{\sum_{j=1}^N \frac{\omega_j(0)}{K_j}}{\sum_{j=1}^N \frac{1}{K_j}}. \quad (8)$$

From Eq.(8), we then conclude that the consensual circulation parameterization ω_c **depends on the distribution of initial conditions $\{\omega_k\}$ and on the coupling strength K_k for $k = 1, 2, \dots, N$ but does not depend on the coupling matrix L and therefore not on the topology of the coupling network**. However, we shall see that L directly affects the convergence rate towards the consensual orbit $\mathcal{S}(t)$.

III. NETWORK OF COUPLED HOPF OSCILLATORS

In this section, we focus on the situation where $H_k \equiv H$ for all k and where the underlying Hamiltonian reads as $H(x, y) = H(x^2 + y^2) = H(r^2)$. The circular symmetry implies that the consensual limit cycle \mathcal{L}_c is a circle and the circulation is a uniform rotation with the consensual frequency given by Eq.(8). Due to the cylindrical symmetry, it is advantageous to express the dynamics in polar coordinates:

$$\mathcal{O}_k = \begin{cases} \dot{r}_k &= 2(1 - r_k^2)r_k + \sum_{j=1}^N L_{k,j} \cos(\phi_k - \phi_j) \\ \dot{\phi}_k &= -2\omega_k - \frac{1}{r_k} \left(\sum_{j=1}^N L_{k,j} r_j \sin(\phi_k - \phi_j) \right) \\ \dot{\omega}_k &= K_k \left[\sum_{l=1}^N \left(\sum_{j=1}^N L_{k,j} r_l r_j \sin(\phi_l - \phi_j) \right) \right]. \end{cases} \quad (9)$$

Note that in the non-parametric case (i.e. when $\omega_k(t) = \omega_k$), the phase dynamics in Eqs.(9) coincides with the Kuramoto model in presence of a general coupling network as discussed

in [5]. Here, the exact solution of Eqs. (9) on which perturbations will now be added, simply reads as:

$$\begin{aligned} \mathcal{S}_{pc}(t) &= (r_s(t), \theta_s(t), \omega(t), \dots, r_s(t), \theta_s(t), \omega_s(t)) \\ &= (1, -2\omega_c t, \omega_c, \dots, 1, -2\omega_c t, \omega_c) \in \mathbb{R}^{3N}. \end{aligned} \quad (10)$$

Rearranging the variables in Eqs.(9) by using the permutation $3(k-1) + n \mapsto N(n-1) + k$ ($k = 1, \dots, N$, $n = 1, 2, 3$) and linearizing around $\mathcal{S}_{pc}(t)$ enables us to write:

$$\begin{pmatrix} \dot{\rho} \\ \dot{\delta} \\ \dot{\epsilon} \end{pmatrix} = \begin{pmatrix} L - 4\text{Id} & \mathbb{O} & \mathbb{O} \\ \mathbb{O} & L & -2\text{Id} \\ \mathbb{O} & -2[K]L & \mathbb{O} \end{pmatrix} \begin{pmatrix} \rho \\ \delta \\ \epsilon \end{pmatrix} \quad (11)$$

where Id is the identity matrix, $[K]$ is a diagonal matrix with K_1, K_2, \dots, K_N on the diagonal and where $\rho := (\rho_1, \dots, \rho_N)$, $\delta := (\delta_1, \dots, \delta_N)$ and $\epsilon := (\epsilon_1, \dots, \epsilon_N)$ are perturbations. To fulfill the conservation law given by Eq.(6), we further impose the that:

$$\sum_{j=1}^N \frac{\epsilon_j(0)}{K_j} = 0, \quad (\text{here } K_k \text{ is constant for all } k). \quad (12)$$

To explicitly exhibit the influence of the network, we focus on the case where $K_k := K$ for all k . Since L is symmetric, then there exists an orthogonal matrix V such that $V^T L V$ is a diagonal matrix $[\lambda]$ with its spectrum $\{\lambda_k\}_{k=1}^N$ on the diagonal. The network being connected, there exists a unique j such that λ_j is zero and the rest of the spectrum are all strictly negative. Without loss of generality, we assume $\lambda_1 = 0$. Changing the basis of the system by means of a (3×3) -bloc matrix with V^T on its diagonal, gives us:

$$\begin{pmatrix} \dot{\tilde{\rho}} \\ \dot{\tilde{\delta}} \\ \dot{\tilde{\epsilon}} \end{pmatrix} = \begin{pmatrix} [\lambda] - 4\text{Id} & \mathbb{O} & \mathbb{O} \\ \mathbb{O} & [\lambda] & -2\text{Id} \\ \mathbb{O} & -2K[\lambda] & \mathbb{O} \end{pmatrix} \begin{pmatrix} \tilde{\rho} \\ \tilde{\delta} \\ \tilde{\epsilon} \end{pmatrix}. \quad (13)$$

The upper left $(N \times N)$ -bloc in Eqs.(13) has N real negative eigenvalues and the rest of the system is described by the following (2×2) -blobs:

$$\begin{pmatrix} \dot{\tilde{\delta}}_k \\ \dot{\tilde{\epsilon}}_k \end{pmatrix} = \begin{pmatrix} \lambda_k & -2 \\ -2K\lambda_k & 0 \end{pmatrix} \begin{pmatrix} \tilde{\delta}_k \\ \tilde{\epsilon}_k \end{pmatrix}. \quad (14)$$

For $k = 1$, we have:

$$\dot{\tilde{\delta}}_1 = -2\tilde{\epsilon}_1 \quad \dot{\tilde{\epsilon}}_1 = 0.$$

This is a direct consequence of the conservation law Eq.(6) and on the restriction imposed by Eq.(12). For $k \neq 1$, the eigenvalues of the System 14 are:

$$\alpha_{\pm} = \frac{1}{2}\lambda_k \pm \frac{1}{2}\sqrt{\lambda_k^2 + 16K\lambda_k} < 0.$$

For a simple, connected graph, the spectrum $\{\lambda_k\}_{k=1}^N$ is negatively defined (c.f. [6]) which ensures an (exponential) asymptotic convergence to the consensual state. More precisely, we have a stable focus for $\lambda_k \in] -16K, 0[$ and a

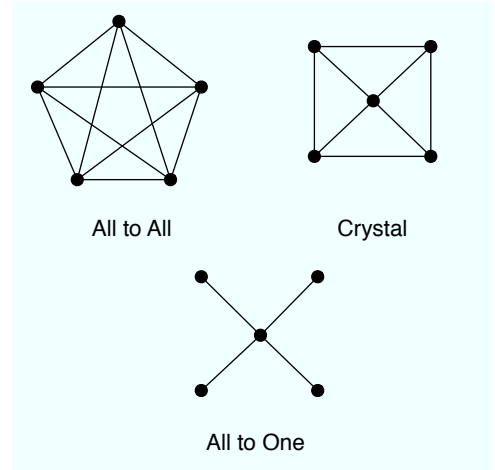


Fig. 1. Three types of network topologies with respective Fiedler number $\mathcal{F}_{(\cdot)}$: “All to All” ($\mathcal{F}_{\text{AtA}} = -5$), “Crystal” ($\mathcal{F}_{\text{Cry}} = -3$) and “All to One” ($\mathcal{F}_{\text{AtO}} = -1$).

stable node for $\lambda_k \in] -\infty, -16K[$. The relaxation time is given by $\tau_{relax} = \mathcal{F}^{-1}$ where \mathcal{F} is the algebraic connectivity (i.e. the Fiedler number - c.f. [7]) of the coupling network. Remember that \mathcal{F} is the largest, non-vanishing, eigenvalue of the associated Laplacian matrix.

IV. NUMERICAL SIMULATIONS

In Figures 2, 3 and 4, we report numerical simulations performed with five Hopf oscillators defined when $H(x, y) = x^2 + y^2$ and $g(H) = 1 - H$. Three different topologies of the interaction network are considered: “All to All”, “Crystal” and “All to One” (c.f. Figure 1).

The learning mechanism can be observed in Figures 2, 3 and 4 and the final consensual frequency is given by Eq.(6). All three figures have the same time scale so that we can fully appreciate the fact that the convergence rates $\rho_{(\cdot)}$ clearly obey:

$$\mathcal{F}_{\text{AtA}} < \mathcal{F}_{\text{Cry}} < \mathcal{F}_{\text{AtO}} \Rightarrow \rho_{\text{AtA}} > \rho_{\text{Cry}} > \rho_{\text{AtO}}.$$

The smaller the Fiedler number, the faster the convergence and thus, the convergence rate does explicitly depend on the topology of the network.

V. CONCLUSIONS AND PERSPECTIVES

Among the numerous possibilities of implementing the DHL learning rule, networks of limit cycle oscillators with adapting frequencies offer a yet unexplored research topics with potential for applications. In this note, we are able to explicitly appreciate the interplay between the DHL learning rule on one hand and the connectivity of the underlying interaction network on the other hand. In particular, the possibility to analytically calculate the consensual circulation parameterization (c.f. Eq.(6)) characterizing the circulation of the final common attractor and the observation that the the topology of the network participate only to the convergence rate are truly remarkable features. At this preliminary stage, we do not yet offer a complete and mathematically rigorous treatment of the rich underlying dynamics.

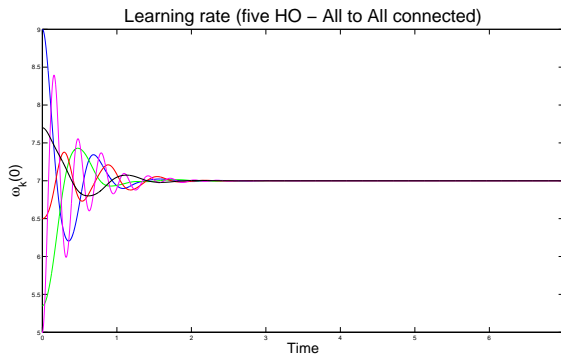


Fig. 2. Time evolution of the circulation parameterization for $\omega_k(t)$ for five Hopf oscillators with $K_1 = 1$, $K_2 = \frac{1}{2}$, $K_3 = \frac{5}{4}$, $K_4 = 5$, $K_5 = \frac{1}{3}$, $\omega_1(0) = 9$, $\omega_2(0) = 5.35$, $\omega_3(0) = 6.5$, $\omega_4(0) = 5$, $\omega_5(0) = 7.7$ and with the network topology “All to All”. The consensual frequency, given by Eq.(8), is here $\omega_c = 7$.

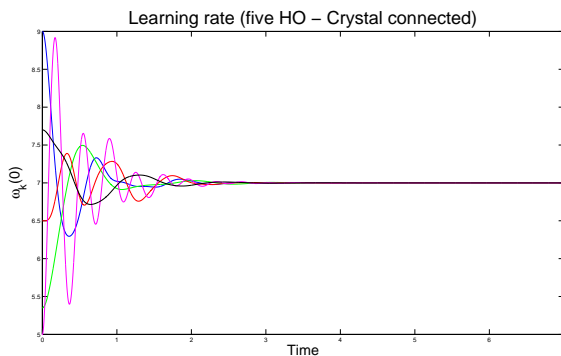


Fig. 3. Time evolution of the circulation parameterization for $\omega_k(t)$ for five Hopf oscillators with $K_1 = 1$, $K_2 = \frac{1}{2}$, $K_3 = \frac{5}{4}$, $K_4 = 5$, $K_5 = \frac{1}{3}$, $\omega_1(0) = 9$, $\omega_2(0) = 5.35$, $\omega_3(0) = 6.5$, $\omega_4(0) = 5$, $\omega_5(0) = 7.7$ and with the network topology “Crystal”. The consensual frequency, given by Eq.(8), is here $\omega_c = 7$.

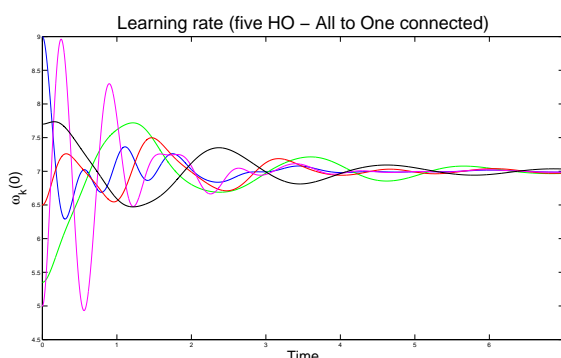


Fig. 4. Time evolution of the circulation parameterization for $\omega_k(t)$ for five Hopf oscillators with $K_1 = 1$, $K_2 = \frac{1}{2}$, $K_3 = \frac{5}{4}$, $K_4 = 5$, $K_5 = \frac{1}{3}$, $\omega_1(0) = 9$, $\omega_2(0) = 5.35$, $\omega_3(0) = 6.5$, $\omega_4(0) = 5$, $\omega_5(0) = 7.7$ and with the network topology “All to One”. The consensual frequency, given by Eq.(8), is here $\omega_c = 7$.

Several open questions among which the characterization of the basin of attraction \mathcal{B} of the consensual state, by constructing ad hoc Lyapunov functions, remain to be discussed. In particular, the dependence of \mathcal{B} on the set of coupling parameters $\{K_k\}_{k=1}^N$ and for coupling networks which can be modeled by multi-edge graphs remain yet to be unveiled.

ACKNOWLEDGMENT

The authors thank Ludovic Righetti for numerous and fruitful discussions shared during the elaboration of this work.

REFERENCES

- [1] L. Righetti, J. Buchli, and A. Ijspeert, “Dynamic hebbian learning in adaptive frequency oscillators,” *Physica D*, vol. 216, pp. 269–281, 2006.
- [2] M.-O. Hongler and D. Rytter, “Hard mode stationary states generated by fluctuations,” *Zeitschrift für Physik B*, vol. 31, pp. 333–337, 1978.
- [3] F. Schweitzer, W. Ebeling, and B. Tilch, “Statistical mechanics of canonical-dissipative systems and applications to swarm dynamics,” *Physical Review E*, vol. 64, pp. 211 101–211 112, 2001.
- [4] F. Schweitzer, *Brownian Agents and Active Particles*. Berlin, Germany: Springer, 2003.
- [5] A. Jadbabaie, N. Motee, and M. Barahone, “On the stability of the kuramoto model of coupled nonlinear oscillators,” in *Proc. of the American Control Conference*, Boston, U.S.A., June 2004, pp. 4296–4301.
- [6] J. L. Gross and J. Yellen, *Handbook of Graph Theory*. Florida, U.S.A.: CRC Press LLC, 2004.
- [7] R. Olfati-Saber and R. M. Murray, “Consensus problems in networks of agents with switching topology and time-delays,” *IEEE Trans. Automat. Contr.*, vol. 49, pp. 1520–1533, Sept. 2004.



Julio Rodriguez is a Ph.D. Student at the Ecole Polytechnique Fédérale de Lausanne (EPFL), Switzerland. He received his Master in Mathematics in 2007 at Geneva University. After one year of teaching assistant at the Section of Mathematics, Geneva University, he joined the doctoral school of Manufacturing Systems and Robotics and started his Ph.D., centered on nonlinear dynamical systems and stochastic processes. In particular, his current research activities focus on assemblies of coupled nonlinear oscillators, synchronization and learning

behaviors as well as collective motion of self-propelled agents.



Max-Olivier Hongler is Adjunct Professor at the Ecole Polytechnique Fédérale de Lausanne (EPFL), Switzerland. His basic education (at the Universities of Geneva, Switzerland, and Bristol, United Kingdom) is in theoretical physics, a domain in which he obtained a PhD degree from the University of Geneva in 1981 for his studies of non-linear stochastic models in off-equilibrium statistical physics. He then occupied research positions at the University of Texas, Austin, at the University of Toronto and at the University of Lisbon, Portugal. He was Invited Professor in theoretical physics at the University of Bielefeld, Germany, in 1992-1993. His main research interests include applied stochastic processes, optimal control and non-linear dynamics. At the EPFL, he teaches lectures in non-linear vibrations, in analytical dynamics, in supply-chains modeling and in stochastic models of manufacturing systems. He is Director of the Doctoral Program in Production and Robotics at the EPFL and Associate Editor of the IEEE Transactions on Industrial Informatics.

About a New Kind of Autonomous, Self-adapting Agents and the Library Game Environment

Herwig Unger, Daniel Berg
Fakultät für Mathematik und Informatik
Lehrgebiet Kommunikationsnetze
58084 Hagen, Germany
kn.wissenschaftler@fernuni-hagen.de

Self adapting agents with local knowledge should be able to manage global resources in dynamic networks automatically. In this paper the library game is introduced – a simulation which uses the metaphor of migrating libraries that try to find paths through the network in such a way, that the satisfaction of all book-consumers reaches a maximum.

Keywords—self-adaption; learning; agent; Library Game

I. MOTIVATION

Computer networks of big companies today become more and more complex, i.e. not only the number of machines is growing but also the number of connected networks as well as the specialization of the machines within the network (which may be equipped with special hard- or software). Furthermore, the dynamics of cooperation in more and more complex development processes result in a permanent change of user groups accessing and changing data and programs on the servers in the system. In such a manner the task of system administrators becomes an extremely tedious one, since a lot of different requests must be considered. Since no single administrator may oversee the huge amount of factors influencing the system behaviour and also do not have access to configure all the several networks in a respective manner, the system behaviour will be less and less an optimal one. The purpose of the present contribution is to consider a new kind of autonomous and self adapting agents, which are able to make automatic decisions on which machine in a complex system which data shall be stored. Differing to existing works, less theoretical aspects but more applicability is in the foreground of our consideration. With our agents we intend to model a multicriterial decision process, taking user behaviour as well as network parameters and economic influences into account. In order to present our approach in a well defined analyzable environment, we first abstract from real networks and setup a similar environment for our considerations: the so called library game environment, which shall also demonstrate similarities in the solution of problems from different areas like computer networks, traffic organization or tasks derived from a financial and economic background. Then we briefly introduce a new kind of an autonomous, self adapting agent which is able to extract complex behavior in a process similar to human abstraction. The agents can choose

from a small set of basic, atomic actions and combine them within a learning- and adaption process to achieve a more complex behaviour in order to increase its satisfaction which is a measure for its success. The last sections of the present contribution describe our simulation setup and the results. In these simulations we address mostly the task where data shall be located to and when it is worth to migrate them to which other places in a complex network. Future work will discuss more detailed possibilities also to learn pricing strategies and the impact of combinations of different influencing factors.

II. THE LIBRARY GAME SETUP

Following our outline, the library game environment shall be introduced more formally at first. We consider a set of players P , consisting of 2 groups, server or service provider (in our case libraries) S and Customers C . Therefore $P = S \cup C$ and furthermore let us assume for the moment that $S \cap C = \emptyset$, i.e. each player is either a service provider (library) or customer. In detail the set of service providers will be defined by the ordered set $S = \{s_i | i = 1(1)n\}$, the set of customers by $C = \{c_j | j = 1(1)m\}$ respectively. To simplify the problem, we assume that the game is played in a (geographic) neighborhood, where any 2 players $p_i, p_j \in P$ have a distance given by $d(p_i, p_j)$ with $d \in \mathbb{R}$.

Each player may have some parameters and attributes. In detail we need functions to obtain:

1. $B(p_i)$: the current budget of p_i
2. $I(p_i)$: any fixed payments, costs (-) or income (+) of p_i per time unit
3. $N(p_i)$: a request function for services of p_i in each time unit and finally
4. $F(p_i)$: the current service fee of p_i per service unit for any customer.

It is clear that these values have some special cases, for the moment we can easily see that $I(c_i) \geq 0, I(s_i) \leq 0, N(s_i) = 0$ and $F(c_i) = 0$.

The request $N(c_i) \forall c_i \in C$ is a fixed (over all customers power-law) distributed function, determining how many goods

(books) a customer wants to obtain from any library per time unit (e.g. per month). Consequently, a respective satisfaction σ for all $c_i \in C$ can be defined by

$$\sigma(c_i) = \frac{G(c_i)}{N(c_i)}$$

where $G(c_i)$ is the number of books which c_i with its current budget $B(c_i)$ really could rent from a library in this time unit. It is clear that every customer strives to increase its satisfaction until 1.

To define the library fully, some more rules are needed as follows.

1. Each customer $c_i \in C$ must pay for the transport of goods from and to the libraries; these costs are proportional to the distance. The costs for the transport are $const_1 * d(c_i, s_j)$.
2. The goal of customers is to increase their satisfaction.
3. The goal of libraries is to survive. A library survives, if its budget $B(s_j)$ is $const_2$ months not lower than zero.

Consequently, each customer c_i will rent books at the cheapest location, whereby costs are determined from the server s_j and transport costs from the distance, only. With a monthly fixed income I , the number of goods c_i obtained from s_j can be calculated by

$$(\tilde{g})(c_i, s_j) = \frac{I(c_i)}{(F(s_j) + const_1 \cdot d(c_i, s_j))}$$

With these definitions the book rental Matrix G can be determined for each time unit (month) t by:

$$G(t) = \begin{pmatrix} g(c_1, s_1, t) & g(c_1, s_2, t) & \dots & g(c_1, s_n, t) \\ \dots & \dots & \dots & \dots \\ g(c_o, s_1, t) & g(c_o, s_2, t) & \dots & g(c_o, s_n, t) \end{pmatrix}$$

where t denotes the number of the respective discrete time steps in the game simulation. It is clear, that this matrix may change if the libraries and customers change their location and / or payments are changed. Since every customer tries to obtain the highest possible number of goods in order to increase its satisfaction σ , it is clear that

$$g(c_i, s_j) = \begin{cases} (\tilde{g})(c_i, s_j) \leftrightarrow (\tilde{g})(c_i, s_j) < (\tilde{g})(c_i, s_k) \quad \forall k = 1(1)o, k \neq j \\ 0 \quad \text{else} \end{cases}$$

In case equal $(\tilde{g})(c_i, s_j)$ exist, one being different from zero is randomly chosen.

Remarks:

1. In $G(t)$ each line (row) represent one customer each column one library
2. After each time step (month) t , the customer satisfaction $\sigma(c_i)$ can therefore be calculated by

$$\sigma(c_i, t) = \frac{\sum_{j=1}^o g(c_i, s_j, t)}{N(c_i)}$$

i.e. a $G(c_i)$ can be defined by

$$G(c_i) = \sum_{j=1}^o g(c_i, s_j, t)$$

3. The budget of c_i after t can be calculated by

$$B(c_i, t) = B(c_i, (t-1)) - \sum_{j=1}^o [g(c_i, s_j, t)(F(s_j) + const_1 \cdot d(c_i, s_j))] + I(c_i)$$

4. The budget of any library s_j can be determined by

$$B(s_j, t) = B(s_j, (t-1)) - \sum_{i=n}^o [g(c_i, s_j, t)(F(s_j))] + I(s_j)$$

The next sections describe the algorithms used by the providers and customers in detail.

III. THE LIBRARY GAME AGENT

A. Definitions to understand the agents' behavior

It is clear that service providers (libraries) $s_j \in P$ as well as customers $c_i \in P$ are autonomous agents, i.e. isolated units which can act on their own. In later sections we will mostly consider the 2 cases, where service providers may change their location and / or service's fee while most other parameters are fixed so far. However in all cases we intend to make the agents able to learn by one and the same algorithm which will be described in that section in detail. Therefore, of course, some more definitions are needed. Most of them concern values to describe the inner behaviour of an agent and its interaction with its environment.

1. The Event e

An event is a tuple $e = \{z_A, a, z_E, r\}$ where z_A describes the state of the environment the agent may see before it is doing any activity, while z_E is the state the agent sees after completing this activity. Both, z_A and z_E must be from the set of states Z of the considered system. The activities of an agent may be selected from a set of elementary activities $a \in A$, which must be defined and fixed for each agent. Finally, after the execution of an activity, the agent obtains a reward $r \in \mathfrak{R}$.

2. The event tape E

All events executed by an agent (or at least a bigger number of τ of such events) are kept on the so called event tape of this agent and may be recalled for any analysis or knowledge extraction. Since we consider always one agent at the moment, we do not add the agent's name to the identifier of the event tape and just call it E . Furthermore we write for simplification instead of $Z_a(e_i)$ mostly $Z_{a,i}$. In such a manner the event tape is an ordered set given by $E = \{e_i \mid e_i = (z_{a,i}, a_i, z_E, i, r_i) \wedge z_{a,i+1} = z_{e,i} \forall i = 1(1)(|E|-1)\}$.

Note that $|E|$ denotes the actual length of the event tape.

 3. The Intelligence q of an agent

Each agent is able to compose several elementary instructions to a sequence of instructions under a name. This ability is something like an abstraction process and naturally the length of sequences learnt will increase with time and experience of the player. To consider this ability of an agent the intelligence q is introduced to be the maximum length of any instruction sequence the agent may store. I.e., the actual intelligence will be denoted by $q = 1(1)q_{\max}$, where q_{\max} is a constant for the maximal reachable intelligence.

 4. The Instruction Memory M

The instruction sequences which an agent may build in the abstraction process depending on its current intelligence will be kept in a special instruction set memory M . In such a manner $M = \{m_1, m_2, \dots, m_c\}$; where c is the maximum number of instruction set to be kept and each instruction $m \in M$ consists of course of a set of events, i.e. $m_i = \{e_1, e_2, \dots, e_k\} \forall i = 1(1)c$. Since the instruction sequences are extracted in an abstraction process from the contents of the event tape E it is clear that $z_A(e_{j+1}) = z_E(e_j)$ and $k \leq q$. Furthermore, $\forall m_i \in M : m_i \subseteq E$ and finally $|m_i| = k$ is called length of instruction sequence, which must be $\leq q$.

 5. Distancefunction d

In several stages of our library game and other game setups it will be necessary to compare two states z_i and z_j . Not in every case every component of a state is absolutely equal to the other one. That is why a distance function $d(z_i, z_j)$ is introduced and used to determine if two states are similar (almost equal) or not. If $d(z_i, z_j) < \varepsilon$, then z_i and z_j are called similar or equivalent and we write $z_i \sim z_j$.

 6. Curiosity p

Every learning process requires that the agent is able to explore its environment, i.e. have a random component allowing him to do new, so far undetermined steps in its behavior. The curiosity p of an agent is the probability describing how often the agent does not follow any known instruction sequence but has fully random behaviour for a given amount of steps.

 7. Reward of an instruction sequence R_Σ

The goal of each agent is of course to get a maximum profit or satisfaction from his activities. So after every activity an agent may obtain a reward $r \in \mathfrak{R}$ from the environment, which can be used to evaluate the success of an activity or instruction set. While the reward of each activity is a simple value, the reward of any sequence of activities is given by the sum of the rewards obtained in each step:

$$R_\Sigma(e_a, e_b) = \sum_{i=a}^b r_i(e_i), a < b, \{e_a \dots e_b\} \subset E$$

Shorter we can also write for any $m_i \in M$:

$$R_\Sigma(m_i) = \sum_{i=1}^{|m_i|} r_i(e_i) \forall e_i \in m_i$$

 8. LRU (Last recently used memory) L

Last but not least we need an intermediate memory for the extraction of information from the event tape E . Mostly it is important, to process parts of E , which are similar / equal to the last processed sequence of events and activities. This is the content of the LRU memory L : $L = \{l_{last}, l_1, l_2, \dots, l_k\}$ at discrete time point $t = t_{last}$, i.e. l_{last} is the last executed sequence while higher indices of l_i denote sequences which have been executed in the farer past.

- Let seq_length be the length of the considered (last) instruction sequence on E , given as a fixed value for the moment.
- Then l_{last} is determined by $l_{last} = (e_{t-seq_length}, \dots, e_t)$ with $e_j \in E$
- The other elements of L are given by $l_i \in L \leftrightarrow z_A(e_j(l_{last})) \sim z_A(e_{j-x_i}(l_i))$
 $\forall i = 1(1)k \wedge l_i \subset E$
 Of course, j runs from $j = 1(1)seq_length$. In this process either the whole event tape or only a part of it (a finite history) maybe considered. If we require that
 – $x_i < t$ we obtain an infinite horizon while
 – $x_i < const$ results in a finite case with a finite event horizon of the agent.

 B. The agents' algorithm

This section presents the agents' algorithm which is executed by the agents in an infinite loop. Beside writing down all events and the observation of the environment on a tape an agent must meet a decision in each situation. For the implementation we intended to implement a behaviour similar

to the human one. Due to its event tape the agent may remember former situations and may decide whether his behaviour in such states was successful or not. In case a state is reached again and a successful activity sequence is known, the agent repeats it in the hope of another positive reward from doing so. If no successful activity is known, the agent can only try any random, elementary activities. The same the agent shall do in any state from time to time in order to be able to optimize its behaviour or to investigate any new appearing possibilities to obtain a higher reward than so far.

In detail, the agent has to execute the following algorithm.

```

init Z = Z0 // initial state
init E = {}
init M = {} // init empty event tape and memory
init L = {} // empty last instruction memory
init q = 1 // reactive behaviour at start

for (;;)
{
    if (p) // random behaviour
    {
        for i = 1(1)q
        {
            random (a)
            make e = (z, a, zE, r)
            z = zE
            write (E, e)
            //seq_length = q
        }
    }
    else if (∃m ∈ M : za(e1(m)) ~ z)
    {
        // Point with known successful
        // instructionset at first search in M
        for i = 1(1)|m1 // execute that
        {
            make (ei(mi))
            z := ze(ei(mi))
            write (E, ei)
            //seq_length = |m1|
        }
    }
    else
    {
        t = compose_seq_with_biggest_reward (E, z)
        //compose a sequence by choosing a event
        //sequence from tape E which maximizes the
        //reward!
        if (!isEmpty(t))
        {
            for i = 1(1)|t|
            {
                make (ei(ti))
                z := ze(ei(ti))
                write (E, ei)
            }
        }
        else // unknown position or no successful
        {
            // sequence known here
            random (a)
            make e = (z, a, ze, r)
            z := ze
            write (E, e)
            seq_length := 0
        }
    }
    evaluate (E, M, seq_length)
    // process results from last step
}

```

Beside reacting to each situation in an optimal manner the agent also has to evaluate and adapt his activities for any

situation and to learn the best behaviour. This is done within the function *evaluate()* after each executed step as described in the next subsection.

C. The evaluation procedure

The evaluation procedure considers the success of the last executed activity sequence written to the event tape. In order to ensure the success of an instruction sequence, it must be found several times (minimal MIN_i times) on the event tape and during each application should have shown a suitable reward behaviour. Depending on the reward obtained and the state of the instruction memory, the following reactions may be reasonable.

- while the instruction memory still has empty positions, any successful instruction sequence with a reward > 0 can be kept
- if the memory is full, an instruction sequence can be replaced, if the current sequence guarantees a better reward for the same initial state or guarantees a globally higher reward for any other maybe so far unknown initial state.
- if the memory is full and no optimizations can be found for a long time (T_{MAX}) it is assumed that improvements can be found only with higher expenditure, i.e. longer instruction sequences which are only possible with a higher intelligence of the individuum. Therefore in this case the intelligence q must be increased by 1.

The above described behaviour is achieved by the function *evaluate()*:

```

function evaluate (E,M, seq_length) {
    build (L) // build LRU mem
    if |L| < MINi break // no activity, if sequence not
    // MINi t times on event tape

    ∀ lj ∈ L count RΣ (lj) = ∑i=1|lj| ri(ei(lj))

    set  $\bar{R}_\Sigma = \frac{\sum_{j=1}^{|L|} R_\Sigma (l_j)}{|L|}$ 
    //average instruction set reward

    if NOTFULL (M) ^ (Rz(llast)>0) ^ llast ∉ M
    //no activity with same za
    {
        add (M; llast)
        T = 0
    } // fill instruction memory

    if FULL (M) ^ ∀ i :  $\bar{R}_\Sigma \gg R(m_i)$ , (mi ∈ M)
    {
        MIN_R_replace(M, llast)
        T = 0
    } // replace globally sequences
    // with much less known reward
}

```

```

if FULL (M) ^  $\exists m_i \leftrightarrow z_a(m_i) \sim z_{A(l_{last})}(R(m_i) < \bar{R}_\Sigma)$ 
{
  replace (M, mi, llast)
  T = 0
} // replace a worse sequence in known situation
if T > TMAX // if no change for
// a long time, increase intelligence
{
  T := 0
  q := q + 1
}

```

IV. IMPLEMENTATION

The LibraryGame is implemented in Java using the P2PNetSim framework. P2PNetSim is a highly scalable simulation tool that makes it possible to implement large p2p network simulations and many other kinds of simulations within large groups of individuals even based on social interaction.

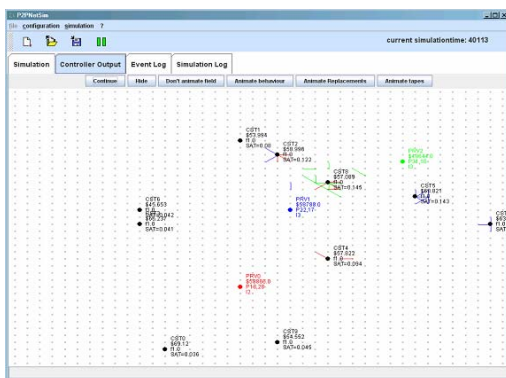


Figure 1: The LibGame in the P2PNetSim Environment

Customers and Providers within this context are modelled as interacting peers communicating via messages with each other. At each simulation time step they can perform actions like requesting services (customers), serve requests and change their positions (providers). $T=50$ time steps form a simulation cycle. Within one cycle the positions of all providers remain constant. After one cycle is over, the customers receive new payments and the providers initiate an evaluation- and migration procedure before the next cycle begins as described in the previous sections.

Some additional parameters have to be considered for the implementation of the LibraryGame simulation:

- **Tapesize**
The sections above implied a potential infinite tape size. For the simulation set-up the tape is implemented as FIFO-memory with a fixed size of 1.000.000. To simulate an 'infinite' band this value is high enough, but it strongly depends on the given field-size on which the game is played.
- **FieldSize**
This is the dimension of the field on which the library game is played. For the example simulation it is set to 20x20.
- **Memorysize**
The maximum number of sequences which can be

stored in a provider's memory. Like tapesize, the optimal value for memorysize finally depends on other simulation parameters.

- **intelligenceIncreaseThreshold**
This variable gives the number of cycles, a provider's memory needs to be unchanged before its intelligence is increased. This value is set to 100.
- **initialCuriosity**
 $0 < \text{initialCuriosity} < 1$: This value gives the propability that a providers chooses a random sequence instead of choosing an existing sequence from tape or from memory. Several simulation-runs showed that this value has to be relatively high (>0.7) to enable the providers to find acceptable sequences. However, if a certain number of sequences was found, such a high value tends to destroy those sequences. In this simulation we used a value of 0.80.
- **processesPerCycle**
This variable defines the number of simulation steps a provider remains at a certain position to serve the customers' requests before it migrates to a new position. This value is fixed to 50. A cycle can be understood as somewhat like a month in real-life situation.
- **defaultServicePrice** ($F(c_i)$)
The fee a provider gets every time a customer consumes a service. This is fixed to 3.0 for all services of all providers.
- **transportCostsPerUnit**
When a customer consumes a services from a provider, the provider has to pay transport costs in addition to the service itself. To calculate this transport costs the Euclidian distance between the customer and provider is multiplied by the transportCostsPerUnit. For each cycle the customer then chooses the provider with the chapeast transport costs. For the simulation discussed here, the transportCostsPerUnit is constantly fixed to 2.0.
- **customerPayment**
After each cycle, the customers gets a 'monthly payment' of $\text{customerPayment} = 2.0$

A. Customer's Setup

The customers get randomly chosen positions which stay constant during the simulation and a request frequency $0 < f \leq 1$. A request frequency of 1 means, that the customer performs a request at every simulation timestep of a cycle.

The customers commonly have different, power-law distributed request frequencies given by:

$$f_i = \begin{cases} \frac{i \cdot \ln \varepsilon}{e^{n-1}} & \forall 1 < i < n \\ 1 & \text{if } n=1 \end{cases}$$

where n is the number of customers and ε is the lowest request frequency for customer $n-1$. To simplify simulation analysis, ε is set to 1, meaning that all customers have a request frequency of 1.

Within a cycle that consists of $T=50$ simulation time steps, a provider with a request-frequency of f_i can perform at most $50f_i$ requests. Usually there will be less requests, because a provider may be too far away and especially in the end of a cycle a customer may have ran out of money. The customer then has to wait for the next cycle, in which he gets his 'monthly payment'.

This results in a decreasing satisfaction value for this customer. A customer's satisfaction for a certain cycle is defined as

$$sat_{Customer_i} = \frac{\text{requests_performed_within_one_cycle}}{\text{simulationsteps_per_cycle} * f_i} ; 0 \leq sat_{customer_i} \leq 1$$

The over-all satisfaction then is the average satisfaction over all cycles. The satisfaction of a provider is directly dependant on its balance.

B. Provider's Setup

Following the LibraryGame definition the providers actually have to pay for migration-activities. But in first instance we are interested in the paths, a provider takes through the LibraryGame map. So providers don't get a payment at all, and they don't have to pay for position changes. Therefore, the satisfaction of a provider can directly be measured by observing its balance.

C. Simulation Results

Figure 2 shows some screenshots of a simulation run with the above discussed setup. One provider (red dot) offers a service to three customers (black dots). The red lines represent the sequences stored in memory. In a first phase (figure a to b) the sequences in memory are concentrated around the customers. The intelligence is not big enough yet, to model paths that are long enough to lead from one customer's position to another while preserving a big reward.

This situation starts changing at $T_{cycle} = 80.000$. The first paths occur which lead from one attractive area to another (figure 1c, from Customer1 to Customer0) Even though this paths could disappear by being replaced by other, more attractive paths, sooner or later they will be re-established and strengthened due to the growing intelligence. (see fig. 2e, 2f). The closer the positions of two providers are, the sooner a path between them will be generated. In this example the relation

$$d(cst0, cst1) < d(cst0, cst2) < d(cst1, cst2)$$

implies the order in which the paths between the customers most likely will be established.

After approximately 0.5 Million cycles and an intelligence of ~ 60 the memory content shows sequence combinations which finally involve all customers. It is possible to extract one path from the memory which is an optimum to serve all customers and to maximize their satisfactions.

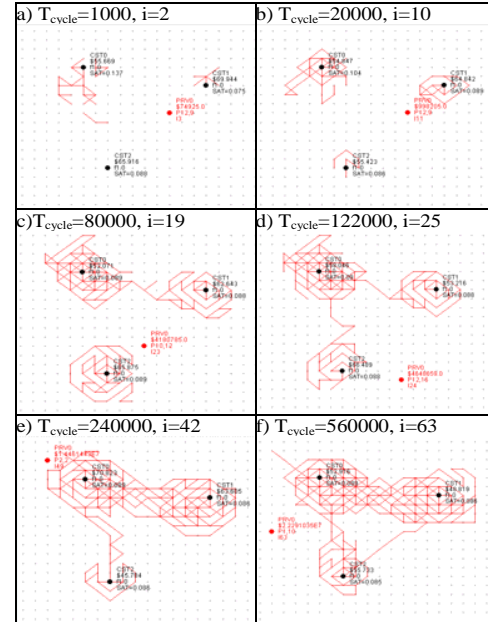


Figure 2: The LibraryGame Simulator; i: intelligence; T_{cycle} : simulation cycle – one cycle is 50 simulation steps

V. DISCUSSION & OUTLOOK

The algorithm is able to find an optimal path on which a provider could walk to maximize the satisfaction of all customers. But it still converges very slowly. To speed up the convergence, it may make sense to reduce the providers' curiosity during the game. This would reduce the effect, that sequences which actually are acceptable and could be used as subsequences for better paths just disappear. Also, the composition of random walks could be optimized. One optimisation which is already used in this simulation is to forbid duplicate path sections within the composition of a random sequence. This prevents the customer of performing too many and too tight circles around an attractive position. Another possibility would be to give a preferred direction as a tendency to the providers when composing random walks. This tendency would be changed from time to time and would enforce the provider to leave attractive positions and therefore raise the probability to enter other attractive regions.

In further researches it has to be found out, if this algorithm could be used to make more providers cooperating with each other in such a way, that the providers dynamically 'share' the customers to provide a maximum over-all-satisfaction for all of them. For this it would make sense to give a 'preferential threshold' to the customers, that make them use a certain provider for a while, even if it is not the cheapest provider anymore. This would correspond to real-life-situations, where consumers do not immediately change the provider when he raises the price. They would still prefer

this provider 'by habit' at least a while before they come to the conclusion to change. Providers then would have a chance to leave their (pseudo-) optimal position to explore the environment without having a too high risk of loosing all of their customers.

Further works will account competing providers with more differentiated pricing strategies and with a 'character'. This should enable a provider to decide to be defensive, aggressive or cooperative according to other providers.

VI. REFERENCES

- [1] Coltzau, H.: „Specification And Implementation Of A Parallel P2P Network Simulation Environment“, 2005, Diplomarbeit
- [2] n.n.: *“Logistic Network Design”*,
In: SWISSLOG, Feb. 2007
http://www.swisslog.com/wds-index/wds-consult/wds-cons-network_design.htm
- [3] Koller, D., Pfeffer A.: “Representations and Solutions for Game-Theoretic Problems” Artificial Intelligence
- [4] Milojicic, D.; Kalogeraki, V.; Lukose, R.; Nagaraja, K.; Pruyne, J.; Richard, B.; Rollins, S. and Xu, Z.: *“Peer-to-Peer Computing”*, Technical Report HPL-2002-57, HP Laboratory Paolo Alto, Mar. 2002.
- [5] Brediny, B.; Maheswaran, R.; Imer, C.; Basar, T.; Kotz, D.; Rus, D.: *“A GameTheoretic Formulation of MultiAgent Resource Allocation”* Proceedings of the Fourth International Conference on Autonomous Agents, 2000
- [6] Bredin, J.: *“Market-Based Mobile-Agent Planning: A Thesis Proposal”* 1999, <http://citeseer.ist.psu.edu/bredin99marketbased.html>
- [7] Bredin, J.; Kotz, D.; Rus, D.: *“Economic Markets as a Means of Open Mobile-Agent Systems”* 1999, <http://citeseer.ist.psu.edu>

Global Structure Constraint Model for Object Representation

Miao Liu and Dongwei Guo and Jie Ma and Yanbin Liu and Chunguang Zhou
 Collage of Computer Science and Technology, Jilin University, Changchun, China 130012
 Email: cgzhou@jlu.edu.cn

Abstract—We present a novel object representation model based on the Global Structure Constraint (GSC). In our approach, the object is described as a constellation of points which are placed at all the representative patches with small color variations. The color information and spatial relations of these patches are reserved by these points to build the color model and shape model. To demonstrate the ability of its representation, we use it together with the searching algorithm to locate target objects in images. The experimental results demonstrate that it is a simple, effective and efficient representation.

I. INTRODUCTION

Given digital images, choosing an appropriate image representation will greatly facilitate the consequently image processing methods, such as image localization, recognition and retrieval systems. There is broad agreement upon the suitability of representing objects as collections of local parts and their mutual spatial relations. Restricting the description to local parts of the image leads to higher robustness against clutter and partial occlusion than traditional global representations (for example, global appearance projected by the principal components analysis (PCA)), whereas incorporating spatial relations between parts adds significant distinctiveness to the representation. The common approach is to employ graph-based representations that deal separately with local parts (nodes of the graph) and spatial relations (arcs of the graph) [1], [2], [3], [4], [5]. The problem with this approach is the complexity of considering both local properties and spatial relations described separately in nodes and arcs, where learning and matching graph representations are known to be very expensive.

As for the contents presented by images, two clearly separated domains are the so-called "things" and "stuff" domains [6], [7], which correspond respectively to entities with discriminant geometry (object) and texture-rich materials with loose geometry (for example, natural landscapes such as forest, river, dessert, and so forth). Entities in these two domains seem to be represented in a fundamentally different way in human vision [7], suggesting the need for different models representing each of them [1].

In this paper, in the GSC model the object is represented as several landmark points which locate in the main patches with small color variations. The color information and spatial relations of these points are reserved and used to build two models, shape and color. The dimension of GSC model can be very low, such as only 26 points for the human face. To

demonstrate the ability of this model, we adopt Genetic Algorithm (GA) [8], [9] to optimize the transformation parameters for the GSC model to locate the target.

II. GLOBAL STRUCTURE CONSTRAINT MODEL

A. Sample

By digital image capture device, the real-world scenarios can be discretized to digital images with some specific resolution, which can be processed by computers. Digital images with large resolution can be compressed to low resolution. These two kinds of processes both can be considered as sampling and compressing representation procedures, which cannot ruin the understanding to the image contents by human brain as long as the result resolutions are not too low. Here, we give an analogously sampling and compressing representation of images.

B. Patches and Landmarks

The patches with small texture variations can be segmented by statistical means. However, in practice we can line out the functional areas of the target object and then mark several key points on each area to depict its main color structure.

C. Statistical Model of GSC

For a 2D image, we represent the n landmark points $\{p_1, \dots, p_n\}$ for a single example as two vectors, which are the shape vector $\mathbf{x} = (x_1, \dots, x_n, y_1, \dots, y_n)^T$ and the color vector $\mathbf{c} = (c_1, \dots, c_n)^T$. c_i is the mean or representative color value of the neighbor region of point $p_i = (x_i, y_i)$. Given the training set of s examples, we can label landmarks and generate the learning vectors \mathbf{x}_j and \mathbf{c}_j . Before analyzing statistically, we transform the shape vectors into a model coordinates in which the shapes of objects are normally considered to be independent of their original position, orientation and scale.

Suppose now we have sets of points \mathbf{x}_j which have been transformed into the model coordinate system. We can model the shape model of GSC, \mathbf{S}_{GSC} , as the mean of training set simply.

$$\mathbf{S}_{GSC} = \frac{\sum_{j=1}^s \mathbf{x}_j}{s} \quad (1)$$

However, the color model of GSC, \mathbf{C}_{GSC} , at landmarks should be modeled representatively to the target class and

independently to the imaging environment.

$$\mathbf{C}_{GSC} = \frac{\sum_{j=1}^s ((\mathbf{c}_j - \lfloor \downarrow_n \text{Min}C_j \rfloor)^T \times (\text{SpanRatio}_j \times \mathbf{I}))}{s} \quad (2)$$

where $\text{Min}C_j = \min_{i=1}^n (c_{j,i})$ and $\lfloor \downarrow_n$ concatenate copies of its operand vertically. $\text{SpanRatio}_j = \frac{\text{Sup}C}{\max_{i=1}^n (c_{j,i}) - \min_{i=1}^n (c_{j,i}) + 1}$ with $\text{Sup}C$ is the superior limit of image color value.

III. SEARCHING WITH GSC MODEL

A. GSC Model Parameters

Having GSC models, what to do is to find out the optimal transformation for fitting GSC model to the target image well. To deal with rigid transformation, function T_{stat} with parameter vector $stat = (T_x, T_y, S_x, S_y, \theta)^T$ designates the Euclidean transformation defining the position, (T_x, T_y) , the scale, (S_x, S_y) , and orientation, θ , from the model coordinate system to the image coordinate system. For in-stance, if applied to a single point (x, y) ,

$$T_{stat} \begin{pmatrix} x \\ y \end{pmatrix} = \begin{pmatrix} T_x \\ T_y \end{pmatrix} + \begin{pmatrix} S_x \cos \theta & -S_y \sin \theta \\ S_x \sin \theta & S_y \cos \theta \end{pmatrix} \begin{pmatrix} x \\ y \end{pmatrix} \quad (3)$$

B. Searching Algorithms

Many searching algorithm can be adopted. The key things about GA [8], [9], which is exploited here as searching algorithm, are described as follow.

1) *Chromosome Coding*: Chromosomes are represented by bit strings. The way to represent T_x , T_y , S_x and S_y are to use a bit string of length eight, and θ is coded as a twelve-bit string. The transformation $T_{C \rightarrow I}$ from chromosomes of bit string C to their interpretation I and the inverse transformation $T_{I \rightarrow C}$ are formulated as,

$$I = T_{C \rightarrow I}(C) = \frac{[C]_D}{2^{len} - 1} \times (I_{sup} - I_{inf}) + I_{inf} \quad (4)$$

$$C = T_{I \rightarrow C}(I) = \left[\frac{I - I_{inf}}{I_{sup} - I_{inf}} \times (2^{len} - 1) \right] \quad (5)$$

where len is the length of bit string, I_{sup} and I_{inf} are the superior and inferior limits of the interpretation, $[]_D$ and $[]_B$ mean to get the decimal and binary value.

2) *Fitness Function*: The fitness function is defined as followed.

$$fitness = \frac{1}{1 + A} \quad (6)$$

with

$$A = \sqrt{\frac{1}{n} \left(\sum_{i=1}^{n-n_{NII}} (\mathbf{M}(i) - \mathbf{C}(i))^2 \right) + k \times n_{NII}}$$

where M is the color model of GSC and C is the color information of GSC, after being transformed to the image coordinates with transformation parameters using (3), in target image. There are also some processes for C before computing $fitness$ with (6), such as the color information must be

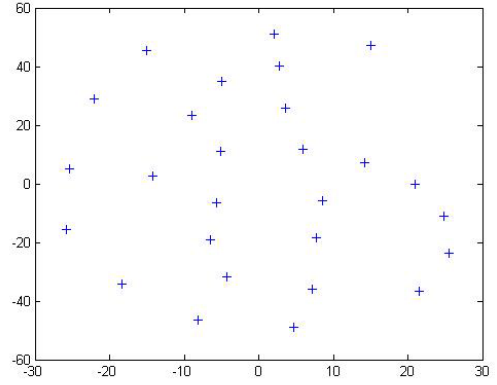


Fig. 1. 27 Landmark points of GSC shape model for number '6' in the model coordinates

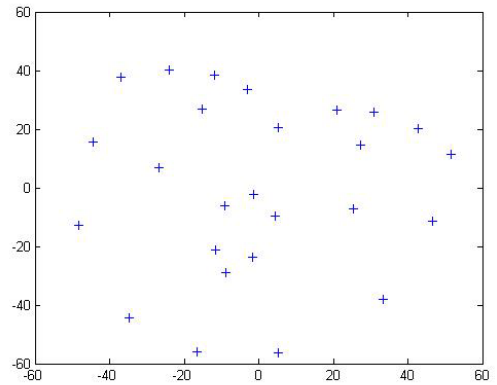


Fig. 2. 26 Landmark points of GSC shape model for human face in the model coordinates

uniformed to the range of M . n is the total number of the landmarks of GSC model and n_{NII} is the number of GSC landmarks not in the target image after transformation. k is a constant.

IV. EXPERIMENTAL RESULTS

First we take a simple digits test on number 6 and 9 because these two numbers are the same if the rotation is not considered. Fig. 1 is the shape of GSC model for the digit, number 6. Table I are results of the 10th, 20th, 30th and 40th iterations, the numbers under each image is the transformation parameters. Table II lists the final results for different kinds of '6' and '9'. Results describe that GSC can find out the proper parameters under the variation of scale and rotation.

To obtain a quantitative evaluation of the performance of the representation we trained GSC for human face on 20 hand labeled face images, from FERET database [10] in which the resolution of image is 256×384 , and tested it on a different set of 100 labeled images with the population size 50 and iteration times 100. The shape model of GSC for human face is shown in Fig. 2. In Table III, the first two rows D_x and D_y means the average differences between the searching results S

TABLE I
TEST RESULTS ON NUMBER '6'

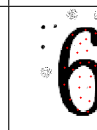
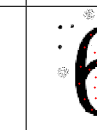
	iterations=10	iterations=20	iterations=30	iterations=40
Image				
T_x	116.813	120.268	105.065	104.374
T_y	131.435	138.496	133.452	134.461
S_x	1.375	1.506	1.686	1.686
S_y	1.421	1.504	1.594	1.649
θ	-0.963	-0.932	-1.570	-1.509

TABLE II
TEST RESULTS ON DIFFERENT KINDS OF NUMBER '6' AND '9'

Image				
T_x	150.156	139.504	165.529	220.103
T_y	140.556	96.081	169.255	191.547
S_x	1.756	1.657	1.787	1.750
S_y	3.258	1.654	1.524	3.256
θ	1.923	-2.982	-0.740	1.958

and the labeled landmarks L on x and y axis respectively. The third row gives the result *fitness* values. The columns mean, minimum and maximum means the statistical results for the set of the 100 images. In these 100 test images, the algorithm can find the proper displacement status for 89 images and the result is not satisfied for the other 11 images yet. Table IV shows some result images after 25, 50 and 75 iterations respectively.

V. DISCUSSION AND CONCLUSION

We have demonstrated that the Global Structure Constraint model has the ability to represent target objects. The advantages of this kind representation are as followed. And it has several advantages such as that the representation is simple, the computational resumption is decreased and can deal with translation, scale and rotation intrinsically without other strategies, such as multi-resolution and model rotation operations. Besides, GSC model has other assistant functions.

TABLE III
THE STATISTICAL RESULTS ON THE SET OF 100 LABELED IMAGES

Unit: Pixels	mean	minimum	maximum
$D_x = \frac{1}{n} \sum_{i=1}^n S_{i,x} - I_{i,x} $	7.518	1.956	35.986
$D_y = \frac{1}{n} \sum_{i=1}^n S_{i,y} - I_{i,y} $	15.313	2.594	92.668
<i>fitness</i>	0.0182	0.0009	0.0574

TABLE IV
SOME TEST RESULT IMAGES OF HUMAN FACE

Iter. 25	Iter. 50	Iter. 75
 (136.240, 214.963, 1.208, 1.378, -2.844)	 (136.240, 226.338, 1.227, 1.617, -2.910)	 (133.480, 216.385, 1.347, 1.336, -2.898)
 (122.440, 131.066, 1.326, 1.435, 3.243)	 (125.200, 133.910, 1.326, 1.580, 3.312)	 (138.188, 184.894, 1.211, 1.035, 3.467)

However, the GSC model has its disadvantages which we are attempting to overcome.

ACKNOWLEDGMENT

The authors would like to thank the support from the National Natural Science Foundation of China under Grant No. 60433020, 60673099 and 60773095.

REFERENCES

- [1] Jaume Amores, Nicu Sebe and Petia Radeva: *Context-Based Object-Class Recognition and Retrieval by Generalized Correlograms*. IEEE Trans. Pattern Analysis and Machine Intelligence, vol. 29, no. 10, pp. 1818-1832 (2007)
- [2] D. Crandall, P. Felzenszwalb, and D. Huttenlocher: *Spatial Priors for Part-Based Recognition Using Statistical Models*. Proc. IEEE International Conference on Computer Vision and Pattern Recognition, vol. 1, pp. 10-17 (2005)
- [3] P. Hong and T.S. Huang: *Spatial Pattern Discovery by Learning a Probabilistic Parametric Model from Multiple Attributed Relational Graphs*. Journal of Discrete Applied Math, vol. 139, nos. 1-3, pp. 113-135 (2003)
- [4] R. Fergus, P. Perona, and A. Zisserman: *Object Class Recognition by Unsupervised Scale-Invariant Learning*. Proceedings of IEEE International Conference on Computer Vision and Pattern Recognition, vol. 2, pp. 264-271 (2003)
- [5] M. Weber, M. Welling, and P. Perona: *Towards Automatic Discovery of Object Categories*. Proceedings of IEEE International Conference on Computer Vision and Pattern Recognition, pp. 101-108 (2000)
- [6] C. Carson, S. Belongie, H. Greenspan, and J. Malik: *Blobworld: Image Segmentation Using Expectation-Maximization and Its Application to Image Querying*. IEEE Transaction on Pattern Analysis and Machine Intelligence, vol. 24, no. 8, pp. 1026-1038 (2002)
- [7] A. Pentland, R.W. Picard, and S. Sclaroff: *Photobook - Content-Based Manipulation of Image Databases*. International Journal on Computer Vision, vol. 18, no. 3, pp. 233-254 (1996)
- [8] Tom M. Mitchell: *Machine Learning*. McGraw-Hill Education (Asia) Co. and China Machine Press (2003)

- [9] Dongwei Guo, Chunguang Zhou and Dayou Liu: *A Niching Genetic Algorithm Based on Clustering and Resource Competition*. Journal of Computer Research and Development, vol. 40, pp. 1424-1430 (2003)
- [10] P.J. Phillips, H. Wechsler, J. Huang, and P. Rauss: *The FERET database and evaluation procedure for face recognition algorithms*. Image and Vision Computing Journal, Vol. 16, No. 5, pp. 295-306 (1998)



Miao Liu received the MSc degree in Computer Science in 2003 from Jilin University, China. Now she is a PhD candidate and her research interests include biometrics and image processing.



Dongwei Guo received his PhD degree from Jilin University in 2002. Now he is an associate professor in the College of Computer Science and Technology, Jilin University. His research interests include computational intelligence and networking security.



Jie Ma is a PhD candidate in the College of Computer Science and Technology, Jilin University. His research interests include pattern recognition and image processing.



Yanbin Liu is a PhD candidate of Artificial Intelligence. He has published several papers. The current research regions include multi-agent system and optimization algorithm.



Chunguang Zhou is a professor in the College of Computer Science and Technology, Jilin University. His research interests include the computational intelligence theory and its application in image processing, business intelligence, bioinformatic, biometrics, machine olfaction and gustation. He has published more than 100 papers in the areas of his interests.



ALPEN-ADRIA
UNIVERSITÄT
KLAGENFURT



SECOND INTERNATIONAL WORKSHOP ON NONLINEAR DYNAMICS AND SYNCHRONIZATION

INDS'09

JULY, 2009 (KLAGENFURT, AUSTRIA)

The Second International Workshop on Nonlinear Dynamics and Synchronization (INDS'09) is a two-day international workshop bringing together international researchers, developers and practitioners from different horizons to discuss the latest advances in nonlinear dynamics and synchronization. INDS'09 will serve as a forum to present current and future works as well as to exchange research ideas pertaining to various aspects in this field of nonlinear dynamic systems and synchronization. INDS'09 will feature contributed as well as invited papers and will include poster and demo sessions.

The major focus of this inter-disciplinary workshop lies on the following areas:

- Theoretical fundamentals of synchronization**
- Nonlinear systems and synchronization**
- Experiments of nonlinear dynamics and synchronization**
- Simulation of nonlinear dynamics and synchronization**
- Applications of nonlinear dynamics and synchronization:**
 - Self-organized traffic management systems
 - Self-organized intelligent supply chains and logistics systems
 - Cybernetics
 - Systems control
 - Robotics
 - Cooperative advanced driver assistance systems
 - Pattern recognition
 - Computational intelligence models (soft computing and machine learning)
 - Cellular neural networks and applications
 - Image processing (incl. scene analysis)
 - Signal processing (incl. speech processing and recognition)
 - Self-reconfigurable systems
 - Self-healing systems
 - Self-testing systems
 - Coupled oscillatory systems
 - Bio-computing, Neuro-computing, Biology, Bio-chemistry
 - Chaos control
 - Communication (wired and wireless), networking and sensor networks
 - Cryptography and security
 - Social sciences, psychology, business and management

We look forward to meeting you again in Klagenfurt to INDS'09.